LOCKHEED MARTIN ENERGY RESEARCH LIBRARIES
3 4456 0515540 8

DOCUMENT COLLECTION

1

ORNL-4401
UC-20 – Controlled Thermonuclear Processes

THERMONUCLEAR DIVISION
ANNUAL PROGRESS REPORT
FOR PERIOD ENDING DECEMBER 31, 1968

OAK RIDGE NATIONAL LABORATORY
CENTRAL RESEARCH LIBRARY
DOCUMENT COLLECTION
LIBRARY LOAN COPY
DO NOT TRANSFER TO ANOTHER PERSON
If you wish someone else to see this document, send in name with document and the library will arrange a loan.
UCN-7969
(3 3-67)

OAK RIDGE NATIONAL LABORATORY
operated by
UNION CARBIDE CORPORATION
for the
U.S. ATOMIC ENERGY COMMISSION

Printed in the United States of America. Available from Clearinghouse for Federal Scientific and Technical Information, National Bureau of Standards, U.S. Department of Commerce, Springfield, Virginia 22151
Price: Printed Copy $3.00; Microfiche $0.65

LEGAL NOTICE

This report was prepared as an account of Government sponsored work. Neither the United States, nor the Commission, nor any person acting on behalf of the Commission:

A. Makes any warranty or representation, expressed or implied, with respect to the accuracy, completeness, or usefulness of the information contained in this report, or that the use of any information, apparatus, method, or process disclosed in this report may not infringe privately owned rights; or

B. Assumes any liabilities with respect to the use of, or for damages resulting from the use of any information, apparatus, method, or process disclosed in this report.

As used in the above, "person acting on behalf of the Commission" includes any employee or contractor of the Commission, or employee of such contractor, to the extent that such employee or contractor of the Commission, or employee of such contractor prepares, disseminates, or provides access to, any information pursuant to his employment or contract with the Commission, or his employment with such contractor.

LOCKHEED MARTIN ENERGY RESEARCH LIBRARIES

3 4456 0515540 8

ORNL-4401

Contract No. W-7405-eng-26

THERMONUCLEAR DIVISION
ANNUAL PROGRESS REPORT
for Period Ending December 31, 1968

JUNE 1969

OAK RIDGE NATIONAL LABORATORY
Oak Ridge, Tennessee
operated by
UNION CARBIDE CORPORATION
for the
U. S. ATOMIC ENERGY COMMISSION

Reports previously issued in this series are as follows:

ORNL-2693	Period Ending January 30, 1959
ORNL-2802	Period Ending July 31, 1959
ORNL-2926	Period Ending January 31, 1960
ORNL-3011	Period Ending July 31, 1960
ORNL-3104	Period Ending January 31, 1961
ORNL-3239	Period Ending October 31, 1961
ORNL-3315	Period Ending April 30, 1962
ORNL-3392	Period Ending October 31, 1962
ORNL-3472	Period Ending April 30, 1963
ORNL-3564	Period Ending October 31, 1963
ORNL-3652	Period Ending April 30, 1964
ORNL-3760	Period Ending October 31, 1964
ORNL-3836	Period Ending April 30, 1965
ORNL-3908	Period Ending October 31, 1965
ORNL-3989	Period Ending April 30, 1966
ORNL-4063	Period Ending October 31, 1966
ORNL-4150	Period Ending April 30, 1967
ORNL-4238	Period Ending October 31, 1967

Contents

INTRODUCTION

ABSTRACTS

1. PLASMA THEORY AND COMPUTATION 1

1.1 Synopsis 1

1.2 Abstracts of Material Available as Preprints 2
1.2.1 Resonant Loss-Cone Instabilities 2
1.2.2 Resonant Loss-Cone Instabilities in Mirror-Confined Plasmas 2
1.2.3 Warm-Plasma Stabilization of Resonant Loss-Cone Instabilities 3
1.2.4 Propagation of Ion Acoustic Waves in a Magnetic Field 3
1.2.5 A Stochastic Model of Electron Cyclotron Heating 3

1.3 Brief Reports of Work in Progress 4
1.3.1 Brillouin Diagram Solutions of Real Dispersion Relations 4
1.3.2 Growth Rates of Flutelike Loss-Cone Modes 5
1.3.3 Flutelike Gyroharmonic Instabilities in Multicomponent Plasmas 8
1.3.4 Explosive Instabilities 10
1.3.5 Loss-Cone Modes in Finite-Length Plasmas 12
1.3.6 Microinstabilities in Hot Electron Plasmas 13
1.3.7 Unstable Waves in Beam-Plasma Systems 14

1.4 New Projects 18
1.4.1 Numerical Simulation of Plasma 18
1.4.2 Diamagnetic Equilibria of Hot-Electron Plasma in a Simple Mirror 22

2. TARGET PLASMAS 25

2.1 Introduction 25

2.2 INTEREM 26
2.2.1 Introduction 26
2.2.2 Description of Facility 27
2.2.3 Diagnostics 29
2.2.4 Results 32
2.2.5 Instability Studies 36
2.2.6 Discussion 39

2.3 IMP (Injection into Microwave Plasma) 40

2.4 Electron Trapping in Mirrors by Electron-Cyclotron Heating 41
2.4.1 Introduction 41
2.4.2 Experiment 42
2.4.3 Results 42
2.4.4 Discussion 43

3. INJECTION AND ACCUMULATION: NEUTRAL INJECTION EXPERIMENTS (DCX-1.5) 45

3.1 Introduction 45
3.2 Apparatus 45

3.3 Experimental Observations 47
3.3.1 Gross Effects 48
3.3.2 Betatron Frequencies 49

3.4 Comparisons 51

4. INJECTION AND ACCUMULATION: MULTIPLE-PASS EXPERIMENTS (DCX-2) 52

4.1 Introduction 52

4.2 Instabilities in the DCX-2 52
4.2.1 The Modified Negative Mass Instability 53
4.2.2 Observations of Modified Negative Mass Instability 55

4.3 Microinstability-Coupled Drift Waves 58

4.4 Effect of the Modified Negative Mass Instability on the DCX-2 Plasma 62
4.4.1 Effect of the Modified Negative Mass Instability on the Injected Plasma 65
4.4.2 Effect of the Modified Negative Mass Instability on the Background Cold Plasma 67
4.4.3 Model of the Central-Peak Proton Group Behavior 69

4.5 Turbulent Heating Experiments in DCX-2 74
4.5.1 Experimental Configuration and Diagnostics 75
4.5.2 Results of the Initial Experiments 76

5. ELECTRON-CYCLOTRON HEATING 79

5.1 High-Beta Plasmas 79
5.1.1 Introduction 79
5.1.2 High-Power 5.5-mm Microwave Technology 80
5.1.3 Diamagnetic Measurements of 30%-Beta Plasma 87
5.1.4 Instability-Accelerated Particles 91
5.1.5 Off-Resonance Heating 93
5.1.6 Specific Electrodissociation Neutron Production 94

5.2 Scattering and Energy Loss Rates in Hot-Electron Plasmas 96

6. TURBULENT HEATING 98

6.1 Burnout V 98
6.1.1 Introduction 98
6.1.2 Plasma Radial Profile 99
6.1.3 Spectroscopic Diagnostics 99
6.1.4 Energy Fluctuations 101
6.1.5 Effect of Helium Impurity 102
6.1.6 Doppler Broadened Neutral Emission 102
6.1.7 Magnetic Field Strength Effects and Heating Efficiency 104
6.1.8 High-Frequency Correlation Studies and RF Effects 105
6.1.9 Plasma Losses Induced by Turbulent Heating 107

6.2 Turbulent Heating of Electrons 108
6.2.1 Introduction 108

6.2.2 The Experimental Dispersion Relation 108
6.2.3 Experimental Strong Turbulent Heating 111
6.2.4 A Simple Gigacycle Correlator 111

6.3 Reducing Molecular Hydrogen in Plasma Devices 112

7. PLASMA PHYSICS 113

7.1 Ion Acoustic Waves 113
7.1.1 Introduction 113
7.1.2 Landau Damping of Electrostatic Ion Waves in a Uniform Magnetic Field 113
7.1.3 Simultaneous Measurements of Ion Acoustic Wave Potential and Plasma Density Perturbation to Yield γ_e 115
7.1.4 Dispersion of Ion Acoustic Waves 116
7.1.5 A More Sensitive Technique for Observing Ion Acoustic Wave Dispersion Near ω_{pi} 116
7.1.6 Wave Focusing to Produce Nonlinear Behavior 117
7.1.7 A Calculation of $\lambda_{\text{ion acoustic wave}}/\lambda_{\text{Debye}}$ as a Function of T_e/T_i for Propagation at Frequencies Near ω_{pi} 118
7.1.8 Wave and Wavelike Phenomena Predicted by the Linearized Wave Theory Near ω_{pi} 119

7.2 Electrostatic Ion Cyclotron Waves 120
7.2.1 Introduction 120
7.2.2 Dispersion Relation of Electrostatic Ion Waves in a Magnetic Field 121

7.3 Pseudowaves 124
7.3.1 Introduction 124
7.3.2 Experimental Investigations of Pseudowaves 124
7.3.3 Computer Simulation Studies of Ion Burst Excitation 128

7.4 Plasma Sheaths 130
7.4.1 Introduction 130
7.4.2 A Transient Sheath – Discovered by Ion Acoustic Waves 130
7.4.3 Experimental Langmuir Sheath Study 131
7.4.4 Computer Simulation Studies of a Plasma Sheath Evolution 134

7.5 Plasma Generation Techniques 135
7.5.1 Introduction 135
7.5.2 Generating a Quiescent Plasma in a Magnetic Field 136
7.5.3 Resonant Microwave Plasma Generation in an Iron-Core Min-B System 137

7.6 Diagnostics 137
7.6.1 Introduction 137
7.6.2 A Simple Technique for Measuring $T_{e\parallel}$ in a Magnetic Field 137

7.7 Far-Infrared Laser-Interferometer for Electron Density Measurement 138
7.7.1 Introduction 138
7.7.2 CH_3CN Laser 138
7.7.3 Michelson Interferometer 140
7.7.4 Conclusions 141

7.8 Plasma Stabilization 141
7.8.1 Introduction 141
7.8.2 Experiments 141
7.8.3 Discussion 143
7.8.4 Theory 143

8. TOROIDAL MULTIPOLES 145
8.1 Introduction 145
8.2 Quadrupole Experiments with a Microwave-Generated Plasma 146
8.2.1 Comparison of Dipole and Quadrupole Magnetic Configurations 146
8.2.2 Comparison of First and Second Model Quadrupole Cavities 146
8.2.3 Electron Temperature Determination in the $\lambda = 3$ cm, 200-W Microwave Plasma 147
8.2.4 Change in Heating Zone 149
8.2.5 Obstacle Experiments in the Microwave-Generated Plasma 149
8.2.6 Effects of Introducing Supports 150
8.2.7 Nature of the Decay of the 3-cm Microwave Plasma 152
8.2.8 Effect of Azimuthal Electric Field on Microwave-Generated Plasma 153
8.3 Preliminary Observations on Combined Operation of the Hydrated Titanium Washer Gun and Microwave Heating 155
8.4 Improvement in the Magnetic Field Strength 157
8.5 Helical Hexapole 158

9. ATOMIC AND MOLECULAR CROSS SECTIONS 160
9.1 High Excited Rydberg States of H_2 160
9.2 Further Studies of Excitation Heating of Ions 164
9.3 Cross Section of Hydrogen Particles in Magnesium Vapor 164
9.4 Electrodisintegration of the Deuteron 165
9.5 Photoionization of Krypton Between 300 and 1500 eV. Relative Subshell Cross Sections and Angular Distributions of Photoelectrons 166
9.6 Production of Hydrogen Atoms 166
9.7 Hydrogen Atom Energy Analyzer 167
9.8 Evaluation of a Magnetic Shield of Four Nested Cylinders 168
9.9 Detector Evaluation 170
9.9.1 Johnston Multiplier 170
9.9.2 Channel Electron Multiplier 171
9.9.3 Funnel Channel Multiplier 171
9.9.4 Detector Evaluation Summary 174
9.10 Atomic and Molecular Processes Information Center 174

10. ENERGETIC-PARTICLE INJECTORS FOR PLASMA PHYSICS EXPERIMENTS 176
10.1 Introduction 176
10.2 Space-Charge Neutralization 176
10.3 Ion Source Filaments 179
10.4 5-keV H^+–10-keV H_2^+ Injector 180
10.5 Solar Wind Experiment 181
10.6 Hydrogen Clusters 181

11. MAGNETICS AND SUPERCONDUCTIVITY 182
11.1 Review of Our Basic Work on Superconductivity 182
11.2 Steady-State Stability of Composite Superconductors 184

11.3 Winding Techniques for Superconducting Magnets 186

11.4 Liquid-Helium Level Detector 193
11.4.1 Introduction 193
11.4.2 Construction Details 194
11.4.3 Principle of Operation 195
11.4.4 Experimental Results 196
11.4.5 Discussion 197

11.5 Progress on the IMP Facility 197
11.5.1 Introduction 197
11.5.2 Phase I 198
11.5.3 Conductor Selection 199
11.5.4 Structural 202

12. FUSION FEASIBILITY 203

12.1 Introduction 203

12.2 The Feasibility of Controlled Fusion 203
12.2.1 General Remarks 203
12.2.2 Some Plasma Considerations 204
12.2.3 Engineering Considerations 206
12.2.4 Conclusions 208

12.3 Neutronics Calculations and Cost Estimates for Fusion Reactor Blanket Assemblies 209

12.4 A Diffusion Process for Removing Tritium from the Blanket of a Thermonuclear Reactor 209

12.5 The Sputtering of Niobium at 1000°C by 20-keV D^+ 210

12.6 Work in Progress 212

13. DESIGN AND ENGINEERING: SERVICE REPORT 213

PUBLICATIONS, ORNL REPORTS, AND PAPERS 214

Introduction

H. Postma

The Target Plasma Program continues to progress. The construction of IMP is proceeding more slowly than previously envisioned; yet the understanding of the targets themselves gained through the INTEREM experiments has been both timely and encouraging. While the complete understanding of the stability of the target electron cyclotron plasma in INTEREM may take much time, the essential characteristics are now known, and if the scaling ($\omega_{pe}/\omega_{ce} \sim 1$) holds at higher field, IMP will indeed have a suitable target for efficient trapping and the proper medium for stabilizing through Landau damping.

To provide the suitable beams for injection, the ion source group has had striking success in creating intense low-energy ion beams. They have begun now to pursue the promising method of hydrogen atom cluster formation and acceleration – a method particularly suited for target plasma injection.

We see reported for the first time the elegant but difficult engineering that goes into the microwave power sources essential to both the target plasma and high-beta devices. The equally difficult development of cryoengineering and superconducting coil design for IMP is given in another section.

One area that the fusion feasibility studies underline as being essential to eventual fusion economics is that of high-beta plasmas. We see in ELMO an experimental example of a stable 40% beta plasma, annular in shape and with high energy densities. The beginnings of the understanding of this plasma through equilibrium calculation and plasma simulation are given in the theory section.

The mechanisms that produce hot-ion plasmas with high densities through turbulent heating are yielding both to experimental and theoretical studies. Improved diagnostics and the development of high-frequency correlators are speeding this process.

We note with satisfaction that the understanding of DCX-2 is nearly complete. More important, the theory developed is not restricted to DCX-2, but accounts for many results obtained in a variety of open-ended devices with or without magnetic wells for both high and low densities. At the same time we appreciate the understanding of finite plasma effects in DCX-1.5. We see, too, in many of the wave propagation studies the detailed coupling of theory, plasma simulation, and experiments that leads to understanding and permanence.

The work in toroidal multipoles has shown that simple ways still exist that can solve difficult levitation problems. The ominous sign through the physics experiments is that plasma lifetime in such average minimum-B wells depends not on supports but on plasma physics stability problems. There is an urgent question, too, that the physical phenomena responsible for losses occurring in this toroidal device may not be the same as for those occurring in stellarators.

We have in the reported cross-section research the studies of fundamental atomic processes coupled to the injection of beams, the evaluation and innovation of diagnostic techniques indispensable in almost all energetic-particle plasma research, and the collection of cross-section data so necessary for evaluating and interpreting results or projecting ideas.

Throughout all these areas we have the steady hand of theory, tying together turbulent heating, target plasmas, and high-beta plasmas. We see forming the important area of plasma simulation and look forward to its guidance in nonlinear regimes and in suggesting eventually which experiments will be most worthy in undertaking.

Finally, the emergence of fusion feasibility studies this year gave renewed confidence that fusion power was both a feasible engineering task and of value to society. These studies urged again the importance of high-beta plasmas and pointed out clearly the remaining engineering tasks.

It has been a vital and productive year, and, while adequate plasma confinement remains elusive, we see more rapid progress and understanding.

Abstracts

1. PLASMA THEORY AND COMPUTATION

We have examined the linear stability of a spatially uniform plasma whose distribution functions model the velocity-space properties of target plasmas. Most of the results are presented as abstracts of published reports. In brief, if electron temperatures are too low, one loses the important stabilizing influence of Landau damping. If the electron temperature is too high, new classes of ion-ion interaction may occur. The optimum electron temperature is roughly that of the hot ions. Regarding the two-ion-group problem, we find that stability is best achieved by raising the warm-ion temperature T_W to about 10% of the hot-ion temperature T_H. Under these conditions and for relative densities $N_W/N_H \gtrsim 0.1$, the flutelike ($k_{\parallel} = 0$) modes are linearly stable. The question of explosive nonlinear instabilities is still under consideration; nonlinear wave interactions may permit negative-energy waves to grow by providing an energy exchange mechanism through wave-wave coupling. For $T_W/T_H \lesssim 0.05$, rapidly growing flutelike modes may occur when $N_W/N_H \gtrsim 0.01$, provided the hot-ion density is large enough. The frequency and wavelength of the fastest-growing modes are related to resonance conditions between the warm-ion hybrid frequency and hot-ion cyclotron harmonics, resulting in the excitation of high-frequency, short-wavelength modes in the buildup stage of a typical target plasma experiment (in which $N_W/N_H \gg 1$). These instabilities may saturate at relatively low levels through rapid phase mixing, and may not be catastrophic to hot-ion accumulation. The nonlinear evolution of flutelike modes is to be attacked by the recently initiated plasma simulation effort. Effects associated with finite plasma length (along magnetic field lines) may play a significant role in determining stability boundaries for these modes. Viable approaches to this problem are being sought through solution of the coupled Vlasov-Poisson equations. The smooth density variation of interest here may introduce dissipative effects capable of triggering the growth of negative-energy waves. The technological problem of producing a suitable target plasma is likely to be related to electron stability problems. Since efficient (rapid) resonant microwave heating of electrons probably leads to non-Maxwellian hot-electron distributions, the various instability mechanisms available to the electrons must be reviewed. Here we limit ourselves to an electrostatic mode, about which relatively little has been published, although the well-known electromagnetic modes may be equally important. The observed finite-beta equilibrium of some microwave-heated plasmas is being investigated through a hierarchy of techniques ranging from semiempirical description of the observed magnetic field using arbitrary arrays of current loops to a microscopic description in terms of plasma distribution functions. Some of these efforts are discussed briefly. These studies, together with investigations of possible heating mechanisms, are aimed at understanding the basic limitations in microwave plasma production, although the present efforts represent only a first attempt at searching out the dominant features. New information on the spectral composition of the rf oscillations apparently associated with turbulent electron heating is compared with well-known beam-plasma interactions. It is shown that most of the rf comes from electron plasma oscillations in the background plasma driven to large amplitude by the slow space-charge wave on the electron beams. An interesting interaction between the slow space-charge wave on one beam and a cyclotron wave on the opposing beam does not appear to have been observed, possibly because of insufficient beam density. This interaction is expected to be effective in trapping primary beam electrons, since it

transfers parallel energy from one beam into perpendicular energy of the opposing beam.

2. TARGET PLASMAS

The concept of using a plasma containing cold ions to trap an injected fast atom beam by charge exchange was discussed in earlier reports. It was pointed out at that time that if the electron component could be made warm, improved stability of the trapped energetic ions might be expected. To implement this concept, it is necessary to generate a plasma with the ratio of the densities of target ions to neutrals of the order of 10^3. We have chosen, as a start, to examine if such a high degree of ionization may be maintained in equilibrium in a plasma where the electrons are heated by radio-frequency power at the electron cyclotron frequency (ECH) and the source of particles results from ionization of the ambient neutral gas.

As a first step in this study, it was decided to remove the constraint imposed by cold-plasma stabilization of the expected flute instability by generating an ECH plasma in a magnetic well. The INTEREM facility was modified for this purpose by the addition of quadrupole windings. Plasmas, generated by ECH, were found with $n_{e_H} \lesssim 10^{12}$ cm^{-3}, $\langle E \rangle \sim 10^5$ eV, in volumes of 2 to 10 liters. In optimum conditions, these parameters may be reached with the neutral density $n_0 \sim 1 \times 10^{11}$ cm^{-3}. The maximum density agreed, as expected, with the cutoff density ($\omega_{pe} \sim \omega_{ce}$). However, the mean confinement time of the energetic particles is estimated to lie between 1 and 30 msec, perhaps an order of magnitude shorter than estimated from classical scattering into the loss cones of the mirrors. Further, fluctuations in the stored energy, high-frequency noise, and axial current suggest the presence of a microinstability in the energetic component. In addition, both the stored energy and maximum density are limited when the fluctuations become intense. If the instability threshold scales as $\omega_{pe}^2/\omega_{ce}^2$, as expected for many microinstabilities, this should pose no threat to the attainment of a target density of $\sim 10^{13}$ cm^{-3} if the magnetic field may be raised to $\sim$20 kG. A test of this scaling is anticipated in the IMP facility, which will also permit study of plasma at lower pressures and ion plasmas with densities up to $\sim 10^{11}$ cm^{-3} if a suitable target density may be produced.

3. INJECTION AND ACCUMULATION: NEUTRAL INJECTION EXPERIMENTS (DCX-1.5)

Work was concentrated on an exposition of the Z-mode high-frequency instability ($\omega \gtrsim \omega_{ci}$). It is thought to be a Harris-like instability, driven by the highly anisotropic ion velocity distribution ($T_{\parallel}/T_{\perp} \approx 0.005$). The instability is observed in the hot-ion density range of $2 \times 10^6 \lesssim n_{avg} \lesssim 3 \times 10^7$ cm^{-3}, with $m = 1$, 2, and 3 modes progressively dominating as the density is raised. Studies of the associated electron ejections along field lines, of rf spectral line widths, and of changes in the radial distribution of hot ions all indicate that the instability is concentrated at smaller radii, where the trapping and subsequent rearrangement of plasma provides larger density. High-resolution studies of the $m = 1$ and 2 rf signals show line structure at regular frequency intervals. This regularity has been related to the proton axial bounce frequency in experiments which included variation of the magnetic field gradient. It is concluded that this instability and the similar ones reported in the PHOENIX II and ALICE (Baseball) plasmas are in fact the same mode. Detailed comparisons of the DCX-1.5 experimental findings with theory are being developed and will be given in a later report.

4. INJECTION AND ACCUMULATION: MULTIPLE-PASS EXPERIMENTS (DCX-2)

The phenomena observed in the DCX-2 and described previously are now well understood. The behavior is dominated by a newly discovered instability, the modified negative mass instability. In this process the counterstreaming injected energetic ions are phase bunched by a mechanism dependent on the finite length of the plasma. The resulting intense electric field at the proton gyrofrequency spreads the energy of the injected particles and produces the so-called central-peak distribution – a major component of the hot plasma having essentially no axial energy – from ions produced in the background gas.

Most of the injected plasma is lost to the injection duct. By careful arrangement of the experimental conditions, it has been possible to observe this loss directly. A flutelike disturbance moves azimuthally at ion precession frequency, expanding radially with a velocity of about 10^5 cm/sec. This

drift wave is correlated with the proton gyrofrequency activity and may be dependent upon it for growth. In the absence of effects which have not yet been taken into account in the theory of this instability, it would be expected to be damped in the DCX-2.

Loss of particles from the central-peak distribution apparently is by charge exchange, but the possibility of other loss processes has not been completely ruled out.

Preliminary turbulent heating experiments have been performed using the DCX-2 magnetic field and a hydrogen arc. Microsecond pulses of 2000 to 4000 A have been passed through the arc by condenser discharge up to 100 keV. The arc resistivity shows an abrupt increase at a critical value of condenser voltage. There is appreciable plasma loss during the discharge in the form of plasmoids, but the arc is not extinguished.

5. ELECTRON-CYCLOTRON HEATING

The efforts of the microwave heating group have been concentrated in two major areas of interest. The first is the development of high-power millimeter-wavelength microwave sources for plasma production and heating. The second is the experimental study of the high-β electron-cyclotron plasma (ECP) produced in the ELMO facility.

The development of a 1-kW 55-GHz power source for ELMO is described, as is its use simultaneously with a 35-GHz power source. Both sources are fed into the ELMO cavity for two-frequency heating. The magnetic field is adjusted so that the heating is simultaneously resonant and nonresonant. The development of a 10-kW 55-GHz power source, its associated waveguide transmission system, and the component development program for this system are described.

More detailed measurements of the stored energy and spatial distribution of the stable plasma in ELMO have been made. Two techniques, total flux measurements and magnetic field surveys, have been the principal diagnostics. A model of the plasma has been developed, based on these measurements, which is consistent with other diagnostics. The model is of a stable, hollow annular plasma with a β of $\sim 40\%$.

Experiments were conducted on the plasma when it was intentionally made unstable at low ambient gas pressure. The studies have shown that both ions and electrons are accelerated to the walls during the instabilities. Radioactivity from both electron acceleration (photonuclear processes) and deuteron acceleration [(d,n) processes] has been seen.

Neutrons from Coulomb dissociation of deuterons are normally produced by the high-β ECP's in the ELMO facility. The neutron production has increased by about an order of magnitude when operating with two-frequency heating. An attempt to correlate the neutron emission with the total stored energy and temperature is also described. The study indicates that there is a serious disagreement between the measurements and the theory.

Studies of the decay of electron-cyclotron-heated plasmas are being carried out in the Long Solenoid Facility. The purpose of these studies is to measure the cross sections for scattering of energetic electrons into the mirror loss cone.

6. TURBULENT HEATING

Turbulent heating experiments at ORNL use direct-current electron beams up to several amperes, with accelerating potentials of more than 10 kV, for plasma generation and trapping in magnetic mirror devices. Both ions and electrons may be heated, the degree of heating depending upon the adjustment of the physical and electrical parameters. In this report period the ion heating device, Burnout V, was operated in a new "supermode," yielding densities $>10^{13}$ cm^{-3}, ion temperatures >1 keV, with an efficiency $>5\%$ and a containment of many ion transit times. Diagnostics measuring spectral radiation, diamagnetism, neutral particle emission, and D-D reaction products were used and are described.

The heating mechanism is still not clear, but we have collected wave data from both the hot-ion and hot-electron plasmas by means of new correlation techniques developed for gigahertz frequencies. Transient electric fields >1000 V/cm and space potentials up to the beam accelerating potential are observed. Data from the hot-electron plasma were reduced to an experimental dispersion relation and are given; they do not adequately fit theory, though we advance some ideas. We consider a method for the removal of impurities in the hot-ion device.

7. PLASMA PHYSICS

The basic studies of low-frequency modes of oscillation in plasmas include not only studies of the properties of waves and wave-plasma interactions but also investigations into new techniques for generating plasmas and into developing new diagnostic techniques. New areas include wave studies in magnetically supported plasmas, computer simulation studies of waves, plasmas, and plasma sheaths, nonlinear-waves studies, microwave plasma generation in a low-pressure min-B system, and studies of a new wavelike phenomenon due to coherent free-streaming motions of plasma particles.

The areas of investigation can be broken down into the following six categories: (1) ion acoustic waves, (2) electrostatic ion cyclotron waves, (3) pseudowaves, (4) plasma sheaths, (5) plasma generation techniques, and (6) diagnostics. The ion acoustic wave studies include experimental and theoretical ion Landau damping in a magnetic field, simultaneous measurements of wave potential and plasma density perturbation to yield γ_e, wave focusing to produce nonlinear behavior, experimental and theoretical dispersion near ω_{pi}, linearized Vlasov theory calculations for wave and wavelike phenomena near ω_{pi}, and a calculation for the variation of wavelength/Debye length with T_e/T_i at frequencies near ω_{pi}. The electrostatic-ion-cyclotron-wave studies include dispersion measurements both above and below ω_{ci} for several angles of propagation. The study of pseudowaves – free-streaming particles accelerated by gridded electrodes – included not only an experimental investigation of their properties but also a computer simulation study of their nonlinear excitation mechanism. The plasma sheath studies included experimental and theoretical study of a transient plasma sheath, an experimental study of Langmuir sheaths, and a computer simulation study of the evolution of a plasma sheath. In the plasma generation studies we have, by proper design of an electron gun, generated an extremely quiescent plasma in a magnetic field; in addition we have generated a plasma at low pressures in a min-B system using microwaves at cyclotron resonance. In the diagnostic development studies we have found a simple technique for measuring $T_{e\parallel}$ in magnetic fields.

In order to measure electron plasma densities in the density regime which approaches or exceeds microwave cutoff, a far-infrared laser ($\lambda = 337\ \mu$) has been developed for use with a Michelson interferometer. The CH_3CN laser operates cw or on long pulses at partial pressures of 0.1 torr of CH_3CN and 0.5 torr of H_2 with excitation by 1.0 A of discharge current. The maximum power output is about 35 mW over a wide operating range of pressures and currents.

A prototype Michelson interferometer has been built with a Mylar beam splitter and translating mirrors which is capable of resolving phase shifts of 10°. As a proposed application, Burnout V would offer about 50° plasma-induced phase shift due to its 10^{13}-electron/cm^3 density and 5-cm diameter.

In another area, we have tried to understand the mechanism which transports a large electron flux across the magnetic field. An electromagnetic theory is developed which involves a time-changing magnetic field, arising from the motion of charged particles, and the mobility of electrons in a negative potential well, arising from space charge. We describe experiments that have led to these transport models.

8. TOROIDAL MULTIPOLES

The primary emphasis in the multipole program was placed on the determination of the characteristic behavior of hot-electron plasma in the confining magnetic field of the levitated toroidal quadrupole. A comparison of the confining properties of the quadrupole and the dipole (a single hoop) showed that the presence of the magnetic well could account for most or all (depending upon interpretation of the density gradients) of the improved confinement in the quadrupole ($\tau/\tau_{\text{Bohm}} \sim 30$). Using the same microwave-generated plasma, it was found that a reduction in the size of the access holes in the copper quadrupole jacket (from a radius of three magnetic field skin depths to one) resulted in a magnetic field and plasma confined to the inside of the quadrupole cavity with minimum leakage out the access holes.

With the improved quadrupole device, plasma was created (with hundreds of watts of $\lambda = 3$ cm microwave fields) having densities on the order of 10^{12} cm^{-3} (the microwave cutoff density) and electron temperatures of about 100 eV as measured by various techniques, primarily with floating double Langmuir probes; the lifetimes of this plasma are about 80 μsec, corresponding to $\tau/\tau_{\text{Bohm}} \sim 40$.

As a result of the magnetic geometry and the time variation of the current, there are time intervals during each plasma event when either one or two electron cyclotron resonance zones exist. The changes in density and fluctuation level accompanying this shift in heating zones are clearly distinguishable, carrying information about equilibration times across the separatrix.

The introduction of metallic obstacles in the quadrupole has shown that the plasma is maintained by local microwave heating once localization is accomplished at the microwave input port. The introduction of supports, cutting all flux lines (at one azimuth), has shown, first, that the radial loss (intrinsic to the levitated device) is not increased by a set of fine-wire supports (as measured by τ, T_e, and n) and second, that any enhanced support loss is not considerably greater than the classical single-particle support loss.

Following cutoff of microwave fields, the plasma decays, first at a rapid rate and then at a much slower rate. The amplitude ratio of these two decay components has been measured throughout the quadrupole, resulting in a possible interpretation of a 100-eV background plasma having a higher-energy component confined to the mirror regions and also rapidly lost in the azimuthal direction; an alternate possibility is that the rapid loss is caused by residual turbulent motion of the electrons remaining after microwave cutoff.

Measurements have been started to determine the effects of resistively generated electric fields (along the hoops) on plasma confinement; the electric field can be increased deliberately by heating the hoops ohmically. Preliminary results indicate a decrease in density inside the magnetic well and an increase in density outside the magnetic well, in addition to an increase in fluctuation level as the hoop temperature and electric field increase. Preliminary results with the combined operation of both the microwave heating and washer gun indicate an enhanced probe flux (either density or temperature or both) when the microwave fields occur simultaneously with the initial appearance of the gun plasma.

A potential increase in magnetic field strength of an order of magnitude has been made possible by reworking the electromagnetic structure (circuit) of the quadrupole current paths and the primary coils of the iron core to provide a low-inductance configuration. The magnetic field will require back-biasing of the iron core and should result in having five 100-eV-ion gyroradii across the smallest magnetic distance (between ψ_s and ψ_c at the outer magnetic flux bridge of the quadrupole). The impedance of the rebuilt quadrupole agrees with the design calculation, and 8% of the maximum field has been reached with the present 60-Hz power supply; an 18-kJ capacitor bank and switchgear are being readied to supply the full field capability.

The helical hexapole has been lightened by using a thick-wall tube construction, has been levitated, and is being prepared for plasma experiments.

9. ATOMIC AND MOLECULAR CROSS SECTIONS

Extensive measurements of time-dependent decay of the highly excited ($n \geqq 10$) principal quantum states of the H_2 molecule revealed that the lifetimes were being influenced by some uncontrolled parameter. Mixing of the *ns* and *np* states in the electric field of the deflecting plates was observed. The fraction of particles in states $n \geqq 10$ was shown to be dependent on the energy of the ionizing electrons in the accelerator ion source. For both H_2 and D_2 the fraction with $n \geqq 10$ increased by a factor of 3 when the electron energy was decreased from 25 to 16 eV.

A literature survey of absorption oscillator strengths for the λ 977 Å line of C^{2+} has revealed gross discrepancies in the theoretical f value. Using the most recent value of Steele and Trefftz removes an annoying discrepancy in the measured and predicted populations of the 6.5-eV metastable state of C^{2+} in the theory of excitation heating of carbon ions to high temperatures in magnetically confined carbon arcs.

Glass capillary arrays (10 μ in diameter, 1.5 mm long) enclosed in a liquid-nitrogen cavity were used to form a water vapor jet target for ion neutralization. Equivalent hydrogen atom fractions of 0.80 were obtained for 40-keV H_2^+. Kinetic gas streaming from the cavity was proportional to the vapor pressure on the high-pressure side of the array.

Energy losses and angular and energy distributions have been determined for the passage of hydrogen atoms through a 250-Å carbon film in the energy interval 2 to 20 keV. Preliminary results indicate that thin carbon foils may be useful as stripping cells down to energies of 1 keV.

The reduction of stray magnetic fields to less than 10^{-3} Oe is reported. Use was made of four concentric cylinders made of Netic and Co-Netic material.

Performance characteristics of channel multipliers and Johnston multipliers were investigated for detecting low-energy hydrogen particles. Completely resolvable pulse-height distributions were obtained from the channel multiplier for both uv photons and hydrogen particles, indicating the multiplier operates in a gain saturation mode. Installing an auxiliary grid in front of the funnel and Johnston multiplier increased the detection efficiency to near 100%.

Advances in the Atomic and Molecular Information Center include: (1) submission of the manuscript of the monograph *Ion-Molecule Reactions* to John Wiley and Sons for publication, (2) development and test of a workable program for data retrieval, (3) publication of two bibliographies, (4) continued writing on the manuscripts for four monographs.

10. ENERGETIC-PARTICLE INJECTORS FOR PLASMA PHYSICS EXPERIMENTS

Energetic charged- or neutral-particle injectors for plasma physics experiments at Oak Ridge now cover an energy range from a few keV up to 600 keV. A continuing effort is being made to develop and improve these specific injectors as needed for particular plasma physics experiments. The 80-mA, 600-keV H_2^+ DCX-2 injector and the 50-mA (equivalent), 20-keV H^0 DCX-1.5 injector, which has a 55% energy spread, are examples of this work.

Recently those efforts have been supplemented by a study of the limitations imposed on low-energy hydrogen ion beams because of improper space-charge neutralization. For cases where electron densities from ionizing collisions of the ions are inadequate, a technique has been found for properly adding electrons to the beam. For hydrogen ion beams this technique makes a significant improvement in beam brightness either for low energy (hundreds of eV) or for low-pressure drift regions. For example, the beam intensity can be increased at least an order of magnitude for a 100-eV beam with a background pressure of 5×10^{-6} torr.

Other recent work includes the development of a new filament designed for continuous high-current operation of the duoplasmatron ion source. This filament has been tested for continuous 50-A arc operation for tens of hours and for 100-A operation for 3 hr.

Equipment is now being built for an experimental injector using ionized and accelerated clusters of condensed hydrogen atoms. The primary efforts will be to use liquid-helium vapors instead of liquid hydrogen in the cryostat and to obtain an intense beam of clusters in an energy range of interest for plasma physics.

In conjunction with NASA at Houston, Texas, and O. C. Yonts of the Thermonuclear Division, an experiment simulating the effect of the solar wind on the moon's surface is being performed. A sample is being bombarded with 10-keV particles for 400 hr.

11. MAGNETICS AND SUPERCONDUCTIVITY

All our facilities for thermonuclear research presently in operation are employing water-cooled magnet systems, utilizing our existing large dc power installations. Various developmental work on water-cooled magnet coils is still necessary and has been done during this report period. However, our efforts in superconductivity are becoming increasingly important. The design of large superconducting magnet systems is not yet in a state of conventional engineering, and extended developmental work must be done. The physics background as needed for an understanding of the operation of superconducting magnet systems is not yet sufficiently clear, and therefore we try to support our developmental work in superconducting magnets by doing research in such fields of superconductivity as are closely connected with the mentioned engineering application. This basic work on superconductivity is jointly sponsored by the Controlled Thermonuclear Branch of the USAEC and by the George C. Marshall Space Flight Center, NASA.

Our research elucidated greatly the steady-state performance of compound conductors (superconducting thin filaments or thin superconductor layers in stabilizing nonsuperconducting metal matrixes) which are presently generally used for superconducting magnet windings. Independent measurements of heat transfer from metal surfaces to liquid helium were applied to the analysis of current-voltage characteristics of compound conductors in the current-sharing state. Good agreement with our experiments made with compound conductors with

very fine superconducting filaments was obtained by considering the fact that the superconductor current depends in general not only on the temperature and the magnetic field, but also on the voltage along the superconductor. These results will be applied to the theory of compound conductors with "thick" filaments, which heretofore was based on oversimplified models.

Our experiments demonstrated that the steady-state performance of compound conductors is not simply terminated by reaching the maximum nucleate-boiling heat flux. In general, other, more complicated stability criteria are decisive. For bare strips of superconducting Nb-Ti, we derived a method for calculating the stability limit which is based on the assumption that the minimum propagating current is approximately a linear function of the external field H. For these calculations, it is sufficient to know the critical current I_c as a function of field H, the normal resistivity R_n, and the critical field at zero temperature $H_{c2}(0)$. This model predicts sufficiently well the experimental data obtained with bare superconducting strips. However, direct application of this approach to the dynamic stability of compound conductors is not possible.

The design and construction of the magnet and the cryogenic system of the IMP facility are well under way. Extensive tests of the superconducting winding materials produced a wealth of experimental data which showed the great variety of the relevant electrical data of commercial superconductors of similar design. This led first to a final decision on the choice of the superconducting material for the mirror coils. A special type of multifilament NbTi compound conductor was selected, and in tests with the completed mirror coils, the critical short-sample currents have been reached.

The original design of the quadrupole coils considered the same superconducting winding material. However, after performing rigidity tests with non-axially-symmetrical ("racetrack") windings, it seemed advisable to use Nb_3Sn ribbon conductors instead of NbTi conductors. Due to higher current density, the winding volume can be appreciably reduced; the favorable "pancake" winding design can be easily employed, and therefore improved winding rigidity can be expected. Concerning the design of the quadrupole coil cans, experiences with type 310 stainless steel at cryogenic temperatures (made recently at other places) indicate that these coil cans (which are exposed to very high electromagnetic forces) should better be made of Armco 21-6-9 stainless steel. These changes in the design of the quadrupoles caused some unforeseen delay. However, since the tests of the vacuum systems and the superconducting mirror coils were successful, Phase I operation is expected to start in the spring of 1969.

For the IMP project, special cryogenic developmental work has been done. A new winding technique has evolved which is especially important for the odd-shaped quadrupole coils. A new liquid-helium level indicator was designed and successfully tested. This simple device has a linear characteristic and can be used undisturbed by strong external magnetic fields. Care has been taken to reduce the cooldown and the heat leak losses of liquid helium to a minimum, which resulted in other details of cryogenic development.

12. FUSION FEASIBILITY

Power from nuclear fusion will be economical only if the plasma physics problem of adequate containment is feasible and if nuclear engineering problems can be solved. We can optimize the system by solving generally the equilibrium plasma reaction rates and the nuclear and size properties. We obtained self-consistent solutions for the thermalization rates between ions, electrons, and the fusion product alpha particles, we calculated fuel burnup fractions for resulting electron and ion temperatures, and we found the effect of radiation, injected energies, and plasma pressure on reaction rates. Typical and revealing conditions for operation of steady-state D-T open and closed magnetic configurations were obtained.

New solutions to outstanding engineering problems were indicated: a cellular niobium vacuum wall, cooled by lithium or molten salt; a natural lithium breeding blanket with graphite as moderator and support; and large superconducting coils but supplying reasonable fields, with stress supports of titanium. Neutronics with these realistic systems indicate high breeding ratios. New and economical solutions to pumping and tritium recovery were found. Inventory would be low and doubling times short. Sputtering ratios for D^+-Nb were found to be very low (0.0006), pointing to long-lived vacuum walls.

It was found that fusion systems must be large to be really cheap [10,000 MW (electrical)] and that

the costs for the "core" of such systems may be near $10.00/kW (electrical). These studies emphasize that for open systems to be economical, plasma pressures must be high; for closed systems to work, outstanding confinement problems must be solved. The large sizes (10 m diameter) dictated by economics also relieve the confinement problem considerably.

1. Plasma Theory and Computation

1.1 SYNOPSIS

The proposed injection and trapping of energetic ions in a target plasma environment, discussed in Sect. 2, raises several questions of plasma stability. Much of the work described here is directed toward these questions. The main elements of the stability problem for target plasmas are the benefits and hazards of (1) high electron temperature and (2) the coexistence of two distinct groups of ions, a warm Maxwellian group (the target) and the fast non-Maxwellian injected particles.

We have examined the linear stability of a spatially uniform plasma whose distribution functions model the velocity-space properties of target plasmas. Most of the results are contained in the material abstracted in Sect. 1.2. In brief, if electron temperatures are too low, one loses the important stabilizing influence of Landau damping. If the electron temperature T_e is too high, new classes of ion-ion interaction may occur. The optimum electron temperature is roughly that of the hot ions. Regarding the two-ion-group problem, we find that stability is best achieved by raising the warm-ion temperature T_W to about 10% of the hot-ion temperature T_H. Under these conditions and for relative densities $N_W/N_H \lesssim 0.1$, the flutelike ($k_{\parallel} = 0$) modes are linearly stable (the question of explosive nonlinear instabilities is still under consideration; Sect. 1.3.4). For $T_W/T_H \lesssim 0.05$, rapidly growing flutelike modes may occur when $N_W/N_H \gtrsim 0.01$, provided the hot-ion density is large enough. The frequency and wavelength of the fastest-growing modes are related to resonance conditions between the warm-ion hybrid frequency and hot-ion cyclotron harmonics, resulting in the excitation of high-frequency, short-wavelength modes in the buildup stage of a typical target plasma experiment (in which $N_W/N_H >>$ 1). These instabilities may saturate at relatively low levels through rapid phase mixing, and may not be catastrophic to hot-ion accumulation. The desirability of studying the nonlinear evolution of flutelike modes is reflected by the selection of problems to be attacked by the recently initiated plasma simulation effort, described in Sect. 1.4.1. Effects associated with finite plasma length (along magnetic field lines) may play a significant role in determining stability boundaries for these modes. Viable approaches to this problem are being sought through solution of the coupled Vlasov-Poisson equations, as described in Sect. 1.3.5.

The technological problem of producing a suitable target plasma is also of immediate concern, and is likely to be related to electron stability problems discussed in Sect. 1.3.6. Since efficient (rapid) resonant microwave heating of electrons probably leads to non-Maxwellian hot-electron distributions, the various instability mechanisms available to the electrons must be reviewed. In Sect. 1.3.6 we limit ourselves to an electrostatic mode about which relatively little has been published, although the well-known electromagnetic modes may be equally important. The observed finite-beta equilibrium of some microwave-heated plasmas is being investigated through a hierarchy of techniques ranging from a semiempirical description of the observed magnetic field using arbitrary arrays of current loops to a microscopic description in terms of plasma distribution functions. Some of these efforts are discussed briefly in Sect. 1.4.2. These studies, together with investigations of possible heating mechanisms, such as reported in Sect. 1.2.5, are aimed at understanding the basic limitations in microwave plasma production, although the present efforts represent only a first attempt at searching out the dominant features.

A possible alternative technique for target plasma production is turbulent heating, of which the most highly developed form at ORNL uses energetic electron beams in a reflex discharge configuration. During the past year, new information has been obtained on the spectral composition of the rf oscillations apparently associated with the turbulent electron-heating process. The compatibility of these data with well-known beam-plasma interactions is studied in Sect. 1.3.7, where it is shown to support the hypothesis that most of the rf comes from electron plasma oscillations in the background plasma driven to large amplitude by the slow space charge wave on the electron beams. An interesting interaction between the slow space charge wave on one beam and a cyclotron wave on the opposing beam does not appear to have been observed, possibly because of insufficient beam density. This interaction is expected to be effective in trapping primary beam electrons, since it transfers parallel energy from one beam into perpendicular energy of the opposing beam.

Much of the material in this report describes initial stages in the development and implementation of new analytical techniques aimed at easing the constraints which have restricted much of our previous work to linearized theories of infinite, homogeneous low-beta plasmas in uniform magnetic fields. Section 1.3.5 describes an attempt to account for spatial variation of plasma density along the magnetic field. The smooth density variation of interest here may introduce dissipative effects capable of triggering the growth of negative-energy waves. Section 1.3.4 deals with the nonlinear wave interaction which may also permit negative-energy waves to grow by providing a nonlinear energy exchange mechanism. Section 1.4.1 discusses several possible techniques for following the time history of plasma models with high-speed digital computers, techniques which show promise of permitting comprehensive observations of many modes of plasma behavior only suggested by existing analytical techniques. Section 1.4.2 describes some elementary studies of high-beta plasma equilibria motivated by observations in the ELMO facility.

These studies go beyond the normal mode analysis which has characterized much of the past decade of plasma investigations to examine the consequences of these modes for the behavior of realistic systems. Fortunately, observations suggest that many of the complex interactions of waves and particles are useful and nondestructive. Their utilization to advantage may, however, require a greatly elevated level of understanding of the behavior of high-temperature plasmas.

1.2 ABSTRACTS OF MATERIAL AVAILABLE AS PREPRINTS

1.2.1 Resonant Loss-Cone Instabilities[1]

C. O. Beasley, Jr. W. M. Farr
R. A. Dory G. E. Guest
D. J. Sigmar

We consider several aspects of resonant loss-cone instabilities: the general properties of the unstable oscillations, particularly in plasmas containing hot electrons; the stabilization effects resulting from adding low-temperature ions to a hot-ion, hot-electron plasma and varying the energy and angle spread of the hot-ion distribution; and the behavior of these same modes at high densities, approaching reactor values. To date these studies have shown that the instabilities can be weakened or in some cases effectively eliminated by the various procedures studied. Complete stabilization may, however, rely on effects not yet understood, such as the finite length effects mentioned in this report or the effects associated with spatial variation in the confining magnetic field.

1.2.2 Resonant Loss-Cone Instabilities in Mirror-Confined Plasmas[2]

C. O. Beasley, Jr. W. M. Farr
R. A. Dory G. E. Guest
D. J. Sigmar

We consider resonant instabilities (having frequencies near harmonics of the ion gyrofrequency,

[1]Abstract from *Proceedings of International Conference on Plasma Confined in Open-Ended Geometry, Gatlinburg, Tennessee (1967).* Issued as Oak Ridge National Laboratory Proceedings CONF-671127, available from Clearinghouse for Federal Scientific and Technical Information, National Bureau of Standards, U.S. Department of Commerce, Springfield, Va. 22151.

[2]Abstract of paper No. CN-24/G-11 presented at the Third Conference on Plasma Physics and Controlled Nuclear Fusion Research, Novosibirsk, U.S.S.R., Aug. 1–7, 1968. Conference proceedings will be published.

Ω_i) which may occur in dense, energetic mirror-confined plasmas. The Harris dispersion relation for electrostatic oscillations in an infinite homogeneous plasma in a uniform magnetic field is solved for a set of steady-state distribution functions chosen to simulate mirror-confined or electrostatically confined plasma components. The Bers-Briggs procedure is used to obtain spatial and temporal growth rates of unstable waves, and the stabilizing effects of several parameter variations are examined through the resulting changes in (1) these growth rates, (2) marginal stability threshold densities, (3) transition densities at which growth becomes absolute rather than convective, and (4) axial wavelengths of the unstable oscillations. We have surveyed the effects of (1) variations in the electron temperature, (2) variations in the width of the distribution functions, and (3) addition of low-temperature ions to the hot plasma. Although within the present model we find no set of parameters for which high-density mirror-confined plasma is stable, it appears that laboratory plasmas can be effectively stable if (1) the particle distributions approach collisional equilibrium, (2) the ion and electron temperatures are roughly equal, and (3) the plasma length does not exceed a value around 100 ion gyroradii. Low-temperature ions are impractical for stabilizing the resonant modes near higher harmonics of gyrofrequency ($\omega \approx \ell\Omega_i$, $\ell = 2, 3, 4, \ldots$).

1.2.3 Warm-Plasma Stabilization of Resonant Loss-Cone Instabilities[3]

J. D. Callen[4] W. M. Farr
R. A. Dory G. E. Guest

A warm Maxwellian plasma can stabilize velocity-space instabilities which might otherwise occur in a hot non-Maxwellian plasma with which it coexists. The relative densities and temperature of the two species required for stabilization of resonant ($\omega \approx \ell\Omega_i$, the ion gyroharmonics) loss-cone modes in a mirror-confined hot-ion plasma are evaluated for a model plasma whose density is spatially uniform but whose velocity-space distribution function simulates the loss-cone effect of mirror confinement. Marginal stability boundaries are given and compared with several simple but inexact criteria. The dominant features of the stability boundaries are explained on the basis of cutoff of propagation of the unstable waves. Temporal growth rates of the absolutely unstable modes are found to decrease significantly with increasing warm-plasma density.

[3]This paper is being submitted for publication in *Physics of Fluids*. It is currently available as ORNL-TM-2397.

[4]Institute for Advanced Study, Princeton, N.J.

1.2.4 Propagation of Ion Acoustic Waves in a Magnetic Field[5,6]

R. A. Dory Glenn Joyce[7]

The properties of low-frequency electrostatic waves propagating at various angles to a magnetic field in a plasma are studied. Numerical calculations are used to determine the phase velocities, group velocities, damping decrements, and propagation directions for frequencies between zero and twice the ion cyclotron frequency. A model is presented which simulates experimental time-of-flight studies of finite wave packets generated by sine-wave bursts.

1.2.5 A Stochastic Model of Electron Cyclotron Heating[8]

H. Grawe[9]

We calculate analytically the energy gained by an electron during one transit of an idealized one-dimensional magnetic mirror field B in the presence of a given microwave electric field. The heating rate is defined as this energy gain over the transit time. It depends on the initial energy and the position of the turning point of the electron. The heating rate for relativistic electrons not crossing the resonance surfaces (on which the microwave frequency equals the local nonrelativistic electron

[5]This work is supported in part by the National Aeronautics and Space Administration under grants NGR 16-001-043 and NsG 233-62.

[6]Abstract from ORNL-TM-2341 (June 1968). Submitted for publication in *Physics of Fluids*.

[7]Consultant from University of Iowa, Department of Physics and Astronomy, Iowa City, Iowa 52240.

[8]Submitted for publication in *Plasma Physics*.

[9]On leave from Institut für Plasmaphysik, Garching bei München, Germany.

gyrofrequency) can be comparable with that of "resonant electrons."

A comparison of the heating rate and energy loss rates from multiple collisions and radiation suggests an equilibrium at energies of 10^2 to 10^3 keV, depending on the mirror ratio, microwave field strength and frequency, and the density of the cold-electron group responsible for the collisional energy losses. The fraction of electrons heated to this equilibrium energy is calculated.

The results are in good agreement with the experimental measurements.

1.3 BRIEF REPORTS OF WORK IN PROGRESS

1.3.1 Brillouin Diagram Solutions of Real Dispersion Relations

R. A. Dory Joyce Monard[10]

1.3.1.1 Description. – We would like to write down a little of the lore of computer solutions of dispersion relations of the form $1 = \epsilon F(\omega, k; p)$ where F is real when the wave frequency ω and wave number k are real. The multiplier ϵ gives the usual multiplicative dependence of waves in infinite uniform plasma on the plasma density, $\epsilon = \omega_p^2/\Omega^2$, where ω_p is plasma frequency and Ω is gyrofrequency. F also depends on other plasma parameters p: anisotropy, energy spread, species concentrations, and so on. The ϵ factor is assumed to contain the only dependence on density.

We use a two-dimensional version of a well-known graphical technique: the parameters p and ϵ are chosen; then F is evaluated in the ω-k plane. Wherever F takes on the value $1/\epsilon$, there is a propagating solution ω, k to the dispersion relation. Analysis of the loci of these solutions gives nearly all the information one normally asks.

The procedure is simple, efficient, and complete (finds all real solutions). The simplicity and completeness result from using $F(\omega, k; p)$ directly rather than trying to solve the dispersion relation for $\omega(k)$ or $k(\omega)$. The method is efficient because one normally wishes to know the density dependence of the solutions. Thus a single calculation of F on a grid in the ω-k plane allows solution of many values of ϵ.

We use a simple contouring package called SCAN to analyze the array F_{ij} of values of F on the ω-k grid. This finds all solutions of the dispersion relation except those caused by variation of F over distances smaller than the grid size. Having found the locus or contour where F takes on a given value $1/\epsilon$, SCAN plots the contour using either a CALCOMP plotter or cathode ray tube output device. When one contour is finished, another is added without recomputing the values F_{ij}. These contours may be regarded as level curves on the three-dimensional surface $Z = F(\omega, k)$.

The procedure is useful where one wishes to consider many values of ϵ and where the properties of waves propagating in a given direction are of interest. For arbitrary propagation in three dimensions, a set of ω-k diagrams is required, each having labels (say) of two angles specifying the propagation direction. For an azimuthally symmetric system, one needs only a reduced set with a single direction label.

1.3.1.2 Example. – We present in Fig. 1.1 a sample diagram for propagation across the magnetic field in a plasma with a warm Maxwellian ion species and a hot loss-cone species[11] of the $j = 1$ type, where the perpendicular velocity distribution has a peak with half width at half maximum of 60% of the peak velocity, and a neutralizing cold inert background species.

The vertical axis is k and the horizontal is ω. The resonance lines $\omega = \Omega, 2\Omega, 3\Omega, \ldots$ lie at 0.5, 20.5, 40.5, 60.5 on the horizontal scale. The vertical scale gives $5k_\perp\rho/\pi$, where ρ is the mean gyroradius of the hot ions.

1.3.1.3 Interpretation. – 1. Where contours cross the resonance lines $\omega/\Omega = \ell = 1, 2, 3, \ldots$ to lie on the left side, the propagating waves are negative energy waves. Instability results if for some density these can couple to the positive energy waves associated with the next lower harmonic, for example near $k_\perp\rho \cong 3\pi$ and $\omega \cong 2.8\Omega$ where the $\ell = 2$ (positive energy) and $\ell = 3$ (negative energy) waves couple. No coupling of $\ell = 1$ to $\ell = 2$ occurs in this example, but the higher coupled modes are seen to be unstable for sufficient density.

2. Generally an instability is present if one of the contours has a horizontal tangent ($d\omega/dk =$

[10]Summer student from University of Tennessee, Department of Physics, Knoxville, Tenn.

[11]G. E. Guest and R. A. Dory, *Phys. Fluids* **8**, 1853 (1965).

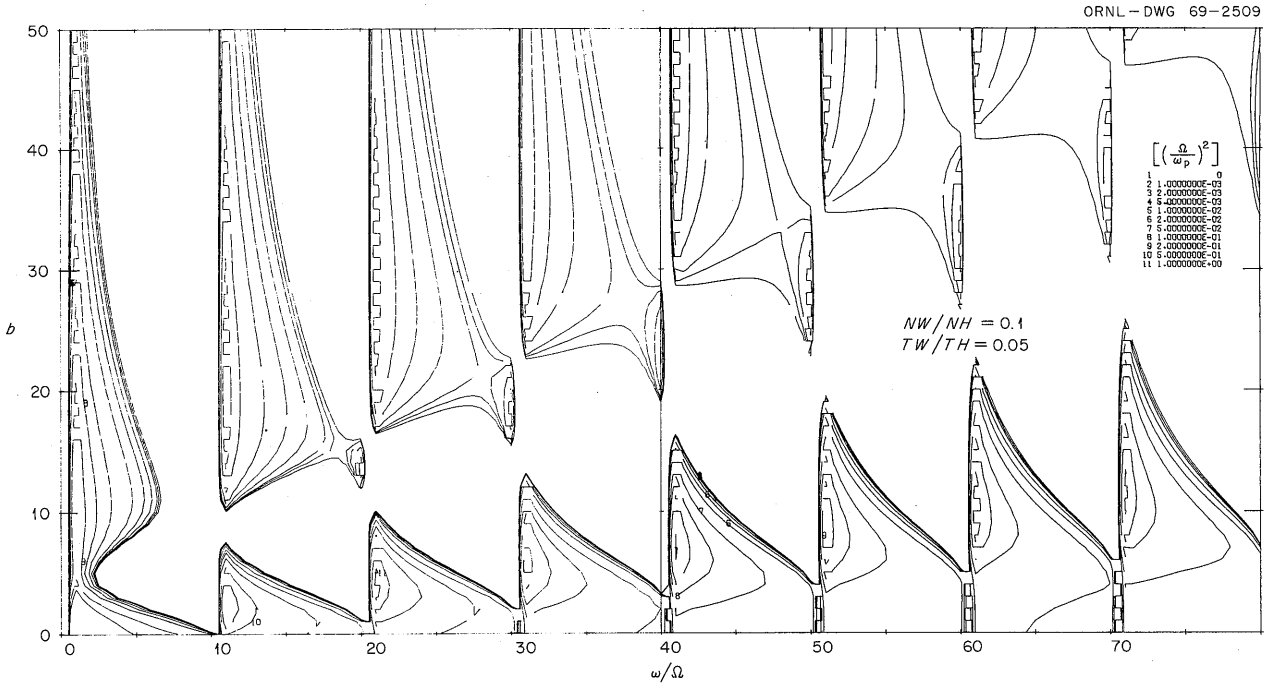

Fig. 1.1. Brillouin Diagram Used in Example of Sect. 1.3.1.2.

$V_{\text{group}} \to \infty$ is not permitted relativistically of course, but calculations including relativistic dynamics usually leave the conclusion unchanged). One must be careful to avoid misinterpreting structure whose scale length nears the spacing of the grid on which $F(\omega, k)$ is evaluated. In Fig. 1.1, the behavior near the gyroharmonics has this origin because of infinities in F.

3. One finds the minimum threshold densities from the saddle points of the surface $Z = F(\omega, k)$. The saddle appears as the center of a nested set of hyperbolae in the ω-k plots.

4. The curvature of the surface $Z = F(\omega, k)$ gives a qualitative estimate of growth rate of instabilities. If the regions of hyperbolic contours are restricted to small ranges of ω and k, the instabilities have relatively low growth rate and saturate at a small value when ϵ is increased (example, the $\ell = 2 - \ell = 3$ mode). If the structure is broad, the instability has relatively high growth rate (example, $\ell = 4 - \ell = 5$ mode).

5. Pass bands and stop bands in ω and k are obvious from the diagrams. Here again care must be taken to differentiate between numerical resolution and physical properties.

For further examples of this technique, see Sect. 1.3.7.

1.3.2 Growth Rates of Flutelike Loss-Cone Modes

R. A. Dory Joyce Monard[10]

Frequent requests for detailed information about the modes described by Dory, Guest, and Harris[12] and the need to check growth rate calculation procedures for the two-species model (Sect. 1.3.3) have led us to collect various data on the single-species uniform-plasma modes propagating across (in the azimuthal direction) a plasma with non-monotonic distribution f_0 of velocity component $v_\perp$ normal to the magnetic field.

[12]R. A. Dory, G. E. Guest, and E. G. Harris, *Phys. Rev. Letters* 14, 131 (1965).

ORNL-DWG 69-2510

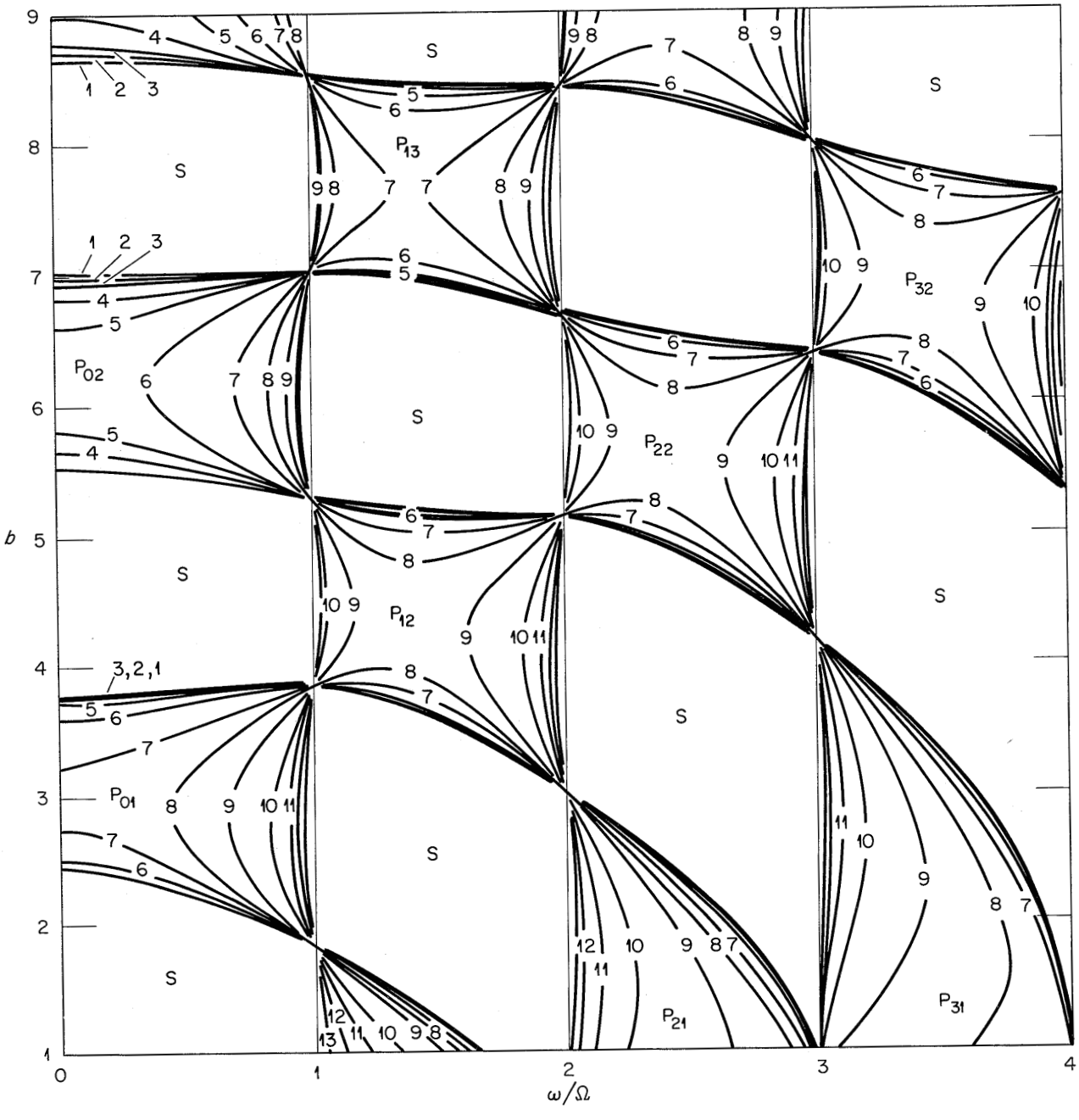

Fig. 1.2. Wave Plot for δ-Function Distribution. Curves are for following values of ϵ^{-1}: (1) 0.0, (2) 0.001, (3) 0.002, (4) 0.005, (5) 0.01, (6) 0.02, (7) 0.05, (8) 0.1, (9) 0.2, (10) 0.5, (11) 1.0, (12) 2.0, (13) 3.0. $b \equiv k_\perp V_\perp/\Omega$.

Other properties of the modes are given by Crawford *et al.*[13] and Bers *et al.*[14]

[13]Consult *Bibliography of Stanford Reports, Papers and Conference Presentations on Plasma Physics*, SU-IPR Report No. 255 (July 1968).

[14]Consult Massachusetts Institute of Technology, Research Lab of Electronics Quarterly Progress Reports, 1965 to 1968.

The Brillouin diagram (see Sect. 1.3.1) given in Fig. 1.2 is for a δ-function distribution at $v_\perp = V_\perp$. The range of $w = \omega/\Omega$ (wave frequency over gyrofrequency) is 0 to 4 and that of $b \equiv k_\perp V_\perp/\Omega$ is 1 to 9. We note pass zones $P_{\ell m}$ where wave propagation occurs and stop zones S where there are no propagating waves. The zones alternate to form a distorted checkerboard pattern with

corners at integer values of ω/Ω and at values of b where the residues $H_\ell(b)$ are zero. The dispersion relation is

$$1 = \epsilon \sum_{-\infty}^{\infty} \ell \, H_\ell(b)/(\ell - w) \, , \tag{1}$$

where

$$\epsilon = \omega_p{}^2/\Omega^2$$

and

$$H_\ell \equiv (\Omega/k_\perp)^2 \int d^3v \, v_\perp^{-1} J_\ell^2(k_\perp v_\perp/\Omega) \frac{\partial f_0}{\partial v_\perp} \, .$$

Zone label $P_{\ell m}$ corresponds to possible instabilities at Re $(\omega/\Omega) = 0$ for $\ell = 0$ and Re $(\omega/\Omega) \approx \ell + \frac{1}{2}$ for $\ell \neq 0$, with $k_\perp V_\perp/\Omega \approx m\pi$ when $\ell = 0$ and $k_\perp V_\perp/\Omega \cong (m + \ell - \frac{1}{2})\pi$ when $\ell \neq 0$.

The effect of spreading the velocity distribution to one of the Poisson j distributions $[u^j/(j!e^{-u})$, where $u \equiv v_\perp^2/\alpha_\perp^2$ and $j^{1/2}\alpha_\perp$ is then peak velocity] of ref. 12 is to decouple the positive and negative energy waves and to remove the high-m stop bands. We recall from ref. 14 that for $j < 3$ all modes are stable.

The estimate given in ref. 12 for the FWHM of the peak in the j distributions is incorrect because of improper implicit expansion of $x^{1/2}$ about $x = 0$. The correct result is $\delta v_\perp(\text{FWHM})/V_\perp(\text{peak}) \cong [(\ln 4)/j]^{1/2}$, good to 2% for $j = 1, 2, 3, \ldots$.

We now display growth rate as a function of j, ϵ, ℓ, and m. Figure 1.3 shows $\gamma = \text{Im}\,\omega$ for the mode P_{01} as a function of ϵ with j as a curve label. Figure 1.4 presents the same data replotted to display γ as a function of $j^{-1} = (\delta v_\perp/V_\perp)^2/\ln 4$, with ϵ as a curve label. In both of these figures, the value of b is varied near π to maximize γ (zone P_{01}).

In Fig. 1.5 we show the ϵ dependence of γ for $j = 30$ when γ is maximized near $k_\perp V_\perp/\Omega = \pi$, 2π, and 3π (zones P_{01}, P_{02}, and P_{03}). Figure 1.6 shows P_{12} data for $j \to \infty$, with γ maximized near $k_\perp V_\perp/\Omega \cong 3\pi/2$.

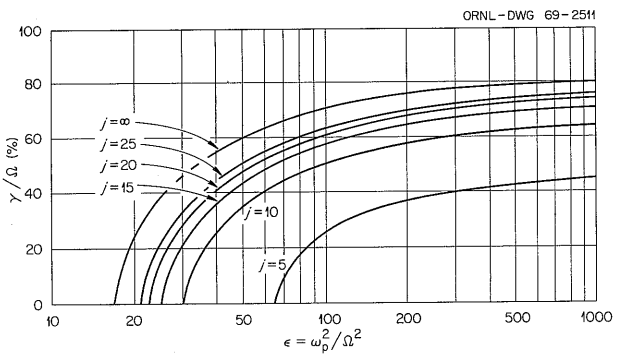

Fig. 1.3. Growth Rate of Zero-Frequency Mode as Function of Density and Energy Spread.

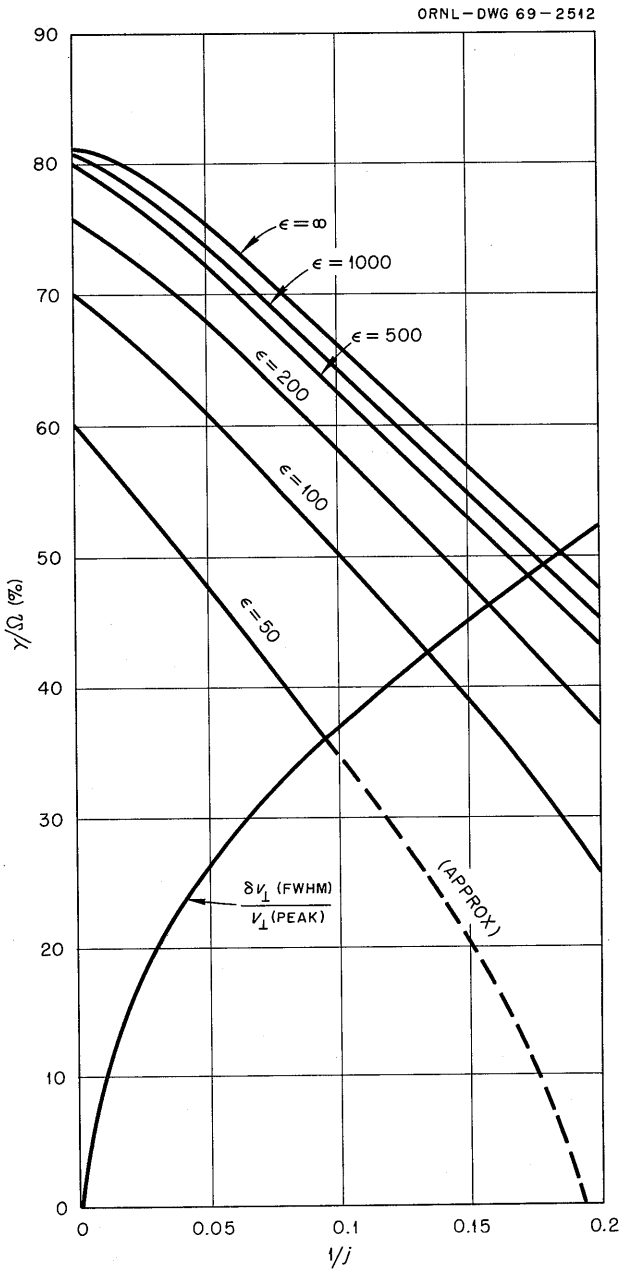

Fig. 1.4. Growth Rate of Zero-Frequency Mode as Function of Density and Velocity Spread.

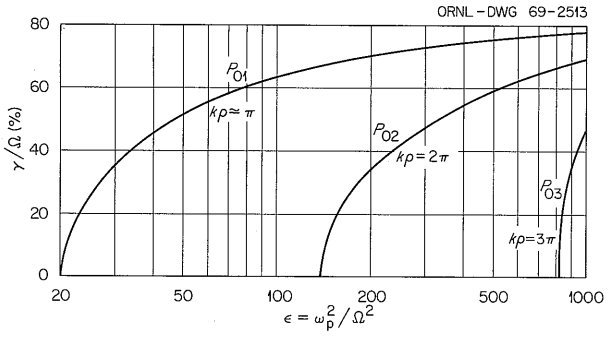

Fig. 1.5. Growth Rate of Zero-Frequency Mode as Function of Density for $k\rho \equiv k_\perp V_\perp/\Omega \simeq \pi$, 2π, 3π.

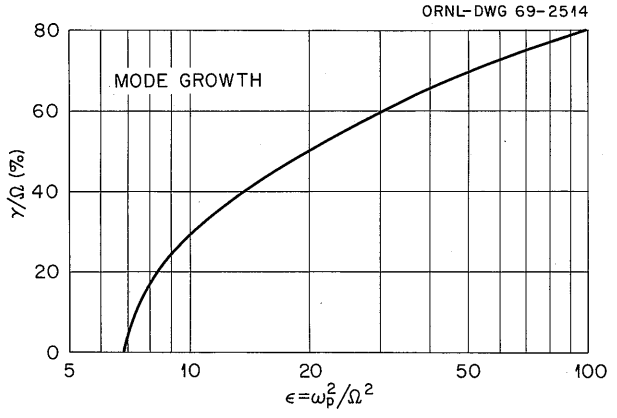

Fig. 1.6. Growth Rate of the Longest-Wavelength Mode with $1 < \mathrm{Re}\,(\omega/\Omega) < 2$. Here γ is maximized over $k_\perp V_\perp/\Omega$ near the value $3\pi/2$.

We would like to point out that the growth rates are easily found by singling out two resonant terms, say ℓ_1 and $\ell_2 = \ell_1 + 1$, in the ℓ sum of Eq. 1 and solving the resulting quadratic. To improve accuracy, the rest of the ℓ terms may be treated approximately by setting $w \simeq (\ell_1 + \ell_2)/2$ in them and re-solving the quadratic. If the resulting w is much displaced from $(\ell_1 + \ell_2)/2$, this new w may be put into the nonresonant terms and another solution found. The process will fail for b's such that $H_{\ell_2} \simeq 0$, where coupling of ℓ_1 to $\ell_3 = \ell_1 + 2$ becomes the dominant feature. This possibility is easily recognized and corrected.

The P_{0m} modes are especially easily solved since one knows from symmetry that $\mathrm{Re}\,\omega = 0$ and that the $\ell = \pm 1$ terms will usually be dominant.

Finally we would like to call attention to the zero slope portion at the upper right-hand corner of zone P_{01} in Fig. 1.2. This represents the unstable coupling of the negative energy wave $\omega/\Omega \lesssim 2$ to the positive energy wave $\omega/\Omega \gtrsim -2$ in the presence of the not-quite-zero contributions from $\ell = \pm 1$. This unstable mode has frequency just under Ω and has low growth rate. It occurs only for a small range of density at high values. Because it lies very close to the gyroharmonic, resonance detuning by relativistic effects[14] or magnetic field variation will probably cause it to disappear.

1.3.3 Flutelike Gyroharmonic Instabilities in Multicomponent Plasmas

R. A. Dory W. M. Farr
G. E. Guest

The techniques described in Sects. 1.3.1 and 1.3.2 facilitate the study of necessary conditions for stabilization of the well-known flutelike ($k_{\parallel} = 0$) high-frequency electrostatic instabilities which may occur when a hot non-Maxwellian plasma component exists together with a less-energetic Maxwellian group (assumed here to be of the same species). A sufficient condition for stability with respect to these modes is $\partial f_0/\partial v_\perp \leqq 0$ for the total distribution function. This condition can be satisfied by suitable adjustment of relative densities and temperatures of the non-Maxwellian and Maxwellian groups (for brevity we shall designate these simply as "hot" and "warm" particles), as shown, for example, in the reference of Sect. 1.2.3. But less restrictive necessary conditions may be desirable if the resonant loss-cone modes (Sect. 1.2.3) are stabilized by other means.

We simulate the velocity-space effects of mirror confinement in the usual way[11] and derive stability boundaries in the plane of relative density–relative temperature $(N_W/N_H - T_W/T_H)$ using the techniques of Sects. 1.3.1 and 1.3.2. Typical results are shown in Fig. 1.7. Here, the "hot" particle density parameter, $\epsilon = \omega_p^2(H)/\Omega^2$, is set at $\epsilon = 1000$, appropriate for hot-ion plasmas of fusion interest. The hot-particle distribution function models mirror confinement in a trap of mirror ratio 2 to 3 (in the language of ref. 11, $j = 1$). The three boundaries shown correspond to frequency ranges $\Omega < \omega \leqq 2\Omega$, $2\Omega < \omega \leqq 3\Omega$, and $4\Omega < \omega \lesssim 5\Omega$.

These results may be understood in terms of elementary wave properties in this plasma:

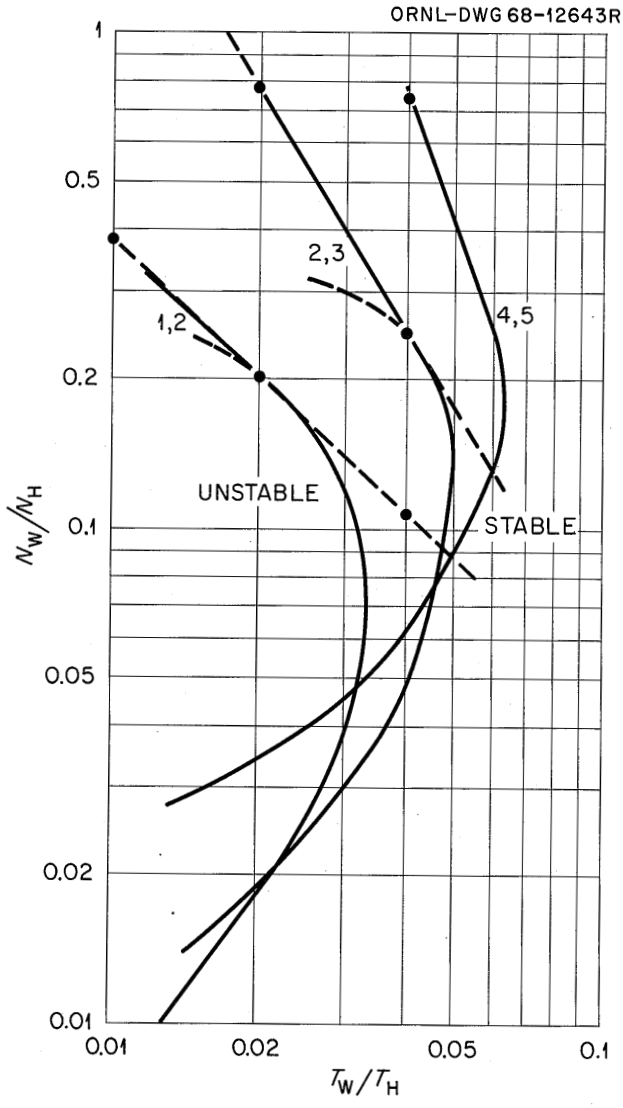

Fig. 1.7. Stability Boundaries for Flutelike ($k_{\parallel} = 0$) Modes in a Plasma Containing Maxwellian Ions (Density N_W, Temperature T_W) and Mirror-Confined Ions (N_H, T_W) of the Same Species. The three boundaries shown are for Re $(\omega/\Omega) \sim$ 2, 3, and 5.

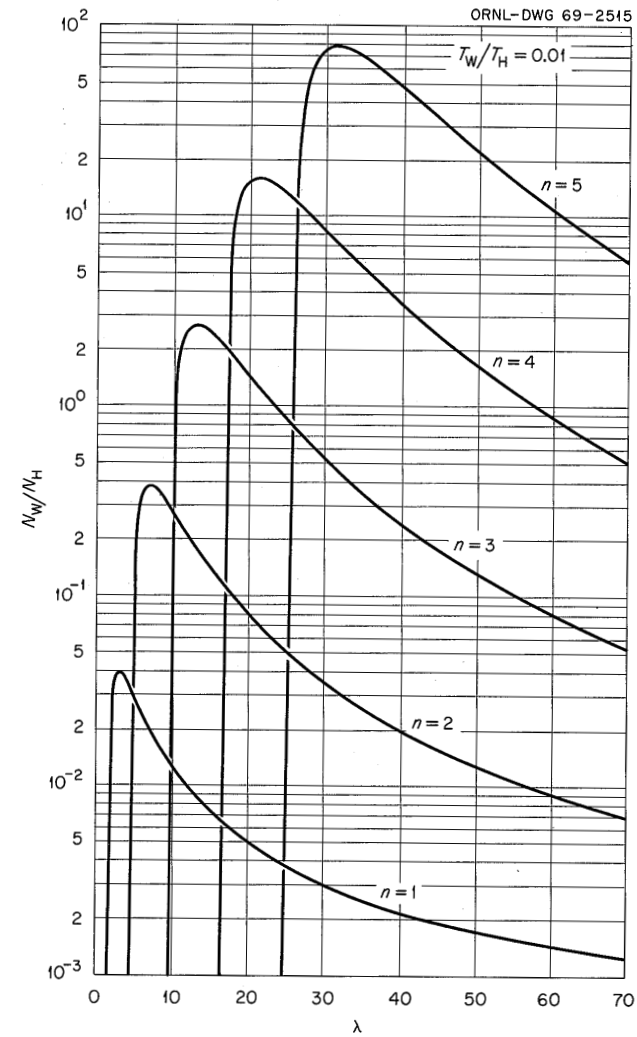

Fig. 1.8. Zeros of

$$\sum_{\text{species}} \omega_p^2 \left\langle \frac{1}{v_\perp} \frac{\partial}{\partial v_\perp} J_n^2 \left(\frac{k_\perp v_\perp}{\Omega} \right) \right\rangle$$

for the Two-Component Plasma with $T_W T_H = 0.01$. $\lambda \equiv k_\perp^2 < v_\perp >^2 / 2\Omega^2$.

1. The upper (nearly linear) portion of the boundary corresponds closely to the conditions under which the cyclotron wave with $\omega \lesssim n\Omega$ has negative kinetic power, while the wave with $\omega > (n-1)\Omega$ has positive kinetic power. That is,

$$\sum_{\text{species}} \frac{\omega_p^2}{k^2} \left\langle \frac{1}{v_\perp} \frac{\partial}{\partial v_\perp} J_m^2 \left(\frac{k_\perp v_\perp}{\Omega} \right) \right\rangle \begin{array}{l} < 0, \; m = n \; , \\ > 0, \; m = n - 1 \; . \end{array} \tag{1}$$

Since this criterion depends on relative density, relative temperature, and wavelength, it is helpful to construct curves along which the weighted averages (above) vanish. An example is shown in Fig. 1.8, where we plot zeros of (1) in the N_W/N_H-λ plane ($\lambda \equiv k_\perp^2 \rho_H^2/2$) for $T_W/T_H = 0.01$. Notice that condition (1) requires that λ increase as N_W/N_H decreases.

2. The lower portion of the boundary relates to the wave-propagation cutoff which occurs when

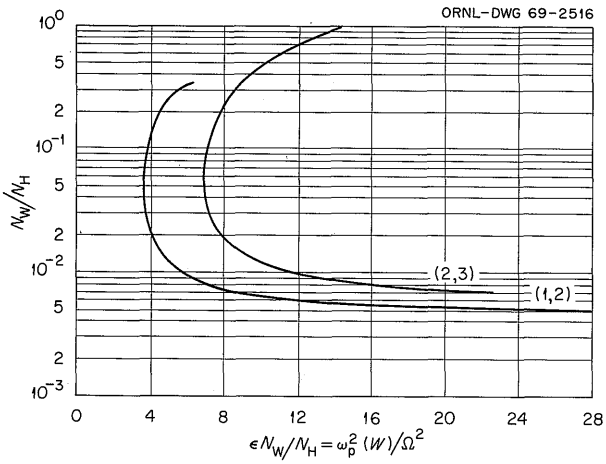

Fig. 1.9. Threshold Densities for Flutelike Modes in a Two-Component Plasma with $T_W/T_H = 0.01$. Curves shown are for Re $(\omega/\Omega_i) \sim 2$ and 3.

wavelengths decrease to values comparable with warm-particle gyroradii.

3. Threshold densities are related (but not simply) to the condition for warm-ion hybrid frequency resonance with the nth gyroharmonic:

$$\frac{\omega_p^2(W)}{\Omega^2} \approx f(\lambda, n) \to n^2 - 1 \text{ as } \lambda \to 0 .$$

Since we have defined $\epsilon = \omega_p^2(H)/\Omega^2$, this requires $\epsilon \times N_W/N_H \approx n^2 - 1$. Figure 1.9 shows the behavior of $\epsilon \times N_W/N_H$ at the threshold for growth as N_W/N_H is varied. The excursion to large values as N_W/N_H decreases indicates the approaching cutoff of propagation.

Within the stability boundaries discussed above, temporal growth rates of unstable modes may approach the gyrofrequency, Ω. Since growth may occur over a wide band of relative densities if T_W/T_H is small, minimum relative temperatures of $\sim 10\%$ may be necessary to suppress these modes in multicomponent plasmas. Although the stability boundaries shown here are derived for hot and warm particles of the same species, they may be extended easily to systems containing heavier cold impurities, for example. Similar conclusions are anticipated.

1.3.4 Explosive Instabilities

E. G. Harris[15]

Explosive instabilities are nonlinear instabilities which occur in plasmas in which negative energy waves may propagate.[16,17] They are called explosive because the amplitude of the disturbance can become infinite in a finite time. The instability occurs through the nonlinear coupling of two positive energy waves and one negative energy wave or two negative energy waves and one positive energy wave. In either case, all three waves may grow without violating the conservation of energy.

Consider the interaction of three monochromatic waves with complex amplitudes C_1, C_2, and C_3. The Hamiltonian for the system may be written as

$$\begin{aligned} H = {} & S_1\hbar\Omega_1 C_1^* C_1 + S_2\hbar\Omega_2 C_2^* C_2 + S_3\hbar\Omega_3 C_3^* C_3 \\ & + \hbar M_1 C_1^* C_2^* C_3^* + \hbar M_1^* C_1 C_2 C_3 \\ & + \hbar M_2 C_1^* C_2^* C_3 + \hbar M_2^* C_1 C_2 C_3^* \\ & + \hbar M_3 C_1^* C_2 C_3^* + \hbar M_3^* C_1 C_2^* C_3 \\ & + \hbar M_4 C_1^* C_2 C_3 + \hbar M_4^* C_1 C_2^* C_3^* . \end{aligned} \tag{1}$$

Here, Ω_1, Ω_2, and Ω_3 are the (positive) frequencies of the waves; $\hbar$ is Planck's constant and will not appear in the final results. The sign of the energy of a wave is given by

$$S_i = \left[\frac{(\partial/\partial\omega)[\omega\ \epsilon(\mathbf{k}, \omega)]}{|(\partial/\partial\omega)[\omega\ \epsilon(\mathbf{k}, \omega)]|} \right]_{\omega=\Omega_i} = \pm 1 . \tag{2}$$

The amplitudes have been normalized so that the energy of a wave is given by $S_i\hbar\Omega_i C_i C_i$. The asterisk denotes a complex conjugate. The coupling constants M_1, M_2, M_3, and M_4 must be determined from a theory of nonlinear interactions.

---

[15] Consultant from the University of Tennessee, Physics Department, Knoxville, Tenn.

[16] R. E. Aamodt and M. L. Sloan, *Phys. Rev. Letters* **19**, 1227 (1967).

[17] M. N. Rosenbluth, B. Coppi, and R. N. Sudan, paper CN-24/E-13 presented at the Third International Conference on Plasma Physics and Controlled Thermonuclear Research, Novosibirsk, U.S.S.R., 1968 (to be published).

The Hamiltonian equations of motion are:

$$\dot{C}_i = \frac{dC_i}{dt} = \frac{-i}{\hbar}\frac{\partial H}{\partial C_i^*}, \tag{3}$$

from which

$$\dot{C}_i = -iS_1\Omega_1 C_1 - iM_1 C_2^* C_3^* - iM_2 C_2^* C_3 - iM_3 C_2 C_3^* - iM_4 C_2 C_3 , \tag{4}$$

with similar equations for C_2 and C_3. We shall assume that waves 1 and 2 are positive energy waves and that 3 is a negative energy wave. In the absence of nonlinear interactions, the solution would be:

$$C_1(t) = A_1 e^{-i\Omega_1 t} , \tag{5}$$

$$C_2(t) = A_2 e^{-i\Omega_2 t} , \tag{6}$$

$$C_3(t) = A_3 e^{+i\Omega_3 t} . \tag{7}$$

In the presence of nonlinear interactions, we shall assume solutions of the above form but allow A_1, A_2, and A_3 to be time-dependent. Then

$$\begin{aligned}\dot{A}_1 = &-iM_1 e^{i(\Omega_1+\Omega_2-\Omega_3)t} A_2^* A_3^* \\ &-iM_2 e^{i(\Omega_1+\Omega_2+\Omega_3)t} A_2^* A_3 \\ &-iM_3 e^{i(\Omega_1-\Omega_2-\Omega_3)t} A_2 A_3^* \\ &-iM_4 e^{i(\Omega_1-\Omega_2+\Omega_3)t} A_2 A_3 ,\end{aligned} \tag{8}$$

with similar equations for A_2 and A_3. We shall assume that

$$\Omega_1 + \Omega_2 - \Omega_3 = 0 . \tag{9}$$

Then all of the terms on the right-hand side of Eq. (8) except the first contain rapidly oscillating factors and may be neglected if the nonlinear interaction is sufficiently weak. Assuming this to be the case we obtain:

$$A_1 = -iM_1 A_2^* A_3^* , \tag{10}$$

$$A_2 = -iM_1 A_1^* A_3^* , \tag{11}$$

$$A_3 = -iM_1 A_1^* A_2^* . \tag{12}$$

This set of nonlinear equations can be solved exactly. The solution is particularly simple if one of the amplitudes (we shall suppose that it is A_1) vanishes at $t = 0$. Then the solution is:

$$\int_0^{|A_1|} \frac{dx}{\sqrt{(|A_{20}|^2 + x^2)(|A_{30}|^2 + x^2)}} = |M_1| t , \tag{13}$$

where A_{20} and A_{30} are the initial values of A_2 and A_3. If we assume that $|A_{20}| = |A_{30}|$, then the integral is elementary and

$$|A_1| = |A_{20}| \tan |M_1 A_{20}| t . \tag{14}$$

We see that the amplitude of wave 1 grows from zero to infinity in a time

$$t_\infty = \frac{\pi}{2|M_1 A_{20}|} . \tag{15}$$

As an application of these ideas, we shall consider an unmagnetized plasma with a distribution function for the electrons

$$f(v) = n_1 \delta(\mathbf{v}) + n_2 \delta(\mathbf{v} - \mathbf{V}) . \tag{16}$$

The ions are assumed to be infinitely massive. The dielectric function is

$$\epsilon(\mathbf{k}, \omega) = 1 - \frac{\omega_{p1}^2}{\omega^2} - \frac{\omega_{p2}^2}{(\omega - \mathbf{k}\cdot\mathbf{V})^2} . \tag{17}$$

The equation $\epsilon(\mathbf{k}, \omega) = 0$ has four roots. When all four frequencies are real, three roots correspond to positive energy waves and one to a negative energy wave. We shall consider the coupling of two of the positive energy waves and the negative energy wave. Conservation of momentum requires that

$$\mathbf{k}_1 + \mathbf{k}_2 + \mathbf{k}_3 = 0 . \tag{18}$$

For simplicity we shall choose

$$\mathbf{k}_1 = \mathbf{k}_3 , \tag{19}$$

$$\mathbf{k}_2 = -2\mathbf{k}_1 , \tag{20}$$

$$\Omega_1 \cong \Omega_2 \cong \omega_{p1} , \tag{21}$$

$$\Omega_3 \cong k_3 V - \omega_{p2} . \tag{22}$$

Equation (9) gives

$$\Omega_3 = 2\omega_{p1} , \tag{23}$$

so

$$k_3 = k_1 = \frac{2\omega_{p1} + \omega_{p2}}{V} \tag{24}$$

Wave 3 is the negative energy wave. All wave vectors are taken to be parallel or antiparallel to the direction of **V**.

The coupling constant M_1 for an unmagnetized plasma has been calculated elsewhere[18] and shown to be

$$M_1 = \frac{U}{\hbar m^2} R_1 R_2 R_3 \int d^3v\, f(\mathbf{v}) \frac{1}{\lambda_1 \lambda_2 \lambda_3} \left[\frac{k_1^2(\mathbf{k}_2 \cdot \mathbf{k}_3)}{\lambda_1} + \frac{k_2^2(\mathbf{k}_1 \cdot \mathbf{k}_3)}{\lambda_2} + \frac{k_3^2(\mathbf{k}_1 \cdot \mathbf{k}_2)}{\lambda_3} \right] , \tag{25}$$

where

$$\lambda_i = \Omega_i - \mathbf{k}_i \cdot \mathbf{v} , \tag{26}$$

$$R_i = \left[\frac{4\pi e^2 \hbar \Omega_i}{U k^2 |(\partial/\partial\omega)(\omega\epsilon)|_{\Omega_i}} \right]^{1/2} , \tag{27}$$

and U is the volume of the system.

After some algebra, we can use Eq. (16) in Eq. (25) to obtain M_1 and substitute the result into Eq. (15) to obtain

$$\frac{1}{\omega_{p1} t_\infty} = \frac{9}{20\sqrt{2\pi}} \sqrt{\frac{\omega_{p2}}{\omega_{p1}}} \left(\frac{\delta n_{20}}{n_1} \right) , \tag{28}$$

where δn_{20} is the initial perturbation in density due to wave 2. In obtaining Eq. (28), we have assumed that $\omega_{p2} \ll \omega_{p1}$ and used

$$\frac{1}{8\pi} E_{20}^2 = \frac{\hbar \Omega_1 |A_{20}|^2}{U |(\partial/\partial\omega)(\omega\epsilon)|_{\Omega_i}} \tag{29}$$

and

$$k_1 E_{20} = 4\pi e \delta n_{20} . \tag{30}$$

A more interesting case of an explosive instability occurs when a wave propagates perpendicular to a magnetic field in a plasma which has a loss cone distribution. (See Sects. 1.3.1 and 1.3.3.) This is being investigated by J. Fukai and E. Harris.

1.3.5 Loss-Cone Modes in Finite-Length Plasmas

C. O. Beasley H. Grawe[9]

A model of a mirror-confined plasma is used to investigate instabilities in inhomogeneous plasmas. The plasma is assumed to be infinite and uniform in the direction perpendicular to the (uniform) magnetic field, but confined by a parabolic potential to a finite region along the magnetic field. The corresponding distribution may be written

$$F_0 = \frac{1}{\pi^{3/2} \alpha_{\parallel} \alpha_\perp^2 j!} e^{-(z^2/L^2) - (v_\parallel^2/\alpha_\parallel^2)} \times \left(\frac{v_\perp}{\alpha_\perp} \right)^{2j} e^{-v_\perp^2/\alpha_\perp^2} ,$$

where we have included the effect of a loss cone in velocity space. This model, though not a true mirror-confined equilibrium, should allow a study of the effects of plasma inhomogeneity along the magnetic field on plasma instabilities provided other effects such as magnetic field inhomogeneities do not dominate. In some cases, such as plasmas with little spread in perpendicular energy, the model gives a close approximation to reality.

The Vlasov and Poisson equations for this model lead to an exact integral equation for the perturbed potential. In integrating the Vlasov equation over velocity space, one separates the ϕ and $v_\perp$ integrations and performs them first, since the $v_\parallel$ variable is coupled with the spatial variable z. By assuming that the perturbed potential ϕ is periodic along the direction of the magnetic field, which may always be done if ϕ vanishes at some point representative of the boundaries of the system, one may write this potential as a Fourier sum. One may then do the

[18] E. G. Harris, to be published in *Advances in Plasma Physics* (Wiley, New York).

$v_{\parallel}$ integration to obtain an expression for the perturbed charge density along the magnetic field. Finally, Poisson's equation with appropriate boundary conditions leads to an integral equation for the perturbed charge density.

For even potentials, we use the boundary conditions $\phi(0) = 1$, $\phi'(0) = 0$ (ϕ the perturbed charge density). For odd potentials, we use $\phi(0) = 0$, $\phi'(0) = 1$. These boundary conditions, plus the constraint that the potential vanish at some point represented by the boundary of the system, determine the eigenvalue ω_p^2 and the eigenfunction ϕ for this integral equation for each frequency ω for a given set of plasma parameters). By examination of the eigenmodes of a range of frequencies, one may determine the marginally stable frequencies and densities and growth rates of unstable modes.

1.3.6 Microinstabilities in Hot-Electron Plasmas

C. O. Beasley G. E. Guest
W. M. Farr D. J. Sigmar

Electrostatic instabilities may occur in non-Maxwellian plasmas as a result of ion-ion interaction in the presence of hot electrons or electron-electron interaction in the presence of cold ions. We extend earlier work[19,20] on these instabilities and report on zero-frequency, $k_{\parallel} \neq 0$ modes not mentioned by these authors. In the case of ion-ion modes, a second less-energetic species of ions is included in the calculation, and in the case of electron-electron modes, a low-temperature electron component is included. For the ion-ion modes, the electron contribution determines a critical electron temperature ($T_{e\ \mathrm{crit}} \gtrsim 3.5E_{\parallel i}$) below which the modes are cut off (Fig. 1.10). For the electron modes, no such cutoff exists. Except for this difference, one can immediately convert the ion-mode results into electron-mode results simply by relabeling the gyrofrequency, gyroradius, etc. In the ion-ion case, the electron contribution vanishes in the limit of high electron temperature, while in the electron-electron case, the ion contribution vanishes in the limit $\omega \sim \omega_{ce} \gg \omega_{pi}$. In these limits, the threshold density is determined solely by the characteristics of the mirror distribution. It is a strong function of the anisotropy, and in a loss-cone plasma, depends on the spread in perpendicular energy. Figure 1.11 shows the threshold density for a weak ($j = 1$) and a strong ($j = 5$) loss cone as a function of the anisotropy. Absolutely unstable modes at Re $\omega \sim (n + \frac{1}{2})\omega_c$ with temporal growth rates $\omega_i \lesssim \omega_c/2$ can occur for $\omega_p^2/\omega_c^2 \lesssim 0.3$, at wavelengths $\lambda_{\parallel}/\rho < 1$, $\lambda_{\perp}/\rho > 2$, where ω_c is the gyrofrequency and ρ the gyroradius. Addition of cold plasma raises the thresholds for absolute instabilities but lowers the marginal or convective threshold, thus allowing for a region of convective instability with growth lengths of $O(10\rho)$. These

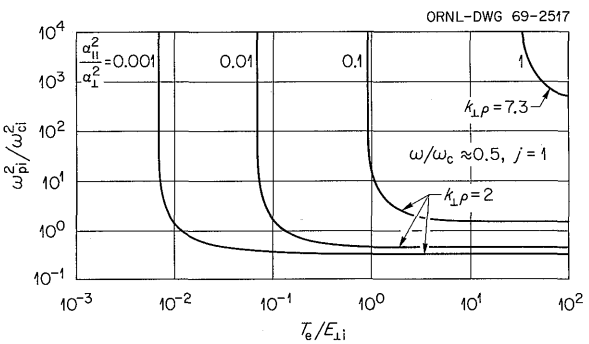

Fig. 1.10. Marginally Stable Density as Function of Electron Temperature (over Perpendicular Ion Energy) for Several Anisotropies $\alpha_{\parallel}^2/\alpha_{\perp}^2$.

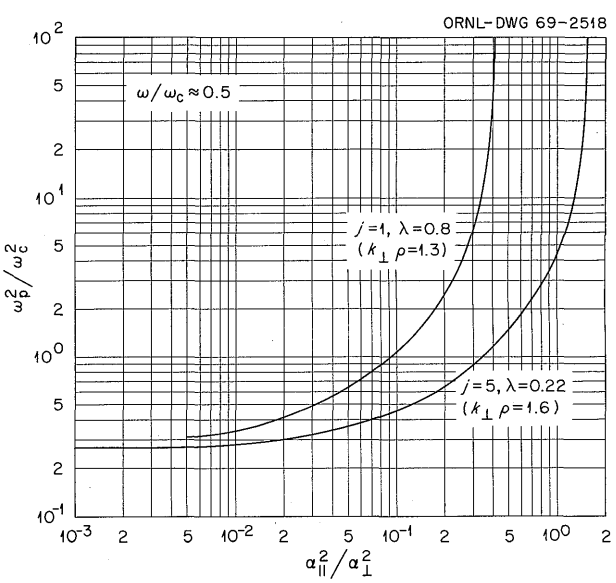

Fig. 1.11. Marginally Stable Density vs Anisotropy in the Limit $T_e \to \infty$ for a Weak Loss Cone ($j = 1$) and Strong Loss Cone ($j = 5$). See ref. 11 for definition of j.

[19] A. V. Timofeev, *JETP* **12**, 281 (1961).

[20] L. S. Hall, W. Heckrotte, and T. Kammash, *Phys. Rev.* **139**, A1117 (1965).

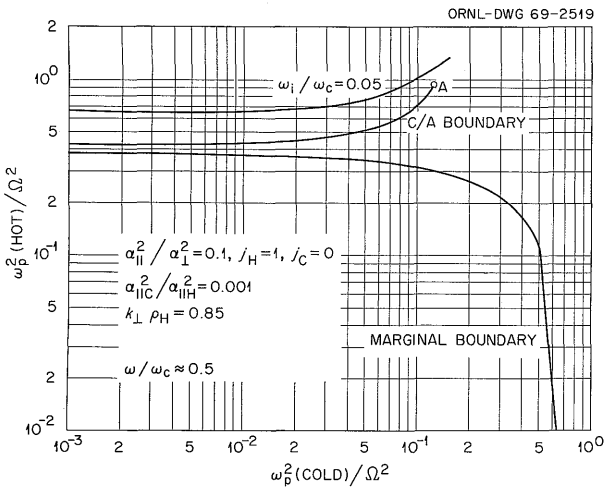

Fig. 1.12. Curves of Marginal Stability, Convective-Absolute Transition Boundary, and Constant Temporal Growth Rate in the Plane of ϵ_H and ϵ_C, $\epsilon = \omega_p^2/\Omega^2$. Here $j(\mathrm{hot}) = 1$, $j(\mathrm{cold}) = 0$, $(\alpha_{\parallel}^2\ \alpha_{\perp}^2)(\mathrm{hot}) = 0.1$, $\alpha_{\parallel}^2(\mathrm{cold})/\alpha_{\parallel}^2(\mathrm{hot}) = 0.001$, $\omega/\Omega \approx 0.5$, $k_{\perp}\rho_H = 0.85$.

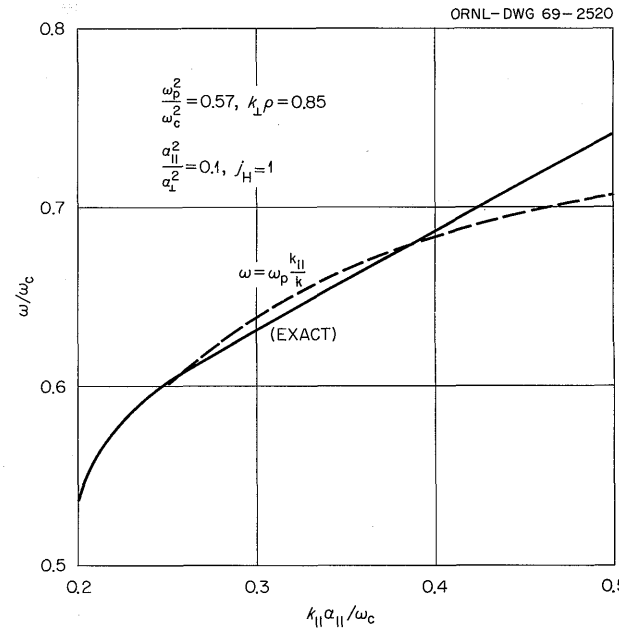

Fig. 1.13. Comparison Between the Exact Dispersion Curve and $\omega = \omega_p k_{\parallel}/k$.

results are illustrated in Fig. 1.12. At point A (Fig. 1.12) one finds a spatial growth rate of $|\lambda_{\parallel i}| = 7.6\rho$, for example. Note that the marginal threshold curve intersects the horizontal axis at $\omega_p/\omega_c = 0.8$, which is equal to the value of the frequency ω/ω_c. This supports the notion that the fundamental mode is a plasma oscillation. Figure 1.13 shows this clearly in an ω-$k_{\parallel}$ diagram.

The zero-frequency modes are absolute, having similarly large temporal growth rates, but occur at densities $\omega_p^2/\omega_c^2 \gtrsim 40$. They require a spatial resonance condition $\lambda_{\perp} \approx 2\rho$ and cannot propagate if cold plasma is present.

Analytic estimates for thresholds, critical electron temperature, limiting growth rates, onset of absolute growth, and influence of a cold species are supported by extensive numerical solutions. A detailed technical report on this work is in preparation.

1.3.7 Unstable Waves in Beam-Plasma Systems

G. E. Guest R. A. Dory

The development of high-frequency diagnostic techniques for the hot-electron plasmas produced by turbulent heating has permitted observation of regular trains of oscillations having frequencies near the electron plasma frequency, ω_{pe} (hence typically $\sim\Omega_e/10$), and phase velocities along the magnetic field near the electron-beam speed. In order to make a provisional identification of the type of interaction responsible for the generation of these waves, we have calculated threshold conditions, growth rates, frequencies, and wavelengths of electrostatic instabilities expected to occur in plasmas containing two oppositely directed, spatially homogeneous beams of monoenergetic electrons passing through a homogeneous background plasma. Ions were assumed to be infinitely massive for the present purposes.

The dispersion relation appropriate to this model is well known:

$$\frac{\Omega_e^2}{\omega_p^2} = \frac{k_{\perp}^2}{k^2}\left[\frac{1}{(W-H)^2-1} + \frac{1}{(W+H)^2-1}\right] + \frac{k_{\parallel}^2}{k^2}\left[\frac{1}{(W-H)^2} + \frac{1}{(W+H)^2}\right] + \frac{N_e}{N_b}\left(\frac{k_{\parallel}^2}{k^2}\frac{1}{W^2} + \frac{k_{\perp}^2}{k^2}\frac{1}{W^2-1}\right) .$$

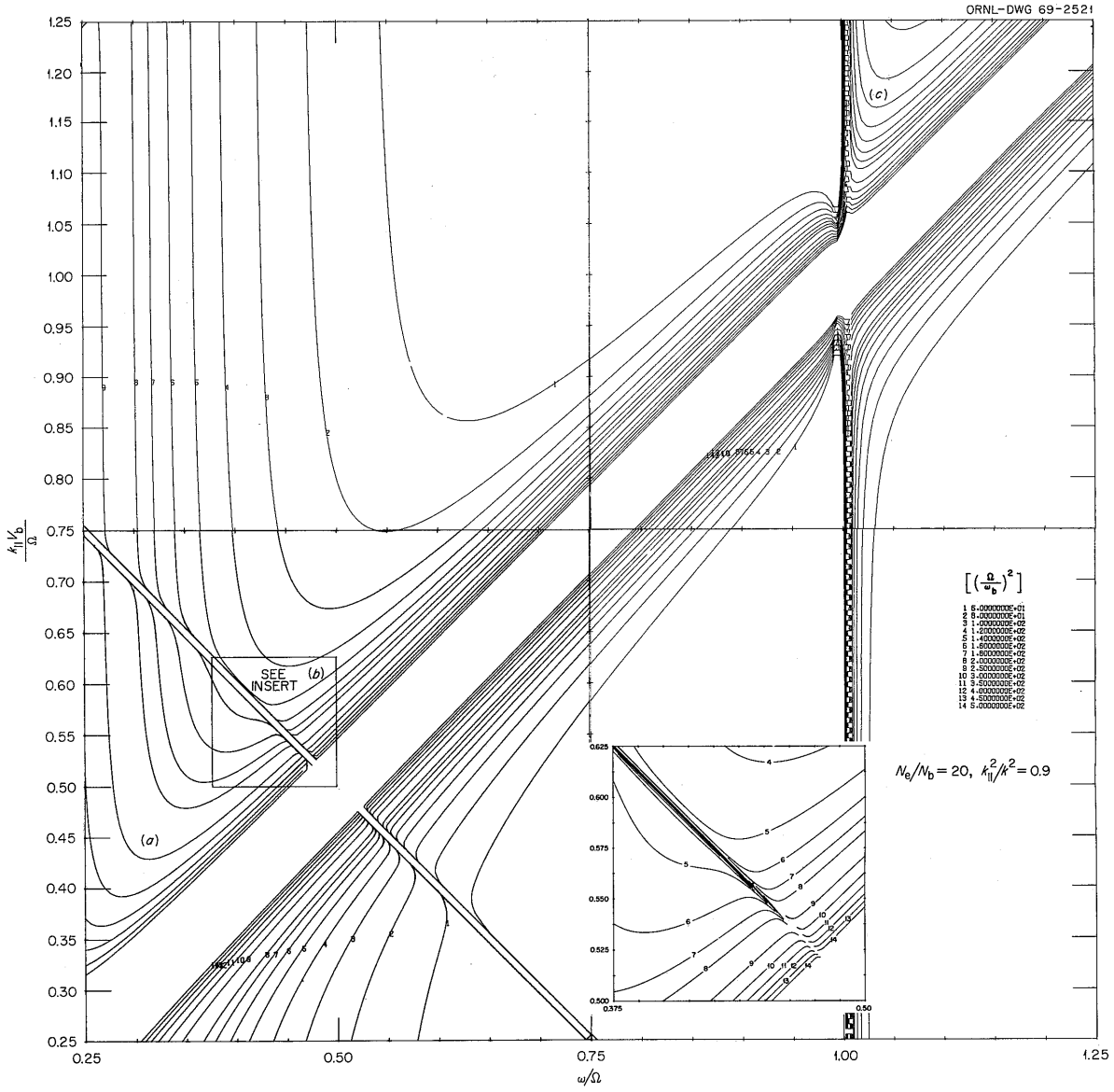

Fig. 1.14. Brillouin Diagram for the Plasma Model of Sect. 1.3.7. $N_e/N_b = 20$, $k_{\parallel}^2/k^2 = 0.9$.

Here $W \equiv \omega/\Omega_e$, $H \equiv k_{\parallel}v_b/\Omega_e$, $\omega_b^2/\Omega_e^2 = mN_b/(\epsilon_0 B^2)$, and N_e and N_b denote plasma and beam densities. The various unstable wave interactions anticipated in such a plasma are suggested by the Brillouin diagram shown in Fig. 1.14 (here $N_e/N_b = 20$ and $k_{\parallel}^2/k^2 = 0.9$):

a) slow space-charge wave on the beams coupling to plasma oscillations in the background plasma;

b) slow space-charge waves on one beam coupling to cyclotron waves on the opposite beam; and

c) slow space-charge waves on the beams coupling to cyclotron waves in the background plasma.

For plasma parameters typical of the ORNL beam-plasma experiments,[21] type *a* modes are unstable over a broad range of frequencies and wavelengths; type *b* and type *c* modes grow only over much narrower bands. This behavior is illustrated

[21] R. V. Neidigh *et al.*, paper CN-24/L-2, presented at the Third Conference on Plasma Physics and Controlled Nuclear Fusion Research, Novosibirsk, U.S.S.R., Aug. 1–7, 1968.

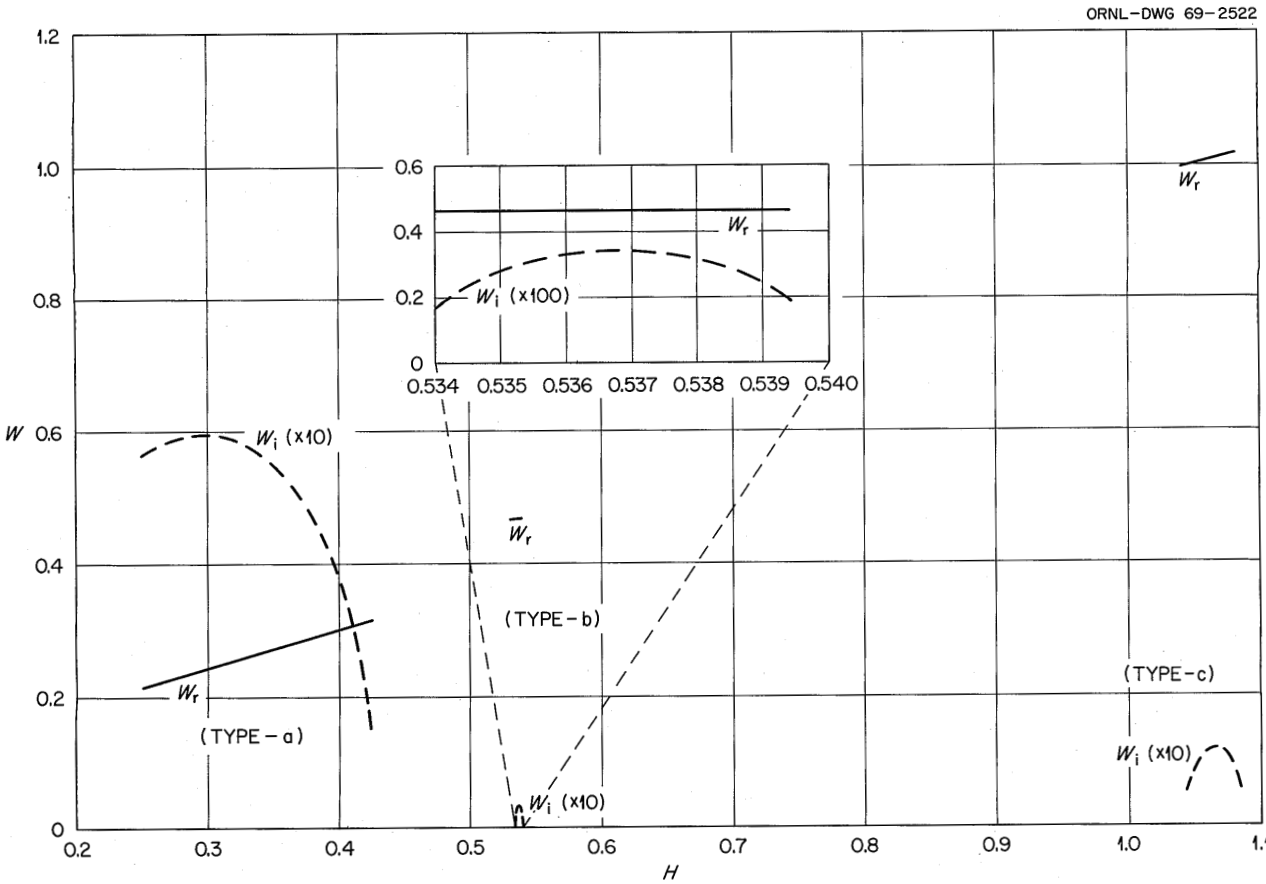

Fig. 1.15. Growth Rate and Frequency for Type *a* Instabilities. $\omega_p^2/\Omega_e^2 = 0.004$, $N_e/N_b = 20$, $k_{||}^2/k^2 = 0.9$.

in Fig. 1.15, where we plot frequency and growth rate in the unstable bands for plasma parameters and propagation angle corresponding to curve 9 of Fig. 1.14: $\omega_b^2/\Omega_e^2 = 0.004$, $N_e/N_b = 20$, and $k_{||}^2/k^2 = 0.9$. Stable frequencies and wavelengths can be read directly from Fig. 1.14. Growth rates of type *b* modes are greatest for $k_{||} \approx k_\perp$, for which the Brillouin plot is shown in Fig. 1.16. Even in this optimum case, type *b* growth rates are roughly an order of magnitude smaller than the other two modes.

Since the present plasma model assumes each electron group to be monoenergetic, it cannot account for the dissipation resulting from thermal spread in particle speeds. One such dissipation, cyclotron damping, is important if

$$(W - 1)/H \lesssim \sqrt{T_e/E_b},$$

where T_e is the temperature of the background electrons and E_b is the beam energy. Since $(W - 1)/H \sim 0.01$ for type c modes, strong cyclotron damping of this mode should occur for $T_e \gtrsim 10^{-4} E_b$; that is, for electron temperatures greater than a few electron volts. By contrast, Landau damping of type *a* modes requires $T_e \sim E_b$.

In Fig. 1.17, we plot the type *b* wave parameters vs beam density, ω_b^2/Ω_e^2, for $k_{||} \approx k_\perp$ and $N_e/N_b = 20$. Shown here are the marginally stable values of H, together with the maximum growth rate and the corresponding frequency. The range of unstable frequencies is very narrow: $\Delta W/W \approx 1.4 \times 10^{-3}$ for $\omega_b^2/\Omega_e^2 = 0.007$, and is proportional to ω_b^2/Ω_e^2 over the range shown. Because of the weak growth and narrow band behavior, spatial inhomogeneities may stabilize these modes in the experimental plasmas.

We therefore expect type *a* modes to dominate the observed rf spectrum and seek to compare the experimental observations with this model calculation by assuming that the observed frequencies and

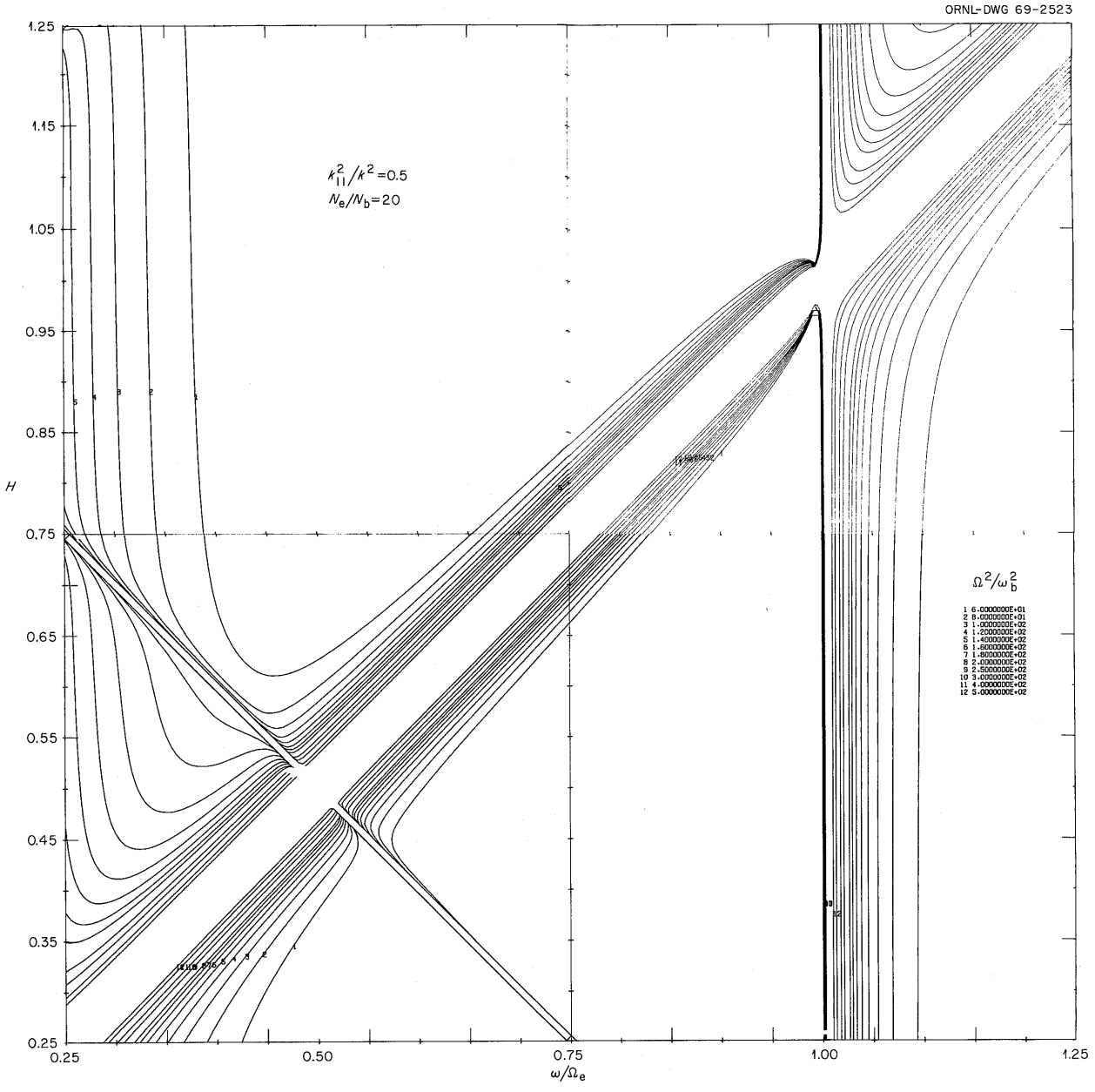

Fig. 1.16. Brillouin Diagram for the Plasma Model of Sect. 1.3.7. $N_e/N_b = 20$ and $k_{||}^2/k^2 = 0.5$.

wavelengths should be those of the fastest-growing modes. Thus we can plot (W, H) for maximum growth rate as a function of beam density (through ω_b^2/Ω_e^2) for various values of N_c/N_b. Data of this sort are presented in ref. 21. Uncertainties in the experimental plasma parameters and major idealizations in the present theoretical model prevent firm conclusions, but it is likely that the observed signals are electron plasma oscillations driven to large amplitude by coupling of the slow space-charge waves on the beams.

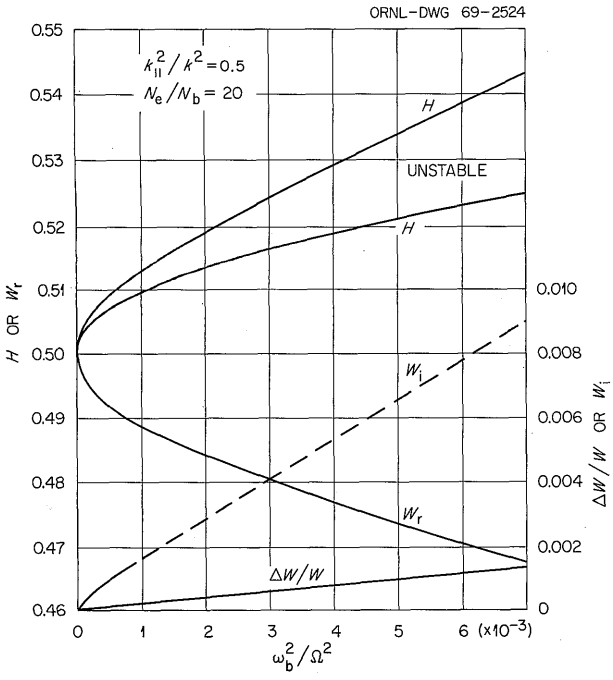

Fig. 1.17. Type *b* Wave Parameters vs ω_b^2/Ω_e^2 for $k_{\parallel} = k_{\perp}$. Marginally stable values of H, frequency (W_r = Re ω/Ω_e) and growth rate (W_i = Im ω/Ω_e) for maximum growth, and width, $\Delta W/W$, for the unstable band of frequencies.

1.4 NEW PROJECTS

1.4.1 Numerical Simulation of Plasma

R. A. Dory H. K. Meier

The theory of small perturbations about a simple plasma equilibrium gives a large amount of information useful in the study of plasma confinement. However, this theory does not answer such questions as saturation levels of unstable growth, effect of instability on plasma distribution, mechanisms and rates of particle loss, and so on. Much effort has been directed toward remedying this through quasi-linear theory or turbulence theory. The effort has been partially successful, but many interesting and even crucial areas have not yet been treated nor are likely to be in the near future.

An alternative approach is to use numerical techniques and computers, taking advantage of any available overlap with the analytical techniques mentioned above to provide checks and guidelines for procedures. We have begun studies of numerical methods (*simulation* for short) related to those that have been and are being used by others. For historical and bibliographic references, we suggest the proceedings of two recent symposia[22,23] and note especially the quite complete survey given by Birdsall at the Williamsburg meeting. To this bibliography we add an early effort from the field of particle accelerators,[24] where many of the same techniques lead to new stable equilibria despite Coulomb repulsion among the beam particles.[25]

The present studies are in the very initial phase of searching for solvable interesting problems and for viable techniques. The few concrete portions represent building blocks with which results are eventually to be obtained.

The task of plasma physics is to predict and influence the behavior of a large number of particles (of the order of order 10^{16}) under the influence of both externally applied electric and magnetic fields and internal fields whose sources are currents and charge imbalances in the particles. To treat such a problem realistically on a computer by following the motion of each of the particles is not yet possible. For example, assuming about two orders of magnitude improvement in speed of computing (one nanosecond per operation), the setting up of 6×10^{16} initial coordinates would require two years of computation time. To advance the coordinates through *simulation time* would require orders of magnitude more computation time. The storage requirements too are of the wrong *order of order* of magnitude to be feasible in the near future.

Since the problem is so huge, one must resort to model calculations: that is, to take into account those effects that seem most likely to be important and neglect the rest. This of course is normal procedure – the trouble is that with only the "important" effects, the problem is still too formi-

[22] *Symposium on Computer Simulation of Plasma and Many-Body Problems*, NASA report SP-153 (1967).

[23] "Conference on Numerical Simulation of Plasma," *Bull. Am. Phys. Soc.* **13**, 1744 (1968); proceedings available as Los Alamos Scientific Laboratory report LA-3900 (1968).

[24] R. A. Dory, Midwestern Universities Research Association report No. 654, *Nonlinear Azimuthal Space Charge Effects* (thesis, University of Wisconsin, Department of Physics, 1962).

[25] R. A. Dory, *Plasma Phys.* **6**, 511 (1964).

dable, and one must reassess "importance" and find further or better approximations.

We outline some approaches and attempt to summarize the results.

1.4.1.1. Vlasov Equation Solving. — In the limit of many particles in the Debye sphere, the Vlasov equation is traditionally applied, using internal fields averaged over distances like the Debye length λ_D. Microfields with shorter wavelengths than λ_D are neglected or occasionally included through Fokker-Planck diffusion coefficients. The problem is described by $f(\mathbf{x}, \mathbf{v}, t)$, the phase-space particle distribution function, which is followed through time using Vlasov's equation:

$$\frac{\partial f}{\partial t} + \mathbf{v}\frac{\partial f}{\partial \mathbf{x}} + \mathbf{a}\frac{\partial f}{\partial \mathbf{v}} = 0 \quad or \quad = \frac{\partial f}{\partial t}\text{Fokker-Planck} \ , \quad (1)$$

where $\mathbf{a}$ is the single-particle acceleration,

$$\mathbf{a} = (e/m)(\mathbf{E} + \mathbf{v} \times \mathbf{B}) \ ,$$

with $\mathbf{E}(\mathbf{x}, t)$ and $\mathbf{B}(\mathbf{x}, t)$ given by the sum of external and internal fields. The internal fields are determined from Maxwell's equations using charge and current densities

$$\rho = \int d^3v \, f \quad \text{and} \quad \mathbf{j} = \int d^3v \, f\mathbf{v} \ , \qquad (2)$$

which are smooth over distances like the Debye length.

Maxwell's equations combined with (1) and (2) are treated as an initial value problem, beginning with interesting initial conditions $f(\mathbf{x}, \mathbf{v}, 0)$, $\mathbf{E}(\mathbf{x}, 0)$, and $\mathbf{B}(\mathbf{x}, 0)$.

If the model problem is one-dimensional so that $\mathbf{x}$, $\mathbf{v}$, $\mathbf{E}$, and $\mathbf{B}$ become scalars, a relatively simple procedure can be used. Armstrong and Montgomery[22,23] as well as Feix and Grand[22,23] perform Fourier (in x) and Hermite (in v) expansions of $f(x, v, t)$ and follow the evolution in time of the amplitudes $f(k, m, t)$, where k is the wave number and m is the Hermite function subscript.

A fundamental difficulty appears because in the *free-streaming* problem, where $E \equiv 0$ and $\partial f/\partial t + v\,\partial f/\partial x = 0$, the distribution becomes a very complicated function of v as time progresses, at least when viewed without doing some sort of smoothing or coarse-grained averaging. In Fig. 1.18 we show the evolution of phase space in such a problem (figure after one of Lynden-Bell)[26]. The shaded area contains (say) a uniform phase density of particles. The unshaded area contains nonparticles. Obviously the initial density variation in x space disappears in time as a result of *phase mixing*, in free streaming. One can of course solve the free-streaming problem exactly, either by physical intuition $[f(x, v, t) = f(x - vt, v, 0)]$ or by transformation techniques using analytical methods for treating limits. Neither approach is a priori practicable when the interaction fields are present, but numerical treatments can be done at least in principle. Unfortunately, programming physical intuition or analytical limit theory is a difficult task, and it seems more likely that one can succeed side-stepping the difficulties with subtle rearrangements of the techniques.

The Fourier-Hermite approach in one dimension required the use of a very large number, $m_{max} \approx 10^3$, of $f(k, m, t)$ as a function of m. This could be tolerable, but the number m_{max} rises linearly in time as the problem progresses, so that the finite capacity of the computer restricts the length of time the computation can be run. The extension of this technique to two or three dimensions appears impractical. Truncating the m series resulted in errors which propagate toward low m values, where they have a large effect on the course of the problem.

We can suggest two ways to avoid the trouble. Both involve using Fourier expansions in v instead of the Hermite series. For a fundamental *period* in the v direction, we choose a number V above which we will never permit particles to exist. If q is the velocity *wave number*,

$$f = \sum_k \sum_q \exp(ikx + iqv)\, f(k, q, t) \ ,$$

then free streaming drives nonzero amplitudes $f(k, q, t)$ toward large q values at a rate k. The motion of these amplitudes is strongly suggestive of propagation of a wave in the k-q transform space, which suggests two ways to follow the motion. First, one could give a width, height, and location (q value) for peaks in the initial amplitudes $f(k, q, 0)$ and follow these very few numbers through time. Second, one can invent truncation methods which eliminate or at least deemphasize unphysical wave reflection at the cutoff in q. Preliminary results confirm that the second procedure is effective in free-streaming examples.

---

[26] Lynden-Bell, *Monthly Notices Roy. Astron. Soc.* **136**, 101 (1967).

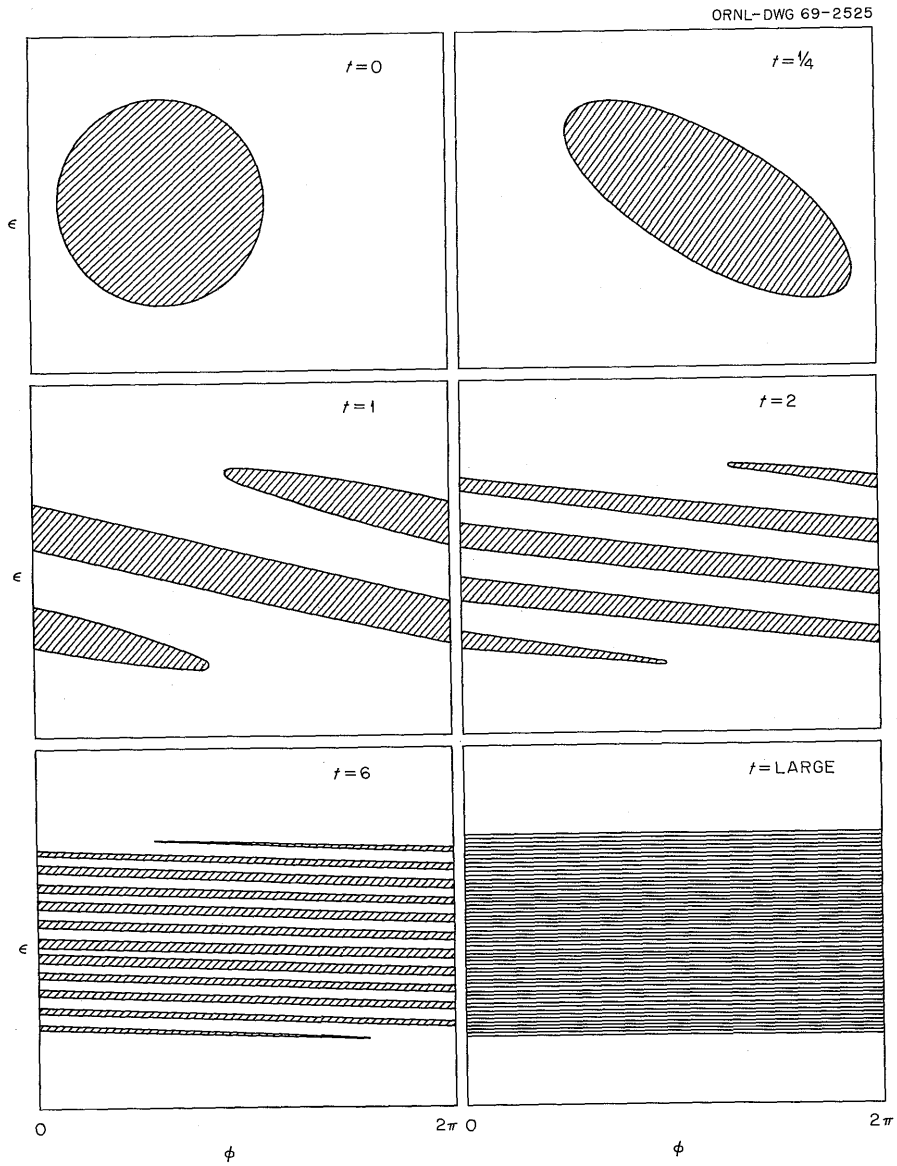

Fig. 1.18. The Evolution of Phase Space in a Free-Streaming Problem. From Lynden-Bell[26].

The idea behind both these suggestions is that there is a *natural* description of the motion of phase space and that mathematical difficulties should be reduced if this is found. The Fourier expansions here are natural ones for problems near the spatially uniform equilibrium $f(\mathbf{x}, \mathbf{v}, t) = f_{EQ}(\mathbf{v})$.

Having found natural coordinates and stable truncation methods, one would presumably be able to give accurate solutions to a problem using only a few parameters to describe the system. If this is true, then there is reasonable hope that two- and three-dimensional problems might be solvable. If not, there seems to be little hope for this approach to plasma dynamics, and one would be forced to concentrate on other approaches such as those described later.

A similar process (expanding in natural eigenfunctions[24]) exists for treating motion near equilibria other than the spatially uniform one. For example, an equilibrium with a sinusoidal potential well will exhibit the usual phase mixing in large energy regions of phase space but will have pendulum-equation phase mixing at small energy, so that an azimuthal phase variable (ϕ in Fig. 1.19)

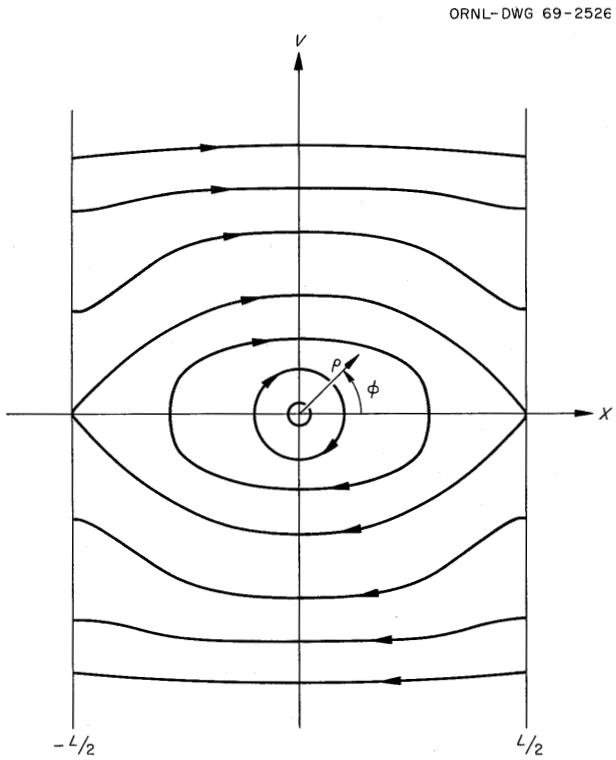

Fig. 1.19. Phase Trajectories in a Sinusoidal Potential Well. Phase mixing occurs for closed orbits as well as open ones because the orbit period is a function of energy.

will tend to disappear in time, while dependence of f on the radial phase variable ρ will become very complicated in time.

The generalization is: in action-angle variables of the motion in an arbitrary equilibrium, one will find that f becomes independent of angle and on a fine-grained scale becomes a rapidly oscillating function of the action variable. Finding the coarse-grained dependence[27] on action is the heart of determining toward what equilibrium the system would like to go.

An alternate suggestion to following waves in the transformed phase space is to find appropriate procedures for replacing complicated f's by coarse-grained ones. The condition one would like to fulfill is that no physics be lost in this process. To know what did get lost one should have fairly inexpensive ways to solve the fine-grained problems for comparison.

[27]Ref. 25 describes the thermodynamics of collision-free systems.

A second approach for solving the Vlasov equation is to follow the motion of contours of constant f in the phase space, realizing that each point in phase space follows the motion of any particle which happened to be located at that phase point. Knowing the motion of f contours, one may reconstruct enough of f to perform the moment integrals; Eq. (2) provided only that the contours do not become too complicated.

This method has been used fruitfully by Berk, Nielsen, and Roberts,[28] and others,[29] but the tendency of phase space to become complicated limits its effectiveness to rather simple problems. We do not yet know a trustworthy way to do the smoothing necessary to follow a problem for any long time.

1.4.1.2. Particle Following. – If one uses smoothed fields in the single-particle motion equations, he can represent real systems by 10^4 to 10^6 particle clouds and in one-dimensional systems, at least, hope to obtain meaningful results. Such studies have been described in ref. 24 and in the work[22,23] of Bers, Birdsall, Buneman, Byers, Dawson, Hockney, Morse, and others.

In some cases the number of clouds available has been large enough so that statistical fluctuations in *cloud* density do not cause electric fields large enough to obscure the plasma phenomena being studied. In two and three dimensions this is no longer true, and one is forced to experiment with smoothing techniques for reducing the fields caused by poor statistics.

In considering the idea of a cloud as a group of particles whose internal motion is unimportant to the problem at hand, we have observed a natural way to subdivide the particle interactions into long- and short-range contributions. If $f_0(\mathbf{x}, \mathbf{v}, t)$ is

$$\sum_{i=1}^{N} \delta[\mathbf{x} - \mathbf{x}_i(t)]\, \delta[\mathbf{v} - \mathbf{v}_i(t)] ,$$

which obeys the Boltzmann equation with non-smoothed interaction fields, then f_0 may profitably be expanded in both $\mathbf{x}$ and $\mathbf{v}$ in terms of Hermite polynomials with weight function $\exp[-(x^2/x_0^2) - (v^2/v_0^2)]$. Keeping only the lowest-order amplitudes and choosing $x_0 \sim \lambda_D$ and $v_0 \sim$ (say) $(2kT/m)^{1/2}$,

[28]See H. Berk, C. E. Nielsen, and K. V. Roberts (submitted to *Physics of Fluids*, 1969).

[29]Ref. 28 refers to early work by D. Depackh.

we should obtain the Vlasov equation. By keeping higher-order amplitudes we should obtain the Vlasov equation with force terms modified in a way that prevents phase-space structure from becoming too complicated. The sequence of higher-order approximations will lead to ways to improve cloud-following approaches.

We plan to use cloud following in conjunction with the Vlasov equation methods for cross-checks on the validity of smoothing procedures.

1.4.1.3. Problems Amenable to Simulation. – It appears likely that a two-dimensional particle-following code will give credible information on the following types of problems:

1. Does the drift cyclotron instability really exist? In a mirror? In a magnetic well?
2. How do flute modes behave when the ratio R/ρ of system radius to gyroradius is not much larger than unity?
3. Can the classical flute modes, diochotron modes, Burt-Harris modes, and drift cyclotron be distinguished when $R/\rho \approx 1$ to 10?
4. How do radial boundaries affect the modes?

Saturating amplitudes and nonlinearly important wavelengths will be interesting results of a well-constructed code.

1.4.1.4. Ancillary Matters. – To make simulation feasible, one needs highly efficient means to solve Maxwell's equations with suitable boundary conditions and sources given by Eq. (2). These well-known methods for this are available: (1) Fourier expansion, solution, and inversion; (2) iterated relaxation solution of finite difference equations (FDE) approximating the Maxwell equations; and (3) direct inversion of the matrix associated with the FDE.

For use in method 1, we have implemented and tested a simple FORTRAN version of the Cooley-Tukey[30] Fast Fourier Transform procedure, which cuts computing time by orders of magnitude, and we plan to implement the twice-faster modification suggested by Bergland.[31]

For reduced problems where $\mathbf{j}$ is negligible and Poisson's equation in two dimensions determines a potential function, method 3 has been implemented by O. Buneman[32] of Stanford to yield an extremely fast solution. We have operated and tested a version of this which solves $\nabla^2\phi = -\rho$ in a rectangular region in Cartesian coordinates. Also available is a version which operates in a rectangle in the R-Z plane of a cylindrically symmetric system. This could be applied to Fourier components to solve a three-dimensional problem.

We have found a relatively simple polynomial fraction approximating the conformal mapping[33] $W = \mathrm{sd}(\sqrt{2}\,Z)$ which maps a square in the complex Z plane into a circle in the W plane. The sd is the Jacobian elliptic function with modulus $m = m_1 = \frac{1}{2}$. This will provide a convenient way to use Buneman's codes for more natural circular boundary conditions.

1.4.1.5. Acknowledgments. – We thank C. K. Birdsall and C. M. Van Atta for an interesting study group at the University of California Lawrence Radiation Laboratory, Livermore. We would like to acknowledge informative discussions with K. R. Symon, C. E. Neilsen, C. O. Beasley, and most of the authors from the two symposia cited. Special thanks are due to O. Buneman and R. Hockney for information and details of their potential-solving routines.

1.4.2 Diamagnetic Equilibria of Hot-Electron Plasma in a Simple Mirror

R. DeLozier[34]
R. A. Dory
P. H. Edmonds
O. C. Eldridge[35]
E. A. Ferguson
G. E. Guest
J. Park[34]
C. E. Parker

Three calculations are being made of the equilibrium of hot-electron plasma in the mirror configuration of the ELMO facility.[36] The primary purpose is to determine the electron distribution from available experimental data.[37] A secondary purpose is to study equilibria and stability of high-β plasma.

---

[30] J. W. Cooley and J. W. Tukey, *Math. of Comp.* **19**, 297 (1965).

[31] G. O. Bergland, *Comm. of the Assoc. for Comp. Mach.* 11, 703 (1968).

[32] Private communication (1968).

[33] H. Kober, *Dictionary of Conformal Representations*, Dover Publications, Inc., 1952.

[34] Applied Science Department, Computing Technology Center.

[35] Consultant from the University of Tennessee, Knoxville, Tenn.

[36] *Thermonuclear Div. Semiann. Progr. Rept. Apr. 30, 1967*, ORNL-4150, sect. 4.2.

[37] Sect. 5.1, this report.

The data[37] give measurements during turnoff of the change in magnetic field on axis and outside the plasma, and the change in total flux through an external loop. In the first calculation, by P. H. Edmonds,[37] the field from an annular double layer of current filaments was considered. Parameters were varied until the experimental data were well reproduced.

A second calculation used a computer code developed by S. R. Fisher[38] of New York University. The code treats a guiding center hot-electron plasma in which the perpendicular and parallel pressures are specified functions of the magnetic flux and magnetic field. Currents are obtained from the pressure gradients and the self-consistent magnetic field from Maxwell's equations through a finite difference scheme. A typical result is shown in Fig. 1.20, which gives the change in magnetic field as a function of distance along the axis. This plot agrees well with experiment. Through comparison with experimental data, we confirm the current filament model determination[37] of density, temperature, and location of the plasma.

In the third approach, a self-consistent equilibrium is calculated from trial distribution functions for cold ions, cold electrons, and hot electrons. The trial distributions can be any function of invariants of single-particle trajectories in the equilibrium fields. Invariants used here are energy $W = \frac{1}{2}mV^2 + e\Phi$, magnetic moment $\mu = mV^2/2B$, and angular momentum $P_\theta = \frac{1}{2}rV_\theta + e\psi/2\pi$, where $\psi(r, z)$ is the flux function and $\Phi(r, z)$ the electric potential. We have used the trial distributions

$$f(W, \mu, P_\theta) = C\mu \exp(-W/\Theta) \exp[-(P_\theta - L_0)^2/(\Delta L)^2]$$

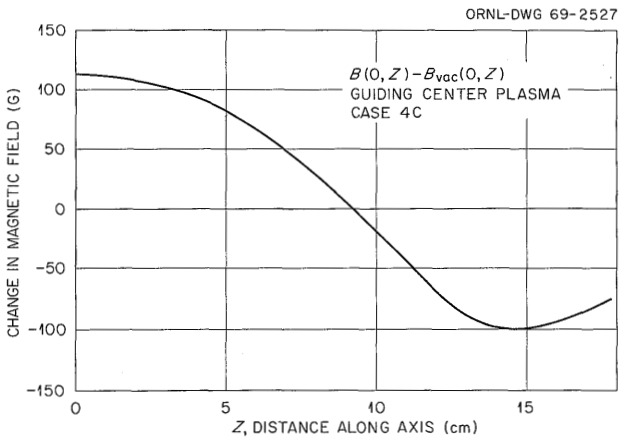

Fig. 1.20. Magnetic Field Change Caused by High-Density Hot-Electron Plasma.

to represent the loss-cone distribution for a mirror ratio of 2.

The adjustable constants are density αC, temperature Θ, and parameters L_0 and ΔL, which determine the radial location of the plasma by giving the peak and spread of the distribution in angular momentum. From charge and current densities obtained by integrating the distributions over all velocity space, the fields are found by direct integration using Green's functions. To give a rough simulation of the experiment, we begin with the vacuum magnetic field, with zero temperature and with zero potential. Parameter Θ is stepped upward, and another equilibrium is found through iteration of the equations, using the previous equilibrium as an initial guess. Further stepping of Θ gives a sequence of equilibria through which plasma could pass if so inclined, but of course this is not necessarily the correct dynamics of a single experiment.

Sample results are shown in Fig. 1.21, which gives the midplane magnetic field as a function of radius for several electron temperatures. The peak electron density here is $n_e = 6 \times 10^{11}$ cm^{-3}. In Fig. 1.22 we show contours of constant β,

$$\beta = \frac{B^2_{vac} - B^2}{B^2_{vac}},$$

for $\Theta = 600$ keV. These equilibria qualitatively reproduce the available experimental data; their stability and the dynamic factors which determine the set of adjustable constants preferred by the plasma are unresolved questions. A numerical simulation of the system dynamics may prove feasible, and this should help to answer these questions.

For now, one can offer the hypothesis that flute instability permits the plasma to move quickly in the radial direction until it reaches a radius where the conducting end walls of the rf cavity are nearby along the magnetic lines. At this radius, line-tying[39] stabilization of the flute modes could stop the radial motion, and a stable equilibrium could result. The observed location of the hot-electron annulus is roughly consistent with this interpretation.

---

[38] This code is a modification of a code by John Killeen, LRL, Livermore.

[39] G. E. Guest and C. O. Beasley, *Phys. Fluids* **9**, 1798 (1966).

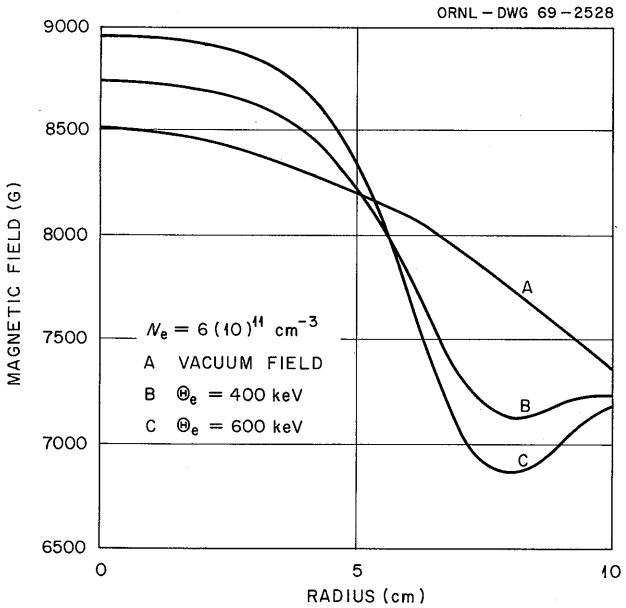

Fig. 1.21. Radial Variation of Midplane Magnetic Field Calculated for Hot-Electron Plasma. $N_e = 6 \times 10^{11}$ cm^{-3} with mean electron energies of zero (A), 400 keV (B), and 600 keV (C).

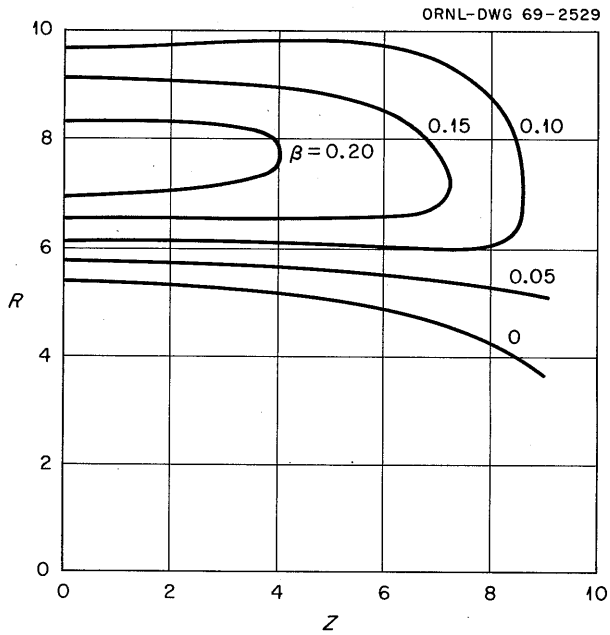

Fig. 1.22. Calculated Contours of Constant Plasma Pressure (in Percent) for the 600-keV Case.

2. Target Plasmas

2.1 INTRODUCTION

J. L. Dunlap N. H. Lazar

The target plasma program aims at creating a dense hot-ion plasma through injection of energetic atoms into a hot-electron target plasma. The program continues to be motivated by expectations of enhanced stability of the energetic-ion plasma and by prospects for hot-ion densities such that $(\omega_{pi}/\omega_{ci})^2 \gg 1$.

Our initial report[1] considered these motivations at some length. The buildup calculations there which defined certain desired parameters of the system still appear adequate; we are working toward target densities of about 10^{13} cm^{-3} coupled with the injection of some tenths of an ampere (equivalent) of energetic atoms, ambient neutral pressures in the range 10^{-7} to 10^{-6} torr, and maintenance of a high degree of ionization (ratio of target density to density of charge-exchange centers of about 10^3). However, the theoretical picture regarding hot-ion instability is now considerably more detailed, and we take this opportunity to review it.

The initial prospect that an energetic-ion plasma will be more stable in a hot-electron environment was based primarily on the thought that a warm-electron component would suppress all long axial wavelength ion instabilities through Landau damping. This thought has since been found to be valid only for $\omega_{pi}/\omega_{ci} < 1$. Additionally, two new and potentially dangerous instability mechanisms have been treated theoretically. At high densities ($\omega_{pi}/\omega_{ci} > 1$, $n_i > 2 \times 10^{10}$ for $B \approx 20$ kG) new resonant ($\Delta\omega/\omega_{ci} \ll 1$) instability modes which result from a coupling of plasma oscillations analogous to sound waves with ion-cyclotron waves have been studied with a wide range of electron density, temperature, and ion anisotropy.[2] These modes are calculated to propagate with very long wavelengths ($\lambda/\rho_i \sim 10^2$), and thus axial magnetic field gradients may favorably affect their growth. The second class of instabilities has a rather nonresonant (i.e., $\Delta\omega/\omega_{ci} \approx \frac{1}{2}$) character, has maximum growth with $k_{\parallel}\rho \sim 1$ to 10, and is found to be produced by the presence of the hot-electron component, particularly for $T_e \gg T_i$.[3] Despite these new theoretical developments, we feel the prospects of stability remain good. Neither of the two new modes has, as yet, been experimentally identified; certainly the presently limiting modes are expected to be suppressed;[4] and the experimental evidence of the fast-atom injection studies in the simple-mirror INTEREM configuration showed stability of the accumulated ion plasma at $\omega_{pi}/\omega_{ci} \approx 1$.

Our program quite naturally concentrates on the electron-cyclotron heating techniques originally developed at this laboratory by R. A. Dandl and his co-workers.[5] The preceding report[1] summarized the initial relevant developments, the triple-mirror operation of INTEREM with energetic neutral injection, and design of superconducting coils for the mirror-quadrupole facility IMP. The program has been more heavily emphasized during the present report period, as can be seen from the

---

[1] R. A. Dandl, G. E. Guest, and N. H. Lazar, *ORNL Target Plasma Program*, ORNL-4080 (April 1967).

[2] *Thermonuclear Div. Semiann. Progr. Rept. Oct. 31, 1967*, ORNL-4238; C. O. Beasley, Jr., *et al.*, Third Conference on Plasma Physics and Controlled Thermonuclear Research, Novosibirsk, U.S.S.R., Aug. 1–7, 1968, paper CN-24/G-11.

[3] D. J. Sigmar and G. E. Guest, sect. 1 of this report.

[4] J. G. Cordey *et al.*, Third Conference on Plasma Physics and Controlled Thermonuclear Research, Novosibirsk, U.S.S.R., Aug. 1–7, 1968, paper CN-24/H-5; J. F. Clarke *et al.*, *ibid.*, paper CN-24/H-6.

[5] M. C. Becker *et al.*, *Nucl. Fusion, Suppl.*, Part I, 345 (1962).

following sections. Initially, we give details of two elements of the program that involve in situ feed (i.e., target ion and electron feeds by ionization of ambient neutral gas within the target):

1. *The INTEREM Experiment.* – The facility has been modified to mirror-quadrupole geometry to permit operation in magnetic well geometry with $B_0 \sim 3$ kG and heating on closed field contours (heating frequency 10.6 GHz). Experiments with this configuration have demonstrated the suitability of this geometry for producing electron-cyclotron-heated (ECH) plasmas with a relatively small cold-particle density. Measurements of the plasma parameters have indicated that energetic-electron densities approaching the cutoff density $n \lesssim 10^{12}$ cm^{-3} are possible with optimum conditions but that the ratio of the target density to neutral density is only ~ 3 to 5. The plasma lifetime appears to be limited to values below that calculated from classical scattering, and the poor confinement is attributed to microinstabilities. A discussion of these results and the implication for the scaling experiments in IMP are included in Sect. 2.

2. *The IMP Experiment.* – The magnetic field strength, heating frequency, and base vacuum properties limit the usefulness of the INTEREM experiment. IMP will have higher fields, higher heating frequencies, and lower base pressures. These features will permit a scaling in heating frequency and therefore in density to test the concept of in situ heating. The configuration is suitable for hot-ion trapping, so some stability studies of the combined ECH and hot-ion populations are also permitted. Since the facility is not yet operational, here we will deal with its role within the framework of the target plasma program. Engineering details are presented in Sect. 11.5.

Consideration is also being given to possible alternatives to in situ feed, that is, cold ion and electron feed to the target from *outside* the target region and trapping of these particles by application of electron-cyclotron heating. Section 2.3 describes work on a fundamental aspect of such feed – measurement of the trapping efficiency of electrons drifted into the resonantly heated region. The results are roughly in agreement with estimates based on a simple model of the process. Work is also in progress toward a future modification of the INTEREM facility to a mirror-octopole configuration, one that will allow studies of target creation with drifted feed. Details are left to the next progress report.

2.2 INTEREM

M. C. Becker
C. W. Blue
J. L. Dunlap
G. R. Haste
W. J. Herrmann[6]
N. H. Lazar
O. D. Matlock

2.2.1 Introduction

The motivation for the addition of quadrupole coils to the simple-mirror INTEREM facility is described above. In brief, the experiment was designed to study the properties of an electron-cyclotron-heated (ECH) plasma in a minimum-B geometry and, in particular, to establish the conditions under which such a plasma may be generated at low pressures. If the plasma heating mechanism produced the ideal mirror-confined energy distribution and the plasma losses were entirely governed by electron-ion and electron-electron scattering into the loss cones, the required feed rate of neutral atoms could be reduced below what has been obtained in the past. The ratio of target ion density, n_t, to neutral density inside the plasma, n_0' (n_0 is the ambient neutral density), would then be significantly greater than is observed in simple mirror geometries.[1]

The simple demonstration of a large improvement in the ratio n_t/n_0 through the use of magnetic well geometry, however, was not successful. Flutes, which are seen in the plasma decay in simple mirror geometry, are not present in the minimum-B configuration. Nevertheless, the plasma in minimum-B exhibits fluctuations, and the lifetime of the energetic component is found to be limited below the values computed from mirror loss due to electron-ion and electron-electron scattering (assuming a Maxwellian electron distribution). We are unable, at present, to identify the specific mechanism which drives the fluctuations and so are unable to make predictions as to the scaling of the loss rates (and, therefore, the required neutral feed rate) with change in magnetic field strength or density. We suggest the possibility that at higher fields, higher densities

[6]On leave of absence from the Institut für Plasmaphysik, 8046 Garching bei München, Germany.

may be possible, and we point to two facts which offer some degree of optimism: (1) If the fluctuations are caused by a microinstability, as appears to be supported by the experiments, it is possible that thresholds could scale as $\omega_{pe}^2/\omega_{ce}^2 = n_e/B^2$. (2) Experimentally, in simple mirror configuration the observed plasma density has been observed to rise as the field is increased – with a scaling not very different from n_e/B^2.

Although a decided improvement in n_t/n_0' in the magnetic well, when compared with the earlier INTEREM mirror configuration, was not demonstrated, several significant results should be noted. These are as follows: (1) Effective electron-cyclotron resonant heating occurs in a minimum-B configuration, which proves the symmetry of the simple mirror field is not required for efficient heating. (2) The cold-electron cyclotron frequency at some point in the plasma volume must be resonant with the heating frequency to produce a steady-state plasma. (3) Hot dense plasmas are produced in the magnetic well configuration at pressures much lower than can be reached using a simple mirror geometry. (4) The energetic-electron component reaches densities in optimum conditions approaching 10^{12} cm^{-3} even at the lowest neutral density – $n_0 = 1.4 \times 10^{11}$ cm^{-3}. The density is never observed to be significantly greater than the cutoff density ($n_c = 1.4 \times 10^{12}$ cm^{-3}). (5) The energetic-electron distribution functions were measured for energies above ~ 30 keV and showed a mean energy, $\langle E \rangle$, of ~ 100 keV, almost independent of operating parameters. (6) The volume filled by the plasma seems to be determined, principally, by the location of the resonant heating surface for cold particles. In this determination, the modification of the vacuum magnetic field by the finite β,

$$\beta = \frac{n \langle E \rangle}{\beta_0^2/8\pi},$$

of the confined plasma must be taken into account. (7) The stored energy in the plasma reached ~ 25 J. In this case, for the estimated volume of 11 liters, we obtain an average energy density of $\sim 2 \times 10^{16}$ eV/cm^3 or $\beta \approx 6\%$. At higher fields, with smaller plasma volumes, $\beta \sim 10$ to 20%. (8) The hot-electron confinement time, during equilibrium, is estimated to lie in the range 1 to 30 msec. However, after shutting off the applied power, the observed plasma decay time at low pressures is about an order of magnitude longer and corresponds, approximately, to what is expected from classical scattering. (9) Correlation of radial and axial particle losses with radiation bursts at high frequency (approximate harmonics of ω_{pe}, ω_{ce}) are noted both in the equilibrium state and during decay.

2.2.2 Description of Facility

The previous INTEREM[7] facility consisted of a large vacuum tank ($1.25 \times 1.25 \times 2.7$ m) pumped by several unbaffled 20-in. oil diffusion pumps; a pair of coils, arranged for 2:1 mirror ratio, which could produce a central field in excess of 4000 G; and a microwave-frequency power source of 20 kW capability at 10.6 GHz (corresponding to the electron cyclotron frequency at $B = 3870$ G). For the modified facility, quadrupole coil windings were cast in epoxy and arranged about a new perforated copper cavity, as shown in Fig. 2.1. At the time this coil system was inserted in the existing tank, the vacuum system was rebuilt by replacing the 20-in. pumps with four 10-in. pumps, each with Freon-cooled baffles. Additionally, large areas of liquid-nitrogen-cooled surfaces were placed in the vacuum tank to further reduce the water vapor background and permit base pressures below 10^{-7} torr with a large reduction in organic contaminants.

All detailed plasma measurements were carried out using a field shape most nearly analogous to that designed for the IMP geometry,[8] that is, with a high wall-mirror ratio in the midplane. The flux lines and surfaces of constant magnetic field $|B|$ were calculated by M. Rankin, C. E. Parker, and E. A. Ferguson.[9] In their calculation, the current conductors were replaced by filaments or loops. Each mirror coil was approximated by 90 loops; the quadrupole coils (including the end turns) were approximated by ten filaments per coil. The results of the calculations for the $|B|$ surfaces and flux lines in the two planes between the quadrupole conductors are shown in Fig. 2.2. The flux lines

[7] M. C. Becker *et al.*, *Thermonuclear Div. Semiann. Progr. Rept. Oct. 31, 1967*, ORNL-4238, p. 59.

[8] See sect. 2.3 of this report.

[9] The authors wish to thank M. Rankin, C. E. Parker, and E. A. Ferguson for preparing the necessary codes and carrying out the field calculations.

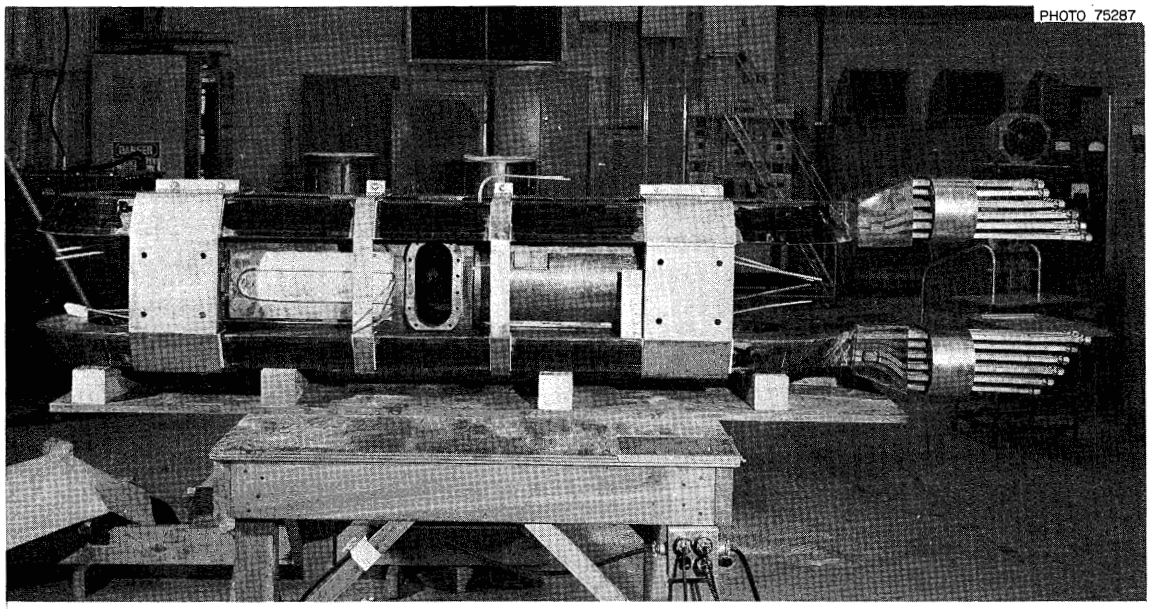

Fig. 2.1. Photograph of Quadrupole Coils in Place About the Inner Vacuum Cavity.

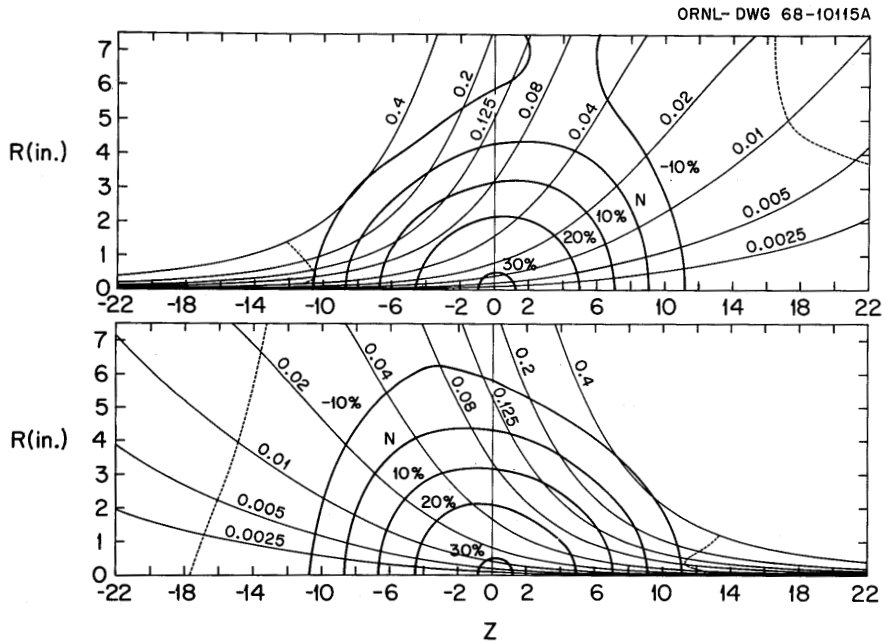

Fig. 2.2. Flux Lines and Surfaces of Constant Values of Magnetic Field for Nominal (N) Currents and Those +10, +20, and +30% from the Nominal in the Two Planes Between the Ioffe Bars. The numbers on the flux lines indicate the distance of the lines from the axis in the mirror throat ($z = \pm 22$ in.).

are identified by the distance in inches from the axis at which they intersect the plane through the mirror maxima ($z = \pm 22$ in.). The nominal field (N) was chosen so that the $|B|$ surface on which the cyclotron frequency of cold electrons is resonant with the applied heating frequency was approximately midway between the axis and the wall. $|B|$ surfaces are also indicated for 10, 20, and 30% above the nominal current values.

The flux lines in the two planes are slightly different because of the influence of the turns at the ends, which are in the sense to add axial

field at the east end and oppose the mirror field at the west end. This is most clearly illustrated by the dashed lines, which give the position at which the total field strength corresponds to the value at the opposite end of the flux line where it strikes the wall. Particles which have scattering times longer than the time of flight along the flux line will leave the plasma at the end of the flux line which has the lower field. In the upper drawing, this means scatter-dominated particles will leave the plasma at $z = -22$ in. only if they are on flux lines between 0.005 and 0.02 in. from the axis. In the other plane, all scatter-dominated particles inside the 0.02-in. flux line will leave through the axial mirror at $z = +22$ in. Particles which have a time of flight much longer than their scattering time, for example, particles ~ 1 to 5 eV (depending on density), should leave the plasma through both ends of the cavity in about equal numbers.

Electrons which are heated become relativistic, and their cyclotron frequency changes proportional to their total energy. For example, an electron of 500 keV is in resonance with the applied frequency at a field which is twice as high as for a cold electron. The highest energy at which electrons can remain in resonance somewhere in the 2:1 mirror field is ~ 500 keV for the $+30\%$ field and about 350 keV in the nominal field case. Particles with energies higher than 500 keV or 350 keV, respectively, have probably been heated by nonresonant interaction with the heating field.[10]

Because of the replacement of the real currents by only a small number of current-carrying filaments, some errors in the absolute value of the magnetic field strength are unavoidable. The accuracy in the absolute values decreases with increasing radius and in approaching the mirrors.

2.2.3 Diagnostics

The plasma parameters are determined, principally, using four tools: (1) the diamagnetic flux change, from which we may establish the total stored energy; (2) the currents leaving the plasma axially along the flux lines, which we can relate to line density; (3) energy spectra from bremsstrahlung radiation, which we can interpret in terms of electron energy; and (4) high-frequency (microwave) noise, which is used to seek the cause of plasma fluctuations.

2.2.3.1. Diamagnetic Flux. – A 30-turn coil was wrapped about the cavity, and the time-integrated flux change through it due to the presence of the plasma was measured. In using this technique, which was originally worked out for this application by R. A. Dandl,[5] we were restricted to integrated measurements of flux changes, since the time constant for penetration of the signals through the copper cavity prevented time-related information on a scale more rapid than ~ 10 msec. Nevertheless, gross monitoring of the plasma diamagnetism is most significant, since one can easily show that the observed flux change, $\Delta\Phi$, is related to the total stored energy $n_{e_H} \langle E \rangle V$ by the relation

$$\Delta\Phi = n_{e_H} \langle E \rangle V \left[\frac{1}{1 + (l/R)^2} \right]^{1/2} k ,$$

where R is the radius of the pickup coil and k is a conversion factor depending on the electronic integrator properties. This expression is derived assuming the plasma may be replaced by an equivalent dipole, of length l, placed on axis. As will be discussed below (Sect. 2.2.4.2), $l \approx R$ for almost all conditions, and this is taken into account in the results given. However, three other effects influence the accuracy of the measurement. First, the flux lines are not exactly perpendicular to the plane of the loop (see Fig. 2.2). Second, plasma energy stored close to the wall will have a larger influence on the signal than the energy stored near the axis; that is, the dipole approximation may not be suitable. Finally, if we are interested in total stored energy and not just perpendicular energy, we must make some estimate of the energy parallel to the flux lines. These three effects tend to result in an uncertainty in the quoted stored energy, perhaps as much as 50%.

Although the total stored energy is an interesting parameter, it would be more informative to extract either the plasma density or mean energy from the results. For this information, the plasma volume and either of the other two parameters are needed. The difficulties of volume determination will be described below. In any case, the absolute density estimates, due to uncertainties in all the

[10] H. Grawe, sect. 1 of this report.

measurements, clearly cannot be relied on to better than a factor of 2. Relative measurements, however, are more reliable.

2.2.3.2. Axial Current Measurements. – In attempting to find an independent determination of plasma density, we are guided by the near independence of ionization rate on electron energy. The ionization rate coefficient (σv) is shown in Fig. 2.3 as a function of energy. The average of this coefficient over the electron energy distribution is only weakly dependent on the shape of the distribution and, for electrons in the "energetic" component ($E > 1$ keV), is taken to be 1.2×10^{-8} cm^3/sec for molecular hydrogen gas.

The electron current flowing to a probe is given by the simple expression:

$$I = e\left[n_{e_H} n_0 \left\langle \sigma v \right\rangle_{\text{hot}} + n_{e_c} n_0 \left\langle \sigma v \right\rangle_{\text{cold}}\right] A l ,$$

where A is the area of the detector projected back along flux lines into the plasma, l is the average plasma length, n_0 is the neutral density, and n_{e_H} and n_{e_c} are the densities of the hot and cold electron components.

During the steady state, the measurement of hot-electron density is confused by the higher ionization rate (and unknown density) of cold electrons. Further, the preferential loss of scattered particles through the weaker mirror field along a flux line adds to the uncertainties. Therefore we have used the hot-electron density determined only from measurements of the current resulting from ionization during decay after waiting a suitable interval for the cold particles present during steady state to escape. We find the currents through the two mirrors are equal during decay, implying the particles are sufficiently cold so as to scatter many times in their time of flight through the mirrors.

A typical detector which was developed to measure this current is shown in Fig. 2.4. The defin-

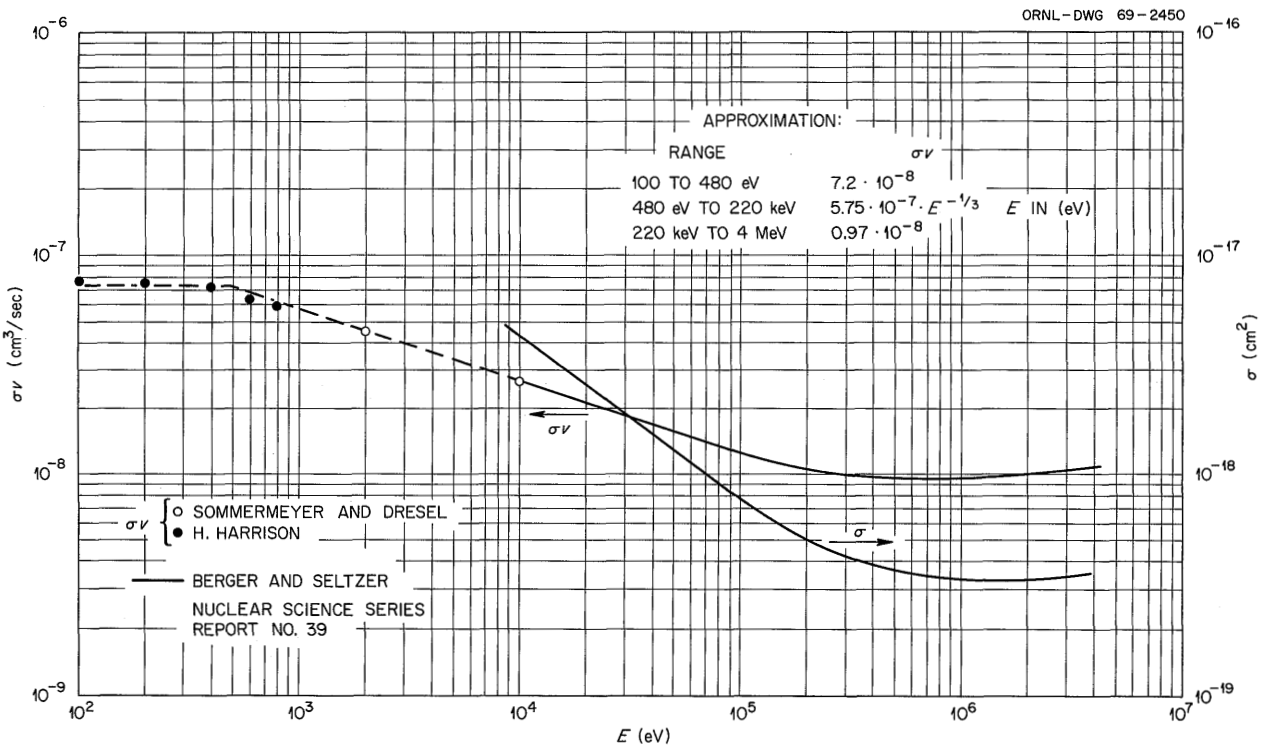

Fig. 2.3. Ionization Rate Coefficient σv as a Function of Electron Energy. The data are taken from: M. J. Berger and S. M. Seltzer, *Studies in Penetration of Charged Particles in Matter*, sect. 10, Tables of Energy-Losses and Ranges of Electrons and Positrons, *Nucl. Sci. Ser.*, Report No. 39; K. Sommermeyer and H. Dresel, *Z. Physik* 141, 307 (1955); H. Harrison, *The Experimental Determination of Ionization Cross-Sections of Gases Under Electron Impact*, Catholic University Press, 1956.

ORNL-DWG 68-6418A

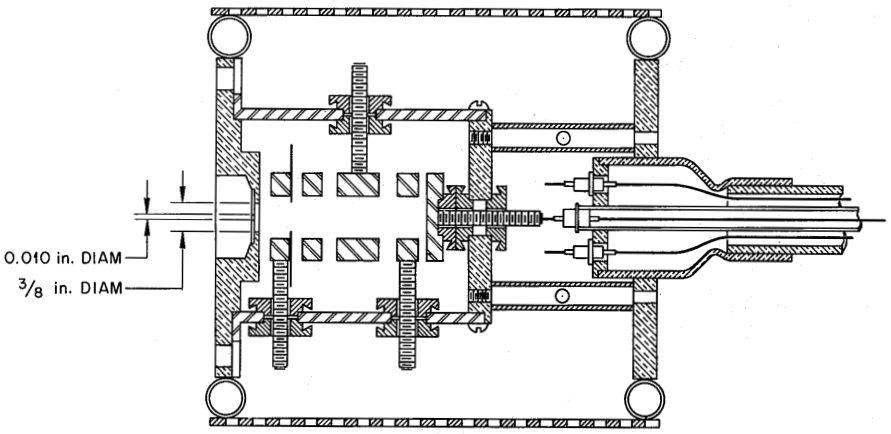

Fig. 2.4. Detector Used to Analyze Current Flowing Out of Plasma Along Flux Lines.

ing aperture, held at wall potential in all measurements, is only 0.025 cm in diameter in order to reduce space charge influences. Ions (or electrons) are repelled by the first electrode, and the axial energy of the other species may be analyzed by examining the current to the collector as a function of the voltage of the third electrode. The combination of fourth electrode and collector is used to suppress secondary emission from the collector. All electrodes are coated with carbon black to reduce secondary emission.

This arrangement allows us to examine the space potential of the plasma, as well as the current, by noting the voltage at which saturation ion current occurs. Typical curves obtained either with ions or electrons reflected by the first electrode are shown in Fig. 2.5. As can be seen in the figure, saturation electron current is obtained at wall potential – as expected from the positive space potential indicated by the ion curve. In the decay period, there is evidence that the space potential is close to wall potential.

2.2.3.3. Bremsstrahlung. – The use of bremsstrahlung radiation to establish the mean electron energy in a plasma is an old concept. The adaptation of this standard technique for use in ECH plasmas, however, where the radiation field near the vacuum container can exceed 100 R/hr, was not trivial. R. A. Dandl and W. B. Ard were primarily responsible for this development.[5] The x-ray spectrum from free-free and free-bound scattering is determined from a well-collimated 3 × 3 in. NaI(Tl) detector. Because of the enormous x-ray flux from all the walls, care must be taken to reduce the scattered radiation from the wall in the line of sight of the collimator. This is done by replacing the region of the cavity with a thin aluminum window (~0.006 in. thick). Scattered radiation is shielded from the window and its mount by a thick lead shield – in effect creating a "black hole" to look into.

The rate of detected x rays may be calculated from the expression

$$R(E_\gamma) = \epsilon \Omega V \int_{E_\gamma}^{\infty} (n_t + n_0)\, \sigma(E_\gamma, E)\, v\, f(E)\, dE \ ,$$

where

$$\int_{1\,\mathrm{keV}}^{\infty} f(E)\, dE = n_{e_H}$$

is the hot-electron density, v the electron velocity, $n_t + n_0$ is the total density of scattering centers, ϵ the detector efficiency, Ω the solid angle subtended by the detector (assuming a point source), V the observable volume of plasma, and $\sigma(E_\gamma, E)$ the bremsstrahlung cross section.[11] Nonrelativistically, the latter may be approximated as

$$\sigma(E_\gamma, E) = \frac{k}{E_\gamma} \cdot \frac{1}{E} \cdot$$

In the relativistic limit, σ is also approximately inversely proportional to $(E_\gamma E)$ but increases, as well, logarithmically with E. In most measurements, only the nonrelativistic approximation was used, since the bulk of the radiation was at low energies.

[11] W. Heitler, *The Quantum Theory of Radiation*, Clarendon Press, Oxford, England, 1960.

ORNL-DWG 68-8439A

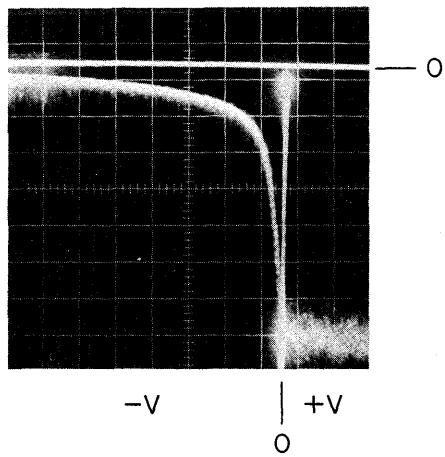

(*a*) ELECTRON CURRENT
VERTICAL: 10^{-6} A/DIV
HORIZONTAL: 20 V/DIV

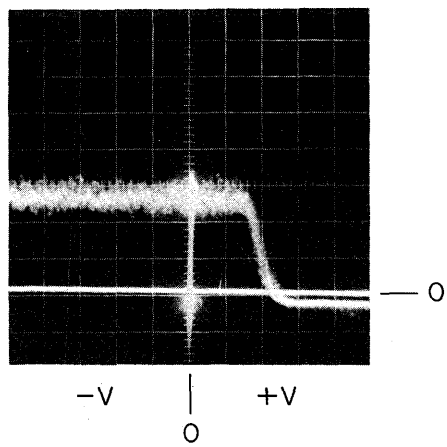

(*b*) ION CURRENT
VERTICAL: 10^{-6} A/DIV
HORIZONTAL: 20 V/DIV

Fig. 2.5. Current Observed as a Function of Retarding Potential on the Third Electrode in Detector Shown in Fig. 2.4. (*a*) Ions repelled by first electrode. (*b*) Electrons repelled by first electrode.

After correcting for detector response and air and window absorption, the observed spectrum was unfolded into the particle distribution function by differentiation of the smoothed data. These calculations were carried out on line using an LINC-8 computer. The code for these computations and the interfacing with the computer were carried out by J. E. Francis.

2.2.3.4. Microwave Noise Measurements. – The detected noise signal which is radiated into *K* band has been shown[5] to be related to the total stored energy in the plasma in simple mirror geometries. We have examined this signal as a function of time and correlated the fluctuations in it with the observation of instabilities. In addition, a superheterodyne receiver was constructed using the harmonics from a slowly swept local oscillator having a fundamental frequency range between 8 and 12 GHz. The signals, mixed with the oscillator, were amplified in a narrow-band-pass amplifier with a central frequency of 30 MHz, and the output was displayed on a synchronized oscilloscope to produce a frequency spectrum.

2.2.4 Results

2.2.4.1. Qualitative Observations. – Hot-electron plasmas with stored energy of at least several joules could be created at all pressures in the range 5×10^{-7} torr to 2×10^{-5} torr. In general, the only necessary condition appeared to

be the presence of a magnetic surface where the cold-electron cyclotron frequency was resonant with the heating frequency somewhere inside the confinement volume. When the magnetic field was raised so that resonance with the heating frequency did not exist in the volume, no plasma was observed. If, however, a plasma was first created with the field slightly reduced, it could then be indefinitely maintained if the coil current was then raised so that resonance (based on the vacuum field) no longer existed. This observation seems to demonstrate the finite β of the plasma, which produces a diamagnetic field sufficient to reduce the vacuum field so that resonance of the cold-electron "cyclotron" motion with the heating power can exist in the plasma volume.

Since the plasma flowing to the walls effectively cleans the surface upon which it strikes, a clear indication of the volume filled by the plasma can be deduced from the wall markings after experiments of several hours. The plasma, qualitatively, was found on those flux lines which pass through resonant heating surfaces. Detailed information on the plasma volume, including measurements of the distribution of hot electrons, is described below – these results essentially confirm these rough observations.

When the quadrupole coils are not energized, that is, using a simple mirror field configuration, hot, dense plasmas are seen only at pressures above 5×10^{-6} torr. Further, at pressures below 1×10^{-5} torr, as the power is raised, a threshold is reached when the stored energy suddenly disappears. Such a sudden disappearance of plasma is not seen when the magnetic well is used.

2.2.4.2. Spatial Distribution of Hot Density. – From an analysis of the current during the decay of the plasma, we have indicated that we may deduce the line density of energetic electrons. Such analyses have been carried out during a series of decays using a current detector which could be scanned radially in a plane between the quadrupole conductors. The results are shown in Fig. 2.6 for several values of the central field.

The most obvious feature is the current maximum on axis. This is distinct from the observations in some simple mirror experiments which indicate a cylindrical, or ring-shaped, hot-electron spatial distribution.[12] The second feature is the limitation of the radial extent, in most cases, to those flux lines which pass through a cold-particle resonant heating surface. The principal exception

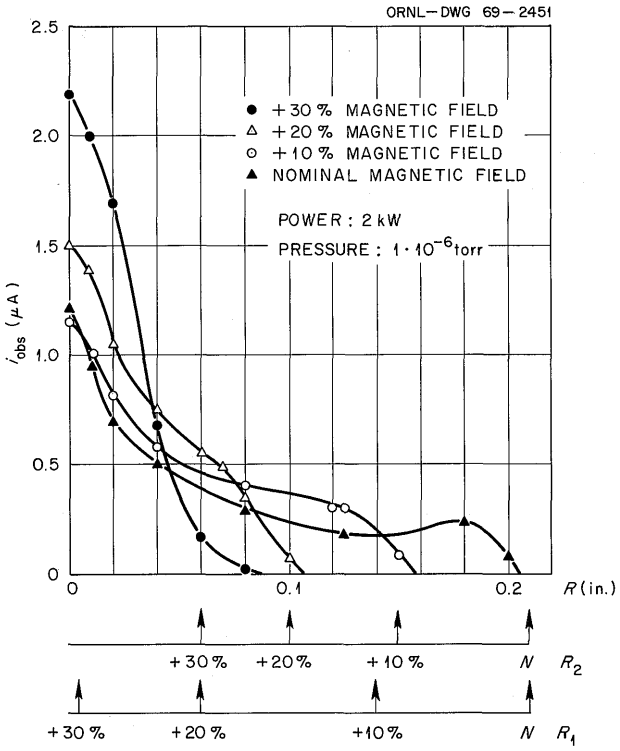

Fig. 2.6. Maximum Current Flowing Along Flux Lines During Decay as a Function of Distance from Horizontal Plane. The distance may be related to the flux lines indicated in Fig. 2.2. The arrows indicated by R_1 represent the positions of the flux lines tangent to the resonant $|B|$ surfaces calculated from the vacuum field. The arrows indicated by R_2 indicate the positions of the flux lines tangent to surfaces which are used to estimate the plasma volume given in Table 2.1.

to this observation occurs when the field is raised to 30% above nominal. Here, the magnetic surface (in vacuum) which results in resonance is essentially just a point on axis. In this case, the large observed radial size is attributed to cold-particle resonance occurring at the larger radii as a result of the plasma diamagnetic field.

Obstacles have been inserted axially through the mirrors in order to attempt to establish the plasma length along flux lines. Some influence on the microwave mode pattern in the cavity can be detected as the obstacle (a 2×12 in. plate) is moved axially, but these mode variations have

[12] R. A. Dandl *et al.*, sect. 5.1 of this report; H. Ikegami *et al.*, Third International Conference on Plasma Physics and Controlled Thermonuclear Research, Novosibirsk, U.S.S.R., Aug. 1–7, 1968, paper CN-24/J-5.

only a small influence on the stored energy ($\lesssim 10\%$). In each case, no large change in stored energy was seen until the obstacle was moved in to at least 12 in. from the midplane, and the total stored energy decreased by a factor of 2 when the obstacles were moved to 22 cm from the midplane. In some cases the obstacle strongly influenced the stored energy when it was still significantly outside the resonant field surface. Two explanations account for this observation: (1) The obstacle interferes with low-energy (< 10 keV) particles which, if allowed to live, would eventually gain perpendicular energy and, therefore, accumulate closer to the midplane. (2) The hot electrons which contribute to the stored energy exist out to the resonant zones and, as a result of scattering, are even found axially beyond them. We cannot distinguish between these options.

The volume of the plasma is needed to interpret several other measurements. We assume the plasma length is defined by the axial obstacle. However, the dimension perpendicular to the flux lines is more difficult to establish. From the spatial distribution of currents (Fig. 2.6), we find the last flux line on which currents are observed (R_2). In some cases, these lines are at some distance from the flux lines tangent to the vacuum field resonant surfaces (R_2). Since plasma diamagnetism will alter the location of the surface, but probably not its shape, we have estimated the volume of the plasma from the positions of the flux lines at which the current reaches zero, but we retain the shape (Fig. 2.2) of the vacuum field. Since these shapes are nearly ellipsoidal, we calculated the volume from the expression

$$V = \frac{4}{3}\pi l a^2 .$$

The results of these estimates are given in Table 2.1.

2.2.4.3. Electron Energy Measurements. – A typical electron energy distribution, $f(E)$, determined from unfolding the bremsstrahlung spectrum, $I(F)$, is shown in Fig. 2.7. Surprisingly, numerous observations showed that the shape of the distribution was almost unaffected by pressure, power, or field variations – principally the intensity varies with power. The mean energy of the distribution is ~ 100 keV.

Table 2.1. Estimated Plasma Volumes for Various Field Configurations

Magnetic Field Configuration	Axial Length, l (cm)	Radial Dimension in Midplane (cm)	Volume (liters)
N	21.6	11.0	10.8
+10%	21.6	9.5	8.2
+20%	21.6	6.7	4.1
+30%	21.6	4.8	2.1

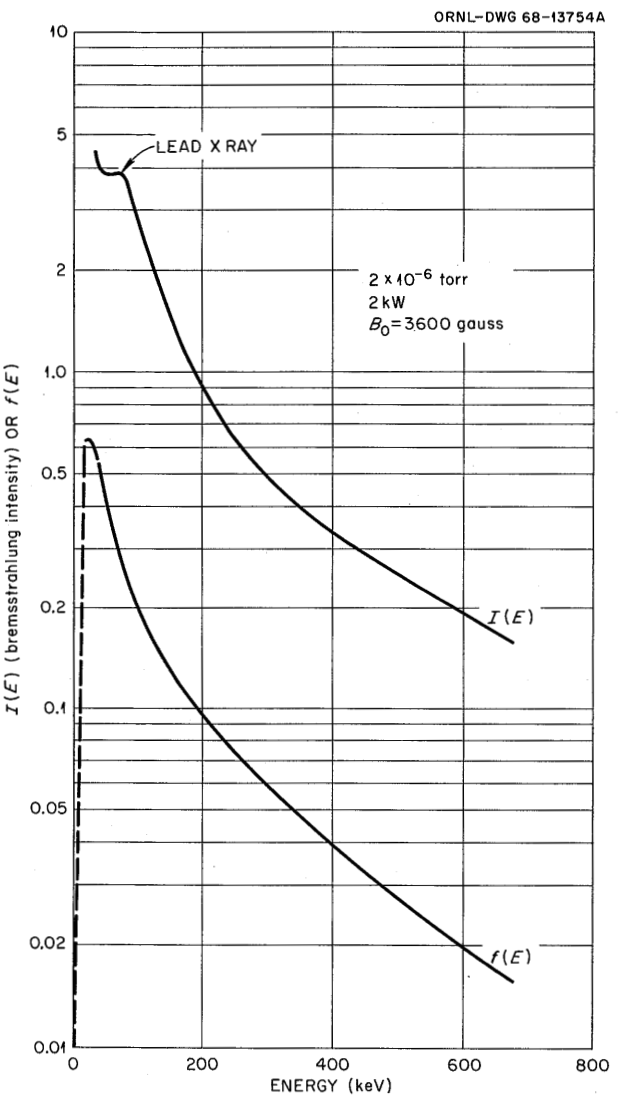

Fig. 2.7. Electron Energy Distribution Function $f(E)$ Determined from the Bremsstrahlung Spectrum $I(E)$.

The tail of the distribution is masked, to a degree, by insufficient statistics. However, the presence of a small component of high-energy electrons was determined from an analysis of the axial current decay. Particularly at higher pressures where instabilities do not interfere ($p > 5 \times 10^{-6}$ torr), current is observed for several seconds after the power is turned off. Assuming that energy is lost only by ionization, we estimate that perhaps 10% of the hot-electron population have energies in excess of 0.5 MeV, with some electrons with energy as high as 3 MeV.

2.2.4.4. Density of Hot Electrons. – The absolute density determined from the observed current from ionization during decay depends, of course, on the axial density distribution. Taking the points where the stored energy decreases by one-half for the length of the plasma yields the results given in Fig. 2.8 for the axial density as functions of power and pressure for the nominal

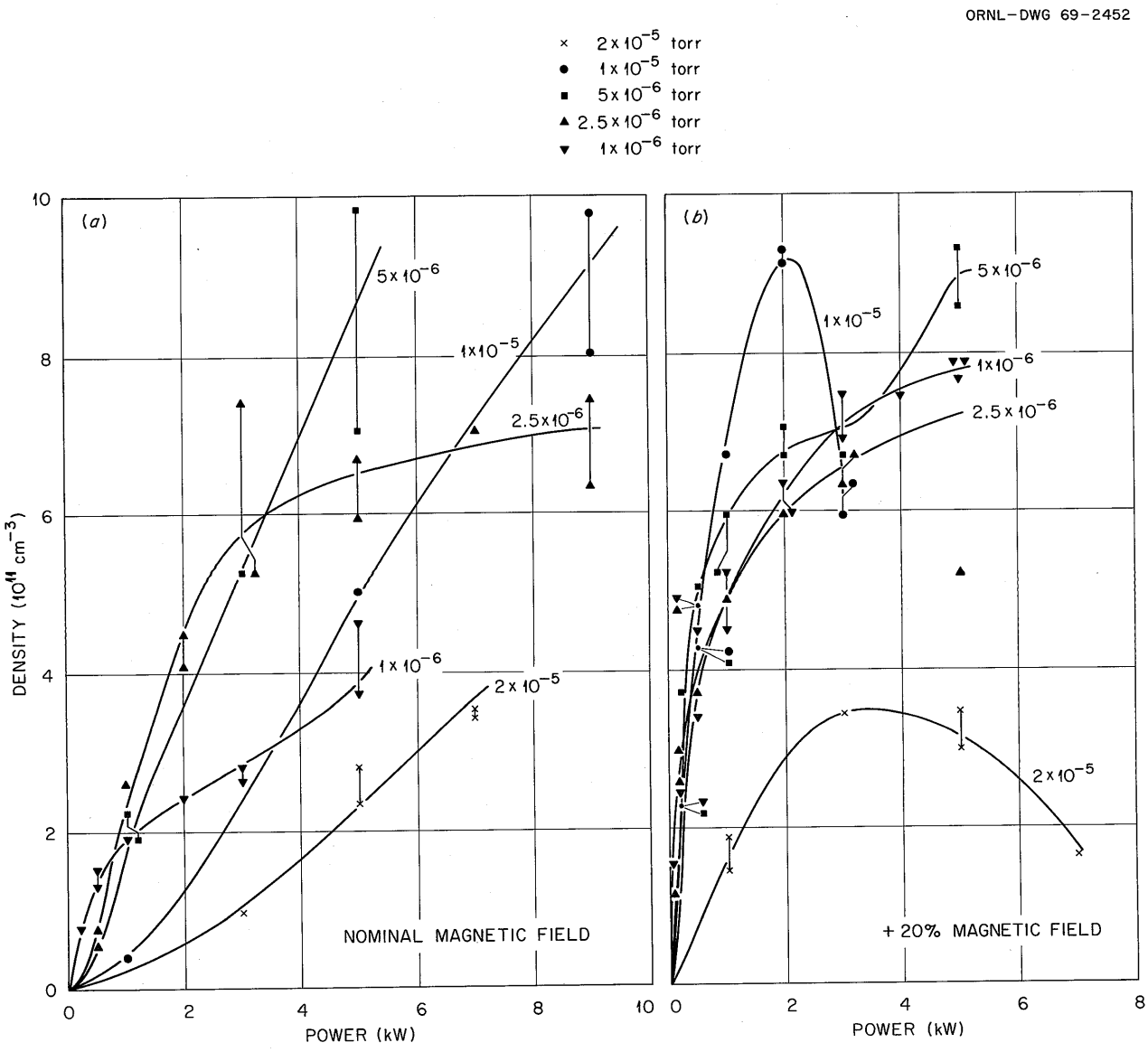

Fig. 2.8. Density of Energetic Electrons on Axis for (*a*) Nominal and (*b*) +20% Field as a Function of Heating Power for Several Values of Neutral Pressure. The values of pressure shown are those indicated by the ion gage. The neutral molecular density for hydrogen gas is obtained by multiplying by 14.1×10^{16} particles cm^{-3} $torr^{-1}$.

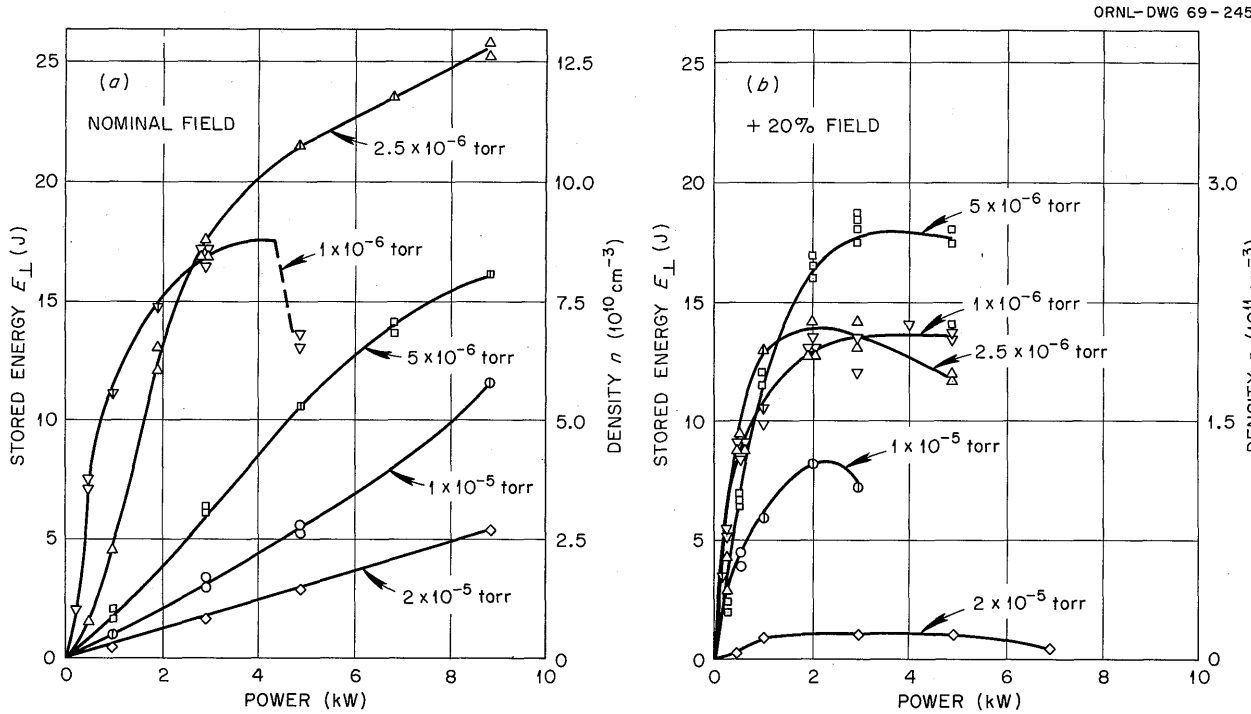

Fig. 2.9. Stored Energy and Estimated Average Density of Electrons as a Function of Heating Power for Several Values of Indicated Pressure at (*a*) Nominal and (*b*) +20% Field.

(N) and 20% higher field. In Fig. 2.9 we present the observed stored energy for the same parameters. Assuming the volume and mean electron energy do not depend on pressure or power, in Fig. 2.9 we also indicate the average density for these cases. From these figures we can see that the energetic-electron density increases with power, as long as the power is not too high. At the lower powers, the density increases as the pressure is lowered. However, both the electron density and stored energy are seen to be limited at high powers for all pressures (except perhaps at pressures above 1×10^{-5} torr in some cases). At high powers, the axial current and stored energy exhibit large amplitude fluctuations – approaching 100% modulation in the current during steady state under some conditions. It is not surprising, therefore, that the density deduced from the current in these cases varies nonreproducibly from one turnoff to another. Fluctuations in the decay also lead to uncertainties in the proper value of current to relate to "equilibrium" energetic density. This uncertainty, amounting to $\sim 25\%$, combined with uncertainty in the axial length of the flux line, results in reliability to only a factor of 2 in the density measurement from the axial current.

2.2.5 Instability Studies

The basic reason for the construction of the magnetic well geometry was to suppress the "low" frequency instabilities of the plasma, independent of cold-plasma density, and thus to extend the pressure range suitable for ECH plasma generation down to lower pressures than was possible with simple mirror configurations. In experiments in INTEREM using a simple mirror configuration, we have found direct evidence of radial losses associated with a repetitive low-frequency fluctuation during the plasma decay after the cold plasma has had time to flow out the mirrors ($\sim$200 μsec). However, we must stress that the presence of this phenomenon during decay is no proof that during the steady state, such losses dominate the plasma equilibrium – as Dandl has repeatedly shown in his experiments.[5] The evidence merely indicates that flute instability is likely to play a significant role in establishing the range of equilibrium, as a function, say, of cold plasma density, which can exist in simple mirrors. In any event, with the magnetic well configuration, no evidence of low-frequency instability is seen in the plasma decay.

ORNL-DWG 68-13147R

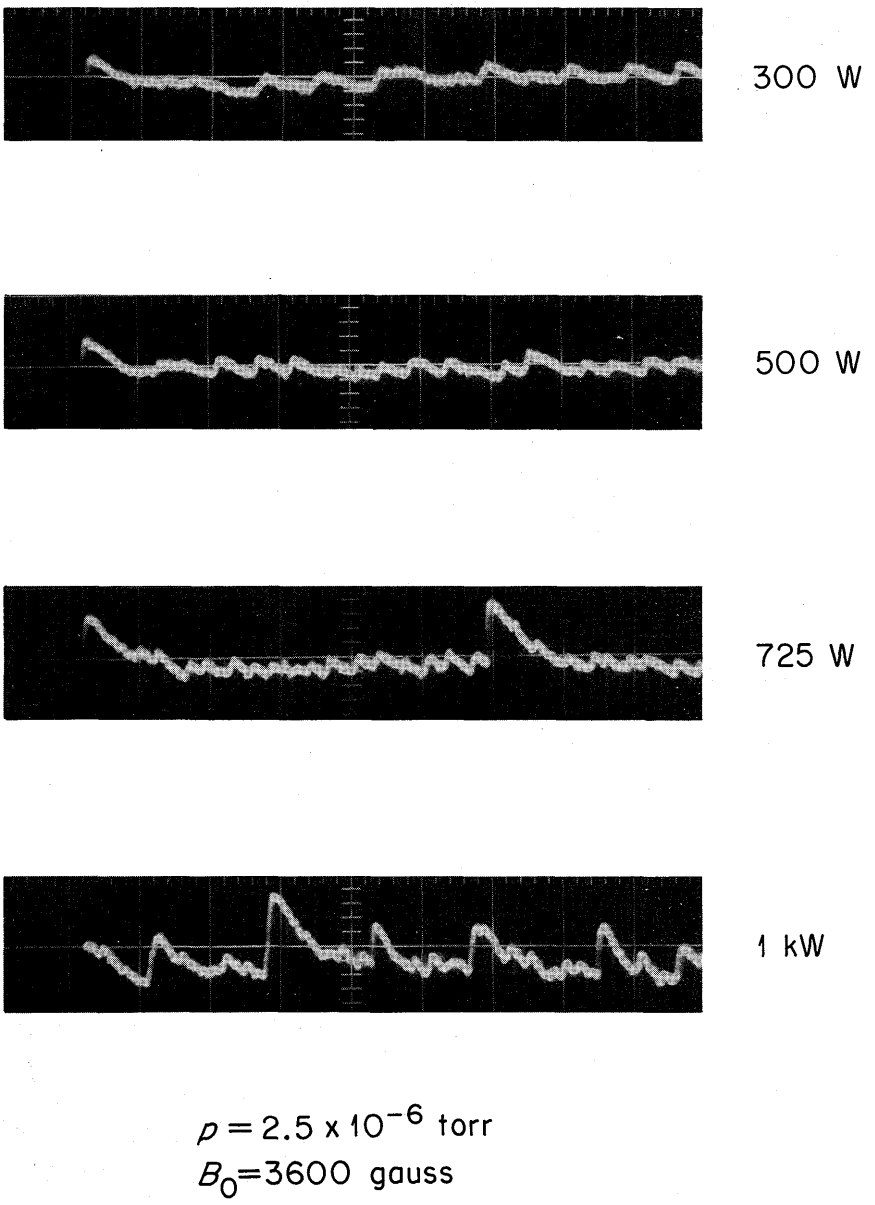

Fig. 2.10. Fluctuations in $\Delta\Phi$ Observed from Coil Wrapped Around Cavity for Four Values of Applied Power. B_0 = 3600 G corresponds to +20% field.

Other fluctuations, however, are seen in the plasmas produced in magnetic well geometry. In Fig. 2.10, we show the increase in repetition frequency of the fluctuations seen in the derivative of the diamagnetic flux signal as a function of applied microwave power. At the lowest pressures, similar fluctuations are present with applied powers below 50 W. Fluctuations show up in the K-band noise, in the fast diamagnetic flux, in the axial currents, and in large x-ray bursts from a radial skimmer. At the higher fields, with smaller plasma volumes, these fluctuations always are correlated, as shown in Fig. 2.11. For lower magnetic field values, the correlations are not quite as good, perhaps as a result of the larger plasma volumes. It is informative to note that all the fluctuations are preceded by a high-frequency noise burst, and on this evidence, we suggest that a microinstability in the plasma is the probable source of the fluctuation.

ORNL-DWG 68-13145R

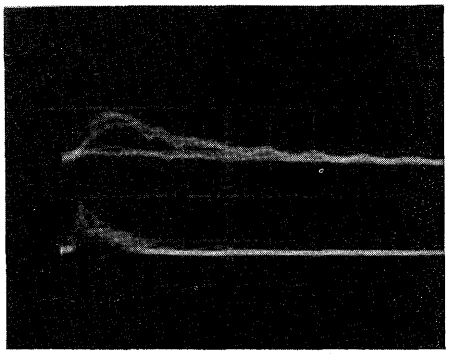

$p = 2.5 \times 10^{-6}$ torr; POWER = 2 kW
$B_0 = 3600$ gauss

$\frac{d\phi}{dt}$

rf NOISE ABOVE 16 GHz
SWEEP SPEED = 0.2 μsec/cm

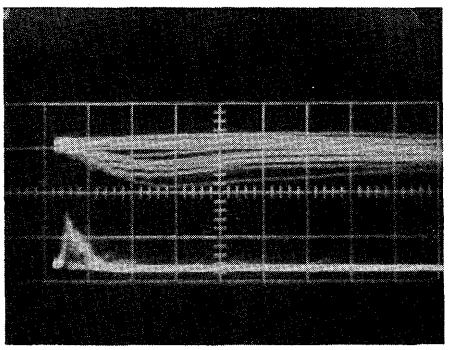

i_{AXIAL}

rf NOISE ABOVE 16 GHz
SWEEP SPEED = 0.5 μsec/cm

Fig. 2.11. Correlation of Fluctuations in Diamagnetic Flux ($d\phi/dt$) and Axial Current (i_{axial}) with Noise Bursts at Frequencies Above 16 GHz. $B_0 = 3600$ G corresponds to +20% field.

We have made an attempt to identify the microinstability mechanism with, at present, no success. Using the superheterodyne arrangement described in Sect. 2.2.3.4, we have measured the frequency spectrum of the radiated noise. A typical spectrum is shown in Fig. 2.12. When the magnetic field is changed, the spectral content changes only in intensity, not in shape, and when the power is raised, the spectrum is similar to that seen at the original field. The peaks seen at ~8.5 and 11.5 GHz have been identified. The spectrum near 8.9 GHz arises from signals mixing with the second or fourth harmonic of the local oscillator, the peak near 11.5 GHz from mixing with the third harmonic. The peaks, obviously, are very broad, although roughly peaked near a harmonic of the electron cyclotron frequency somewhere in the plasma volume (not at the heating frequency, which is 10.6 GHz). The frequency may, perhaps irrelevantly, also be related to low harmonics of the electron plasma frequency (which is within a factor of 5 of the heating frequency in most cases, closer at higher power, and would

ORNL-DWG 68-13146R

$P = 1 \times 10^{-6}$ torr
POWER = 1 kW

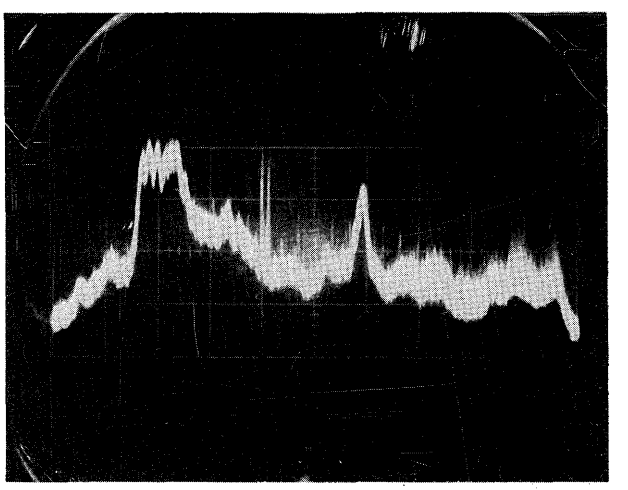

12.4 10.6 8.2
(HEATING FREQUENCY)
LOCAL OSCILLATOR FREQUENCY (GHz)

Fig. 2.12. Frequency Spectrum Determined from Superheterodyne Receiver for Frequencies in K Band.

always be expected to show a broad frequency spectrum due to density fluctuations).

2.2.6 Discussion

From an examination of the data presented above, we are struck by several trends. The mean electron energy and energy distribution are almost independent of the heating power, field magnitude, or pressure (except for the cold-electron component). At a given pressure, as the power is raised, the energetic-electron density rises and then saturates. Fluctuations, which were present at lower power, become more frequent and appear to dominate in the plasma losses.

The maximum density observed occurs near the center of the volume and, in general, approaches $n_{e_H} \sim 10^{12}$ cm^{-3}, that is, where $\omega_{pe} = \omega_{ce}$. The density decreases radially. The plasma is observed to fill the volume defined by the magnetic surface at which resonance between the cold-electron cyclotron motion and the heating fields occurs. The location of this surface is affected, of course, by the diamagnetism of the confined plasma.

As we stressed in the Introduction, the parameter of greatest significance for a target plasma is the ratio n_t/n_0'. Since the ionization probability of a neutral atom passing through the plasmas in INTEREM is not greater than 50%, the internal and external neutral densities are about equal ($n_0 = n_0'$). In the optimum cases, in INTEREM $n_e/n_0 \approx 3$ to 5. In order to assess the major influences on n_e/n_0, we may write the equilibrium power and particle equations

$$P = \frac{n_{e_H} \langle E \rangle fV}{\overline{\tau}}, \tag{1}$$

$$\frac{n_{e_H}}{\overline{\tau}} = n_{e_H} n_0 \langle \sigma v \rangle_H \left[1 + \frac{n_{e_c} \langle \sigma v \rangle_c}{n_{e_H} \langle \sigma v \rangle_H} \right] \eta . \tag{2}$$

In Eq. (1), P is the power absorbed by the plasma, $\langle E \rangle$ is the mean plasma energy, and V the volume. Since the particles may not leave the plasma with their mean energy, we introduce the factor f to express the average fraction of the mean energy carried off by a particle as it escapes the field. $\overline{\tau}$ is then the mean particle lifetime. This expression is valid if the power carried off by the cold particles can be neglected, and at the lowest pressures we have established this to be true. In Eq. (2), $\langle \sigma v \rangle_{H,c}$ are the ionization rate coefficients averaged over the hot or cold electron distributions, and η is the fraction of cold electrons which are trapped for a sufficiently long time to become hot.

The parameters f and η are not yet known, but we may assume that neither of them exceeds unity and thus obtain bounds on $\overline{\tau}$. Taking $f = 1$ and a volume of 4.1 liters ($\sim$20% field), at 1 kw, $\overline{\tau}_{max} = 32$ msec. The minimum value of $\overline{\tau}$ is determined from $\eta = 1$, $\overline{\tau} \cong 0.5$ msec. For a Maxwellian distribution with a temperature of 100 keV, a density of 10^{12} cm^{-3} would have a lifetime of $\sim$0.15 sec (consistent with the observed decay times). In order to establish a better limit on $\overline{\tau}$, we are in the process of devising an experiment to determine the parameter f. We are forced to the conclusion, however, that unless instabilities are limited, the short lifetime will severely restrict the range of pressure for which an equilibrium at the required density can be maintained with in situ gas ionization as the sole electron source.

Some speculation on the instability mechanism is, perhaps, in order. Two possibilities come to mind, and others may be possible: (1) unstable electromagnetic (whistler) mode, (2) oblique electrostatic mode. Ikegami *et al.*[12] report that in their hollow-shell ECH plasma, whistler modes may be triggered by a rapid heating pulse during plasma decay. Sudan[13] has determined the conditions for instability in a relativistic bi-Maxwellian electron plasma and finds that for sufficiently large anisotropy, unstable whistler modes should grow at frequencies near $\omega \sim (1 - \gamma)\omega_{CR}$, where ω_{CR} is the relativistic electron cyclotron frequency for the mean of the distribution and $\gamma = T_{\parallel}/T_{\perp}$. Although this mode represents a possible mechanism for the observed instability, there are some disturbing inconsistencies. Primarily, it is not clear why it is not seen in the simple mirror configurations at higher cold-plasma density. M. Farr[14] has estimated the influence of a second cold group of electrons on the instability, and it would appear the cold group could not have a decisive affect. Nevertheless, we observe the

[13] R. N. Sudan, *Phys. Fluids* **8**, 153 (1965).

[14] M. Farr, private communication.

effects strongly only in the quadrupole configuration, and then principally when the cold density is reduced.

D. Sigmar and G. Guest[3] have calculated the instability thresholds for electrostatic "loss-cone" modes with oblique propagation across the magnetic field for energetic (but nonrelativistic) plasmas, including the influence of a cold-electron population. Briefly summarized, they find instability thresholds for $(\omega_{pe}/\omega_{ce})^2 \sim 1/10$ to 1 for sufficiently high anisotropy. The frequency should occur in a band around $\omega_{ce}/2$ for perpendicular wavelengths near the gyroradius. They observe that the presence of cold plasma alters the mode so that it becomes convectively rather than absolutely growing. If this transition represents an observable phenomenon, perhaps this mode would most nearly correspond to the observations.

It may be important, as well, that the plasma heating mechanism, if localized in the resonant regions, can result in $v_{\parallel} \sim$ constant in the midplane for those electrons which have become relativistic. In that event, the electrons leaving the heating region approximate streams in the midplane, which should tend to destabilize both these modes.

Since the instability threshold scales with $(\omega_{pe}/\omega_{ce})^2$ in the mode calculated by Sigmar and Guest and the unstable whistler mode may be expected to have growth rates which also scale with the same parameter, we have some theoretical justification for expecting higher densities with stronger magnetic field strengths. However, the INTEREM facility cannot be extended to significantly higher fields. Further, we are at a technical limit in the base pressure in INTEREM, so that a measure of the variation of $\bar{\tau}$ with pressure in a plasma using 3-cm heating power is not presently feasible. It therefore appears necessary to proceed to the experiments in IMP to provide scaling points toward a full-scale target plasma.

2.3 IMP (INJECTION INTO MICROWAVE PLASMA)

W. B. Ard	N. H. Lazar
R. J. Colchin	L. A. Massengill
J. L. Dunlap	T. F. Rayburn
R. S. Edwards	R. G. Reinhardt
D. P. Hammond[15]	E. R. Wells

Certain inadequacies in the INTEREM apparatus, summarized in Sect. 2.1, clearly indicate the need for extending such studies of target plasma formation with in situ feed to include an experimental environment characterized by higher magnetic field, higher microwave heating frequency, and better base vacuum. The IMP facility is being constructed to provide this environment. The field configuration is again a mirror-quadrupole, but design criteria call for $B_0 = 20$ kG, a 2:1 axial mirror ratio, and closed modulus B surfaces out to 1.3 B_0. The higher field will permit resonant heating with frequencies as high as 55 GHz, the present limit at which significant steady-state power can be obtained. In addition, the IMP facility will use high-vacuum construction techniques and pumping equipment to provide significantly lower base pressure and a cleaner environment than does the INTEREM apparatus.

Initially, greatest emphasis will be placed on those experiments in IMP which will provide a more definitive test of the concept of in situ feed. We must discover whether or not the observed limitations of the INTEREM plasma can be relaxed enough to permit electron densities to reach 10^{13} cm^{-3} with ambient neutral pressures in the range of 10^{-7} to 10^{-6} torr. The battery of diagnostics described in the previous section will all be available. In addition, IMP will incorporate a neutral injector for which at least 25 mA at 20 keV is expected. During this phase of the operation, the injector will function primarily as a near-unequivocal diagnostic[16] for the target density and the ratio of target to neutral densities near the center of the ECH plasma.

A 10^{13}-cm^{-3} target density in IMP with an ambient pressure of 10^{-6} torr of molecular hydrogen would be suitable for accumulating peak hot-ion densities approaching $(\omega_{pi}/\omega_{ci})^2 \approx 10$. These figures assume only the current levels anticipated from the initial injector assembly. The stability of such a plasma will, naturally, be of great interest. However, stability studies will be compromised somewhat by the small size of the plasma, since growth for some theoretically predicted modes requires wavelengths longer than the IMP plasma can provide. Nevertheless, successful operation of the IMP facility will permit serious

[15] On leave of absence from Culham Laboratory, Culham, England.

[16] M. C. Becker *et al.*, *Thermonuclear Div. Semiann. Progr. Rept. Oct. 31, 1967*, ORNL-4238, p. 61.

consideration to be given to a facility of larger scale based on the concept of in situ feed.

Section 11.5 gives some engineering considerations of IMP.

2.4 ELECTRON TRAPPING IN MIRRORS BY ELECTRON-CYCLOTRON HEATING

W. B. Ard

2.4.1 Introduction

A possible approach to the problem of producing a satisfactory "target plasma" is to form the plasma by trapping particles in the mirror region that are applied by a plasma source outside the mirrors. This method would, in principle, eliminate the need of neutral particles in the target plasma region. It seems, at least to this author, that there is no alternative to this approach to the target plasma problem.

One method of trapping particles from the "feed" plasma in the mirror is to heat some of the feed electrons to a sufficiently high energy that they become mirror contained. The electrons are freely streaming through the mirror, so that the heating must be accomplished in a time less than that required for the electrons to transit the mirror. Electron-cyclotron heating can give electrons an appreciable amount of transverse energy in a short time, and the purpose of this investigation is to determine the efficiency of this method of trapping streaming electrons in a mirror.

The assumption we make in order to discuss trapping with microwave heating is that, at some region inside the mirror where the magnetic field is such that electrons are in resonance with the heating frequency, the electrons undergo a non-adiabatic change in transverse energy, and that the electron motion is otherwise adiabatic. In order to find the transverse energy change, ΔE, required to trap the electrons, we simply require

$$E/B_0 < \frac{E_\perp(r)}{B_r} , \tag{1}$$

where E is the total energy of the electron, B_0 is the magnetic field in the mirror throat, and $E_\perp(r)$ is the perpendicular energy at a point inside the mirror where the magnetic field is B_r ($B_r < B_0$). For simplicity we take B_r as the resonant magnetic field.

Let the initial energy of the electron as it enters the mirror be $E_0 = E_{\perp 0} + E_{\parallel 0}$. The initial transverse energy at B_r is then equal to

$$\left(\frac{B_r}{B_0}\right) E_{\perp 0} \text{ or } \left(\frac{B_r}{B_0}\right)(E_0 - E_{\parallel 0}) .$$

Equation (1) then becomes:

$$E_0 + \Delta E < \frac{B_0}{B_r}\left[\left(\frac{B_r}{B_0}\right)(E_0 - E_{\parallel 0}) + \Delta E\right] = E_0 - E_{\parallel 0} + \left(\frac{B_0}{B_r}\right)\Delta E \tag{2}$$

and

$$\Delta E > E_{\parallel 0}/(R - 1) , \tag{3}$$

where $R = B_0/B_r$ is the effective mirror ratio. Although the actual mirror ratio can be larger than R, there is no advantage as far as trapping is concerned.

We see that the energy given to an electron must be of the order of its initial parallel energy. The energy that can actually be given to an electron in one transit of the resonance region can be estimated by assuming that the electron is in resonance with the microwave field for a time Δt equal to the time required for the phase of the electron in its orbit to change 180° with respect to the phase of the microwave field, that is,

$$\Delta t = \frac{\pi}{\Delta\omega} , \tag{4}$$

where $\Delta\omega = \omega_0 - \omega$, ω_0 is the frequency of the microwave field, and ω is the Larmor frequency of the electrons. If we write

$$\Delta\omega = \frac{d\omega}{dz}\Delta z = \frac{d\omega}{dz}\frac{dz}{dt}\Delta t , \tag{5}$$

we have

$$\Delta\omega = \frac{d\omega}{dz} v_\parallel \Delta t = \frac{e}{mc}\frac{dB}{dz} v_\parallel \Delta t , \tag{6}$$

and Eq. (4) becomes

$$\Delta t = \left(\frac{\pi mc}{ev_{\parallel}\, dB/dz}\right)^{1/2} = \frac{4.2 \times 10^{-4}}{(v_{\parallel}\, dB/dz)^{1/2}} . \qquad (7)$$

The perpendicular energy gained by the electron in this time is then

$$\Delta E = \mathcal{E} v_{\perp} \Delta t , \qquad (8)$$

where $\mathcal{E}$ is the electric field strength of the microwave field.

If we assume that $v_{\perp} \approx v_{\parallel} \approx v$ and $dB/dz \approx 10^2$ G/cm, we can get an order of magnitude relation for the energy gained in one transit. From Eqs. (7) and (8), we then have

$$\Delta E \approx 0.3 \mathcal{E} E^{1/4} . \qquad (9)$$

For trapping we require $\Delta E > E_{0\parallel}$; thus $\mathcal{E}$ must be of the order of magnitude of E_0, where $\mathcal{E}$ is in volts per centimeter and E_0 is in electron volts, if an appreciable fraction of the electrons are to be trapped. Of course, even small microwave electric field strengths will be sufficient to trap some electrons if the electron distribution contains some electrons with very small $E_{\parallel}$.

2.4.2 Experiment

The Long Solenoid facility was used for an experiment to determine the efficiency of trapping electrons in a mirror with modest microwave power. For these experiments the currents in the solenoid coils were adjusted to produce a magnetic mirror region near each end of the machine with a more or less uniform field connecting the two regions. A microwave discharge in one of the mirrors produced a plasma that was allowed to stream down the uniform field and through the second mirror region. Baffles were placed between the two mirrors in order to limit the streaming plasma to a small column and to reduce the neutral gas pressure as much as possible in the second mirror.

The plasma column was brought through the second cavity, 4 cm off the magnetic axis. The purpose of this was that electrons that became trapped in the mirror would precess out of the column due to the magnetic field gradient and would strike a target located in the midplane of the mirror 90° in azimuth from the position of the plasma column. The number of electrons striking the target was measured by counting x rays emitted from the target.

The target also functioned to prevent the containment of trapped electrons in the mirror. This was necessary in order to reduce secondary ionization in the mirror by the trapped particles. Nevertheless, some secondary ionization could occur, and it was necessary to limit the time duration of the microwave field. It was found that no appreciable secondary ionization was produced during the first 200 μsec of the pulse; that is, the counting rate was independent of time during the first 200 μsec.

Another possible source of error was the ionization of gas in the mirror by electrons in the plasma column. Since these electrons would be produced inside the mirror, a large fraction of them would be trapped to start with.

2.4.3 Results

The measurements were taken by turning the trapping microwave power on for 75-μsec intervals and counting the number of x rays emitted from the target during the pulse. The x rays were counted by photographing the output of the pulses from the x-ray detector on an oscilloscope. Since the pulse widths from the detector were about 1 μsec, the counting rate had to be kept below about 30 x-ray pulses per trapping pulse. Therefore the counting rate was determined by averaging over many trapping pulses.

The number of electrons traversing the mirror per second was estimated by monitoring the saturation ion current to a collector placed in the plasma column.

The contribution to the counting rate from secondary ionization in the mirror by the plasma column and by the trapped electrons was determined by changing the pressure in the mirror and measuring the count rate as a function of pressure.

Results from a typical set of measurements are shown in Fig. 2.13. The count rate is seen to vary approximately linearly with pressure, so that the curve can reasonably be extrapolated to zero pressure. In fact the slope is small enough that the base pressure is sufficiently close to zero pressure that little error should be introduced by the extrapolation.

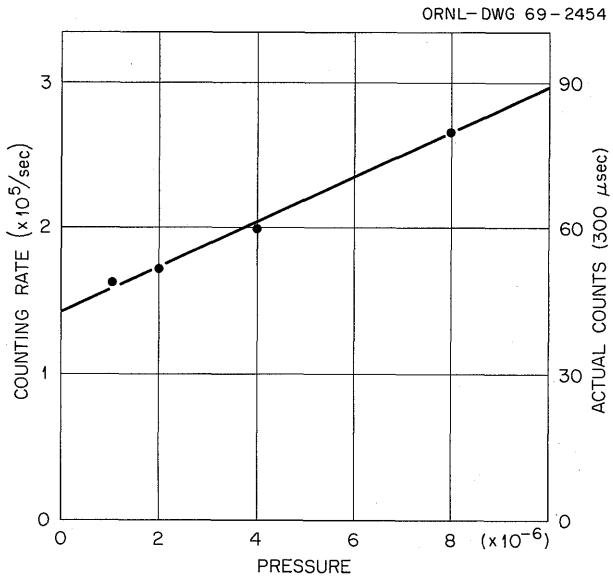

Fig. 2.13. Count Rate of X Rays from Target as a Function of Background Pressure.

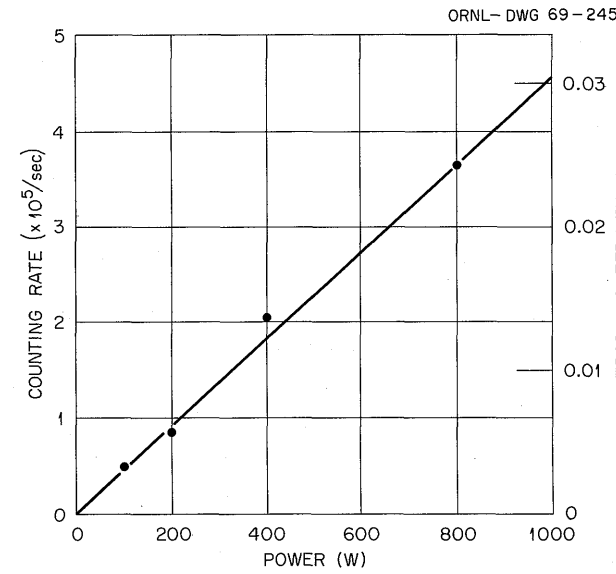

Fig. 2.14. Trapping Efficiency as a Function of Microwave Power.

In order to determine the number of electrons actually striking the target, one must know the fraction of the total emitted x rays detected by the x-ray detector and the number of x rays emitted per electron striking the target. The fraction of x rays detected depends on the solid angle subtended by the detector and absorption between the target and the detector. The absorption was due to a 0.005-in. Mylar window, a 0.002-in. aluminum window, and 10 cm of air. At 8 keV, 50% of the x rays were absorbed. The solid angle subtended by the detector, aperture diameter $\frac{1}{8}$ in., 22 in. from the target, was 2.5×10^{-5} sr.

Assuming the x rays are emitted into 4π sr, the detector detects only about 1 in 10^6 of the emitted x rays.

The number of x rays emitted per electron striking is somewhat uncertain, since it depends on the energy of the electron. Most of the x-ray pulses detected indicated that they were K x rays from the copper target, so that one could conclude that few of the electrons were more than about 20 keV. Electrons with energy less than about 10 keV would not produce enough energetic x rays to be detected. The efficiency for the production of K x rays by electrons in the range 10 to 20 keV is about one or two K x rays per 1000 electrons incident on the target. If we assume an average yield of 1.5 x rays per 1000 electrons, we get an estimate of the number of electrons trapped per second as

$$N \approx 6 \times 10^8 C ,$$

where C is the number of x rays counted per second. Extrapolating the curve in Fig. 2.13 to zero pressure gives a counting rate of about 1.5×10^5 per second, and we get an estimate of about 10^{14} electrons per second trapped.

Measurement of the current to the collector in the plasma column gives a value of about 10^{16} electrons per second traversing the mirror and hence a trapping efficiency of about 1%.

Figure 2.14 shows the dependence of the counting rate and hence the trapping efficiency as a function of microwave power in the mirror region. The maximum trapping efficiency was about 2.5% at a power of 800 W. Further increases in power increased the count rate; however, at counting rates over 3 or 4×10^5 per second, the pulses were difficult to resolve, and therefore the count rate could not be determined with any accuracy.

2.4.4 Discussion

It is apparent that the results of this experiment yield only an estimate for the actual efficiency of trapping electrons by microwave electric fields. However, the estimate should be within a factor

of 2 of the actual efficiency. While only the electrons that gained more than 10 keV were detected, it can be argued that these are really the only electrons that would contribute very much to the final trapped plasma density, since at high plasma densities, low-energy electrons scatter too rapidly to be considered mirror contained.

These results seem quite good from the point of view of building up a target plasma from a warm toroidally contained plasma. An electron would only make about 50 transits of the torus before being trapped and heated in the mirror. Even with Bohm loss rates in the torus, the average electron is much more likely to be trapped in the mirror than to be lost from the torus. Since the scattering rate for hot electrons in the mirror can be quite small, even a 1% trapping rate could sustain a density in the mirror considerably larger than the density in the torus. However, if the density in the mirror is to be larger than the torus density, ions must be contained in the mirror by a negative space potential.

3. Injection and Accumulation: Neutral Injection Experiments (DCX-1.5)

R. J. Colchin
J. L. Dunlap
R. S. Edwards
L. A. Massengill
R. G. Reinhardt
W. J. Schill
E. R. Wells

3.1 INTRODUCTION

Experiments and calculations this last year concentrated on an exposition of the Z mode, initially described in earlier reports.[1,2] It is thought to be a Harris-like instability, driven by DCX-1.5's highly anisotropic ion velocity distribution ($T_{\parallel}/T_{\perp} \approx 0.005$).

Experiments ended in June, and DCX-1.5 was subsequently removed to make room for assembly of the IMP facility. Experimental work accomplished before termination is reported in the succeeding sections. The apparatus employed is described in Sect. 3.2, results are reported in Sect. 3.3, and comparisons with the observations of PHOENIX II and ALICE (Baseball) are drawn in Sect. 3.4. Much of our work in mirror geometry complements the ALICE and PHOENIX II efforts with stabilized fields. An important supplement is a demonstration of the existence of betatron motions. Still to be completed is a detailed comparison of these experimental findings with theory. Efforts in this direction are presently being brought to fruition and will be reported later.

3.2 APPARATUS

The apparatus employed was, for the most part, the same as described in the earlier reports,[1,2] but some adaptations were made for Z-mode studies. The one major change involved modifying the liner and magnetic coil configurations to accommodate betatron oscillation measurements. Equipment applications and modifications are discussed below.

The plasma was formed in a liner which constituted a separate vacuum region inside the main vacuum tank. Two different liners were employed. During the bulk of the experiments, the configuration was that labeled A in Fig. 3.1. Just before termination of our studies, an additional set of magnetic field coils was added. This necessitated change of the liner to configuration B. This second liner differed from the first in that it contained no provision for titanium pumping. As a consequence, background gas pressures were higher, limiting attainable average plasma densities to less than 10^7 particles/cm^3. Only betatron frequency measurements were conducted in this last configuration.

Gridded cold-plasma detectors[3] were employed both in the measurement of peak positive plasma potentials and in the detection of electrons ejected during Z-mode bursts. A radial array of 11 detectors was situated in one end-wall. During Z-rf bursts the potentials on axis rose from their normal 100- to 200-V levels and peaked at values such as those shown in Fig. 3.2. Potentials then returned

[1] *Thermonuclear Div. Semiann. Progr. Rept. Apr. 30, 1967*, ORNL-4150, pp. 36–46.

[2] *Thermonuclear Div. Semiann. Progr. Rept. Oct. 31, 1967*, ORNL-4238, pp. 28–38.

[3] *Ibid.*, pp. 28–30.

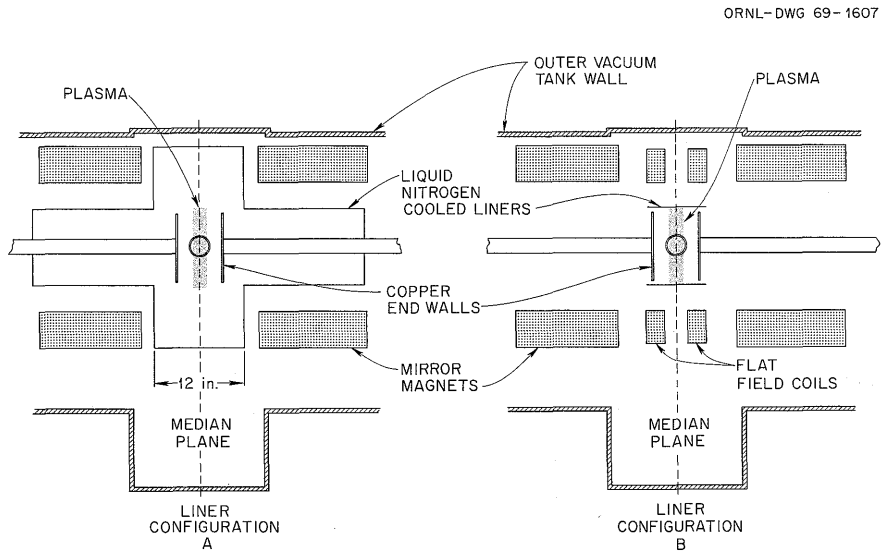

Fig. 3.1. Liner Configurations Under Normal Operation (*A*) and with Flat Field Coils Added (*B*).

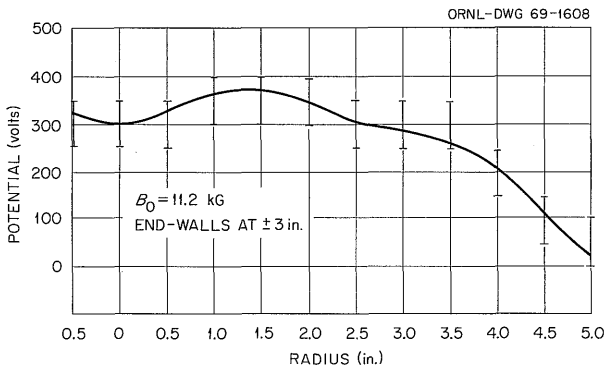

Fig. 3.2. Peak Values of Plasma Potential During *Z*-Mode Bursts, as a Function of Radius. Density was $\cong 2 \times 10^7$ particles/cm^3.

to normal upon termination of the burst. Since, as will be shown later, the *Z*-mode instability was localized near the axis, it was of interest to compare density values in this central region with those average values measured by secondary-emission detectors[3] (SED). Data (Fig. 3.3) were taken under both strong and weak instability conditions. For weak instability, it is estimated that the central density (defined as the average density between $0 \leqq R \leqq 1.5$ in. and $Z = \pm 0.75$ in.) was seven times that given by SED measurements.

Radio-frequency emission was monitored by detectors of two types. One was the crown probe,[4] capable of $\dot{B}_\theta$, $\dot{B}_z$, and electrostatic measurements. The second type, capacitatively coupled to the plasma, was the array of five button probes shown in Fig. 3.4. This array was aligned along the magnetic field for the purpose of phase correlating *Z*-mode signals at different longitudinal positions. Each button was a copper disk, $\frac{3}{8}$ in. in diameter. Because *Z*-mode activity occurred principally near the axis, it was often advantageous to move the detector array to smaller radius while maintaining a separation from the plasma itself by advancing the movable scraper.

In the hope of heating trapped electrons, 35-GHz microwave power was directed at the plasma from a waveguide opening into the liner. Power transmitted into the liner was a few watts. However, the *Q* of the structure was extremely low, due to open ports accommodating diagnostics, beam, and end-walls, and we were unable to estimate the microwave fields.

Anticipating that microwave heating of electrons would lower normally positive plasma potentials, provision was made for lithium beam[3] potential determinations. This technique rests on uncertain ground when the velocity of the lithium beam atoms

[4] J. L. Dunlap *et al.*, *Phys. Fluids* **9**, 199 (1966).

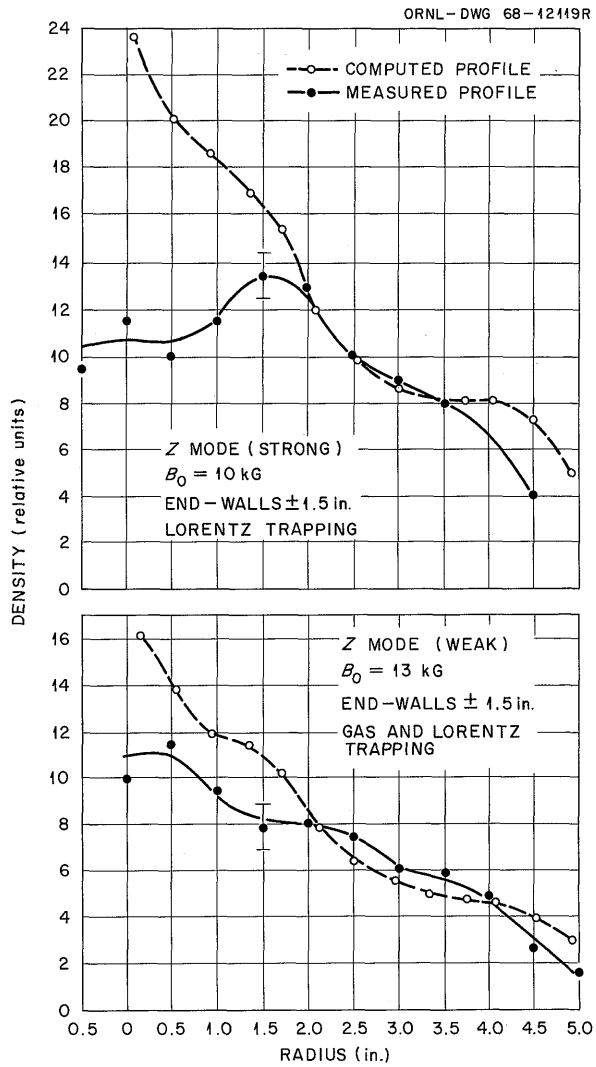

Fig. 3.3. Measured and Computed Hot-Ion Radial Density Profiles. Measurements from ion saturation current to gridded cold-plasma collectors. Computed curves were for ionization from a beam simulated by five injection trajectories, all in the median plane but spaced 0.25 in. apart. The injected current associated with each trajectory was such as to model the actual beam profile. Error bars represent uncertainties in extracting data from oscillograms.

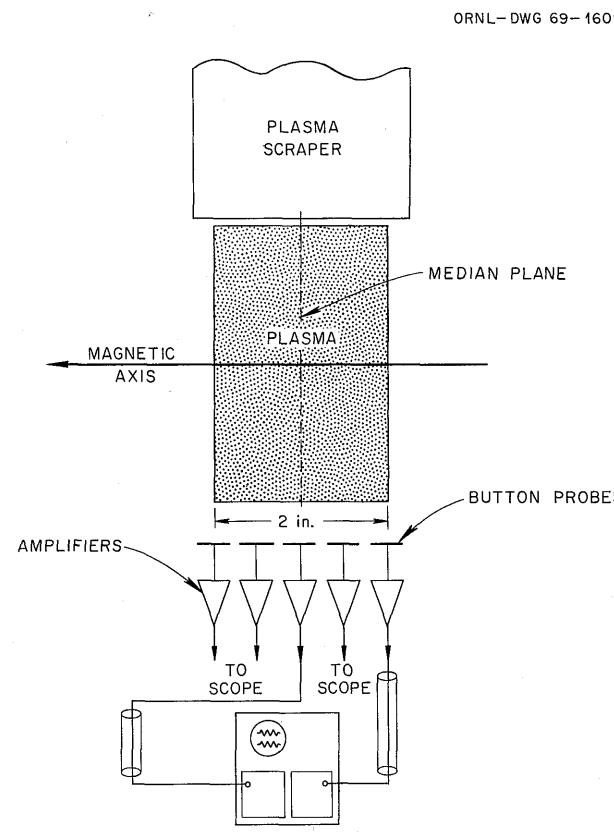

Fig. 3.4. Schematic of RF Probe Array Used in Z-Mode Phase Correlation Measurement.

is comparable with the phase velocity of instability waves, as here at ω_{ci}. Agreement between potentials measured during Z-mode activity by gridded cold-plasma collectors and by the lithium beam technique convinced us that the latter method did indeed give reliable results.

3.3 EXPERIMENTAL OBSERVATIONS

Before going further, two definitions are in order. In the following, "cyclotron harmonic" or simply "harmonic" is taken to mean ω_{ci}, $2\omega_{ci}$, or $3\omega_{ci}$. "Mode number" is equivalent harmonic number, mode $m = 1$ occurring around ω_{ci}, $m = 2$ around $2\omega_{ci}$, etc.

Observing Z-mode rf at low resolution on a spectrum analyzer, we noted frequency bands near the cyclotron harmonics. Usually the frequencies were near a single harmonic; occasionally they existed simultaneously at 1 and $2\omega_{ci}$ or at 2 and $3\omega_{ci}$.

Upon increasing the spectrum analyzer's resolution, we noted that a given band of frequencies actually consisted of discrete frequencies separated by nearly equal intervals. Under a second heading (Sect. 3.3.2) it is shown that one frequency was essentially at the cyclotron harmonic and that the others were spaced away from that harmonic by

multiples of the betatron frequency. Information was also obtained concerning the symmetries (about the median plane) of these oscillations.

3.3.1 Gross Effects

Z-mode signals were observed at hot-ion densities (SED) of $2 \times 10^6 \lesssim 3 \times 10^7$ cm^{-3}. At lower densities these signals were washed out by detector system noise; at higher densities the θ mode became the completely dominant high-frequency instability. Between these limits the Z mode, θ mode, and stable flute all existed. All three were relatively weak below $n \approx 10^7$ cm^{-3}, and the Z mode dominated the high-frequency spectrum.

Z-mode behavior was characterized by separated rf bursts, the separation being rather regular under some conditions, rather irregular under others. At a density of approximately 10^7 particles/cm^3, typically 600 to 800 larger bursts occurred per second, each of $\cong$0.5 to 1 msec duration. Coincident with each rf pulse was the ejection of electrons from the ends of the plasma. These electrons possessed energies below 50 eV, and principally in the range 10 to 20 eV. They appeared most copiously at onset. Accompanying electron ejection, plasma potentials rose (Fig. 3.2), falling again at at the end of the pulse. A physically reasonable model of this behavior is as follows: Instability potential fluctuations, particularly at onset, reduced the height of the normally positive potential barrier by 10 to 20 V. This allowed electrons near the top of the potential well to escape, thereby causing plasma potentials to rise. This, in turn, decreased the subsequent number of escaping electrons.

Instability activity occurred most abundantly near the center of the plasma, within $r \approx 2$ to 2.5 in. This conclusion is drawn from several sources. First of all, electrons were ejected with greatest intensity within 2 in. of the axis. During a series of measurements with gridded probes, single-pulse electron emission was observed in the presence of an $m = 2$ mode. During some bursts, electron emission was centered off axis. For bursts centered on axis, electrons with energy greater than 20 eV were commonly seen out to a radius of 1.25 in. Less-common larger bursts caused electron emission to 3.75 in.

Another indication that Z-mode activity took place mainly near the axis came from the measurements of rf line widths detailed in Sect. 3.3.2. Spectrum analyzer displays at high dispersion (in liner configuration B) disclosed cyclotron-harmonic line widths of less than 0.3 MHz for both $m = 1$ and $m = 2$ modes. If we rule out the possibility of activity in a thin annular region at larger radii and associate the harmonic line width with a spread in local gyrofrequency, this spread implies activity at radii of less than 2.5 in.

A third, indirect, indication of the instability's location may be gleaned from Fig. 3.3. Under weak instability conditions the plasma density was found to peak at the center, in approximate agreement with the simple model calculations. At higher densities and with a more virulent instability present, this peak disappeared, in disagreement with model calculations. This observation suggests that the instability modified the radial plasma profile near the axis, that is, at positions where instability potential fluctuations were, presumably, largest.

Figure 3.5 shows mode amplitudes as functions of density. Three density scales have been provided, two calibrated in terms of average density and a third for peak values. At lower densities the peak scale should have most closely corresponded to values experienced by the instability. This does not hold true at higher densities, with correspondingly increased instability activity. Under these conditions (Fig. 3.3) the density no longer peaked at the instability location near the axis, and densities in the instability region were more akin to the average. It is interesting to note that no net plasma loss was recorded by an SED looking at the whole plasma during periods of increased Z activity. This observation supports the view that the plasma was being rearranged away from the center rather than being lost.

Besides the density dependence of mode number shown in Fig. 3.5, modes also exhibited a dependence on magnetic field strength, as illustrated in Fig. 3.6. The Z-mode number was rather weakly influenced by end-wall position, and then only in density regimes near mode overlap (Fig. 3.5).

We sought to define minimum $k_\perp$ values for the instability by limiting the plasma radius. Limitation was imposed through the use of a movable scraper (Fig. 3.4), which, unfortunately, decreased plasma density up to one Larmor diameter away. Instability signals at ω_{ci} disappeared for limiting radii less than 1.5 in., corresponding to $k_\perp \gtrsim 0.25$ cm^{-1}. In a similar manner, it was determined that $k_\perp \gtrsim 0.15$ cm^{-1} for $m = 2$ modes.

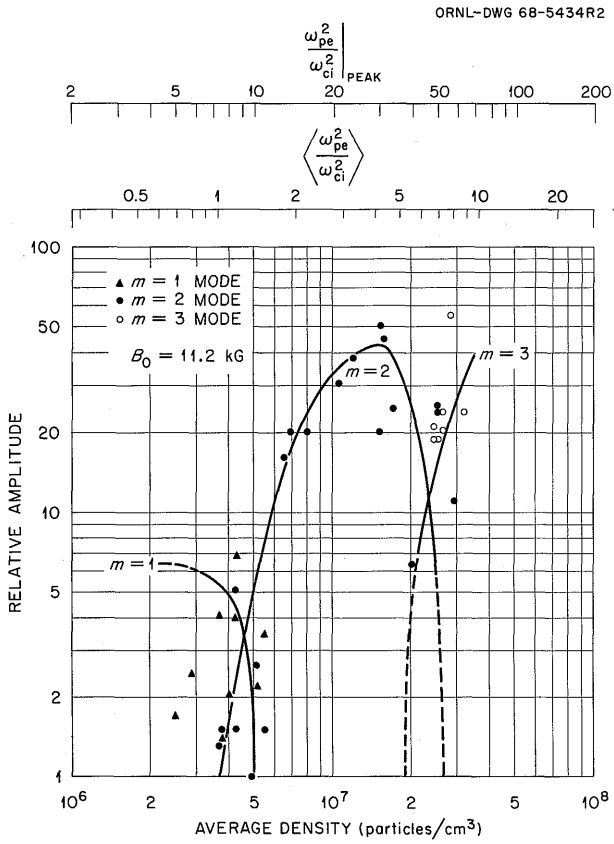

Fig. 3.5. Relative Z-Mode Amplitude as a Function of Density. Some scientific license, supported by other observations like these, has been exercised in drawing the curve fits and extrapolations.

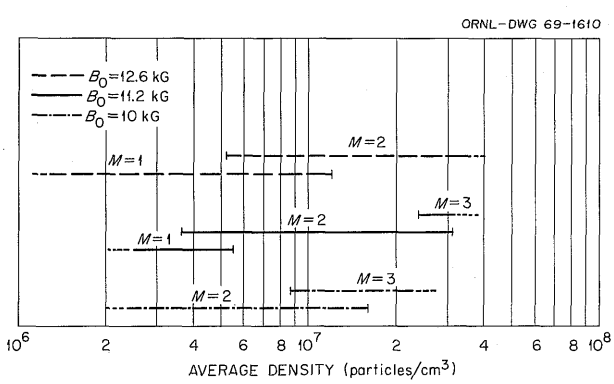

Fig. 3.6. Density Ranges for Z-Mode Observations as Functions of Magnetic Field Strength. All satellite frequencies were included in these measurements.

Earlier efforts[4] had led to the expectation that Harris-like modes might be stabilized by microwave heating of electrons. We were able to substantially reduce the rf amplitude of $m = 2$ mode signals by this technique, but could not suppress them completely. Partial stabilization was achieved only when the microwave resonance zone was close to the plasma center. Lithium beam measurements indicated that plasma potentials on axis were lowered by about 100 V from normal values of 140 to 180 V. No potential reversal was recorded.

3.3.2 Betatron Frequencies

As noted previously, closer inspection of the Z-mode rf bands revealed internal structure. We apply the term "satellites" to those frequencies shifted from the cyclotron harmonic. Satellites were observed both above and below $n\omega_{ci}$ in liner configuration A (Fig. 3.1). In liner B, satellites appeared only below the harmonics, as indicated in Fig. 3.7, which is intended as a schematic representation of radiation displayed by a spectrum analyzer. Usually either the ω_{ci} or the $2\omega_{ci}$ group of frequencies dominated, depending on density. Limited pumping in liner B restricted our investigations to lower densities and hence to frequencies below $3\omega_{ci}$. In all experiments, B_0 was 11.2 kG.

Because the satellite frequencies of Fig. 3.7 appeared at regular intervals below $n\omega_{ci}$, we attempted to relate these frequency intervals to a natural oscillation of the system. An obvious choice was the betatron or Z-bounce frequency. This frequency can be derived from the approximate force law

$$F_z = -\mu \frac{\partial B}{\partial z},$$

where μ = magnetic moment. Since B_z in DCX-1.5 had a nearly parabolic dependence on z,

$$\frac{1}{zB_0}\frac{\partial B}{\partial z} \simeq \text{constant},$$

from which it follows that

$$\ddot{Z} + v_\perp^2\left(\frac{1}{2zB_0}\frac{\partial B}{\partial z}\right) Z = 0 .$$

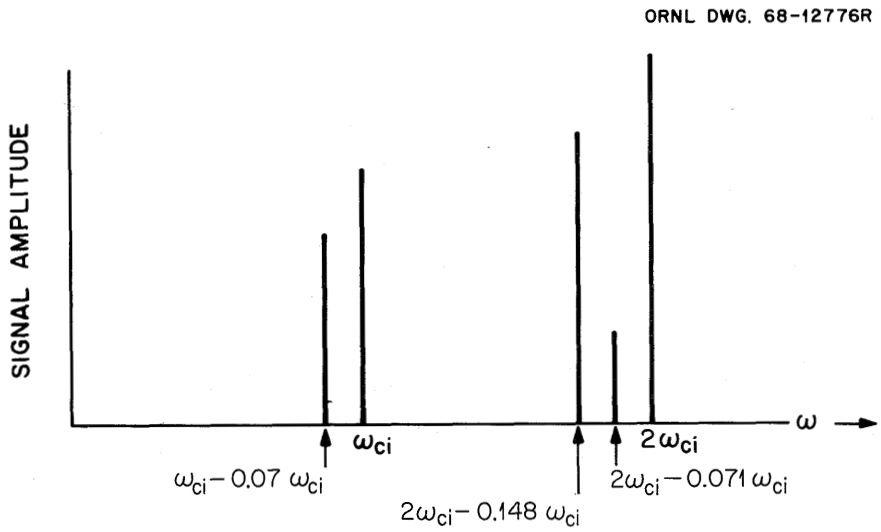

Fig. 3.7. Schematic of Z-Mode Frequencies and Amplitudes as Observed on a Spectrum Analyzer During Betatron Oscillation Experiments. Usually, only one set of frequencies was dominant, depending on density.

This equation implies simple harmonic motion with frequency

$$\omega_B = v_\perp \sqrt{\frac{1}{2zB_0}\frac{\partial B}{\partial z}}\,.$$

In order to determine if the observed satellite frequency spacing was purely a magnetic field effect, we decided to vary the magnetic field gradient. This was accomplished by adding an additional set of coils, labeled "flat field coils" in configuration B of Fig. 3.1. The central magnetic field was held constant at 11.2 kG, while field gradients were flattened by increasing current in the flat field coils and simultaneously decreasing current in the regular mirror windings.

Frequencies computed from the above equation are plotted on the lower solid curve of Fig. 3.8. The upper solid line is $2\omega_B/\omega_{ci}$, or twice the lower curve. Data from the three satellites depicted on Fig. 3.7 are also plotted, showing frequencies which decrease with approximately the predicted slope. From these data we conclude that satellites are directly associated with ion bounce motions.

An attempt was made to measure phase relations of potential oscillations along magnetic field lines. The rf detection system is diagrammed in Fig. 3.4 and was placed in liner A. Because of the simultaneous presence of more than one frequency component, it was impossible to make unequivocal symmetry assignments for each spectral component. An antisymmetric $m = 1$ mode was observed, its phase shifting by 180° across the midplane. This is believed to be the lower $m = 1$

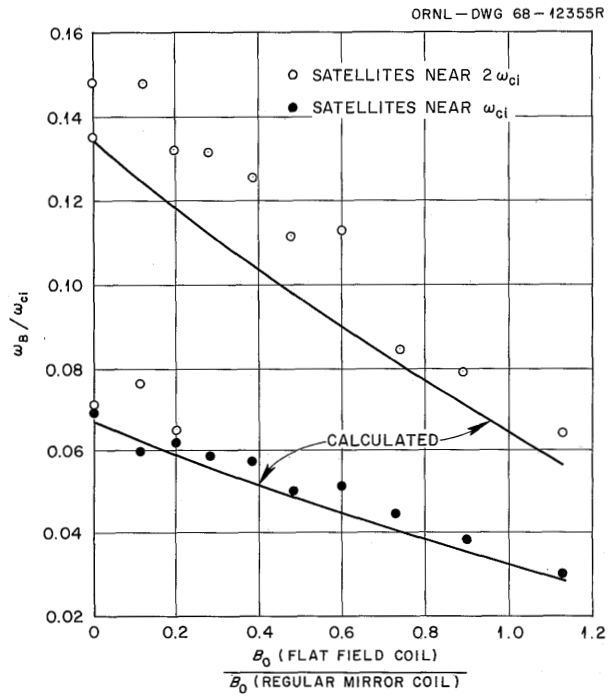

Fig. 3.8. Normalized Betatron Frequency as a Function of the Relative Contributions from Flat Field and Regular Mirror Coils. Total B_0 was held fixed at 11.2 kG.

frequency component. All observations near $2\omega_{ci}$ showed potential oscillations in phase along the magnetic field. In addition, beats between $m = 2$ frequency components were found with a frequency corresponding to ω_B. From these observations it can be concluded that there was a mode of odd symmetry present near ω_{ci}, while the principal modes of oscillation near $2\omega_{ci}$ were of even symmetry. Also, near the second harmonic, frequencies separated by ω_B existed simultaneously.

3.4 COMPARISONS

The Z mode as observed in the simple mirror field of DCX-1.5 bears a striking resemblance to instabilities occurring in the ∇B-stabilized fields of PHOENIX II[5–7] and ALICE (Baseball).[8–10] Because of the many similarities it can only be concluded that these are one and the same mode. The paragraphs below compare our observations with those of the PHOENIX II and ALICE groups.

All three experiments observed burst-like rf radiation. Associated with these bursts was the ejection of electrons from the ends of the plasma. In each experiment, plasma potentials rose as electrons were emitted.

The details of these effects varied somewhat. The other plasmas exhibited burst lengths of 1 to 10 msec, as compared with 0.5 to 1 msec for DCX-1.5. The difference is probably due to the higher densities in ALICE and PHOENIX II. Peak potentials in ALICE were 0.9 to 2 kV, 200 V in PHOENIX II, and 400 V in DCX-1.5.

All groups have detected bands of radiation at the first three harmonics. The amplitude of this radiation was density dependent, and modes appeared in succession with increasing density. The threshold densities were somewhat higher in ALICE and PHOENIX II as compared with DCX-1.5, most probably due to their lower anisotropy.

Microwave heating has been tried, with very similar effects in DCX-1.5 and ALICE. In both cases, heating of electrons reduced the instability amplitude but did not entirely eliminate it. In PHOENIX II, higher harmonics of the Z modes ($\gtrsim 3\omega_{ci}$) were quenched, but an apparently new mode was excited at ω_{ci}.

Frequency structure within a given rf band has been reported by all three groups. PHOENIX II observes a spacing of approximately one bounce frequency. Such measurements are complicated in ALICE and PHOENIX II by temporally changing magnetic fields of lower symmetry. In the steady fields of DCX-1.5, this splitting was traced to ion bounce motions.

Finally, PHOENIX II has observed an $m = 2$ antisymmetric mode. This was not detected in DCX-1.5, possibly because of the dominance of symmetric oscillations. However, an antisymmetric $m = 1$ mode was observed in DCX-1.5.

---

[5] W. Bernstein *et al.*, *Plasma Physics and Controlled Nuclear Fusion Research*, vol. II, p. 23, IAEA, Vienna, 1966.

[6] W. Calvert *et al.*, *Proceedings International Conference on Plasma Confined in Open-Ended Geometry, Nov. 1–4, 1967, Gatlinburg, Tenn.*, CONF-671127, p. 1.

[7] J. G. Cordey *et al.*, to be published in the *Proceedings of the Third IAEA Conference on Plasma Physics and Controlled Nuclear Fusion Research*, Novosibirsk, U.S.S.R., Aug. 1–7, 1968.

[8] C. C. Damm *et al.*, *Proceedings International Conference on Plasma Confined in Open-Ended Geometry, Nov. 1–4, 1967, Gatlinburg, Tenn.*, CONF-671127, p. 27.

[9] C. C. Damm *et al.*, to be published in the *Proceedings of the Third IAEA Conference on Plasma Physics and Controlled Nuclear Fusion Research*, Novosibirsk, U.S.S.R., Aug. 1–7, 1968.

[10] C. C. Damm *et al.*, *Controlled Thermonuclear Research Annual Report*, UCRL-50002-68, p. 36 (1968).

4. Injection and Accumulation: Multiple-Pass Experiments (DCX-2)

J. F. Clarke
J. S. Culver
S. M. DeCamp
J. C. Ezell
J. E. Francis
G. G. Kelley
J. F. Lyon
E. C. Moore
J. E. Robinson[1]
R. F. Stratton
J. P. Wood

4.1 INTRODUCTION

The main features of the DCX-2 plasma behavior are now well understood. The dominant instability activity at the proton gyrofrequency and its harmonics was found to be due to a previously unrecognized instability (the modified negative mass instability). The electric fields produced act to spread the perpendicular energy of the initially injected protons and to heat cold protons produced from the background gas. The energetic plasma formed from the background protons has very little energy parallel to the magnetic field and is, in fact, the central peak distribution.

The principal loss mechanism for the injected energetic particle distribution, called the sidelobe plasma, appears to be a low-frequency drift instability which carries these particles to the nearest obstacle, the injection duct. There is a correlation between this drift wave and the modified negative mass instability, and there may be a causal relationship between them. The drift instability occurs at a density well below the expected threshold.

No losses other than by charge exchange have been found in the central peak distribution of particles, but it has not been confirmed that other loss processes do not exist.

[1]Summer research participant from Massachusetts Institute of Technology.

4.2 INSTABILITIES IN THE DCX-2

In ref. 2 we showed that the dominant microinstability in the DCX-2 was the modified negative mass instability (MNM). This instability, discovered independently by one of us (G.G.K.) and by B. B. Kadomtsev, has proved to be of considerable importance in explaining the results of at least three experiments (DCX-2, PR-5, and DECA-II).[3]

The modified negative mass instability occurs because ions trapped in a magnetic well oscillate rapidly back and forth between regions of strong magnetic field. The response of an ion to any slow growing perturbation is governed by the average motion of the ion over its entire orbit between the mirrors. The most important parameter influencing the response to cyclotron-frequency instabilities is the average gyrofrequency seen by the ion. This average cyclotron frequency is velocity dependent, and it is this property which produces the modified negative mass instability. Figure 4.1 shows schematically how the instability occurs. An incipient ion clump at A decelerates ions at B. These ions penetrate further into the mirror, see a higher average cyclotron frequency,

[2]J. F. Clarke and G. G. Kelley, *Phys. Rev. Letters* **21**, 1041 (1968).

[3]J. F. Clarke, *Bull. Am. Phys. Soc.* **13**, 1491 (1968); J. F. Clarke and G. G. Kelley, to be published in *Nuclear Fusion*.

ORNL-DWG 68-8451

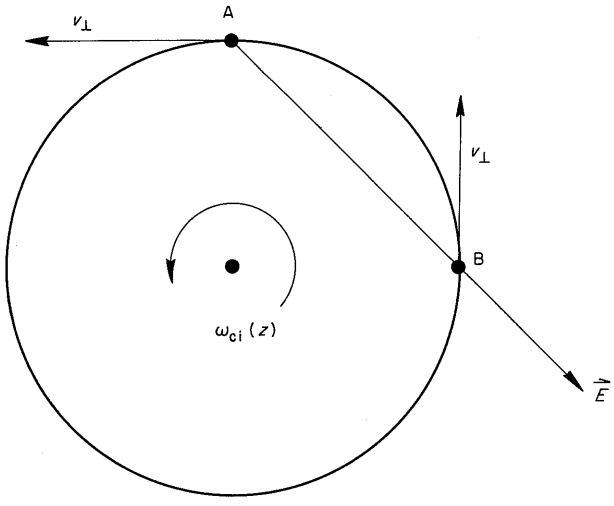

Fig. 4.1. Physical Model of the Modified Negative Mass Instability. Particle B loses perpendicular velocity to the clump at A and penetrates further into the magnetic mirror than the clump. Since its average cyclotron frequency increases, it catches up with the clump.

and catch up with the ions at A. Thus the clump grows.

In ref. 4 a theoretical description of the instability was presented which served to specify the main characteristics which one might hope to observe in an experiment, and it was on the basis of this theory that the mode identification was made in the DCX-2. Since then an improved theoretical description has been formulated which allows one to evaluate the effect of finite length on the instability.

In addition to this microinstability, whose effect is described in the next section, we have identified a low-frequency drift wave which causes direct losses of the injected ions. In addition to its importance as a direct loss mechanism in the machine, this low-frequency mode may demonstrate the occurrence of a coupling between a cyclotron-frequency instability and a low-frequency wave. Drift waves would otherwise be expected to be damped in the DCX-2.

[4] J. F. Clarke *et al.*, *Plasma Physics and Controlled Nuclear Fusion Research*, Novosibirsk, U.S.S.R., CN-24/H-6, 1968 (to be published).

4.2.1 The Modified Negative Mass Instability

The physical basis of the MNM instability is the dependence of a particle's average cyclotron frequency on its pitch angle. A theoretical description of this effect can be obtained if one considers the solution of the Vlasov equation obtained by the method of characteristics. The perturbed distribution function f_1 is obtained in terms of the unperturbed distribution function f_0 and the perturbed potential ϕ by integrating along the unperturbed orbits:

$$f_1 = \frac{q}{M} \int_{-\infty}^{t} dt' \nabla\phi \cdot \frac{\partial f_0}{\partial \mathbf{v}} . \tag{1}$$

The new instability results when one considers the particular unperturbed orbits appropriate for a particle in a spatially varying magnetic field. In such a field a particle's phase is given by

$$\Delta\Psi = \int_0^t \omega_{ci}\Big(z(t)\Big)\, dt . \tag{2}$$

Since in a mirror, $z(t)$ is periodic with the bounce frequency $\omega_B = 2\pi/\tau_B$, we can write this as

$$\Delta\Psi = \overline{\omega}_{ci} n\tau_B + \int_{n\tau_B}^{t} \omega_{ci}(t')\, dt' . \tag{3}$$

If the change in cyclotron frequency seen by the particle in its orbit is such that $\Delta\omega_{ci} \ll \omega_B$, the phase increment represented by the second term is negligible, and we can write

$$\Delta\Psi = \overline{\omega}_{ci} t , \tag{4}$$

where

$$\overline{\omega}_{ci} = \frac{1}{\tau_B} \int_0^{\tau_B} \omega_{ci}(t)\, dt . \tag{5}$$

Thus the unperturbed orbit depends on the average cyclotron frequency of the particle in the spatially dependent field. The dependence of $\overline{\omega}_{ci}$ on the particle's velocity is responsible for the MNM instability.

In the DCX-2, since the ions are in a nearly constant magnetic field, their z motion is essentially a free flight between the mirrors. Thus

our unperturbed orbits are functions of the constant velocities $v_{\parallel}$ and $v_{\perp}$ and the constant frequencies ω_B and $\bar{\omega}_{ci}$ over a spatial interval $-a < z < a$.

Once f_1 is specified, we obtain the dispersion relation from Poisson's equation, which can be written as

$$-\nabla^2\phi + \frac{q}{\epsilon_0} n(z) = \frac{q}{\epsilon_0}\int dv^3 f_1 ,$$

where $n(z)$ is the electron density. One then argues that since the electrons are much more responsive to electric fields along the direction of B than the ions, one can solve this equation by considering the ions as a perturbation.[5] For the case of a plasma of infinite extent perpendicular to the magnetic field with hot ions and cold electrons we obtain

$$\frac{\partial}{\partial z}\left[\frac{n(z)}{n(0)} - \frac{\omega^2}{\omega_{pe}^2}\right]\frac{\partial\phi}{\partial z} + \frac{\omega^2 k_\perp^2}{\omega_{pe}^2}\phi = \frac{q}{\epsilon_0}\int dv^3 f_1 , \quad (6)$$

where $n(0)$ is the midplane electron density. One then proceeds to solve Eq. (6) with standard perturbation techniques. If we define $\phi_q(z)$ as the eigenfunctions of the left side of Eq. (6), we obtain an approximate dispersion relation

$$\frac{k_\perp^2\omega^2}{\omega_{pe}^2} = \lambda_q - \frac{\omega^2}{\omega_{pe}^2}\omega_{pi}^2\int 2\pi v_\perp dv_\perp dv_\parallel \left[\sum_{n,m}\frac{J_n^2(k_\perp\rho)|A_m^q|^2 a}{(\omega - n\bar{\omega}_{ci} - m\omega_B)}\left(\frac{m\pi}{a}\frac{\partial f_0}{\partial v_\parallel} + \frac{n}{\rho}\frac{\partial f_0}{\partial v_\perp}\right)\right] , \quad (7)$$

where λ_q is the eigenvalue of the eigenfunction ϕ_q, which we have Fourier analyzed on the interval $-a < z < a$ seen by the hot protons:

$$\phi_q(z) = \sum_m A_m^q e^{-im\pi z/a} .$$

Since the scale length of the potential variation along the axis l is much greater than the length of the proton region $2a$, we can simplify the dispersion relation by taking

$$\lambda_q \approx \left(\frac{\pi}{l}\right)^2 \quad 1 - \frac{\omega^2}{\omega_{pe}^2}$$

and

$$|A_m^q|^2 a = \delta_{m,0} .$$

Then, using the distribution function

$$f_0 = \frac{n_{\text{Cold}}}{n_{\text{Hot}}}\frac{\delta(v_\perp)\,\delta(v_\parallel)}{2\pi v_\perp} + \frac{\delta(v_\perp - v_\perp^0)}{4\pi v_\perp}\left[\delta(v_\parallel - v_\parallel^0) + \delta(v_\parallel + v_\parallel^0)\right] \quad (8)$$

to describe the injected plasma in the machine, Eq. (7) reduces to

$$1 = \frac{\omega_{pc}^2}{\omega^2 - \bar{\omega}_{ci}^2} + \omega_{pi}^2\sum_n\left[\frac{n^2 J_n^2(x)\,p_\perp}{x^2(\omega - n\bar{\omega}_{ci})^2} + \frac{n}{(\omega - n\bar{\omega}_{ci})\,k_\perp x}\frac{\partial J_n^2}{\partial v_\perp}\right] , \quad (9)$$

where $x = k_\perp\rho$, $\omega_{pc}^2 = q^2 n_{\text{Cold}}/M\epsilon_0$, $\omega_{pi}^2 = q^2 n_{\text{Hot}}/M\epsilon_0$ and $p_\perp = \rho \times \partial\omega_{ci}/\partial v_\perp$ is the parameter which is responsible for the MNM instability. This parameter is negative for mirror-confined particles since the average cyclotron frequency increases when $v_\perp$ decreases. For the DCX-2, $p_\perp$ is estimated by computing particle trajectories. It turns out that for injected particles in the DCX-2 field, $p_\perp$ is a very sensitive function of the pitch angle and the precise field shape. Our best estimate for our nominal field shape and injection pitch angle is

$$p_\perp = -3 \times 10^{-3} .$$

However, small variations in the actual field shape, due to small deviations in coil position, and in the injection pitch angle, which can be affected by plasma potential as well as the field shape, could change this value by factors of 2 or 3. Equation (9) gives instabilities with frequencies

[5] J. G. Cordey, private communication.

$$\frac{\Delta\omega}{\bar{\omega}_{ci}} = \frac{n}{2}\left[\frac{1}{2}\left(\frac{\omega_{pc}}{\bar{\omega}_{ci}}\right)^2 \delta_{n,1} + \frac{1}{x}\frac{\partial J_n^2}{\partial x}\left(\frac{\omega_{pi}}{\bar{\omega}_{ci}}\right)^2\right] \tag{10}$$

and growth rates

$$\frac{\gamma}{\bar{\omega}_{ci}} = n\left(\frac{\omega_{pi}}{\bar{\omega}_{ci}}\right)\frac{J_n}{x}\sqrt{|p_\perp| - \left(\frac{\Delta\omega}{\bar{\omega}_{pi}}\right)^2 \frac{x^2}{J_n^2}}\,. \tag{11}$$

4.2.2 Observations of Modified Negative Mass Instability

The instability is flutelike by assumption and has no apparent density threshold. In fact, since the injected plasma has a small thermal spread, one would expect a very low threshold. We have observed the instability down to

$$\left(\frac{\omega_{pe}}{\omega_{ci}}\right)^2 = 10^{-2}\,.$$

This fact, together with the flutelike nature, is quite sufficient to distinguish the observed instability from a Harris mode. In addition, the frequency of the instability is predicted to be above but close to the average cyclotron frequency. Absolute frequency measurements show the fundamental instability to occur within a range of 10 to 60 kHz above the central field value in the machine. This frequency shift is close to what one would estimate from the calculations of $\bar{\omega}_{ci}$ by orbit tracing of the injected ions. However, for the reasons given above with respect to the uncertainty in $p_\perp$, it is difficult to make an exact comparison with theory. One indication that the average cyclotron frequency is indeed the critical quantity for this instability is the remarkable sharpness (3 kHz) of the unstable frequency. Only an averaging process could produce such sharpness of resonance in a nonuniform field. We shall return to this point in the next section.

As can be seen from Eq. (11), the growth rate increases with the square root of the density until the second term under the square root exceeds the $|p_\perp|$ term. This represents a cutoff effect. One can picture the MNM instability as a coupling between an ordinary positive-energy ion cyclotron wave represented by the third term on the right of Eq. (9) and a new negative-energy wave introduced by the occurrence of an energy-dependent cyclotron frequency in the second term. When the ordinary cyclotron wave is cut off, the instability is stabilized. The appearance of ω_{pc}^2 in Eq. (10) shows that cold resonant ions contribute to this cutoff for the first harmonic of the instability. Higher harmonics can only be cut off by hot ions.

The spectrum observed in the DCX-2 is shown in Fig. 4.2. Below a critical partial pressure of hydrogen in the system, all harmonics are observed to be unstable. We find in Fig. 4.2*b* that when hydrogen gas is added to the system, the odd harmonics disappear. The fourth harmonic is phase correlated to the second in this latter case, as shown in Fig. 4.2*c*. Therefore its appearance probably does not represent a separate instability. Figure 4.2*d* shows a higher dispersion view of the first harmonic below the critical pressure, and Figs. 4.2*e* and 4.2*f* show the same spectra above the critical pressure with hydrogen and deuterium. The explanation of these data given by Eq. (11) is that the fundamental instability is cut off by a critical density of cold H^+ (Figs. 4.2*d* and *e*). The resonant nature of the cutoff is demonstrated by the fact that no concentration of cold deuterium plasma produces cutoff (Fig. 4.2*f*). Beyond cutoff the second harmonic is still unstable (4.2*b*) and produces a fourth harmonic by a nonlinear distortion of the clumped ions distribution (4.2*c*).

In Figs. 4.3*a* and *b* we show the predicted cutoff density with various amounts of cold H^+ in the system as a function $|p_\perp|$. Figure 4.3*c* shows the relation of the existence of the fundamental rf to the buildup of cold plasma. From known ionization cross sections, we can calculate that the observed cold-ion current corresponds to a minimum ratio of cold H^+ to injected H^+ of 30% for a hot-ion density at cutoff of 4.5×10^7 cm^{-3}. From Fig. 4.3*a* this would indicate a value of $|p_\perp|$ close to that estimated on the basis of our orbit calculations. On the other hand, as shown in Fig. 4.3*b*, the growth rates predicted by Eq. (11) with this value of $p_\perp$ are several times those observed (20 to 80 μsec). In addition, examination of Figs. 4.2*e* and 4.2*f* shows that unstable frequencies are observed on either side of the dominant frequency. Thus our approximation to the general dispersion relation cannot reproduce all of the observed details of the instability.

Upon close examination of the side bands, we find them to be located at multiples of the ion bounce frequency; this is shown in Fig. 4.4. If we make the crude assumption that these side-

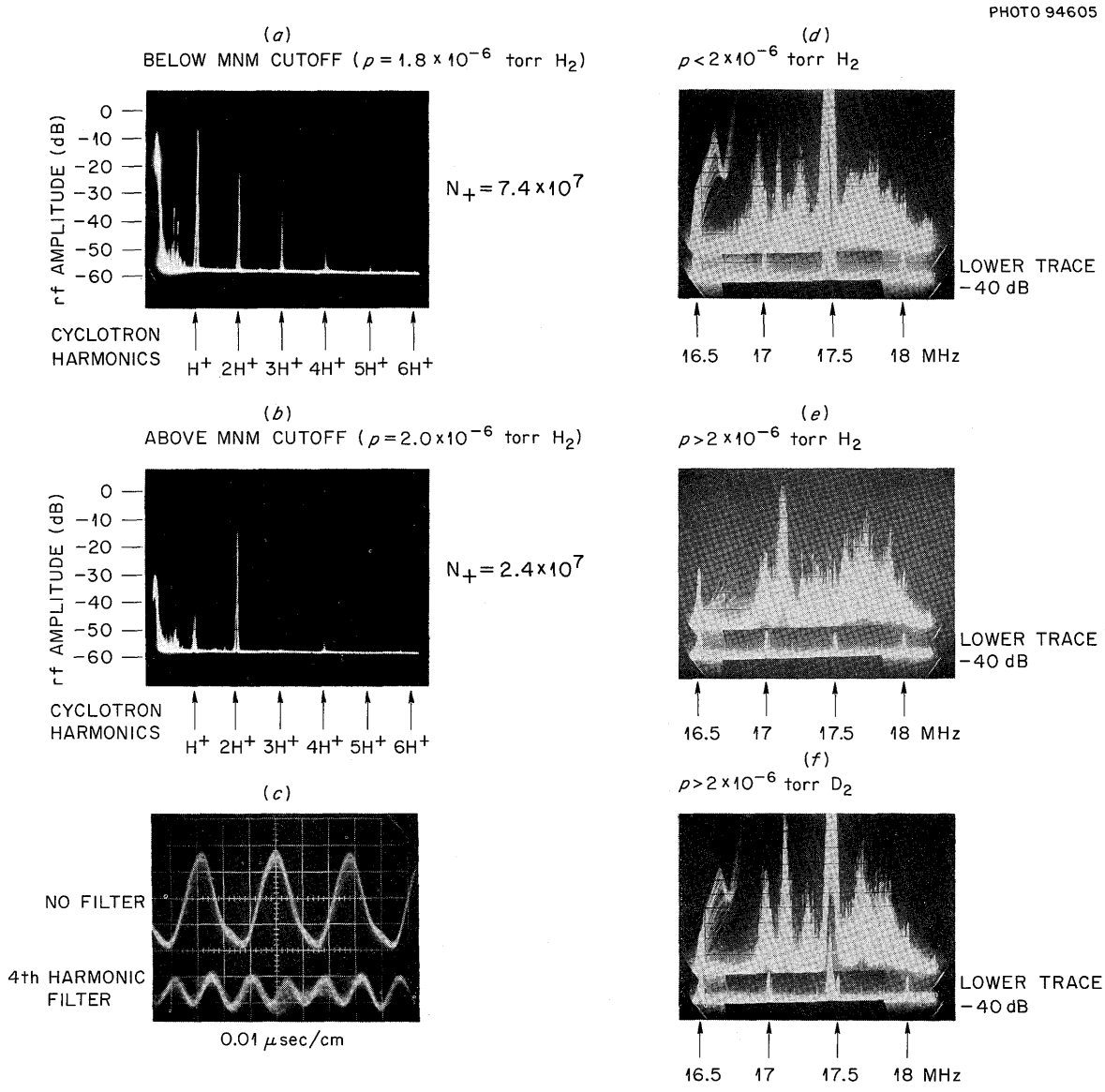

Fig. 4.2. An Overall Picture of the RF Activity in the DCX-2 (*a*) Below and (*b*) Above the Fundamental Cutoff. (*c*) The fourth harmonic is phase correlated to the second above transition and thus probably does not represent an independent instability mode. (*d*) and (*e*) The fundamental frequency in more detail below and above the cutoff. The side bands at the ion bounce frequency are apparent. (*f*) The cutoff is due to the presence of resonant cold H^+, since the substitution of a similar D_2 plasma does not produce cutoff.

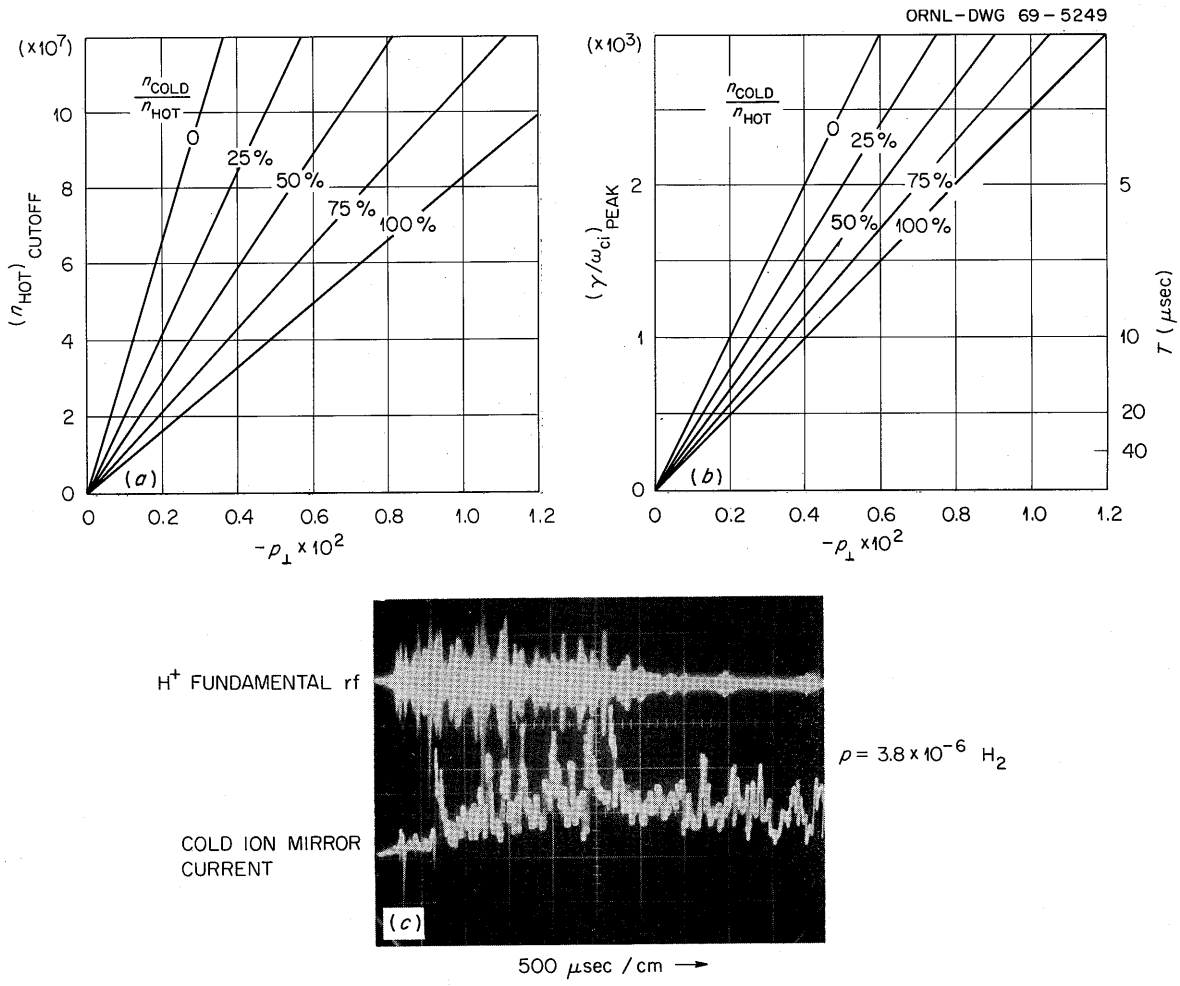

Fig. 4.3. (*a*) and (*b*) **The Theoretical Change in the Cutoff Density and Peak Growth Rate with Cold-Plasma Density as a Function of the MNM Index $p_\perp$.** (*c*) The bottom trace shows the buildup of cold plasma in the machine as reflected in the cold-ion current leaving through the mirrors. When the cold-ion density reaches a level of 30% of the hot density, cutoff of the fundamental instability mode occurs, as shown by the top trace of Fig. 4.3c.

band instabilities occur independently (i.e., choose $|A_m^q|^2 a = \delta_{mm'}$), the dispersion relation predicts instabilities displaced from the dominant instability frequency by $\Delta\omega = \pm m\omega_B$, with growth rates

$$\frac{\gamma}{\bar{\omega}_{ci}} = \frac{J_1}{x}\left(\frac{\omega_{pi}}{\omega_{ci}}\right)\sqrt{\left[|p_\perp| - 2k_m\rho p_{\parallel} - k_m^2\rho^2 - \frac{1}{4}\left(\frac{\omega_{pi}}{\omega_{ci}}\right)^2 \frac{1}{J_1^2}\left(\frac{\partial J_1}{\partial x}\right)^2\right]}\,, \quad (12)$$

where $k_m = \pi m/a$ and $p_{\parallel} = \rho\, \partial\bar{\omega}_{ci}/\partial v_{\parallel}$. We have neglected the cold-plasma cutoff effect since the side bands are shifted far from resonance with the cold ions. The most obvious difference from the main instability is the reduction in growth rate due to the presence of potential variation along the magnetic field, which is represented by the k_m terms in Eq. (12). Aside from explaining the existence of the observed side bands and their reduced amplitude relative to the dominant mode, this approximate treatment has little to add to our

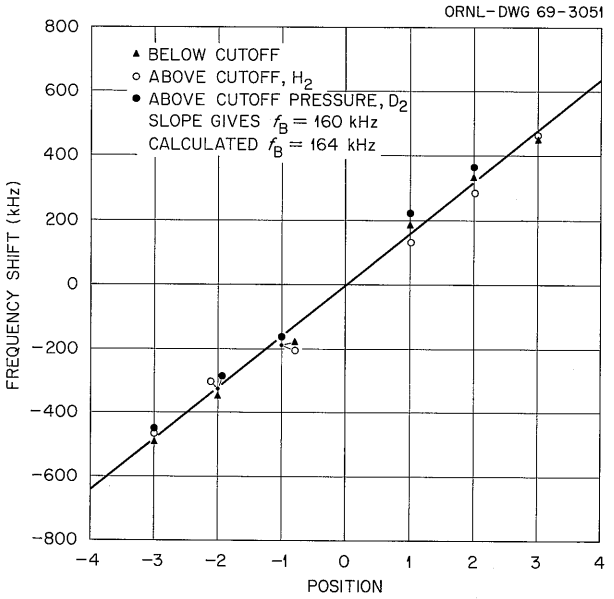

Fig. 4.4. The Frequencies of the Side Bands of Figs. 4.2*d*, *e*, and *f* Plotted vs an Integer Representing Their Position. The slope of the line gives the bounce frequency. The occurrence of these frequencies reflects the effect of finite length on the instability.

Table 4.1. Characteristics of the MNM Instability

	Predicted	Observed
$k_\perp \rho_i$	0.5	$\cong 0.5$
$k_\parallel$	0	$\ll 0.01\ \mathrm{cm}^{-1}$
$\frac{\omega_{pe}}{\omega_{ci}}$ at threshold	0	<0.1
$\frac{n_{\mathrm{Cold}}}{n_{\mathrm{Hot}}}$ at cold-plasma cutoff	50%	$>30\%$
Frequency shift, $f - f_{ci}$	37 kHz	20 to 60 kHz
Growth rate, γ/ω_{ci}	15×10^{-4}	1 to 5×10^{-4}
Parametric dependence of γ	$\propto\left(\frac{\omega_{pi}}{\omega_{ci}}\right)$	$\propto\left(\frac{\omega_{pi}}{\omega_{ci}}\right)$

fundamental understanding of the instability. A more detailed analysis would perhaps reveal the interaction between the side bands which produces the particular intensity distribution found experimentally. However, it is more than likely that nonlinear effects play a large role in such detailed questions.

Table 4.1 is a comparison of the predicted instability characteristics with those observed. The agreement is good except for the magnitude of the growth rate. This could be explained by the rapid energy spreading produced by the instability.

Questions as to the effect of the instability on the injected plasma are of considerable interest. Aside from the expected effect of energy spreading ($\Delta E_\perp/E \cong 0.5$ to 1), we believe that the MNM instability contributes to direct radial particle transport due to its coupling to a low-frequency drift wave, which is examined in the following section.

4.3 MICROINSTABILITY-COUPLED DRIFT WAVE

A relationship has been seen between the high-frequency microinstability and low-frequency signals in experiments on the Alice[6] and Phoenix 1A[7] devices, as well as in the DCX-2. The causal relationship between these signals has not been determined in these other devices, but we believe, at least in DCX-2, that the MNM instability is producing the low-frequency effects, since otherwise drift waves would be expected to be damped.

In the DCX-2, 97% of the injected ions are lost radially to the injection duct, which acts as a radial limiter. As long ago as 1964[8] a quasi-periodic variation of the integrated charge-exchange flux, with a frequency on the order of an ion precession time in the mirrors, was noted. Unfortunately the signals were erratic, and detailed interpretation was impossible.

By working with low-density plasmas and with low power input to the instability, we have been able to observe these low-frequency effects develop in a coherent manner. The most easily observed low-frequency effect is an amplitude modulation of the MNM instability. This is shown in Fig. 4.5*a*. We can also see that this modulation is correlated with the detection of ions of energy greater than 850 V exiting along the field.

[6] L. G. Kuo *et al.*, *Phys. Fluids* **7**, 988 (1964).

[7] C. C. Damm *et al.*, *Phys. Fluids* **8**, 1472 (1965).

[8] *Thermonuclear Div. Semiann. Progr. Rept. Oct. 31, 1964*, ORNL-3760, p. 13.

PHOTO 94607

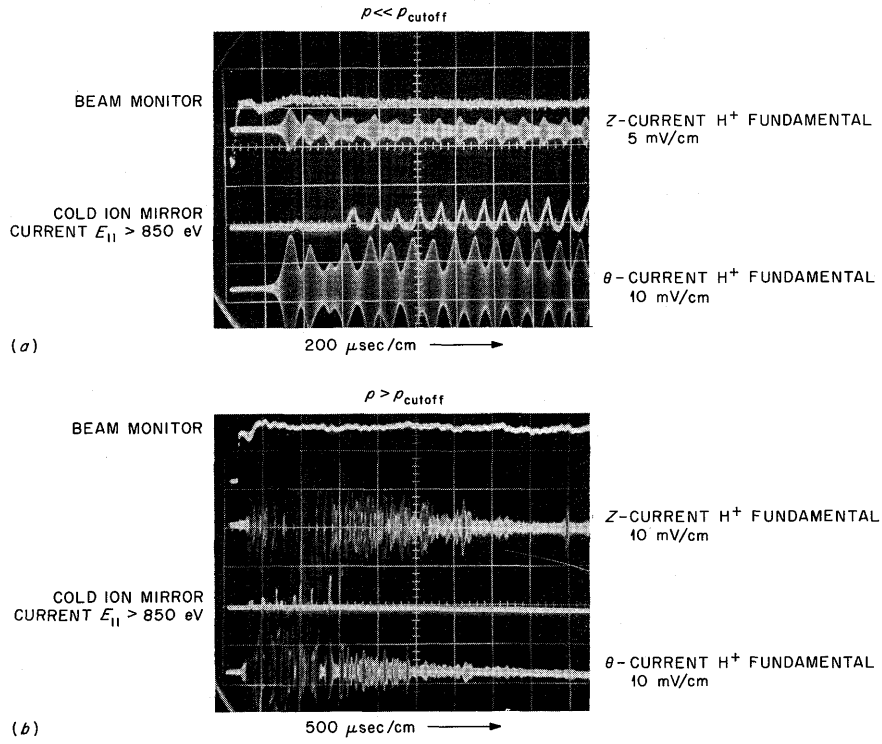

Fig. 4.5. (*a*) The Steady-State Drift-Wave Oscillation Present at Low Pressure Reflected in the Amplitude Modulation of the MNM Instability. The correlation of the ejection of ions of energy greater than 850 V reflects the oscillation of the plasma potential correlated with the MNM instability amplitude. (*b*) The turbulent nature of these oscillations at a pressure above cutoff and the fact that the large plasma potential oscillations responsible for the ejection of the cold ions are confined to the period of strong fundamental activity. Autocorrelation of the data shown reveals approximately the same drift-wave frequency as at lower pressures but with a coherence time of only a few cycles.

Time-resolved energy analysis of these ions shows that this energy reflects an increase in plasma potential rather than an increase in temperature of the cold ions. Figure 4.5*b* shows that the modulation of the instability becomes more pronounced and its periodicity less obvious as the pressure is raised. This is the situation corresponding to the modulated hot-ion density measurements of 1964. We can see from these data that the large plasma potential fluctuations are related to the existence of the fundamental MNM mode, since these fluctuations are strongly attenuated above the cutoff of this mode.

Phase measurements on the envelope of the MNM signal show that it is in phase along the field and has an $m = 1$ azimuthal distribution rotating in the direction of the ions. The observed frequency is in the range of the hot-ion mirror precession frequency and also of the frequency of rotation in the radial electric field due to the plasma potential.

These data suggest that an ion drift wave is responsible for these effects. The theory of such a wave in an infinitely long cylinder of plasma has been developed.[6,7] The only subtlety is in defining a gradient for the DCX-2 field. Numerical computation of ion orbits in the field shows that ions experience practically all of their precession during reflection at the end of the relatively flat central field region. Since their transit through this region is rapid compared with a precession time, it is reasonable to define an effective magnetic field gradient by the relation

$$\omega_M \equiv \frac{w_\perp + 2w_{||}}{qBr}\left(\frac{1}{B}\frac{dB}{dr}\right)_{\text{eff}} , \tag{13}$$

where ω_M is given by orbit tracing of particles with $w_\perp$ and $w_{||}$ perpendicular and parallel energies.

Then, taking a density distribution independent of radius and a small ion excess to provide a plasma potential, we obtain waves of frequency

$$\omega = -\frac{m}{2}(\omega_M + \omega_E) \pm \frac{m\omega_M}{2}\sqrt{1 - \frac{16\omega_{pi}^2}{\alpha^2 v_\perp^2}} , \tag{14}$$

where $\omega_E = E_r/rB$ and α is determined from the radial boundary conditions. For the DCX-2 plasma of radius $R_p = 15$ cm, αR_p equals 3.85. Equation (14) predicts unstable flutes for ions of Larmor radius ρ when

$$\left(\frac{\omega_{pi}}{\omega_{ci}}\right)^2 > \left(\frac{\alpha\rho}{4}\right)^2 , \tag{15}$$

which gives a density threshold for the injected particles of 8×10^8 cm^{-3}. Above this density we would expect catastrophic radial plasma transport. In fact the injected plasma density never approaches this critical density because radial plasma losses commence at a much lower density. We shall return to this point. At densities much below this threshold, Eq. (14) predicts two stable $m = 1$ waves at frequencies

$$\omega \cong -\omega_E , \tag{16}$$

$$\omega \cong -(m\omega_M + \omega_E) ,$$

where the minus sign indicates rotation in the ion direction. We have been able to identify the oscillation in the DCX-2 as the former of these waves in the following way.

By injecting only a short pulse of ions into the machine at a high gas pressure, we can prepare a known density of ions before any instability has a chance to develop to appreciable amplitude. Under these conditions we can monitor the plasma potential and MNM envelope as shown in Fig. 4.6*a*. One sees that as the plasma potential decays, the period of the oscillation lengthens. Using the measured radial variation of plasma potential at early times to obtain the radial electric field and assuming that this field scales with the mean plasma potential shown in Fig. 4.6, we can plot the period of the oscillation against radial electric field. The results are shown in Fig. 4.6*b*, along with theoretical periods calculated from Eq. (14). The data indicate that the oscillations are the lower branch of the stable ion drift wave.

In Fig. 4.7 we show the result of increasing the density of injected ions. Equation (14) indicates that for this density range ($n \sim 10^7$ cm^{-3}) the oscillation should merely shift in frequency. Instead we see evidence of large potential fluctuations and rapid loss of particles. The latter conclusion follows from the fact that at the highest density shown, the plasma potential, cold-ion production, and MNM instability signals all go to zero, indicating a loss of hot ions.

Direct measurements of radial particle transport confirm these conclusions. Figure 4.8*a* shows the signal to particle detectors located outside the 15-cm plasma radius determined by the injector snout and located at 90° intervals from this snout in the direction of ion rotation. Regular pulses of particles are seen with time delays between the probes appropriate for the drift wave of Fig. 4.6. When the MNM signal reaches a maximum, a large increase in particle collection is seen on the detector. The phase relation that this suggests is as shown in Fig. 4.8*d*. A low-frequency wave with the charge distribution shown would give a maximum rf signal at position 7 (Fig. 4.8*d*) because of the excess hot-ion density there. The $E \times B$ drift produced by this charge would then give the enhanced signal at the particle probe. When the density is raised, this MNM–drift-wave coupling is increased as seen in Fig. 4.8*b*, and the radial loss also increases. This corresponds to the large loss indicated in Fig. 4.7 by the plasma potential measurements.

An estimate of the radial transport rate can be obtained from measurements of the power deposited on a target vs the target distance from axis. These measurements show that the injected ion plasma extends about 6 cm radially beyond the beam injector on the side of the machine opposite the beam injector. Assuming that these protons have moved this radial distance in half a flute period (and therefore hit the beam injector a half period later) gives a radial transport velocity of 1.2×10^5 cm/sec for a 10-kHz drift frequency.

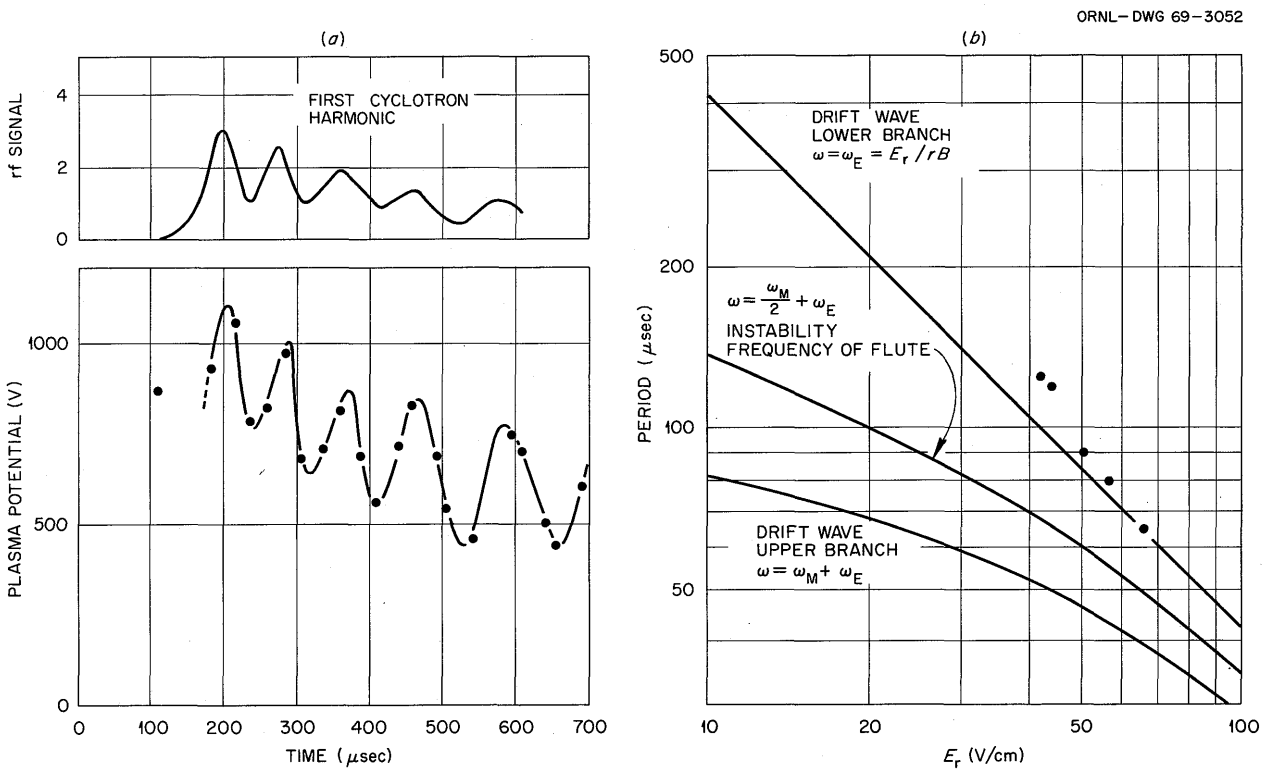

Fig. 4.6. (*a*) **The Results of a Direct Measurement of Plasma Potential and MNM Amplitude Made Under Conditions when the Injected Beam Is Pulsed On for a Short Period (≅100 μsec).** After injection, the plasma potential and rf activity decay with time. A plot of the observed period vs the radial electric field obtained from the average plasma potential of Fig. 4.6*a* is shown in Fig. 4.6*b*, along with the theoretical period of a drift wave. The data indicate that we are observing the lower branch of the drift wave well below the instability threshold.

Taking $v_r = E_\theta/B_z$ gives $E_\theta = 11$ V/cm, in reasonable agreement with other measurements of electric field strengths. Since the average distance an ion must move radially to be lost to the beam injector is about this same distance (6 cm), the average side-lobe proton loss time might be expected to be about half a flute period (~ 50 μsec), in fair agreement with the loss times in Table 4.2 (see Sect. 4.4.1).

It should be emphasized that these large losses occur at densities at least an order of magnitude lower than the critical density for the onset of the flute. This fact, together with the observation that there is a close coupling between the rf amplitude and the low-frequency oscillations, leads us to believe that the MNM instability is coupling to this low-frequency phenomenon in a way which reenforces it.

A further indication of the effect of coupling is seen in the data of Fig. 4.9. From the pitch angle spread in the injected particles, we would expect a drift wave excited by the asymmetric injection to be damped in about five periods. However, Fig. 4.9 shows that one can achieve a stable oscillation in the presence of this damping. This requires an energy feed from some source. One can see the plasma potential fluctuations reflected in the ion current trace of Fig. 4.9 begin to damp until the microinstability grows to a sufficient amplitude to establish a steady state. The same effect is seen in Figs. 4.8*a* and *b*. At low density the rf and the drift wave are uncoupled, and the drift wave damps. When the rf attains sufficient amplitude, both it and the drift wave are enhanced.

That the microinstability amplitude maximum rotates with the drift wave is indicated by the

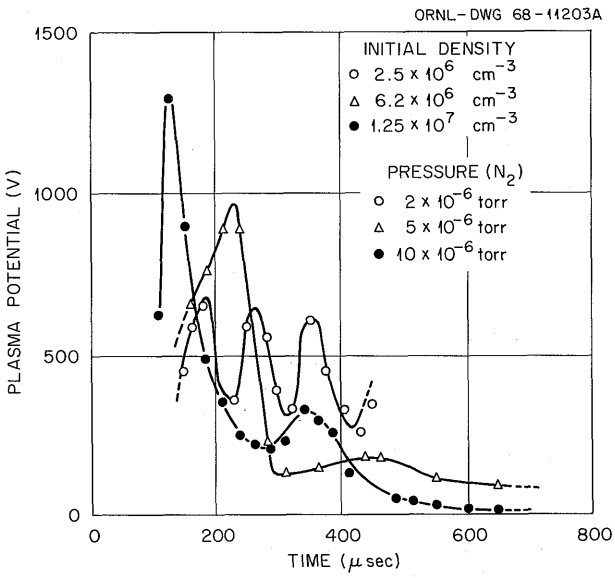

Fig. 4.7. The Plasma Potential as a Function of Time and Initial Ion Density. The lowest ion density gives regular oscillations corresponding to the drift wave of Fig. 4.6*b*. At higher densities the oscillations become larger, and a loss of ions is indicated at the highest density, where the potential goes to zero. This density is close to the usual steady-state value and is more than an order of magnitude below the flute threshold.

amplitude modulation shown in Fig. 4.9. However, it can be seen in a more elegant manner in the data of Fig. 4.10. This shows the central instability peak of Fig. 4.2*d* at lower pressure with much higher dispersion and continuous injection. The sharpness of the individual lines composing the group was mentioned previously as evidence for the reality of the average cyclotron frequency concept. Here we wish to note that there are two sets of lines spaced at $\pm\omega_E$ and $\pm 2\omega_E$ from the center line and that the lower side bands are of smaller amplitude than the upper ones.

The spectra can be understood if we note that the instability frequency seen by a probe will be modulated at the rotation frequency of the ions in the drift wave. Thus a density modulation by the drift wave produces both amplitude and frequency modulation of the microinstability:

$$S = (1 + \alpha \cos \omega_E t) \cos (\omega_c t + \beta \sin \omega_E t) .$$

The Fourier transform of this expression is

$$S_\omega = \sum_{-\infty}^{\infty} J_n(\beta) \left(1 + \frac{n\alpha}{\beta}\right) \left[\frac{\delta(\Omega_+) + \delta(\Omega_-)}{2}\right] ,$$

where $\Omega_\pm = \omega \pm (\omega_c + n\omega_E)$. Thus the lower side bands are of smaller amplitude than the upper; and multiples of ω_E appear in the spectra. It should be noted that it is essential for the same modulation frequency to appear in the amplitude and phase of the signal to obtain this result, which is known as vestigial single-side-band modulation.

Figure 4.10*b* illustrates the behavior of the machine as the power input is raised by increasing the pressure. The individual lines broaden and merge because the steady-state balance between rf pumping and drift-wave damping is upset, causing the plasma density to fluctuate. Finally the line width approaches that of Fig. 4.2*d*, which indicates the rapid pulsing of the rf activity which characterizes the machine operation at the highest densities.

4.4 EFFECT OF THE MODIFIED NEGATIVE MASS INSTABILITY ON THE DCX-2 PLASMA

This section deals with the role that the dominant modified negative mass instability, described in Sect. 4.2, plays in the observed DCX-2 plasma behavior, specifically its effect on the injected plasma (the energetic trapped protons from H_2^+ beam breakup) and the background cold plasma (cold protons produced by ionization of background hydrogen gas).

The main effect of the MNM instability on the injected protons (side-lobe group) is to spread their perpendicular energies and increase their loss rate by more than an order of magnitude over charge exchange, possibly through coupling to the low-frequency drift wave described in the preceding section. The main effect of the instability on the background cold plasma is to create a new group of energetic protons (central-peak proton group) from it by ion cyclotron resonant heating of cold protons. This instability-produced group of energetic protons has higher density, higher energies, and longer lifetime, and is more stable than the injected plasma. Thus the creation of the central-peak proton group by the modified negative mass instability helps to offset the increased loss of the injected plasma by the same

PHOTO 94608

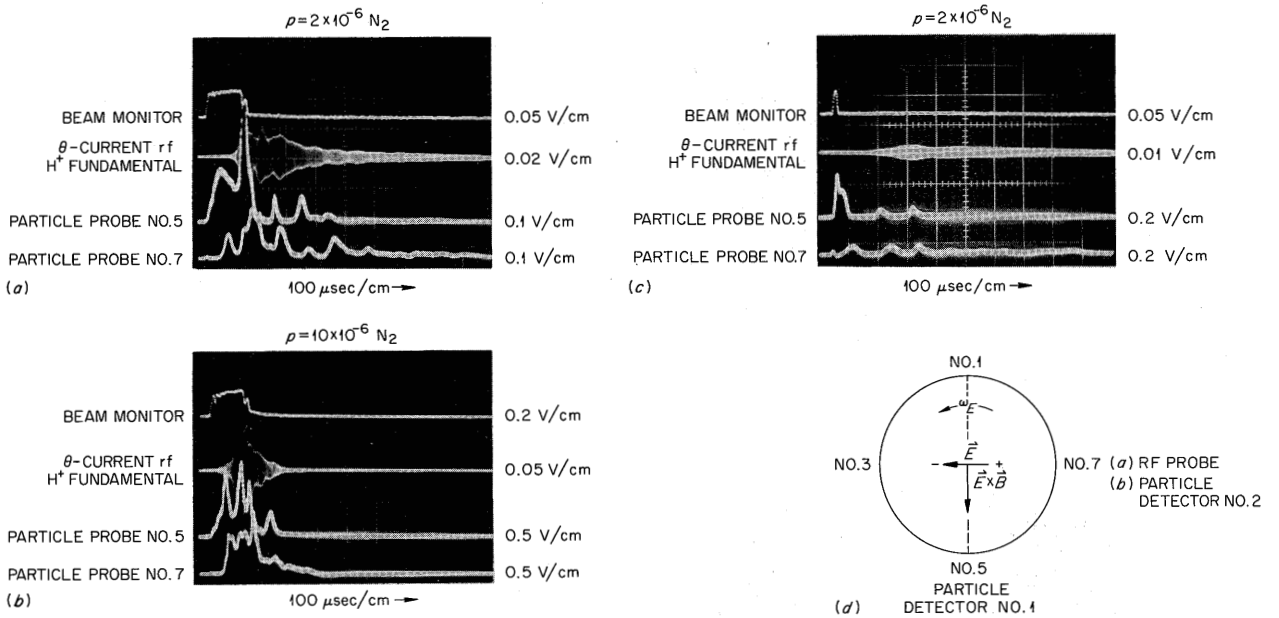

Fig. 4.8. The Detection of Radial Particle Transport by Two Probes Separated in Azimuth by 90° and Located Outside the Radius of the Injected Plasma Is Shown in Fig. 4.8*a* and *b* Under Conditions Corresponding to the 2×10^{-6} Torr and 10×10^{-6} Torr Case of Fig. 4.7. The large increase in radial transport when the MNM instability and the drift wave couple is evident in these figures. The damped drift wave for low densities and weak MNM instability is shown in Fig. 4.8c. The location of the detectors and the electric fields explaining the observations are shown in Fig. 4.8*d*.

PHOTO 94609

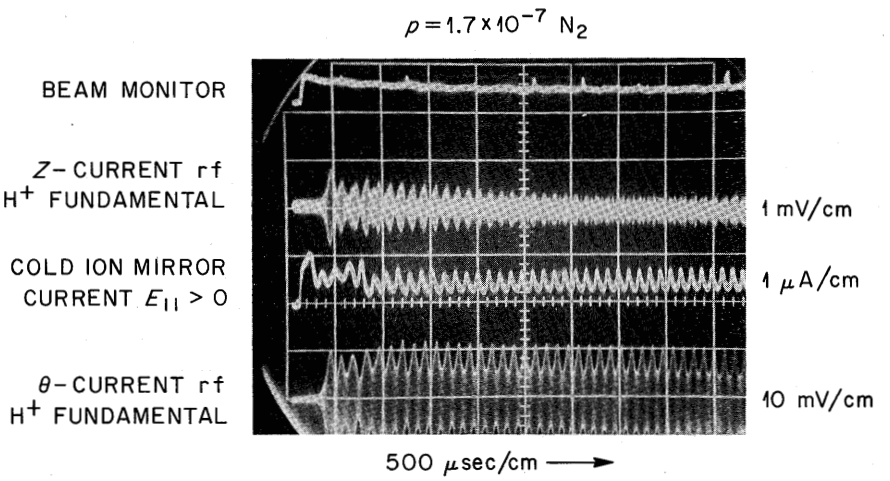

Fig. 4.9. The Steady State Achieved at Low Pressure by the Drift Wave as Reflected by the Cold-Ion Mirror Current and the MNM Amplitude. The initial amplitude of the ion current is seen to fall because the drift wave is damped. When the MNM instability attains sufficient amplitude, this damping is overcome, and a steady-state oscillation results.

PHOTO 94610

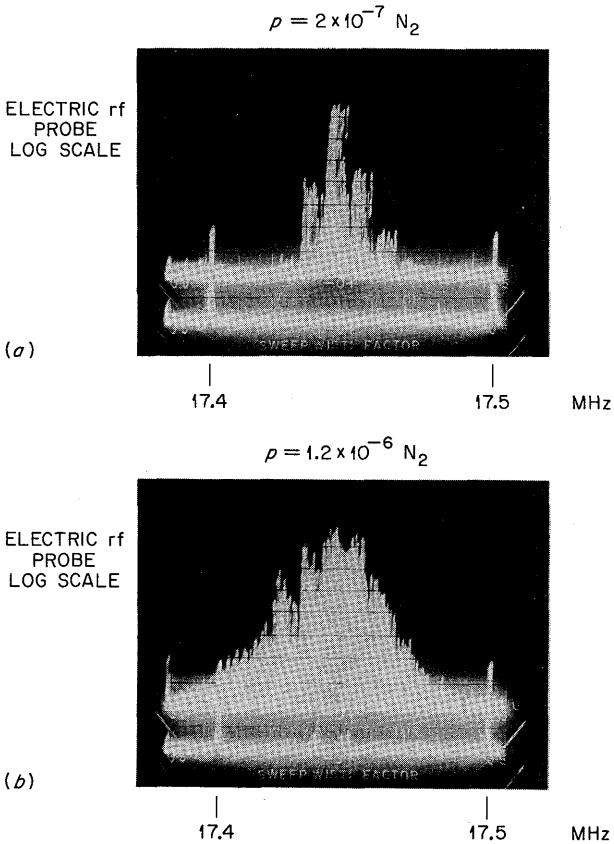

Fig. 4.10. (*a*) and (*b*) High-Dispersion RF Spectra of the Fundamental MNM Instability Mode. The multiple unequal-amplitude side bands are at the drift-wave frequency and indicate the coherent amplitude and frequency modulation of the MNM instability by the drift wave. The line width in *a* is instrumental. As the pressure is raised, the ion density is observed to remain approximately constant, indicating increased losses. The broadening of the spectral lines as the pressure is raised reflects this increased loss of hot particles, which results in a decreased coherence time for the drift wave.

ORNL-DWG 68-8223A

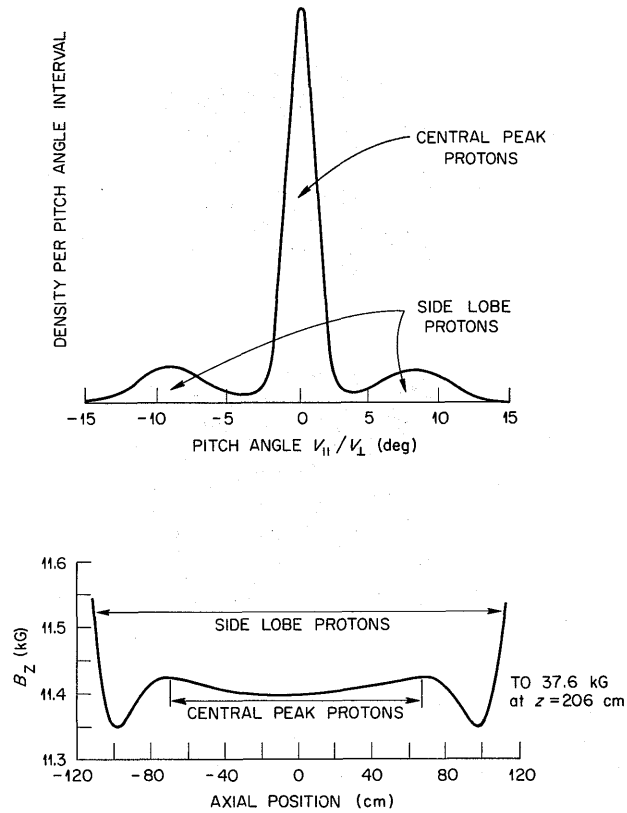

Fig. 4.11. Pitch-Angle Distribution of the Energetic ($W > 50$ keV) Charge-Exchange Neutrals Seen from the Machine Midplane. The measured magnetic field configuration that produces a strong central-peak proton group is also shown. The 540-keV H_2^+ beam injector is located at an axial position of +107 cm.

instability. The net result is that no limit in energetic-proton density is observed when the plasma feed is varied over three orders of magnitude with the modified negative mass instability present, although the energetic-plasma density is always less than it would be in the absence of instability.

Although the properties of these two energetic proton groups have been discussed in detail in previous reports,[4,9–11] a brief review of the plasma characteristics relevant to the following discussion is given for the reader's convenience. Figure 4.11 shows the usual steady-state pitch angle distribution of the energetic protons trapped in DCX-2, obtained by using a highly collimated scanning silicon-barrier detector. As can be seen,

[9] *Thermonuclear Div. Semiann. Progr. Rept. Oct. 31, 1964*, ORNL-3760, pp. 18–21.

[10] *Thermonuclear Div. Semiann. Progr. Rept. Apr. 30, 1965*, ORNL-3836, pp. 27–29.

[11] P. R. Bell *et al.*, *Plasma Physics and Controlled Nuclear Fusion Research*, Culham, England, vol. II, p. 77, 1965.

there are two separate energetic proton groups: the central-peak proton group (heated protons) and the counterstreaming side-lobe proton group (injected protons). The central-peak proton group is characterized by a very low parallel energy $[(E_{\parallel})_{CP} \lesssim 100$ eV], whereas the side-lobe proton group is characterized by a parallel energy distribution corresponding to the axial velocity distribution of the injected H_2^+ beam $[(E_{\parallel})_{SL} \sim 1.3$ to 5 keV]. Figure 4.11 also shows the central magnetic field shape that produces a strong central-peak proton group, and the different axial extents of the two energetic proton groups trapped in this field.

Unless otherwise noted, the results discussed below were obtained with energetic-proton plasmas produced by breakup of a 540-keV H_2^+ beam on a hydrogen gas background. These hydrogen gas breakup results illustrate the essential features of the energetic plasma behavior and its origin. The same basic mechanisms seem to occur with the other gas breakup and arc breakup plasmas studied, and the hydrogen gas breakup results discussed below will also be related to these other results.

4.4.1 Effect of the Modified Negative Mass Instability on the Injected Plasma

Typically, 95% of the injected protons are lost from the side-lobe plasma by other than classical (charge exchange) means, with most, if not all, of these protons going to the beam injector. Section 4.3 showed a correlation between radial losses of energetic ions ($E \gtrsim 1$ keV) and a low-frequency drift wave, which is correlated with the dominant MNM instability. Here we will be concerned with determining the extent of these losses under different plasma conditions.

At early times in the beam pulse (before the onset of the MNM instability), the side-lobe proton group is observed to contain a large number of protons only at 270 keV (from breakup of the 540-keV H_2^+ beam) and a smaller number at 180 keV (from breakup of the small 540-keV H_3^+ beam component). As shown in Sect. 4.2, this group of newly trapped protons is unstable with respect to the modified negative mass instability, resulting in intense electric fields with frequencies very close to multiples of the average proton cyclotron frequency seen by these protons.

The first effect of the modified negative mass instability on these side-lobe protons is to spread their perpendicular energies about a 270-keV peak, from less than 100 keV up to a maximum perpendicular energy of 1.5 MeV, without significantly affecting their initial parallel energy distribution. This spreading of the side-lobe proton perpendicular energies is observed to start with the onset of the proton gyrofrequency electric field from the modified negative mass instability. The perpendicular energy spreading of the side-lobe protons produces two opposing effects on a side-lobe proton's lifetime. A side-lobe proton that loses perpendicular energy has a much shorter lifetime against charge-exchange loss but also a smaller probability of being lost to the beam injector, while a side-lobe proton that gains perpendicular energy has a much longer lifetime against charge-exchange loss but a higher probability of being lost to the beam injector. The probability of loss increases with side-lobe energy since the amount of loss-free area available for a precessing side-lobe proton decreases with increasing proton orbit size.

The energetic-proton losses from the side-lobe proton group have been determined from measurements of the total power deposited on the beam injector, the power deposited on a radially movable side-lobe plasma target (beyond the axial extent of the central-peak group), and the energy distribution of charge-exchange neutrals from the side-lobe proton group at two axial locations. Although the beam injector and plasma target power measurements generally agree with the charge-exchange current measurements, they are much less accurate than this more direct measurement of the classical component of the side-lobe proton loss. Values for the average direct (to the beam injector) side-lobe loss time τ_l can be obtained from the energetic-proton current input I_+ to the side-lobe group from beam breakup, the side-lobe energetic-proton density N_{+SL} and volume V_{SL}, and the total side-lobe charge-exchange current I_{cx} and mean charge-exchange time $\overline{\tau}_{cx}$ by using the equilibrium current relation

$$I_+ = I_l + I_{cx} = \frac{eN_{+SL}V_{SL}}{\overline{\tau}_l} + \frac{eN_{+SL}V_{SL}}{\overline{\tau}_{cx}} . \qquad (17)$$

Solving for $\overline{\tau}_l$ gives

$$\overline{\tau}_l = \frac{\overline{\tau}_{cx}}{I_+/I_{cx} - 1} \tag{18}$$

or

$$\overline{\tau}_l = \overline{\tau}_{cx}\left(\frac{I_+\overline{\tau}_{cx}}{eN_{+SL}V_{SL}} - 1\right)^{-1} . \tag{19}$$

The value of $\overline{\tau}_l$ can be gotten from a direct measurement of I_{cx} in steady state by inference from

$$N_{+SL} = G\int_0^\infty I_{cx}\,dt$$

after beam turnoff (G is a geometry factor).

Table 4.2 shows these results for a hydrogen gas breakup plasma below the cutoff pressure for the modified negative mass instability, and for a deuterium arc breakup plasma at the same pressure. Although the side-lobe densities N_{+SL} for these two cases differ by more than two orders of magnitude (7.8×10^6 vs 1.1×10^9), the fraction of the total side-lobe proton loss due to charge exchange I_{cx}/I_+ is not much different (4.7% vs 9.2% respectively). For hydrogen gas breakup, the calculated direct loss time is about 20 times faster than the measured mean charge-exchange time ($\overline{\tau}_{cx}$) for the side-lobe protons, and about a hundred times faster than that expected if no instability had occurred (τ_{cx_0}). For the deuterium arc breakup case, the two separate estimates for the loss time τ_l differ considerably, reflecting an unexplained larger value of the side-lobe density as calculated from the number of side-lobe charge-exchange neutrals after beam turnoff relative to the density calculated from the steady-state charge-exchange current energy spectrum. The direct loss times for the deuterium arc breakup case are longer than for the hydrogen gas breakup case, ranging from a fortieth to four-tenths of the charge-exchange loss time expected if no instability had occurred.

As the pressure is raised above cutoff of the MNM instability with hydrogen gas breakup, the side-lobe proton density increases from 50% to a factor of 3, depending on the plasma conditions. This increase in density reflects a corresponding decrease in the side-lobe loss time with the large decrease in amplitude of the proton gyrofrequency signal from the MNM instability. The spread in perpendicular energies of the side-lobe protons also decreases as the large-amplitude MNM instability rf changes from the proton gyrofrequency to its second harmonic. A correspondence between the side-lobe loss rate and the amplitude of the proton gyrofrequency activity from the MNM instability may also be seen by comparing arc and gas breakup (see Table 4.2). With arc breakup, the proton gyrofrequency signal has a relatively low amplitude, and the side-lobe proton loss rate is less than with hydrogen gas breakup below cutoff.

Table 4.2. Side-Lobe Proton Losses

	Hydrogen Gas Breakup (Below Cutoff)	Deuterium Arc Breakup
P, torr	2.3×10^{-6}	2.2×10^{-6}
N_{+SL}, ions/cm^3	7.8×10^6	1.1×10^9
$N_{+CP\ (center)}$, ions/cm^3	3.9×10^7	1.1×10^9
I_{cx}/I_+, %	4.7	9.2
$\overline{\tau}_{cx}$, msec	1.2	2.1
$\overline{\tau}_l$, μsec	$58 = \frac{1}{20}\overline{\tau}_{cx} = \frac{1}{134}\tau_{cx_0}$ $62 = \frac{1}{19}\overline{\tau}_{cx} = \frac{1}{124}\tau_{cx_0}$	$212 = \frac{1}{10}\overline{\tau}_{cx} = \frac{1}{40}\tau_{cx_0}$ $3410 = 1.62\,\overline{\tau}_{cx} = 0.4\,\tau_{cx_0}$

4.4.2 Effect of the Modified Negative Mass Instability on the Background Cold Plasma

In our previous reports we have generally used injected-particle accountability,

$$eN_+V = \beta I_{inj}\tau_{loss} ,$$

to describe the total energetic trapped plasma. This implied that the dominant central-peak proton group was created from the injected protons by some mechanism through which some side-lobe protons lost their original relatively large parallel energy to become the very low parallel energy central-peak protons. There are serious objections to this explanation of the central-peak origin, however. The description of the energetic-proton plasma as two distinct groups, each characterized by a well-defined parallel energy, would tend to suggest separate origins for the two proton groups. The suggestion that some side-lobe protons lose almost all of their parallel energy [from $(\bar{E}_{||})_{SL} \sim$ 1.3 to 5 keV to $(\bar{E}_{||})_{CP} \sim 100$ eV] to become central-peak protons is in sharp contrast with the observation that the side-lobe protons do not significantly change their parallel energy (corresponding to the parallel velocity of the injected beam) while undergoing a large spread in their perpendicular energies. A mechanism for generation of the central peak from the injected distribution would have to result in a rapid loss of parallel energy for those protons that it affected, while leaving the parallel energy of the other side-lobe protons unchanged. This process would also have to be unilateral; otherwise the flow would be larger in the opposite direction, with the higher-density central-peak group feeding the lower-density side-lobe group. There is in fact no evidence to support the direct generation of the central peak from the side lobes, and not only are there strong arguments against it, but also there is direct evidence that the origin of the central-peak group lies in the background cold plasma.

If the central peak is generated from the background plasma, no elaborate scheme for losing parallel energy is needed. Instead, a mechanism that heats cold protons to MeV energies is required. Such a mechanism is found in ion cyclotron resonant heating by the intense, nearly resonant electric fields of the MNM instability. Strong evidence that these fields heat cold protons to form the central-peak group is found in the observed evolution of the central-peak energy distribution described below. In addition, all the other evidence to be presented is consistent with this explanation, and no contradictory evidence has been found. Ion cyclotron resonant heating as a possible mechanism for creation of the central-peak group has been mentioned previously[12] and was also suggested by Stix.[13] There may be some nonresonant heating occurring as well, as presumably happened with lithium arc breakup, when harmonics of the lithium ion gyrofrequency were seen when the beam was on.

The number of protons in the central-peak group is usually much larger than that in the side-lobe group. However, under certain conditions (hydrogen gas breakup above a critical pressure) the central-peak group essentially disappears, providing a clue to its origin. Figure 4.12 shows the rf spectrum and the proton pitch-angle distribution obtained with hydrogen gas breakup of the injected beam, both below and above the cutoff pressure for the fundamental of the MNM instability. As can be seen, the presence of the central-peak group is correlated with the presence of a strong line at the proton gyrofrequency. Just above the cutoff pressure, the proton fundamental rf falls by more than a factor of 200, and the central-peak group essentially disappears. At still higher pressures the proton cyclotron fundamental increases in strength, and a weak central-peak proton group returns.

Figure 4.13 shows the time behavior of the proton fundamental rf (top trace in Figs. 4.13*a*, *b*, and c and the third trace in Fig. 4.13*d*), a "central-peak" signal (second trace in these figures), and their time correlation. It was obtained with hydrogen gas breakup at pressures above the cutoff pressure for the modified negative mass instability. The other traces can be ignored in the present discussion. The proton gyrofrequency signal rises to a peak, has large-amplitude bursts for a varying time that decreases in length with increasing pressure above the cutoff pressure, and then drops to a much smaller amplitude for the remainder of the beam-on time. This decrease in amplitude is correlated with a sudden increase in amplitude of activity at the second harmonic

---

[12] *Thermonuclear Div. Semiann. Progr. Rept. Apr. 30, 1965*, ORNL-3836, p. 16.

[13] T. H. Stix, private communication, 1966.

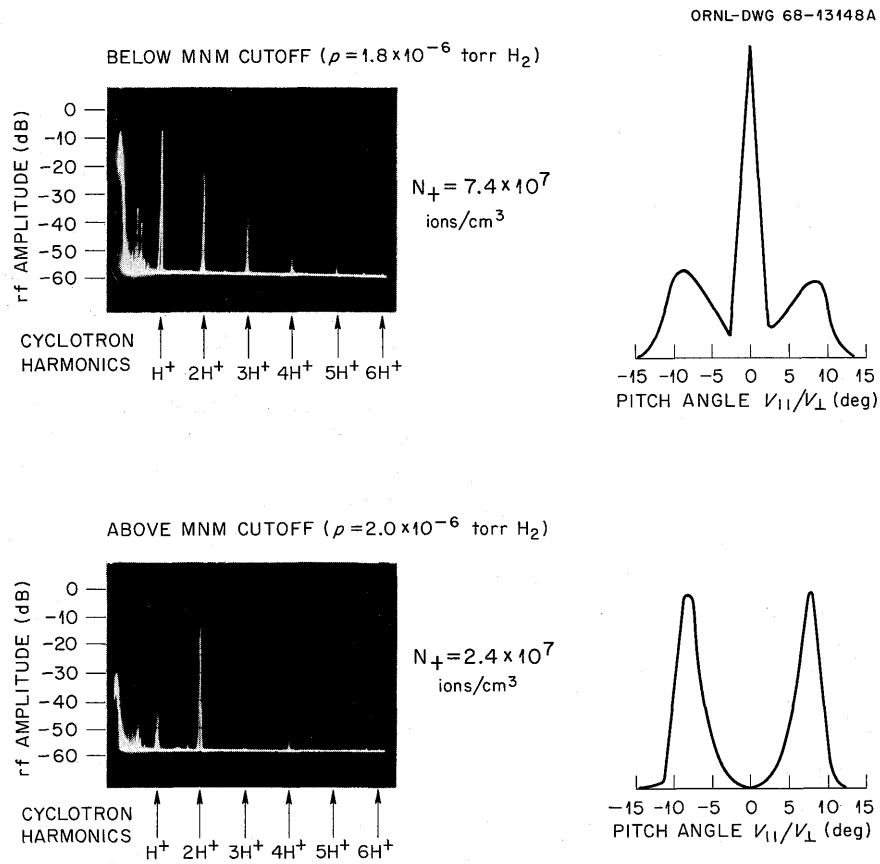

Fig. 4.12. Proton Cyclotron Harmonic Spectrum and Energetic-Proton Pitch-Angle Distribution Obtained Below and Above the Cutoff Pressure for the Modified Negative Mass Instability.

of the proton gyrofrequency. The "central-peak" signal (second trace) is the signal from a foil neutral detector collimated to accept energetic neutrals ($E > \sim 50$ keV) originating from ions with pitch angles between $-3°$ and $+3°$. Because of the wide range of pitch angles accepted, some beam dissociation neutrals are also counted in this signal. The dashed curves superimposed on the "central-peak" traces indicate the approximate beam contribution measured with the energetic-proton plasma suppressed, so that the actual central-peak charge-exchange signal is the difference between the two curves.

Figures 4.13*a*, *b*, and *c* show that there is good detailed time correlation between the fundamental rf and the central peak for the 50-, 10-, and 1-msec durations of these figures. Figure 4.13*c* shows that the central-peak signal does not start to rise until the first peak of the rf signal, and Fig. 4.13*d* shows a case in which the central-peak signal did not start to fall until after the large-amplitude proton gyrofrequency signal had stopped (third trace).

A direct measurement of the average time behavior of the lower-energy part of the central-peak proton group was obtained by counting the charge-exchange neutrals from the central-peak maximum (0° pitch angle) in the energy interval 50 to 90 keV, averaged over many beam pulses. These counts were recorded as a function of time after the beam trigger signal (also used to trigger the traces in Fig. 4.13) using a multichannel pulse-height analyzer in a multichannel scaling mode. These results are shown in Fig. 4.14. This figure shows that the difference between the "central-peak" signal and the beam signal (dashed curve)

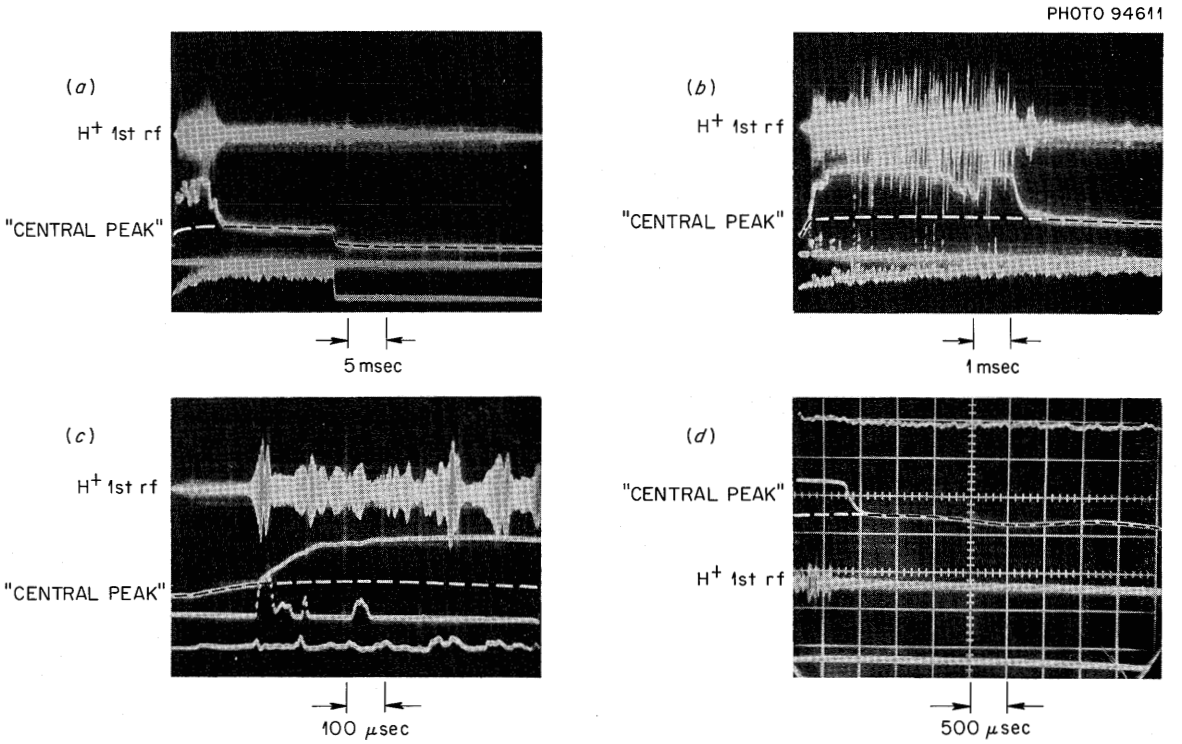

Fig. 4.13. Correlation Between the Proton Cyclotron Fundamental RF and a "Central-Peak" Signal.

in Fig. 4.13*a* is a fair representation of the central-peak behavior at low energy. However, the averaging over the many beam pulses needed for good counting statistics in Fig. 4.14*a* smooths over details in the central-peak charge-exchange signal and produces the downward step 21 msec after beam turnoff (caused by a 1-msec variation in beam-on time).

Figure 4.14*b* shows that the central peak starts 250 to 300 μsec after the beam trigger signal and reaches more than half of its peak amplitude in the next 50 μsec (300 to 350 μsec). This fact is to be compared with the development of the proton gyrofrequency activity, which starts about 200 μsec and reaches peak amplitude about 325 μsec after the beam trigger signal at this pressure. This measurement agrees with the conclusion drawn from Fig. 4.13*c*, namely, that the central peak starts when the proton gyrofrequency activity is already at large amplitude. Other evidence also shows that the proton gyrofrequency fields are the cause, rather than just an effect, of the central-peak proton group. The large-amplitude proton gyrofrequency signal does not change significantly when the central-peak proton group is suppressed through the insertion of an obstacle, or through changes in the central magnetic field shape that do not allow the central peak to be formed [no large nearly resonant (flat) field region].

4.4.3 Model of the Central-Peak Proton Group Behavior

A model for the origin and subsequent development of the central proton group can be made in terms of slightly off-resonance ion-cyclotron heating, with individual protons cycling up and down in energy as their velocities come into and out of phase with the electric field. The measured frequency of the modified negative mass instability peak in the rf spectrum is about 10 to 60 kHz from the nominal central-field proton cyclotron frequency (17.374 MHz), and the width of this rf peak varies from less than 3 kHz at low plasma density to 30–50 kHz under normal hydrogen gas breakup conditions, and over 100 kHz with arc breakup

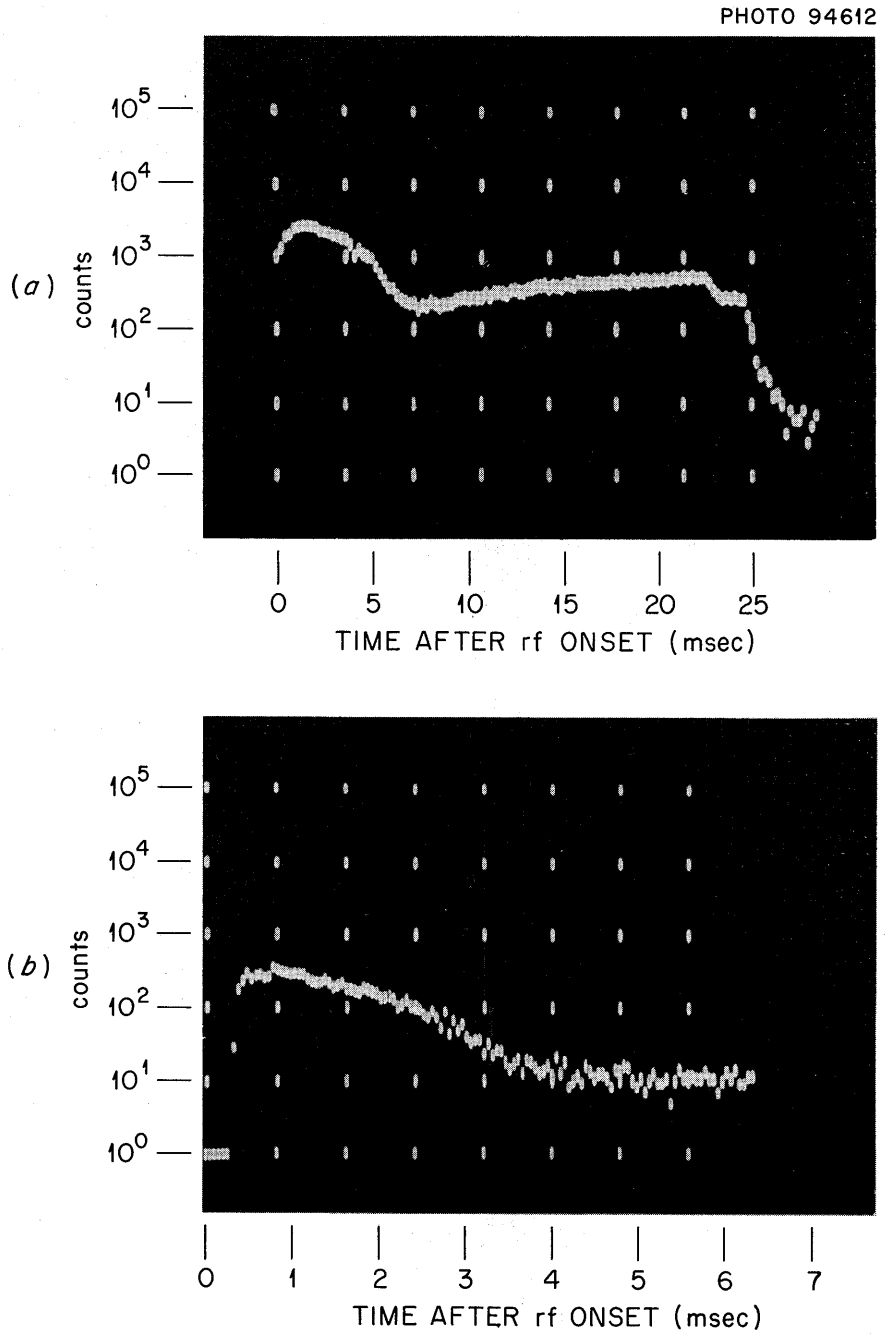

Fig. 4.14. Charge-Exchange Current from the Central-Peak Maximum (0°) in the Energy Range 50 to 90 keV vs Time After the Beam Trigger Signal. The time scales are (*a*) 50 μsec/point and (*b*) 200 μsec/point.

plasmas. The central magnetic field is not perfectly flat, with 5- to 10-G ripples in the magnetic field on axis (out of 11.4 kG) under the best "flat field" conditions. In addition there is a sag in the central magnetic field of ~30 G under the conditions which maximize the central-peak density (see Fig. 4.11), corresponding to a spread of ~45 kHz in the central-peak proton gyrofrequency. The perpendicular energy of an ion with initial perpendicular energy $W_{\perp_0}$ in a circularly polarized electric field

$$E_x = -E_0 \sin \omega_{RF} t ,$$

$$E_y = E_0 \cos \omega_{RF} t ,$$

with magnetic field in the z direction is

$$W_\perp(t) = W_{\perp_0} + \sqrt{W_{\perp_0} W_{\perp_{max}}}\,[\cos(\Delta\omega\, t - \phi) - \cos\phi] + W_{\perp_{max}} \sin^2 \frac{\Delta\omega}{2} t , \qquad (20)$$

where

$$\Delta\omega = \omega_{RF} - \omega_{ci} ,$$

$$\phi = \left(\tan^{-1} \frac{\dot{y}}{\dot{x}}\right)_{t=0} ,$$

and

$$W_{\perp_{max}} = \frac{2e^2 E_0^2}{m(\Delta\omega)^2} = 48 \left[\frac{E_0(\mathrm{V/cm})}{\Delta f(\mathrm{kHz})}\right]^2 \mathrm{keV} ,$$

the maximum perpendicular energy for initially cold protons. In general the initial energy is small compared with $W_{\perp_{max}}$, and the terms containing it can be ignored at onset of the electric field. Thus at the onset of the rf, all the protons stay together as they cycle upward in energy. The time-averaged distribution function for these protons (number of protons oscillating in energy multiplied by the probability per unit energy interval of finding these protons at an energy $W_\perp$) is given by

$$f(W_\perp) = N_+ [\pi W_\perp^{1/2} (W_{\perp_{max}} - W_\perp)^{1/2}]^{-1} \qquad (21)$$

and is shown in Fig. 4.15. The steady-state distribution of proton energies might be expected to look like this distribution, since new cold protons are continuously being added to the heated proton population to replace the energetic protons being lost. If the energetic-proton loss time is long compared with the energy cycling time, then the details of the proton loss probability as a function of energy will not influence the shape of the proton energy distribution, only its amplitude (density).

Actually E_0 and Δf are not constants, but have a range of values that changes with time and proton energy. The instability electric field amplitude changes with time [often in an irregular, stochastic (bursts) fashion], and since it also varies with position, the electric field seen by a proton changes with its energy (orbit size) and the position of its guiding center. The beat frequency Δf also changes since the instability frequency f_{RF} depends on density and has a finite width (30 to

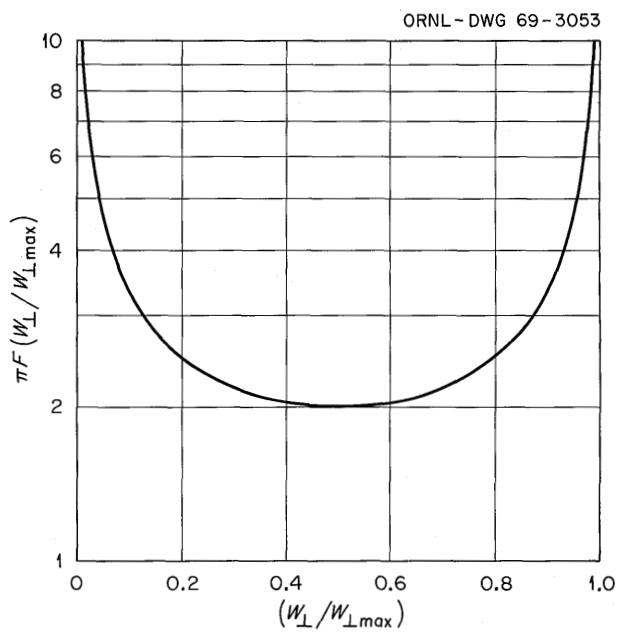

Fig. 4.15. Perpendicular Proton Energy Distribution Initially Expected from Protons Oscillating in Energy with $W_{\perp_0} = 0$. Subsequent changes in the heating parameters E_0 and Δf introduce a large spread in the amplitudes of the protons' energy excursions and in the energies about which they oscillate, producing a very broad peak in the steady-state energy distribution of the central-peak protons.

50 kHz), and a proton's gyrofrequency depends on its energy through its relativistic mass $[f_{ci}(W) - f_{ci}(0) \approx 18.5W(\text{MeV})\ \text{kHz}]$ and through the change in average magnetic field seen by a proton as its orbit size and the axial and radial location of its guiding center in the magnetic field change.

Although these changes in frequency and electric field are small, they represent large changes in the heating parameters Δf and E_0 and can produce a large change in the amplitude of a proton's energy oscillation:

$$W_{\perp_{max}} \propto (E_0/\Delta f)^2 .$$

Since they can occur on a time scale short compared with the energy oscillation period $(2/\Delta f)$, especially for the larger-amplitude energy oscillations (small Δf), they produce a spreading in energy and can explain the high average energy of the distribution. The power absorbed by the central-peak protons is quite large in steady state:

$$P_{CP} \approx \left(\frac{N_+ V\bar{E}}{\tau_l}\right)_{CP} = \left(\frac{N_+ V\bar{E}}{\bar{\tau}_{cx}}\right)_{CP} \sim 100\ \text{W},$$

if charge-exchange loss for the central peak is assumed.

The initial coherence in the motion of the background ions expected at the time of appearance of the rf is in fact seen. By this time the background cold-proton density has built up to an appreciable density n_{+CO} ($\sim 5 \times 10^7$ cold ions/cm^3) since the average cold-proton loss time (free flight time) is larger than the rf onset time. Since the rf spectrum shows a large narrow peak at early times, this value of $E_0/\Delta f$ should determine the early behavior of these cold protons. This original proton group should stay together (heat), independent of their initial phases with respect to the instability electric field as explained before, and should be identifiable as a group until they spread out in energy due to changes in $E_0/\Delta f$, or until enough new cold protons ($\sim n_{+CO}$) have been ionized and heated to mask the original oscillating group. The latter time should be comparable with or less than the time needed to accumulate n_{+CO} (the rf onset time).

Figure 4.16 shows the time-resolved evolution of the central-peak proton energy distribution measured at low pressure (in order to slow down the development of the central-peak group by increasing the onset time). During the first 50 μsec of the proton gyrofrequency signal, the bulk of the central-peak group is found in the range 130 to 205 keV. In the next 50 μsec this group has moved to higher energy (205 to 290 keV), leaving less protons at lower energy, and the higher-energy part of the distribution ($W_\perp > 300$ keV) has increased in density. During the next 100 μsec the peak is back at lower energy, and the energy distribution starts to broaden, with the lower part of the energy distribution increasing the fastest. In the period 200 to 1000 μsec after the rf onset, the central-peak energy distribution has become very broad (almost flat), with the largest increase in density being at the higher energies. The central-peak energy distribution slowly changes for a much longer time ($\sim$100 msec) before a steady-state energy distribution is reached.

The evidence presented in this section and the last confirms the ideas presented above about the origin of the central-peak proton group and its subsequent behavior, namely, that the central-peak proton group is created from the background cold plasma by slightly nonresonant ion-cyclotron heating, with the result that the central-peak protons cycle in energy. No losses other than by charge exchange have been found in this group, but it has not been proved that such losses do not exist.

Unfortunately it has not been possible to measure the efficiency with which the side-lobe-generated rf fields couple energy into the central-peak plasma. The overall efficiency of conversion of beam energy into central-peak energy can be found, however, and is only about 0.5%. Nevertheless, since most of the power in the side-lobe plasma is lost to the injector, it may be that the actual heating process is quite efficient. The possibility of generating a central-peak-type plasma by direct generation of rf fields appears promising.

Figure 4.17 shows the total energetic-proton density (central peak plus side lobe) obtained in the machine midplane with hydrogen gas breakup and hydrogen arc breakup as the side-lobe input power was varied over three orders of magnitude, at a constant beam energy. The arc breakup results appear to be just a high-density (high breakup fraction) continuation of the gas breakup results. There is also support for this opinion in the similarity of the overall heating efficiencies, side-lobe proton loss rates, proton energy distributions, and rf spectra obtained with gas breakup and arc breakup plasmas. The energetic-proton density

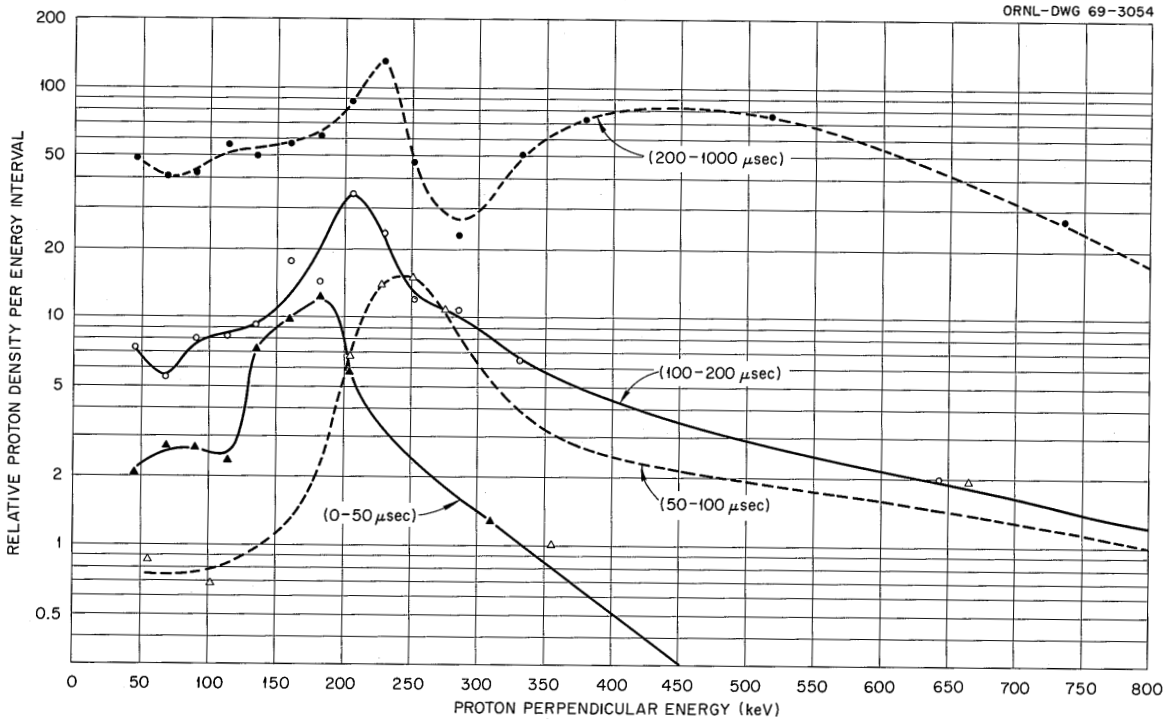

Fig. 4.16. The Central-Peak Proton Energy Distribution at Different Times (0 to 50, 50 to 100, 100 to 200, and 200 to 1000 μsec) After the Onset of the Proton Cyclotron Fundamental RF.

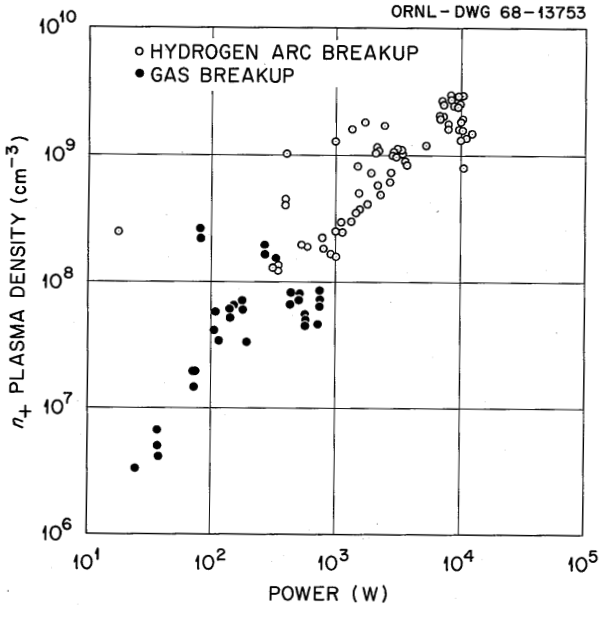

Fig. 4.17. Dependence of Total Energetic-Proton Density on Power Input to the Side-Lobe Proton Group from 540-keV H_2^+ Beam Breakup.

continues to increase over three orders of magnitude in the side-lobe input power, with the MNM instability present at all densities. This dependence of density on input power shows that there is no limit on the energetic-proton density imposed by the MNM instability, although the density is reduced (by one to two orders of magnitude) below that expected if no instabilities had occurred and if all injected protons had remained at 270 keV until decaying by charge exchange on the background gas.

Since the side-lobe injection energy was held constant at 270 keV in Fig. 4.17, there was no real distinction between input power and current. In Fig. 4.18 the side-lobe injection energy was varied with deuterium arc breakup, and the total energetic-proton density is shown vs the power input to the side-lobe group. It was not possible to keep the side-lobe input current constant in this experiment, the side-lobe input current changing a factor of 4 as the injection energy was varied over a factor of 2 (from 270 keV down to 132 keV). The magnetic field was changed along with the injection

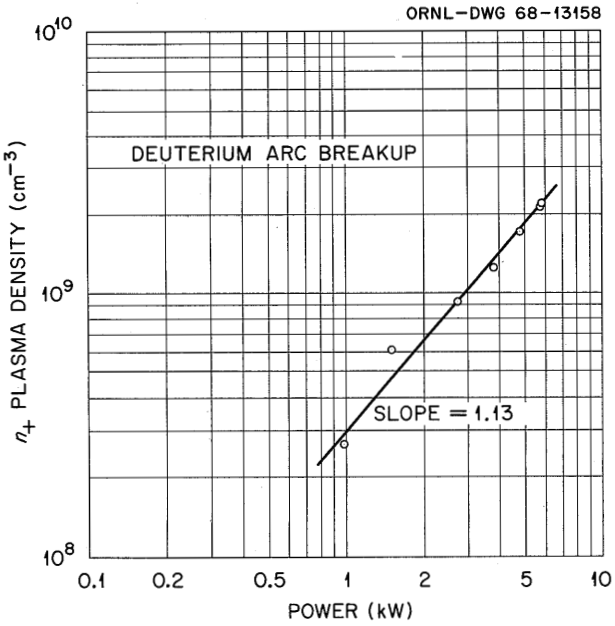

Fig. 4.18. Dependence of Total Energetic-Proton Density on Side-Lobe Input Power when Injection Energy is Varied.

energy so as to keep the H_2^+ beam trajectory constant, and the variation of breakup fraction with beam energy was taken into account in the calculation of input power. Again, a linear variation of energetic-proton density with input power is obtained, although the total energetic-proton density is made up of comparable central-peak and side-lobe components.

Some conclusions can be drawn from the preceding results. First, since almost all of the injected protons apparently are carried to the beam injector by a drift instability possibly sustained by the MNM instability, we will try to find means to reduce this loss. Second, since the overall heating efficiency of the central-peak protons is very low, presumably because of the very low efficiency of power transfer from the side-lobe protons to the electric field, we will try to couple power into the central peak by more direct ion cyclotron resonant heating. Third, it is encouraging that no limit on plasma density has been found and that no non-charge-exchange losses from the central-peak proton group have been observed as yet. Fourth, it may be desirable to use another method (besides accumulation of injected protons or ion cyclotron resonant heating of cold protons) to prepare an energetic-proton plasma in DCX-2, perhaps less energetic but much denser than the present DCX-2 plasma. An exploration of this possibility, turbulent heating of an arc plasma, is presented in the next section.

4.5 TURBULENT HEATING EXPERIMENTS IN DCX-2

We are exploring turbulent heating of an arc plasma in DCX-2 as an alternative to the injection-accumulation and injection-heating methods presently used to build up the trapped plasma. Although we are not abandoning the high-energy ion-injection approach, we are encouraged by the turbulent heating results obtained in mirror systems by Zavoisky,[14,15] Scott,[16] Neidigh,[17] and others. For instance, Zavoisky reports[14] plasma densities of 1 to 3×10^{13} cm^{-3}, ion and electron temperature of 3 to 5 keV, and heating efficiencies of 10 to 15%, and Neidigh, using a different method, reports somewhat lower figures in Sect. 6.

Turbulent heating offers some important advantages over the present molecular-ion-injection approach. The chief advantage is that turbulent heating methods can heat plasmas with densities of a few times 10^{13} ions/cm^3 to temperatures of a few keV in the order of a microsecond. With the injection-accumulation approach, the rate of filling the plasma volume is so slow that even weak (low growth rate) instabilities, resulting in modest loss rates, can limit the plasma density to a relatively low value. For example, dissociating half of a 30-mA H_2^+ beam in a trapping volume of 100 liters leads to a filling rate of only 7.5×10^{11} protons cm^{-3} sec^{-1}. A second advantage of turbulent heating is its high efficiency. Overall turbulent heating efficiencies of 10 to 15% have been reported by Zavoisky and Neidigh (Sect. 6), compared with an overall heating efficiency of $\sim$1% for the injection-heating process that produces the central-peak proton group from cold protons. Turbulent heating imparts a relatively high energy density (β) to the trapped plasma. Zavoisky reports plasma energy densities of $\sim 5 \times 10^{16}$ eV/cm^3

[14] M. V. Babykin *et al.* *Soviet Phys. JETP* (English Transl.) 25, 421 (1967).

[15] E. K. Zavoisky *et al.*, *Plasma Physics and Controlled Nuclear Fusion Research*, Novosibirsk, U.S.S.R., CN-24/L-1, 1968 (to be published).

[16] T. H. Jensen and F. R. Scott, *Phys. Fluids* 11, 1809 (1968).

[17] R. V. Neidigh *et al.*, *Plasma Physics and Controlled Nuclear Fusion Research*, Novosibirsk, U.S.S.R., CN-24/L-2, 1968 (to be published).

for densities of 1 to 3×10^{13} cm^{-3}. Although the energy density in the DCX-2 plasma is also high ($n\bar{E}_+ \sim 2 \times 10^{15}$ eV/cm^3), it is heavily weighted by the very high average proton energy (800 keV).

Turbulent heating in DCX-2 would also increase the available plasma volume. Eliminating the beam injector would move the nearest radial plasma limiter from 15 cm to 46 cm from axis, reducing any radial transport loss times by a factor of 3 and any radial diffusion loss times by an order of magnitude. Another advantage of turbulent heating over molecular ion injection is the much smaller anisotropy and near equality of the ion and electron temperatures of the plasma created. The injection-accumulation and injection-heating processes produce a large spread in the perpendicular energies of the trapped protons without affecting their parallel energy distribution. The resulting high anisotropy ($T_{\perp i}/T_{\parallel i} \sim 10^3$) can lead to Harris-type instabilities. Turbulent heating produces much more isotropic plasmas and under certain conditions nearly equal ion and electron temperatures, compared with $T_{\perp i}/T_e \sim 3 \times 10^4$ typically for the DCX-2 plasma.

While turbulent heating offers these advantages over the present molecular-ion-injection approach, it may have its own limitations. An obvious disadvantage of turbulent heating could be a high plasma loss rate due to plasma turbulence continuing after the end of the heating pulse. However, Zavoisky reports that this does not occur, that the plasma is relatively quiescent after the heating pulse with a large fraction of the heated plasma decaying smoothly with a lifetime of 10 to 30 μsec. Any other possible disadvantages must be found and studied before turbulent heating can be evaluated as an alternative or complement to our present methods of building up the DCX-2 plasma. Leading up to this objective, some preliminary experiments on turbulent heating of the DCX-2 arc have been conducted and are reported below. Their purpose has been to see whether an arc could be pulsed to high voltage without being extinguished, to develop and test the diagnostics needed to study such a plasma, and to see if any significant heating of ions is obtained.

4.5.1 Experimental Configuration and Diagnostics

In our turbulent heating experiments, a high-voltage pulse is applied to the DCX-2 arc electrodes from a capacitor bank, producing a large current which flows along the magnetic field axis and interacts with the arc plasma. Our experiment differs from those of Zavoisky and others in the substitution of a deuterium arc plasma for their deuterium-loaded titanium washer gun plasmas. Our method allows operation at low ambient pressure.

A schematic diagram of the experimental configuration used to obtain most of the results discussed below is shown in Fig. 4.19. The numbers identify different components of the capacitor discharge circuit and various diagnostic probes, showing their approximate axial and azimuthal locations. The high-voltage power supply can deliver up to 5 mA at 130 kV, although it was not used at over 90 kV in the experiments described below. The dc arc power supply is inductively isolated from the discharge circuit by the 100-μH coil. The discharge voltage is varied by changing the spacing of the untriggered air spark gap. With this configuration, discharge currents of up to several kiloamperes are obtained.

The arc inductance, measured from the ringing frequency of the discharge current signal, is about 4 μH, much larger than any other inductance in the arc discharge circuit. The 0.1-μF capacitance and 4-μH inductance of the discharge circuit give a critical damping resistance of $2\sqrt{L/C} = 12.6\ \Omega$. The turbulent arc resistance, measured from the shape of the discharge current signal, varies from about 2 Ω to more than 15 Ω.

There are three current diagnostics: a noninductive 0.1-Ω resistor to measure the total discharge current, a Rogowsky coil inside the copper vacuum liner to measure the arc current, and a Rogowsky coil in the dc arc power supply lead. The discharge voltage is known from the minimum setting on the high-voltage power supply that causes breakdown and from the arc inductance times the initial rate of change of the arc current. The time dependence of the arc voltage is calculated from

$$1/C \int_0^t i_{\text{arc}}\, d\tau.$$

Low-frequency instability rf (<2 GHz) is studied with our standard radial electric probes and magnetic loop probes. Higher-frequency rf oscillations are studied with 3-cm and 12-mm horns and diode mixers. An 8-mm interferometer is also being installed to follow the variations in arc density up to 1.5×10^{13} electrons/cm^3. The DCX-2 cryo-

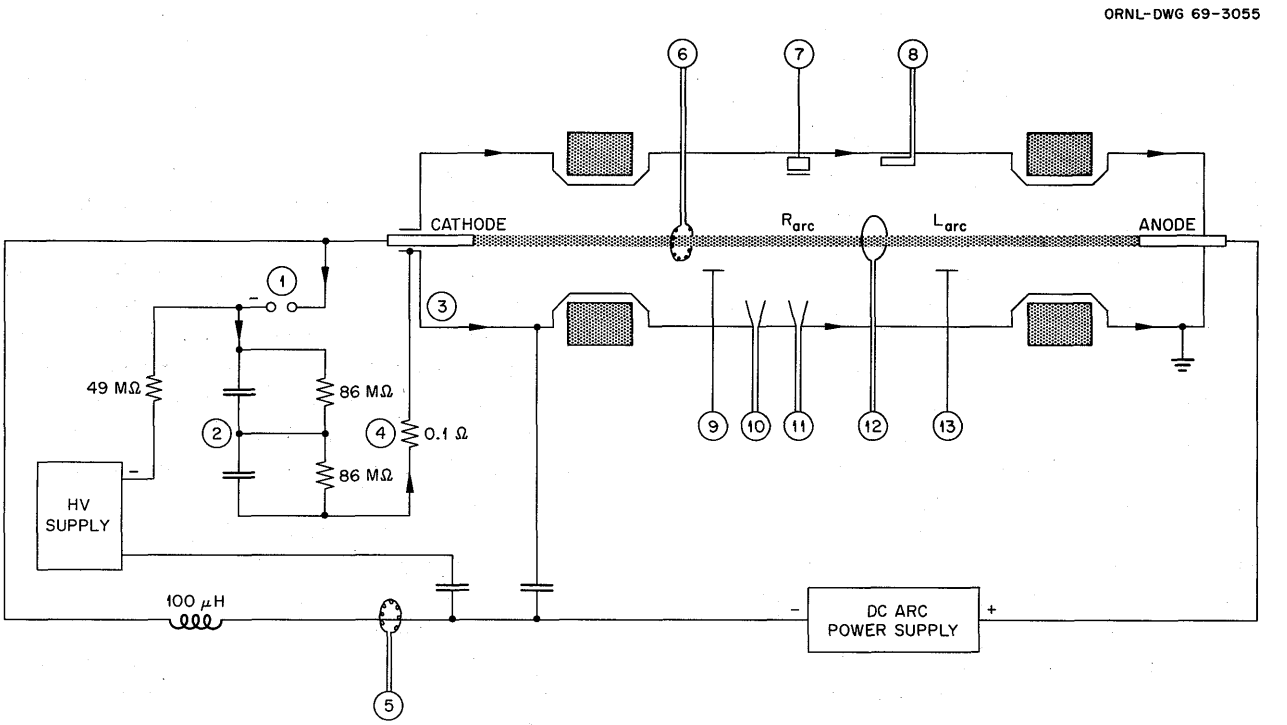

Fig. 4.19. The Experimental Configuration Used for Turbulent Heating Studies in DCX-2. The capacitor discharge circuit consists of (1) an untriggered air spark gap; (2) two 50-kV, 0.2-μF capacitors connected in series; a deuterium arc characterized by R_{arc} and L_{arc}; and (3) the DCX-2 copper vacuum liner, which serves as the return path for the capacitor discharge current. The arc diagnostics include (4) a noninductive 0.1-Ω resistor in the capacitor discharge current return path, (5) a Rogowsky coil in the dc arc power supply lead, (6) a Rogowsky coil to measure the arc current, (7) a gamma-ray detector, (8) a radial electric and magnetic loop rf probe (one of several), (9) and (13) biased plasma collector plates, (10) and (11) 12-mm and 3-cm microwave horns, and (12) a diamagnetic loop.

genic energy analyzer (liquid-nitrogen-cooled silicon-barrier detector and preamplifier) has been modified to allow selection of a window from seven different thicknesses of aluminum and beryllium foils. This arrangement will allow determination of electron temperature from measurements of total gamma-ray intensity vs absorber thickness. Biased probes are used to measure radial transport of ions and electrons from the arc, and integrating diamagnetic loops are used to measure the perpendicular plasma pressure $(n_e kT_e + n_i kT_i)$.

4.5.2 Results of the Initial Experiments

The initial small-scale experiments exploring the possibility of using a turbulently heated plasma in DCX-2 have had three purposes: (1) to see if an arc could be pulsed to high voltage without being extinguished, flooding the plasma region with high-pressure gas from the arc electrodes; (2) to develop and test the diagnostics needed to study the high-density, low-energy pulsed conditions of turbulent heating; and (3) to see if an arc could be heated to a few keV at densities near 10^{13} and still have a significant fraction of this plasma left after the heating (current) pulse is over. The first two goals of the experiment have been successful. The arc is not extinguished when it is pulsed to high voltage, and the diagnostics described above are in use. The arc exhibits an anomalous (turbulent) resistivity above a certain discharge voltage, but it is not yet known whether a significant density of ions is heated to high energy.

The top traces in Fig. 4.20 show the two kinds of pulsed-arc current signal obtained from the non-inductive resistor in the return current path of the capacitor discharge circuit. The bottom traces are the time integral of this current and are proportional to the voltage across the arc. The arc current behavior is either underdamped (Fig. 4.20*a*) or overdamped (Fig. 4.20*b*), depending on whether the arc discharge voltage is below or above a critical voltage V_D respectively.

PHOTO 94613

(*a*)

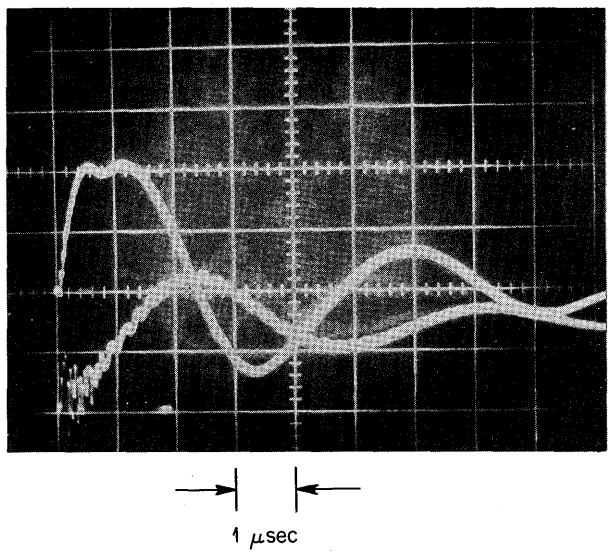

1 μsec

(*b*)

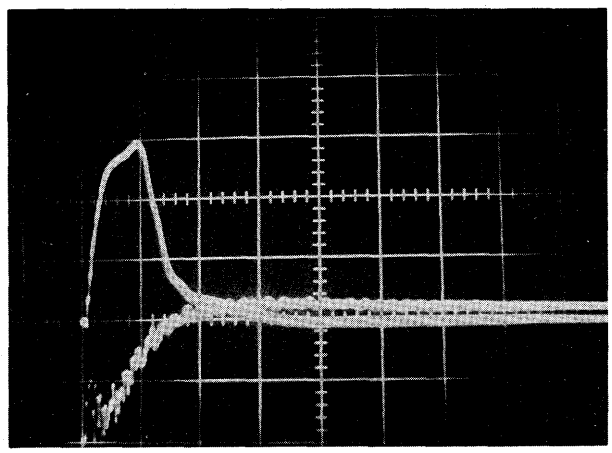

1 μsec

Fig. 4.20. Pulsed-Arc Current Signal and Its Integral (Arc Voltage) Below and Above the Transition Voltage. The peak arc currents in *a* and *b* are 0.94 and 2.67 kA, corresponding to initial arc voltages of 23 and 48 kV respectively.

This change in arc current behavior can be interpreted in circuit terms as due to a change in the arc resistance R_{arc} from below the critical damping resistance $Z_c = 2\sqrt{L/C}$, to above it. The arc resistance can be calculated from Figs. 4.20*a* and *b* either from the $\exp(-R\ \Delta t/2L)$ decrease in amplitude of successive arc current maxima or from V_{arc}/i_{arc} at the arc current maxima (when the $L\ di/dt$ voltage contribution is zero), assuming that $dL_{arc}/dt \ll R_{arc}$ at these times. These calculations show that the resistance of the underdamped arc is approximately constant at 2 to 4 Ω (much less than $Z_c = 13\ \Omega$) throughout the time of the current discharge, values in agreement with the 2- to 5-Ω resistance of the dc arc at low current (50 to 150 A).

For the overdamped arc, the arc resistance changes during the discharge time, from 2 to 4 Ω to more than 13 Ω. This change occurs after the peak of the current pulse. Up until this time, the overdamped arc exhibits approximately the same behavior and value of resistance as the underdamped arc. Scott[18] has observed a similar change in plasma current behavior, due in his case to a sudden current penetration of the plasma. However, in our case the time for the current to penetrate through the arc is calculated at about 0.1 μsec, whereas the arc resistance change occurs after 1 μsec or more.

Similar behavior has been noted in other experiments. Figure 4.21 shows turbulent electrical conductivity as a function of electric field measured by Demidov[19] and by Hamberger[20] in toroidal turbulent heating experiments.

These conductivity values are called turbulent since they are much lower than that calculated by Spitzer for Coulomb scattering. The decrease in electrical conductivity near 0.4 V/cm is attributed to the onset of ion sound waves, and the further decrease near 30 V/cm is attributed to a two-stream instability. It appears that the transition we observe is the first (low electric field) transition. For the DCX-2 arc the resistance values

[18] F. R. Scott, private communication, 1968.

[19] B. A. Demidov, N. I. Elagin, and S. D. Fanchenko, *Soviet Phys. "Doklady"* (English Transl.) 12, 467 (1967).

[20] S. M. Hamberger and M. Friedman, *Phys. Rev. Letters* 21(10), 674 (1968).

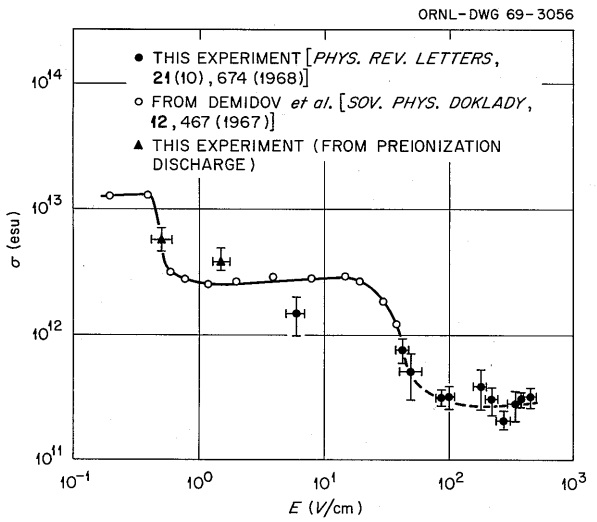

Fig. 4.21. Dependence of Turbulent Electrical Conductivity on Applied Electric Field.

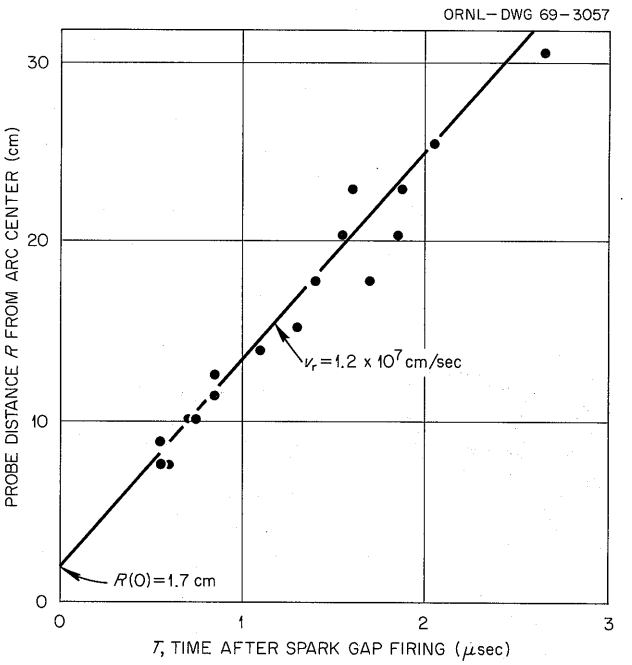

Fig. 4.22. Arc Plasmoid Position vs Time After Spark Gap Firing.

calculated from these measurements are 4.2 Ω for the low-field region (<0.4 V/cm), 22 Ω for the intermediate-field region (0.6 to 20 V/cm), and 155 Ω for the high-field region (>~100 V/cm). These calculated values are in fairly good agreement with the measured values of 2 to 4 Ω below V_D and over 13 Ω above V_D. The low electric field transition is associated with the Dreicer (runaway) field $E_D \approx 2 \times 10^{-12} n/T_{(ev)}$, which for the DCX-2 arc parameters is about 1 to 3 V/cm. This corresponds to a voltage drop of only ~0.5 to 1.5 kV along the bulk of the arc. Since we observe this transition for discharge voltages between 20 and 30 kV for the lower-density arcs and do not observe it up to 60 kV for the higher-density arcs, we believe that large electrode potential drops (sheaths) account for the rest of the discharge voltage. These regions are small in axial extent (≲5 cm), and the average electric field there must be several kilovolts per centimeter or greater.

The pulsed high-current arc is observed to be unstable. A burst of microwave radiation is observed on an *X*-band diode mixer at the time of the current pulse, and plasma dumps are observed on plasma collector plates. These plasma dumps are large, although not large enough to extinguish the arc. Figure 4.22 shows a plot of the radial distance of the plasma collector from the arc center vs the time after the spark gap firing at which plasma is first collected on the plasma collector plates. The data extrapolate back at $T = 0$ to a value for the arc radius which agrees with other estimates of the arc radius. The data closely fit a line of constant slope, indicating a constant radial velocity of 1.2×10^7 cm/sec out to large radius. This does not correspond to a uniform radial expansion of the arc but rather a motion of plasmoids across the magnetic field. Evidence for this conclusion is obtained from the lack of good axial correlation of these plasma dumps and from the large variation in signal amplitude and arrival time seen at the larger distances from the arc. Apparently at the smaller radius the plasma dumps always hit the collector plate, giving reproducible signals, whereas at larger radius the plasma dump may or may not hit the collector plate. The plasmoids have a constant radial velocity $V_r = E_p/B_z$ as expected in the absence of cross-field short-circuiting of the polarization field. The onset time for this disturbance (<<0.1 μsec) is consistent with the estimated growth time of high-density hydromagnetic flutes driven by the large radial electric field of the discharge.

5. Electron-Cyclotron Heating

5.1 HIGH-BETA PLASMAS

M. C. Becker[1]
R. A. Dandl[1]
H. O. Eason
P. H. Edmonds
A. C. England
J. C. Ezell
R. L. Livesey
M. W. McGuffin
A. H. Snell[2]

5.1.1 Introduction

The efforts of the microwave heating group have been concentrated on two major areas of interest. One area is the field of high-power 5.5-mm microwave technology, the existence of which is very basic to the ECH target plasma program. The other area of interest is the experimental study of the high-β microwave plasma in the ELMO facility.

In order to obtain sufficient coupling of the microwave electric field to the cold plasma so as to maintain breakdown of the gas bled into the cavity, it has been necessary to have in the magnetic confinement field a region of electron cyclotron resonance. It has also been an experimental fact that plasmas formed in cavities employing midplane launching of the electromagnetic energy have generally been limited to $\omega_{pe} \cong \omega_{ce}$. This condition necessitates the development of high-power millimeter sources to permit 10^{13} densities in 20-kG fields. The advantage of this wavelength scaling is illustrated by an observed order-of-magnitude increase in stored energy for the case when the plasma is formed by 8-mm power, under conditions almost identical to the 3-cm-heated-plasma case. The obvious desirability of high density in hot-electron target plasmas and the obviously more fusion-like nature of very energetic plasmas such as the ELMO high-β plasma have caused us to stress the development of high-power millimeter-wave technology. Some aspects of this development work (related to the 10-kW, 5.5-mm ELMO source) are described in Sect. 5.1.2.

During this reporting period the high-β plasma experimental program was concerned with refining the measurements of the steady-state parameters, such as the energy density and detailed shape of the high-β plasma, as well as the corroborating measurements of total perpendicular energy and average electron kinetic energy. The dimensions of the annular plasma well (which was first described in April 1967)[3] and typical values of energy density in the annulus have been more accurately determined by unfolding diamagnetic profile measurements; these are described in Sect. 5.1.3.

It has been suggested that a high-β hot-electron plasma, such as the ELMO plasma, might be used in an electron ring accelerator.[4] Experiments conducted in ELMO were aimed at detecting accelerated ions in the macroinstabilities observable at low gas pressure. This work was in lieu of the obviously more ambitious accelerator experiments. The results are described in Sect. 5.1.4.

In the course of development of the high-power 5.5-mm microwave source, the 5.5-mm 1-kW driver was used in conjunction with 800 W of 8-mm power to investigate off-resonance heating, and some of these data are shown in Sect. 5.1.5.

A rather significant increase in neutron flux was observed when employing the off-resonance heating arrangement. An attempt to quantitatively relate

[1]Instrumentation and Controls Division.

[2]Assistant Director, Oak Ridge National Laboratory.

[3]R. A. Dandl, *Bull. Am. Phys. Soc.* **12**, 461 (1967).

[4]A possibility suggested by both Harold Furth and Herman Postma.

electrodissociation neutron emission to hot-electron plasma experimental parameters by an electron temperature function is described in Sect. 5.1.6.

Finally, detailed experiments dealing with the low-pressure instabilities are still in progress and will be reported later. Suffice it to say that the relationship between the cold-plasma density and stability and the high-β equilibrium between cold-plasma feed and hot-plasma losses is much more involved than a one-step flute threshold.

5.1.2 High-Power 5.5-mm Microwave Technology

5.1.2.1. Introduction. – In view of the previously mentioned advantages of employing millimeter-wave cw power sources for ECH and because of the almost total lack of commercial availability of such sources, a support program[5] was initiated in mid-1963 for the development of a liquid-cooled traveling-wave-tube (TWT) amplifier having a minimum saturated power output of 1 kW cw, center frequency of 55.0 GHz, bandwidth of 1.0 GHz, minimum saturated gain of 15 dB, and other specifications generally compatible with the ECH application. Such extension of the state of the millimeter-wave tube development art, using a severed coupled-cavity slow-wave structure, was accomplished through use of extreme care in the areas of mechanical tolerances, beam control, and vacuum technology. The development was facilitated by lack of restrictions upon beam voltage, dc-to-rf conversion efficiency, size, weight, cooling requirements, noise performance, or spurious frequency content in the output. This successful program produced a TWT (Hughes experimental type-designation HAV-2) which met or exceeded all design objectives. The program was then extended with a revised objective of increasing the power output capability from a single tube to 5 kW cw, with other general characteristics comparable with the HAV-2. This program resulted in experimental TWT type-designation HAV-3. A recent survey paper by Forster[6] describes these tubes in the perspective of the present state of the millimeter-wave tube development art (Hughes commercial type-designations 813-H and 819-H are used in ref. 6).

The objectives of the continuing program were then directed toward improved compatibility with the ECH application, with special emphasis upon those characteristics affecting the simplicity and reliability of simultaneous operation of a sizable number of such tubes. Most notable in this area was perhaps the development of collectors for the tubes which can operate at ground potential rather than at a "depressed" potential. This modification enables considerable simplification of power supply and cooling equipment by elimination of the need for a "floating" collector power supply and by permitting water cooling of the collector rather cooling with an oil circulation system and an additional heat exchanger. (The 1-kW TWT was redesigned in the process of incorporating the grounded collector, and it now has Hughes experimental type-designation HAV-2A.) Subsequent efforts in the support program have been devoted to the fabrication of additional tubes for use in ECH in the ELMO facility, along with the improvement of tube life and reliability, reduction of spurious mode content in the output, general assistance in application and maintenance of tubes in use at ORNL, and continuing optimization of the tube characteristics for compatibility with the ECH application.

The TWT amplifier employing a severed coupled-cavity slow-wave structure is well suited for operation into the adverse microwave load characteristics presented by ECH devices. Since suitable ferrite devices for load isolation at 55 GHz are not available (the present state of the art is perhaps a few tens of watts), the microwave power source must operate at times with a large amount of power reflected from the load. Reflected power passes through the slow-wave structure of the TWT and is dissipated in the external "sever" termination with little effect other than additional ohmic heating of the structure due to transmission losses. Thus the frequency "pulling" and "moding" effects common to oscillators are not present in the TWT amplifier. The TWT can tolerate relatively large amounts of reflected power since this power is not required to be dissipated within the internal structure of the tube, as in a klystron amplifier. In addition to permitting stable high-gain operation, another less obvious advantage of the severed structure is that the driver tube is quite effectively isolated from the effects of reflected power at the TWT output. Finally, there are very obvious advantages in using a high-gain amplifier "chain,"

---

[5]ORNL subcontract 2300 with Hughes Research Laboratories, a Division of Hughes Aircraft Co., 3011 Malibu Canyon Road, Malibu, Calif.

[6]D. C. Forster, "High Power Millimeter Wave Sources," pp. 301–46 in *Advances in Microwaves*, vol. 3 (ed. by L. Young), Academic, 1968.

ORNL-DWG 69-1022

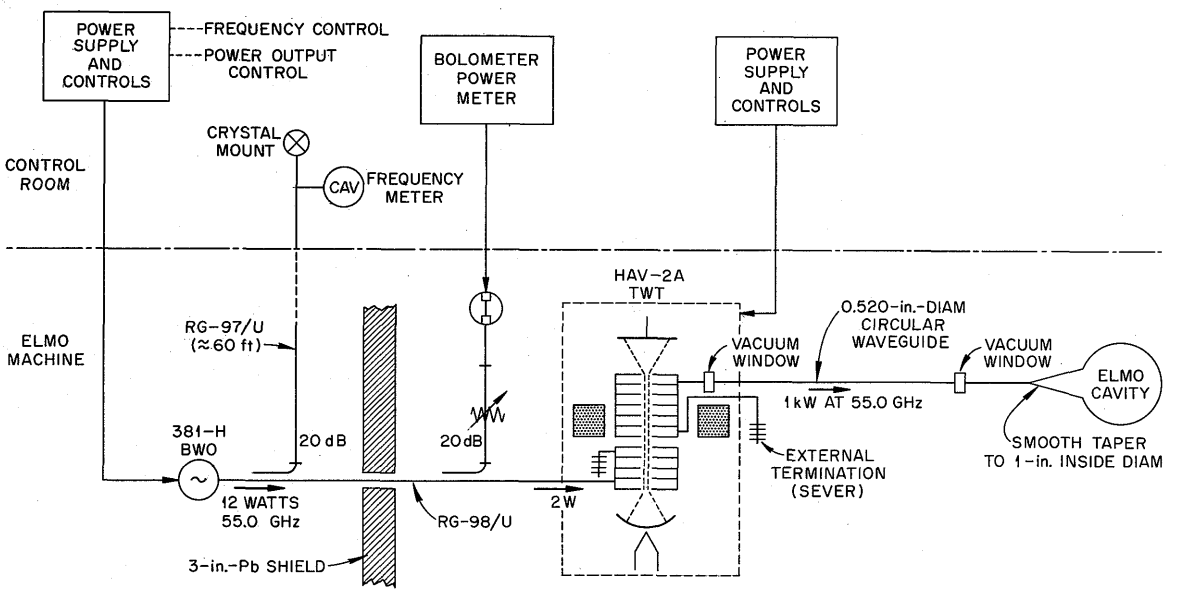

Fig. 5.1. Simplified Schematic Diagram of 1 kW at 55.0 GHz CW Power Source as Used on the ELMO Facility.

especially when multiple output tubes are involved, since coherence is readily attained and control and modulation of the total rf output can be accomplished at a low rf level without necessity for switching large dc currents at high voltages.

5.1.2.2. 1-kW 55-GHz Power Source. – Early in this report period, the installation of a single HAV-2A traveling-wave tube was completed, and its output was connected to the ELMO cavity for ECH experiments. One of the high-voltage power supplies with integral high-speed control and protective circuitry (originally developed as a beam voltage supply for the WJ-282 1-kW cw 35-GHz oscillator)[7] was used to meet the beam requirements of 0.4 A at –27 kV dc. The WJ-282 heater voltage supply, solenoid supply, and ion pump supply were also adapted for use with the HAV-2A, and a comprehensive electrical interlock system was installed for fail-safe operation. The TWT was mounted in a magnetic shield adjacent to the ELMO machine at the location formerly occupied by the WJ-282 tube mount. Increased transmission losses (due to the longer waveguide run necessitated by displacement of the WJ-282 mount) reduced the maximum usable output from a single WJ-282 to approximately 850 W for later experiments involving simultaneous use of power at 35 and 55 GHz (Sect. 5.1.2.3 and Sect. 5.1.5). No modifications were required to the ELMO cavity for 55-GHz operation, since its original design had anticipated ultimate use in this frequency range.

The arrangement of the basic waveguide circuitry and control and monitoring functions is shown in schematic form in Fig. 5.1. Frequency control is accomplished by beam voltage adjustment of the Hughes 381-H backward-wave oscillator[8] (BWO) which is used as a driver. Control of the 381-H output power (and hence control of the HAV-2A output) is accomplished by variation of the accelerating anode potential of the 381-H. This electrode controls the BWO beam current, and rapid turnoff of the microwave power for diagnostic purposes is accomplished by rapid switching of its potential.

The HAV-2A output is connected to the vacuum window on the ELMO tank with a straight 0.520-in.-ID circular waveguide which mates with the output of the TWT. The water-cooled waveguide vacuum window assembly on the ELMO tank was adapted from the design used on the HAV-2A. It incorporates a $\lambda/2$ thick beryllium oxide disk

[7] *Thermonuclear Div. Semiann. Progr. Rept. Oct. 31, 1965*, ORNL-3908, sect. 3.2.2.

[8] As manufactured by Hughes Aircraft Co., Electron Dynamics Division, Torrance, Calif.

brazed into the copper waveguide. The waveguide is tapered to 1 in. in diameter inside the ELMO tank and is then terminated abruptly in a 1.-in.-diam opening in the cavity wall. This tapered transition was incorporated to improve the impedance match to the cavity.

The principal problem encountered in operation of the HAV-2A for ECH experiments has been the lack of "on-line" monitoring of the output power due to the obvious difficulties in designing and fabricating a directional coupler for the highly oversized circular waveguide, in which many modes of propagation are possible. The alternative (which has been used until the present time) has involved the accurate calibration of power output (as measured by a well-matched calorimetric water load) against operating voltages, drive power, and frequency. Frequent calibration checks and the excellent reproducibility of plasma conditions lend confidence to the use of the power-output calibration, but with the obvious disadvantage that the power output is known only for certain combinations of conditions. This difficulty is expected to be eliminated very soon by the use of an oversized rectangular waveguide directional coupler based upon the general coupled-wave theory developed by Miller.[9] Construction of this coupler has been completed, and low-power tests have indicated excellent performance of coupling, directivity, and mode discrimination. High-power operation is expected to present no serious problems, since the unit is water cooled and will have no abnormally high microwave electric field gradients.

5.1.2.3. Two-Frequency Excitation of the ELMO Cavity. – Simultaneous operation of the WJ-282 and the HAV-2A, with the outputs of both tubes connected to the ELMO cavity for investigation of nonresonant microwave heating, presented few problems. Although some mutual coupling exists through the cavity, the slow-wave structures of the tubes present a large mismatch outside their normal operating frequency ranges. The precaution of installing a waveguide low-pass filter ahead of the 35-GHz output power sensor eliminated the possibility of spurious indications due to the coupled 55-GHz power. Since 35-GHz waves will not propagate in the fundamental-mode waveguide used at the detectors on the decoupled ports of the 55-GHz oversized waveguide directional coupler, no future difficulty is anticipated when this component is installed. A tendency was noted for low-level oscillation of the HAV-2A when normal voltages were applied with no plasma present and with no region of 19.65-kG resonance field present in the cavity. The cavity presents a very severe impedance mismatch to the output of the tube under these conditions. This oscillation produces little inconvenience, however, since it can be eliminated by a slight reduction in beam voltage under "standby" conditions. Prompted by these observations, recent tests at Hughes[5] (using a water-load termination with an adjustable reactive element for control of mismatch) have indicated unconditional stability at load VSWR's up to 2.5:1 for an HAV-2A. This demonstration of performance is quite commendable for a state-of-the-art device, since many other high-power microwave tubes having lesser performance levels would almost certainly have failed under this extreme condition.

5.1.2.4. 10-kW 55-GHz Power Source. – The installation of a microwave power source employing two type HAV-3 TWT amplifiers is nearing completion on the ELMO facility. Output power up to 5 kW cw from each of these tubes will be fed into the ELMO cavity through separate oversized rectangular waveguides. The HAV-2A 1-kW cw source now being used for ECH experiments will be relocated and used as a driver amplifier for the two HAV-3 tubes. The large dc power supplies for meeting the HAV-3 beam requirements of 0.9 A at −45 kV have been received and installed. Each of these units also incorporates an insulated heater voltage supply, a line voltage regulator, and a high-speed electronic crowbar with integral sensing circuitry for protection of the HAV-3 against body current values exceeding its 8-mA maximum rating. Power supplies for focusing solenoids and ion pumps have been installed, and an extensive system of interlocks has been incorporated for personnel safety as well as to protect the tubes against loss of coolant flow, loss of waveguide pressurization, loss of focusing, waveguide arcs, overheating, improper voltages, or other abnormal conditions. X-ray shielding has been installed around the collectors of the tubes for personnel protection, although Hughes personnel have reported no dangerous radiation levels.

5.1.2.5. Transmission-Line Considerations for High-Power Millimeter Wave Sources. – As previously mentioned, the output terminals for the HAV-2A and the HAV-3 are oversized circular waveguide

[9]S. E. Miller, "Coupled Wave Theory and Waveguide Applications," *Bell System Tech. J.* **33**, 661–719 (May 1954).

of 0.520-in. inside diameter (for comparison, the internal dimensions of standard WR-15 rectangular waveguide for operation over the frequency range of 50 to 75 GHz are 0.148 by 0.074 in.). This large circular waveguide was used on the tubes to reduce rf transmission losses and to facilitate construction of a waveguide vacuum window capable of reliable operation at the 5-kW cw output power level.

Although power is transmitted principally in the TE^0_{11} (fundamental) mode in the circular waveguide, there exists in this large waveguide the possibility of propagation of approximately 15 higher-order modes. In addition, there exists the possibility of degeneration of the fundamental mode and most of the higher-order modes into orthogonal components (corresponding to rotation of the plane of symmetry of the characteristic field patterns about the waveguide axis). These facts are of little consequence for transmitting ECH power into the ELMO cavity through a straight circular waveguide of uniform or progressively increasing cross section (as was done in the HAV-2A application) since multiple scattering of the waves is inevitable and is indeed desirable. The possible existence of coupling to higher-order modes becomes extremely important, however, in a more elaborate transmission system incorporating bends, directional couplers, power dividers, etc., or constrictions in the waveguide cross section. The difficulties in making waveguide measurements in the presence of higher-order modes are fairly obvious, due to the fact that the transverse field distribution is not well defined and also varies along the length of the guide. The most serious problem arises, however, from the effect of "trapped-mode" resonances within the transmission system.

A very simple system which illustrates the production and effect of such trapped-mode resonances is shown in Fig. 5.2. The swept-frequency oscillator is connected to a length of oversized waveguide by means of a long smooth tapered transition. The oversized waveguide is in turn connected to a

ORNL-DWG 69-1021

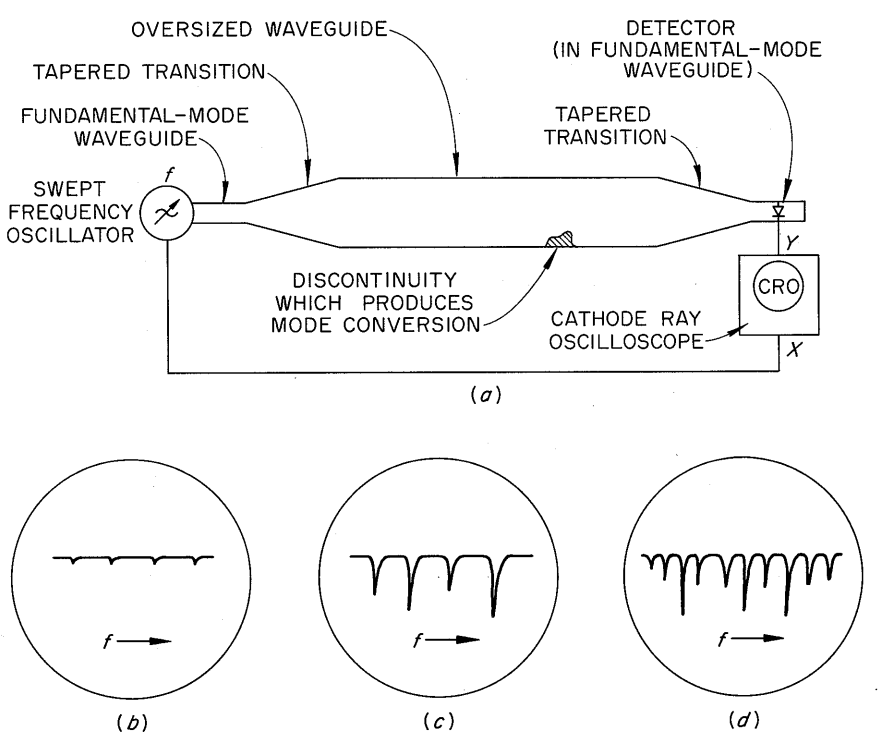

Fig. 5.2. (*a*) A Simple System for Demonstrating the Production and Effect of Trapped-Mode Resonances; (*b*), (*c*), and (*d*) Typical Power vs Frequency Plots Which Would Be Obtained on the Cathode Ray Oscilloscope for the Following Conditions: (*b*) Low Mode Conversion Showing Small-Amplitude Resonance Absorptions; (*c*) High Mode Conversion Showing Large-Amplitude Resonance Absorptions; (*d*) Decreased Frequency Spacing of Resonance Absorptions as the Length of Oversized Waveguide or Its Cross-Sectional Dimensions Are Increased.

detector in fundamental-mode waveguide by a similar tapered transition. The detector output is applied to the Y-axis input of a cathode-ray oscilloscope, and a voltage proportional to the frequency of the oscillator is applied to the X-axis input. A discontinuity which produces conversion to higher-order modes is introduced into the section of oversized waveguide. Since only the fundamental mode can propagate in the fundamental-mode waveguide, the higher-order modes will be totally reflected by the tapered transitions. The higher-order modes are thus "trapped" between the two tapered transitions, and multiple reflections give rise to resonance of these modes at frequencies for which the electrical spacing of the equivalent reflection planes is an integral multiple of $\lambda_g/2$.

Typical oscilloscope presentations for different conditions are shown in Fig. 5.2*b*, *c*, and *d*. Resonance absorption of the trapped modes causes considerable loss in the total transmitted power as a function of frequency. The magnitude of this loss depends upon both the degree of coupling to the mode and the attenuation constant of the waveguide. Since the Q factor of such a "trapped-mode resonator" may be very high, the fraction of the power absorbed may also be quite large for even a slight degree of mode conversion. Such trapped-mode resonances are not confined to elements of a transmission system which produce total reflection of the higher-order modes. They exist between any two impedance mismatches for the mode in question, and the effect differs in degree only, dependent upon the impedance magnitudes, the attenuation constant of the waveguide, and the coupling coefficient between the fundamental mode and the higher-order mode. An identical effect is noted in conventional impedance matching in fundamental-mode waveguide, in which the effect of a discontinuity is compensated by the insertion of an equal impedance at a distance of $n\lambda_g/2$ from the discontinuity. Multiple reflections increase the dissipation losses in the region between the two equal impedances. The absorption effect can be much more pronounced in the high-mode case, however, due to the more optimum coupling to the effective high-Q resonant cavity by way of a small mode conversion coefficient. There is thus cause for extreme concern to minimize coupling and impedance mismatch to higher-order modes in an oversized waveguide system. Although it is possible in principle to accomplish efficient single-frequency operation between the frequencies of adjacent trapped-mode resonances, it is impractical to do so in the millimeter region, where even modest laboratory transmission lines are many wavelengths long and there is little frequency separation between adjacent resonances. It is also necessary to provide some latitude for frequency adjustment in order to optimize the operating conditions of the traveling-wave tubes.

5.1.2.6. Component Development Program for Oversized Waveguide. – As a result of the problems discussed in the preceding section concerning the difficulties in the use of oversized waveguide for efficient high-power transmission, and the lack of precedent in the open literature, a program of oversized waveguide component development has been under way within the RF Heating Group in order to achieve efficient power transmission and monitoring for the 55-GHz systems. After a thorough study, a waveguide having a rectangular cross section of 0.460 by 0.410 in. was selected as an optimum compromise for use in these systems. This compromise was based upon the following interrelated considerations:

1. Minimizing the attenuation per unit length (attenuation of this guide in OFHC copper is ≈0.05 dB/ft, as compared with ≈0.5 dB/ft for standard WR-15 waveguide).
2. Maximizing the power-handling capability (waveguide arcing is a very serious problem in high-power cw transmission systems).
3. Minimizing trapped-mode resonances in the transmission region between the TWT output and the waveguide vacuum window at the ELMO vacuum tank (since transformation to 0.520-in.-diam cross section is necessary at these points).
4. Facilitation of the design and construction of directional couplers for power division and monitoring, and of the design and construction of waveguide bends necessary for changes in direction as required by the plasma experiment.
5. Elimination of the lack of control over generation of orthogonal-mode components which is characteristic of circular waveguides. (The cross section chosen is not square; hence orthogonal modes in this waveguide are not degenerate; that is, they have different propagation velocities, even though they may be excited separately.)
6. Minimizing the possible number of higher-order modes (within the limitations imposed by other considerations).

The oversized waveguide transmission system proposed for use with the 10-kW 55-GHz power

source is illustrated in Fig. 5.3. The output power of the HAV-2A traveling-wave tube is monitored by means of an oversized waveguide directional coupler and fed into a power divider through a dissipative attenuator pad. The equal power outputs of the power divider are fed through adjustable attenuators to tapered transitions, where the waveguide size is reduced to the standard WR-15 cross section. The individually adjustable drive power for the HAV-3 tubes is monitored by means of directional couplers in standard WR-15 waveguide. The power outputs of the individual HAV-3 traveling-wave tubes are monitored by oversized waveguide directional couplers, and are transmitted through vacuum windows to the ELMO cavity by means of individual oversized waveguides. The use of well-matched multimode attenuator pads (which have 15 dB fundamental-mode attenuation) on both decoupled ports enables a single oversized waveguide directional coupler to serve for both output-power monitoring and reflected-power monitoring. Complete control of the power input to the cavity is accomplished by variation of the HAV-2A drive power.

The power divider which will be used initially in the ELMO system consists of a simple bifurcation parallel to the *H* plane which transforms the oversized rectangular waveguide into two half-height waveguides. The half-height waveguides are then tapered to full height for connection to the adjustable attenuators. Such a power divider is matched at the input port for the $TE^{\square}_{10}$ (fundamental) mode and higher modes of the TE_{m0} family, but is not matched at the output ports, and therefore does not have true hybrid properties. A 3-dB directional coupler has been designed using theory given in ref. 9, and is expected to produce superior performance for use as a power divider in the HAV-3 drive circuit.

Bend radius is critical for oversized waveguide applications in that the difference in phase constants between the inside and the outside of the bend produces a distributed coupling between the fundamental mode and higher-order modes. (Consider the interesting analogy to the conditions which require a rotational transform of the magnetic field in toroidal plasma devices.) Bends for the transmission system have been designed according to the data given by Quine,[10] which were in turn based upon the work described in ref. 9.

The arrangement of Fig. 5.3 is considered to be the minimum acceptable system for driving the inputs of the HAV-3 TWT's with the output from a single HAV-2A, optimizing simultaneously the drive-power levels of the individual HAV-3's, and performing the necessary monitoring of power flow. It is readily seen that many possibilities for trapped-mode resonances exist even in such a basically simple system. The most serious limitation is imposed by the fact that the input waveguides for the HAV-3 tubes are of standard WR-15 size, and the tapered transitions which are therefore necessary for connections to these inputs produce total reflection of all incident higher-order modes. However, since the 1-kW output capability of the HAV-2A considerably exceeds the total input requirements of the HAV-3's (≈100 W each), dissipative padding is permitted between elements of the system which reflect higher-order modes. The trapped-mode resonances can therefore be effectively damped without introducing undue dispersion in the phase and amplitude characteristics of the system. It is certain that mode absorbers will have to be developed which produce selective attenuation of the higher-order modes without attenuation of the fundamental $TE^{\square}_{10}$ mode if the output power capability of the HAV-2A is to be used efficiently in driver service for a larger group of HAV-3 tubes.

Design, fabrication, and tests have been completed on initial models for all component types required for the transmission system illustrated in Fig. 5.3. Fabrication and testing is in progress on the balance of the components required for the complete system. All components have been fabricated at ORNL with the exception of the waveguide vacuum window assemblies used for entry to the ELMO vacuum tank, which were fabricated by Hughes. Extensive use has been made of numerical-controlled machine tools for fabrication of the coupling arrays for directional couplers and for the production of electroforming mandrels. Electroforming techniques have been used in the fabrication of directional couplers, tapered transitions, bends, and the power divider. Special tooling has been developed for fabrication of circular-to-rectangular waveguide transitions, large-radius waveguide bends, and flange joints.

The 381-H BWO has been used routinely for swept-frequency testing of the oversized waveguide

[10] J. P. Quine, "*E*- and *H*-Plane Bends for Oversized Rectangular Waveguide," *IEEE Trans. Microwave Theory and Techniques* **MTT-13**, 54–63 (January 1965).

ORNL-DWG 69-1020

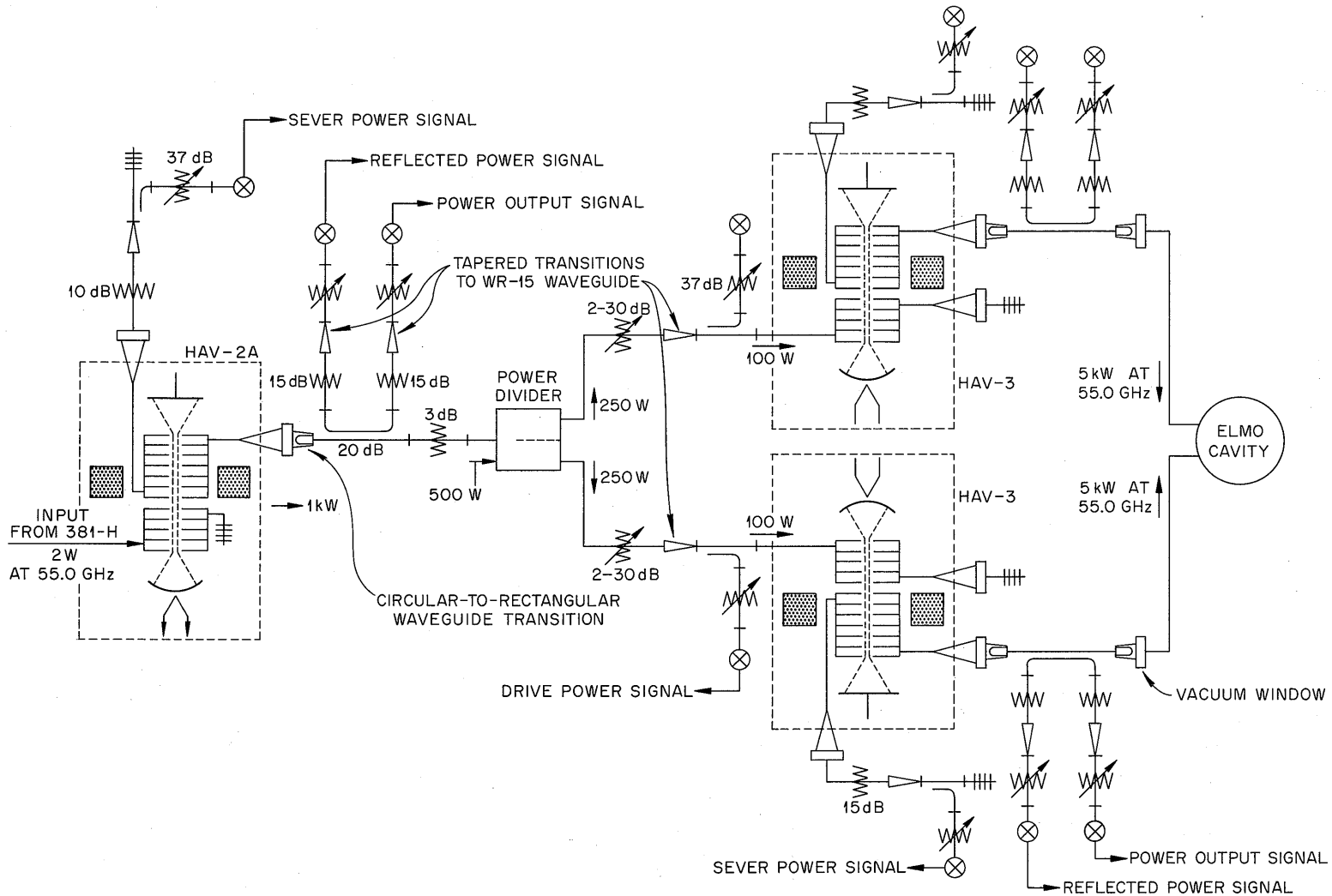

Fig. 5.3. Schematic Diagram of Proposed Oversized Rectangular Waveguide Transmission System for 10kW at 55.0 GHz Power Source.

components. Due to the critical need for system components, it has thus far been expedient to concentrate measurement emphasis upon quantitative $TE^{\square}_{10}$ (desired) mode characteristics of individual components for basic performance tests, and upon qualitative performance of the components in combination for the assessment of the effect of higher-order modes. It is expected that the complete transmission system will be tested in this manner prior to installation on the ELMO facility. A complete determination of the higher-mode characteristics of individual components would be desirable both for optimization of the component characteristics and for predicting the performance of components used in combination. It is expected that development effort on oversized waveguide components will continue for some time in order to further optimize the transmission system for the ELMO installation and thereby gain the knowledge and experience necessary for most efficient and economical realization of the millimeter-wave power requirements of the IMP program.

5.1.3 Diamagnetic Measurements of 30%-Beta Plasma

One of the major areas of study over this report period has been in the interpretation of diamagnetic data. The main objective is to determine as accurately as possible the stored energy density and the spatial configurations of the plasma. Essentially, two separate techniques have been used. First, simple diamagnetic flux measurements were made with axis-encircling loops, and second, detailed diamagnetic field surveys were taken with Hall probes.

With the development of very low-drift electronic integrators and careful elimination of stray thermal, contact, and induced potentials, the diamagnetic loops present an excellent steady-state monitor of the total perpendicular stored energy. However, there are basic uncertainties in the inferred energy density, which are caused by finite geometry effects and by the presence of macroscopic currents.

An important characteristic of the ECH plasma produced in ELMO is the existence of a stable high-β equilibrium condition. To augment the data available from diamagnetic loop measurements, a spatial survey of the diamagnetic field was conducted. These data were then compared with magnetic field profiles computed from a simple plasma model, and from the best fit the dimensions of the plasma and the depth of the diamagnetic plasma well were calculated.

The diamagnetic field measurements were made with a Hall probe element on the end of a long probe; the probe was enclosed in a water-cooled tube to minimize thermal effects on the probe sensitivity. The probe was calibrated at the center of the machine against an N.M.R. magnetometer. As the experiment was to measure small changes in a large field, the linearity of the Hall element was very important. The linearity was tested by placing the probe in the mirror throat and plotting measured field as a function of mirror current. The maximum measured integral nonlinearity was about 8% and could well be due to errors in the current measurement.

The data of a typical run (the computer fit was made for this set of data) are shown in Fig. 5.4*a*. The reproducibility of a point is within 5%; the symmetry about the median plane is quite excellent. A similar scan was then made along a line parallel to the axis of the machine but displaced 8 in. off axis (this was just outside the copper microwave cavity), and the results are shown in Fig. 5.4*b*. These data were taken on the same day and under the same conditions as those shown in Fig. 5.4*a*.

The aim is now to obtain a reasonable plasma model which reproduces this same diamagnetic field profile and which is not in conflict with the other diagnostics. The first attempts showed that the plasma is hollow and has a large axis-encircling current. The magnitude of this current can be found by taking the data of Fig. 5.4, assuming a dipole variation for large distance, and then calculating $I_\theta = 2\int_0^\infty H\,dz$.

The basic model used is shown in Fig. 5.5 and consists of a rectangular pressure profile. The plasma currents due to the pressure gradient are then only on the surface and are given by

$$\nabla p = J_\theta \times B_z$$

or

$$I_1 = \frac{2nkT}{B_1} L$$

and

$$I_2 = \frac{2nkT}{B_2} L ,$$

where $2L$ is the plasma length.

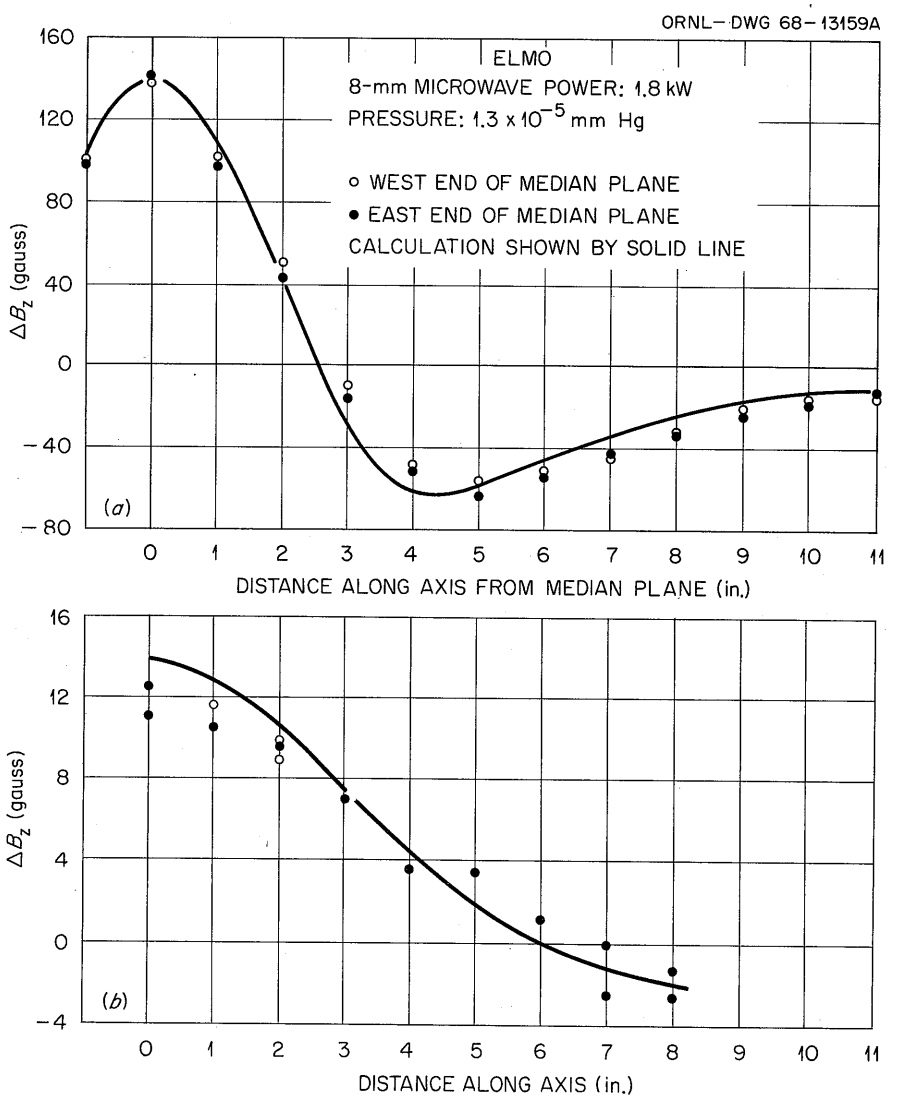

Fig. 5.4. Experimental Data from Diamagnetic Field Survey and Final Computed Result. (*a*) Plasma magnetic field on-axis experimental data. (*b*) Plasma magnetic field off-axis experimental data.

In an attempt to approximate the actual pressure profile more closely, an extra pair of current surfaces was included. The effect of this is to add a step to the pressure profile. This is shown in Fig. 5.6, with a sketch of the actual model used in the calculation. Each row contained 20 loops; the currents in each loop in the two outer rows were set equal and similarly the currents in the two inner rows. Values for the dimensions of the array and for the axis-encircling current were selected; then, normalizing on the central on-axis diamagnetic field, the inner and outer individual currents were calculated. The computer then calculated the field at each data point. The best fit was obtained on a hit-or-miss technique and is shown in Fig. 5.4. The location of the loops in the cavity is shown in Fig. 5.7. The corresponding dimensions and currents are given in Table 5.1. Because of the closeness of the fit, the axis-encircling current is accurate to better than 10%. Small changes in the plasma length shifted the zero-field crossover position in rough proportion, so the length is also accurate to better than 10%. Decreasing the inner radius gives a better fit to the off-axis data but appreciably steepens the slope of the curve at the zero crossover position (already too steep) and introduces large errors in the far field data. A variation of more than 0.5 cm (~10%) in this radius

ORNL-DWG 69-2456

$$\nabla p = J_\theta \times B_z$$

$$\frac{I_1}{2L} = \frac{nkT}{B_1}$$

$$\frac{I_2}{2L} = \frac{nkT}{B_2}$$

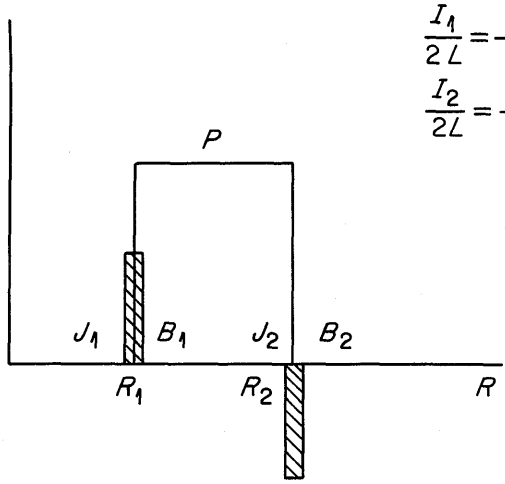

Fig. 5.5. Basic Plasma Model Used for Calculation.

ORNL-DWG 68-13156A

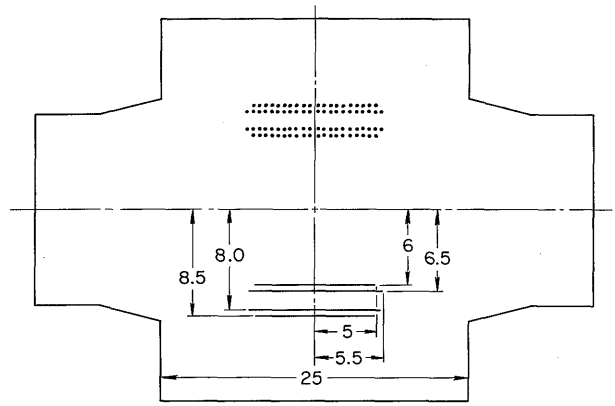

ALL DIMENSIONS IN cm

Fig. 5.7. Schematic of Microwave Cavity Showing Best Fit Current Loop Configuration.

ORNL-DWG 69-2457

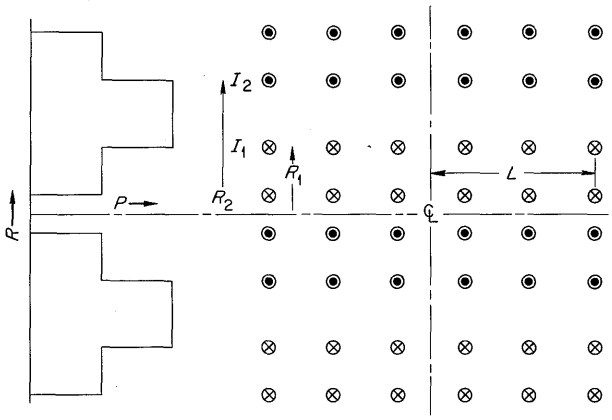

Fig. 5.6. Current Loop Array Used in Calculation with Equivalent Plasma Pressure Profile.

Table 5.1. Summary of Model Parameters

Parameter	Calculated	Experimental
Mean outer radius, cm	8.25	11 (skimmer probe)
Mean inner radius, cm	6.25	~8 (skimmer probe)
Step width, cm	0.5	
Plasma length, cm	10.5	<12 (cavity length)
Total outer current, A	14,538	
Total inner current, A	13,938	
$\frac{I_1}{I_2}\left(=\frac{B_2}{B_1}\right)$	1.043	1.045 (vacuum fields)

produces a rapidly deteriorating fit. However, the value is very dependent on the off-axis data, which are not very accurate. The outer radius was then adjusted to give the best all-over agreement within 0.5 cm. Thus the general accuracy is of the order of 10%, and with this simple model the solution appears to be unique.

With this particular model, the radial variation of magnetic field was then calculated at the median plane of the device and added to the vacuum magnetic field to give the shape of the plasma magnetic well, which is shown in Fig. 5.8. The well depth is 1.4 kG in a vacuum field of about 7.7 kG, giving a maximum β of 33%. The well width is 2 cm, which sets a maximum limit on the mean energy – namely, that the Larmor diameter is of this order – and gives a maximum temperature of 1.5 to 2.0 MeV. This is very close to the actual temperature as measured by bremsstrahlung. The plasma is apparently one Larmor diameter wide, as if there is a unique drift surface.

The mean perpendicular energy at the bottom of the well is 0.08 J/cm^3, which for a temperature of 1 MeV gives a density of 5×10^{11}/cm^3 for the energetic electrons.

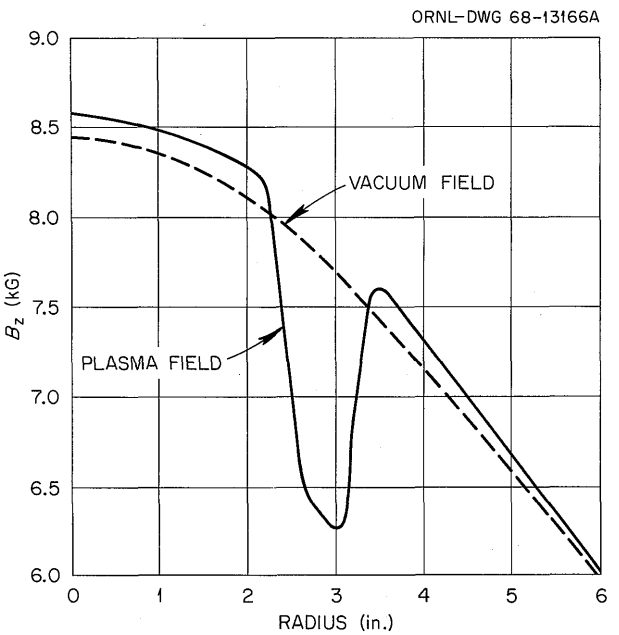

Fig. 5.8. Radial Field Profile at the Midplane from Cavity Loop Model.

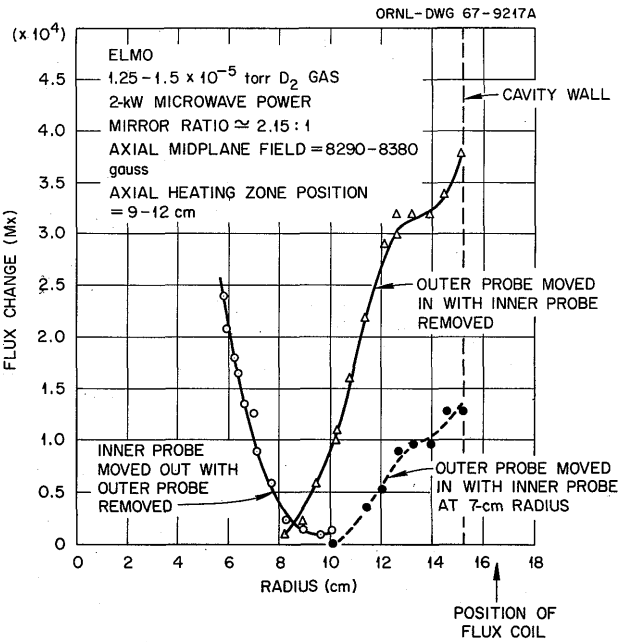

Fig. 5.9. Diamagnetic Signal as a Function of Probe Position.

The dimensions as obtained from this model can be compared with the data obtained from radial skimmer measurements. In Fig. 5.9 is shown the variation of diamagnetic signal measured with axis-encircling loops as a function of the position of the radial skimmer probes. The most unambiguous measurements are those made from the outside, and indicate an outer plasma radius of 11 to 12 cm, which is considerably more than calculated from the field survey. A possible explanation for this discrepancy is that a typical electron, although it spends most of its life in the region of high β, makes several excursions out of this area, and thus as the probe is inserted these electrons are wiped out before the probe enters the main plasma. In support of this hypothesis is the abrupt increase in x-ray flux as the probe is inserted, indicating that the electrons striking the probe are energetic and so gain energy in some other region.[11]

When the internal skimmer probe is run outwards there is no corresponding increase in x-ray flux; it is probable that the inner probe is simply extinguishing the electron source.

We have no good explanation as to why the high-β plasma is apparently hollow and has a specific radius. A possible explanation is that the line tying and hence the stability is better for the magnetic field line connecting with the edge of the cavity (Fig. 5.7). It has been suggested by L. S. Hall[12] that the effect is due to the nonpenetration of the microwaves into the plasma, so that the power is entirely absorbed on the surface. This would require at the surface a density of about $10^{13}/cm^3$ for the 8-mm radiation. This is somewhat higher than is actually estimated, and it can easily be shown that for a fully relativistic plasma the ratio $\omega_{pe}/\omega_{ce} \leqq \beta/2$. In addition, when the field survey was repeated with the mixed 8- and 5.5-mm microwave power, the experimental data obtained were essentially identical with those obtained from the simple 8-mm power configuration; this would not be expected from the above explanation.

A computer study has been made of the diamagnetic equilibrium using distribution functions and magnetic fields compatible with those in the ELMO device. The results of this study are described in Sect. 1.4.2 of this report and would suggest that the plasma configuration inferred from the experiments is at least an equilibrium one; however, these computer experiments have not as yet suggested any mechanism for the appearance of the annulus.

[11] *Thermonuclear Div. Semiann. Progr. Rept. Apr. 30, 1967*, ORNL-4150, sect. 4.2.3, p. 65.

[12] Private communication.

5.1.4 Instability-Accelerated Particles

When ELMO is operated with high-level 8- and 5.5-mm power, large energetic-particle "dumps" occur during instabilities when the gas pressure is lowered. These instabilities are attributed to the lack of cold-plasma stabilization. The threshold pressure for the stability is $\sim 1 \times 10^{-5}$ torr gage but varies somewhat with operating conditions. A large fraction of the stored energy ($\sim$90%) is lost in instabilities with a rise time of $\sim \frac{1}{4}$ μsec and a total duration of ~ 1 μsec. Large x-ray, rf, and microwave noise bursts are observed during the instabilities.

Studies were made to determine if particle acceleration was occurring during the instabilities. When a large group of energetic electrons is lost, one can expect space charge fields to develop with a total potential on the order of the value of the mean electron energy. In the absence of cold-plasma stabilization, such fields could be expected to accelerate ions.

At the suggestion of A. H. Snell, a search was made for the reaction $^{12}C(d,n)^{13}N$, which has a low deuteron energy threshold (328 keV).[13] The experiment involved a search for the 10-min activity of ^{13}N produced on cylindrical graphite-tipped probes, which had been inserted radially and axially into the cavity.

A 10-min positron activity was discovered in the probe tips, but an activity of $\sim$10 min was also found on the copper probe holding the carbon tip. Because of this latter unexpected result the work proceeded in two separate directions. The following section describes the photonuclear activation studies. Next are described the deuteron activation experiments.

5.1.4.1. Photonuclear Studies. – The $\sim$10-min activity on the copper probe holder was identified as the 9.8-min positron activity of ^{62}Cu resulting from a (γ,n) process on ^{63}Cu. Later, the 12.8-hr activity from ^{64}Cu was also found. The isotope ^{64}Cu can be produced either by a (γ,n) process on ^{65}Cu or by neutron capture in ^{63}Cu, although the cross section for neutron capture is much smaller than for a (γ,n) process.

The most striking feature of these (γ,n) processes is that they require very high-energy photons. The nucleon binding energy for ^{63}Cu is 10.84 MeV, and for ^{65}Cu it is 9.91 MeV.[14] Hence x rays of energies greater than these thresholds must interact to produce these reactions. The maximum photon energies observed in the bremsstrahlung radiation of the plasma under steady-state stable conditions are less than 8 MeV. These radioactive isotopes are not observed on copper-tipped probes inserted in the plasma under stable operation. We are drawn to the conclusion that the instability accelerates electrons by several million electron volts from below 8 MeV to above 10 MeV. We can also put an upper limit on the energy acquired by electrons during the instability. To produce ^{11}C from ^{12}C by a (γ,n) process requires a minimum photon energy of 18.7 MeV. This isotope is not a gas and would not tend to desorb as in the case of ^{13}N. A careful search has failed to reveal any evidence of the 20.3-min half-life of ^{11}C, implying that few electrons are accelerated above this threshold. Under similar operating conditions, a higher 10-min activity is seen on probes inserted radially into the plasma on the midplane as compared with the activity on probes inserted axially from one end. This implies that the accelerated particles are lost primarily but not exclusively in the radial direction.

Probably the simplest acceleration mechanism that could act on the electrons is betatron acceleration. The instability dumps a large fraction of the plasma, allowing the magnetic field to quickly rise and accelerate a small fraction of the remaining plasma.[15] A plasma energy-exchange mechanism of this type was previously proposed to explain a rapid increase of the neutron production at turnoff with a 3-cm microwave plasma.[16]

Bremsstrahlung measurements are nearly impossible during an instability. However, we have extracted a small amount of spectral information about the accelerated particles using the copper-tipped probe data for probes inserted from the end. The total yield of radioactive atoms is proportional to:

1. the initial number of "parent" atoms (atoms with one neutron more in the nucleus),
2. the (γ,n) cross section for the "parent,"
3. the flux of photons with energies above the threshold.

---

[13] T. W. Bonner *et al.*, *Phys. Rev.* **15**, 1398 (1949).

[14] J. A. Harvey and M. D. Goldberg, *American Institute of Physics Handbook*, to be published.

[15] This possibility was first suggested by W. B. Ard (1963) and calculated by G. G. Kelley (1968).

[16] *Thermonuclear Div. Semiann. Progr. Rept. Apr. 30, 1963*, ORNL-3472, sect. 3.1.2.

The measured cross sections[17] are assumed to have the same shape between threshold and 18 MeV. Since both ^{62}Cu and ^{64}Cu are found in the probe, a well counter detects both with approximately equal efficiency if the counting bias is properly set and if proper accounting is made for alternate modes of decay for ^{64}Cu. Both isotopes have the same irradiation time. The total number of radioactive atoms is given by the initial rate of decay times the mean life. Hence,

$$\frac{\text{No. of } ^{62}\text{Cu atoms}}{\text{No. of } ^{64}\text{Cu atoms}} \simeq \frac{\text{isotopic abundance of } ^{63}\text{Cu}}{\text{isotopic abundance of } ^{65}\text{Cu}} \times \frac{\sigma(\gamma,n) \text{ for } ^{63}\text{Cu}}{\sigma(\gamma,n) \text{ for } ^{65}\text{Cu}} \times \frac{F(E > 10.8 \text{ MeV})}{F(E > 9.9 \text{ MeV})} ,$$

$$0.5 \simeq \frac{0.691}{0.309} \times \frac{1}{1.19} \times \frac{F(E > 10.8 \text{ MeV})}{F(E > 9.9 \text{ MeV})} ,$$

$$\frac{F(E > 10.8 \text{ MeV})}{F(E > 9.9 \text{ MeV})} \simeq 0.26 .$$

We conclude that the spectrum of electrons striking the probe is dropping rapidly near 10 MeV.

We have also produced 2.4 and 24 min activity in silver-tipped probes from the decay of ^{109}Ag and ^{107}Ag respectively. The 24-min activity can only be produced by a photonuclear process with a minimum photon energy of 9.53 MeV. The 2.4-min activity can either be produced by a photonuclear process with a minimum photon energy of 9.18 MeV on ^{109}Ag or a neutron capture in ^{107}Ag.

It is possible to extend this procedure with other isotopes, but there is great difficulty in normalizing to a constant irradiation time (or total number of incident electrons). Hence it is difficult to utilize the silver data along with the copper data in a spectral analysis.

In principle this procedure could be used to investigate the photon flux through the probe during steady-state operation, similar to our previous photonuclear studies.[18] However, in contrast to these old measurements involving a determination of the neutron production, we must look for radioactivity from a material with a low nucleon binding energy. Unfortunately, there is a dearth of suitable isotopes with nucleon binding energies between 6 and 8 MeV which have radioactive daughters.

The activity seen in copper and silver probe tips is primarily obtained through pure photonuclear processes, since the photonuclear cross section is 100 to 1000 times the cross section for an (e,ne') reaction.[19] Even though the electrons penetrate several millimeters into the probe tip, the resulting bremsstrahlung would have a far greater effect.

5.1.4.2. Deuteron Activation Studies. – We have produced good evidence for a ^{12}C$(d,n)^{13}$N reaction on graphite-tipped probes during instabilities. Our original experiments were undecisive because of variations in success in producing activity on the probe tips. Some of the difficulty was probably due to alternate instability modes or low-power operation resulting in variations in the accelerated deuteron energy and power density. Also, when arc electrode graphite was used, activity was usually seen after irradiation, but it was often not seen or was much weaker when reactor-grade graphite was used. Spectral analysis has shown no impurities in the arc electrode graphite that could be responsible for the observed activity if it were produced by other processes.

It was conceivable, however, that during the operation of the machine, radioactive copper that had been sputtered from the cavity walls could be deposited on the probes. The accuracy of the counting statistics is not good enough to distinguish between a 10-min ^{13}N activity and a 9.8-min ^{62}Cu activity. Chemical removal[20] of the copper on the probes was performed, but no trace of radioactive copper could be found. The activity remained in the carbon after the treatment. A lathe was used to remove a thin surface layer (~0.025 cm) of graphite from the tips. The activity was found to be largely confined to the graphite turnings (dust) with a small amount of activity remaining on the probe tip body. Chemical removal of copper from the dust and subsequent counting showed no radioactive copper; the activity remained in the dust. Heating of active probe tips to a dull red (600 to 700°C) for ~1 min removed about half of the activity, implying that the active material was most probably a gas bound to the surface.

[17] G. E. Coote *et al.*, *Nucl. Phys.* **23**, 468 (1961).

[18] *Thermonuclear Div. Semiann. Progr. Rept. Apr. 30, 1967*, ORNL-4150, sect. 4.2.3.

[19] M. B. Scott *et al.*, *Phys. Rev.* **100**, 209 (1955).

[20] We are indebted to W. R. Laing and L. J. Brady of the Analytical Chemistry Division for providing us with the chemical procedure to remove sputtered copper from the probe tips.

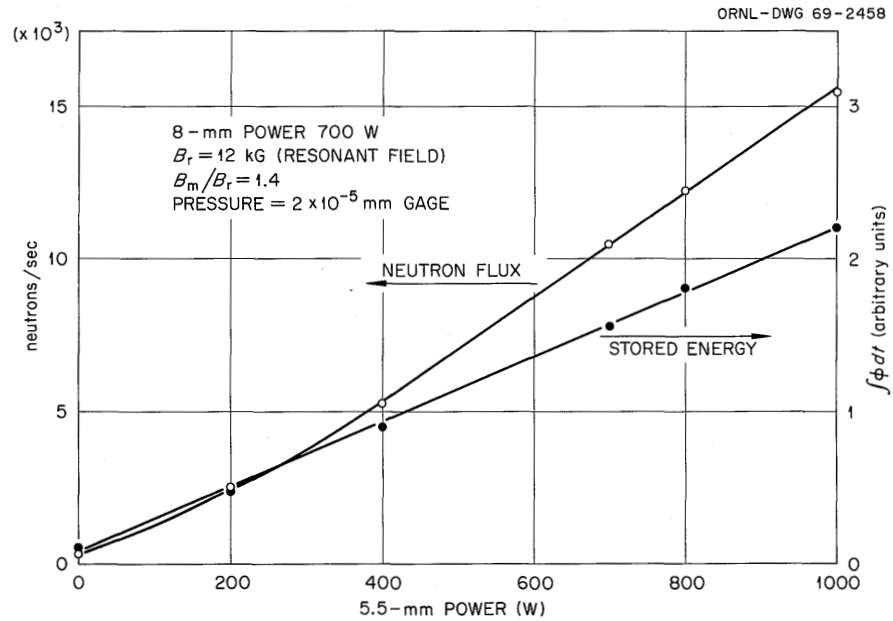

Fig. 5.10. Off-Resonance Heating with 5.5-mm Power.

Operation of the machine on hydrogen produced no activity in the graphite probe tips. The (p,γ) process can also be used to produce ^{13}N from ^{12}C, but the cross section is ~100 times smaller; hence little effect is expected. However, if a photonuclear process were causing the effect, we should still expect to see activity. The evidence strongly suggests that we have produced ^{13}N by a (d,n) process on ^{12}C. A rough calculation suggests that we are accelerating $\gtrsim 10^8$ deuterons/cm^2 above the (d,n) threshold energy onto the probe surface during each instability.

5.1.5 Off-Resonance Heating

Since the 1-kW cw driver for the high-power 5.5-mm microwave amplifier became available during this reporting period, it seemed an attractive possibility (while the 10-kW amplifier is in preparation) to use the driver in parallel with the existing 8-mm microwave source (which requires the other half of the cubicle) to investigate nonresonant heating.

It is obvious that the high-β annulus observed in the 2-kW 8-mm experiments cannot be due to fundamental frequency ECH because the annulus resides in a vacuum magnetic field about half of the resonant field (B_r). Even resonant coupling at the second harmonic frequency[21] is an implausible mechanism when one considers the high relativistic energy of the average energetic electron in the annulus; for example, a 2-MeV electron in the spatial region of the annulus would have to resonate at its 11th harmonic. Both 8- and 5.5-mm power were simultaneously applied to the plasma formed in the simple magnetic mirror ($B_m/B_{00} = 2.0$, $B_r(8\text{ mm})/B_{00} \cong 1.4$) whose field value was such that no resonance existed for 5.5-mm power (since $f\,5.5\text{ mm}/f\,8\text{ mm} = 55\text{ GHz}/35\text{ GHz} = 1.57 > 1.4 \cong B_m/B_r$). The total energy ($n_eT_eV$) dependence on power (as measured diamagnetically) for the same total applied power was slightly greater than that obtained when using the 2-kW 8-mm source alone. The obvious effectiveness of the off-resonance 5.5-mm heating is illustrated in Fig. 5.10, where the total perpendicular energy and neutron flux are strong functions of off-resonance power. Although a detailed correlation with the off-resonance heating theory of Grawe[22] is beyond our diagnostic capabilities at this time, the above results are in good qualitative agreement with Grawe's theory.

---

[21] H. Ikegami *et al.*, *Phys. Rev. Letters* **19**, 778 (1967).

[22] H. Grawe, *Plasma Phys.* 11, 151 (1969).

5.1.6 Specific Electrodissociation Neutron Production

An interesting side effect in these experiments (Sect. 5.1.5) was a much larger neutron flux than was observed with the same total 8-mm power alone, causing us to examine more critically electrodissociation of the deuteron as the mechanism responsible for neutron production. We have attempted in the following analysis to relate in terms of energetic feasibility the following essentially nonspatially dependent and therefore relatively accurate (approximately 10%) measurements: total stored perpendicular energy, total steady-state neutron emission rate, and neutral gas pressure outside the plasma, which is taken as nuclear target density. We have derived a temperature function dependent on a linear product of the above measured parameters for several electron energy distributions. The calculational details of the diamagnetic and neutron emission as a function of electron energy are included so as to indicate the possible accuracy of the method.

5.1.6.1. Diamagnetic Measurements of Total Energy. – The total energy measurements involve taking the integral of the voltage induced, $e = n\,\Delta\phi/\Delta t$, in a 100-turn loop of diameter D placed around the outside of the microwave cavity and essentially in the midplane.

Linear electronic integration then gives a voltage

$$e = 10^{-8}\,\frac{n}{\tau}\int\frac{\Delta\phi}{\Delta t}\,dt = 10^{-6}\,\frac{\Delta\phi}{\tau}, \qquad (1)$$

or

$$\Delta\phi = e\tau \times 10^{6}\,. \qquad (2)$$

The net flux, $\Delta\phi$, is in maxwells when $e\tau$ is in volt-seconds; τ is the integrator time constant.

Note that

$$\frac{n_e T_e}{B} \cong \frac{2\Delta B}{8\pi}, \qquad (3)$$

where ΔB is the diamagnetic field and B is the vacuum field in the region of the annulus.

Using a solenoidal approximation for the high-β shell, the total flux out of the plasma is

$$\Delta\phi_0 = \Delta B\,\frac{V}{l} = \frac{4\pi n_e T_e}{B}\,\frac{V}{l}, \qquad (4)$$

where V is the volume of the annulus and l is its full length.

$\Delta\phi$ is related to $\Delta\phi_0$ by a geometric factor which can, for tightly spaced coaxial current shells, be regarded as a ring of dipoles and closely approximated by

$$\Delta\phi = \Delta\phi_0\,\frac{l}{\sqrt{l^2 + D^2}} = \frac{4\pi n_e T_e}{B}\,\frac{V}{\sqrt{l^2 + D^2}}\,. \qquad (5)$$

Combining (2) and (5) to obtain $n_e T_e V$ (the total perpendicular energy) in terms of the measured parameters,

$$n_e T_e V \cong J = 8 \times 10^{-5}\,Be\tau D\sqrt{1 + \frac{l^2}{D^2}}\,, \qquad (6)$$

in units of 100 J. Typically, B = 6500 G, D = 50 cm, and $e\tau$ ranges from 0 to 0.08 V-sec.

Since the flux integrals can be measured to a few percent and since D can be made much larger than l, $\Delta\phi$ can be a rather accurate measure of total stored perpendicular energy without knowledge of plasma dimensions. The principal errors in this diagnostic result from nondiamagnetic currents and to a lesser extent the value of B. Large drift currents which have been observed do cause an error, but only in the sense of making $n_e T_e V$ slightly (10%) smaller than that obtained from diamagnetism alone.

5.1.6.2. Coulomb Dissociation Neutrons as a Measure of $N_e\,f(T_e)$. – The number of neutrons resulting from Coulomb dissociation of deuterons by electrons above 2.2 MeV is also a quantitative measure of total energy, given some distribution function. A cross section for Coulomb dissociation was calculated as a function of energy by Gordon Soper.[23] This cross section can be fairly accurately (~5% at 4 MeV) represented by the straight line $\sigma_e = 4 \times 10^{-30}\,(E - 3)$, E in MeV, σ_e in square centimeters.

Assume an anisotropic energy-multiplied distribution function as representative of the relativistic electron population:

$$dn_e = \frac{n_e E}{T_e^2}\,\epsilon^{-E/T_e}\,dE\,. \qquad (7)$$

[23] *Thermonuclear Div. Semiann. Progr. Rept. Oct. 31, 1962*, ORNL-3392, p. 62.

For such a distribution the diamagnetically measured total energy $J = 2n_e T_e V$ or the electron density used in the neutron calculation is half the density of a Maxwellian. For J in units of 100 J,

$$n_e = \frac{J\, 3 \times 10^{14}}{T_e V} \; (T_e \text{ in MeV and } T_e \cong T_{e\perp}) \; ; \quad (8)$$

then

$$dn_e = \frac{JE\, 3 \times 10^{14}}{T_e^3 V} \epsilon^{-E/T_e} \, dE \; , \quad (9)$$

and the total number of neutrons, M, produced by electrons in the energy interval dE is:

$$dM = dn_e V n_0 \sigma_e C = \frac{J n_0 E(E-3)}{T_e^3} \epsilon^{-E/T_e} \, dE \quad (10)$$

(n_0 in units of 10^{12}/cc and M in units of 3.6×10^7/sec), where n_0 is a pessimistically large target density, that is, the neutral gas density measured by a vacuum gage, and M is the neutron source strength, measured with a standard-source-calibrated ^{3}He proportional counter.

Using 3 MeV as the linearly approximated threshold for the D(e,n)H reaction and integrating from this threshold to ∞ gives:

$$M = \frac{J n_0}{T_e} (3 + 2T_e) \, \epsilon^{-3/T_e} \; . \quad (11)$$

This expression is plotted in Fig. 5.11 and labeled "modified Maxwellian." Note that $M/Jn_0 = 2$ is only satisfied by $T_e = \infty$. This same integral is plotted with a 6-MeV cutoff, an unreasonably high upper limit for the ELMO geometry.

The neutron production rate for a delta function is also shown in this figure. Experimental observations of M/Jn_0 are shown as vertical lines. These lines are not meant to be a statistical representation, but show rather the typical values and the maximum value that can be repeatedly observed. For example, one can adjust the plasma parameters so that M/Jn_0 ranges from 0.1 to 2.4, and the particular value can be observed for shot after shot with a largest observed value of 2.4.

5.1.6.3. Conclusion. – The electron distribution in ELMO should be cut off above 6 MeV by synchrotron radiation and nonadiabatic effects. The maximum M/Jn_0 for this cut-off distribution is seen on Fig. 5.11 to be 0.25. Values of specific neu-

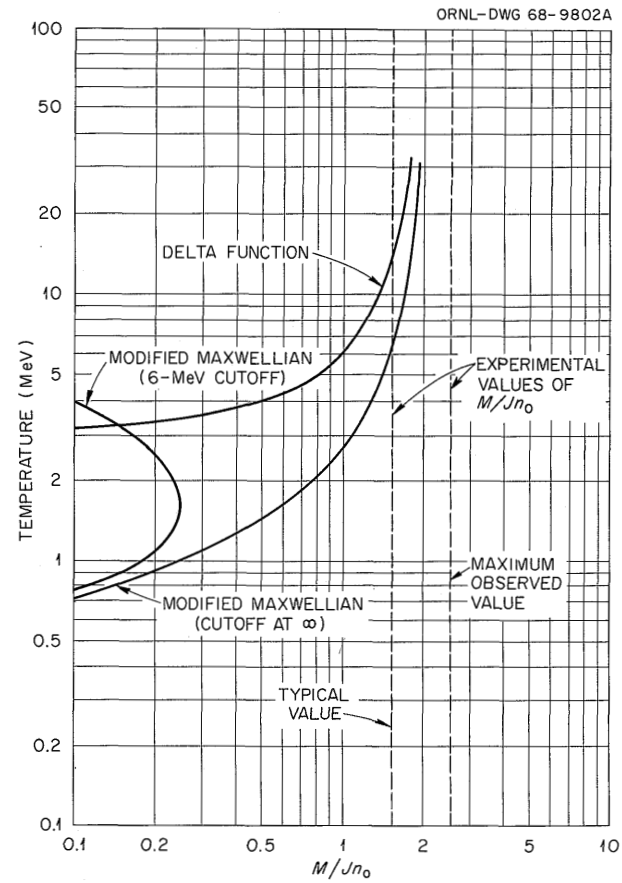

Fig. 5.11. Temperature vs Specific Neutron Production.

tron production (i.e., M/Jn_0) as high as 2.4 have been observed, and these then require a Coulomb dissociation cross section 9.6 times that calculated. For a 4-MeV delta function distribution, the binary cross section would have to be a factor of 5 larger to be in good experimental agreement. More accurate calibration of gages and counters, now in progress, might change the maximum specific neutron production by about a factor of 2. So either the numerical value of the calculated Coulomb dissociation cross section is somewhat too low or some other process involving more target deuterons or enhancement by many-body effects might be the cause. If the discrepancy is simply due to a numerical error in the binary cross section, careful calculation combined with cross-section measurements should solve the problem. If, however, the discrepancy becomes greater in the soon-to-start high-power 5.5-mm experiment, then more radical causes such as multibody effects mainly observable in dense relativistic gases will

have to be considered. See Sect. 9.4 for additional remarks.

5.2 SCATTERING AND ENERGY LOSS RATES IN HOT-ELECTRON PLASMAS

W. B. Ard

Measurements of the spectral intensity of bremsstrahlung from energetic electrons have been used to determine the energy distribution functions of electrons in a microwave-heated plasma. By making the spectral measurements as a function of time in a decaying plasma, information about scattering and cooling rates of the electrons can be obtained, and this can be compared with the classical rates.

The plasma used for these experiments was produced in the Long Solenoid Facility by electron-cyclotron resonance heating. The measurements were limited to conditions with rather high background neutral pressure since stability against flutes in the simple mirror system required cold-plasma conductivity to the end walls.

The spectra were obtained by gating the pulse-height analyzer on for a 20-msec period of time after the heating power had been turned off and the plasma allowed to decay for a fixed period of time. In order to obtain good statistics, spectra from 1000 decays were accumulated for each delay time. Since each point represented an average over many different plasmas and also over long periods of time, spectra obtained for a delay time early in a run were compared with spectra for the same delay time obtained late in the run. If the two spectra were different, the data from the run were not used. The spectra were corrected for the absorption in the windows and air path between the NaI scintillator and the plasma and for the effect of the iodine K edge in the scintillator.

The distribution function of the electrons is obtained from the spectra by the following relation:

$$F(E) \propto -\frac{E}{v}\frac{dI(E)}{dE}, \tag{1}$$

where E is the electron energy, $I(E)$ is the spectral intensity at the energy E, and v is the velocity of the electron at the energy E. Equation (1) is derived from the following considerations:

The energy radiated by an electron in traversing a distance dx through matter is proportional to the nature of the matter and the distance dx, and independent of the electron energy. That is,

$$d\mathcal{E} = KNZ^2\, dx\ ; \tag{2}$$

N is the number of nuclei per cubic centimeter with charge Z and

$$K = \frac{16}{3}\left(\frac{m_0 c^2 r_0^2}{137}\right).$$

The energy is radiated uniformly over the spectrum up to the electron energy. Therefore the energy radiated per unit time per unit energy by an electron of energy E is proportional to v/E below the energy E and is zero above the energy E. The spectral intensity, $I(E)$, of radiation from a distribution of electrons is:

$$I(E) \propto \int_E^\infty \frac{v}{\mathcal{E}} F(\mathcal{E})\, d\mathcal{E}\ , \tag{3}$$

where $F(\mathcal{E})$ is the number of electrons with energy $\mathcal{E}$. Since the definite integral in Eq. (3) is a function only of its lower limit, we can differentiate Eq. (3) with respect to this lower limit and obtain

$$\frac{dI(E)}{dE} \propto -\frac{v}{E} F(E)\ . \tag{4}$$

The results are only preliminary; however, an attempt has been made to compare the observed time behavior of the distribution function with a simple model of the decay. This model assumes that electrons lose energy by inelastic collisions with a constant background density of neutral molecules and are scattered out of the mirror off a constant density of scattering centers. The energy of an electron is assumed to follow the following relation in time:

$$E(t) = (E_0^{4/3} - K_1 t)^{3/4}\ , \tag{5}$$

which results from integration of the empirical relation for the energy loss rate for electrons in gases,

$$\frac{dE}{dt} = -\Delta E\, N_0 \sigma v \propto E^{-1/3}\ . \tag{6}$$

The loss rate of particles is assumed to be:

$$\frac{dF(E)}{dt} = \frac{K_2 F(E)}{E^{3/2}} . \tag{7}$$

The distribution function obtained from spectra taken during the first 20 msec of the decay is taken as the initial distribution and followed in time according to Eqs. (5) and (7) numerically. The constants K_1 and K_2 are adjusted in order to attempt to make the calculated distributions at later times coincide with the distributions obtained from the spectra taken at the corresponding times in the decay. Figure 5.12 shows a comparison between the observed distributions and the calculated ones for the values 4 keV$^{4/3}$/msec and 1 keV$^{3/2}$/msec for K_1 and K_2. The agreement is good at higher energies but not very good at low energies. However, the 20-msec time intervals during which the spectra were taken are too coarse to be valid for the low energies, at which the distribution is changing rapidly. There might also exist systematic errors in determining electron density at the lower energies due to uncertainties in correcting the spectra.

The value 4 keV$^{3/2}$/msec for K_1 is in agreement with published data for the cross section for ionization of hydrogen by electrons, the mean energy loss per ionization, and our estimated pressure of 2×10^{-5} mm during the decay.

The value of 1 keV$^{3/2}$/msec for K_2 is difficult to resolve at this time. The decay rate should be given by

$$\frac{dF(E)}{dt} = \frac{k_1 N + k_2 N_0}{E^{3/2}} F(E) = \frac{K_2 F(E)}{E^{3/2}} ,$$

where N is the total electron density and N_0 is the neutral density. One would expect $k_1 \approx 10^2 k_2$ (scattering from charged particles); however, $N_0 \approx 10^2 N$ in this experiment, and N is, of course, time dependent. An estimate of k_1 from theoretical considerations is $\approx 10^{-11}$/msec, so $K_2 = 3 \times 10^{-1} + 3 \times 10^{-1} = 0.6$ from this estimate and is close to the estimated value from the experiment. However,

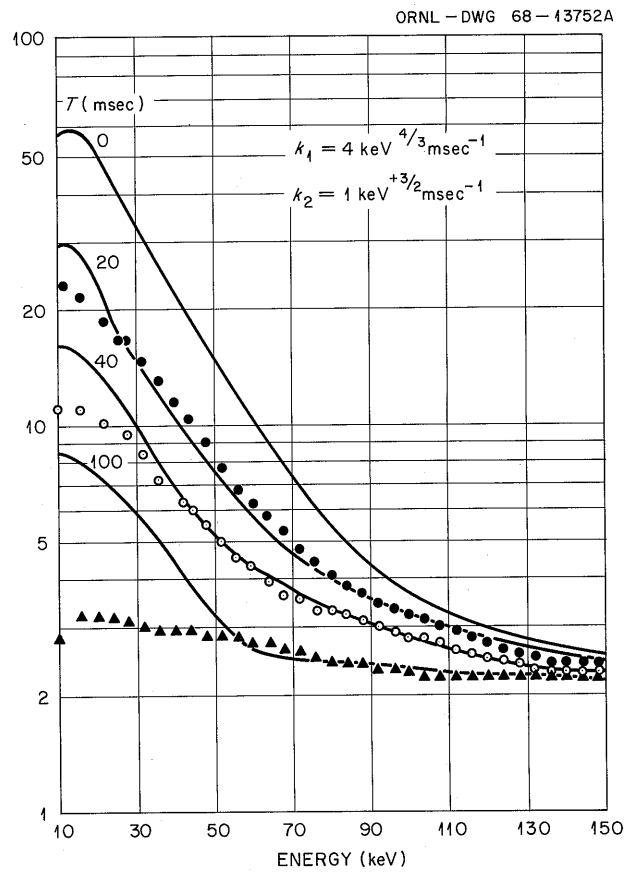

Fig. 5.12. Comparison of Measured and Calculated Distribution of Electrons in Decaying Plasma. Solid lines are measured distribution, and points are calculated. Density is in arbitrary units.

10^{-11} is probably a high estimate of k_1, and 3×10^{10} is probably also high for the electron density during most of the decay; thus $K_2 = 0.6$ is also high. The more likely lower value for K_2 implies a large deviation from the value 1 which fits the measured data.

However, these results are only preliminary, and considerably more work must be done in improving the measurements of the distribution functions, electron densities, and neutral densities before a reliable value for the scattering rates can be obtained.

6. Turbulent Heating

6.1 BURNOUT V

6.1.1 Introduction

R. V. Neidigh

Temperature and density of the "mode II" steady-state plasma in Burnout V are bracketed in Fig. 6.1, and given in greater detail with descriptive material in several publications.[1-3] In the latter part of 1968 we operated Burnout V in a new, visually and diagnostically different plasma mode; we call it a "supermode" because both temperature and density are greater (by a factor of 2) than in the previous mode II plasma. The presence of carbon and copper impurities has limited ion temperature in mode II; though prior to recent improvements the plasma could be pulsed into the supermode, the copper and carbon spectral intensities would then rise over a period of a few seconds, and the plasma would again revert to mode II (or even to the nonheating mode I). By increasing the cooling on the anode cavity we have been able to keep impurities at their mode II level while the beam is at the "supermode" level, about 15% higher than the mode II power level of 60 kW. A helium experiment we describe in Sect. 6.1.5 supports the assumption that impurities limit the plasma temperature. Other diagnostics used on the supermode – spectral intensity dependence on radius, diamagnetic signals, Doppler broadening of Balmer lines, correlation of plasma potentials, plasma losses, and heating efficiency – are discussed in the following paragraphs.

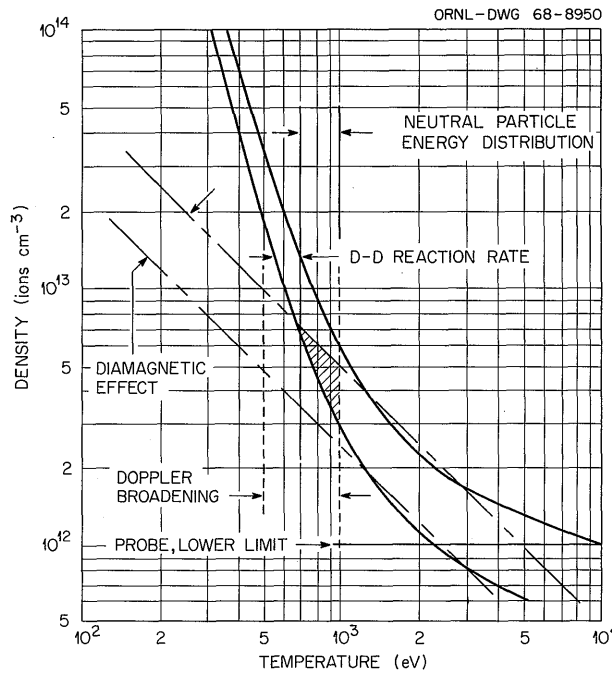

Fig. 6.1. Summary of Temperature and Density Measurements on the Mode II Plasma. The Doppler-broadened Balmer lines indicated a temperature between the limits shown by the vertical dashes. D-D reaction rates determined by 3-MeV proton emission from the plasma place limits on the temperature-density product, indicated by the heavy solid lines. Diamagnetic effect, long dashes, also gives a temperature-density product. Energy distribution of neutral particle emission, vertical solid lines, gives the best temperature resolution. The shaded area, common to all the diagnostics, yields the most probable values for the temperature and density.

[1] I. Alexeff, W. D. Jones, and R. V. Neidigh, *Phys. Rev. Letters* 18, 1109 (1967).

[2] *Thermonuclear Div. Semiann. Progr. Rept. Oct. 31, 1964*, ORNL-3760, p. 30; *Apr. 30, 1965*; ORNL-3836, p. 38; *Oct. 31, 1965*, ORNL-3908, p. 52; *Apr. 30, 1966*, ORNL-3989, p. 46; *Oct. 31, 1966*, ORNL-4063, p. 36; *Apr. 30, 1967*, ORNL-4150, p. 71; *Oct. 31, 1967*, ORNL-4238, p. 73.

[3] R. V. Neidigh *et al.*, paper CN-24/L-2, IAEA Third Conference on Plasma Physics and Controlled Nuclear Fusion Research, Novosibirsk, U.S.S.R., Aug. 1–7, 1968, to be published in *Nuclear Fusion; Bull. Am. Phys. Soc.* 13, 881 (1968).

6.1.2 Plasma Radial Profile

R. V. Neidigh S. R. Sowder[4]

In order to determine the radial extent of the supermode, we optically scanned the plasma using photomultiplier tubes, lenses, and filters. The filters were chosen to pass either Balmer β (4862 Å, FWHM = 8.0 Å) or a region from 5200 to 6500 Å where a molecular band system of deuterium exists. It was found that the molecular pass band contained impurity spectra and therefore had to be disregarded in this experiment. Intensity vs position of the Balmer line was Abel-inverted to get intensity vs radius. These data were taken before the supermode could be maintained in the steady state for long periods. So, in order to scan the whole plasma, we had to scan in several periods. We therefore scanned only when the energetic neutral particle detector current indicated a supermode plasma. As a result each scan was made up of about a dozen different supermode events; see Fig. 6.2. Here is shown a composite to make the entire radial scan in the median plane. The light intensity repeated itself so well that separate tracing events are scarcely detected. The Abel inversion, also shown, was found to be exponential from 1.5 to about 6.0 cm. It is slightly brighter from the axis to 1.5 cm, the beam radius, than the extrapolated exponential and is essentially flat beyond 6 cm to the edge of the plasma. The radial profile of the intensity is, of course, the result of competing processes. Dissociation and charge exchange may leave an excited neutral, distorting an intensity distribution which naively might be thought to resemble the electron density distribution. We have shown in Sect. 6.1.6 that the effect of delayed cascading into the $n = 4$ level significantly distorts the intensity distribution as well. Thus we see that comparison of the radial profiles of mode II and the supermode, though possible from Fig. 6.2, may not be meaningful in detail. It is thought that the intensity decrease in the supermode is significant, however, and may result from reduced penetration into the plasma of the unionized 5-eV neutral atoms from the Franck-Condon dissociation.

[4]1968 Summer Participant, Southern Missionary College.

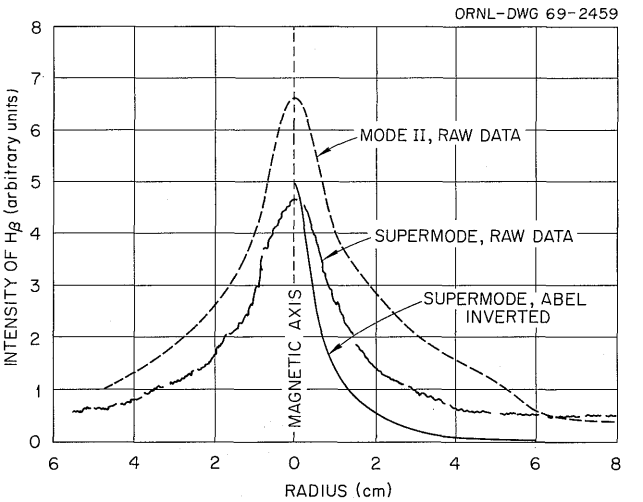

Fig. 6.2. Spectral Intensity Distribution of Mode II and the Supermode. The curves were made with a Balmer β, 4862 Å, FWHM = 8.0 Å, filter. Most notable feature is the overall intensity decrease in the supermode, indicating reduced penetration by the 5-eV Franck-Condon neutral atoms. The Abel-inverted curve shows a departure from exponential at $R < 1.5$ cm, the region of the electron beam.

6.1.3 Spectroscopic Diagnostics

R. Hefferlin[5] R. V. Neidigh

A summary of spectroscopic results for Burnout V in mode II and supermode is presented in Table 6.1. They represent spectroscopic diagnostics on deuterium atoms (the deuterons being invisible) and on other species which assist in determining plasma properties. Results 1–6 are from light along a sector with radii of 1.5 and 6 cm. Result 7 is from light through a diameter of the image. Results 8–11 are from light across the entire image.

This study is very preliminary, but we can draw some tentative conclusions. (*a*) In the supermode we find intensities of both atomic and molecular spectra lower than in mode II, but impurity spectra are at about the same level of intensity. This cannot be interpreted as a decrease in ion or electron density but only as a decrease in neutral density, since the charge-exchanged neutral-particle flux is greater in the supermode by more than a factor of 2

[5]Consultant, Southern Missionary College.

Table 6.1. Spectroscopic Results

	Mode II	Supermode
Species identification		
D I	2×10^6 cm^{-3}	7×10^9 cm^{-3}
D_2 (molecule)	1.5×10^{10} cm^{-3}	Present
CD	Present	Present
Cu I	10^{12} cm^{-3}	10^{12} cm^{-3}
Cu II	10^5 cm^{-3}	10^8 cm^{-3}
C I	Absent	Absent
Other impurities (unidentified); weak lines	Present	Present
Excitation temperature (relative spectrum line intensities force-fitted to Boltzmann distribution)		
D I		
Cool group (center spike, Fig. 6.4)	(1) 0.2 eV, n large	(2) 0.2 eV, n large
Hot group (broadened wings, Fig. 6.4)		(3) 0.2 eV, n large
D_2 (molecules), rotational mode		(4) $\sim$0.02 eV
Cu I		(5) 0.6 eV
Cu II	(6) 2.4 eV	(6) 2.4 eV
Electron density, from cool D I line profiles	(7) 6×10^{13} cm^{-3}	
Ordered motion (spectrum line tilt)		
D I narrow profiles		
Frequency	(8) $-0.05\omega_{ci}$	
Maximum energy	(9) 1 keV	
Cu II		
Frequency	(10) $+\omega_{ci}$	(10) $+\omega_{ci}$
Maximum energy	(11) 3.7 keV	

Comments on Table 6.1

The numbers given in the species identification are relatively accurate to within 20% but probably not absolutely accurate to better than a factor of 5. The following comments correspond to the numbered data of Table 6.1:

1. Deviation from Boltzmann distribution (log plot shows more slope toward higher energy). The figure given is a fit of straight line on log graph for deuterium levels $n = 4$ through $n = 7$ (D_β through D_ϵ). All integrated line intensities were approximated by height × FWHM.

2. Deviation from Boltzmann distribution as in No. 1. The figure given is a fit for levels $n = 5$ and $n = 6$ (D_γ and D_δ). Notice the figure is the same as in No. 1.

3. Fit for levels $n = 5$ and $n = 6$ (D_β and D_γ). Notice the figure is the same as in Nos. 1 and 2.

4. Visual comparison with spectrum scans on Burnout IV. For these scans, calculation was made from three bands of $I^1\Pi - B^1\Sigma$. Also rough agreement from two perturbed bands of $G^1\Sigma - B^1\Sigma$. Notice T = room temperature. Error about 10%.

5. Upper energy levels 6.16 eV (two spectrum lines), 6.52 eV (two spectrum lines), and 3.80 eV (one spectrum line). gf values from Corliss and Bozman in National Bureau of Standards Monograph 53. Error perhaps 5%, but the figure depends entirely on the 3.80-eV-level spectrum line.

6. Many spectrum lines allowed fit to many energy levels. Error perhaps 10%, partly because, in the absence of known gf values, all f's were set equal to 0.2.

7. The narrow line profiles for $D_{\alpha,\beta,\gamma,\delta}$ were measured. The dependence upon wavelength of these four line widths suggested several competing processes. Instrumental broadening and Zeeman broadening were subtracted. The remaining width, when fitted to the GKS theory [R. A. Hill, *J. Quant. Spectry. Radiative Transfer* **4**, 857 (1964)], gave the number in the table.

8. The symbol means that ω is one-twentieth of cyclotron angular frequency (10^8 rad/sec) and that the motion is retrograde. It is not clear whether the motion is "solid disk" motion or cycloidal motion.

9. This figure was arrived at from the distance (from axis) to which the tilted line could be seen.

10. Disk-type motion at cyclotron angular frequency.

11. Same comment as No. 9.

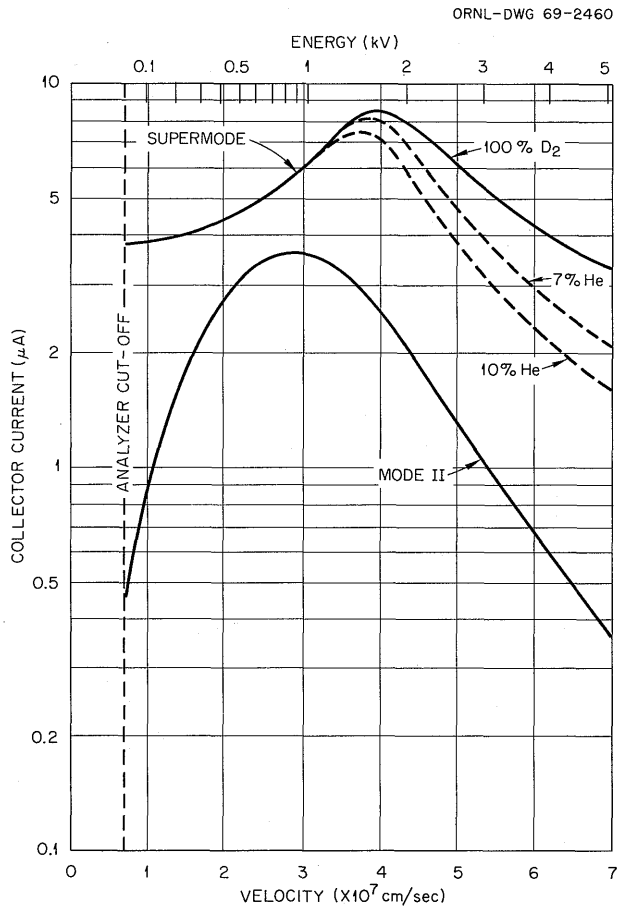

Fig. 6.3. Energy Distribution in Mode II and Supermode. The ordinate is actual detector current. Note the change in the high-energy part of the distribution of the supermode as helium was added. No correction for the varying efficiency of the analyzer with energy or cross sections was made, so the curves had best be considered relative, not absolute.

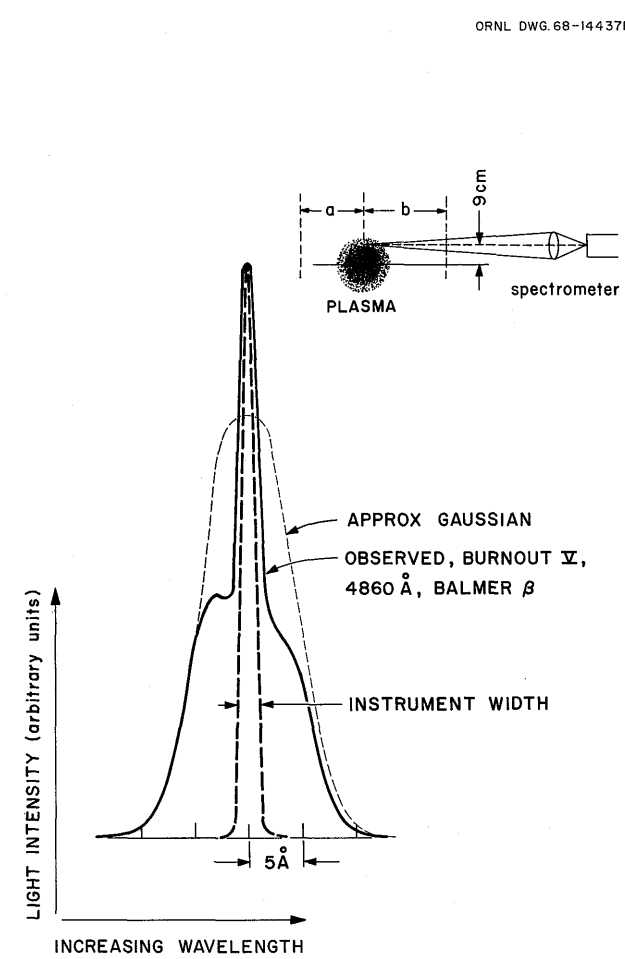

Fig. 6.4. Doppler-Broadened Balmer β Line. This broadened line at 4860 Å was of a sector through the plasma at 9 cm from the magnetic axis. The fit to a Gaussian (light dashed curve) is very good above 1 keV. There is some broadening of the center line. Instrument width was made by scanning the cold plasma of a discharge tube.

(the neutral-particle flux for the two modes is compared in Fig. 6.3). (*b*) The density of neutral copper appears to be abnormally high in both modes. We doubt this number, and must check it carefully. (*c*) Excitation temperatures were determined by separating the line intensities into two groups, a cool group using the intensity of the center spike (Fig. 6.4) and a hot group, at least ten times as abundant, using the line ("wing") on either side of the spike. (*d*) Electron density from the line profile of the cool group, probably correct to within a factor of 2, is the maximum density on the magnetic axis. (*e*) Spectrum line tilt gives a greater energy for copper ions than for deuterium in mode II. The deuterium energy may appear less than its real value because Doppler broadening makes the photographs difficult to read and because of delayed cascading into the excited levels. This is discussed further in Sect. 6.1.6.

6.1.4 Energy Fluctuations

R. V. Neidigh F. R. Scott[6]

Bursts involving rapid perpendicular plasma energy changes have been observed under conditions which show fast neutral atom emission.

[6]Consultant, University of Tennessee.

These bursts are also visually related with rapid radial expansion of the plasma. We associate the bursts, which are observed with a 5-in.-diam flux loop, with rapid loss of plasma energy. From a calibration of the flux loop, we determine that the steady-state perpendicular energy per unit length of the plasma is 5×10^{16} eV/cm. Energy decreases with an e-folding time of 10 μsec; the plasma recovery time is of the order of 200 μsec. During a burst a cathode current of the order of 4000 A is observed.

In addition to these large excursions the flux loop observes moderate fluctuations in the perpendicular energy ($\sim$10%) which occur approximately every 200 μsec. These fluctuations have buildup and decay times of the order of 30 to 50 μsec and are always initially in the direction of increasing perpendicular plasma energy. In addition to perpendicular plasma energy variation observed on the flux loop, there is a strong high-frequency oscillation at the ion gyrofrequency (20 MHz) in the midplane. It is damped or missing during the large burst and takes $\sim$200 μsec to increase to its steady-state amplitude; compare radiation from the supermode shown in Fig. 6.8.

The mode observed by the loop is mode II, not the supermode. The presence of the flux loop acts as a plasma limiter, causing a higher impurity level than normal, preventing the supermode. If we assume that the total number of high-energy ions per unit length is 3×10^{13} (integrating the particle density over the plasma radius) we get approximately 1600 V per electron-ion pair in the plasma.

The big difference between the bursts in Burnout V and other experiments reported in the literature[7] is that here the initiation is after steady-state conditions have been achieved. This requires that there be an internal energy storage (the plasma) equivalent to $\sim$0.5 J which can be released in less than 10 μsec.

It appears that these bursts are not limiting either plasma temperature or density, since they occur after irregular and lengthy (compared with the buildup time of 200 μsec) periods of maximum stored energy. Triggering may be internal, but we believe it is more likely to be caused by an uncontrollable power fluctuation initiated by a spark in the vacuum chamber, external to the magnetic mirrors. The bursts are a fortunate diagnostic related to stored energy and containment time in a way that will reveal minimum values for these quantities.

6.1.5 Effect of Helium Impurity

R. V. Neidigh

A small, but measured, amount of helium bled into the deuterium supermode plasma changed the energy distribution of charge-exchanged flux from the plasma. The high-energy end of the observed distribution was lowered by the presence of helium. The data are shown in Fig. 6.3. This is in qualitative agreement with a previously reported observation[1] that a helium contamination of about 10% in the mode II plasma reduced the D-D reaction rate from 10^3 reactions cm^{-3} sec^{-1} to less than 1 cm^{-3} sec^{-1}, since the energetic portion of the distribution is largely responsible for fusion reactions.[8] It therefore seems likely that the helium contaminant would have a more severe cooling effect on mode II than on the supermode, but no quantitative checks with reaction rates have yet been made.

We cannot yet assure ourselves that the lowering of the high-energy tail by the presence of helium is due to enhanced charge exchange. Un-ionized helium in the core of a burned-out plasma is several orders of magnitude less than Franck-Condon D^0 if ionization is from the 1S state, and it is larger if the ionization is from the higher excited levels. These measurements must be quantitatively compatible with the reduced reaction rates before we can assign certainty.

6.1.6 Doppler-Broadened Neutral Emission

I. Alexeff, R. V. Neidigh, J. R. McNally, F. R. Scott[6]

In the supermode, broad neutral emission lines have been observed, as shown in Fig. 6.4. The

[7] M. V. Babykin *et al.*, *Zh. Eksperim. i Teor. Fiz.* **52**, 643 (1967), *Soviet Phys. JETP* (English Transl.) **25**, 421 (1967); B. A. Demidov, N. I. Elagin, and S. D. Fanchenko, *Dokl. Akad. Nauk SSSR* **174**, 327 (1967), *Soviet Phys. "Doklady"* (English Transl.) **12**, 467 (1967); T. H. Jensen and F. R. Scott, *Phys. Fluids* **11**, 1809 (1968).

[8] J. G. Linhart, *Plasma Physics*, p. 199, North-Holland, 1961; L. M. Goldman *et al.*, *Phys. Fluids* **7**, 1005 (1964); M. Widner, private communication.

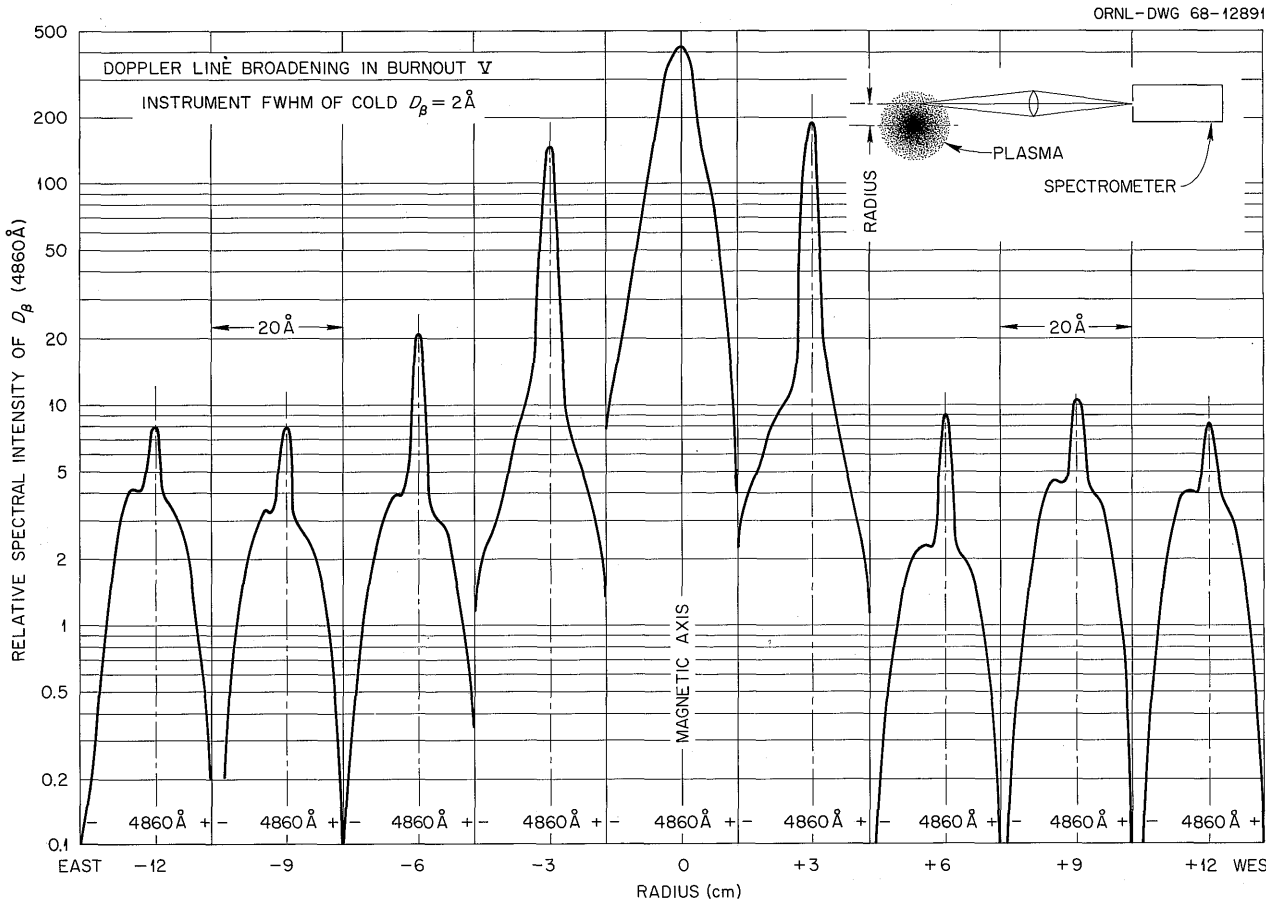

Fig. 6.5. Composite of Balmer β Lines for Different Sectors. The scan from left to right is from short to long wavelength at each sector. Only 20 Å are shown. Note that the asymmetry is the same on each side of the magnetic axis, excluding a disk-like rotation of the plasma.

figure shows deuterium Balmer β intensity observed along a narrow sector in the median plane whose average distance to the plasma axis is 9 cm. The wavelength resolution is approximately 2 Å, which accounts for some, but not all, of the width of the central spike, as the figure shows. We believe this spike is from cool (5 to 7 eV) atom emission, excited in the dissociation process as well as by inelastic electron collisions. The broad wings fit a Gaussian profile for a Maxwellian distribution of deuterium neutrals with a $T_i \approx 1$ keV. However, emission from the low-energy portion of this distribution is abnormally low if the line intensity is due only to Doppler broadening. The slight asymmetry in the distribution emphasizing the blue side of the line is common to all sectors on either side of the arc, as shown in Fig. 6.5. This fact excludes an azimuthal rotation of ions contributing to the broadening. These striking effects, observed here for the first time, are examined in further detail in the following paragraphs.

Since we observe the plasma through a longer vacuum space on the near side than exists on the far side, delayed cascading into the $n = 4$ level (for 4861-Å Balmer β line) may be responsible for the asymmetry. The shifted peak, ~3 Å, corresponds to a deuteron velocity of about 2×10^7 cm/sec. Since there is a 20-cm vacuum space on the far side and a 70-cm space on the near side, the particle transit times are

$$\tau = \frac{20}{2 \times 10^7} = 10^{-6} \text{ sec} .$$

Therefore, for τ's greater than about 10^{-6} sec, more radiation will be contributed from the forward direction than backward (up to 3.5 times). Levels

Table 6.2. Cascade Times

Approximate Relative Intensities	Low Level	Upper Level	τ	Upper Level	τ	Upper Level	τ
6	4s	– 5p	$\underline{1.3} \times 10^{-6}$ sec	6p	$\underline{2.2} \times 10^{-6}$ sec	7p	$\underline{3.6} \times 10^{-6}$ sec
6	4p	– 5s	$\underline{2.3}$	6s	$\underline{4.3}$	7s	$\underline{5.6}$
60	4p	– 5d	0.7	6d	$\underline{1.2}$	7d	$\underline{1.8}$
60	4d	– 5p	$\underline{5.9}$	6p	$\underline{11}$	7p	$\underline{14}$
200	4d	– 5f	0.4	6f	0.8	7f	$\underline{1.4}$
600	4f	– 5d	$\underline{20}$	6d	$\underline{50}$	7d	$\underline{100}$
500	4f	– 5g	0.02	6g	0.7	7g	$\underline{1.6}$

which cascade into the $n = 4$ levels are to be considered for $\lambda = 4861$ Å, in Table 6.2.[9] Those τ's which are underlined will give rise to a forward peaking of the Doppler-broadened λ 4861 Å line at about 3 Å or less. At 6 Å, τ should be $<0.5 \times 10^{-6}$ sec. The strong magnetic field of Burnout V will reduce these τ values slightly. These cascade effects would be superimposed on the radiation resulting from direct capture into the $n = 4$ level.

Experimentally, the asymmetry was eliminated by placing a glass plate in the optical path on the near side, making the distance the same as on the far side. Also, the asymmetry could be reversed by interchanging the dimensions of the near and far sides.

If the neutral density distribution obtained is due to a similar ion density distribution before charge exchange (in fact one must correct for charge-transfer cross sections), then the fit of the wings of the neutral emission lines to a Doppler-broadened Maxwellian velocity distribution has a mean thermal energy of 1 keV. This ad hoc fit is true of the on-axis data as well as the off-axis data. The wing fit indicates that the distribution is Maxwellian from the mean energy of 1 keV to at least four times this energy. This also means that thermonuclear reaction rates computed for $T_i = 1$ keV can be observed and used for diagnostics.

[9] C. W. Allen, *Astrophysical Quantities*, p. 63, University of London, Athlone Press, 1955.

6.1.7 Magnetic Field Strength Effects and Heating Efficiency

R. V. Neidigh

Since hot plasma also implies magnetic bottles for containment, it is pertinent to see how ion temperature, density, and containment times have changed as we have gone to higher field strengths in the Burnout devices. The magnetic geometry of the mirror machine with mirror ratio of 2 has always been used. Containment time has not been specifically measured for each change in field strength but has been deduced from energy and plasma storage and feed-rate calculations, and has increased from a few transit times in Burnout IV to about 700 transit times in Burnout V, while hot-ion velocity has increased only a factor of 4. The range of the increase in stored energy as magnetic field strength has been raised, as is shown in Fig. 6.6. Indeed, we have not yet found an upper limit closing this portion of the graph. On the other hand we also have not yet determined the scaling laws.

Assuming that the heating process is similar to other turbulent heating experiments in which 10% energy transfer occurs, we anticipated approximately the same efficiency in Burnout V. This value, in our steady-state device, can be determined from a calculation using the total stored energy ($nkTV \approx 1.6$ J), the energy input rate from the beam (volts $\times$ amperes $\approx 70 \times 10^3$ J/sec), the total stored particles ($nV \approx 3 \times 10^{16}$ ions), and the

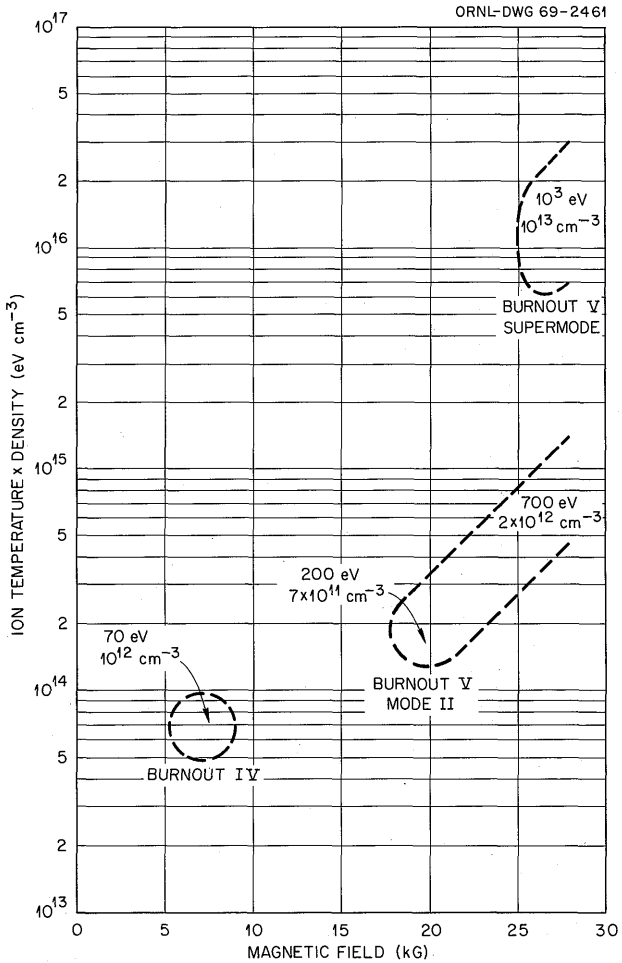

Fig. 6.6. Effect of Magnetic Field Strength on Ion Temperature and Density. Burnout II and III were short-duration experiments to convert the techniques which produced the highly ionized plasma in Burnout I to mirror machines and are not shown. Burnout IV and V are also mirror devices with midplane magnetic field strengths as indicated. It is not completely clear that magnetic field strength is alone responsible for the increase in stored energy since plasma volume was increased by tenfold as well.

particle feed rate (2×10^{19} atoms/sec). Rearranging to get efficiency:

$$\frac{\text{total stored energy}}{\text{energy input rate}} \times \frac{\text{particle feed rate}}{\text{total stored particles}}$$

$$= \frac{(1.6)(2 \times 10^{19})}{(70 \times 10^{3})(1 \times 10^{16})} \approx 5\% \ .$$

We think this is a minimum value for efficiency, since we have used conservative experimental data.

6.1.8 High-Frequency Correlation Studies and RF Effects

I. Alexeff

In previous experiments with our hot-electron plasma we have successfully used a sampling oscilloscope to obtain auto- and cross-correlations.[10] Similar sampling oscilloscope techniques have been applied to the hot-ion plasma in the Burnout device. Two special impedance-matched high-frequency probes were installed in the Burnout V machine so that both auto- and cross-correlation functions could be obtained. The probes could be moved independently – radially, azimuthally, and axially – so that correlations could be obtained in these three directions. Correlation studies were made using both a Tektronix sampling oscilloscope and a Hewlett-Packard spectrum analyzer which was capable of studying oscillations up to 2 kMHz. These high-frequency techniques give much information on the stochastic heating process present in Burnout V. The results can be included under the following categories:

1. *General characteristics of the oscillations* (i.e., frequency range, width of spectral peak, and amplitude of oscillations).
2. *Axial, radial, and azimuthal correlations.* The results tend to show that there is little azimuthal correlation, which is optimum for stochastic heating of ions in the azimuthal direction.
3. *Radial studies as they reflect on radial diffusion.* We find that, as in the hot-electron case, the radio-frequency turbulence is restricted to regions near the plasma core – presumably by the plasma self-shielding. The surface of the plasma seems not to be lost by turbulent diffusion to the wall.

6.1.8.1. General Character of the Plasma Oscillations. – First, we discover that, as in the hot-electron case, intense microwave oscillations are present and are observable only if the probes are inserted into the plasma. The oscillations are not detected at the surface of the plasma. Thus there is evidence that the plasma shields the oscillations and confines them in the core of the plasma.

[10] I. Alexeff *et al.*, *Phys. Rev. Letters* 21, 344 (1968); see also sect. 6.2.4, this report.

PHOTO 94465

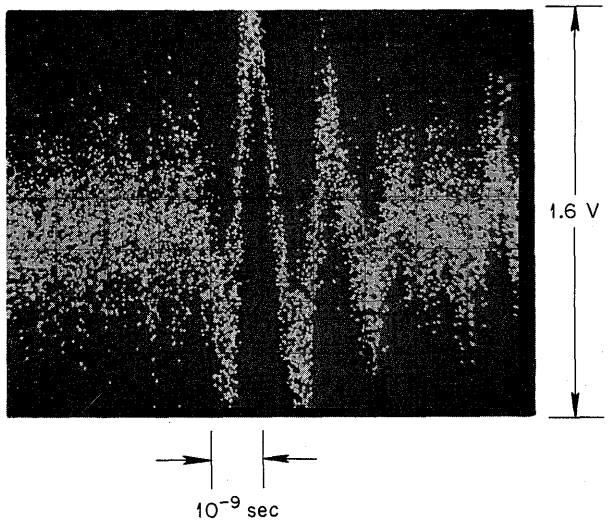

Fig. 6.7. Approximate Autocorrelation Function as Produced by a Single Sampling Oscilloscope.

PHOTO 94466

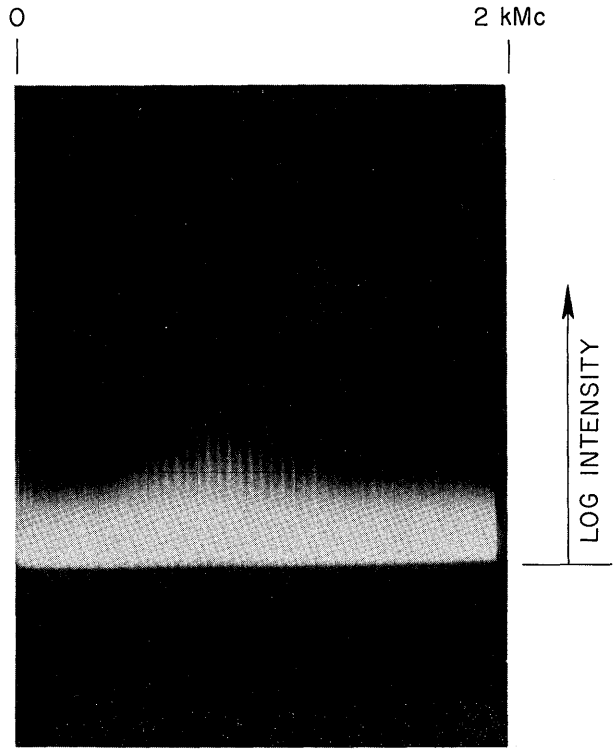

Fig. 6.8. Frequency Spectrum as Seen by a Hewlett-Packard Spectrum Analyzer. Note fine structure – not understood as yet.

Techniques using probes that do not penetrate the plasma, in general, cannot reveal the character of the oscillations. The amplitude of oscillations increased a factor of 4 between the radius of $7\frac{1}{2}$ cm from the magnetic axis and the radius of 5 cm from the magnetic axis when the probes were located on the midplane of the machine. When the probes were brought closer to the magnetic axis than 5 cm they were destroyed. The sampling oscilloscope showed high-amplitude oscillations with a peak-to-peak voltage of over 2 V, a frequency of $\sim$1 kMHz, and coherence time of several cycles. This is shown in Fig. 6.7. We note that voltage oscillations on the order of 1 V, when reflected back through the impedance transformations in the cable, correspond to electric fields at the probe tip on the order of kilovolts per centimeter, an extremely intense rf field. In addition, this high electric field is located 5 cm from the magnetic axis, and extrapolation suggests that the fields on the axis are a factor of 16 higher still. The intense radiofrequency spectrum shows a broad distribution, when studied with the spectrum analyzer, that is peaked at about 800 MHz. The frequency spread is approximately 30%. The Hewlett-Packard analyzer yields data which suggest that the peak is composed of distinct lines, as shown in Fig. 6.8, spaced approximately 50 MHz apart, but the fine structure may be instrumental.

If we attempt to identify the observed 1-kMHz frequency with some frequency characteristic of the plasma, we find that the frequency is about 40 times too high to correspond to the ion cyclotron frequency. The frequency is far too low to correspond to the electron cyclotron frequency or to the electron plasma frequency. However, it agrees very well with the ion plasma frequency. Its period is about one-fourth the transit time of the electron beam across the apparatus and is commensurate with standing waves due to electromagnetic modes, $v \approx c$, between the two mirror coils. Thus we can tentatively say that we have coupling from the electron beam to the ion plasma frequency, which may result in the intense ion heating we observe. We do notice that maximum rf activity is coincident with energetic atoms emitted from the plasma.

In the hot-electron case we have the electron beam apparently coupling to the electron plasma oscillations, and presumably this is why we produce hot electrons. In burnout V the plasma density is too high for the electron plasma frequency

to couple to the transit time of the electron beam. Presumably the electron beam is now coupling to ion plasma oscillations and is heating the ions, as observed. This explanation perhaps shows why hot electrons and hot ions cannot be observed at the same time in the same machine. Since the plasma electron and the plasma ion frequencies are different, the coupling of a given frequency to the electron beam occurs at different densities.

6.1.8.2. Correlation Measurements. – In these measurements the probes were not brought closer to the magnetic axis than 10 cm because the plasma was operating in a very energetic mode and movement of the probes closer than 10 cm to the magnetic axis resulted in probe destruction. In any case, the probes did not last longer than 30 min due to intense sputtering.

A turbulent spectrum is observed in the device when, and only when, the plasma is also emitting energetic neutral particles, produced via charge exchange, into the neutral-particle detector. The behavior of the correlation functions is as follows: First, we find that the amplitude of the signal damps very rapidly as one moves the probe radially outward. This demonstrates that the rf activity is restricted to the plasma core. In this case we find both the autocorrelation and the cross-correlation functions dropping as the probes are moved outward. The cross-correlation signal shows no phase shift within experimental limits as the outer probe is moved to larger radii. Within the limits of measurement this says that if there is a radial velocity then it must be greater than 6×10^9 cm/sec.

We find that for axial correlation measurements, both the autocorrelation measurement and the cross-correlation measurement do not change appreciably as the probe separation is varied from 0 to ~ 2 cm. There is a very slight phase shift present which could correspond to an axial velocity of $\approx 6 \times 10^9$ cm/sec, but this velocity is barely detectable and should be regarded as a lower limit. The electric field along magnetic field lines fluctuates strongly in phase, and there is no tendency for particles to be accelerated along field lines into the mirrors. Thus there appears to be no tendency to heat particles in the axial direction.

We find that for the azimuthal correlations the autocorrelation function on a given probe is preserved as the probe is moved but that the cross-correlation function drops very rapidly. There is also no visible phase shift as the probes are separated, which says that if there is an azimuthal velocity, the velocity must be greater than 6×10^9 cm/sec. Thus the adjacent magnetic field lines show strong electric fluctuations which are random with respect to each other, and particles should be heated very rapidly in the azimuthal direction.

6.1.8.3. Radial Loss of Plasma by Turbulent Diffusion. – A most interesting conclusion which is derived from the radial correlation studies on the hot-electron and the hot-ion plasma is that the rf activity is confined to the plasma core, where the electron beam is traversing the plasma. Apparently the plasma shields its outer surface from the activity going on the core. The outer surface of the plasma is found *not* to have strong rf activity, and consequently the outer surface of the plasma should *not* be lost by turbulence-induced diffusion. This suggests that one of the criticisms of the turbulent heating process – that the turbulence may produce strong radial plasma losses – may not be valid for the turbulent heating produced in the hot-electron and the hot-ion plasma mirror machines at ORNL.

6.1.9 Plasma Losses Induced by Turbulent Heating

I. Alexeff

The losses due to turbulent heating in mirror machines at ORNL may not be serious. In the experiments on hot-electron heating we have demonstrated that the heating efficiency in this steady state must at least be several percent.[11] If the steady-state heating efficiency were 100%, the plasma losses during the heating phase perhaps could not be greater than about 30 times those losses occurring in the quiescent afterglow, which were due to simple classical scattering of hot-electron particles into the mirror loss cones. Otherwise, in the steady state, the rate of energy loss would exceed the rate of energy input.

A second set of observations showed that strong radio-frequency activity in the hot-electron plasma is confined to the plasma core. This is easily understood, because the oscillations present appear to be electrostatic plasma oscillations occurring primarily along magnetic field lines; thus the electric fields obey the classical screening law

[11] I. Alexeff, R. V. Neidigh, and W. F. Peed, *Phys. Rev.* 136, A689 (1964).

for radiation in plasmas when a magnetic field is absent. Since these oscillations have been demonstrated to be considerably below the electron plasma frequency, the electromagnetic fields do not propagate but are evanescent with a very short decay length of a centimeter. Since these oscillations are confined to the central core of the plasma, we suspect that the heating efficiency should be large. Also, because radio-frequency energy is not lost through the plasma surface, the plasma confinement should not be affected by the turbulent heating, since the outer surface of the plasma does not receive turbulent electric energy.

Similar effects were observed in the hot-ion plasma, although in this case we do not understand the details of the heating and the screening mechanism. We do make the following observations.

First, the electric fields along magnetic field lines are well correlated, so there is little tendency for plasma ions to be accelerated into the loss cone. Thus turbulence-induced plasma loss along field lines should not occur.

Second, the electric field is observed to be confined to the plasma core. Apparently the plasma shields the electric fields from the surface and confines them near the magnetic axis. Thus the plasma surface does not receive electric field energy and should not be lost radially by turbulent diffusion. Indeed, equating the known loss time for plasma due to charge-exchange process with the power input from the beam gives almost complete equality. There is no power being lost by other processes than charge exchange within the measured limit of accuracy of about 20%. So turbulent losses of ions either radially or axially cannot be greater than the charge-exchange losses. Turbulence losses must therefore correspond to a plasma lifetime longer than 20 μsec, which is the charge-exchange lifetime.

6.2 TURBULENT HEATING OF ELECTRONS

6.2.1 Introduction

R. V. Neidigh

Electrons have been heated by beam-plasma interaction in various magnetic field geometries, but with temperatures exceeding 100 keV and with densities greater than 10^{11} cm^{-3} in mirror machines that have midplane field strengths up to 2000 G and mirror ratios greater than 2.5.[3,12] In this report period we began investigating the oscillating electric fields within the plasma volume in order to seek the heating mechanism. To study these oscillations, we developed constant-impedance probes and used transmission lines coupled to traveling-wave oscilloscopes in order to measure electric field strengths and coherence times at frequencies up to 3×10^9 Hz.[10] A simple method related to correlation techniques, but using a single sampling oscilloscope, permitted estimation of the auto- and cross-correlation of the signals. The results are to be published[3] and are abstracted in Sect. 6.2.3. A complete correlator functional above 2×10^9 Hz was constructed, and its performance vindicated our use of the simpler techniques. A report describing this correlator is to be published.[13] The abstract appears as Sect. 6.2.4. We report here an experimental dispersion relation found by using the techniques described above and discuss the lack of definitive agreement with theory.

6.2.2 The Experimental Dispersion Relation

R. V. Neidigh

We begin by investigating the electric fields within the plasma volume.[10] Constant-impedance probes penetrate the visible plasma but do not greatly alter electron temperature in the unprobed portion, and therefore we think that they give reliable information. The time-resolved measurement of the electric field was displayed on a traveling-wave oscilloscope and is shown in Fig. 6.9. The sweep speed is indicated by the 10^{-9}-sec interval markers. These waves indicate electric field fluctuations at the time of observation. No two oscilloscope traces made at different times but with identical plasma parameters have ever been alike. Of the four selected, none is typical. Number 1 is notable because it shows an electric field oscillating at the electron gyrofrequency. This is very

[12] M. V. Babykin *et al.*, *Zh. Eksperim. i Teor. Fiz.* **52**, 643 (1967), *Soviet Phys. JETP* (English Transl.) **25**, 421 (1967).

[13] I. Alexeff *et al.*, *A Simple Gigacycle Correlator*, ORNL-TM-2379 (Sept. 26, 1968), to be published in *International Journal of Engineering Science*; R. V. Neidigh *et al.*, *Bull. Am. Phys. Soc.* **13**, 1499 (1968).

ORNL-DWG 68-7971A

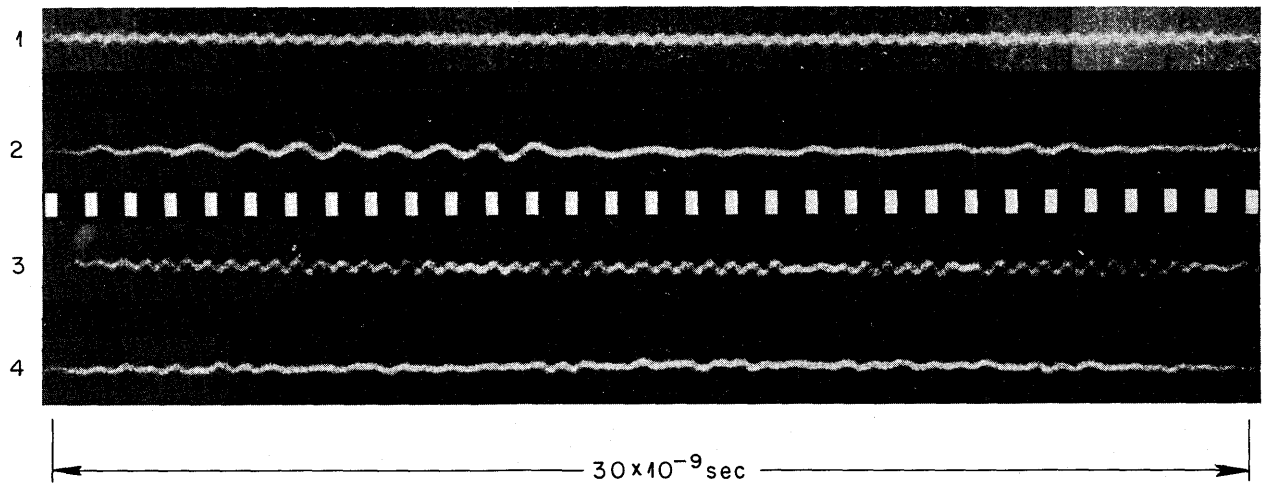

Fig. 6.9. Fluctuating Waveforms. Signals were recorded at random from the steady-state plasma. Vertical time markers are at nanosecond intervals.

rare. The wave train of No. 2 builds to maximum amplitude in a few cycles, lasts a few cycles, and then changes. Number 3 seems to change phase every few cycles. Number 4 shows some identifiable wave trains of only two or three cycles. These signals show that the plasma exhibits coherent oscillations that persist for several cycles, then suddenly change phase, frequency, and amplitude in a random fashion. The oscillations generally occur at frequencies near the electron plasma frequency, which, in most of the plasma region, is somewhat less than the electron gyrofrequency. The amplitudes of the potential oscillations, together with correlation lengths, are in accord with expectations based on the particle-trapping arguments suggested by Thomas Stix in a 1964 paper.[14] That is, background electrons can be trapped in a fluctuating wave on the beam and lead to a rapid damping of that wave. Electric field strengths greater than 1000 V/cm are observed over a correlation length long enough to approach the applied beam potential but short compared with the axial length of the beam.

Data obtained with a sampling oscilloscope and shown in Fig. 6.10 yield similar information and in addition the autocorrelation and cross-correlation of oscillations studied by one and by two probes. The three photographs are for different sets of plasma parameters and show the following: (1) Frequencies vary from 0.2×10^9 Hz to nearly 1×10^9 Hz. The traces marked 1 are of a fixed probe, and the traces marked 2 are of a probe movable along the Z axis. Note the phase shift. (2) The average phase velocity of the wave along the magnetic axis, as found from the average frequency and average wavelength, is 0.3 to 0.7 of the velocity of the incident electron beam. (3) The frequency of the oscillation is below but near the electron plasma frequency and 0.3 to 0.6 of the electron cyclotron frequency. (4) The oscillations are correlated for a time corresponding to one or two cycles, and their average wavelength corresponds to a few centimeters and does not appear to be a standing wave between parts of the apparatus.

We considered the scaling properties of the instabilities predicted in a linear theory using a plasma system made up of two oppositely directed monoenergetic electron beams passing through a cold background plasma in a uniform magnetic field. We solved the dispersion relation for (complex) frequency as a function of (real) correlation length and show in Fig. 6.11 the experimental dependence of frequency and correlation length for maximum growth rate on the plasma parameters: the square of the ratio of beam plasma frequency to gyrofrequency, and the relative densities of background and beam electrons. The outstanding features of the observed waves are phase speeds 0.3 to 0.7 of the beam speeds and frequencies similarly related to the electron gyrofrequency.

[14] T. H. Stix, *Phys. Fluids* 7, 1960 (1964).

PHOTO 75633

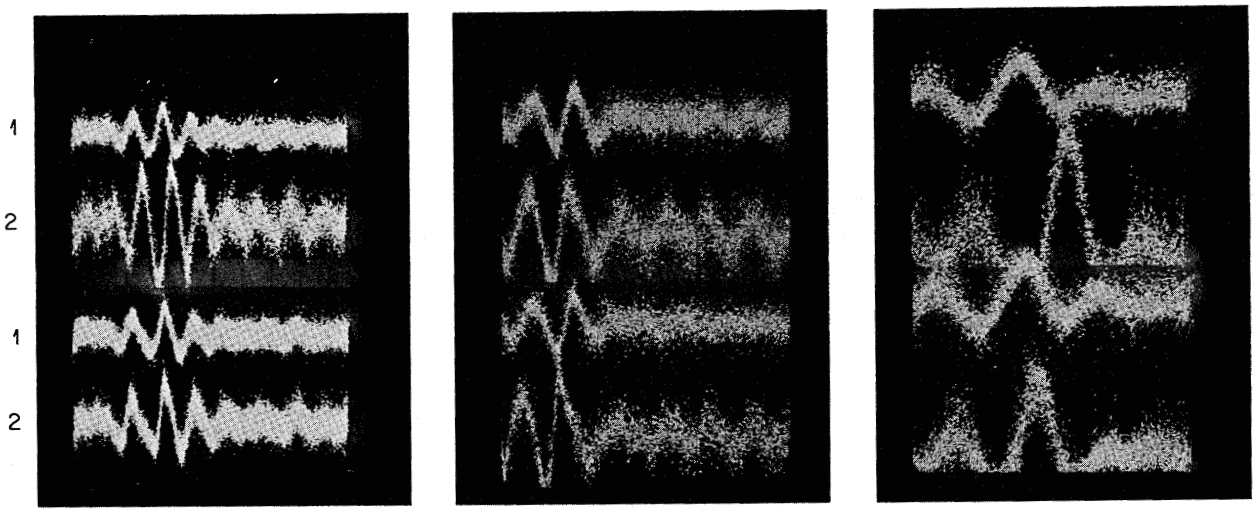

5×10^{-9} sec cm^{-1} 2×10^{-9} sec cm^{-1} 0.5×10^{-9} sec cm^{-1}

Fig. 6.10. "Correlated" Plasma Probe Signals. These signals were obtained by a sampling technique. Samples of V at t and $t + \Delta t$ over many thousands of cycles are stored. The result is a kind of correlation, that is,

$$\frac{1}{n} V_0(t) \sum_{i=1}^{n} V_i(t + \Delta t) ,$$

where $V_0(t)$ is the chosen peak voltage of an oscillating signal at which a trigger circuit was activated to record the data.

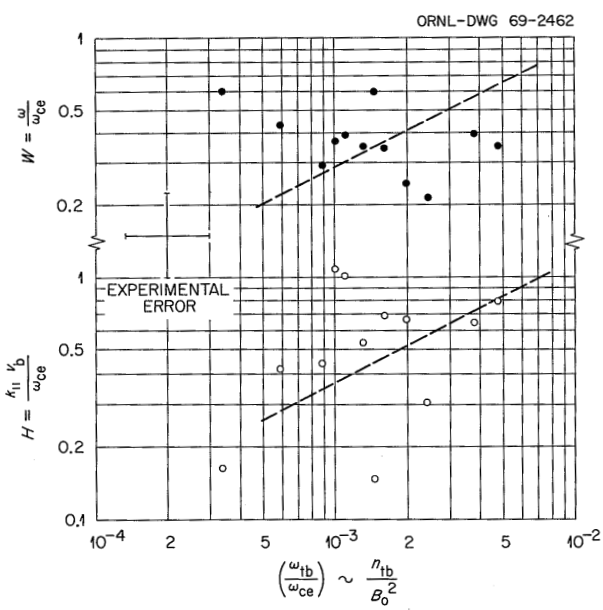

Fig. 6.11. Experimental Dispersion Relation. The two graphs relate the growing waves we observe to plasma frequency through their correlation periods. The data points have a possible error shown by the error circle. The error does not account for the lack of constancy in plasma-to-beam ratio for maximum growth rate. Absolute values for the abscissa are not presently known but are relatively accurate.

The relation to plasma frequency at present is not well known, for the lack of an absolute density measurement; therefore the abscissa is only relatively accurate. A plasma-to-beam density ratio for maximum growth rate will have the slope shown by the dotted lines, and the data should approximate this relation if the theory is pertinent. They do not seem to, even considering the experimental error shown by the error circle. It seems that relating this electron heating experiment to theory will be more difficult than expressed in Sect. 6.2.3.

6.2.3 Experimental Strong Turbulent Heating[3]

R. V. Neidigh
I. Alexeff
G. E. Guest
W. D. Jones
D. C. Montgomery[15]
D. J. Rose[16]
F. R. Scott[6]
W. L. Stirling

Experiments at ORNL are exploring the strong turbulent interaction between a steady-state magnetically collimated electron beam and its self-generated plasma.

The technology to maximize ion heating is being developed in Burnout V, a simple mirror device with magnetic fields of 50-25-50 kG, with an axial electron beam (6 A at 10 kV) which gives a beam power density in the plasma exceeding 1 kW/cm^3. Necessary, but not sufficient, evidence for a true thermonuclear temperature is the observed 10^3 sec^{-1} cm^{-3} plasma source of 3-MeV protons identifying D-D reactions. Spectral measurements of recombination radiation reveal a line width corresponding to an ion energy of 0.5 keV and an energy distribution that can be followed up to 2 keV. Analysis of charge-exchanged neutral atoms reveals the energy spectrum in more detail with a maximum between 100 and 500 eV and as much as 10% near 1 keV. A flux of 3×10^{14} cm^{-2} sec^{-1} of 100-eV deuterons escapes the midplane perimeter. Calorimetric probes measure a plasma heating effect equivalent to 0.5-keV ion bombardment at 2.5×10^{12} cm^{-3}. The rate of decrease of spectral radiation toward the plasma center establishes an electron density of at least 2.5×10^{12} cm^{-3}. The confinement time, 2×10^{-4} sec estimated from density and energy balance, agrees well with the measured spectral-light decay time and is equivalent to hundreds of ion transits through the plasma. A direct diamagnetic decay measurement gives a shorter τ of 20 to 50 μsec, but confirms our values for ion density and temperature. Ion heating has been observed to increase strongly with increasing magnetic field strength, suggesting a direction for future development.

In previous experiments, electrons were heated to temperatures exceeding 100 keV with densities greater than 10^{11} cm^{-3}. To study these oscillations, special impedance-matched probes now have been used to measure plasma electron oscillation frequencies up to 4 kMc, coherence times, and electric field values with the aid of traveling-wave-tube oscilloscopes. Simple methods related to correlation techniques have been used to estimate the auto- and cross-correlations on the signals observed on two electrostatic probes, with the aid of sampling oscilloscopes used as high-speed gates. These techniques allow us to observe "average" frequencies up to 2 kMc and "average" wavelengths which are observed to be a few centimeters. These data have been compared with a simple linear theory, and good agreement has been obtained. All these new techniques aid us in determining the dispersion relation and other important quantities for the plasma electron oscillations, and help us in determining the direction for future progress.

6.2.4 A Simple Gigacycle Correlator[14]

I. Alexeff
R. V. Neidigh
W. R. Wing[17]

A gigacycle (beyond 2000 Mc) correlator has been developed with commercially available components. The basic components comprise two sampling oscilloscopes, a pulse generator, an analog multiplier, a waveform averager, and a display oscilloscope. The oscilloscope output permits "real time" display of the correlation functions as they are computed over 100 sampling points. The device can correlate over a time interval that is adjustable from 2 nsec to 100 μsec. The instrument offers an improvement in frequency response of three orders of magnitude over any of the automatic correlators presently in the literature. Its

[15]Consultant, University of Iowa, Iowa City.

[16]Consultant, MIT, Cambridge, Mass.

[17]Student guest, University of Iowa, Iowa City, summer 1968.

maximum sensitivity without preamplification is about 2 mV. Its particular advantage is that it needs no alterations of its commercially available components, leaving them free for individual conventional use. Use of a single sampling oscilloscope for correlation studies is also discussed.

6.3 REDUCING MOLECULAR HYDROGEN IN PLASMA DEVICES

I. Alexeff

Molecular hydrogen in many experiments (target plasmas) is not desired because under electron bombardment it dissociates to eject ~5-eV neutral atoms – Franck-Condon neutrals – that penetrate deeply into the plasma and cause losses by charge exchange. We suggest that one may reduce molecular hydrogen from plasma devices by lining them with a suitable material which would prevent hydrogen, once dissociated, from recombining. Such techniques are well known from ion source development work, and techniques are presently being used to eliminate molecular hydrogen in discharges.[18]

In general, atomic hydrogen once formed will not recombine unless in the presence of a catalyst. A Pyrex glass vessel will not catalyze the reaction, especially if the glass has been etched with hydrofluoric acid; for example, a Wood's tube is used for producing atomic hydrogen for studying chemical reactions in intersecting atomic beams. A Wood's tube is a long glass discharge tube with a hole at the midpoint so the gas-emitting region is well removed from the metal electrodes where recombination takes place; large percentages of atomic hydrogen – on the order of 90% or better – exist, and these hydrogen atoms have the temperature of the walls of the vessel. Thus the atomic hydrogen, formed with an energy of ~5 eV, does not retain its kinetic energy but is cooled to the temperature of the glass wall.

The electrodes which are used in discharge tubes and ion sources can also be chosen to reduce recombination. Aluminum works well, presumably because of the oxide layer, yet iron is very bad. Thus by coating the internal cavity structure of a microwave-heated plasma or a turbulently heated plasma with a noncatalyzing coating we might greatly reduce the amount of molecular hydrogen in the device and the resulting charge-exchange cooling of the hot plasma by fast Franck-Condon neutrals emitted from the dissociated molecular hydrogen.

In microwave discharges, in some cases, ceramic coatings could be rapidly destroyed by the plasma and the microwave fields. Geller[19] presently uses ceramic linings for his cavities; he finds that with metal walls, undesirable instabilities develop. He uses long pulses of microwave power of up to 25 kW. The best cavity material for lining is zirconia (zirconium oxide), which is flame-sprayed on the cavity wall. Apparently fused quartz also works well, but the dielectric constant of Pyrex renders it rather unsatisfactory for microwave work. In using these linings, one must make sure that the plasma is present *before* the microwave power is turned on; then the plasma absorbs the microwave power, and large standing electric fields are not present.

Thus ceramic or glass linings for plasma apparatus seem feasible, and we will begin experiments using these techniques in the turbulent heating devices.

There is, of course, a second (and difficult) technique for removing molecular hydrogen from the system; this is to run the walls of the apparatus at a temperature of ~2500°C, in which case the molecular hydrogen will be dissociated according to the Saha equation. This hot-wall technique is practical for feeding the hydrogen in through a hot, incandescent tube to result in atomic hydrogen. In small plasma units it is perhaps possible though not appealing to make all the walls incandescent.

[18] Private communication, C. F. Barnett and Sheldon Datz.

[19] R. Geller, CEN, Saclay, France, private communication.

7. Plasma Physics

7.1 ION ACOUSTIC WAVES

7.1.1 Introduction

We have continued to do basic experiments on ion acoustic waves in simple discharge-tube plasmas; however, we have extended these basic studies to these waves in magnetically supported plasmas, and are commencing to study nonlinear ion acoustic waves. Relevant theoretical studies have also been carried out.

In the linear regime in B-field-free plasmas we have made (velocity) dispersion measurements (Sect. 7.1.4) which agree with the prediction of both macroscopic theory and our new Vlasov theory for finite-length sine-wave trains; recent calculations using macroscopic theory suggest, however, that measuring relative electron and ion density perturbations might be a more sensitive way to observe dispersion than making velocity variation measurements (Sect. 7.1.5). We have also checked experimentally the relationship between wave potential and density fluctuation,

$$\frac{eV_{\text{wave}}}{kT_e} = \gamma_e \frac{\Delta n}{n},$$

predicted by our calculations using macroscopic theory, and find that $\gamma_e = 1$ (Sect. 7.1.3).

In the linear regime in magnetically supported plasmas we have studied contaminant-ion Landau damping; we find, for example, that for propagation perpendicular to the magnetic field the Landau damping is immeasurably small for frequencies below the contaminant ion cyclotron frequency but is present for higher frequencies (Sect. 7.1.2). Both effects are in good agreement with our theoretical calculations (Sect. 7.1.2).

In the nonlinear regime in B-field-free plasmas we have, by wave focusing, produced density perturbations on the order of 25%, a value which seems already to be producing nonlinear effects (Sect. 7.1.6). We have made calculations of $\lambda_{\text{wave}}/\lambda_{\text{Debye}}$ for $\omega > \omega_{pi}$ and find that, under some conditions, ion waves may be able to propagate above the ion plasma frequency and still have $\lambda_{\text{wave}}/\lambda_{\text{Debye}} \gtrsim 1$ (Sect. 7.1.7); calculations based on a linearized Vlasov theory, however, suggest that the waves would be too small to be physically observable (Sect. 7.1.8).

7.1.2 Landau Damping of Electrostatic Ion Waves in a Uniform Magnetic Field

A. Hirose[1] W. D. Jones
I. Alexeff N. A. Krall[2]
D. Montgomery[3]

We have studied Landau damping of electrostatic ion waves due to contaminant helium ions in a xenon plasma as a function of frequency and propagation angle in a uniform magnetic field. To summarize the results for

$$\omega_{ci}^{\text{Xe}} \ll \omega \lesssim \omega_{ci}^{\text{He}},$$

damping for perpendicular propagation is immeasurably small. The damping is recovered for $\omega > \omega_{ci}^{\text{He}}$.

Electrostatic ion waves in a uniform magnetic field have been theoretically studied by several

[1]Consultant, University of Tennessee, Knoxville.
[2]University of Maryland, College Park.
[3]Consultant, University of Iowa, Iowa City.

authors in the so-called "electrostatic approximation," in which the two normal modes with $\mathbf{E} \perp \mathbf{B}$ decoupled into a purely transverse one.[4-7] In the present experiment, the contaminant Landau damping method[8] is investigated in a uniform magnetic field. A xenon plasma is contaminated with a small amount of helium ions, the thermal velocity of which is in the same order as the velocity of ion acoustic waves supported by xenon ions. For a wave frequency ω satisfying

$$\omega_{ci}^{\mathrm{Xe}} \ll \omega \ll \omega_{ci}^{\mathrm{He}} ,$$

where ω_{ci} is the cyclotron frequency, the ion wave propagates with the ion acoustic velocity[8]

$$(kT_e)^{1/2} M_{\mathrm{Xe}}^{-1/2} .$$

The damping rate due to helium is

$$\frac{k_i}{k_r} = \epsilon \sqrt{\frac{\pi}{8}} \left(\frac{T_e}{T_i}\right)^{3/2} \sqrt{\frac{M_{\mathrm{He}}}{M_{\mathrm{Xe}}}} \times \frac{1}{\cos\theta} e^{-M_{\mathrm{He}} T_e / 2M_{\mathrm{Xe}} T_i \cos^2\theta} , \qquad (1)$$

where k_i and k_r are the imaginary and real parts, respectively, of the wave number; ϵ is the number density ratio of helium to xenon ions; T_e and T_i, electron and ion temperatures; M_{Xe}, the mass of a xenon ion, and M_{He}, the mass of a helium ion; and θ is the angle at which the wave propagates to the magnetic field. In Eq. (1) we have assumed that $T_e \gg T_i$ and that $\lambda_{\mathrm{wave}} \gg \lambda_{\mathrm{Debye}}$. This equation resembles that of Stepanov[4] for electron Landau damping of electrostatic ion waves in a magnetic field. If $\omega_{ci}^{\mathrm{He}} \ll \omega$, one can compute that the usual Landau damping is recovered.[9]

The plasma is produced by electrons streaming through a gridded probe. In the plasma column, no appreciable electron drift is present, which gives us a fairly quiescent plasma. The column is 60 cm long, and its maximum diameter is about 6 cm. The wavelength is always much smaller than the column diameter. The electron temperature is about 1 eV, and the ion temperature is about 0.05 eV. The density is on the order of $10^9/\mathrm{cm}^3$. Two long thin wire probes are used as an exciter and a receiver. They are so movable that propagation at any angle to the magnetic field can be investigated.

Damping measurements are made using sine-wave bursts in plasma both without and with helium.[8] To obtain the net damping due to helium ions, we subtract the damping without helium from the damping with helium. This last step eliminates ambiguities caused by electron Landau damping and geometrical effects on the wave amplitude. The results are as follows:

1. For propagation parallel to the magnetic field, the measured damping agrees with that obtained with no magnetic field.[8]

2. As Fig. 7.1 (top) shows, for wave frequencies such that $\omega_{ci}^{\mathrm{Xe}} \ll \omega \ll \omega_{ci}^{\mathrm{He}}$, the experimental angular dependence of the damping is in excellent agreement with what is predicted by Eq. (1). One striking result is that the Landau damping disappears[10] as θ approaches 90°.

3. The Landau damping, which vanishes near 90° for $\omega < \omega_{ci}^{\mathrm{He}}$, appears again as the magnetic field is decreased so that $\omega > \omega_{ci}^{\mathrm{He}}$. In Fig. 7.1 (bottom) the perpendicular damping normalized by parallel damping is shown as a function of $\omega/\omega_{ci}^{\mathrm{He}}$. For complete recovery of Landau damping, we find experimentally that a wave frequency which is about four times the helium cyclotron frequency is required.

Interesting effects are predicted theoretically at $\theta = 90°$ (ion analogs of the "Bernstein modes") but are confined to a very narrow range of angles. Because of finite angular spreads in the k vectors

[4] K. N. Stepanov, *Zh. Eksperim. i Teor. Fiz.* **35**, 1155 (1958) [*Sov. Phys. JETP* **8**, 808 (1959)].

[5] W. E. Drummond and M. N. Rosenbluth, *Phys. Fluids* **5**, 1507 (1962).

[6] D. G. Lominadze and K. N. Stepanov, *Zh. Tekhn. Fiz.* **34**, 1823 (1964) [*Sov. Phys. – Tech. Phys.* **9**, 1408 (1965)].

[7] R. W. Fredricks, *Plasma Phys.* **2**, 197, 365 (1968).

[8] I. Alexeff, W. D. Jones, and D. Montgomery, *Phys. Rev. Letters* **19**, 422 (1967). Several methods of measuring the ion temperature, all of which are consistent, were presented.

[9] G. V. Gordeyev, *Zh. Eksperim. i Teor. Fiz.* **23**, 660 (1952). In this reference, the recovery of Landau damping of electron plasma waves was shown. A similar treatment can be applied to ion acoustic waves.

[10] A. Hirose *et al.*, *Bull. Am. Phys. Soc.* **13**, 1569 (1968).

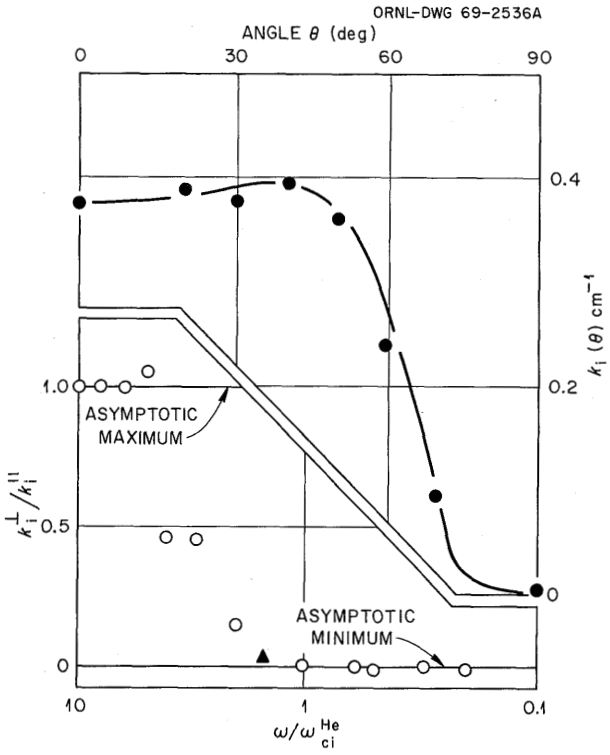

Fig. 7.1. (Top) Angular Dependence of Landau Damping. The solid line is predicted by Eq. (1), where all parameters are known. ϵ, the contaminant factor, is kept fairly constant at $\sim$0.01. The wave frequency $f = 50$ kHz. The magnetic field $B = 400$ G, which gives $f_{ci}^{Xe} = 4.6$ kHz and $f_{ci}^{He} = 152$ kHz, so that $f_{ci}^{Xe} \ll f < f_{ci}^{He}$. (Bottom) Recovery of Landau Damping. The perpendicular damping normalized by the parallel damping is plotted as a function of the frequency ratio ω/ω_{ci}^{He}. Note the complete recovery of the damping for $\omega/\omega_{ci}^{He} \gtrsim 4$.

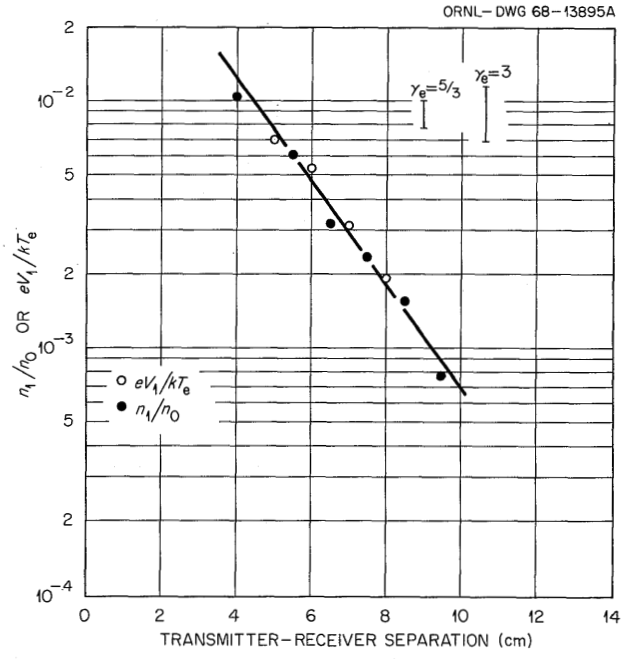

Fig. 7.2. Experimental Ion Acoustic Wave Potential and Plasma Density Perturbation as a Function of Distance. The clustering of both sets of points about the same visual line of best fit seems to indicate an experimental value of $\gamma_e \approx 1$. The lengths of the bars labeled $\gamma_e = {}^5/_3$, 3 show the average vertical separation of the two sets of data points which would be necessary for γ_e to have those values. Note that extrapolation to zero probe separation leads to a ratio of <0.1, indicating linear waves throughout the region of propagation.

of our wave packets, as well as for possible other reasons (high electron-neutral collision frequencies, finite spreads of driving frequencies represented by our sine-wave bursts, etc.), we have not seen these phenomena.

7.1.3 Simultaneous Measurements of Ion Acoustic Wave Potential and Plasma Density Perturbation to Yield γ_e[11]

H. Doucet[12] I. Alexeff W. D. Jones

We have measured and correlated the absolute magnitudes of the potential of an ion acoustic wave and of the accompanying plasma density perturbation. The measurements show that the waves being studied are linear throughout the region of study and that the coupling of the driving voltage to the plasma is very weak, $v_{driving}/v_{wave}$ being of the order of only a few tenths of a percent. The correlation of wave amplitude and density perturbation shows that γ_e, the compression coefficient of the electron fluid, is experimentally equal to 1, indicating isothermal compression of the electrons. Theoretically, using first-order macroscopic theory, it can easily be shown that the quantities measured are related by the following equation: $eV_1/kT_e = \gamma_e(n_1/n_0)$, where V_1 is the wave potential, e is the electron charge, k is Boltzmann's constant,

[11] H. Doucet, I. Alexeff, and W. D. Jones, *Phys. Fluids* 11, 2451 (1968).

[12] Ecole Polytechnique, Paris, France.

T_e is electron temperature, n_1 is the density perturbation due to the wave, and n_0 is the unperturbed density. Simultaneous measurements were made of V_1 and n_1/n_0. T_e was measured by an ordinary Langmuir probe. eV_1/kT_e was then compared with n_1/n_0. Figure 7.2 shows plots of eV_1/kT and n_1/n_0 as a function of the separation between transmitter and receiver electrodes. It is noted that both sets of points lie on the same curve, indicating by the above theoretical relationship that $\gamma_e \approx 1$.

7.1.4 Dispersion of Ion Acoustic Waves[13]

Glenn Joyce[14] I. Alexeff
Karl Lonngren[14] W. D. Jones

We have investigated, experimentally and theoretically, the dispersion of ion acoustic waves in quiescent rare-gas discharge plasmas. Experimentally, various grid systems were used to generate the waves, which were studied using a time-of-flight technique. The experimental results show that two separate propagating phenomena appear. The slower-propagating disturbance is the ion acoustic wave, obeying the theoretically predicted dispersion behavior. The faster-propagating disturbance, though superficially resembling a wave, is composed of bursts of ions accelerated by the driving potentials placed on the grids. Previous theoretical models of ion wave propagation have utilized either purely initial-value or steady-state, boundary-value calculations. We present here a model which more nearly simulates the experimental time-of-flight studies of finite packets of ion waves generated by finite sine-wave bursts.

Figure 7.3 shows dispersion data obtained for the two propagating phenomena in a xenon plasma. The upper set of points shows the observed dependence of the "pseudowave" signal on frequency, whereas the lower set of points shows the observed ion acoustic wave velocity dependence on wave frequency. The two lower curves are theoretical curves showing the predicted dispersion of ion acoustic waves for the conditions of the experiment. The uppermost curve is a visual line of best fit for the ion burst data.

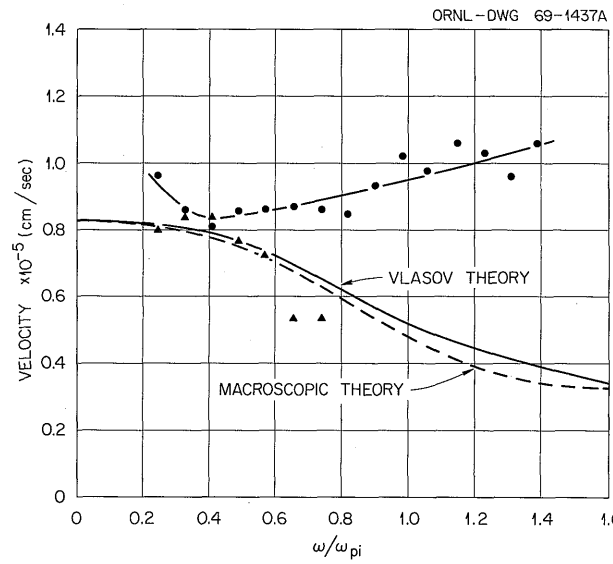

Fig. 7.3. A Comparison of Experimental and Theoretical Dispersion for Ion Acoustic Waves. The lower set of points are the ion wave velocity measured experimentally. The two lower curves show the theoretically expected dispersion for the conditions of the experiment. The Vlasov theory was fitted to the experimental point near $\omega/\omega_{pi} = 0.5$; the v_0 (ion velocity for $\omega \ll \omega_{pi}$) thus obtained was used in constructing the macroscopic theory curve. A temperature ratio of $T_e/T_i = 30$ was used for both curves. The upper set of points shows the observed dependence of the velocity of ion bursts on exciting frequency, the uppermost curve being a visual line of best fit to the data.

7.1.5 A More Sensitive Technique for Observing Ion Acoustic Wave Dispersion near ω_{pi}

H. Doucet[12] I. Alexeff W. D. Jones

In Sect. 7.1.4, an experiment was described in which the dispersion of ion acoustic waves in the vicinity of the ion plasma frequency was given by observing the experimental decrease in the wave phase velocity as the wave frequency approached the ion plasma frequency. A possible criticism of that experiment was that when the wave frequency was sufficiently near the ion plasma frequency for appreciable slowdown to occur, the wave signal was so severely Landau damped that the slowdown measurement was extremely difficult. In the present discussion a more sensitive technique is

[13]G. Joyce, K. Lonngren, I. Alexeff, and W. D. Jones, accepted for publication in *The Physics of Fluids*.

[14]Summer participant, University of Iowa.

suggested theoretically, and the results of an experimental effort to utilize the new technique are described.

In ref. 11 a theoretical derivation was made of the relationship between the potential of a propagating ion acoustic wave and the accompanying plasma density perturbation. In that derivation it was shown that the wave potential V_1 was given equally well by either of the following two (one electron, one ion) equations:

$$V_1 = \frac{m_e}{e}\frac{\Delta n_e}{n_0}(v_\phi^2 - \gamma_e v_e^2) , \tag{1}$$

$$V_1 = -\frac{m_i}{e}\frac{\Delta n_i}{n_0}(v_\phi^2 - \gamma_i v_i^2) . \tag{2}$$

When $v_\phi^2 \approx kT_e/m_i$, that is, when the ion acoustic wave is nondispersive, then $v_i^2 << v_\phi^2 << v_e^2$, where v_e and v_i are the electron and ion thermal speeds, and both Eqs. (1) and (2) reduce to

$$\frac{V_1}{kT_e} = \gamma_e \frac{\Delta n}{n_0} , \tag{3}$$

which is the relationship experimentally investigated in ref. 11. If now, however, we allow the wave to become dispersive, then we note an interesting effect. As the wave disperses, that is, as v_ϕ decreases, the earlier approximation that $v_\phi^2 << v_e^2$ becomes even better; however, the approximation that $v_\phi^2 >> v_i^2$ breaks down. Since the V_1 predicted by Eqs. (1) and (2) are the same, we can combine the two equations into one expression,

$$\frac{\Delta n_e}{\Delta n_i} \approx \frac{1}{v_s^2}(v_\phi^2 - v_i^2) , \tag{4}$$

where $v_s^2 \equiv (\gamma_e kT_e + \gamma_i kT_i)/m_i$. Thus we have a quantity which varies as the *square* of v_ϕ; if v_ϕ is reduced by 30%, for example, Eq. (4) predicts that $\Delta n_e/\Delta n_i$ would decrease by at least 50%. Therefore measuring the density perturbations produced by the wave might be a more sensitive indication of ion acoustic wave dispersion than making a direct velocity measurement. Figure 7.4 shows a quantitative comparison of the rate of variation of the two quantities in the dispersive region around the ion plasma frequency, for a representative value of $T_i/T_e = 1/30$.

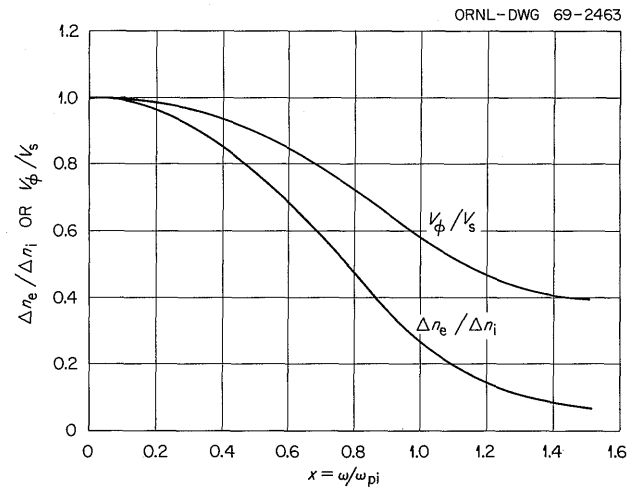

Fig. 7.4. A Theoretical Comparison of the Rate of Variation of Two Quantities Associated with Ion Acoustic Wave Propagation in the Dispersive Region Around the Ion Plasma Frequency. A measurement of the relative variations of electron and ion density perturbations seems to be a more sensitive indicator of dispersion than a measurement of phase velocity variation.

Preliminary experiments have been made to determine $\Delta n_e/\Delta n_i$ for ion acoustic waves near the ion plasma frequency. Although the initial data show a monotonic decrease of $\Delta n_e/\Delta n_i$ with increasing frequency in the vicinity of the calculated ion plasma frequency, in qualitative agreement with the predictions of Eq. (4), the quantitative agreement is from fair to bad. The measurements are complicated by a resonance in the ac ion current (i.e., in Δn_i) to the probe in the neighborhood of one-third to one-half of the ion plasma frequency. The effect of this as-yet-not-understood resonance on the $\Delta n_i/\Delta n_e$ values can be quite appreciable.

7.1.6 Wave Focusing to Produce Nonlinear Behavior

I. Alexeff H. Doucet[12] W. D. Jones

We have made experimental studies of ion acoustic waves in the nonlinear regime. As we have shown earlier,[15] however, our present technique of exciting ion acoustic waves by applying

[15]See sect. 7.1.3.

time-varying potentials to a negatively biased planar electrode in the plasma is very inefficient in terms of generating large-amplitude waves. A technique which we have recently investigated as a possible means of creating a large-amplitude wave is wave focusing. To do this we have used a *cylindrical* grid as the ion wave transmitter. In this way, ion waves generated at the inner surface will propagate inward and will be focused at the cylinder axis. To date, a thin cylindrical wire detector probe has indicated a maximum $\Delta n/n \approx 0.25$ at the axis. With the detector probe located off-axis, both the incoming and outgoing waves could be observed. That the above-noted 25% variation in density may already be sufficiently large to produce interesting nonlinear effects may be indicated by the fact that the wave shape of the wave before it reaches the axis is appreciably different from that of the disturbance which propagates away from the axis after implosion. This is shown in Fig. 7.5, where it can be seen that the incoming signal is both more sharply peaked and larger in amplitude than the outgoing signal. What is responsible for the observed change in wave shape has not yet been studied.

PHOTO 94467

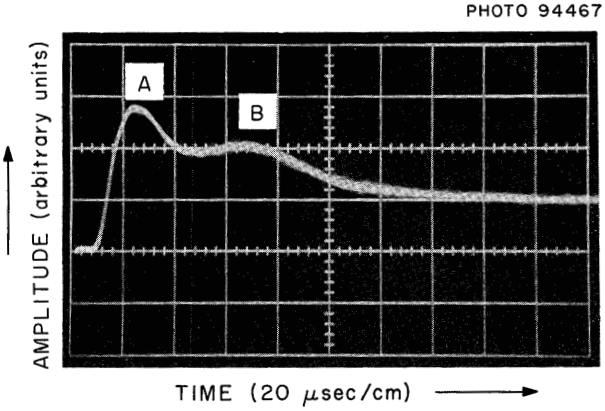

Fig. 7.5. The Wave Shape of Ion Acoustic Wave Signals both Before and After Focusing by a Cylindrical Gridded Transmitter. The waves were excited at the inner surface of the transmitter by a 50-V negative step function (applied at time equal to zero in the photo) and detected by a small probe located at an intermediate position between the cylinder's wall and its axis. Signal *A*, the incoming signal, is seen to be more sharply peaked and larger in amplitude than *B*, the signal propagating outward from the axis after focusing at the axis. Plasma generated from a xenon gas.

7.1.7 A Calculation of $\lambda_{\text{ion acoustic wave}}/\lambda_{\text{Debye}}$ as a Function of T_e/T_i for Propagation at Frequencies near ω_{pi}

H. Doucet[12] I. Alexeff W. D. Jones

For some time now we have been making the assumption that when ion acoustic waves are propagated at frequencies approaching the ion plasma frequency, their wavelength approaches the Debye length. For this reason it was further assumed that in the vicinity of the ion plasma frequency the collective interaction between electrons and ions which characterizes ion acoustic wave behavior would disappear and that ion acoustic waves, per se, would not be expected to propagate at frequencies above the ion plasma frequency. The purpose of the present calculations was to check these assumptions quantitatively. The results show that the basic assumption that $\lambda_{\text{wave}} \to \lambda_{\text{Debye}}$ as $\omega \to \omega_{pi}$ can be in serious error, depending upon the T_e/T_i ratio.

It is elementary to show that the following relationship between wavelength and Debye length is true:

$$\frac{\lambda}{\lambda_D} = \frac{v_\phi/(kT_i/m_i)^{1/2}}{(T_e/T_i)^{1/2}\, f/2\pi f_{pi}} , \tag{1}$$

where v_ϕ is the phase velocity of the wave. Previous work[16] has shown that for $\omega/\omega_{pi} \gtrsim 2$,

$$v_\phi \approx (2.38 + 0.19\, x)\,(kT_i/m_i)^{1/2} ,$$

where $x \equiv \omega/\omega_{pi}$. The same work indicates that for $\omega < \omega_{pi}$, $v_\phi \gtrsim$ the value at $x = 2$. Thus we can say that

$$\frac{\lambda}{\lambda_D} \geqq \left(\frac{T_i}{T_e}\right)^{1/2} \left(\frac{14.9}{x} + 1.19\right) , \tag{2}$$

where the > becomes applicable for $x < 2$, but for $x \gtrsim 2$ the equation becomes fairly exact with the = sign.

Using the loose criterion that λ/λ_D must be $\gtrsim 1$ in order for the wave disturbance to exhibit the collective behavior between ions and electrons

[16] G. M. Sessler and G. A. Pearson, *Phys. Rev.* **162**, 108 (1967).

Table 7.1. Combinations of Frequency and Temperature Ratios Giving $\lambda_{wave} \geq \lambda_{Debye}$

$x = \frac{\omega}{\omega_{pi}}$	T_e/T_i
0.9	∞
2	75
3	39
4	24
5	18
6	13
7	11
8	9
9	8
10	7

characteristic of ion acoustic wave propagation, we can write down the following restrictive relationship between wave and plasma parameters in order for ion acoustic waves to exist at high frequencies:

$$\frac{T_e}{T_i} \sim \left(\frac{14.9}{x} + 1.19\right)^2 . \tag{3}$$

Equation (3) was then used to construct all the pairs of values shown in Table 7.1 except the first. To calculate the "cutoff" frequency for $T_e/T_i = \infty$ (i.e., for $T_i = 0$), we use the "cold" ion plasma phase velocity,[17]

$$v_\phi = \left[\frac{kT_e}{m_i}\left(1 - \frac{\omega^2}{\omega_{pi}^2}\right)\right]^{1/2} , \tag{4}$$

which has a meaning only for $x(= \omega/\omega_{pi}) < 1$. Substituting Eq. (4) into Eq. (1) and setting both sides equal to 1 gives $x_{cutoff} \approx 0.9$.

The table shows that ion acoustic waves can, on the basis of the present considerations, be propagated at frequencies considerably above the ion plasma frequency for sufficiently small T_e/T_i ratios. For example, the table would predict that for the published conditions of Sessler and Pearson's experiments[16] ($T_e/T_i \sim 10$ to 15) it should be possible to propagate ion acoustic waves up to frequencies five to seven times the ion plasma frequency. They report the observation of "ion plasma waves" up to these kinds of frequencies. However, as we show below, using calculations based on the linearized Vlasov equation, the observations of Sessler and Pearson cannot be interpreted as ion acoustic waves, at least not on the basis of linear theory.

[17] L. Spitzer, Jr., *Physics of Fully Ionized Gases*, 2d ed., chap. 3, Interscience, New York, 1962.

7.1.8 Wave and Wavelike Phenomena Predicted by the Linearized Wave Theory near ω_{pi}

H. Doucet[12] I. Alexeff W. D. Jones

If the linearized Vlasov equation is used to calculate the electric field which penetrates into a plasma when an rf voltage is applied to a grid immersed in the plasma, the electric field is found to be representable as the sum of four terms, shown symbolically as follows:[18]

$$E = Q_D + Q_L + Q_e + Q_i . \tag{1}$$

Here Q_D and Q_L result from collective behavior of the plasma and are, respectively, the Debye-shielded exponentially attenuated electric field near the grid and the ion acoustic wave electric field due to the first Landau pole. Q_e and Q_i, however, as has been shown by Hirshfield,[19] Joyce,[20] Dong,[21] and others, represent electric fields due to grid-modified free-streaming motions of the electrons and ions respectively; these two terms appear, even when the collective interaction term in the Vlasov equation is omitted from the equation.

The purpose of the present work was to make a calculation of Q_L/E_0 and Q_i/E_0 for frequencies above the ion plasma frequency, where E_0 is the amplitude of the applied electric field at the grid. In particular we were interested in doing this for the published conditions of Sessler's experiments[16,22] (which are not greatly different, in many respects, from those of our own experiments). The purpose

[18] R. W. Gould, *Phys. Rev.* **136**, A991 (1964); N. Q. Dong, *Bull. Am. Phys. Soc.* **13**, 1569 (1968).

[19] J. L. Hirshfield, *Phys. Fluids* **11**, 411 (1968).

[20] Glenn Joyce, unpublished material.

[21] N. Q. Dong, *Bull. Am. Phys. Soc.* **13**, 1569 (1968); also, unpublished material.

[22] G. M. Sessler, *J. Acoust. Soc. Am.* **42**, 360 (1967).

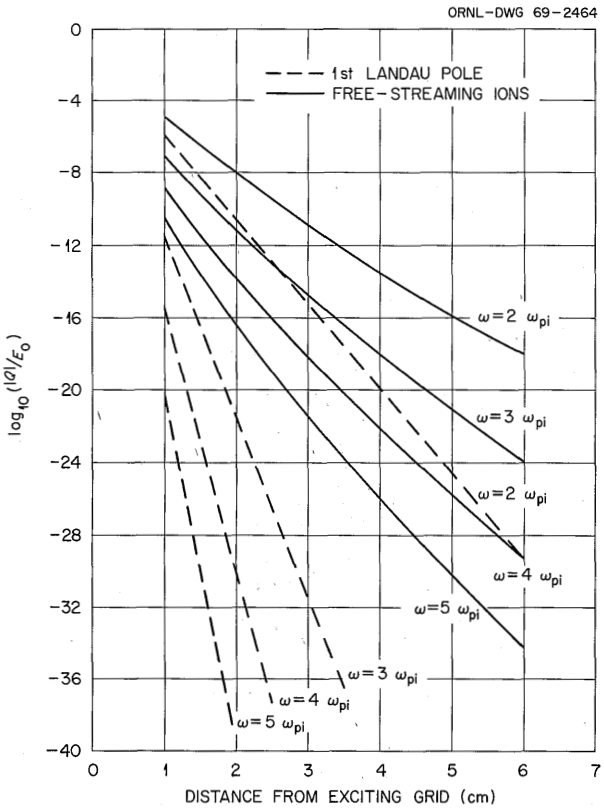

Fig. 7.6. Theoretical Contributions to the Electric Field in a Plasma from the First-Landau-Pole and Free-Streaming-Ions Solutions of the Linearized Vlasov Equation for an RF-Excited Grid in a Plasma. The results show two things: (1) except perhaps at the lowest frequencies and near the grid, the signals would be too small to be detected; (2) the free-streaming-ions contribution is generally orders of magnitude larger than the ion acoustic wave (first Landau pole) contribution.

of the calculations was twofold: (1) to see if, on the basis of linear theory, Q_L and Q_i would be expected to be large enough to be physically measurable, using conventional measuring techniques, and (2) to see which of the two effects would be expected to dominate at these higher frequencies.

Without going into the details of the calculations, the results of the calculations are shown in Fig. 7.6. Here we have plotted $\log_{10}(|Q|/E_0)$ vs distance from the exciting grid. The solid curves show the contribution of the ion streaming term for four different frequencies, while the dashed curves show the corresponding contributions to the electric field due to the first Landau pole (i.e., ion acoustic waves). From these curves, which were calculated for the published conditions of Sessler's experiments and assuming a Maxwellian ion energy distribution, we can make the following statements concerning Sessler's observations: (1) Except, perhaps, at the lowest frequency and shortest distances, neither the ion-acoustic-wave nor the free-streaming-ions contribution would be large enough to be physically observable (Sessler's excitation signals were less than 10 V); Q_j, for example, in the middle range of Sessler's measurements, even for the optimum calculation shown in Fig. 7.6, is on the order of 10^{-13} V. (2) In general, the contribution due to the free-streaming ions is orders of magnitude larger than that expected from ion acoustic waves.

Thus it seems clear that, on the basis of a linear theory, and assuming a Maxwellian ion energy distribution, the "ion plasma waves" reported by Sessler can be interpreted neither as ion acoustic waves nor as free-streaming ions. The theory which Sessler and Pearson[22] have used to interpret their experimental results is a linear theory. In fact, a closer look at their theory reveals that it is identical with the calculations which we have done here for Q_i; that is, their theory does not consider any collective behavior in the bulk of the plasma.

In conclusion, it seems that an adequate theoretical treatment both for the experimental observations of Sessler and Pearson,[22] and for ourselves, for frequencies greater than the ion plasma frequency, still remains to be done. Apparently a nonlinear theory will be required.

7.2 ELECTROSTATIC ION CYCLOTRON WAVES

7.2.1 Introduction

The so-called electrostatic approximation[9] gives a modified dispersion relation of ion acoustic waves in a magnetized plasma. For a highly nonisothermal plasma ($T_e \gg T_i$), the dispersion relation is given by[6,23]

$$\omega^2 = \frac{1}{2}\left[\omega_s^2 + \omega_{ci}^2 \pm \sqrt{(\omega_s^2 + \omega_{ci}^2)^2 - 4\cos^2\theta\,\omega_s^2\,\omega_{ci}^2}\right], \tag{1}$$

[23]T. H. Stix, *The Theory of Plasma Waves*, p. 42, McGraw-Hill, New York, 1962.

where ω_{ci} is the ion gyrofrequency, ω_s is the ion acoustic frequency given by $\omega_s^2 = (T_e/M)k^2$, and θ is the propagation angle with respect to the magnetic field. At $\theta = 90°$, the upper mode becomes the electrostatic ion cyclotron wave which has been observed by several authors.[24-26] The lower mode gives a phase velocity $\sqrt{T_e/M}\cos\theta$, if $\omega \ll \omega_{ci}$. This is identical to one of the two branches of magnetoacoustic waves,[27] $(T_e/M)^{1/2} \ll V_A$, where V_A is the Alfvén speed. Between the two modes expressed by Eq. (1), there exists a frequency gap ($\omega_{ci}\cos\theta < \omega < \omega_{ci}$) where wave propagation is forbidden.

In the present experiment, we investigated the dispersion relations of the two modes of Eq. (1) over a fairly wide frequency range at several propagation angles.

7.2.2 Dispersion Relation of Electrostatic Ion Waves in a Magnetic Field

A. Hirose[1] I. Alexeff W. D. Jones

The dispersion relation of electrostatic ion waves, closely related to ion acoustic waves, is investigated as a function both of the propagation angle with respect to an external uniform magnetic field and of the wave frequency. Four angles are chosen: $\theta = 0$, 55, 70, and 90°. For frequencies above ω_{ci}, the so-called electrostatic ion cyclotron waves are observed; below ω_{ci}, the wave velocity becomes $\sqrt{T_e/M}\cos\theta$. The frequency gap, $\omega_{ci}\cos\theta < \omega < \omega_{ci}$, in which the propagation is forbidden is also observed.

7.2.2.1. Experiments and Results. – The experiment was performed in a xenon plasma column supported by an external magnetic field. The plasma was produced by an electron stream from a gridded anode and had a diameter larger than 6 cm and an axial length of about 60 cm. The plasma density was on the order of 10^9 cm^{-3}. The electron temperature had a value between 0.8 and 1.0 eV, depending on the magnetic field. The ion temperature was estimated to be 0.05 eV.[28]

Phase velocities were measured by the method of time of flight, in which sine-wave bursts propagated between two wire probes, exciter and receiver. These two movable probes were constructed so as to allow the investigation of wave propagation at an arbitrary angle from 0 to 90°.

The maximum magnetic field available was 5.0 kG. Either magnetic field or wave frequency could be changed during the experiment. For the former case, the phase velocity is normalized by the parallel ion acoustic velocity, since the electron temperature showed a slight dependence on the magnetic field.

Perpendicular Propagation.[25] – The wave frequency is kept constant at either 30 or 50 kHz; the magnetic field is varied from 0 to 4.0 kG. Phase velocity parallel to the magnetic field at each magnetic field is used to normalize the perpendicular velocity.

Some propagation patterns are shown in Fig. 7.7. We notice the appearance of dispersion of the wave as the cyclotron frequency approaches the wave frequency; the number of sinusoidal components in received signals is larger than that in the exciting signal. We can see also the shift of these sinusoidal waves to the left, which indicates an increase in phase velocity. However, the envelope of the sinusoidal waves shifts to the right, which indicates a decrease in the group velocity. Further increase in the magnetic field stops propagation of the wave. This cutoff occurs at a frequency very close to the ion cyclotron frequency.

These qualitative observations agree with what is expected from theory. For $\theta = 90°$, Eq. (1) simply becomes

$$\omega^2 = \omega_{ci}^2 + \frac{T_e}{M}k^2 , \qquad (2)$$

which is the electrostatic ion cyclotron wave. As ω approaches ω_{ci} from above, the phase velocity is increased while the group velocity is decreased, which makes the wave quite dispersive. For $\omega < \omega_{ci}$, the wave becomes evanescent, giving pure imaginary k.

In Fig. 7.8 a quantitative comparison with the theory is made. The theoretical curve is given by Eq. (2).

[24] N. D. D'Angelo and R. W. Motley, *Phys. Fluids* 5, 633 (1962).

[25] W. D. Jones, I. Alexeff, and A. Hirose, *Bull. Am. Phys. Soc.* 13, 1568 (1968).

[26] M. Porkolab and G. S. Kino, p. 365 in *Proc. Seventh Intern. Conf. on Phenomena in Ionized Gases*, vol. II (eds., B. Perovic and D. Tosic), Gradevinska Knjiga Publishing House, Belgrade, 1966.

[27] V. L. Ginzburg, *Zh. Eksperim i Teor. Fiz.* 21, 778 (1951).

[28] I. Alexeff, W. D. Jones, and D. Montgomery, *Phys. Rev. Letters* 19, 422 (1967).

PHOTO 94468

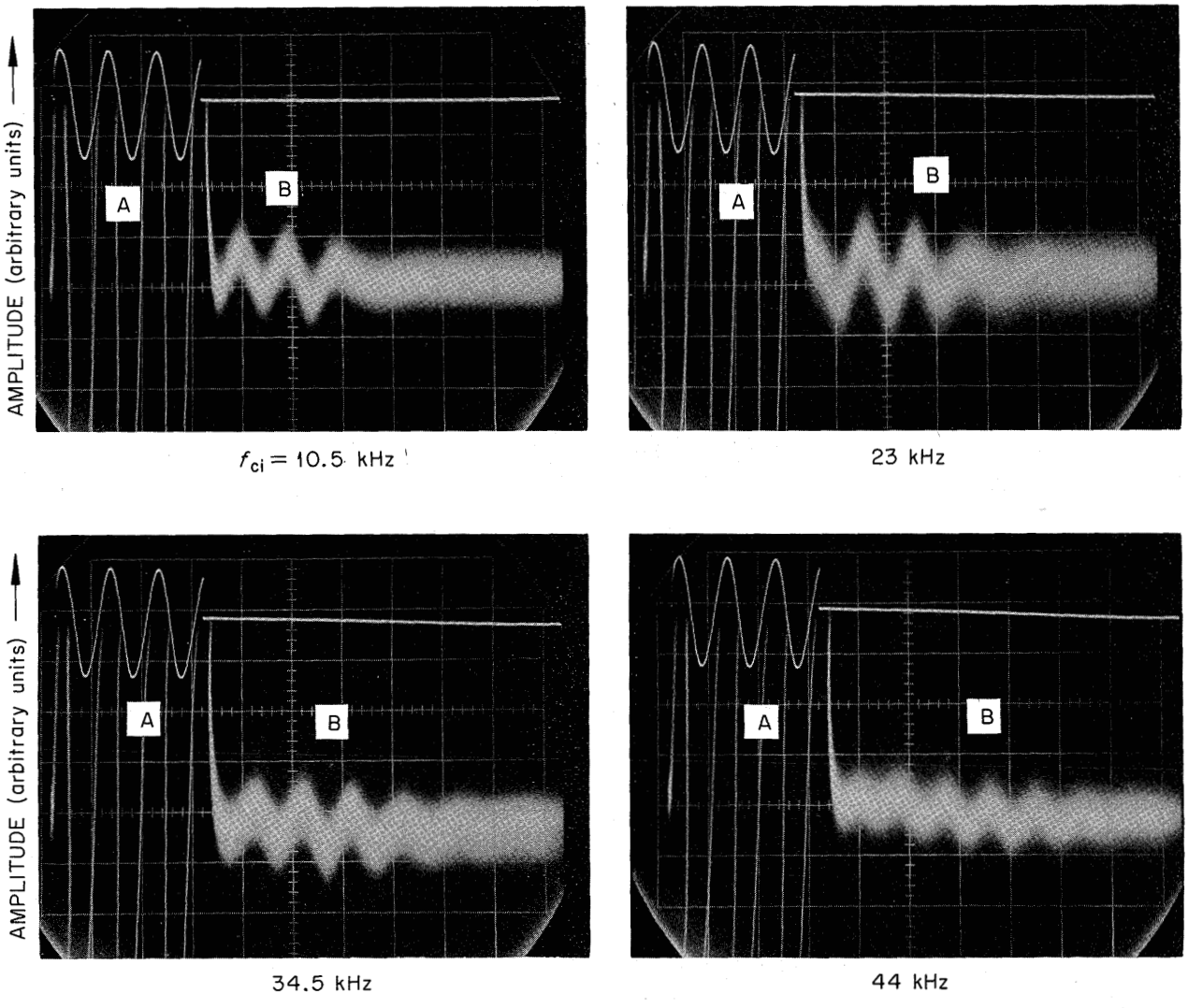

Fig. 7.7. Observation of the Waves Propagating Perpendicular ($\theta = 90°$) to the Magnetic Field. Distance between exciter and receiver is 5.0 cm. The magnetic field is changed to give the cyclotron frequency below each picture. The wave frequency is kept at 50 kHz. The upper trace is the exciting signal; the lower trace is the received signal. Only the received signals labeled B are of interest here. Time (20 μsec/cm) is zero at the left.

Oblique Propagation, θ = 55 and 70°. – The fast mode, which is the electrostatic ion cyclotron wave at $\theta = 90°$, is only slightly changed even at $\theta = 55°$, while the lower cutoff frequency becomes $\omega_{ci} \cos \theta$, below which the magnetoacoustic wave is expected. The magnetic field is kept constant at 5 kG in this case, and the exciting frequency is changed from 10 to 140 kHz.

Figure 7.9 demonstrates the existence of the frequency gap. Frequencies are chosen below, within, and above the forbidden gap. A large difference in the time of flight or phase velocity in the two propagation regions is observed (see Fig. 7.9 captions). Also, we can notice strong damping of the wave in the forbidden gap region.

The results of the phase velocity measurements are shown in Fig. 7.10 without any normalization. The saturating phase velocity at $\omega \gg \omega_{ci}$ gives the ion acoustic velocity, which can be checked from parallel propagation. The agreement between

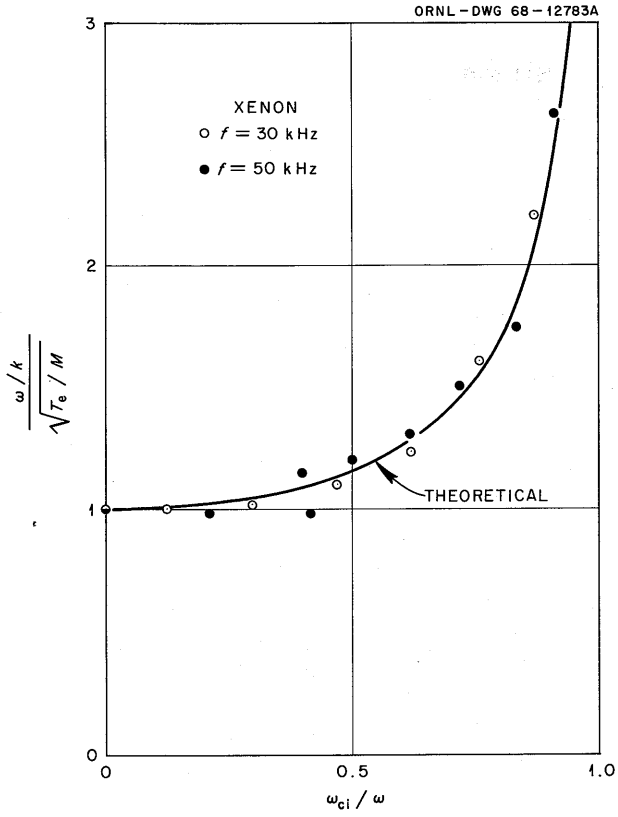

Fig. 7.8. Dispersion Relation of the Perpendicular Propagation. The phase velocity normalized by the ion acoustic velocity parallel to the magnetic field is plotted as a function of frequency ratio, ω_{ci}/ω. The theoretical curve (solid line) is given by Eq. (2). Wave frequency is kept constant at either 30 or 50 kHz.

PHOTO 94496

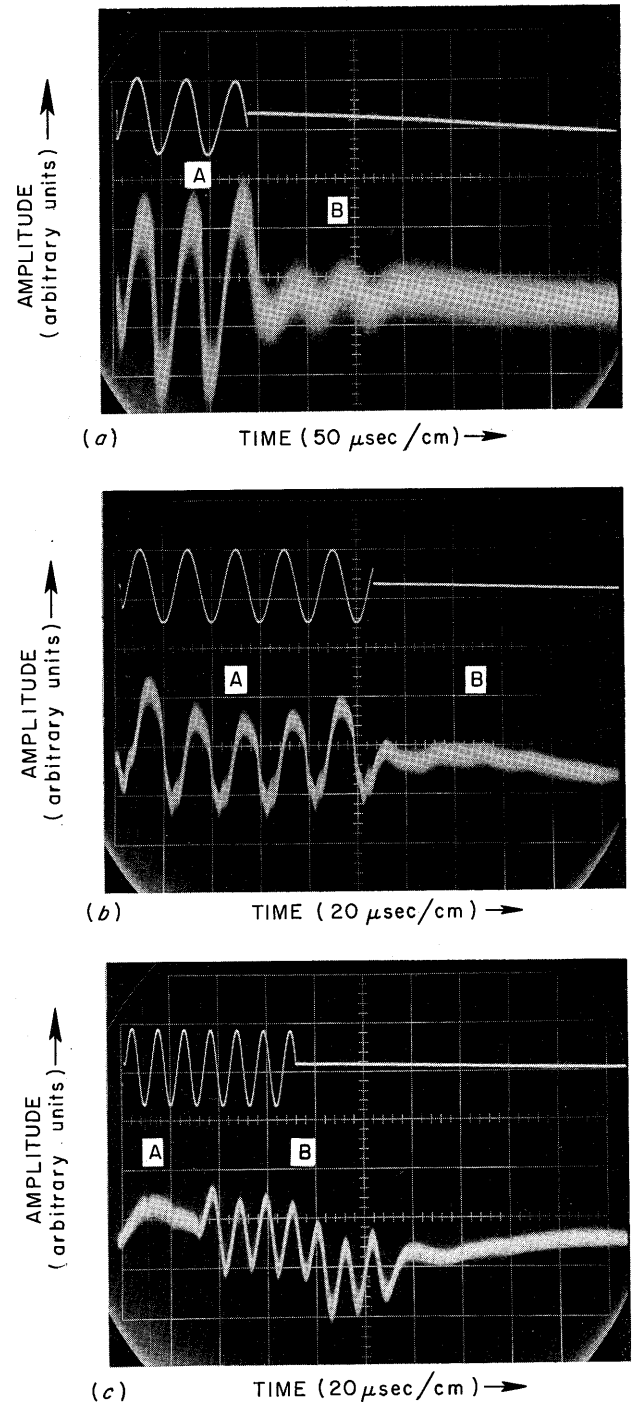

Fig. 7.9. Propagation at $\theta = 55°$. The ion cyclotron frequency is 58 kHz, corresponding to $B = 5$ kG. For each photo, the upper trace is the exciting signal, while the lower trace is the received signal. The signals labeled B are the received signals of interest here. (*a*) $\omega < \omega_{ci} \cos\theta$. Wave frequency $f = 20$ kHz (time scale = 50 μsec/div). Probe distance $d \cong 4.6$ cm. Phase velocity is about 4×10^4 cm/sec. (*b*) $\omega_{ci} \cos\theta < \omega < \omega_{ci}$. $f = 50$ kHz (time scale = 20 μsec/div). $d = 5$ cm. Note a strong damping of the wave although some high-frequency components can be seen. (*c*) $\omega_{ci} < \omega$. $f = 90$ kHz (time scale = 20 μsec/div). $d = 2.5$ cm. The propagation can be observed again, but with a higher phase velocity than that of *a*. The phase velocity is approximately 8.5×10^4 cm/sec.

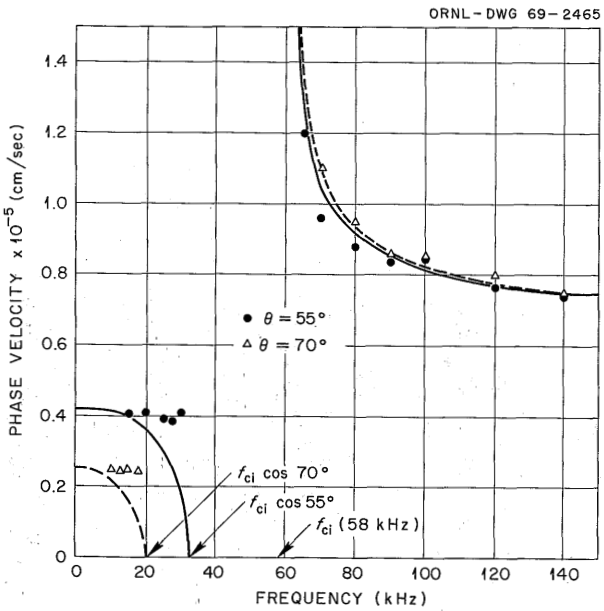

Fig. 7.10. Dispersion Relation at $\theta = 55$ and 70°. Theoretical curves are calculated from Eq. (1). The solid line is for $\theta = 55^\circ$ and the dashed one is for $\theta = 70^\circ$.

theory and experiment for the fast mode is reasonably good. The slow mode, however, does not show appreciable change in the phase velocity, but stays constant very close to $\sqrt{T_e/M}\cos\theta$ up to the frequency $\omega_{ci}\cos\theta$, above which the wave suffers strong damping.

For $\theta = 0$, Eq. (1) simply gives $\omega = \omega_s$ and $\omega = \omega_{ci}$, the latter of which, however, suffers a strong cyclotron damping; $\omega = \omega_s$, the ion acoustic wave propagating parallel to the magnetic field, has been observed without any velocity change or resonance-like phenomena over a wide frequency range in our experiment. Therefore this parallel phase velocity can be regarded as a good tool for measuring the electron temperature as used above.

7.2.2.2. Discussion. – Equation (1) is not valid for purely perpendicular propagation of the ion wave, but is limited[4] by

$$\left|\frac{\pi}{2} - \theta\right| \gg \sqrt{\frac{m}{M}},$$

where m is the electron mass. This inequality comes from the condition that the phase velocity parallel to the magnetic field is much less than the electron thermal speed. However, the ratio $\sqrt{m/M}$ is practically zero if we consider our experimental conditions such as finite spatial spread of the wave packets and finite probe size (including the sheath around it). Also, resonances at harmonics of the ion cyclotron frequency, as expected for purely perpendicular propagation,[7,29] are not observed.

The term "magnetoacoustic" given to the slow mode (characterized by the velocity $\sqrt{T_e/M}\cos\theta$) is not only customary[27] but also it can be shown that the polarization is equal to the usual magnetoacoustic wave known as an MHD wave. Since $\sqrt{T_e/M} \ll V_A$ (Alfvén speed) is well satisfied in our plasma, the two modes are degenerate.

Errors in the phase-velocity measurements are not over 5%, so that unchanging phase velocity of the slow mode is not due to experimental error. Further examination, both theoretical and experimental, may be required to explain the discrepancy. Also, the damping[6] associated with these two modes should be examined by avoiding ambiguities such as geometrical wave attenuation[28] due to finite probe size, etc.

7.3 PSEUDOWAVES

7.3.1 Introduction

An investigation of this new plasma phenomenon has been twofold. On the one hand, we have made extensive experimental investigations aimed at learning the basic properties of these "waves." On the other hand, we have used computer simulation in an effort to gain a theoretical understanding of our observations. The computer simulation, which is based on a nonlinear excitation process, is beginning to yield results which are in qualitative agreement with experimental observations.

7.3.2 Experimental Investigations of Pseudowaves

S. Aksornkitti[30]	W. D. Jones
I. Alexeff	Glenn Joyce[14]
H. Doucet[12]	Karl Lonngren[14]

We have discovered and studied in some detail a new wavelike phenomenon which we have called

[29] I. B. Bernstein, *Phys. Rev.* **109**, 10 (1958).

[30] Department of Electrical Engineering, University of Iowa.

pseudowaves.[31] Although many of their properties superficially resemble those of ion acoustic waves, our studies seem to indicate that "pseudowaves" are coherent bursts of free-streaming ions. These bursts of ions are generated under a wide range of conditions whenever a time-varying potential is placed on a *gridded* electrode immersed in a plasma.

We have somewhat arbitrarily divided the regions of interest for study of the "waves" into four parts: (1) $eV_{exc}/kT_e \gg 1$ and $\omega < \omega_{pi}$, (2) $eV_{exc}/kT_e \lesssim 1$ and $\omega \lesssim \omega_{pi}$, (3) $eV_{exc}/kT_e \lesssim 1$ and $\omega > \omega_{pi}$, and (4) $eV_{exc}/kT_e \gg 1$ and $\omega > \omega_{pi}$. The observations in regions 1 and 4 appear rather unambiguous and are easy to make. The observations in region 2, which has consumed most of our effort in the pseudowaves investigations, have been less clear-cut and more difficult to make. In region 2, not only are the pseudowave signals much weaker, but apparently pseudowaves can couple strongly to ion acoustic waves which are generated simultaneously, both factors adding greatly to the ambiguity of the observations. In region 3, it has been only recently that we apparently have learned empirically how to generate pseudowaves of sufficient amplitude for study at frequencies higher than ω_{pi}. Thus our present knowledge in this region is sparse.

Some effort has been devoted to finding a theoretical model which can successfully predict pseudowaves and their properties in the four regions described. Solutions corresponding to free-streaming ions can be found by using the linearized Vlasov equation to calculate the electric field generated in a plasma by an rf potential placed on a grid immersed in the plasma. Such calculations indicate,[32] however, that such signals would be too small to be observable, at least for frequencies $> \omega_{pi}$ (i.e., in regions 3 and 4). A computer simulation model[33] based on a nonlinear excitation mechanism is presently being tested. According to these simulation studies, ions accelerated into a sinusoidally oscillating potential well can be resonantly "trapped" for short times in the well and then coherently ejected with energies comparable with the well depth. This model has been tested for ω both $< \omega_{pi}$ and $> \omega_{pi}$ for $eV_{exc}/kT_e > 1$ (i.e., for regions 1 and 4). The preliminary results are encouraging; the model seems to be able to predict, for example, the square-root dependence of the pseudowave velocity on the excitation voltage amplitude which has been experimentally observed in regions 1 and 4. Unfortunately, part of the model breaks down for $eV_{exc}/kT_e \gg 1$, and it is not presently known how seriously this violation affects the results. The model has not been tested for regions 2 and 3 (i.e., for $eV_{exc}/kT_e < 1$ – the linear-excitation regime); however, it seems likely that the model may have some relevance to those regions also. Immediately below, we describe a further model which seems intuitively very simple and which is capable of describing the regions 1 and 4 results quite accurately.

Figure 7.11 shows one way by which we think pseudowaves can be generated when a large ($eV_{exc} \gg kT_e$) transient negative potential is placed on a gridded transmitter probe. When the potential well is present, ions will be accelerated toward the grid. An ion reaching the plane of the grid will have acquired the full potential of the applied voltage and will have a velocity given approximately by the formula shown, where V is the magnitude of the applied voltage. If the negative potential is quickly removed just at the time such an ion reaches the grid, then the ion will continue on through the grid and out into the plasma with its

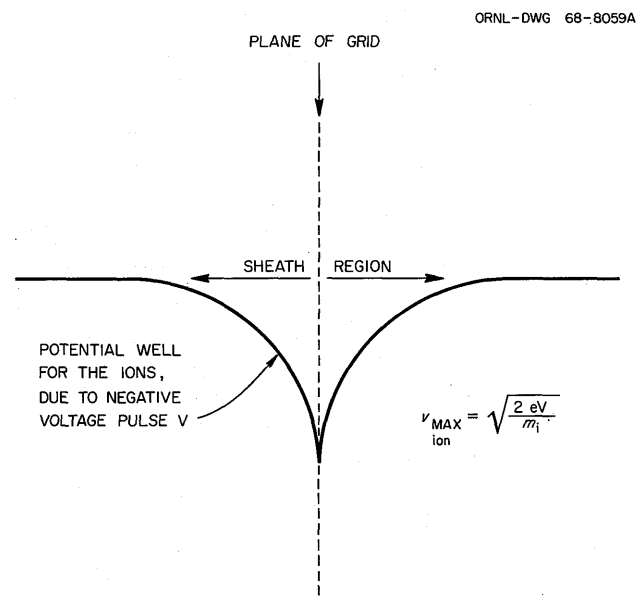

Fig. 7.11. A Model for Pseudowave Excitation when a Large ($eV_{exc} \gg kT_e$) Transient Negative Potential Is Placed on a Gridded Electrode in a Plasma.

[31] K. Lonngren *et al.*, *Phys. Letters* **25A**, 629 (1967); see also sect. 7.1.4, this report.

[32] See sect. 7.1.8.

[33] See sect. 7.3.3.

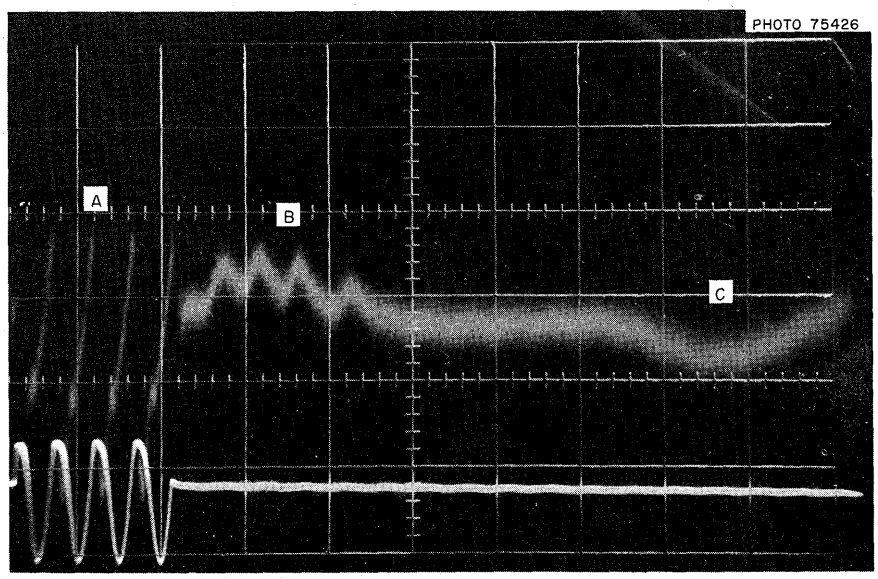

Fig. 7.12. Detection of Pseudowaves and Ion Acoustic Waves, Generated Simultaneously by Sine-Wave Bursts Applied to a Negatively Biased Gridded Transmitter. The lower trace shows the exciting signal on the transmitter, while the upper trace shows the signals received by the detector. The received signal consists of three parts: *A*, a directly coupled electrostatic signal; *B*, a rapidly propagating pseudowave signal; and *C*, a slowly propagating ion-acoustic-wave signal. Note that the ion acoustic wave has been distorted by dispersion and Landau damping, while the pseudowave seems unaffected by the higher-than-ion-plasma-frequency excitation. Sweep = 10 μsec/cm; upper and lower trace vertical scales = 0.2 V/cm and 20 V/cm respectively. Xenon gas was used.

full acquired velocity. Such an ion striking the detector will produce an identical signal to an ion striking the detector due to ion acoustic wave motion. This model obviously predicts that the velocity of pseudowaves should depend upon the amplitude of the exciting voltage; it was just this observation, in fact, which led to our initial discovery of pseudowaves, since we find ion acoustic wave velocity to be independent of exciting-voltage amplitude.

Figure 7.12 shows the detection of both pseudowave and ion-acoustic-wave signals, both waves being generated simultaneously by the same bursts of sine waves placed on the gridded transmitter. Using the arbitrary labeling scheme described above, the pseudowaves here were generated under the conditions characterized by region 4, that is, $eV_{exc} \gg kT_e$ and $\omega > \omega_{pi}$. The lower trace in the photo shows the exciting signal on the transmitter, while the upper trace shows the signals received by the detector. The received signal consists of three parts: *A*, a directly coupled electrostatic signal; *B*, a rapidly propagating pseudowave signal; and *C*, a slowly propagating ion-acoustic-wave signal. Note that the ion acoustic signal has been distorted by dispersion and Landau damping, while the pseudowave signal seems unaffected by the higher-than-ion-plasma-frequency excitation. This represents a second important differentiating characteristic between pseudowaves and ordinary ion acoustic waves. A third important difference between the two phenomena is seen if propagation is carried out in a two-ion-species plasma. For this case we see only one ion acoustic wave, whose velocity is intermediate between the velocities expected for the two separate ion species. We see two pseudowaves, however, one corresponding to each of the two ion masses present.

Figure 7.13 shows some pseudowave propagation data exhibiting the amplitude dependence of the pseudowave velocity on the transmitter excitation voltage, V_{exc}. For these measurements the exciting signals were square-wave voltage pulses of varying amplitudes. The superimposed straight line shows both quantitatively and qualitatively the velocity expected for a $(2eV_{exc}/m_i)^{1/2}$ dependence,

such as is expected on the basis of the simple model shown in Fig. 7.11. In this region the experimental data are in good agreement with the predicted velocities. For $eV_{exc} \approx kT_e = 1$ to 2 eV, however, the velocity points no longer follow the theoretical curve. In this region the velocity of the signal seems to become much less dependent on the exact amplitude of the exciting voltage and to "saturate" at approximately the ion acoustic wave velocity ($\sim 10^5$ cm/sec).

Figure 7.14 shows some preliminary dispersion measurements of pseudowaves, made mainly in region 2 but extending slightly into region 3. Note that as the frequency of the pseudowaves begins to approach the ion plasma frequency ($\sim$150 kHz), the waves become dispersive, as do ion acoustic waves. There are two important differences, however.[31] First, the dispersion is much smaller than observed for our ion acoustic waves. Second, the velocity change is in the opposite direction to that expected and observed for our ion acoustic waves. Coherent sine-wave bursts and a time-of-flight technique, as suggested by Fig. 7.12 and as used in all our previous ion-acoustic-wave studies, were used in obtaining these dispersion data.

We have looked at the damping of pseudowaves as a function of excitation voltage amplitude. Figure 7.15 shows the measured spatial damping wave number. For these measurements, square-wave excitation was used, spanning both regions 1 and 2. Here we see a kind of resonance in the damping at $eV_{exc}/kT_e \approx 1$, apparently followed by a decreased damping for lower excitation voltages. The damping observed for $eV_{exc}/kT_e > 1$ behaves monotonically; this we attribute just to collisions between the free-streaming particles and background gas. If we take the mean free path of the streaming particles to be given by $1/n\sigma$, where n is the background (xenon) gas density and σ is the scattering cross section, then we can use our pseudowave damping data to calculate experimental values for σ. We find that over the range of $\sim$10 to 150 V, σ, which at these speeds is primarily resonant charge exchange, is given approximately by $1 \times 10^{-8} \div$

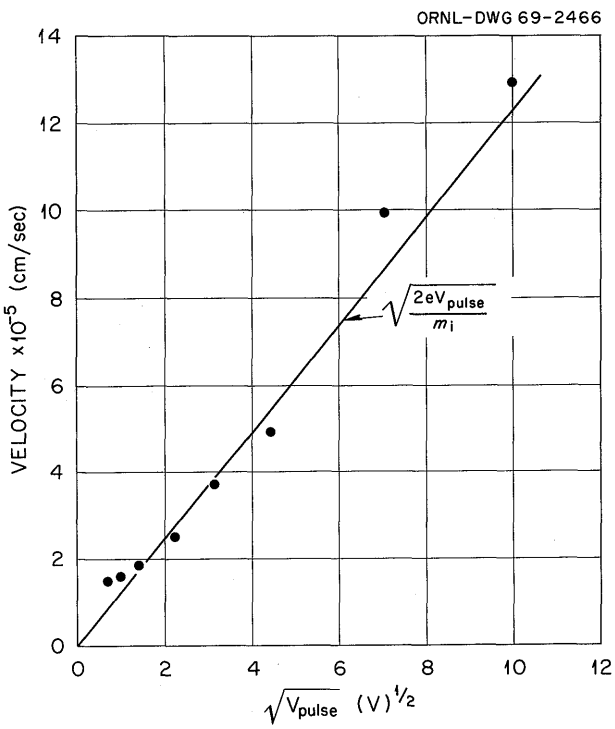

Fig. 7.13. Observed Velocity Dependence on Excitation Voltage Amplitude. The exciting signals were square-wave voltage pulses of varying amplitudes, spanning both regions 1 and 2. The straight line shows the velocity expected on the basis of the simple pseudowave model shown in Fig. 7.11.

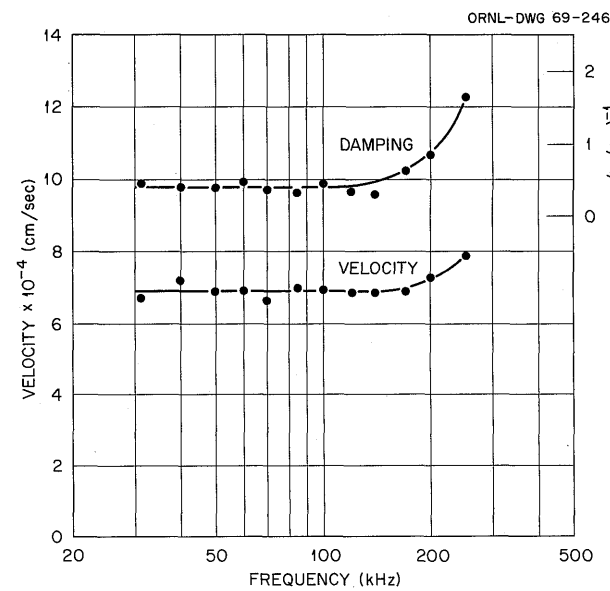

Fig. 7.14. Preliminary Dispersion Measurements of Pseudowaves in Regions 2 and 3. The pseudowaves become dispersive near the ion plasma frequency, as do ion acoustic waves. The dispersion is smaller, however, than we observe for ion acoustic waves, and the velocity change is in the opposite direction to that which we expect and observe for ion acoustic waves.

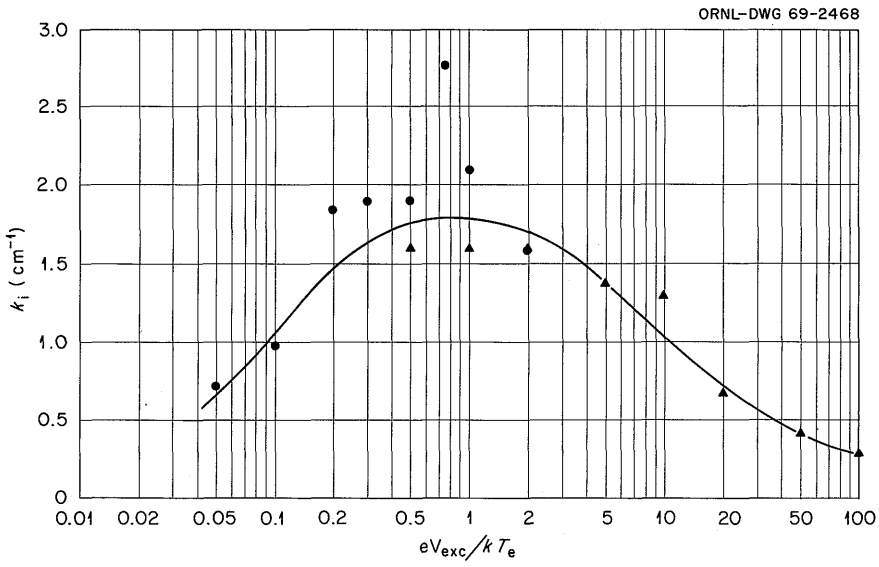

Fig. 7.15. Pseudowave Spatial Damping as a Function of Excitation Voltage Amplitude. For $eV_{exc}/kT_e > 1$ the damping behaves monotonically and is attributed to gas damping due to collisions between the free-streaming ions and background gas. Thus gas damping of pseudowaves gives a simple means of measuring scattering cross sections at low ion energies.

v_{ion}, σ being in square centimeters when v_{ion} is in centimeters per second. The qualitative dependence of cross section on xenon ion energy found here is similar to that which has been reported in the literature[34] for other rare-gas measurements, and the σ value at the highest ion energy measured is within better than a factor of 2 agreement with the theoretical value given by Wannier[34] for the case of xenon ion speeds large compared with atom thermal speeds. Thus gas damping of pseudowaves may represent a simple and accurate means for measuring scattering cross sections at low ion energies.

Three other interesting observations have been made concerning pseudowaves: (1) They are not excited by a flat solid plate – a grid must be used. This is easily understood on the basis of the model shown in Fig. 7.11, since the pseudowaves in that model originate on the opposite side of the transmitter from where the observation is made. (2) In square-wave excitation, a pseudowave is excited only on the positive-going side of the square wave. Again, on the basis of Fig. 7.11, energetic ions would not be expected to leave the potential region until the attractive potential is removed. (3) The velocity of the pseudowave depends on the rise time of the positive-going side of the "square" wave. Figure 7.11, again, would predict this. If, when an ion has reached the grid plane, the attractive potential is not instantaneously removed from the grid, then the ion encounters a retarding potential as it leaves the grid plane and loses some of its acquired energy. All three of these pseudowave characteristics contrast with ion acoustic wave behavior: Ion acoustic waves are excited both by gridded and solid surfaces, they are excited by both sides of a square wave pulse, and their velocity is independent of the excitation voltage rise time.

7.3.3 Computer Simulation Studies of Ion Burst Excitation

M. M. Widner[35] W. D. Jones
I. Alexeff Karl Lonngren[36]

Previous experiments have shown that free-streaming ion bursts can propagate from grids through a plasma with about the same velocity as

[34]E. W. McDaniel, *Collision Phenomena in Ionized Gases*, pp. 164, 439, Wiley, New York, 1964.

[35]ORAU Graduate Fellow, Department of Electrical Engineering, University of Iowa.

[36]Department of Electrical Engineering, University of Iowa.

ion acoustic waves.[37] The velocity of these ion bursts has a dependence upon the excitation frequency which has not been well understood in the past. If the ion burst is free streaming and noninteracting, these dependences must result from the excitation mechanism.

We have studied a nonlinear excitation mechanism numerically using a simple Debye-shielded potential model for the sheath about a grid. The results of these calculations predict that ion bursts are produced and that the burst velocity has the experimentally observed dependence upon excitation frequency and excitation voltage amplitude.

A Debye sheath was assumed to exist about a transparent grid. A Debye sheath represents the actual sheath to first order for small excitation potentials and is chosen for simplicity with the hope of obtaining qualitative information about the excitation process. The plasma enters the calculation only through Debye shielding of the excitation potential and does not interact with the free-streaming ions.

Individual ions were directed toward the sheath from an initial position which was far from the sheath. Initially there was a negligible force on the ions due to the excitation potential. The ions obeyed an equation of motion

$$\frac{d^2x}{dt^2} = \frac{-x}{|x|}\theta_0(2\pi)^2\, e^{-|x|} \sin(2\pi\omega t + \theta) ,$$

where x is position normalized by the electron Debye length, t is time normalized by $1/f_{pi}$, ω is frequency normalized by ω_{pi}, θ_0 is excitation potential normalized by kT_e/e, and θ is the phase of the excitation potential.

As the ions entered the sheath they were accelerated or decelerated depending upon the phase of the excitation signal. Twenty different phases were used for each particular amplitude and frequency. A 360° phase change corresponds to a time change of $1/\omega$. The initial position was kept fixed, while the initial time for each ion was modified corresponding to the source phase. This allows the ions to enter the sheath at random phase, and the results are interpreted from the

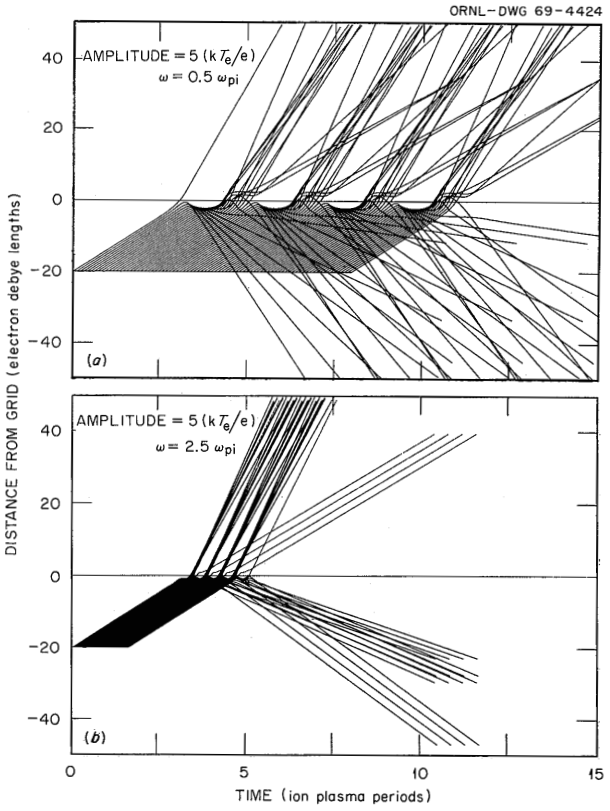

Fig. 7.16. Numerically Computed Ion Trajectories. Ions with initial velocity of $\sqrt{kT_e/m_i}$ enter a Debye-shielded potential at random phase. The ions which pass through the grid are grouped as ion bursts. (*A*) Frequency = $0.5\omega_{pi}$. (*B*) Frequency = $2.5\omega_{pi}$. The velocity of the burst is seen to be greater in *B* than in *A*.

superposition of the ion trajectories as shown in Fig. 7.16. Bursts of ions are clearly present in Fig. 7.16. Most of the ions pass through the grid and are accelerated forward, while only a few are reflected. The ions that pass through the grid have about the same position at a given time and define a burst. The ions in the burst have essentially the same velocity as the burst, thereby preserving it.

The individual ion velocity is representative of the burst velocity after the ion has passed through the grid. If the final velocities of the ions are compared we can determine if a burst of ions is present and, if so, the velocity of the burst. A cluster of ions with nearly the same final velocity would constitute a burst.

[37] See sects. 7.3.2 and 7.1.4, this report; also *Thermonuclear Div. Semiann. Progr. Rept. Oct. 31, 1967*, ORNL-4238, sect. 5.6.

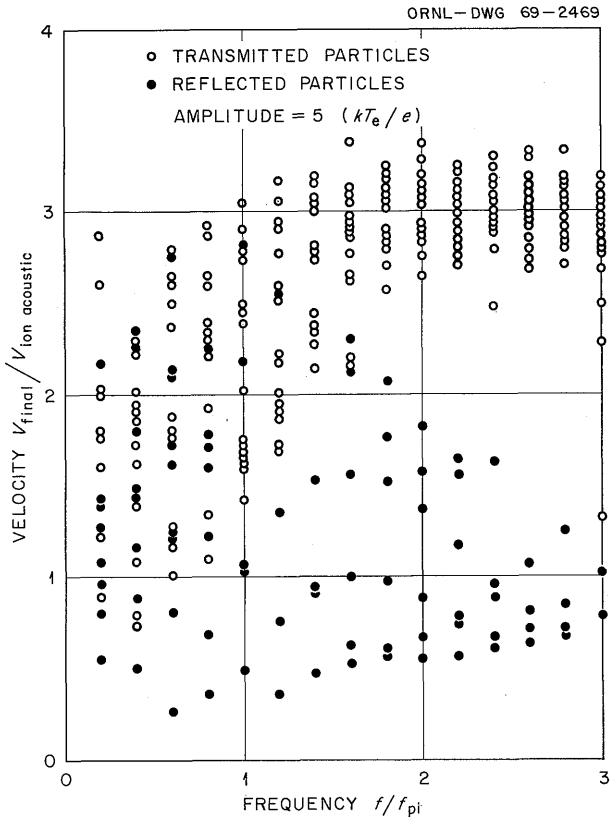

Fig. 7.17. Final Ion Velocity as a Function of Excitation Frequency. Each set of points at a given value of f/f_{pi} constitutes ions entering the sheath at 20 equally spaced points throughout the phase of one cycle.

The dependence of the burst velocity on excitation frequency is shown in Fig. 7.17. The burst is not well defined for frequencies much below the ion plasma frequency. The burst velocity increases as frequency increases and approaches a constant velocity over the higher frequency range. The velocity of these bursts also was proportional to the square root of the excitation potential, as is observed experimentally. The maximum velocity for a burst is $(e\phi/m_i)^{1/2}$, where ϕ is the ac voltage applied to the grid.

In summary, we have seen that a simple Debye-shielded potential model for a grid will predict the formation of ion bursts. The computations show the detailed ion motion which is responsible for the burst formation. The ion burst velocity has the dependence upon frequency and excitation voltage amplitude which is observed experimentally.

7.4 PLASMA SHEATHS

7.4.1 Introduction

Both experimental and computer simulation studies have been made of plasma sheaths. Experimentally, we have studied both the conventional Langmuir sheath and a new transient sheath. The thickness of the Langmuir sheath as a function of voltage was measured using both ion acoustic waves and a hot probe. The transient sheath, which is a sheath that forms in a time comparable with the electron plasma period and evolves into an ordinary Langmuir sheath in a time comparable with the ion plasma period, was observed and studied by means of ion acoustic waves. A one-dimensional fluid model is used in the computer sheath study to compute the response of a plasma slab to a large negative potential applied at the plasma boundary. Both the transient sheath and its subsequent time evolution into a space-charge region resembling a Langmuir sheath result from the numerical study.

7.4.2 A Transient Sheath – Discovered by Ion Acoustic Waves[38]

I. Alexeff Karl Lonngren[14]
W. D. Jones D. Montgomery[3]

We have found that when a high ($eV > kT_e$) negative voltage is placed impulsively on a plate immersed in a plasma, the electric field produced by this voltage penetrates into the plasma to distances much larger than those given by the Debye formula. The penetration of the electric field forms a new type of sheath – a transient sheath. After a long period of time it collapses into a Langmuir sheath. The thickness of this transient sheath is given by $x = (2eV)^{1/2}\,(4\pi ne^2)^{-1/2}$, where x is the sheath thickness (cm), e is the electron charge (esu), V is the applied voltage (statvolts), and n is the ion density (cm^{-3}). We have utilized ion acoustic waves to make an experimental study of these sheaths. In the experiment we follow the time of flight of the leading edge of an ion acoustic wave as a function of distance. When these data are plotted and the resulting straight

[38] I. Alexeff *et al.* (to be published in *Physics of Fluids*, February 1969).

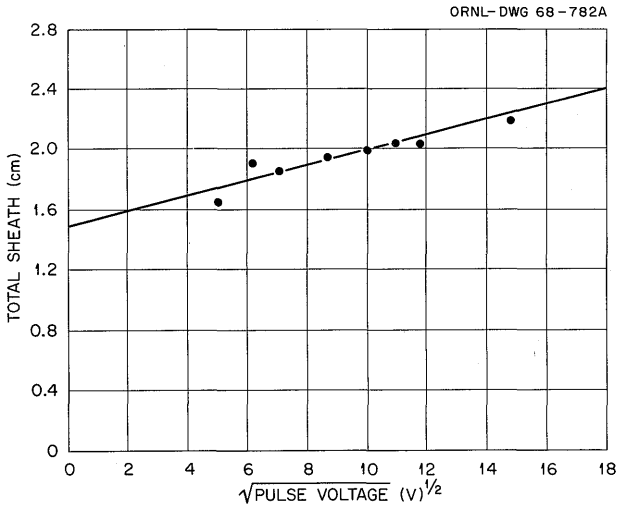

Fig. 7.18. Dependence of Sheath Thickness on Transmitter Exciting Voltage. The data were taken using delta-function exciting voltages having a duration much shorter than an ion plasma period. The straight line corresponds to the transient sheath on the transmitting electrode varying in thickness as $V^{1/2}$. The vertical-axis intercept corresponds to Langmuir sheaths on both transmitter and receiver. The slope of the straight line gives an ion density of 4.2×10^8 cm^{-3}, as compared with a Langmuir probe value of 3.5×10^8 cm^{-3}.

line of propagation distance vs propagation time is extrapolated back to zero time, we find a finite distance. This distance is due to dc Langmuir sheaths plus the transient sheath. Figure 7.18 shows a plot of experimental sheath thickness as a function of transmitter exciting voltage. The straight line corresponds to the transient sheath on the transmitting electrode, varying in thickness with the theoretically expected $V^{1/2}$ dependence. The finite intercept corresponds to Langmuir sheaths on the transmitting and receiving electrodes. Since the thickness of the transient sheath involves only the applied potential and the plasma ion density, measurement of this sheath thickness as a function of voltage permits an unambiguous determination of the ion density.

7.4.3 Experimental Langmuir Sheath Study

M. M. Widner[35] W. D. Jones
I. Alexeff Karl Lonngren[36]

7.4.3.1. Introduction. – The steady-state plasma sheath extending from a negatively biased electrode in a low-pressure discharge has been studied experimentally by two techniques. The perturbation associated with ion acoustic waves propagates many times faster through the sheaths on the transmitting and receiving electrodes than through the plasma. By using time-of-flight data for ion acoustic waves the total sheath thickness on the transmitting and receiving electrodes is obtained. A hot probe was also used to measure sheath thickness. The hot probe potential was found to change abruptly more negative as it was moved from the plasma into the sheath, sharply defining the sheath edge.

The sheath thickness was measured as a function of bias voltage. The dependence agreed well with the collisionless Langmuir sheath equation[39,40] for bias voltages much more negative than the space potential.

7.4.3.2. Experimental Results and Conclusions. – A sheath occurs between a boundary surface and a plasma and is a region in which quasi-charge neutrality breaks down. A negatively biased electrode with $eV \ll -kT_e$ is surrounded by an ion-rich sheath called the Langmuir sheath. The ion space charge limits the current in this sheath as given by the Langmuir-Childs law. The ion current entering the sheath is determined by the ion drift rate in the plasma, which is on the order of $\sqrt{kT_e/m_+}$. The space-charge-limited current is set equal to the ion drift current to obtain the Langmuir sheath thickness as in

$$j_+ = \frac{1}{9\pi}\sqrt{\frac{2e}{m_i}}\,\frac{V^{3/2}}{d^2} = \frac{eN_+\overline{C}_+}{4}, \qquad (1)$$

where j_+ is the ion current density, m_i the ion mass, V the probe potential, d the sheath thickness, N_+ the ion density in the plasma, and $\overline{C}_+$ the average velocity of ions entering the sheath.[39]

The experimental vessel was a 5-liter glass cross containing a xenon plasma. The plasma density was $\sim 10^9$ cm^{-3} with an electron temperature of about 1 eV. The background xenon pressure was $\sim 1\ \mu$ Hg, and the mean free path for ions was long compared with the measured sheath thickness. The apparatus is quite similar to that previously

[39] L. B. Loeb, *Basic Processes of Gaseous Electronics*, p. 334, University of California Press, Berkeley and Los Angeles, 1960.

[40] L. Tonks and I. Langmuir, *Phys. Rev.* **34**, 876 (1929).

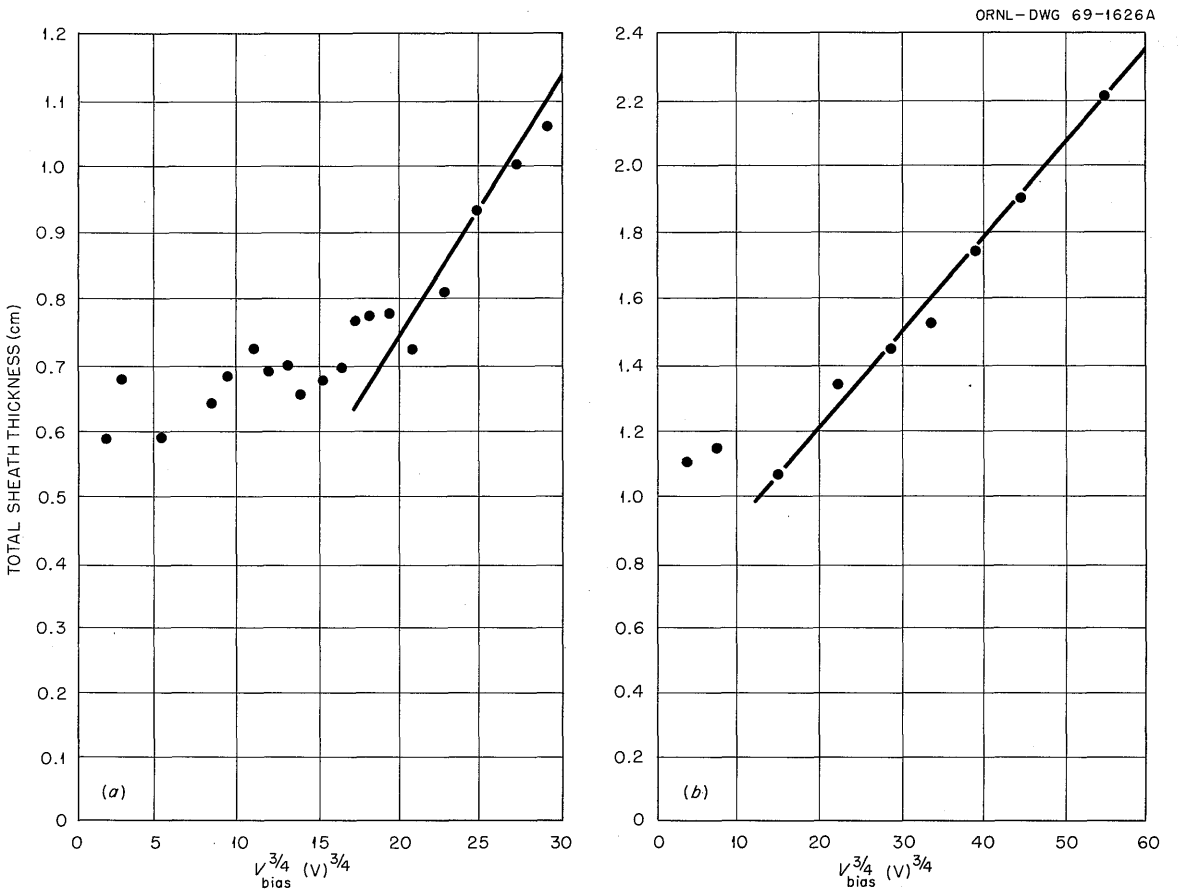

Fig. 7.19. Experimental Langmuir Sheath Measurements Using Ion Acoustic Wave Propagation. The total sheath on the transmitting and receiving electrode is plotted as a function of the $^3/_4$ power of the bias voltage. The two parts of the figure correspond to two different experimental runs with slightly different discharge conditions and different bias voltages. (*a*), bias voltages from 0 to −80 V; (*b*), bias voltages from 0 to −233 V. The intercepts ($V_{bias} = 0$) are unequal for the two graphs due to different transient sheaths on the transmitting electrode, since pulses of different amplitude were used to excite the waves.

described, and the plasma is stable and quiescent.[11]

Ion acoustic waves were transmitted between two copper disks of 1 in. radius. A pulse generator was used to generate the waves on an unbiased disk. The ion acoustic waves were detected on a negatively biased disk. The bias voltage on the receiving electrode was varied and the sheath thickness measured. For a fixed bias voltage a set of time-of-flight vs distance data was taken for ion acoustic waves. The leading edge of the ion acoustic wave signal was used to obtain the time of flight. A straight line is a good fit to the data points and is extrapolated back to zero time, giving an intercept which corresponds to the total sheath on the transmitting and receiving electrodes. The sheath on the transmitter is a Langmuir sheath and a transient sheath.[38,41] A Langmuir sheath exists on the receiving electrode, and it, presumably, is not significantly perturbed by the ion wave.

The hot-probe measurements of sheath thickness were obtained by positioning the hot probe in the center of the discharge and moving it toward the negatively biased receiving antenna. A hot probe will assume the local surrounding potential if there is an ample supply of electrons surrounding it and if it is hot enough to emit electrons. If the probe potential should deviate from the local surrounding potential, it will either emit or collect electrons until it assumes the local surrounding potential. The hot-probe potential was monitored by a very high-impedance voltmeter. The probe potential

[41]See sect. 7.4.2.

would decrease very slowly as it was moved from the center of the discharge toward the biased electrode. When the potential reached about $-kT_e/e$ the potential abruptly changed rapidly more negative, sharply defining the sheath edge. Only the sheath edge was measured and not the sheath profile by this technique since there is not a large supply of electrons in the sheath.

The results of the ion acoustic wave measurements are plotted as the total sheath thickness depending upon bias voltage to the $^3/_4$ power in Fig. 7.19. This is a revealing way to compare the results with the Langmuir sheath equation. Linear dependence in such a plot would be expected for agreement. The voltage range studied was 0 to 80 V negative (Fig. 7.19*a*) and 0 to 233 V negative (Fig. 7.19*b*). Each data point was extracted from the ion acoustic wave data using a least-squares error fit of a straight line to the data points. For bias voltages ~–200 V the plasma became noisy, and for voltages ~–233 V completely unstable. The dependence is almost linear for voltages more negative than ~20 V. The results of the data are tabulated in Table 7.2 and compared with Eq. (1). The plots in Fig. 7.19 are interpreted as having the expected linear dependence for potentials ~–20 to –233 V. The voltage range from 0 to –20 V seems to have a dependence other than that predicted by the Langmuir sheath equation.

The hot-probe data are shown in Fig. 7.20. These data closely resemble the ion acoustic wave data except the Langmuir sheath thickness itself is the ordinate of the plot and not the total sheath. The results are tabulated in Table 7.2 and for potentials more negative than ~–20 V show agreement with Eq. (1). We have assumed particles entering the sheath with a velocity $\sqrt{kT_e/m_i}$ for this comparison.

Table 7.2. Comparison of Experiment with Model

	Slope (cm/V$^{3/4}$)	
	Measured	Calculated
Ion acoustic wave data, Fig. 7.19*a*	0.0384	0.0378
Ion acoustic wave data, Fig. 7.19*b*	0.0283	0.0327
Hot-probe data, Fig. 7.20	0.0188	0.0206

In summary, the plasma sheath on a planar negatively biased electrode in a low-pressure discharge has been studied by ion acoustic waves and a hot probe. The sheath thickness was measured as a function of bias voltage. The model was the collisionless Langmuir sheath equation assuming ions entering the sheath with a velocity of $\sqrt{kT_e/m_i}$. The measurements agreed with the model for potentials much more negative than the space potential.

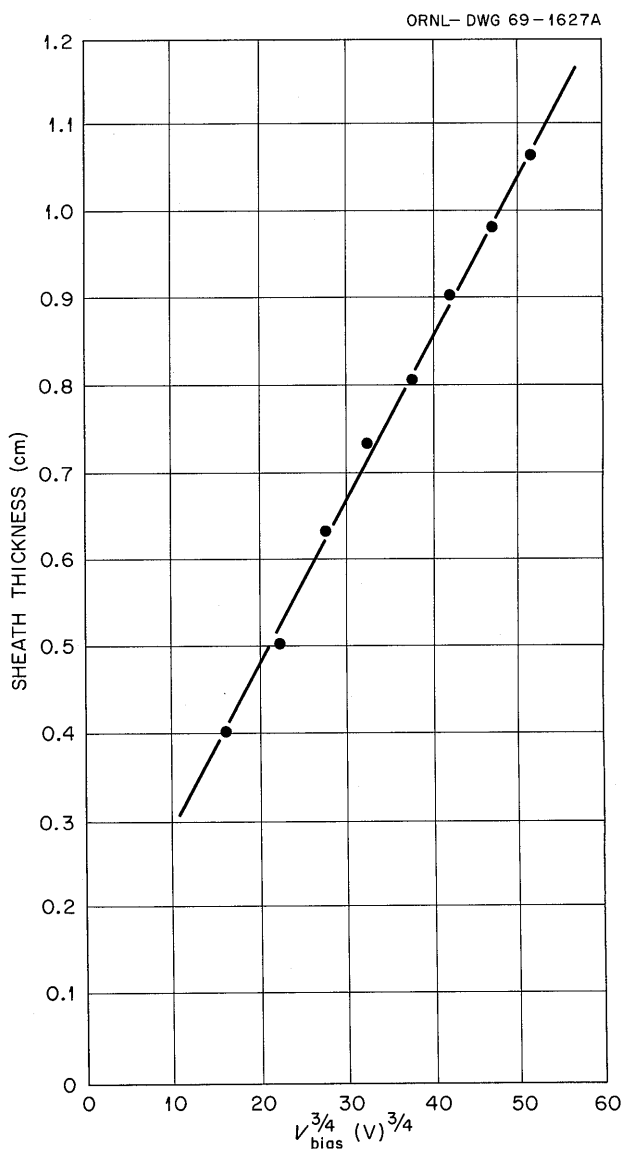

Fig. 7.20. Experimental Langmuir Sheath Measurements Using a Hot Probe. The sheath thickness on the electrode is plotted as a function of negative bias voltage to the $^3/_4$ power.

7.4.4 Computer Simulation Studies of a Plasma Sheath Evolution

M. M. Widner[35] W. D. Jones
I. Alexeff Karl Lonngren[36]

7.4.4.1. Introduction. – The excitation of ion acoustic waves in time-of-flight studies has long been accomplished without understanding the mechanism of excitation.[42] A time-varying potential, whose frequency components are low compared with the ion plasma frequency, produces a propagating ion acoustic wave when applied to an electrode in a plasma. The experimental situation involves excitation potentials $\gg kT_e/e$, which produce a sheath on the transmitting electrode. The sheath produced is not negligible, but intimately related to the excitation of the ion acoustic wave.

Recent experiments have investigated the sheath which develops on a transmitting electrode.[41] A transient sheath develops on a time scale of the electron motion, while the ions remain fixed. As the ions respond to the excitation potential the sheath begins to change as determined by the excitation potential and the plasma quantities.

The sheath development has been studied numerically with a one-dimensional fluid model. A negative potential was applied to a uniform plasma slab corresponding to a situation quite similar to ion acoustic wave excitation. The primary results show the sheath moving into the plasma with the ion acoustic speed and the formation of a space-charge sheath after a few ion plasma periods.

7.4.4.2. Numerical Calculations and Results. – We have studied the nonlinear sheath evolution process numerically using a system of one-dimensional fluid equations. The equations are:

$$\frac{\partial n_i}{\partial t} + \frac{\partial}{\partial x}(n_i v_i) = 0 ,$$

$$\frac{\partial v_i}{\partial t} + v_i \frac{\partial v_i}{\partial x} = -\frac{\partial \phi}{\partial x} ,$$

$$\frac{\partial^2 \phi}{\partial x^2} = n_e - n_i ,$$

$$n_e = e^{\phi} ,$$

where n_i and n_e are the ion and electron densities normalized by the uniform density, v_i the ion fluid velocity normalized by the ion acoustic speed, ϕ the potential normalized by kT_e/e, x the position normalized by the electron Debye length, and t the time normalized by $1/\omega_{pi}$. The electrons are assumed to be in equilibrium since only negative potentials are considered.

A stationary plasma slab was considered initially with the ion and electron densities equal to unity and the ion fluid velocity and the potential equal to zero at all positions. A negative-going step function was chosen as the excitation signal. The step was applied at one plasma boundary while the potential was maintained at zero at the other boundary. The time evolution of the plasma quantities was then studied. The continuity equation advanced the ion density in time, and the equation of motion advanced the ion velocity in time. Poisson's equation was solved for the potential after each time advance.

The accuracy of the solutions was checked by computing an energy relation for the ions and by testing the sensitivity of the solutions to changes in time and distance spacings. Using these techniques, it is believed the numerical solutions are within 5% of the actual solution.

A typical solution to the system of equations is shown in Fig. 7.21. The excitation signal was a negative-going step function of amplitude $20kT_e/e$. The ion and electron densities are plotted as a function of position at several equal time intervals after the step excitation is applied.

A transient sheath formed quickly as the electrons were initially pushed back by the repulsive potential. The ions then began to move toward the boundary, causing the ion density to decrease near the boundary. The sheath began to penetrate into the plasma and began to resemble a space-charge sheath similar to a Langmuir sheath. A Langmuir sheath is a steady-state sheath, however, and this model will not reach a steady-state solution. The results do show that a space-charge sheath develops which does not move appreciably after the first few ion plasma periods.

After a few ion plasma periods the sheath edge moves into the plasma slab with precisely the ion acoustic speed. The disturbance in the quasi-charge neutral region resembles a rarefaction wave as found in ordinary fluid dynamics. It is interest-

[42] W. D. Jones and I. Alexeff, vol. II, p. 330 in *Proc. Intern. Conf. Phenomena Ionized Gases, 7th*, ed. by B. Perovic and D. Tosic, Gradevinska Knjiga Publishing House, Belgrade, 1966; I. Alexeff and W. D. Jones, *Phys. Rev. Letters* **15**, 286 (1965).

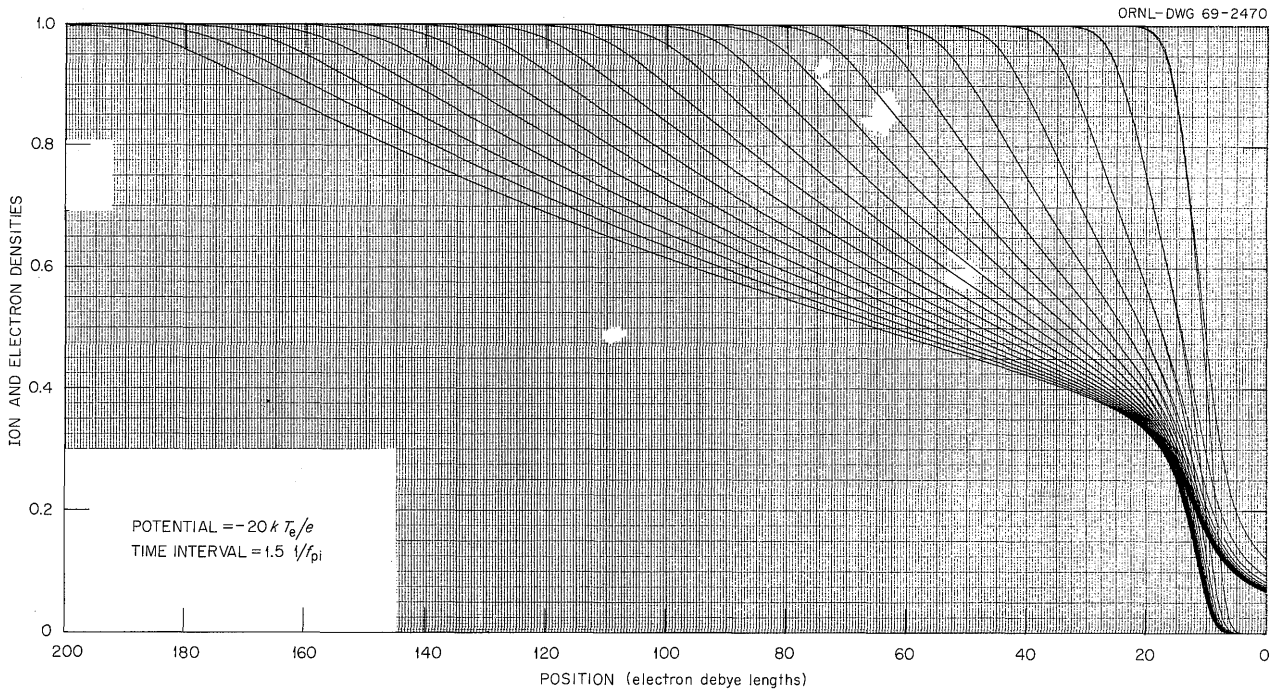

Fig. 7.21. Sheath Development Resulting from a Negative Step Potential Applied to a Plasma Boundary. The electron and ion densities are superimposed, with the electron density being the lower trace of each pair. The leading edge of the sheath moves with precisely the ion acoustic speed after a few initial time periods. An ion space-charge sheath quickly forms, limiting the ion current to the boundary.

ing that charge neutrality is maintained to a high degree except in the space-charge region near the boundary, where most of the potential drop occurs.

In an actual plasma discharge a wave is observed breaking away from the sheath for a negative step excitation. The model does not show such a breakaway, since it is only a one-dimensional model and does not allow plasma to enter the sheath from more than one direction. The model also does not include ion generation in the plasma slab, which also may contribute to the wave separating from the sheath.

In summary, we have studied the development of a sheath on a plasma boundary by numerically solving a set of one-dimensional fluid equations. A negative step potential was applied to the boundary of a uniform plasma slab and the response studied. A transient sheath developed on a time scale of the electron motion as the electrons quickly responded to the negative potential. After several ion plasma periods a space-charge sheath developed near the plasma boundary, limiting the influence of the boundary potential. The leading edge of the disturbance propagated into the plasma with precisely the ion acoustic speed after a few time stops. The disturbance in the quasi-charge neutral region resembled a rarefaction wave as found in ordinary fluid dynamics.

7.5 PLASMA GENERATION TECHNIQUES

7.5.1 Introduction

We have been concerned with two different aspects of plasma generation in magnetic fields. In the first case we were interested in generating a quiescent plasma for basic plasma wave studies in magnetic fields. This we have succeeded in doing by proper design of an electron gun. In the second case we were interested in generating an ECRH plasma in our iron-core min-B magnetic field system, both for the purpose of studying the containment properties of the system – in particular, flute stabilization at low pressures – and to study the basic properties of the resulting plasma. A resonantly generated plasma has been made using low-power microwaves; however, further study has not been made.

7.5.2 Generating a Quiescent Plasma in a Magnetic Field

A. Hirose[1] I. Alexeff
W. D. Jones

By the proper design of an electron gun we have been able to generate rare-gas plasmas in solenoidal magnetic fields with intensities up to 5 kG (the limit of the present system) whose properties are quite similar to those of our magnetic-field-free discharge plasmas. The plasmas typically have $n_e \sim 10^9$ cm^{-3}, $T_e \sim 1$ eV, $T_i \sim 0.05$ eV, and a low-frequency ($<\omega_{pi}$) noise level which seems to be smaller than the random thermal fluctuations of the plasma ions. The plasma column is, typically, 60 cm long with cross-sectional dimensions of approximately 4.5 × 5.5 cm, the rectangular shape and size being dictated by the cathode geometry. The plasma column is terminated at one end by the anode-cathode structure and at the other end by a flat conducting plate whose potential is normally the same as the anode potential, but can be varied.

The plasma is created by ionizing collisions between the background gas and a parallel diffuse beam of energetic electrons from the anode-cathode assembly. This method of creating the plasma, coupled with emission-limited operation of the cathode, decouples the plasma generation rate and the plasma density, thus eliminating a major source of noise commonly encountered due to feedback between plasma and plasma source. The electron beam is diffuse to eliminate the generation of beam-plasma instabilities. Making the beam parallel to the magnetic field lines lessens the chance of exciting cyclotron-related instabilities. Locating the anode at the same end of the plasma column as the cathode eliminates the creation of a relative drifting of plasma ions and electrons, thus removing a source of two-stream instabilities. As described below, the anode-cathode assembly is constructed with the anode close to the cathode. This eliminates the buildup of a dense plasma in the electron gun itself and thus lessens the chances of two-stream and beam-plasma instabilities in the gun. Also, as discussed below, the anode acts like a noise filter between the plasma column and the gun. Finally, the gun is constructed so as to minimize its self-magnetic field.

Figure 7.22 shows, schematically, the construction of the electron gun. The gun consists basically of four elements: the anode A, the cathode

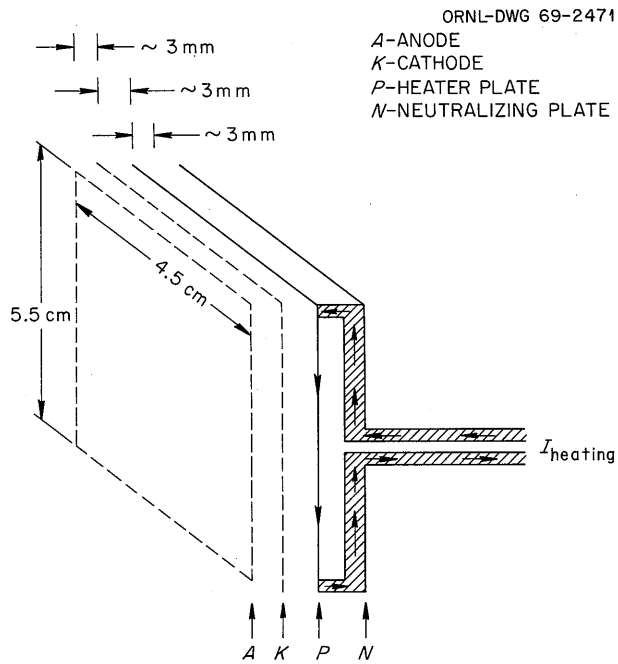

Fig. 7.22. A Schematic Representation of the Four-Element Electron Gun Used in the Generation of Quiescent Rare-Gas Plasmas in a Solenoidal Magnetic Field.

K, the heater plate P, and the neutralizing plate N. The anode is constructed of a 90%-transparent tungsten mesh whose mesh size is smaller than the plasma Debye length. The primary function of the anode is to accelerate electrons into the plasma region; however, the small mesh size of the anode semi-isolates the plasma column from noise fluctuations in the gun and thus probably contributes to the overall quiescence of the plasma. The cathode is an oxide-coated platinum mesh. An oxide coating is used to reduce the operating temperature of the cathode. The cathode is radiation heated by the heater plate. By using radiation heating of the cathode we eliminate "hot spots" which normally occur when a mesh structure is resistance heated by a dc current. The heater plate is constructed of 5-mil-thick tungsten sheet and normally requires about 400 A to heat. The neutralizing plate is made of two sections of ¼-in.-thick water-cooled plate; with the current leads to the two sections connected as shown in the figure, the two sections, to a first approximation, function as one to carry the heating current antiparallel to its direction in the heater plate. Thus, to first order, the magnetic fields of the two currents in

opposite directions neutralize each other in the anode-cathode region, giving a magnetic-field-free electron gun. The dimensions of the gun and approximate spacings of the elements are indicated in Fig. 7.22.

7.5.3 Resonant Microwave Plasma Generation in an Iron-Core Min-*B* System

I. Alexeff W. D. Jones

Preliminary experiments have been made to generate and heat a plasma at low background gas pressures in an iron-core min-*B* system[43] by resonant coupling of microwaves and the plasma at the electron cyclotron frequency matching the microwave frequency. The experiments were done by piping 12-cm microwaves from a 100-W power supply through a few feet of coaxial line to a wire antenna protruding 2 to 3 cm inside the perforated microwave cavity and plasma container located between the iron-core pole pieces. In the system, at the minimum pressure obtainable by the pumping system ($\sim 1 \times 10^{-6}$ torr gage), it was possible to generate a visible well-defined shell of plasma whose shape corresponded roughly to surfaces of constant B in the system and whose radial position could be varied from a small region near the center of the device all the way out to the container walls by varying the magnet current. Although an accurate check was not made to see if the electron cyclotron frequency at the visible plasma surface was exactly equal to the microwave frequency, enough is known from previous correlation measurements of B-field strength and magnet current to know that the two frequencies were comparable.

Efforts to detect energetic x rays, as evidence of plasma heating, were unsuccessful. In view of the small amount of microwave power reaching the cavity, however, this was not surprising. Efforts to utilize a 1-kW microwave power supply have been delayed due to arcing of the coaxial line.

7.6 DIAGNOSTICS

7.6.1 Introduction

We have developed a simple technique for measuring the parallel component of the electron temperature in a magnetically supported plasma. The technique is based on an energy analysis of the ions accelerated through the plasma sheath on an ungrounded plate which terminates the plasma along field lines.

7.6.2 A Simple Technique for Measuring $T_{e\parallel}$ in a Magnetic Field

I. Alexeff W. D. Jones

In the case where electrons are much more mobile than ions, equating ion and electron currents to a floating plate in contact with a plasma shows that the plasma should be positive with respect to the floating plate by the amount

$$V_F \approx \frac{T_e}{2} \ln \frac{m_i}{m_e}, \tag{1}$$

where T_e is in electron volts and V is in volts. Most of this voltage will occur across an electron-rich sheath located near the surface of the floating plate. Thus ions collected by the floating plate will have been accelerated through a potential given by Eq. (1). If, now, a small hole is made through the plate, the accelerated ions at that point can pass on through the plate and be energy analyzed. Equating the maximum observed ion energy to V_F in Eq. (1) allows a value to be calculated for T_e. It can be reasoned that this technique would be valid for any situation where the ion and electron motion to the sheath is unimpeded. In particular, the technique should be applicable to measuring the parallel electron temperature in a plasma contained by a magnetic field of simple geometry.

We have used the above technique to measure the parallel electron temperature in a discharge-type plasma contained in a solenoidal magnetic field.[44] The plasma column was terminated at one end by the plasma source and at the other end by a flat copper disk which could be made to float relative to the plasma. A gridded probe, consisting of a

[43] *Thermonuclear Div. Semiann. Progr. Rept. Apr. 30, 1967*, ORNL-4150, p. 141; *Oct. 31, 1966*, ORNL-4063, p. 124; I. Alexeff, *J. Appl. Phys.* **37**, 2182 (1966).

[44] See sects. 7.1.2 and 7.2.2.

collector and a single repelling grid for electrons, was located behind a $\frac{1}{8}$-in. hole through the copper disk. By varying the potential on the ion collector and measuring the corresponding ion current, a current-voltage characteristic such as is shown in Fig. 7.23 could be found. Ideally, since the thermal energy of the ions in the plasma is negligible compared with the energy acquired in crossing the sheath on the floating plate, an essentially monoenergetic ion beam would be expected. Space-charge effects in the probe itself, however, would be expected to modify the distribution in the manner implied by the characteristic of the figure. Equating the maximum voltage value of ~12.5 V at which an ion current could be detected, for the data shown, to V_F in Eq. (1) yielded a value of $T_{e\parallel} \approx$ 2.2 eV (argon plasma). This value was compared with an electron temperature implied from a velocity measurement made of ion acoustic waves propagating in the plasma column parallel to the magnetic field. The two values agreed within about 30%, the temperature calculated by use of Eq. (1) being the higher.

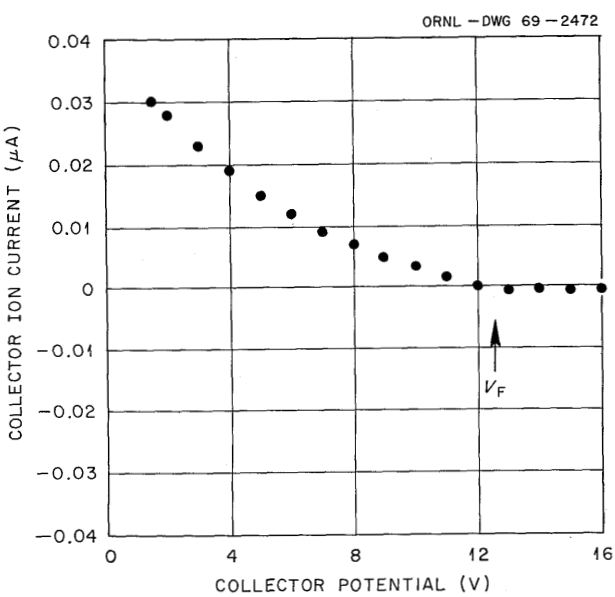

Fig. 7.23. A Current-Voltage Characteristic of the Gridded Probe Used to Determine the Parallel Electron Temperature in a Plasma Column Supported by a Solenoidal Magnetic Field. T_e is simply related to V_F, the collector potential required to stop the most energetic ions accelerated by the plasma sheath surrounding an electrically floating plate.

7.7 FAR-INFRARED LASER-INTERFEROMETER FOR ELECTRON DENSITY MEASUREMENT

C. E. Nielsen[45] J. N. Olsen[46]

7.7.1 Introduction

As electron densities approach 7×10^{13} cm^{-3}, 4-mm microwave diagnostics are limited by cutoff. On the other hand, at shorter wavelengths the 10.6-μ CO_2 laser radiation does not interact usefully with plasmas of less than 10^{15} cm^{-3}. It is of interest then to develop a diagnostic source at an intermediate wavelength (in the far-infrared or submillimeter region), particularly to measure radial electron distributions in Burnout V.

A mercury arc lamp and grating interferometer[47] at 300 μ wavelength has been used to detect densities of 10^{12} to 10^{13} cm^{-3}; however, with the advent[48–51] of the CH_3CN laser at 337 μ, a strong cw coherent source is available. With such a laser and a Michelson interferometer, the Burnout V plasma ($n_e = 10^{13}$, diameter = 5 cm) should provide a 50° phase shift in two passes. Although this method would be more useful and accurate in the 10^{14} to 10^{15} cm^{-3} regime, a 4-mm interferometer can be used in Burnout V as a check.

To this end we have assembled a 35-mW CH_3CN laser operating in a cw mode and a prototype Michelson interferometer with translating mirrors. Preliminary results with this laser-interferometer show phase shifts of about 40° easily; however, an improved method of operation is discussed which makes 10° phase shifts resolvable.

7.7.2 CH_3CN Laser

The laser developed for this work has shown itself to be easily constructed and operated. Ease of construction is due to the very long cyanide

[45]Consultant, Ohio State University, Columbus.

[46]NSF Trainee, Ohio State University, Columbus.

[47]S. C. Brown, G. Bekefi, and R. E. Whitney, *J. Opt. Soc. Am.* **53**, 448 (1963).

[48]H. A. Gebbie, N. W. B. Stone, and F. D. Findlay, *Nature* **202**, 685 (1964).

[49]L. O. Hocker *et al.*, *Appl. Phys. Letters* **10**, 147 (1967).

[50]W. W. Miller and G. T. Flesher, *Appl. Phys. Letters* **8**, 217 (1966).

[51]S. Kon *et al.*, *Annual Report, Institute of Plasma Physics, Nagoya University, April 1966–March 1967*, p. 89.

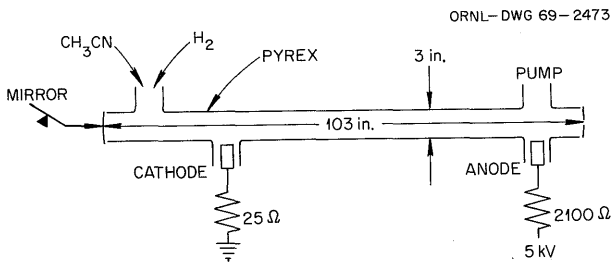

Fig. 7.24. Schematic of CH_3CN Laser.

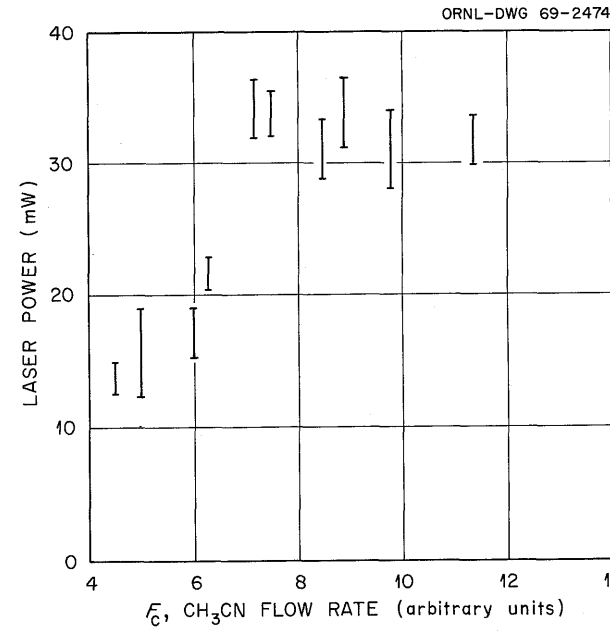

Fig. 7.25. Laser Power as CH_3CN Flow Rate Is Varied.

wavelength of 13.25 mils, which forgives many imperfections in mirror quality. The operating characteristics reflect the strength of the lasing transition, which provides gain over a wide range of CH_3CN and H_2 partial pressures and discharge currents. Let us first consider the physical details, then the resulting output.

The laser cavity (Fig. 7.24) is 103 in. long and of 3-in.-ID Pyrex pipe. The cathode is removed from the mirror at the end to reduce residue formation on the mirror surface; the residue accumulation is much worse near the cathode than the anode. Both the anode and cathode are water cooled, and about 2600 cfm of forced-air cooling protects the glass and O-rings from excessive heating.

Decomposition of the active gas, CH_3CN, necessitates a flowing rather than a closed gas system. The H_2 background gas stabilizes the discharge and has a mass low enough for little collisional deexcitation. The flow rate of each gas and the total pressure are monitored.

The spherically concave aluminum mirrors, which have a 120-in. radius of curvature, are placed 103 in. apart for a less-than-confocal resonant cavity. The anode mirror has a 0.1-in.-diam aperture, providing 2% output coupling[52] of the TEM_{00} mode. The cathode mirror has translational freedom for tuning the cavity resonance. Both mirrors are mounted on flexure plates, which allow adequate alignment to select output only from an axial resonant mode.

Electrical power is supplied by a three-phase, full-wave-rectified Megatherm source with a three-phase, 440-V autotransformer in its primary and a high-voltage vacuum switch in its secondary.

Output power measurements were performed with a platinum resistance thermometer in a Wheatstone bridge circuit. A permanently affixed Cupron heating coil enables direct comparison of radiative with electrical power. Since the slow response of the resistor saturated after a few seconds, the following results were obtained in successive 10-sec discharges. Steady-state operation with a Golay cell shows that these 10-sec discharges may be considered as effectively steady state.

A principal strength of this type of laser is the range of conditions which yield laser action. For example, Fig. 7.25 shows output power vs rate of CH_3CN flow, F_c. The power is observed to rise to a maximum of 36 mW as F_c increases to its middle value and then stays about constant to the maximum flow rate. The vertical bars represent the range of successive discharges. The discharge current was 1.0 A, and when F_c is at its middle value the CH_3CN and H_2 partial pressures are 0.1 and 0.5 torr respectively.

Similarly, Fig. 7.26 shows the variation of output power vs discharge current. The power increases to 40 mW as the current increases to 1.0 A and then remains constant with further increases.

Due to the large diffraction angle of the output power, two 45-in.-focal-length mirrors are used to focus 38% (assuming Fraunhofer diffraction) of the power toward the Michelson detector, 115 in. distant.

[52] A. G. Fox and T. Li, *Bell System Tech. J.* **40**, 453 (1961).

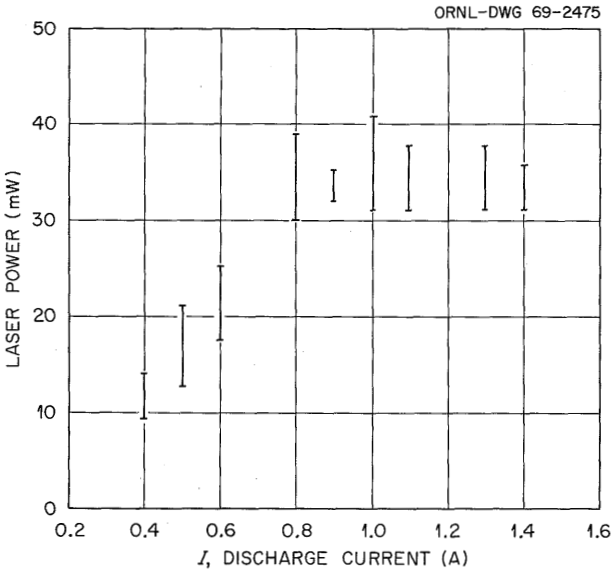

Fig. 7.26. Laser Power as Discharge Current Is Varied. $F_c = 7.0$ throughout.

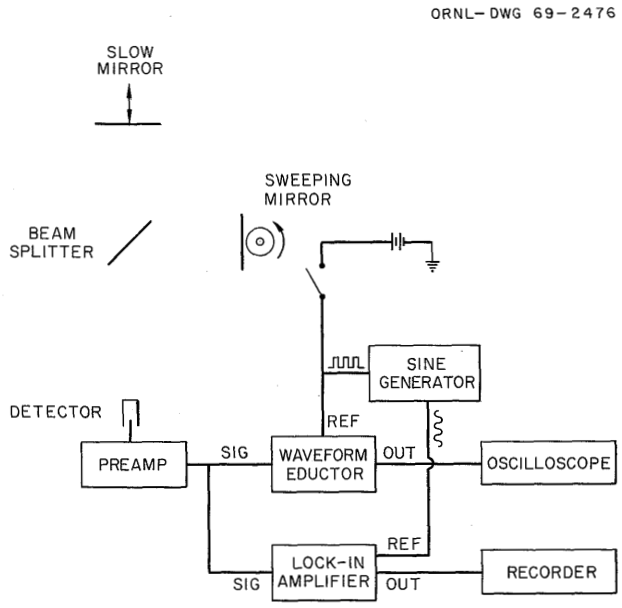

Fig. 7.27. Michelson Interferometer.

7.7.3 Michelson Interferometer

A prototype interferometer has been assembled with Mylar beam splitter and translating mirrors to test a combined laser-interferometer system and especially to establish a lower limit to detectable phase shifts. A brief description of the apparatus precedes some preliminary results and discussion of a method to resolve a few degrees of phase shift.

All components of the interferometer, Fig. 7.27, are mounted upon a cross of 5-in. aluminum channel. The mirrors can then be up to 30 in. from the beam splitter. The 2-mil Mylar beam splitter is chosen[53] to maximize the signal power to 50% of incident power for radiation polarized parallel to the plane of the cross.

The 4-in.-diam mirrors and their micrometer adjustments are each mounted atop two 20-mil flexible plates which enable translation while maintaining alignment. The "slow" mirror is driven by a differential screw through small distances to simulate plasma-induced phase shifts. The "sweeping" mirror is driven by an eccentric wheel rotating at 5 Hz. Its axle is $\lambda/4$ (3.3 mils) off center for a total travel of $\lambda/2$. Thus it sweeps through two fringes per revolution, or 10 fringes per second.

Because of the sweeping mirror's cyclic motion the phase shift due to the slow mirror (or plasma) is carried in the harmonic content of the interferometer signal. This is in contrast to the usual uniformly translating mirror signal, which would be a cosine function shifted in time. The signal, P, can be Fourier decomposed to sums of even and odd harmonics of 5 Hz. Let ϕ_p be the plasma or mirror phase shift:

$$P = P_0 + \cos 2\phi_p \sum_{\text{even}}^{n} a_n \cos 2\pi n 5t$$

$$+ \sin 2\phi_p \sum_{\text{odd}}^{n} b_n \cos 2\pi n 5t \, .$$

Using a Golay cell[54] pneumatic detector, some preliminary results have been obtained which confirm the above analysis. Figure 7.28 shows the signal from the Golay cell during two successive discharges of the laser where the slow mirror is used to impart a phase shift of about 40°. The appearance of a 10-Hz component is clearly visible in the bottom trace. Similar results have been found using a triglycine sulfate ferroelectric crystal and a P.A.R. Waveform Eductor.

This suggests a sensitive method of plasma phase-shift detection that can resolve as little as

[53] J. E. Chamberlin *et al.*, *Infrared Phys.* **6**, 195 (1966).

[54] Loaned by E. E. Bell, Ohio State University.

ORNL – DWG 69 – 2477

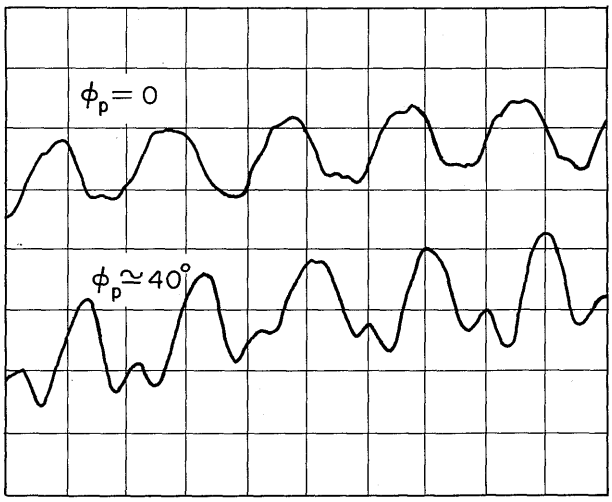

Fig. 7.28. Response of Golay Detector to Laser-Interferometer. Vertical scale is 0.5 mV/cm; horizontal scale is 100 msec/cm.

10° shift. Referring again to Fig. 7.27, one mechanically triggers a sinusoidal reference voltage at 5 Hz. Beating this against the detector signal in a P.A.R. lock-in amplifier, the reference voltage phase is set to maximize the response to the $b_1 \cos 2\pi 5t$ component. Then the slow mirror is driven until $\sin 2\phi_p$ nulls out this component. The plasma density is changed, departure from null is observed, and the slow mirror is moved to renull. The movement can be calibrated; thus $\Delta\phi_p$ is known. This null-renull procedure has the advantage of high sensitivity to ϕ_p but insensitivity to changes in laser output.

7.7.4 Conclusions

The basis for future work is twofold. First, the CH_3CN laser is a reliable cw source of 337-μ radiation with about 35 mW output. Second, the prototype interferometer behaves as expected in preliminary results, showing a 40° phase shift clearly and transmitting a substantial fraction of laser power as signal.

The laser-interferometer system will be adapted to the Burnout V machine, where an $\int n_e \, dl$ of 5×10^{13} electrons/cm^2 will impart a two-pass phase shift of 50°. This should be measurable to about 20% by the proposed null-renull method.

7.8 PLASMA STABILIZATION

E. D. Shipley O. C. Yonts

7.8.1 Introduction

We have previously reported[55] some interesting characteristics of the symmetric arc and the tuned end-wall Penning ion gage. Our original motivation – to increase the electron transport across the magnetic field by using special boundary walls – is satisified by both of these experiments. Our primary effort during the past year has been to try to understand the mechanism by which electrons are transported across the magnetic field.

7.8.2 Experiments

Figure 7.29 shows a schematic of a typical symmetric arc. This discharge is surrounded by a cylinder having a diameter of 3 in. (2- and 4-in. cylinders are also used). The cylindrical symmetry permits Maxwell's electromagnetic theory to be readily applied. The dc potential of the cylinder with respect to ground (bias) can be varied by means of the power supply shown.

The anode can be operated either grounded or as an insulated reflector. Calorimetric measurements can be made of the power reaching this electrode. A typical Faraday cup is shown in the right-hand end wall. The end walls also had several insulated tiny circular areas or surface probes (not shown) having a diameter equal to that of the Faraday cup hole. Langmuir probes were used outside the cylinder to monitor currents.

When the cylinder is biased negatively an ion current flows to the cylinder from the discharge. For an argon discharge at 150 V, 2 A, and 3000 G, the maximum ion current of 200 mA is obtained for –200 V on the cylinder.

When the cylinder is biased positively (argon as above) a large electron current having no bursts flows to the cylinder. A typical characteristic curve is shown in Fig. 7.30. If the reflector is grounded, probe measurements have shown that as the electron current to the cylinder increases, the electron current to the grounded reflectors decreases. The net increase in current to the end

[55] *Thermonuclear Div. Semiann. Progr. Rept. Oct. 31, 1967*, ORNL-4238, p. 93.

ORNL-DWG 68-1940R

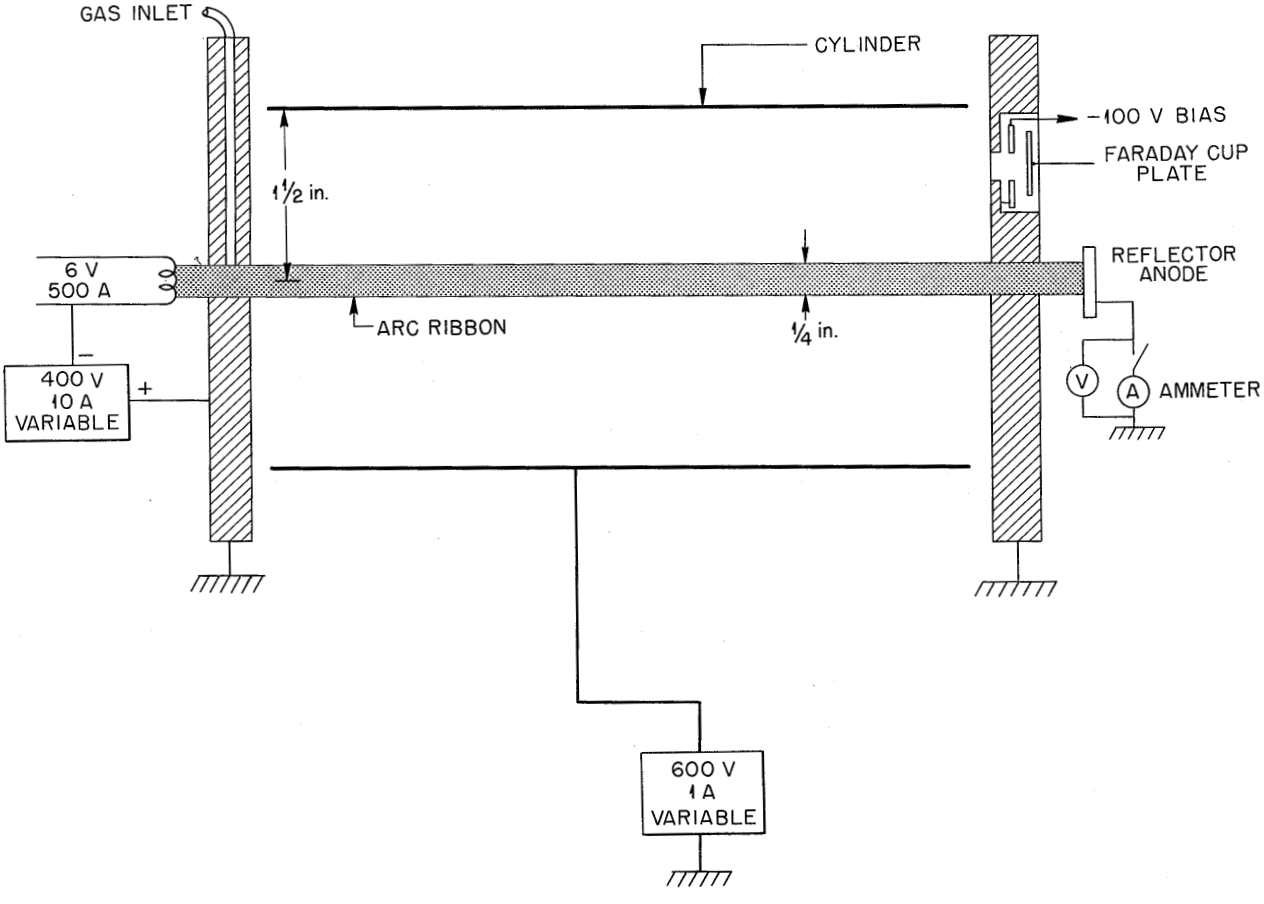

Fig. 7.29. Symmetric Discharge Schematic.

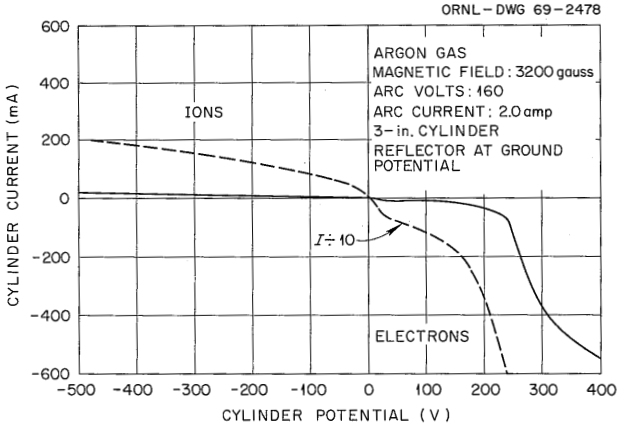

Fig. 7.30. Typical Characteristic Curve for Symmetric Arc.

walls and the cylinder is equal to the decrease in current to the grounded reflector. Approximately one-half the decrease in current to the grounded reflector goes to the cylinder.

When this characteristic was first observed, we thought that the pigging electrons inside the positive cylinder produced ions and electrons by ionization, with the ions going to the end walls and the electrons to the cylinder at equal rates. This, however, is not the case. Use of Faraday cups in the end walls gave an integrated ion current of only 2 mA when some 750 to 1000 mA of electrons were going to the cylinder. We found also that a decrease in electron current to the grounded reflector mentioned was not due to an increase in ions reaching it; calorimetric measurements showed that

the power reaching this electrode decreased with decreasing current. Small surface probes, having a diameter equal to the Faraday cup hole size, mounted flush with the surface of the end walls, gave an integrated wall ion current of approximately 100 mA. Corresponding electron currents to the cylinder were as above, 750 mA or more. The 50/1 ratio of ion current to the wall for surface probe compared with the Faraday cup shows that the ions have transverse energy and are caught by the side of the hole into the Faraday cup. Approximately 98% of the ions have an energy greater than 1 eV for argon.

Langmuir probes placed outside the cylinder show current values down by a factor of 100 over those inside. Surface probes were also used to check discharge from the cylinder ends; there was no detectable discharge.

From the above we conclude that the electrons collected at the cylinder must largely originate in the central arc. The central arc thus acts as a source of electrons, and the cylinder acts as a sink.

7.8.3 Discussion

We seek to explain these large electron transport rates by classical processes since there is so little ionization in the volume and the cylinder current shows no bursts.

The classical diffusion equations for ions and electrons are:

$$F^+ = -D_\perp^+ \frac{\partial n^+}{\partial r} - \mu_\perp n^+ \frac{\partial v}{\partial r}, \tag{1}$$

$$F^- = -D_\perp^- \frac{\partial n^-}{\partial r} - \mu_\perp^- n^- \frac{\partial v}{\partial r}, \tag{2}$$

where F^+ is ion flux, $D_\perp^+$ is ion diffusion coefficient perpendicular to the magnetic field, $\partial n^+/\partial r$ is the radial ion density gradient, $\mu_\perp^+$ is the ion mobility perpendicular to the magnetic field, n^+ is the ion density, and $\partial v/\partial r$ is the radial potential gradient. Terms in Eq. (2) are the same except for electrons. Centimeter-gram-second units are used in all calculations. Equation (1) can easily give our low value for ion flux if there is a positive potential gradient to balance a negative density gradient.

The trouble is with Eq. (2) for electron flux. Both diffusion and mobility are in the same direction but cannot give the large flux observed (10^{16} cm^{-2} sec^{-1} at the cylinder). ($D_\perp^-$ has a value between 1 and 10^3, depending on electron temperature and neutral density.) The diffusion term cannot contribute to the electron transport, since $\partial n^-/\partial r$ is of order 1.

A not too unreasonable value for $\mu_\perp$ is -10^2, and n^- might be as large as 10^{13} cm^{-3}, so the mobility term could satisfy the electron flux if the value of $\partial v/\partial r$ is $+10$ cgs units or 3000 V/cm.

It is difficult to imagine how this large potential gradient can exist over the entire distance from arc to cylinder (almost 5 cm for a 4-in.-diam cylinder). We therefore consider another explanation calling on time-varying electric and magnetic fields which are due to both space charge and space currents.

7.8.4 Theory

The radial component of electron flux is due to variation in the magnetic field H_Z as well as to mobility. The radial component of electron flux due to time-changing magnetic field can be written as

$$F_H^- = n^- \frac{E_\phi}{H} C, \tag{1}$$

where n^- = electron density, H = total magnetic field, $C = 3 \times 10^{10}$ cm/sec, E_ϕ = azimuthal component of electric field defined by the following Maxwell's equation:

$$-\frac{1}{C}\frac{\partial H_Z}{\partial t} = \mathrm{curl}_Z\, E = \frac{1}{r}\frac{\partial}{\partial r}(rE_\phi) - \frac{\partial E_R}{\partial \phi}$$

$$= \frac{1}{r}\frac{\partial}{\partial r}(rE_\phi), \tag{2}$$

since circular symmetry is assumed.

Here H_Z is the Z component of magnetic field arising from the azimuthal drift current density. To calculate the azimuthal drift current density μ_ϕ, we use:

$$\mu_\phi = k|I|n^- \frac{E_R}{H} C, \tag{3}$$

where $|I| = 4.8 \times 10^{-10}$ esu and E_R is radial component of electric field. The factor k permits a nonvanishing azimuthal drift current density due to different azimuthal drift velocities for ions and

electrons ($n^+ \approx n^-$). The value for k is greater than -1 and less than $+1$, depending on the shape of the negative potential well. k is positive when the potential gradient, equal to $-E_R$, increases with increasing r. k is negative when potential gradient decreases with increasing r. A small value for $|k|$ implies that the ion drift velocity almost matches the electron drift velocity. A large value, near unity, for $|k|$ implies a large disparity in these drift velocities.

The following Maxwell equation relates μ_ϕ to H_z:

$$\frac{4\pi\mu_\phi}{C} = \frac{4\pi k|l|n^-}{H} E_R = -\frac{\partial H_z}{\partial r} . \tag{4}$$

The radial component of electron flux due to mobility is defined as follows:

$$F_\mu^- = -|\mu_\perp^-| n^- E_R . \tag{5}$$

The total radial component of electron flux is the sum of Eqs. (1) and (5):

$$F^- = F_H^- + F_\mu^- . \tag{6}$$

The above six equations define and describe the two types of electron transport across the magnetic field. The intuitive idea is that Eq. (6) can give rise to a large radial electron flux due to cyclic but nonturbulent electric and magnetic fields.

The continuity of electron transport requires the following equation be satisfied:

$$-\frac{\partial n^-}{\partial t} = \frac{1}{r}\frac{\partial}{\partial r}(rF^-) = \frac{1}{r}\frac{\partial}{\partial r}(rF_\mu^-) + \frac{1}{r}\frac{\partial}{\partial r}(rF_H^-) . \tag{7}$$

The first term on the right-hand side of Eq. (7) is:

$$\frac{1}{r}\frac{\partial}{\partial r}(rF_\mu^-) = -|\mu_\perp^-| \frac{1}{r}\frac{\partial}{\partial r}(rn^- E_R)$$

$$= |\mu_\perp^-| \frac{H}{4\pi k|l|} \cdot \frac{1}{r}\frac{\partial}{\partial r}\left(r\frac{\partial H_z}{\partial r} Z\right) . \tag{8}$$

The second term on the right-hand side of Eq. (7) is:

$$\frac{1}{r}\frac{\partial}{\partial r}(rF_H^-) = \frac{C}{H}\frac{1}{r}\frac{\partial}{\partial r}(n^- rE_\phi) = \frac{CE_\phi}{H}\frac{\partial n^-}{\partial r}$$

$$+ \frac{Cn^-}{H}\frac{1}{r}\frac{\partial}{\partial r}(rE_\phi) = \frac{CE_\phi}{H}\frac{\partial n^-}{\partial r} - \frac{n^-}{H}\frac{\partial H_z}{\partial t} . \tag{9}$$

Substituting Eq. (8) and Eq. (9) into Eq. (7) gives

$$-\frac{\partial n^-}{\partial t} = \frac{CE_\phi}{H}\frac{\partial n^-}{\partial r} - \frac{n^-}{H}\frac{\partial H_z}{\partial t}$$

$$+ \frac{|\mu_\perp^-| \cdot H}{4\pi k|l| r}\frac{\partial}{\partial r}\left(r\frac{\partial H_z}{\partial r}\right) . \tag{10}$$

The introduction of the factor k seems to be an essential step in the formulation of this problem of electron transport. Since k can be a function of t, the analytical work is difficult. Special cases are being examined which may serve to better identify this electron transport mechanism.

8. Toroidal Multipoles

I. Alexeff W. Halchin
R. A. Dory M. Roberts
W. L. Stirling

8.1 INTRODUCTION

An exciting development in fusion physics has been the production of an apparently stable plasma, usable for detailed studies, in the toroidal multipole magnetic field configuration. One important limitation of the toroidal multipole plasma containment experiments of Dory,[1] Ohkawa,[2] and Eckhartt[3] is the presence of mechanical supports holding the internal conducting hoops that generate the multipole magnetic field; these supports can be a dominant plasma loss mechanism (due just to collisions), and apparently effective shielding is not yet possible.[4]

One scheme to eliminate these obstacles to the plasma is to use electromagnetic levitation to support the internal conductors. The earlier toroidal multipole experiments[1–3] had used octopole configurations (four hoops) with internal supports; and though the early levitron[5] experiments utilized levitation, it was of only a single hoop (dipole), a less favorable confinement geometry.

The ORNL toroidal multipole program is involved with experiments of plasma confinement in two magnetic geometries with levitated internal conductors: the quadrupole and the hexapole. A sketch of the quadrupole configuration is shown in Fig. 8.1.

Our device is a coplanar toroidal quadrupole using liquid-nitrogen-cooled copper liner and hoops with a mean hoop circumference of 1 m. The magnetic field is inductively coupled at 60 Hz. In these experiments, there were 22 gyroradii for 100-eV electrons and ~5 gyroradii for ions of ~1 eV between ψ_s and ψ_c at the outer bridge (the weakest place in the field).

ORNL-DWG 68-12141A

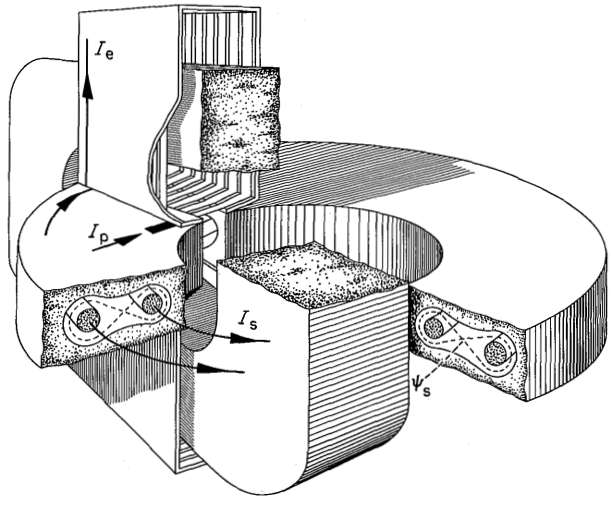

Fig. 8.1. Schematic Drawing of the ORNL Levitated Toroidal Quadrupole, Showing the Primary (I_p), Secondary (I_s), and Eddy (I_e) Currents and the Magnetic Separatrix (ψ_s).

[1] R. A. Dory *et al.*, *Phys. Fluids* **9**, 997 (1966).

[2] T. Ohkawa *et al.*, p. 531 in *Plasma Physics and Controlled Nuclear Fusion Research*, vol. II, IAEA, Vienna, 1966.

[3] D. Eckhartt *et al.*, p. 719 in *Plasma Physics and Controlled Nuclear Fusion Research*, vol. II, IAEA, Vienna, 1966.

[4] H. K. Forsen *et al.*, *Bull. Am. Phys. Soc.* **13**, 266 (1968).

[5] S. A. Colgate and H. P. Furth, UCRL-5392 (1958).

8.2 QUADRUPOLE EXPERIMENTS WITH A MICROWAVE-GENERATED PLASMA

8.2.1 Comparison of Dipole and Quadrupole Magnetic Configurations

Since filling with microwave generation is more uniform than with plasma guns[6] (and uniform filling is important) and production on a specified Mod B surface is possible with microwave heating, we began to use the easily generated electron cyclotron resonance plasmas with pressures near 8×10^{-5} torr. We have been investigating the effect of the quadrupole magnetic well by removing the inner hoop, so we can measure plasma properties with and without the magnetic well, that is, in a quadrupole and in a dipole. The ion saturation current profiles for plasma in the dipole and for comparison in the quadrupole are presented in Fig. 8.2. Plasma is detected up to and through the wall, because there is a large access hole which allows the 1.5-kG magnetic field to leak out a considerably long distance. A probe current of 50 μA indicates a density of 10^{10} cm^{-3} when the ion velocity is taken to be $(3kT_e/m_i)^{1/2}$ with $T_e = 30$ eV.

[6]M. Roberts *et al.*, *Phys. Letters* **26A**, 590 (1968); M. Roberts *et al.*, *Thermonuclear Div. Semiann. Progr. Rept. Oct. 31, 1967*, ORNL-4238, p. 96.

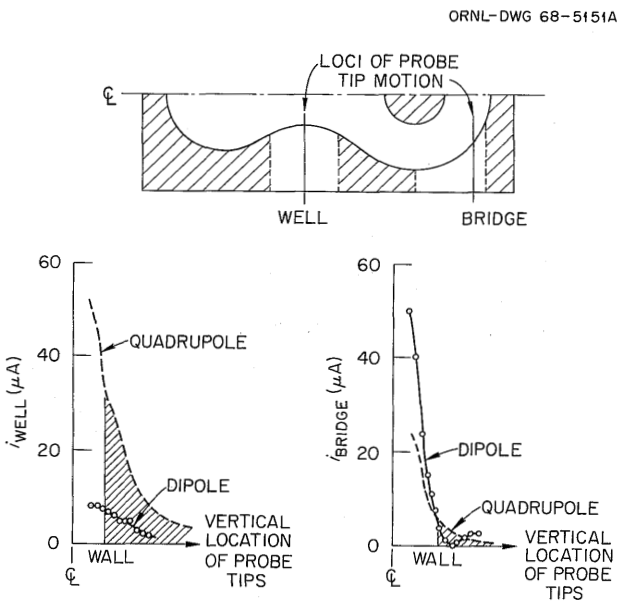

Fig. 8.2. Comparison of Dipole and Quadrupole Ion Saturation Current Profiles.

A summary of the results with the quadrupole and the dipole for the $\lambda = 12$ cm ($P = 40$ W) hydrogen plasma is listed in Table 8.1. The calculation of τ_{Bohm} in Table 8.1 does not take into account the change in density gradients between quadrupole and dipole, evident[7] in Fig. 8.2. If one can assign a factor 3 difference between scale lengths, then τ/τ_{Bohm} for the dipole can approach unity, and the full improvement of $\tau/\tau_{Bohm} = 40$ can be credited to the magnetic well. The fluctuation level in the quadrupole is a constant ($\Delta n/n = 0.05$) in the well region along the probe's line of motion but varies in the bridge region from 0.10 near the center line to 0.25 near the wall, corresponding to the crossing from stable region to unstable region. In a similar experiment with a $\lambda = 3$ cm plasma (in the second model, described in Sect. 8.2.2), T_e and τ each increased a factor of 3 when the dipole was made into a quadrupole. The average well is therefore essential to improving confinement time and density and to reducing fluctuation levels. This is, as far as we know, the first direct demonstration that the average well of multipoles causes a significant confinement enhancement.

Table 8.1. Comparison of $\lambda = 12$ cm Microwave Plasmas in Two Magnetic Configurations

	Quadrupole	Dipole
T_e, ev	30	15
τ, μsec	30	15
τ/τ_{Bohm}	30	$\lesssim 8$
n, cm^{-3}	$8 \cdot 10^9$	$2 \cdot 10^9$
Fluctuation level, $\Delta n/n$		
Well	0.05	>0.25
Bridge	0.10–0.25	>0.25

8.2.2 Comparison of First and Second Model Quadrupole Cavities

A comparison of plasma profiles between two quadrupoles with $\lambda = 12$ cm microwave plasma is

[7]The assistance of T. K. Fowler (Lawrence Radiation Laboratory, Livermore, Calif.) in pointing out this aspect of the data is greatly appreciated.

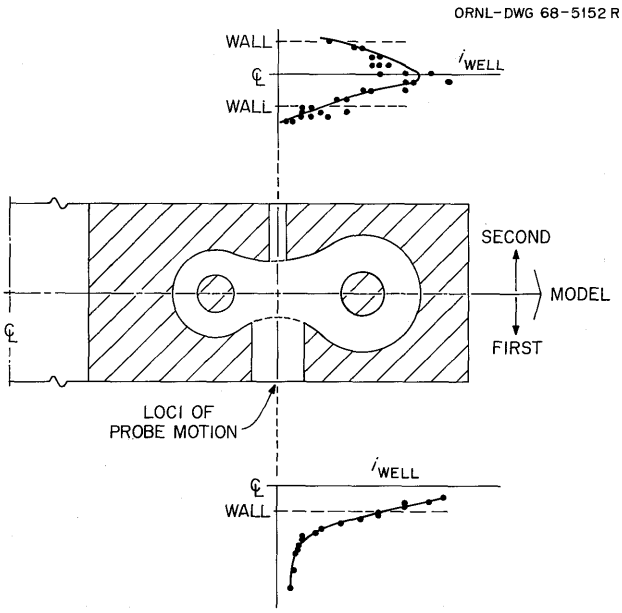

Fig. 8.3. Improvement of Plasma Profile in the Quadrupole by Reduction in the Size of the Access Holes.

indicated in Fig. 8.3, shown in the lower and upper halves of the figure. The first model was used for early experiments, and the second model is presently in use for $\lambda = 3$ cm experiments. The differences are two: first, the access holes, which were $\frac{3}{4}$ in. in diameter in the first model, became $\frac{1}{4}$ in. in the second model, greatly reducing the leakage of both the magnetic field and the plasma; and second, the protruding hump in the first model has been flattened out considerably in the second model for better shaping of the field and to increase the volume of the magnetic well.

8.2.3 Electron Temperature Determination in the $\lambda = 3$ cm, 200-W Microwave Plasma

The confinement of hot-electron ($T_e \gg T_i$) hydrogen plasmas produced by $\lambda = 3$ cm microwave heating is being studied in the levitated toroidal quadrupole. Considerable emphasis has been placed on making a reliable estimate of T_e. Table 8.2 summarizes these results.

When resonant microwave heating is pulsed on, the probe current e-folding buildup time is of order 20 μsec. From the growth rate, $dn_i/dt = n_g \cdot n_e \cdot \sigma_{ionization} \cdot v_{electron}$, and assuming $n_e = n_i$, we calculate that σv is about 5×10^{-8} cm^3/sec (the highest value σv can have), giving a lower limit to the electron temperature of order 100 eV. This is result C in Table 8.2.

Table 8.2. Plasma Electron Temperature Determination

A. X-ray emulsion absorption	$\approx$1–3 keV
B. Double-probe characteristics	>100 eV
C. Probe current buildup time	$\gtrsim$100 eV
D. Four gyroradii across flux bridge	<3 keV
E. Incident microwave power fully used	$\approx$0.3–3 keV

The characteristic curves on the double probes placed in the well but near the heating zones show essentially straight-line behavior up to the maximum applied bias voltage of 300 V, implying that $T_e > 150$ eV. This is indicated as result B in Table 8.2. On the left-hand curve of Fig. 8.4, it is clear that breakdown is occurring over 200 V. These data were taken with microwave power on. Not shown, but at the microwave turnoff, the signal amplitudes do not drop rapidly; they have smooth decays, indicating that at least for the first half e-folding time the temperature remains reasonably constant. From the analysis of probe signal decays after microwave turnoff, we find that the decay time constant is 80 to 100 μsec in the magnetic well and is over 200 μsec in back of the outer bar.

This decay measurement is made when the heating takes place at the inner bar, so that the longer decay accompanies the measured lower temperature in the nonresonant zone. Considering $dE/dt = n_g \cdot \sigma_{excitation} \cdot v_{electron} \cdot \Delta E_{excitation}$, the 80-$\mu$sec decay of T_e (shown on the right side of Fig. 8.4) is consistent with cooling on the background gas by excitation or ionization processes. The measured light signals have nearly the same decay time constant as the probe signals do, further corroborating the fact that electrons with $T_e > 13.6$ eV do exist after microwave turnoff. Following microwave turnoff, increases in the probe current are frequently measured after a 10- to 15-μsec delay; these increases are possibly a result of ionization caused by the remaining hot electrons. After the initial buildup of light and probe signals, the light flux is constant, indicating a constant production rate of plasma particles. Since the current probe

ORNL-DWG 68-6018A

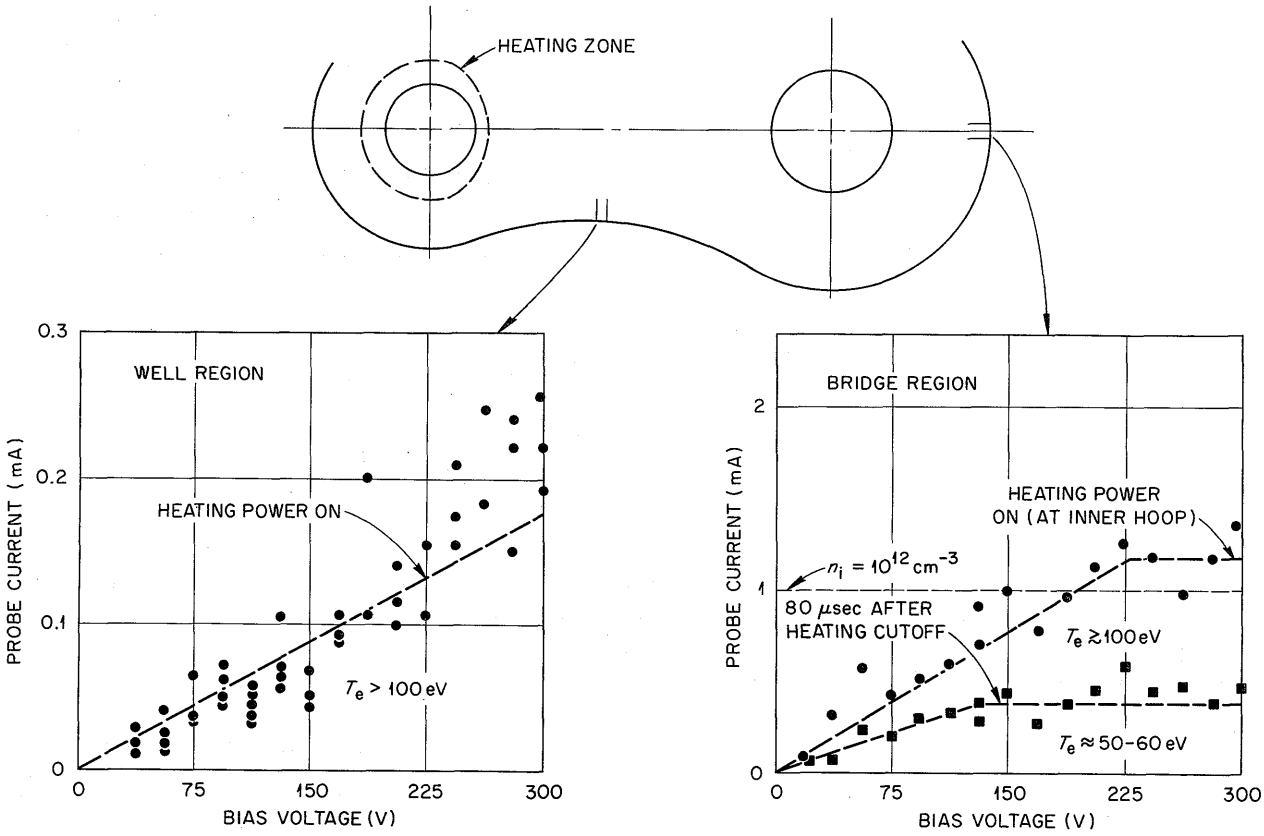

Fig. 8.4. Electron Temperature Measurements in the Magnetic Well and in the Flux Bridge.

signals limit after buildup, this suggests there is an increase in the loss rate at higher densities.

An upper limit to the electron energy can be made by studying the x-ray spectrum using personnel monitoring type x-ray film. In a graded absorption measurement, it was possible to bracket the energy of the x rays (and, hence, the electrons) that caused the image to be on the order of 1 to 3 keV. Of course, this upper limit may apply to only a small fraction of the plasma density. This is the basis for result A in Table 8.2.

Calculating that all the incident microwave power (≈100 W) put into the cavity goes into heating ($n_e \approx 10^{11}$ cm^{-3}) plasma electrons (in 40 μsec), then an upper temperature limit is reached on order 300 eV (or 3 keV if n_e hot = $0.01 n_e$ total). This is result E in Table 8.2.

The final determination of the upper limit is made in terms of the gyroradius of hot electrons. With 1 cm of space between hoop and wall at the bridge and an average of 2 kG magnetic field, 15-keV electrons could have two gyroradii on each side of the separatrix. Assuming these highest-energy electrons to be about $5kT_e/e$, one finds a $T_e \sim 3$ keV (shown as result D in Table 8.2).

These five determinations seem to bracket the electron temperature during the heating and for at least a short time after the heating is turned off to be in the range between 100 and 1000 eV. Using the lower, more pessimistic number and the average value for the magnetic flux as determined by Hobbs and Taylor,[8] the Bohm time is about 2 μsec. Since the decay time is on the order of 80 to 100 μsec, the conservative τ/τ_{Bohm} is on the order of 40.

[8] G. D. Hobbs and J. B. Taylor, *Plasma Phys.* **10**, 207 (1968).

8.2.4 Change in Heating Zone

The computed Mod B contour plots shown schematically in Fig. 8.5 and more accurately in Fig. 8.15 indicate that as the magnitude of the hoop currents increases, there will be a heating zone first encircling the inner bar and then, second, an additional zone encircling the outer hoop. The appearance of the second zone comes when the inner hoop resonance zone intercepts the cavity wall and is essentially confined to a vertical line spaced between the inner hoop and the field zero.

Figure 8.5 illustrates the positions of the heating zones, gives a clear example of the plasma signals in each of the bridge regions, and indicates how they appear out of phase with each other. A probe in the magnetic well region seems to indicate an average (or sum) of the two outer probes, plus transients at the times of heating zone change.

Light signals were measured in the well region and in a bridge region. As the magnetic field varied, the light in the well region took on the same time variation as the well probe. The outer bridge light occurred only when the heating zone was encircling the outer bar.

ORNL-DWG 68-6015R

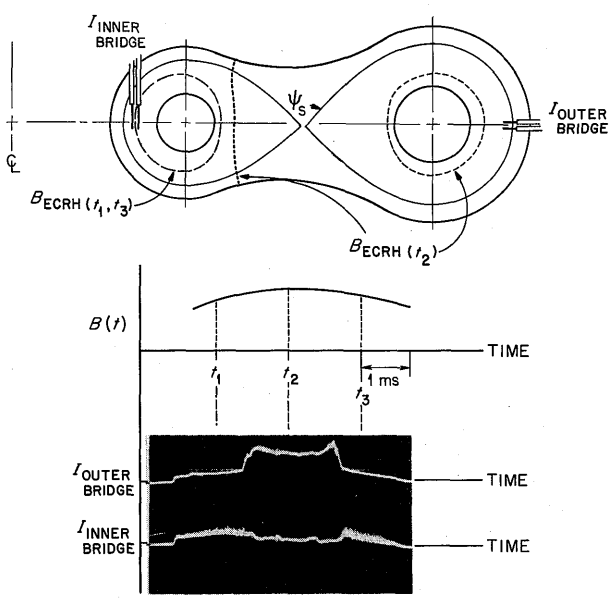

Fig. 8.5. Probe Currents Showing the Effects of Changing the Microwave Resonance Zones. Note the positions of the electron cyclotron resonance heating (ECRH) zones with time.

Thus it appears that a probe in each of the resonance regions (within the separatrix) sees mostly that plasma contained on the self-flux. The two regions are connected, however, by the 20% mutual flux (the other 80% is private to each hoop), and current from the plasma in the neighboring bar's zone does appear on the probe curves as a smaller signal. The time constant for the density in the outer heating zone to drop when the heating zone vanishes into the bar is on the same order of magnitude as the decay time when the microwave power is pulsed off. A second set of hoops (indicated on Fig. 8.15) designed to have 50% mutual flux was built but has not yet been installed.

The fluctuation amplitude appears to accompany the heating zone; that is, the outer bridge probe shows 40-kHz noise when a heating zone encircles the outer bar and not when it is around the inner bar and vice versa for the probe around the inner bridge (see probe currents in Fig. 8.5).

Statistical evidence from x-ray films exposed to various (upper) parts of the cross section at many azimuths indicates that most of the x-ray production is in the region directly above and to each side of the bars but not in the center, the magnetic well region. This implies that the hot electrons are confined to the resonance zones or to the mirror regions and produce x rays there.

8.2.5 Obstacle Experiments in the Microwave-Generated Plasma

A set of experiments was undertaken to determine the effect on the plasma properties of obstacles placed in the quadrupole field. In general, obstacles are defined as objects intersecting some, but not all, flux lines between hoop and wall at one radius; supports, on the other hand, cut all flux lines between hoop and wall. With a $\frac{1}{4}$-in.-diam bar or obstacle located at B (Fig. 8.6), the current signal on a fixed-position double probe placed directly above the obstacle was measured as a function of the bar's vertical position. Resonance heating was taking place around the inner hoop prior to the microwave power cutoff, and the probe amplitude readings were normalized with respect to another probe placed in the wall 105° in azimuth away, minimizing the effects of shot-to-shot fluctuations.

There is no significant decrease in plasma lifetime caused by the introduction of the obstacles at

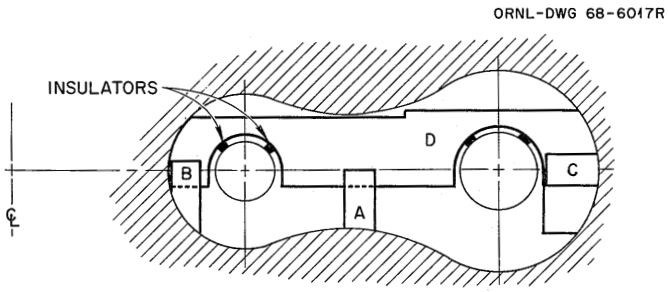

Fig. 8.6. The Effects of Different Conducting Obstacles Placed in the Magnetic Field. (*A*) Little effect. (*B* and *C*) Alters production rate locally: at probe $\left\{\begin{matrix} <1\text{ cm} \\ \approx 3\text{ cm} \\ =8\text{ cm} \end{matrix}\right\}$ from obstacle, probe current is $\left\{\begin{matrix} \text{decreased} \\ \text{increased} \\ \text{unchanged} \end{matrix}\right\}$. (*D*) Prevents formation of plasma.

B or *C*. This implies that the presence of the bar is affecting only the plasma production rate or the microwave field pattern as manifested by the steady-state current amplitude and not the loss rate as determined from the plasma lifetime. Since this effect is strongest in the immediate vicinity of the bar, one concludes that the production by microwave resonance is a local phenomenon occurring uniformly around the machine.

As a second experiment, a similar bar (*C*) was pushed in to touch the outer hoop as a dummy support. Once more the effect of the bar on the steady-state amplitude was maximum in the neighborhood of the disturbance.

A 1-cm-thick conducting obstacle (insulated from the hoops), shown as *D* in Fig. 8.6, was placed 180° from the microwave port and 90° from a set of probes. The plasma is prevented from forming and then forms alternately with the frequency of vibration of the hoops ($f_v \approx 16$ Hz) as the hoops are and are not touching the obstacle. With the obstacle cutting all flux lines, the plasma-forming hot electrons can live at most one or two machine transits, a time (a few microseconds) that is less than the exponentiation buildup time (40 to 50 μsec).

Another, even more drastic, step with even clearer results is the experiment performed by pressing the hoops against the bottom of the cavity with the resonance field energized. No plasma is detected on any probe in this case, demonstrating that plasma completely encircles the hoops on poloidal field lines.

8.2.6 Effects of Introducing Supports

Most existing toroidal multipole confinement experiments[1–3,9] differ from ideal conditions by the presence of hoop supports, by the resistively generated electric fields along the hoops, and by the low magnetic fields (i.e., a few gyroradii across) used. Recent careful experiments[10] in supported hoop octopoles have measured electric fields set up by the presence of the hoop supports, that is, an effect not directly related to support size.

In this work, we try to determine the effect of supports in our levitated device filled with an $n \cong 10^{12}$ cm^{-3}, $T_e = 100$ eV, $\tau_{decay} \cong 80$ μsec microwave resonance generated plasma. The supports were introduced as three sets of insulated wire shafts (through vertical holes in the hoops), along which the hoops rose from rest to the central portion of the cavity. Floating double probes were placed at different azimuthal, cross-sectional, and radial positions, and the values of nv, T_e, and τ were averaged over a number of shots for each variation in support size. Photodiodes were used to monitor the visible light from the plasma. Up to 1 kW of $\lambda = 3$ cm microwave fields were used to produce the plasma in a background of 7×10^{-5} torr of hydrogen. Figure 8.7 shows the behavior of the normalized loss rate [τ_{Bohm} is here strictly a normalizing constant equal[8] to $16(Br^2)e/kT_e$] as a function of normalized size of the supports. For reference, the approximate area ratios of some other multipole experiments are given. Shot-to-shot fluctuations are not shown here, since the greatest uncertainty arises from the temperature measurement. Direct numerical values come from the electrostatic probe characteristics, which show saturation at about 90 eV for the triangle point and no saturation up to 100 eV for the circular points, for which a lower limit of about 100 eV is used. Supporting evidence that the probe interpretation is meaningful comes from saturation data showing a reduction in temperature from $T_e \gtrsim 100$ eV to 50 eV in the expected cooling time of about 80 μsec. Corroborating electron temperature determinations come from the plasma buildup time, yielding a value for $(\sigma v)_{ionization}$ consistent with T_e greater

[9] A. N. Dellis *et al.*, *Bull. Am. Phys. Soc.* **13**, 1527 (1968).

[10] J. A. Schmidt and G. L. Schmidt, *Bull. Am. Phys. Soc.* **13**, 1526 (1968).

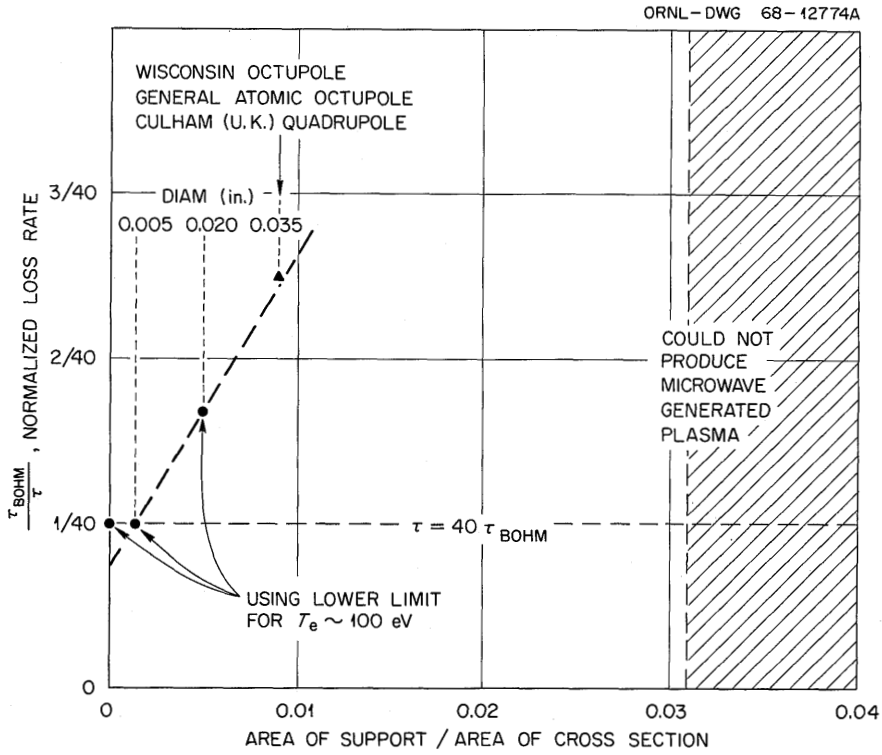

Fig. 8.7. Effect of Support Size on Plasma Loss Rate. The approximate area ratios of some other multipole experiments are given: Wisconsin octopole, R. A. Dory *et al.*, *Phys. Fluids* 9, 997 (1966); General Atomic octopole, T. Ohkawa *et al.*, p. 531 in *Plasma Physics and Controlled Nuclear Fusion Research*, vol. II, IAEA, Vienna, 1966; Culham (U.K.) quadrupole, A. N. Dellis *et al.*, *Bull. Am. Phys. Soc.* 13, 1527 (1968).

or equal to 80 eV, assuming the buildup time is determined solely by ionization phenomena. Total power and magnetic geometry considerations set upper limits on the order of 1 keV, consistent with the photographic film x-ray data also. With the hoops levitated freely, there is a radial loss, indicated by the vertical intercept, that is apparently not altered significantly by the introduction of the set of smallest supports; that is, the radial loss dominates the small (5-mil-diam) support loss. The 20-mil supports do reduce the lifetime measurably, and the 35-mil supports reduce both τ and T_e measurably. Density remains approximately constant at $n_e = 10^{12}$ cm^{-3} ($\omega_{pe} \sim \omega_{cutoff}$) as determined from a double probe in the manner suggested by Chen, Etievant, and Mosher.[11]

We have found that the presence of the electrostatic probes inside the plasma chamber can make as significant an effect upon the T_e and τ results as do the supports; therefore we made measurements with the probes at the periphery of the machine. The straight-line fit to the data can correspond to a sum of the classical single-particle support loss, in which τ_{Bohm}/τ is proportional to the area of support, and a radial loss (represented by the vertical intercept) that is independent of supports. The precision of the data is, however, insufficient to show any enhancement over the direct support loss attributable to any radial loss caused by the presence of the supports (e.g., convective cells caused by supports). The simple theory requires $B \times \nabla B$ drifts, which should reverse with reversed B (which we do not see). With even larger supports than shown, the plasma could not be produced (as indicated by the shading), apparently due to insufficiently long mean free path in which to acquire ionization energy.

It is indicated above that in this quadrupole with a $\lambda = 3$ cm microwave-generated plasma having a

[11] F. F. Chen, C. Etievant, and D. Mosher, *Phys. Fluids* 11, 811 (1968).

τ/τ_{Bohm} about 40, introduction of sufficiently small supports, that is, about 5-mil diameter, has no measurable effect on the three parameters n, T_e, and τ. These data support the contentions that the intrinsic radial loss is not attributable to supports and that any enhanced support loss is not considerably greater than classical single-particle support loss. The magnetic field is being increased more than an order of magnitude (see Sect. 8.4) and will make possible scaling measurements of the support effect. In addition, measurements of the effect of the resistive electric field along the hoops are being carried out to seek understanding of this second nonideal property of an inductively coupled finite-resistivity quadrupole.

8.2.7 Nature of the Decay of the 3-cm Microwave Plasma

A number of characteristics of the microwave plasma behavior have been recently unraveled. This section describes both the plasma generation process and the positional variations of an interesting characteristic of the probe signal decays – the ratio of amplitudes of the fast and slow components of the signal decay.

Using double-probe techniques we have observed that the plasma is initiated both at the microwave entrance port, position R (Fig. 8.8), and at position F, which is 180° in azimuth from R (and is geometrically the same as R, having a dummy waveguide hole). A shock or ionizing front proceeds from R in the direction toward U and simultaneously from F in the same direction, that is, F toward I. The front is indicated in Fig. 8.9 by an arrow; the azimuthal velocity of the front has been measured to be $\sim 10^6$ cm/sec. This measurement was made by comparing the rise time of the probe plasma signals with microwave turn-on time at different azimuths. Once breakdown is achieved at any azimuth, the ionization is maintained by the local microwave field, so that the steady-state flux to the probe is constant with time until microwave turnoff. This implies then that $dn/dt = 0$, or the plasma loss rate is equal to the plasma generation rate by the microwave field.

We have long observed in the afterglow a plasma having a fast decay component of 10 to 20 μsec followed by a slow decay component of 100 to 150 μsec. Figure 8.9 shows three curves which illustrate the variation of the ratio of the fast-decay amplitude, A_f, to the slow-decay amplitude, A_s, as a function of azimuth. Each curve is plotted vs simulated hoop support size, S_s, normalized by the minor cross-sectional area of the torus, S_t. These

ORNL-DWG 68-12773A

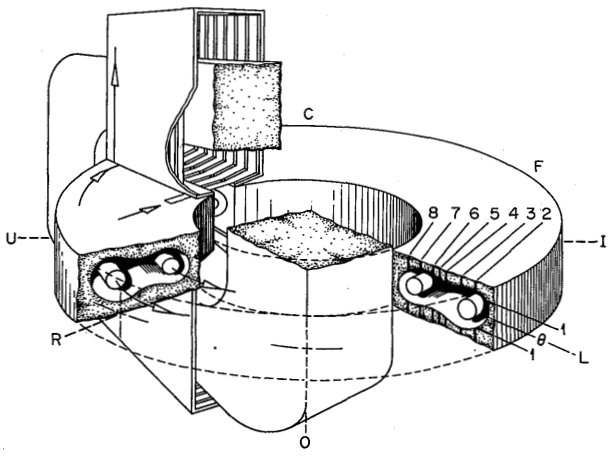

Fig. 8.8. Address Notation of the ORNL Quadrupole. The location of each diagnostic part is designated by a number and letter combination.

ORNL-DWG 68-13152A

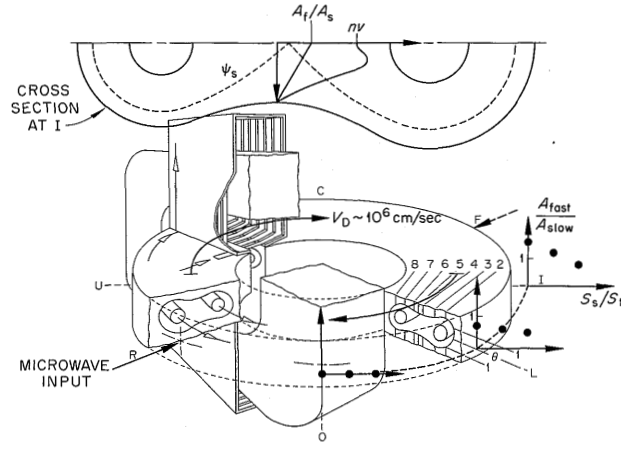

Fig. 8.9. Characteristics of the $\lambda = 3$ cm Microwave Plasma. The ratio of amplitude components in the probe decay (A_f/A_s) is plotted vs normalized probe size at three azimuths. A_f/A_s is also shown as a function of cross-sectional position at azimuthal location I. At I, the probe flux nv shows a peak value on the separatrix as expected. The clockwise drift velocity of the ionization front following microwave field turn-on is indicated by the two arrows labeled V_D.

measurements were made on probes located in the "5" position.

The cross section at I in Fig. 8.9 shows the amplitude variation of probe $I5$ as a function of radius. The occurrence of the maximum flux at $r = {}^5/_{16}$ in. agrees with our calculations for the location of the separatrix, where one would expect the maximum plasma density.

Variations of the ratio A_f/A_s with radius (shown at the top of Fig. 8.9 in the cross section at I) show that the fast component is contained in the magnetic well region. We have intuitively associated the fast component with a higher-energy electron distribution which originates at F (and presumably R) and attenuates rapidly with azimuth. Since this component decays so rapidly with azimuth, we could conclude (in this first, two-temperature model) that the radial loss out of the machine is high compared with the azimuthal drift velocity, even though these electrons are "contained" in the well. The slow-decay component we have associated with the 100-eV-temperature electron distribution.

Another model suggests that the plasma loss rate immediately after microwave turnoff can be equal to the microwave-induced loss rate during steady state. This statement assumes that the microwave fields produce turbulent motion of the particles which, in turn, causes enhanced losses. There is the further assumption made that the turbulent motion continues for some time after the microwave fields are removed and it is the effect of the residual turbulence that we are seeing (i.e., fast decay, A_f) in the absence of the heating fields. It also assumes that the microwave turnoff time is small compared with the fast decay, a measurable relationship. Thus the enhanced initial loss rate would be caused by the particles, which are correspondents with the microwave fields in producing the turbulence.

According to this new model, then, the slow-decay component is the true loss rate of the single-temperature (100 eV) electron plasma. This can be checked by looking at the fast-decay component as a function of microwave input power.

The relaxation from a non-Maxwellian or turbulent spectrum to a Maxwellian or thermal spectrum is on the order of the relaxation time for like-particle scattering. For 100-eV electrons in a 10^{12}-cm^{-3} plasma, this is ~ 30 μsec. This is very close to the measured duration of the fast-decay component of 10 to 20 μsec.

So far, we cannot separate these two suggested models.

8.2.8 Effect of Azimuthal Electric Field on Microwave-Generated Plasma

An important reservation held against a nonsuperconducting quadrupole is the possibility that the resistive electric field contributes to a disturbance of plasma equilibrium and hence enhances the plasma loss. We have begun assessing this effect by heating the hoops ohmically and then making plasma measurements with a controllable IR drop along the hoop. An important first question in this experiment is just what and where this resistive electric field is and at what time during the pulsed field cycle it is present.

In a device with zero resistivity, there would be an electric field (parallel to the hoop) whose magnitude is given by the solid line in Fig. 8.10. The $E_{||}$ in Fig. 8.10 varies temporally as $E_{||}e^{j\omega t}$ and is 90° (in time) ahead of B or I_{hoop}, since the impedance is purely inductive. When $\rho \neq 0$, the electric field parallel to the hoop has a radial profile of peak values as shown in the dashed line of Fig. 8.10 and is less than 90° ahead of B or I_{hoop}. There is little difference between the two cases near the walls or in the well. Only near the hoops (and at the wall) is there a significant change. Figure 8.11 shows the change in electric field caused by the finite resistivity in the hoops. The end result is that the $E_{||}$ field located at $B = 0$ [it is this $E_{||}$ that is small when I_{hoop} (or B) is maximum] is hardly affected by finite resistivity in the hoop; it is only at the $B = 0$ point that the $E_{||}$ (were it in phase with I_{hoop}) could accelerate electrons in a field-free region, causing runaways. The $E_{||}$ field near the surface of the hoops, however, is directly proportional to the resistance and can be in phase with the magnetic field, causing an $E \times H$ force into the hoops. With both toroidal *and* poloidal magnetic fields present (i.e., shear), however, the resistive E could accelerate electrons along field lines. We also find that since the radial and temporal variations of the two contributions to $E_{||}$ are dissimilar, it is possible to look for two effects. First, one can observe the effects of the resistive $E_{||}$ near the hoops resulting from heating them, and second, one can observe the inductive $E_{||}$ near the field zero and the walls (with the hoops cold) by shifting the observation time

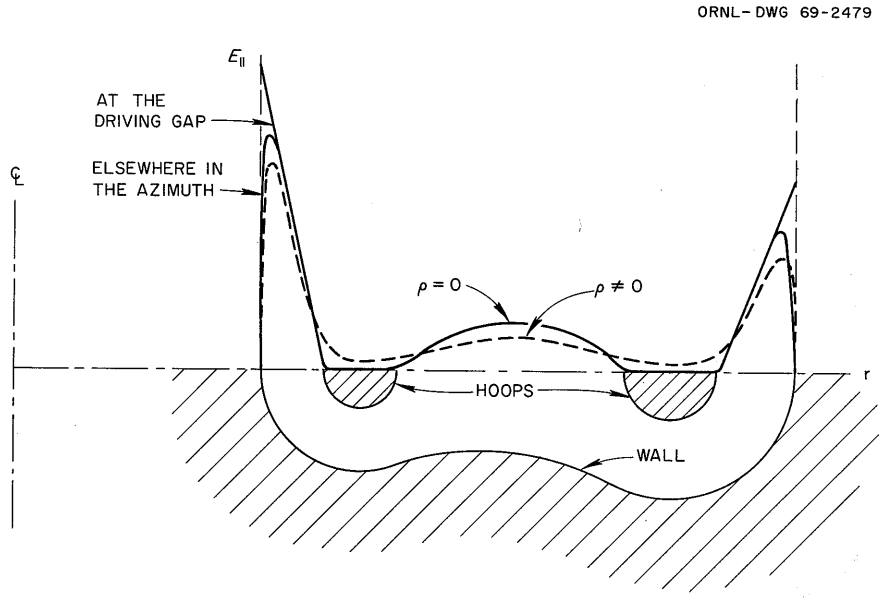

Fig. 8.10. The Approximate Peak Induced Electric Field $E_{\parallel}$ vs the Major Radius r for the $\rho = 0$ and $\rho \neq 0$ Cases for an Inductively Driven Quadrupole.

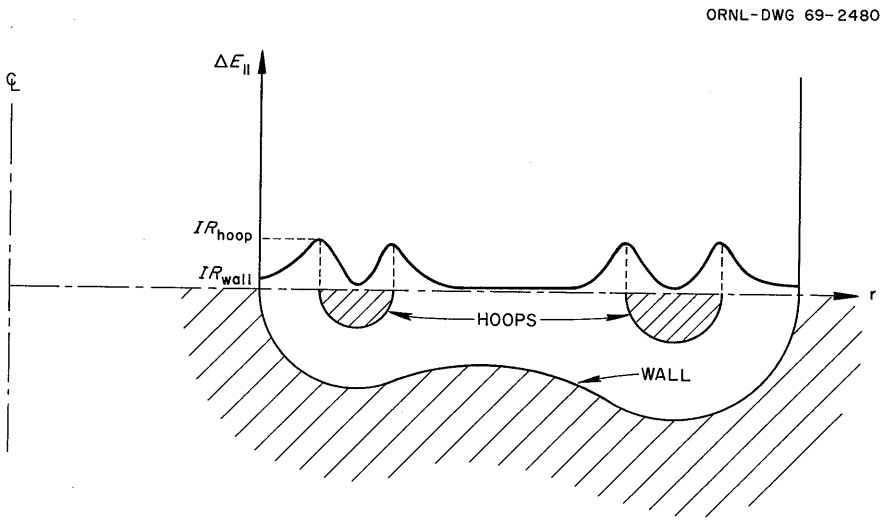

Fig. 8.11. The Approximate Change in Peak Induced Electric Field $E_{\parallel}$ vs the Major Radius r Resulting from Finite Resistivity of Copper.

off the peak magnetic field to an instant when $E_{\parallel}$ (inductive) is not zero. The magnitude of the resistive electric field along the hoop surface is about equal to IR divided by the circumference, equal to about 5 mV/cm. This field at room temperature would be three times higher, equal to 15 mV/cm. The magnitude of the inductive electric field is roughly 150 mV/cm near the walls and about 30 mV/cm in the field zero, both at the instant of zero magnetic field. During the experiment (±1 msec from peak field) the respective maxima near the walls and in the well are 75 and 15 mV/cm.

The measurement of the electric field is inferred from a measurement of the hoop temperature. Since the hoops are levitated during the experiment, we monitor the temperature variation of the hoop temperature with a thermocouple as soon as the levitation period is over. The scope display of the temperature variation allows us to extrapolate to time $t = 0$ when the double-probe observations are made. The output of a Rogowski coil, which reads the hoop current and initiates all measurements at a predetermined value of magnetic field, is monitored simultaneously with the hoop temperature on a dual-beam scope. We thus have our $t = 0$ marker and a means of determining the total energy delivered to the hoops.

Calculations, as well as measurements, show that the inner hoop temperature rises about 50 C° above the boiling point of nitrogen (77°K), to which it is initially cooled. Since half this energy is delivered to the hoop after the probe observations are made, the rise in hoop temperature at time $t = 0$ is about 25 C°. By repeated current pulsing of the hoops, we are able to make plasma observations at any desired temperature above the 100°K minimum value. Since the resistance of the copper hoops increases by a factor of 3 between 77°K and room temperature, we know that the electric field is a factor of 3 greater at room temperature than at 77°K and varies smoothly with temperature at points in between.

Our experimental results are preliminary but are summarized in the following five observations. As the hoop temperature or azimuthal electric field increases:

1. The steady-state probe amplitude measured at the wall of the plasma container increases. This amplitude increase has been seen for probes at the wall near both the outer bridge region and the magnetic well region.

2. The steady-state probe amplitude decreases inside the magnetic well region.

3. Probe flux measurements at the wall made after microwave cutoff show an increase with increasing hoop temperature. This effect appears to have a sharp onset hoop temperature threshold about 30 C° to 40 C° above 77°K.

4. The decay time of the probe signal of statement 3 above has a relatively slow decay (comparable with the slow-decay component, A_s, of Sect. 8.2.7, which appears to decrease with increasing hoop temperature).

5. In general, the low-frequency (~40 kHz) noise level during steady state increases. There is evidence for enhanced high-frequency noise persisting in the plasma decay after microwave cutoff.

6. If we associate probe flux in the well with the density of confined plasma and probe flux at the wall with a measured radial loss, then increasing temperature results in reduced confinement and increased loss (statements 1, 2, and 3 above). These assignments are subject to the following qualification. The distance between the stability limit ψ_c and the wall at the outer bridge is $^1/_{16}$ in., which is also the length of the diagnostic probes. Therefore it is difficult clearly to separate confined plasma from radial loss in these measurements where the positional tolerance is on the order of $^1/_{16}$ in.

8.3 PRELIMINARY OBSERVATIONS ON COMBINED OPERATION OF THE HYDRATED TITANIUM WASHER GUN AND MICROWAVE HEATING

An important aspect of quadrupole field studies is an investigation of the confinement of different types of plasmas. Most of our recent effort has been with hot-electron (microwave-generated) plasmas. In an effort to achieve a hot-ion plasma, we have installed a plasma gun. Our previous usage[6] of these guns revealed a plasma with cold electrons and hot ions on the order of 10 to 100 eV. Comparison of hot-electron and hot-ion plasmas is of interest because of the important role in stability theory played by the ratio T_e/T_i. We have begun combining the two production techniques in the hope of generating a hot-electron plasma from the gun plasma in the absence of a high background pressure.

Figure 8.8 shows our address notation of the diagnostic ports. The gun was located at F, 180° from the microwave input port, and fired into the top of the device at position 5. Figure 8.12 shows double-probe traces taken in position 5 at both I (bottom trace) and L. There is a 5-μsec delay in the arrival of the signal at L as compared with I. This corresponds to a transit time of about 5×10^6 cm/sec. The maximum amplitude corresponds to a density of $\lesssim 10^{11}$ cm^{-3}. In this experiment the background neutral density is $\lesssim 10^{10}$ cm^{-3}.

The effect of a microwave field superimposed on the gun plasma is shown in Fig. 8.13. In these traces the probes are at $I\phi$ and $C\phi$, 45° on either side of the azimuth F at which the gun is located. As shown, the pulsed microwave field produces a large increase or spike in the leading edge of both probe signals. The cw microwave field has a smaller effect, which we believe is due to a lower steady-state amplitude of the cw microwave field. The difference is about a factor of 2. Close examination of the probe signals in Fig. 8.13 shows that there are two peaks in each trace ($I\phi$ and $C\phi$).

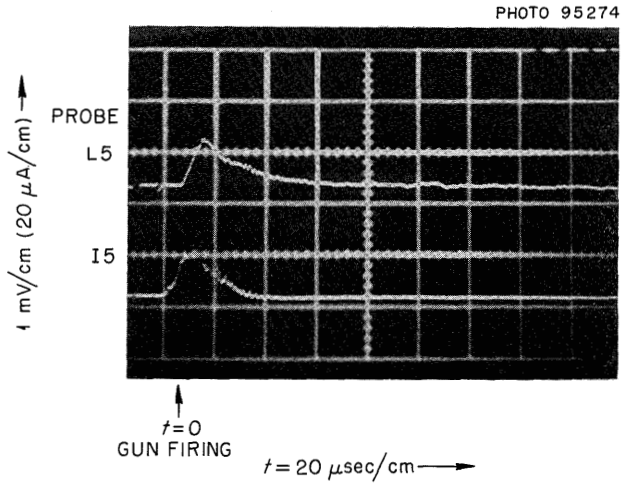

Fig. 8.12. Probe Response to Plasma from Titanium Washer Gun. The gun is fired at $t = 0$.

The second peak occurs about 26 μsec after the first base-line tick mark at the extreme left of each trace. Assuming the tick marks are a measure of

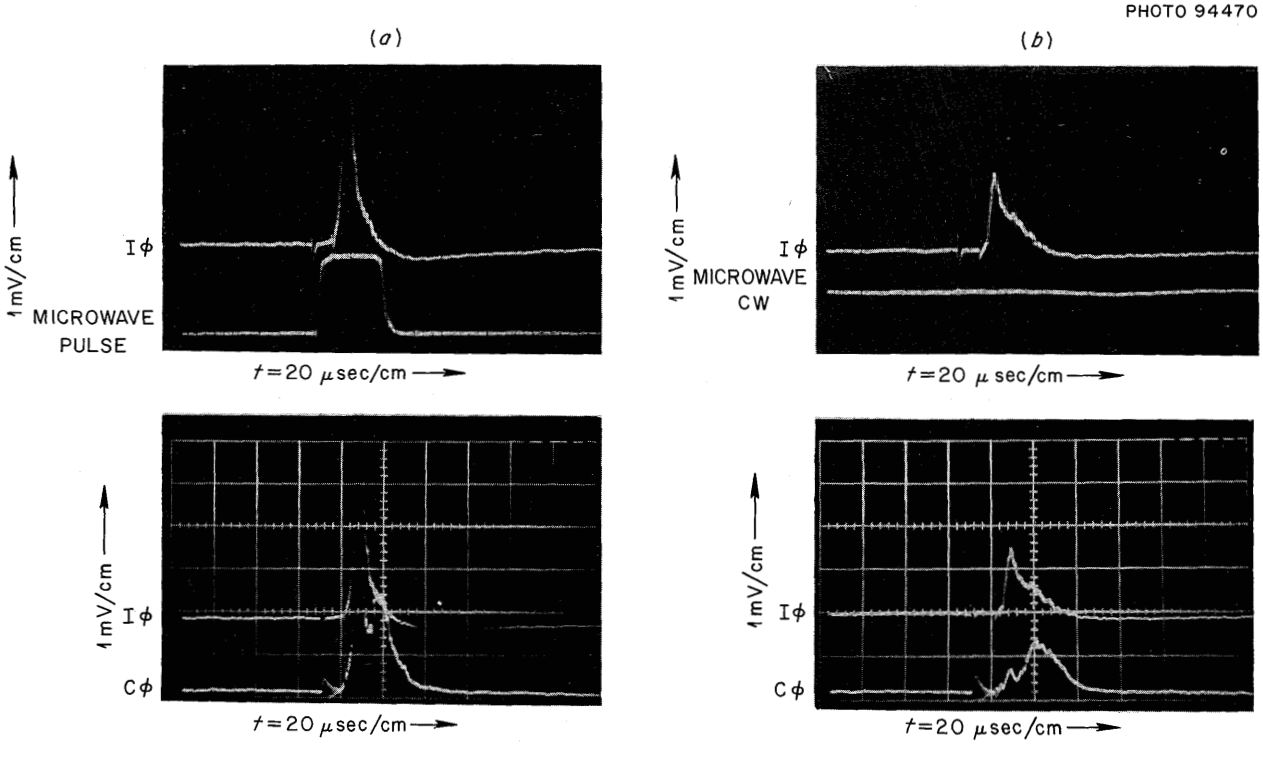

Fig. 8.13. Effect of Microwave Heating Applied to the Gun Plasma. (*a*) A strong enhancement of probe flux is seen (compare with the gun plasma burst in Fig. 8.12) when a microwave pulse occurs simultaneously with the gun plasma burst. (*b*) The enhancement is less noticeable with a lower-power cw microwave field applied to the same gun plasma.

the time of firing of the gun, we may identify the signals 26 μsec later as representing a lower energetic group of particles – ions. The first peak or spike in the traces of Fig. 8.13 corresponds to a more energetic group of particles which arrive at either probe $I\phi$ or $C\phi$ about 16 μsec after the first tick mark. Since this portion of the signal responds to the microwave field, it probably contains energetic electrons which, in comparison with our microwave-generated plasmas, have a density on the order of 10^{11} cm^{-3}. Thus it appears there are energetic electrons (heated locally), drifting azimuthally preferentially from F to I, and ions preferentially in the opposite direction from F to C. Such a separation of charges is consistent with the $B \times \nabla B$ drift the gun plasma experiences on crossing the field at injection. Since the drift velocity of a group of particles is directly proportional to their energy (i.e., $v_D = \frac{1}{2} m v_\perp^2$), one may estimate from Fig. 8.13 that the energetic electrons are twice as energetic as the ions in the slower portion of the signal.

In summary, these data indicate: (1) The gun plasma arrives at the same time at azimuthally symmetric points, proceeding both ways around the torus at $\sim 10^6$ cm/sec, with electrons going preferentially in one direction and ions in the other. (2) The buildup time of the probe signal (nv) is halved from ~ 4 to ~ 2 μsec upon the application of a microwave field to the gun plasma. (In the first case the buildup is of the arrival of plasma, whereas in the second case it is probably a local heating of electrons.) (3) The amplitude of the faster component of the gun plasma burst is enhanced by at least a factor of 2 by the microwave fields, implying an increase in the T_e for fixed n.

For the reasons stated in Sect. 8.2.8, it is not yet possible to determine whether ion losses are enhanced or suppressed.

8.4 IMPROVEMENT IN THE MAGNETIC FIELD STRENGTH

In the first two generations of the quadrupole (first and second models) used for all the experiments described in Sects. 8.2 and 8.3, the return currents in the jacket were carried around the iron pole piece in such a way that an amount of energy approximately three times the energy stored in the quadrupole magnetic field was stored outside the quadrupole. This excess energy was stored in the coupling field between the primary and secondary windings of the transformer formed by the primary coil, hoops, and jacket. As the saturation magnetic field of the iron (and therefore the induced voltage) is limited, an excess field energy or impedance results in a much reduced current in the quadrupole. The excess stored energy can be reduced to about 15% of the quadrupole energy, thereby allowing an increase in quadrupole current by a factor of 4, by placing the primary current winding in close proximity to the secondary current winding (the continuation of the jacket around the pole piece).

The rewinding of the primary coils and matching jacket continuity winding (Fig. 8.14) resulted in a measured quadrupole impedance equal to the calculated 170 nH plus 30 nH in connections. This reduced impedance, coupled with the use of back-biasing of the core (doubling the useful flux change), implies a magnetic field strength plot as shown in Fig. 8.15. The magnetic characteristics of the quadrupole were computed[12] for zero skin depth. This increased magnetic field (84 and 44 kG at the surface of the inner and outer hoops respectively) requires 18 kJ in the form of a 36-Hz half-cycle capacitor discharge yielding a maximum of 400 kA total current. The power supply is being readied, and 8% of the design field has already been reached with the present 60-Hz ac supply.

This is an appropriate place to state clearly two figures of merit for the quadrupole, the number of ion gyroradii and the well depth. The relevant width of the plasma in gyroradii for ions of 100 eV energy is considered to be the shortest distance between the density peak on the separatrix, ψ_s, and the MHD stability limit, ψ_c, determined by the minimum of

$$\oint \frac{dl}{B}\bigg|_{\text{on field line}} .$$

Since the number of gyroradii is determined from the line integral $\int B \cdot dl$, it is the amount of gauss-centimeters or webers per meter that is important; in the toroidal case, $\int B \cdot dl$ is inversely proportional to the major radius (total flux at a given radius is constant), so that the minimum distance

[12]We would like to acknowledge the help of G. D. Hobbs and Culham Laboratory in providing the magnetic field computations.

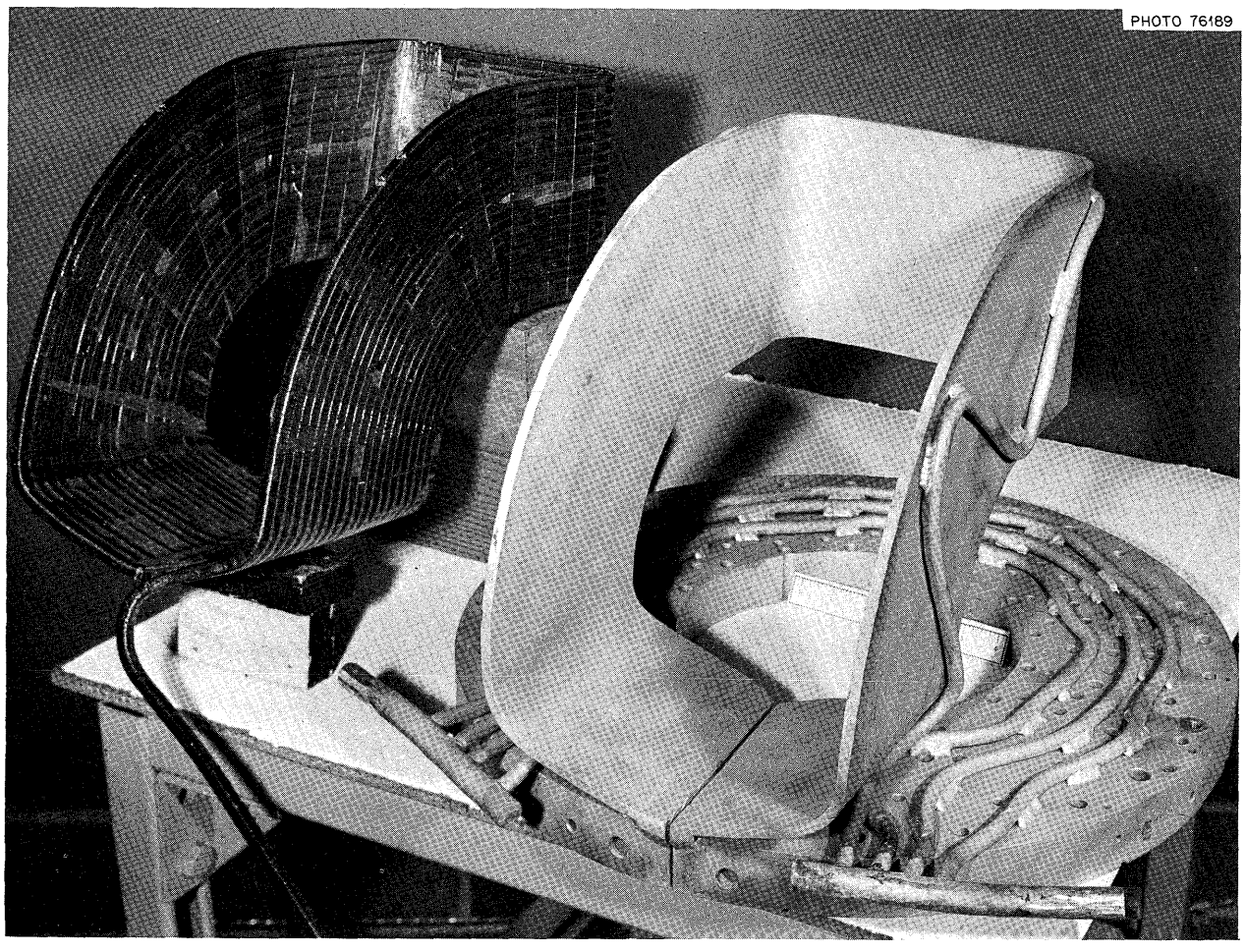

Fig. 8.14. Single-Turn Continuity Winding (Attached to Torus) and Closely Fitting Primary Winding for Low Inductance. The 90° curve in the primary-jacket strip line results from vacuum tank space requirement.

between ψ_s and ψ_c is at the outer bridge. For the maximum design currents (400 kA total), the amount of gauss-centimeters between the outer ψ_s and ψ_c is about 30 kG · 10^{-1} cm ~3000 G-cm, corresponding to about five 100-eV-ion gyroradii. This corresponds favorably to the present and second-generation multipoles envisaged elsewhere.

The second figure of merit is the depth of the magnetic well in the quadrupole and is defined[13] as

$$\frac{\oint dl/B\Big|_{\psi=\psi_c/2} - \oint dl/B\Big|_{\psi=\psi_c}}{\oint dl/B\Big|_{\psi=\psi_c}},$$

equal to 2.5% for our quadrupole, which compares with 3% for the Gulf General Atomic quadrupole.[13]

8.5 HELICAL HEXAPOLE

In addition to the levitated toroidal quadrupole, another device, the levitated helical hexapole, is also under study. The helical hexapole (Fig. 8.16) is structurally a single piece, although at any radial cross section it appears to be a conventional hexapole configuration [the other three "poles" carrying the return currents are in a continuous copper wall (not shown) surrounding the three conductors]. This device has the advantage over the quadrupole of a better ratio of connection length to

[13] T. Ohkawa *et al.*, paper CN-24/C-2 presented at the IAEA Third Conference on Plasma Physics and Controlled Nuclear Fusion Research, Novosibirsk, U.S.S.R., Aug. 1–7, 1968.

radius of bad curvature and more confinement volume; the built-in shear will require the addition of an external toroidal field for comparison purposes. It is necessary to design the hexapole to withstand the magnetic compression forces by its torsional strength; the present structure, having 1.5-in.-diam copper tubes with $\sim \frac{3}{8}$-in. walls (work hardened) with a 21-in. mean major diameter, has been levitated and appears to be sufficiently strong for preliminary investigation.

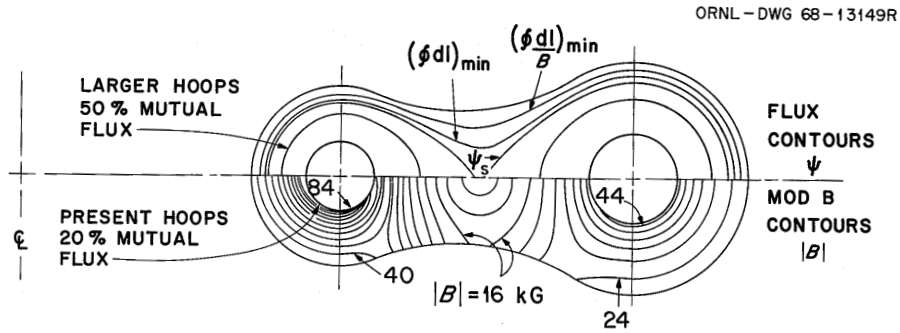

Fig. 8.15. Magnetic Characteristics of ORNL Quadrupole. The values of $|B|$ represent the computed values of peak possible magnetic field strength.

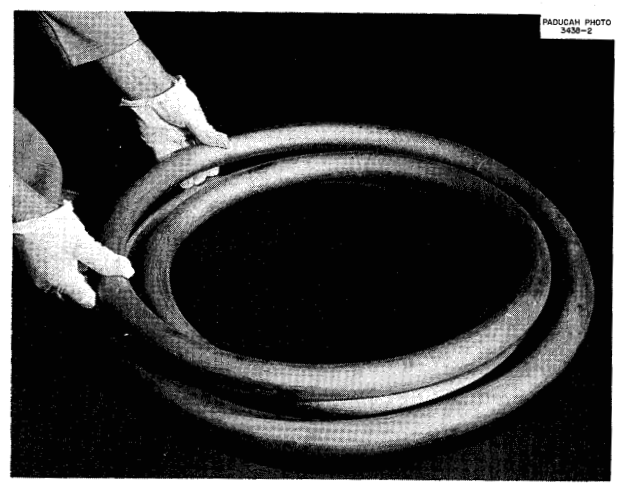

Fig. 8.16. The Helical Hexapole.

9. Atomic and Molecular Cross Sections

9.1 HIGH EXCITED RYDBERG STATES OF H_2

C. F. Barnett J. A. Ray
Arnold Russek[1]

Previous results in the series of experiments studying the population of highly excited n states of the hydrogen molecule indicated that (1) the population of states $n \geqq 10$ for H_2 is a factor of 2 to 3 less than that for hydrogen atoms formed under identical conditions, (2) the highly excited n state population of D_2 is greater than that of H_2, (3) theory predicts that the high-level n states of molecules will be depleted by the process of autoionization in which a $\Delta v = 1$ vibrational transition supplies sufficient energy to eject the n orbital electron into the continuum, (4) theoretical lifetimes of the autoionization states are of the order of 10^{-6} sec for $\ell = 0$ and 10^{-11} sec for $\ell \geqq 0$. Experimentally the technique used consisted in producing molecular ions in a conventional PIG source, accelerating the ions to energies of 100 to 200 keV, and passing the ions through a gas cell where electron capture collisions resulted in energetic molecules in all states of electronic excitation. The particles emerging from the cell were passed through a parallel-plate electrostatic analyzer to remove the ion component. An electrostatic field then stripped the loosely bound electrons, with the nth state ionization depending on the applied electric field, E_n (e.g., a field of 8×10^4 V/cm will ionize all states $n \geqq 10$).

In the previous semiannual report (ORNL-4238) we reported the results of determining the H_2 and HD autoionization lifetimes, which were nearly those predicted by theory. In order to measure lifetime, we varied the distance between the electron capture collision in the gas cell and the electric stripping field. Further detailed measurements of the excited-state transit time dependence have been completed. For small attenuations of the excited-state fraction, linear plots were made of the fraction in states $n \geqq 10$ as a function of transit time. The slope of these curves should be proportional to the autoionization lifetime and should be independent of H_2 energy. For 100-, 150-, and 200-keV H_2 energies the slopes were random and were inconsistent by a factor of 12. The conclusion has been drawn that some sort of decay is being measured that depends on some unknown parameter and not only on autoionization transitions.

The usual practice in the past in analyzing data has been to assume that the fraction of particles captured into state n is proportional to n^{-3}. Intense Stark effect theory predicts that the electric field required to ionize state n is proportional to n^{-4}. From these two conditions it is easy to show that the fraction of particles in state n that are ionized is proportional to $\mathcal{E}^{1/2}$, where $\mathcal{E}$ is the applied electric field. To show the validity of this approach for hydrogen atoms, fraction in states $n \geqq 10$ is plotted as a function of $\mathcal{E}^{1/2}$ in Fig. 9.1*a*. A straight line results with an abscissa intercept corresponding to the experimental condition that the electric field (2×10^3 V/cm) of the electrostatic deflection plates adjacent to the gas cell was sufficient to ionize a few of the very high n states. The same type of plot in Fig. 9.1*b* for 200-keV hydrogen molecules shows a quadratic-type curvature, suggesting that the electron capture into high n states for the molecules is not proportional to n^{-3}. Figure 9.2 shows two additional functional relationships between the fraction with $n \geqq 10$ and the applied field. Figure 9.2*a* results from assuming the capture probability into

[1]Consultant, University of Connecticut.

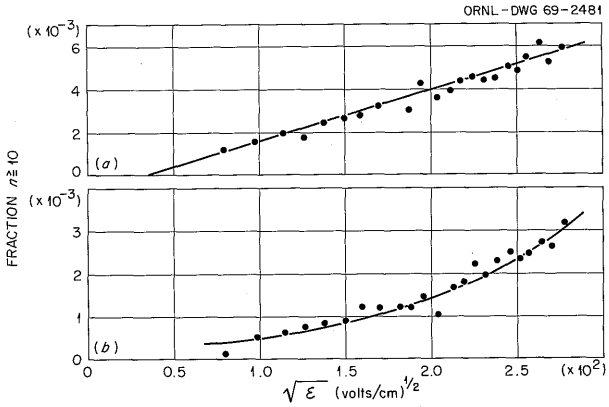

Fig. 9.1. (*a*) Fraction of Hydrogen Atoms in Principal Quantum States $n \geqq 10$ as a Function of the Square Root of the Applied Electric Stripping Field. Results are shown for a 100-keV proton beam charge exchanging in hydrogen. Capture probability (σ_{10}^{n}) proportional to n^{-3}. (*b*) Fraction of H_2 in principal quantum states $n \geqq 10$ as a function of the square root of the applied electric stripping field. Results are shown for a charge-exchanging 200-keV H_2^+ in hydrogen. Capture probability proportional to n^{-3}.

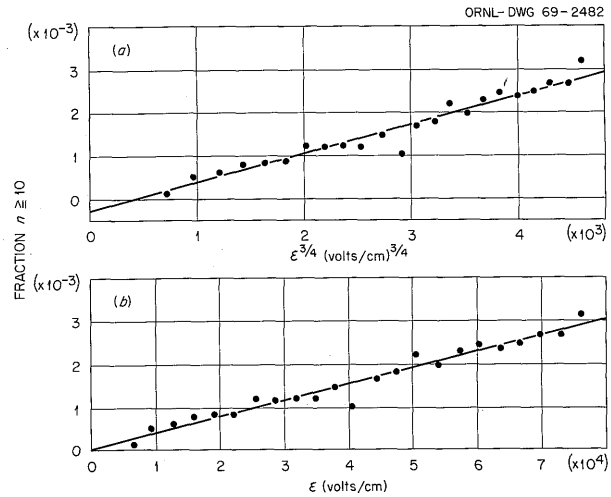

Fig. 9.2. (*a*) Fraction of H_2 in Principal Quantum States $n \geqq 10$ as a Function of the Applied Electric Field to the $\frac{3}{4}$ Power. 200-keV H_2^+ in H_2. Capture probability proportional to n^{-4}. (*b*) Fraction of H_2 in principal quantum states $n \geqq 10$ as a function of the applied electric field (200-keV H_2^+ in H_2). Capture probability proportional to n^{-5}.

state n is proportional to n^{-4}, and Fig. 9.2*b* the capture probability being proportional to n^{-5}. In both plots the straight lines have been drawn by using a least-squares fit to the data points and seem to fit either assumption. Since the experimental conditions impose the boundary condition that the curve must cross the abscissa at $\mathcal{E} = 2 \times 10^3$ V/cm, the data indicate that the capture into state n is proportional to n^{-4} and is a more appropriate fit.

The departure of the capture probability into state n of the hydrogen molecular ion from that of the proton suggests that capture into state n may be dependent on the state of vibrational excitation of the molecule. To test this conjecture, the PIG-type ion source was replaced by an electron bombardment source having an estimated energy resolution of 0.5 eV, so that we could control the ionization energy of the electrons. The H_2^+ molecular ion has a well depth of 3.7 eV with 18 to 19 vibrational levels, whereas the D_2^+ ion has essentially the same well depth but with $\sqrt{2}$ times more vibrational levels. The procedure then was to create molecular ions in either low or high levels of vibrational excitation, accelerate the ions to energies of 100 to 200 keV, convert the ions to molecules by

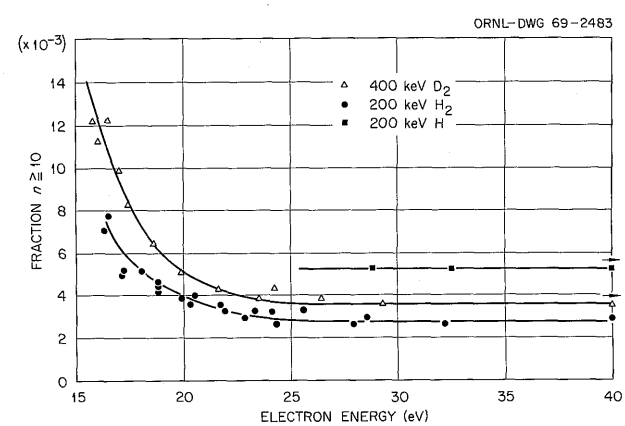

Fig. 9.3. The Fraction of Excited States $n \geqq 10$ for Equivelocity D_2 and H_2 as a Function of the Ion Source Bombarding Energy. Also shown are the values obtained for 200-keV hydrogen atoms.

capture collisions, and analyze the highly excited states as described previously. The results of this study are shown in Fig. 9.3, where the fractions in states $n \geqq 10$ are shown as a function of the electron energy in the ion source. Three curves are shown: (1) 200-keV H, (2) 200-keV H_2, (3) 400-keV D_2. The abscissa scale was calibrated by determining the onset of helium ionization at 24.7 eV.

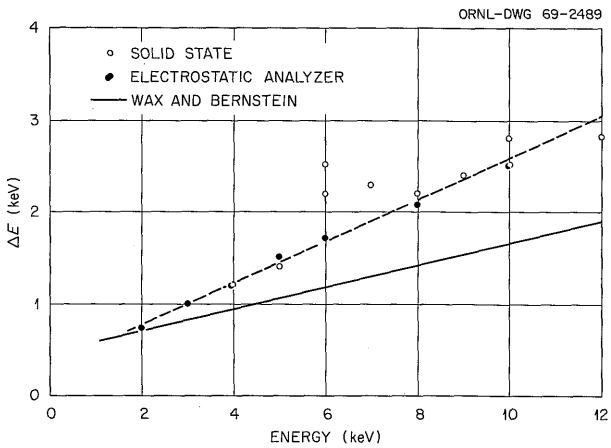

Fig. 9.4. The Dependence of the Yield of 100-keV D_2 in All Principal Quantum States as the Ion Source Electron Bombarding Energy Is Increased.

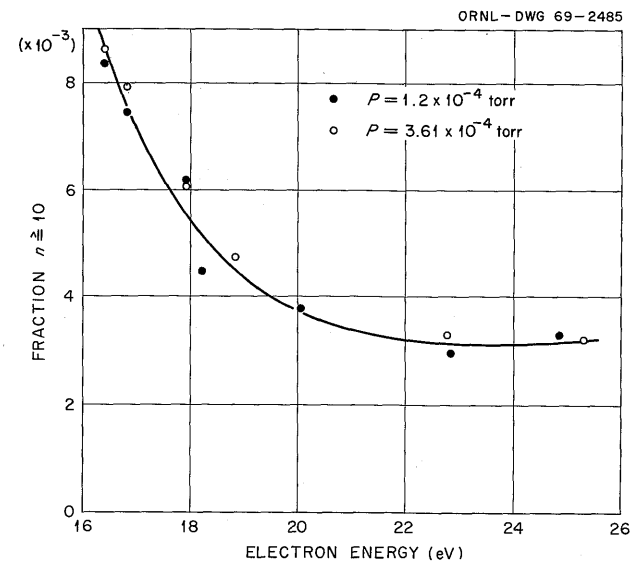

Fig. 9.5. The Effect That a Change in Ion Source Pressure Has on the Excited State Fraction with $n \geqq 10$ as the Electron Energy Is Increased.

For both H_2 and D_2 the fraction in states $n \geqq 10$ increases rapidly as the electron energy decreases from 20 eV down to the appearance energy at 15.7 eV. Again the fraction in states $n \geqq 10$ for D_2 is greater than that of H_2 by a factor of 1.3 at electron energies above 25 eV and increases to 1.5 for states of lower vibrational excitation.

Hayden and Amme[2] have reported a 10 to 15% decrease in the total electron capture cross section as the electron bombarding energy in an ion source was increased. Figure 9.4 shows the results of our measurements of the variation in total capture cross section as a function of the ion source electron energy. Plotted is the ratio of D_2 to D_2^+ (which is proportional to the cross section) as a function of the electron energy. The total yield of D_2 decreases approximately 15% for electron energies greater than 16.5 eV. The decrease at smaller electron energies is not understood but probably results from source operation at electron energies near threshold.

To determine if collisions in the source region were affecting the measured fraction, the ion source pressure was varied by a factor of 3, and the results are shown in Fig. 9.5. The fraction of D_2 in states $n \geqq 10$ is plotted as a function of electron energy for pressures of 1.2 and 3.61×10^{-4} torr. No variation was found between the two conditions.

The theoretically predicted lifetimes of the *ns* and *np* states being of the order of 10^{-7} and 10^{-11} sec, respectively, creates an anomaly with respect to the experimental observations. With short *np* lifetimes of 10^{-11} sec the beam that enters the electric field deflecting region just outside the gas cell will be composed of pure *ns* states. While in the deflector region, state mixing takes place, with the probability of being in the *s* state oscillating (ideally) between 1 and 0, but each time the excited molecule is in the *p* state it decays by autoionization. After the beam leaves the deflector region it is in a mixture of long-lived *s* states and short-lived *p* states, the percentage of the mixture depending on the oscillation time between *s* and *p* states and the time in the deflector field region. This mixture can be varied by varying the accelerating energy, thereby changing the transit time through the deflector field. Thus one should see a beating between the *ns* and *np* states by looking for the maxima and minima in the excited-state fraction as a function of the acceleration energy (or velocity). It can be shown that this beat frequency is:

$$T_2 - T_1 \cong -D\left(\frac{M}{eV_1^3}\right)^{1/2} (\tfrac{1}{2})(V_2 - V_1) ,$$

where D is length of deflector plates, V_1 and V_2

[2]H. C. Hayden and R. C. Amme, *Phys. Rev.* **172**, 104 (1968).

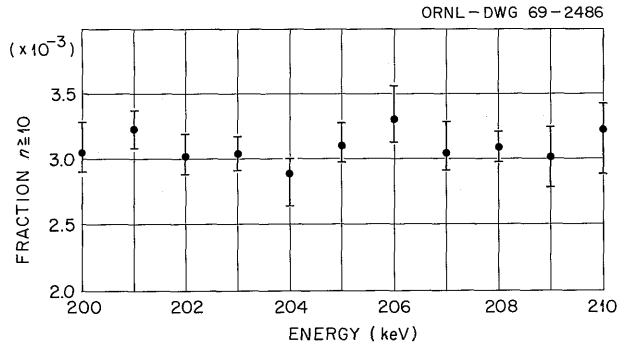

Fig. 9.6. Oscillations Produced by *ns*, *np* State Mixing in the Deflector Region Electric Field. Plotted is the fraction of H_2 in states $n \geqq 10$ as the accelerator voltage is increased 10 kV.

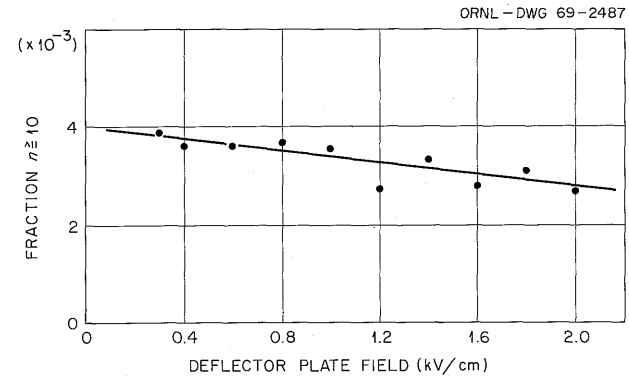

Fig. 9.7. The Influence That the Deflector Region Electric Field Has on the Excited-State Fraction of 200-keV H_2.

are accelerator voltages at successive maxima of the fraction, M is H_2 mass, and e is electronic charge. This beating time is also equal to

$$T_2 - T_1 = \frac{2\pi h}{E_p - E_s},$$

where $E_p - E_s$ is the energy difference between the p and s state in the field-free case but varies linearly with the applied electric field. The fraction of molecules in states $n \geqq 10$ is plotted as a function of accelerator voltage in Fig. 9.6. The error bars indicate the scatter and reproducibility of the data. Although the evidence is not conclusive, an oscillation seems to be present with maxima occurring at approximately 5 keV. This type of curve is very reproducible from day to day. If the maxima do occur at 5 keV, then the calculated beating time is 2.2×10^{-10} sec, resulting in an energy separation between the p and s states of 4.9×10^{-5} eV. The energy separation for the s and p states in the field-free region is $<8 \times 10^{-7}$ eV. We use Bethe's formulation[3] for the energy separation ΔE due to field $\mathcal{E}$:

$$\Delta E = \pm \frac{3}{4}\sqrt{n^2 - 1}\left(\frac{2}{3} n \mathcal{E} a_0\right),$$

where n is the principal quantum number. For an $\mathcal{E}$ field in the deflecting plate region of 2×10^3 V/cm, as used in the measurement to determine the beat frequency, the predicted energy separation is 5.3×10^{-4} eV, which is a factor of 10 greater than inferred from our measurements.

In addition to the change that the accelerator voltage produces on the *s*-*p* ratio, the deflector plate field should also change the *s*-*p* mixture. In Fig. 9.7 the fraction $n > 10$ H_2 has been plotted as a function of the applied field between the deflector plates. The fraction decreases by 35% as the deflector plate field is increased from 0.3 to 2×10^3 V/cm. The fraction in states $\geqq 10$ for hydrogen atoms was independent of this deflecting field.

These two measurements indicate qualitatively that state mixing is taking place in the deflector field. However, if the lifetimes are of the order 10^{-7} and 10^{-11} sec for *ns* and *np* states, then all the excited states should be depleted through the short-lifetime *p* state. Obviously, further quantitative measurements must be made to understand this state-mixing phenomenon.

These measurements have indicated that the electron capture probability is definitely influenced by the level of vibrational excitation of the molecule. The exact dependence of the depopulation of the highly excited levels by autoionization transitions is indeterminate at the present time. The future program seems to lie in the direction of creating known vibrational levels through high-resolution photoionization.

[3]H. A. Bethe and E. E. Salpeter, "Quantum Mechanics of One and Two Electron Systems," p. 326 in *Handbuch der Physik*, vol. 35, Springer-Verlag, Berlin, 1957.

9.2 FURTHER STUDIES OF EXCITATION HEATING OF IONS

J. Rand McNally, Jr.

A paper recently published, on further studies of excitation heating of ions to high temperatures,[4] suggested the possibility of a slightly inverted population of metastable C^{2+*} ions in long magnetically confined vacuum carbon-rich arcs. Based on theoretical oscillator strengths and data from absorption experiments involving two parallel 5.7-m-long arcs, it was reported that the population ratio of metastable to ground state C^{2+} ions in the arc was about 3.3, compared with the value of 1.5 previously predicted[5] for a Boltzmann distribution at $T_e = 40{,}000°K$.

The value of the theoretical absorption oscillator strength used for the λ 977 Å transition involving the ground state of C^{2+} is necessary in interpreting these measurements. The value of 1.08 given by Griem[6] was used in the determination of the population of ground-state C^{2+} ions; however, Wiese, Smith, and Glennon[7] reported 0.81, and Steele and Trefftz[8] recommend 0.69 for λ 977 Å. Thus the measured population ratio may be as small as 2.1 instead of 3.3 as reported. In view of the fact that the λ 1175 Å spectral lines involving the C^{2+*} metastable states were incompletely resolved, as well as the uncertainties in determining n_j and T_e, it seems appropriate to suggest that there is probably no major discrepancy between the measured population ratio and the predicted ratio and, further, that the possibility of an inverted population is probably negated.

This correction does not affect the major thesis of the published paper,[4] which offered additional evidence on the importance of atomic processes in plasmas, namely, the quantized pumping of kinetic energy from electrons to ions under appropriate conditions (via the excitation-heating process) and the unusual dynamic equilibrium that can be established ($T_i = 100T_e$). It does emphasize, however, the importance of accurate oscillator strengths to the interpretation of plasma properties.

[4]J. Rand McNally, Jr., *Plasma Phys.* **10**, 903 (1968).

[5]J. Rand McNally, Jr., *et al.*, *Applied Opt.* **5**, 187 (1966).

[6]H. R. Griem, *Plasma Spectroscopy*, McGraw-Hill, New York, 1964.

[7]W. L. Wiese, M. W. Smith, and B. M. Glennon, *Atomic Transition Probabilities: Hydrogen Through Neon*, NSRDS-NBS 4, vol. I (1966).

[8]R. Steele and E. Trefftz, *J. Quant. Spectry. Radiative Transfer* **6**, 833 (1966).

9.3 CROSS SECTION OF HYDROGEN PARTICLES IN MAGNESIUM VAPOR

C. F. Barnett J. A. Ray

In the previous semiannual progress report (ORNL-4238), cross sections were reported for the electron capture and loss by hydrogen ions and atoms in magnesium vapor. Subsequent measurements have shown that these reported values may be in error by an order of magnitude due to uncertainties in vapor density. A rhodium-plated copper chamber was used as the collision cell, with the magnesium number density determined from published vapor-pressure–temperature curves. The reproducibility of the data was dependent on the temperature history and cycling of the vapor cell, suggesting that the vapor density was dependent on some uncontrollable parameter other than temperature.

The chemical reactivity of magnesium vapor with wall material was investigated by suspending foils of various metals in the vapor cell. Weighing the foils before and after 11.5 hr exposure to magnesium vapor yields the chemical absorption rate of the metal. Table 9.1 presents the results obtained for several metals when exposed to a magnesium vapor pressure of 10^{-5} torr. Rhodium was

Table 9.1. Absorption of Magnesium Vapor by Metal Foils

Foil	Gain in Weight[a] (%)
Ag	10.9
Mo	0
Cu	1.9
Pt	35.8
Rh	131.9
Au	33.4
W	0
SS (304)	0.6
Ta	2.3

[a]Exposure time, 11.5 hr.

the most reactive metal found but was chosen in the present experiment because of its properties to contain cesium. Future magnesium vapor cells should be constructed of either tungsten or molybdenum, in order to be able to deduce vapor pressures accurately.

9.4 ELECTRODISINTEGRATION OF THE DEUTERON

A. Russek C. F. Barnett

Measurements of the neutron production rate in electron-cyclotron-heated plasmas indicate that the rate is approximately a factor of 10 greater than that predicted from the theoretical e + D cross section in the energy region near threshold (Sect. 5.1.6). A study has been made to determine if detailed measurements of the e + D cross section near threshold would provide information as to the physics of the electrodisintegration of the deuteron.

In Table 9.2 the Compton wavelength is tabulated for electron kinetic energies between 2 and 480 MeV. At high energies the Compton wavelength of the incident electron is comparable with the size of the deuteron. At these energies the electron can be used as a probe to study the structure of the deuteron. For these higher energies the Stanford group and others have studied the elastic scattering and electrodisintegration of electrons incident on deuterons.

At low energies, near threshold, the electron wavelength is of the order of 10^{-11} cm and can only sample the extreme outer tail of the deuteron wave function. This part of the wave function depends only on the binding energy of the deuteron and the effective range of nuclear forces and has long been well known. It should be pointed out that the so-called "final-state interaction" (the deviation of the wave function from a simple plane wave for the separating neutron and proton) does influence the cross section at low energies. However, an experiment, with the poor resolution inherent even in an excellent electrodisintegration experiment, could tell nothing more than that it should not be neglected. These considerations indicate that little could be learned about the deuteron structure even if the cross section was measured as a function of scattering angle and energy loss of the incident electron.

Table 9.2. Compton Wavelength for High-Energy Electrons

Kinetic Energy (MeV)	λ, Compton Wavelength (cm)
2	4.9×10^{-11}
120	1.0×10^{-12}
480	2.5×10^{-13}

In plasma experiments such as encountered in ELMO, there is a possibility of three-body interactions, namely, an electron interacting with a second electron while it is interacting with the deuteron. This possibility is due to the fact that the low-energy electron has a large Compton wavelength compared with the size of the deuteron. This particular type of reaction is distinctively different from the usual three-body interaction where two electrons simultaneously interact with the nucleus. For double-event-type reactions it is conceivable that a more efficient energy-momentum transfer to the nucleus would be permitted.

To obtain a rough estimate of the importance of double events, the binary rate can be compared with the tertiary rate. The number of single events (R_1) per target nucleus per unit time can be written as follows:

$$R_1 = n_e v A \left(\frac{r_{nuc}}{\lambda}\right)^3 ,$$

and the number of double events (R_2) can be written as

$$R_2 = \frac{(n_e v A)^2}{2} \left(\frac{r_{nuc}}{\lambda}\right)^3 ,$$

where n_e is the electron density, v is electron velocity, $A = \pi\lambda^2$ = Compton cross-sectional area. If

$$n_e \cong 10^{12} \text{ electrons/cm}^3 ,$$

$$v \cong 3 \times 10^{10} \text{ cm/sec} ,$$

and

$$\lambda = 10^{-11} \text{ cm}^2 ,$$

then

$$R_2/R_1 \cong 5 .$$

If these qualitative theoretical considerations are valid, then they should be found in a plasma experiment with the neutron production rate having an n_e^2 dependence.

9.5 PHOTOIONIZATION OF KRYPTON BETWEEN 300 AND 1500 eV. RELATIVE SUBSHELL CROSS SECTIONS AND ANGULAR DISTRIBUTIONS OF PHOTOELECTRONS[9]

M. O. Krause

Energy spectra of electrons ejected from *M* and *N* subshells of krypton by characteristic x rays of 300 to 1500 eV energy have been measured with an electrostatic analyzer. Krypton was irradiated in the gas phase, and electrons were detected perpendicular to the x-ray beam. From these spectra, relative subshell contributions to the photoionization cross section were obtained for single-electron emission and for double-electron emission, the latter involving simultaneous transitions of *M* and *N* electrons. Angular distributions of photoelectrons from the 3*s*, 3*p*, and 3*d* shells of krypton and the 1*s* shell of neon also have been determined at excitation energies from about 200 to 1100 eV above the respective ionization thresholds. Data on relative cross sections for single photoionization corroborate a theoretical model which uses a Herman-Skillman central potential (Cooper and Manson in the following article). Angular distributions agree satisfactorily with calculations by the same model; this means theory makes dependable predictions regarding the asymmetry parameter and the effect of retardation. Data on double photoionization disagree with results of the electron shake-off theory, which accounts for only about half the observed intensities. This suggests that electron-electron correlation plays an important role.

9.6 PRODUCTION OF HYDROGEN ATOMS

C. F. Barnett J. A. Ray

Our attempts using water vapor jets formed by glass capillary arrays to induce energy dispersion in an energetic-neutral beam have been unsuccessful. The mosaic capillary array was placed in a liquid-nitrogen cylindrical cavity through which the beam passed. The cavities were placed in series with a decelerating potential applied between them so that neutrals would be formed in different equipotential regions. Application of small positive potentials to the cavities resulted in the radial extraction of space-charge-neutralizing electrons from the intense proton beam, thereby causing severe defocusing of the charged beam.

The same geometric single-cavity configuration has been used to determine the jet conversion efficiency of ions to neutrals. The water vapor jet was formed by 10-μ-diam, 1.5-mm-long glass capillaries arranged together in an array approximately 6 mm in diameter. The results are shown in Fig. 9.8 for a 40-keV H_2^+ beam incident on the cavity. Plotted is the percent neutrals formed as a function of the pressure on the high-pressure side of the array. Use of a high-resolution solid-state detector

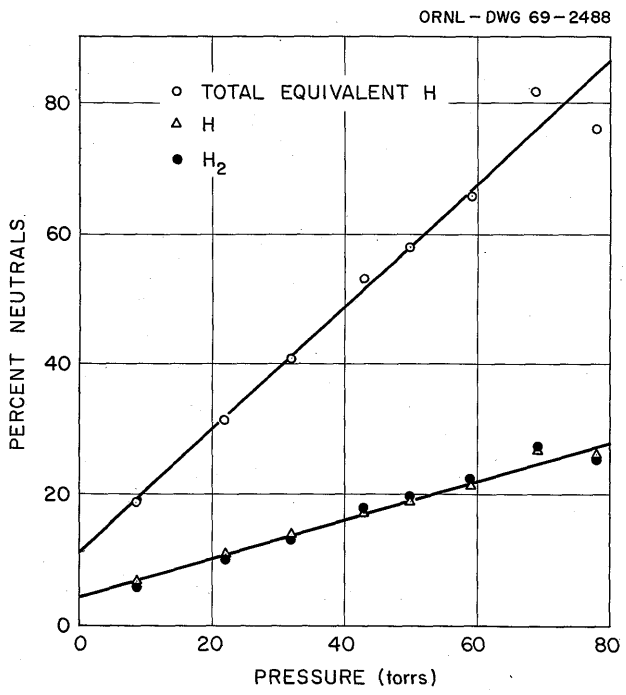

Fig. 9.8. Yield of H and H_2 as a 40-keV H_2^+ Beam Traverses a Water Vapor Jet Formed by a Glass Capillary Array. Array consisted of 10-μ-diam, 1.5-mm-long capillary tubes fused to form a mosaic array 6 mm in diameter.

[9]Abstract of published paper: *Phys. Rev.* **177**, 151 (1969).

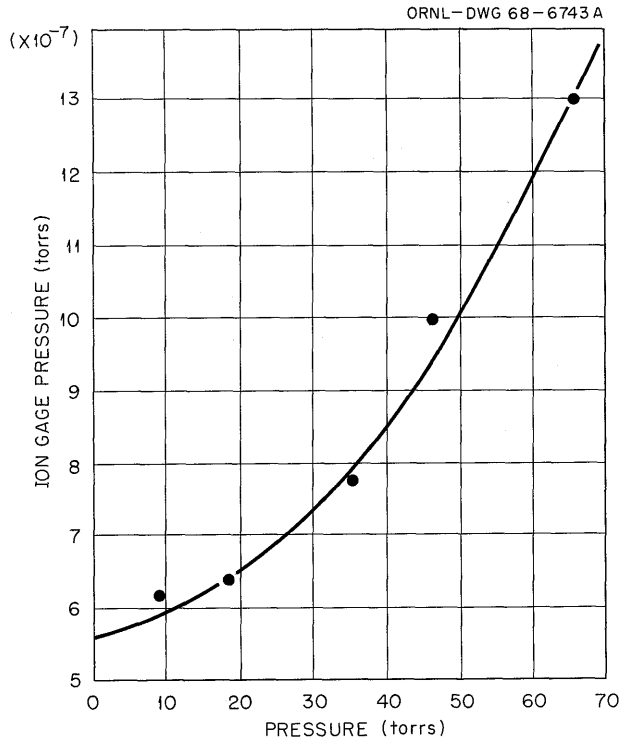

Fig. 9.9. Indications of Kinetic Gas Streaming from a Water Vapor Jet Surrounded by a Liquid-Nitrogen-Cooled Cavity.

permitted the separation of hydrogen atoms formed by dissociative collisions from H_2 formed by electron capture collisions. At this energy the production of atomic and molecular neutral species for a given pressure is the same. The uppermost curve, indicated by closed circles, is the fraction of total atoms in the beam or the sum of hydrogen atoms and twice H_2. The expected conversion efficiency at water vapor equilibrium pressures would be approximately 120% for conversion of H_2 to atomic hydrogen.

With all neutralizer gas cells operating in conjunction with a plasma containment system the kinetic gas streaming is of paramount importance. To obtain an estimate of streaming, an ion gage was mounted in the vacuum region surrounding the gas jet cavity. Figure 9.9 indicates the increase in the pressure of the vacuum region as the driving pressure across the array is increased. The pressure increased by a factor of 2 over the pressure range, corresponding to an 80% conversion.

9.7 HYDROGEN ATOM ENERGY ANALYZER

J. A. Ray C. F. Barnett

To aid in the diagnosis of the energy dispersion of hydrogen particles escaping a plasma, the conversion efficiency, angular divergence, and energy loss characteristics of a thin carbon foil have been investigated for 1- to 10-keV hydrogen atoms. Initially the ion transmission and energy loss of the particles were determined by passing the ions emerging from the back surface of the foil through a parallel-plate electrostatic analyzer. The angular divergence was determined by placing an electron multiplier with a window of large area directly behind the foil and scanning the total transmitted beam with a plate containing a small aperture. Results of these measurements are shown in Figs. 9.10–9.12. Positive ion transmission is shown as a function of energy in Fig. 9.10, and, as expected, the conversion of hydrogen to H^+ increases with particle energy, being about 2% at 10 keV. The angular divergence, which is defined as the full width at half maximum of the transmitted beam, is plotted as a function of incident hydrogen energy in Fig. 9.11. By plotting this angular divergence as a function of E^{-1} a straight line results which is in general agreement with classical scattering theory. The energy loss of the particles in the carbon foil determined by this technique is shown as solid data points in Fig. 9.12. The results were obtained with a 250-Å foil. Shown as the solid line are recent results of Wax and Bernstein[10] for a 100-Å foil. It should be possible to use these results to calibrate carbon foils so that the energy loss spectra obtained could be unfolded to obtain the energy dispersion of the incident beam. In experiments with monoenergetic particles the shape of the energy spectrum as determined by the condenser-plate method was as expected for 10 keV energy in that the curve was approximately Gaussian with a low-energy tail. But for lower energies (2 keV) the low-energy tail disappeared and a high-energy tail appeared. This change of shape, coupled with no direct relationship between particle energy and analyzer resolution, prohibited an unfolding of the measured spectra.

[10] R. L. Wax and W. Bernstein, *Rev. Sci. Instr.* **38**, 1612 (1968).

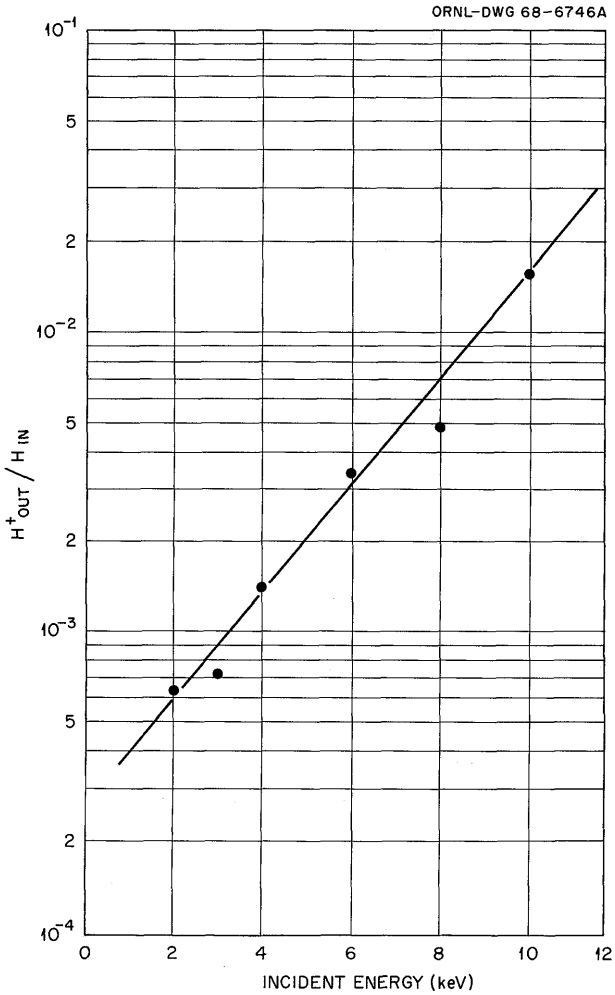

Fig. 9.10. Ratio of Transmitted Ion Current to the Incident Hydrogen Atom Flux for 250-Å Carbon Foil as a Function of the Hydrogen Atom Energy.

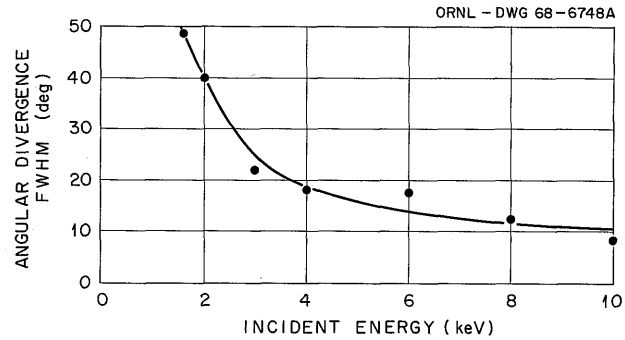

Fig. 9.11. Angular Divergence of Hydrogen Particles Emerging from a 250-Å Carbon Foil.

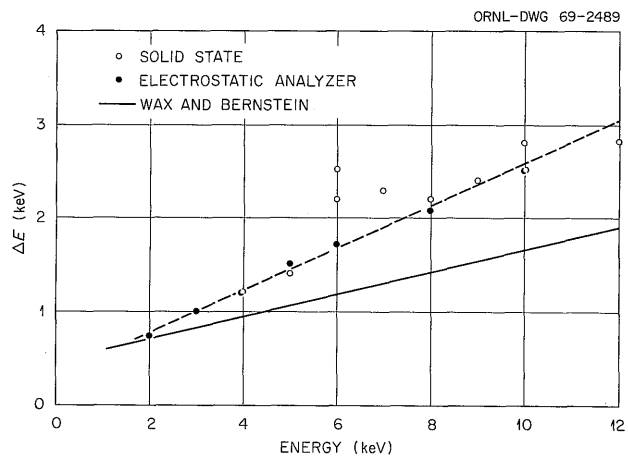

Fig. 9.12. Energy Loss of Hydrogen Particles Passing Through a 250-Å Carbon Foil. Shown also are the results obtained by R. L. Wax and W. Bernstein [*Rev. Sci. Instr.* 38, 1612 (1968)] for a 100-Å foil.

To alleviate these difficulties the energy loss has been determined by mounting the foil at a positive 10-kV potential. The ions emerging from the foil were postaccelerated and were incident on a high-resolution solid-state detector with an energy equal to the initial energy plus the postaccelerating potential minus the foil energy loss. The energy loss was determined by measuring the shift of the detector pulse-height spectrum with the foil in and out of the beam. Results obtained by this method are shown as open circles in Fig. 9.12 and are equivalent to results obtained by the condenser-plate method. The advantages of the solid-state detector technique lie in the simplicity of use and the fact that the resolution is energy independent.

9.8 EVALUATION OF A MAGNETIC SHIELD OF FOUR NESTED CYLINDERS

M. O. Krause

Occasionally in determining cross sections, ambient magnetic fields need to be reduced to a low level to avoid malfunctioning of instruments or intolerable beam deflection. If fields of 10^{-2} Oe or greater can be tolerated, magnetic shields of high-permeability material give satisfactory performance. However, if fields need to be smaller than 10^{-2} Oe, field compensation by means of Helmholtz coils seems to be indicated. Such coils are usually large, cumbersome, and expensive and, also, of

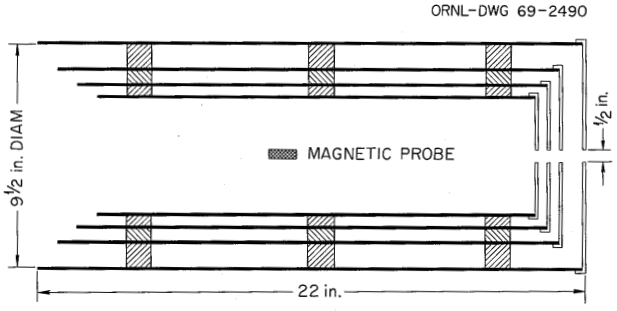

Fig. 9.13. Magnetic Shield of Four Nested Cylinders. The two outer shields are 0.050-in. Netic; the two inner shields are Co-Netic AA. The left end caps are not shown.

limited value whenever fields are highly inhomogeneous in space. It is therefore of interest to explore the potential of high-μ material for low-level shielding. An existing multilayer shield, shown in Fig. 9.13, was evaluated with regard to its attenuation properties and the possibilities of achieving a minimal residual field of less than 10^{-3} Oe.

The shield was manufactured by Perfection Mica, Magnetic Shield Division, and consisted of two inner cylinders of Co-Netic and two outer cylinders of Netic material. The Co-Netic layers provide high attenuation at medium field strengths, and the Netic layers attenuate strong fields without saturating easily. Thus the shield was designed for maximum attenuation of medium to strong fields, but it can also be used in low-level fields where the Co-Netic material almost exclusively determines the shielding quality. The shield was used without any preparation such as degaussing, and a Hewlett-Packard magnetometer served as a probe with a maximum sensitivity of 2×10^{-5} Oe per division. In the laboratory, stray external fields of about 0.5 Oe with excursions up to 1 Oe were present in any direction, and the apparatus could be placed between two iron-free coils providing fields up to 120 Oe. The investigation was, in the main, limited to the behavior of the shield in dc magnetic fields. The following is a short description of the more important measurements and the results:

1. Attenuation at medium field strength: With external field, H_e, in direction of shield axis, attenuation factor is 1000 to 3000 for 10 Oe $< H_e <$ 120 Oe, and it is up to 10,000 with H_e perpendicular to the axis in the same range of H_e.

2. Attenuation at low field strength: For external fields below 1 Oe the field inside the shield, H_i, remains between 1 and 5×10^{-3} Oe regardless of the actual value of H_e and its direction. This limiting residual field is due to the remanent magnetization of the shield and about equal to the (coercive) field in the shield material of the innermost layer. Considering the source of the minimum residual field it would appear as if low-level shielding were limited to H_i in the order of 10^{-3} Oe. As will be shown under point 4, H_i can, however, be reduced further either by controlling the remanence of the shielding material or by introducing a solenoid or Helmholtz-type coils within the shield.

3. Uniformity of H_i within the shield for $H_e \approx$ 0.5 Oe: Mapping of H_i along the axis showed variations of H_i within 1×10^{-3} Oe from $l = 0.38L_i$ to $l = 0.62L_1$ (where L_1 is length of inner cylinder) and within 2×10^{-3} Oe from $l = 0.33L_1$ to $l = 0.67L_1$. Toward the ends of the cylinders the field rises rapidly into the 10^{-2} Oe region; the open-ended configuration accelerates this rise; the uniformity of the field in the center region is, however, quite insensitive to the use or omission of end caps. Tracing H_i in planes perpendicular to the axis yielded the following results: $\Delta H_i < 2 \times 10^{-4}$ Oe from center to wall in midplane, $\Delta H_i < 10^{-3}$ Oe 6 cm off midplane, and $\Delta H_i < 10^{-2}$ Oe 12 cm off midplane (or approximately midway between center and end).

4. Reduction of residual field below 10^{-3} Oe: Two methods are available to accomplish this. (1) Since the residual field inside the cylinder depends on the residual magnetization of the shield, one can change H_i, and in fact zero it, by changing the magnetization of the shield material in such a way that H within the shield is approximately zero. This so-called "remanence control" of the shield[11] requires the addition of two coils near the ends of the cylinder. (2) The more elegant and versatile method is the introduction of small compensation coils inside the shield. These can be Helmholtz pairs or simply a solenoid. In this experiment a solenoid was used, and it proved very easy to reduce H_i to less than 1×10^{-5} Oe. Furthermore, this arrangement allowed the dynamic control of H_i with a corresponding reduction of external magnetic

[11] B. J. Patton, Socony Mobil Oil Co., Inc., Dallas, Tex., recognized first the value and significance of the remanence control (1962 unpublished); see also B. J. Patton and J. L. Fitsh, *J. Geophys. Res.* **67**, 1117 (1962).

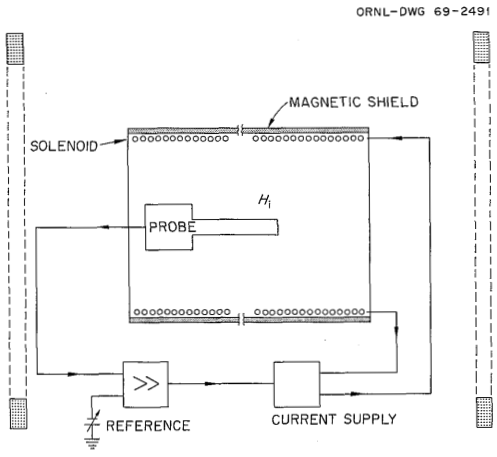

Fig. 9.14. Solenoid and Control Circuit to Regulate Residual Magnetic Field H_i Within a Magnetic Field.

field disturbances. With the setup of Fig. 9.14, which had a feedback gain of about 10, the effective attenuation of the shield was increased by this factor, so that even in a "magnetically hostile" environment with field spikes and abrupt changes of nearly 1 Oe the inside field could be kept at less than 10^{-3} Oe over a period of several days. A steady level of about 10^{-5} Oe could be maintained near the midplane of the shield if a more sensitive probe as well as a greater feedback gain were to be used.

9.9 DETECTOR EVALUATION

C. F. Barnett J. A. Ray

Characteristics of several electron multiplier configurations have been investigated during this report period. Emphasis has been placed on commercially available multipliers that will detect low-energy hydrogen particles escaping a plasma. Desirable characteristics include stability, known detection efficiency, energy sensitivity, and ability to discriminate neutral particles from photons or x rays.

9.9.1 Johnston Multiplier

The Johnston multiplier[12] is a large-area-entrance-window 20-stage BeCu-dynode electron multiplier whose geometry is shown schematically in the inset of Fig. 9.15. The efficiency of the multiplier was determined to be less than 20% due to secondary electrons from the first dynode escaping the multiplier structure. An auxiliary grid has been placed 3 mm in front of the first dynode to repel the primary-emitted secondary electrons into the direction of the second dynode. Plotted in Fig. 9.15 is the detection efficiency (determined by comparing the counting rate of the multiplier with that of a solid-state detector) as a function of the negative bias placed on the auxiliary grid. The data shown are for 20-keV hydrogen particles with –2700 V placed on the first dynode. With increased grid voltage the efficiency increased to a maximum at approximately 100 V greater than the first dynode potential. Detectors with large windows usually are unreliable due to the nonuniformity of response as the particles impinge on the first dynode. Shown in Fig. 9.16 is the efficiency of detection as a 20-

[12]Johnston Laboratories, Baltimore, Md.

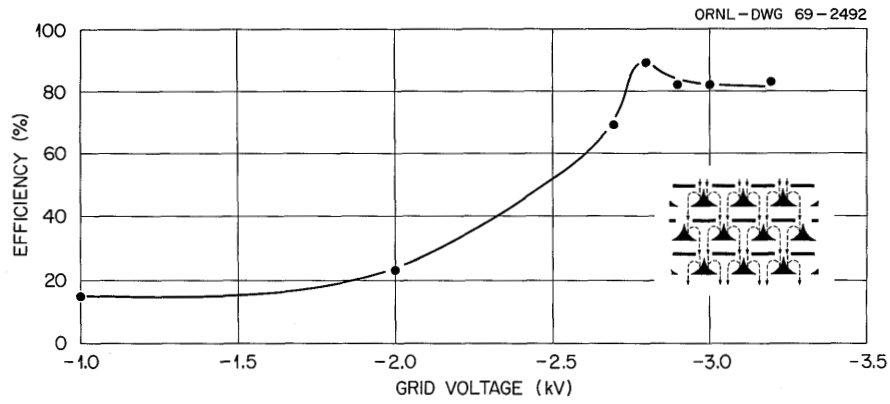

Fig. 9.15. Detection Efficiency of a Johnston Multiplier with an Auxiliary Grid Mounted 3 mm in Front of the First Dynode. Shown is the efficiency as a function of the negative bias on the grid. Negative 2700 V bias applied to first dynode of multiplier.

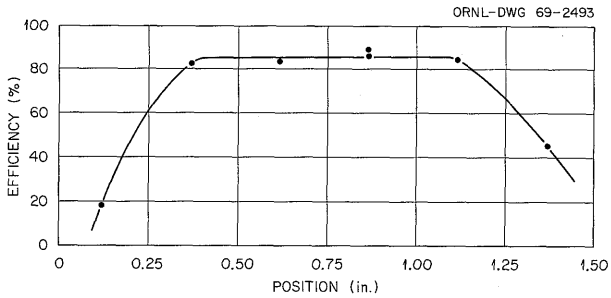

Fig. 9.16. Johnston Multiplier Efficiency as a 0.140-in.-Diam 20-keV Hydrogen Beam Is Scanned Across the Entrance Window. Multiplier dynode voltage, −2700 V; auxiliary grid voltage, −2800 V.

keV, 3.5-mm-diam hydrogen beam is scanned across the entrance of the multiplier. The response is flat over the center 18.7-mm-diam region of the multiplier. Decreased response at the outer regions was probably the resultant of outward radial scattering of the electrons as they travel down the tube.

9.9.2 Channel Electron Multipliers

Channel multipliers[13] consist of annular semiconductor tubing bent into some curved pattern with a potential difference applied across the length of the tube. Secondary electrons emitted from particle impact at the entrance are accelerated by the applied longitudinal electric field, creating additional secondaries from surface collisions. Gains of 10^8 are obtainable with tubes 10 to 15 cm long. A schematic of a typical multiplier is shown in the inset of Fig. 9.17. Also shown is the pulse-height spectrum obtained for 1- and 50-keV hydrogen incident on the multiplier. The increase in the 1-keV hydrogen curve at small pulse heights results from electronic noise. In the past the practice has been to assume that the electron multiplier is 100% efficient if the pulse-height spectrum is clearly resolvable above noise. These data would indicate that 1-keV hydrogen was detected with 100% efficiency; however, in the next section it is shown that the efficiency is independent of the shape of the pulse spectrum. Since the detectors would normally be used in regions of a stray magnetic field, the response was determined as a function of an externally applied field. The results for a constant input 30-keV hydrogen beam are shown in

[13]Bendix Corp., Southfield, Mich., or Mullard, Farmingdale, Long Island, N.Y.

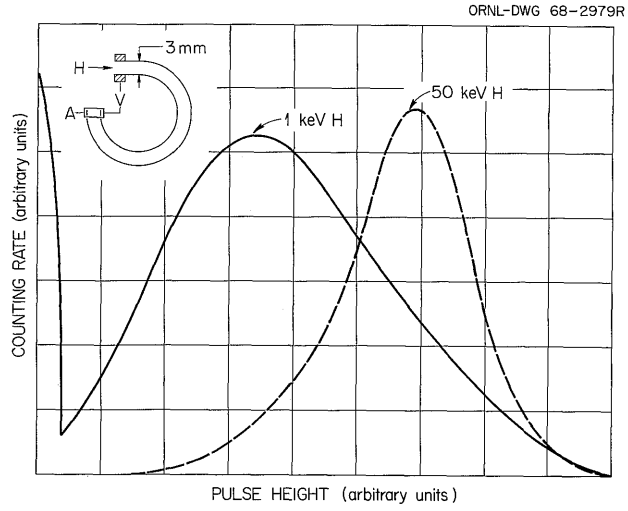

Fig. 9.17. Pulse-Height Spectra for 1- and 50-keV Hydrogen Obtained from a Channeled Multiplier.

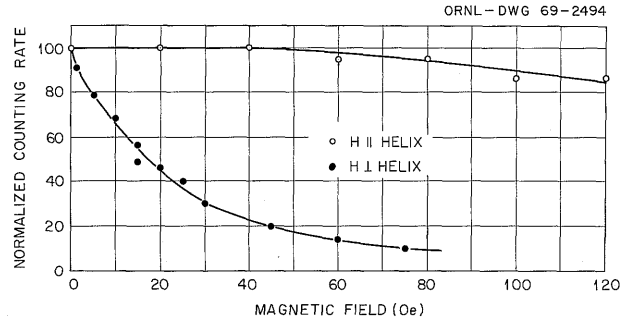

Fig. 9.18. The Effect of an External Magnetic Field on a Channel Multiplier. Upper curve obtained when magnetic field was in the direction of the plane of curvature. Lower curve, the field was perpendicular to the plane.

Fig. 9.18. The upper curve was obtained with the magnetic field applied parallel to the plane of multiplier curvature. A small decrease was found for fields up to 120 Oe. However, when the field was applied transverse to the multiplier plane a rapid decrease in counting rate was observed.

9.9.3 Funneled Channel Multipliers

Some applications involving particle detection require a larger entrance window than the normal 1 to 2 mm available as a channel multiplier. To increase the effective area, the entrance to the tube is flared into a cone or funnel with an entrance diameter of 1 cm, as shown in the inset of Fig. 9.19.

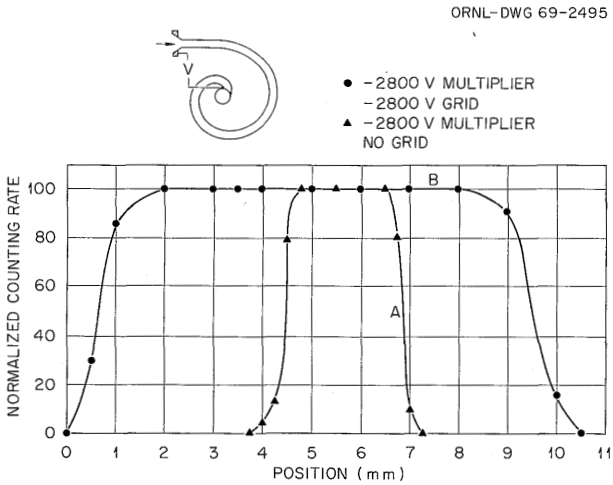

Fig. 9.19. Counting Rate of a Funnel Multiplier as a 20-keV 0.125-mm-Diam Hydrogen Beam Is Scanned Across the 1-cm-Diam Entrance. Operated with negative bias on both front end of multiplier and auxiliary grid.

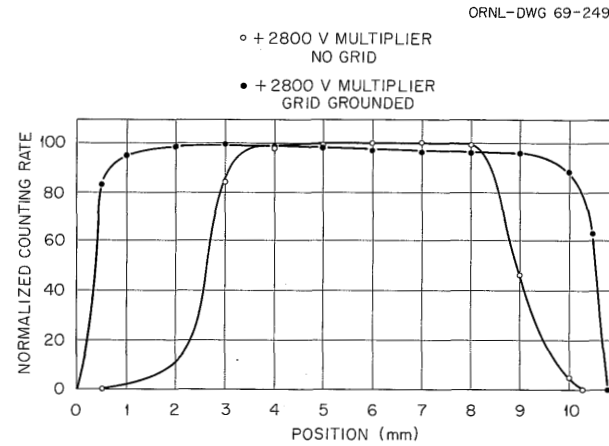

Fig. 9.20. Counting Rate of a Funnel Multiplier as a 20-keV 0.125-mm-Diam Hydrogen Beam Is Scanned Across the 1-cm-Diam Entrance. Operated with front end of multiplier and auxiliary grid at ground potential.

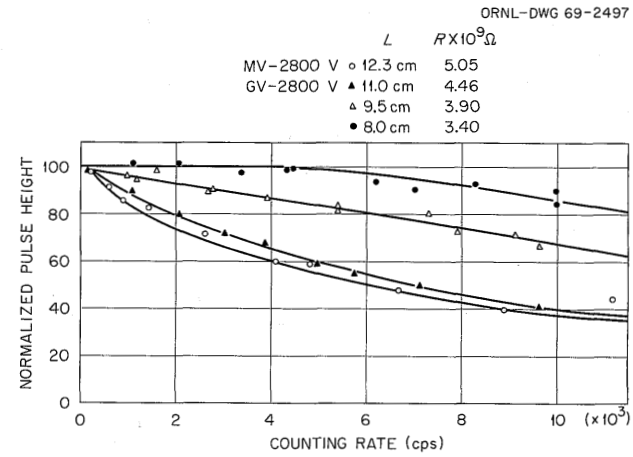

Fig. 9.21. The Variation of Pulse Height or Gain as a Function of Counting Rate for a Funneled Multiplier. 20-keV hydrogen beam incident. The four curves are for various lengths or resistances of multiplier. In the four curves the multiplier voltage and amplifier gain were maintained constant.

Shown also is the counting rate as a 20-keV 0.125-mm diam hydrogen beam is scanned across the entrance. The curve labeled *A* was obtained with the multiplier operating as recommended by the manufacturer,[13] and as is obvious the cone does not result in increased areal response. When a grid is placed at an equi-bias in front of the multiplier, data as shown in curve *B* were obtained. These data were obtained with the entrance at a negative potential. With the entrance at ground potential and the collector at +2800 V, results are obtained as shown in Fig. 9.20, which indicates large areas of uniform sensitivity. As the small-diameter hydrogen beam was scanned across the entrance window the gain or average pulse height decreased as a function of position, with minimum gain found in the central channel region.

Observations were made that the average pulse height decreased as the counting rate increased, implying that the multiplier was being used as an amplifier in a saturation mode caused either by space charge or high tube resistance. A series of tests were conducted in which the multiplier length was decreased in small steps. The results are shown in Fig. 9.21, where the pulse height is plotted as a function of counting rate. Pulse heights are normalized to 100 at counting rates of 200 counts/sec for the 20-keV hydrogen beam. Decreasing the length by 35% permits the tube to operate in the nonsaturating mode for counting rates less than 5×10^3 counts/sec. By increasing the multiplier voltage to 3400 V, thereby increasing the gain, the multiplier gain saturated. These results indicate that the multiplier gain is normally limited by space charge in the collector region. Since the pulse height decreases as the counting rate increases, it was desirable to determine if the efficiency was also a function of counting rate. The

Table 9.3. Detector Characteristics

Detector	Availability	Approximate Cost (dollars)	Gain	Stability to Atmospheric Exposure	Energy Sensitive	Minimum Energy of H or H^+ Detection	Minimum Energy of Heavy Ions	Efficiency, 10-keV H (%)	Fatigue (particle damage)	Discrimination, $h\nu$ vs H^0	Entrance Window Uniformity	Sensitivity
Johnston with grid	Johnston Labs.	2000	10^6	Stable	No	1 keV	1 keV	90	None	?	Good	Counting rates
Channel multiplier with grid	Mullard-Bendix	350	10^8	Stable	No	100 eV	100 eV	100	Gain decrease 2× after 15 hr	No	Good	Counting rates
Funneled multiplier with grid	Mullard-Bendix	500	10^8	Stable	No	100 eV	100 eV	100	Gain decrease 2× after 15 hr	No	Good	Counting rates
Surface barrier detector	ORTEC nuclear diodes	800	Particle energy (eV), 3.7	Stable	Yes	6 keV	20 to 40 keV	100	Fails after total flux $\sim 10^{14}$	No	Good	Counting rates
Magnetic electron multiplier	Bendix	1000	10^5	Stable	No	1 keV	1 keV	60	None	No	Poor	Counting rates
Faraday cup	Workshop	50	1	Stable	No	Few eV	Few eV	100	None	Yes	Good	10^{-12} A with dc electrometer
Secondary emission detector	Workshop	50	2 to 5	Stable	No	100 eV	100 eV	100	None	No	Good	10^{-12} A
Open electron multiplier	Any P.M. tube Mfr.	100	10^5	Unstable	No	1 keV	1 keV	Unknown	Unknown	No	Poor	Counting rates
Thermal		10 to 100		Stable	No				None	No	Good	10^{-7} W

efficiency as determined by comparing the multiplier counting rate to a solid-state detector is shown as a function of counting rate in Fig. 9.22. The efficiency being consistently greater than 100% reflects the fact that the solid-state detector is insensitive to reflected energetic particles. For 20-keV hydrogen the particle reflection coefficient is approximately 0.05; thus it is expected that the funneled multiplier could have an efficiency greater than 100% as measured by this comparison technique.

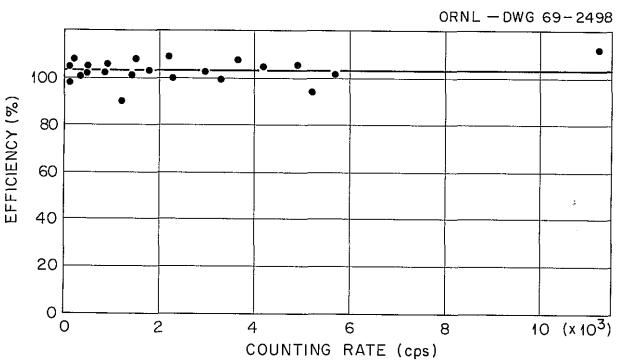

Fig. 9.22. Funneled Multiplier Efficiency Plotted Vs Counting Rate. 20-keV hydrogen incident. Multiplier and grid voltage –2800 V.

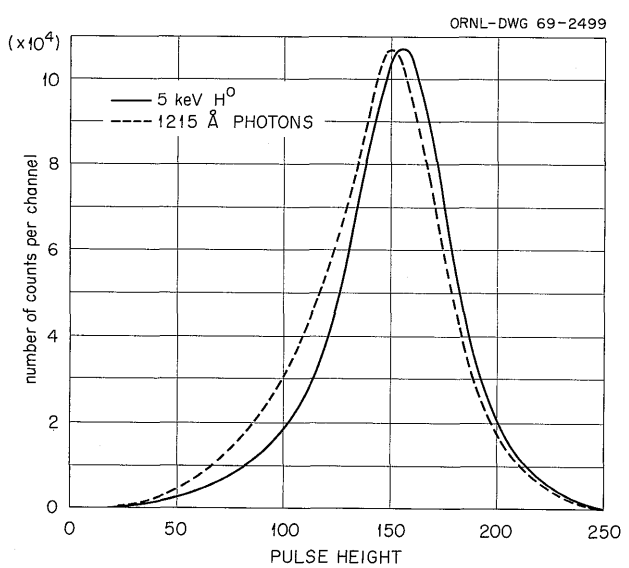

Fig. 9.23. Pulse-Height Distributions Obtained from a Funneled Multiplier for Incident 5-keV Hydrogen Atoms and for 1215-Å Photons.

To determine if the multiplier was capable of discriminating against photons a pulse-height spectrum was obtained for 5-keV hydrogen atoms. The multiplier was then mounted in a vacuum ultraviolet spectrometer and a pulse spectrum obtained for 1215-Å photons. In both cases the multiplier gain and amplifier gains were maintained constant. The pulse spectra obtained are shown in Fig. 9.23. For incident photons the maximum number of photoelectrons emitted per photon is 1 except in the relatively rare cases of Auger transitions. For 20-keV hydrogen atom impact the secondary emission ratio should be at least 3 to 4. Since the multiplier gain is saturated, the output pulse height is independent of the relative number of electrons emitted at the first stage. The pulse spectra shown in Fig. 9.23 are characteristic of one electron being emitted regardless of photon or heavy-particle detection. Therefore no discrimination between photons and hydrogen atoms exists for this type of multiplier.

9.9.4 Detector Evaluation Summary

Shown in Table 9.3 is a summary of detector characteristics that have been investigated in our laboratory during the past five years. This table is placed here as a guide rather than to present absolute numbers. If detailed information is needed, the reader is referred to the continuing series of Thermonuclear Division progress reports.

9.10 ATOMIC AND MOLECULAR PROCESSES INFORMATION CENTER

C. F. Barnett
L. G. Bean
D. A. Griffin
M. O. Krause
J. R. McNally
J. A. Ray
I. A. Sellin
L. D. Vest
M. I. Wilker

The current atomic and molecular physics and chemistry literature is being searched and evaluated on a monthly schedule. These searches provide the basis for the semiannual editions of the series *Bibliography of Atomic and Molecular Processes*. During this report period two bibliographies have been issued, for July–December 1967 and January–June 1968. Delays in publication of approximately four months are encountered in the

process of editing and printing. Since the publication of these bibliographies imposes a large expense on the data center and Laboratory, a survey was made to determine the feasibility of the user sharing the cost by purchasing these publications or to determine if microfiche would be satisfactory. The response to the questionnaire sent to those on our distribution list (1867) was 1331, with 686 indicating they would be willing to pay a nominal sum for the bibliography, and essentially everyone objected to the use of microfiche. Two publishers have declined the offer of publishing these items commercially, and thus the only reimbursable publication route left is through the U.S. Clearing House. At the present time, publication and distribution through the Clearing House seems to be impractical.

After long delays the first monograph, *Ion-Molecule Reactions,* has been completed and sent to the publisher, John Wiley and Sons. Publication date is expected by June or July 1969. The second monograph, which has been in the writing stage for approximately 18 months, has grown to an expected length of 800 printed pages, which defeats the intent of the monograph series. This volume has been divided into three monographs: monograph No. 2, *Excitation by Heavy Particles,* authors E. W. Thomas, Georgia Institute of Technology, and A. Russek, University of Connecticut; monograph No. 3, *Ionization by Heavy Particles,* authors John W. Hooper, Georgia Institute of Technology, Felton Bingham, Sandia Corporation, and A. Russek; monograph No. 4, *Dissociation of Molecules by Heavy Particles,* authors G. W. McClure and J. A. Peek, both of Sandia Corporation. The fifth monograph is approximately 50% complete, authors being C. F. Barnett and I. A. Sellin of Oak Ridge National Laboratory and R. A. Mapleton of Air Force Cambridge Research Laboratories. At the present time there are no plans to start future monographs; however, data compilations are beginning involving the phenomena of sputtering and secondary emission from metallic surfaces.

The revised version of *Cross Sections of Interest to Thermonuclear Research* is proceeding, with an expected completion date in the fall of 1969. Our other publication activities included the translation, referencing, and distribution on a limited basis of a bibliography entitled *Electronic and Atomic Collision Bibliography of Russian Literature for the Years 1946–1966.*

Problems of data storage and retrieval have been partially solved during this report period. Our computer storage now consists of three files: (1) the master file containing the bibliographical information, (2) the reaction file used for retrieval when the collision process and collision partners are specified, and (3) the data file where evaluated data are stored and retrieved. Both the reaction file and data file are cross-linked by accession number to the master file. Tests completed with an 800-reference data base have indicated that the machine retrieval of information is more complete than manual search. In no cases did the machine search fail to retrieve information found through manual search techniques. Presently, all references are being placed on tape for routine search requests.

Ways have been sought to increase the efficiency and decrease the cost of data input and monograph production. For the past eleven months, tests have been carried out with both data input to a computer by remote access and computer text editing using a telephone line link with Van Horn Information Processing Corporation in Washington, D.C. It has been our experience that bibliographical and data input time and efficiency have not been improved by such techniques. Data input by punched cards is much less expensive, more accurate, and less time consuming than remote access. Text editing is feasible but more expensive due to the telephone line charges. For the past two years we have planned to tie in remotely with the K-25 IBM 360 system; however, cost analysis by the Nuclear Safety Information Center has led us to cancel all equipment that had been ordered for remote access. The decision has been made to continue our present system of computer input via punched cards, and retrieval will be on a 24-hr turn-around basis.

10. Energetic-Particle Injectors for Plasma Physics Experiments

R. C. Davis
R. R. Hall
G. G. Kelley
O. B. Morgan, Jr.

10.1 INTRODUCTION

The energy range of charged- or neutral-particle injectors developed at Oak Ridge now extends from a few keV up to 600 keV. These injectors can all be used for either pulsed or dc injection and are exemplified by the 80-mA, 600-keV H_2^+ DCX-2 injector and the 50-mA (equivalent), 20-keV H^0 DCX-1.5 injector which produces a 55% energy spread (full width at half maximum) in the trapped protons. For less demanding vacuum requirements, found for example in some target plasma experiments, currents of 250 mA (equivalent) H^0 at 20 keV are available.

The above injectors are useful for a variety of fruitful plasma physics experiments. However, there continues to be a desire for more intense beams with greater flexibility throughout this energy range and perhaps at even lower energies. Therefore supplementary studies are being made of such basic problems as the space-charge neutralization of low-energy beams and the control of the shape of the ion emission surface. Related engineering problems, for example, the development of a better ion source filament, are also being pursued.

In the near future the present efforts will also be supplemented by experiments to evaluate entirely new sources of energetic particles. The first experiment will be an attempt to build an improved injector by using ionized and accelerated hydrogen clusters as the source of particles.

10.2 SPACE-CHARGE NEUTRALIZATION

One of the most critical requirements for the production of intense ion beams is the space-charge neutralization of the ions by creating an equal density of electrons within the beam. A simple, effective method for obtaining these electrons is to trap those produced by ionizing collisions of the energetic ions with the background gas.[1] With hydrogen ion beams of 10 to 600 keV and with a gas pressure of $\sim 10^{-6}$ torr or greater, it has been demonstrated that dc ion beams can be space-charge neutralized.[1,2] These beams are neutralized if the walls surrounding the drift region are at the same electric potential and if an electron reflector (either an electric or magnetic field) is provided between the drift space and the ion source. The effectiveness of the neutralization depends on the residual positive charge required to hold the electrons. A decrease in the rate of production of electrons reduces the degree of neutralization.

There are at least three typical operating conditions for intense ion beams for which the source of electrons may be inadequate. For very low-energy ions, hundreds of eV for hydrogen ions, for example,

[1] G. G. Kelley and O. B. Morgan, *Phys. Fluids* 4, 1446 (1961).

[2] O. B. Morgan, G. G. Kelley, and R. C. Davis, *Rev. Sci. Instr.* 38, 467 (1967).

ORNL-DWG 69-2500

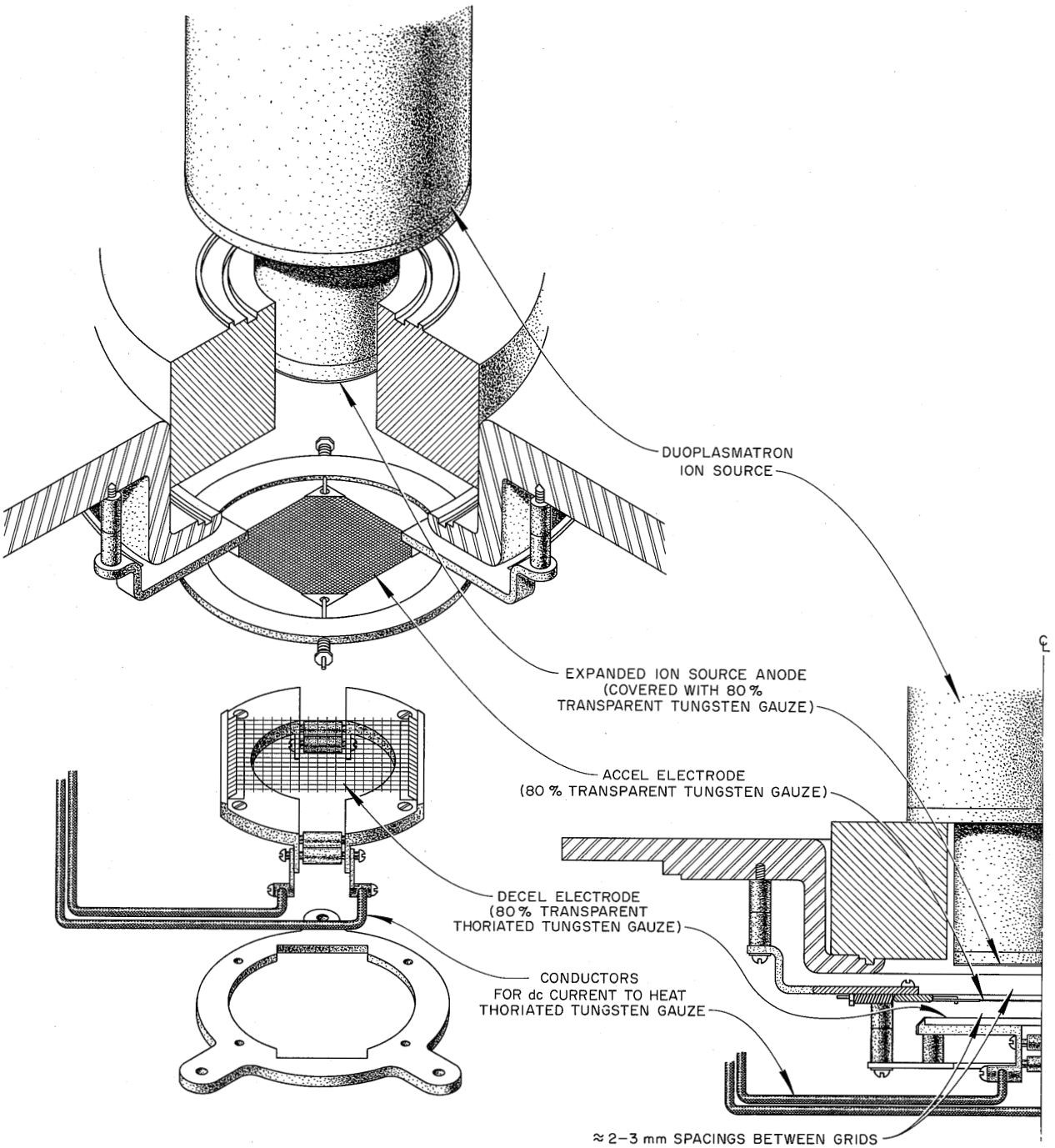

Fig. 10.1. Space-Charge Neutralizing System for Low-Energy Ion Beams.

the ionization cross section has decreased significantly.[3] The production rate is also too low for these and more energetic particles when the background neutral-particle density is reduced to a very low value (pressures much lower than 10^{-6} torr, for example). The third condition is pulsed operation when the beam "on time" is shorter than the ionizing collision time of the beam particles at otherwise satisfactory background pressures.

In some cases where the self-neutralization of the beam does not occur, attempts have been made to add electrons by placing emitters around the periphery of the beam. The electrons produced are accelerated into the positive column of ions, but unfortunately they have their maximum energy (and therefore contribute least to the density) in the center of the ion beam. This, of course, is not an ideal solution, and what is needed is a source of electrons generated intimately within and uniformly across the ion beam cross section.

A method of providing these electrons has been developed. At low energies or for low duty cycle, intense ion beams can usually be more effectively obtained through grids or in some cases multi-apertured electrodes instead of large single apertures. To evaluate the potential advantage of using an effective electron source for these beams, a system is being used that incorporates an accel-decel set of gridded electrodes (Fig. 10.1). A duoplasmatron ion source with an expanded, tungsten-grid-covered anode is used as a source of plasma. The accel-decel gridded electrodes provide an electric field to keep electrons in the drift region from flowing to the positively biased anode. Simultaneously the decel electrode is chosen to be the source of added electrons by making it from an 80%-transparent thoriated tungsten grid. This grid is heated to emission temperatures by an external current source and, except for a few volts potential drop for heating, is maintained at the drift space wall potential. The accel electrode made of tungsten gauze (which will not emit at temperatures at which the thoriated tungsten is a copious source of electrons) is biased at a negative potential of tens of volts to reflect electrons.

A shielded 1.25-cm-diam probe is used to determine the density and profile of the ion beam. The probe has an inner insulated tungsten grid that is used as a secondary electron suppressor and an outer grid maintained at the ground potential of the drift space chamber. The probe results are checked by comparing them with a 5-cm-diam calorimeter. The two current measurements are found to agree within a few percent. The probe can be moved both axially and radially in the beam.

The thoriated tungsten grid was made by hand (a very tedious job), and since the grid was heated to higher temperatures in preliminary exploration than was eventually found to be necessary, it was partially destroyed before as much information could be obtained as was desired. However, it is now known that thoriated tungsten gauze can be obtained commercially and will then be more expendable and also more uniform and rigid than the handmade gauze used here.

Figure 10.2 indicates the typical performance of the system with and without the addition of the electrons as a function of the ion energy for a dc hydrogen ion beam at a background gage pressure of 5×10^{-6} torr in the beam drift region. This information indicates the current to the 1.25-cm-diam probe at a distance of 1 m from the ion source. By scanning radially through the beam with the 1.25-cm-diam probe, the current density was found to be uniform within 20% over at least a 5-cm diameter. Therefore the beam available in a 2-in.-diam circle at 1 m distance at an energy of 100 eV and a pressure of 5×10^{-6} torr is approximately 1200 μA with the added electrons and approximately 96 μA without the electron addition. From the limited information obtained before the grid was destroyed, some general observations can be reported.

Starting at an energy of 1 keV and lowering the energy and observing the probe current as a function of the background pressure (varied by introducing hydrogen gas into the beam drift region), one finds that approximately equal currents can be obtained by increasing the background pressure or by adding the electrons. However, the pressure required is $\approx 5 \times 10^{-4}$ torr. At an energy of $\approx$200 eV or lower the addition of electrons results in higher probe currents than those obtained at any background pressure. At 100 eV the electron addition gives at least a factor of 2 more probe current than can be obtained at the optimum pressure.

It should be emphasized that the magnitude of the numbers reported may not reflect the ultimate potential of this system to produce intense low-energy beams. Very little effort has been invested in the optimization of numerous parameters involved in the system that might significantly increase the

[3]H. B. Gilbody and J. B. Hasted, *Proc. Roy. Soc. (London)*, Ser. A **240**, 382 (1957).

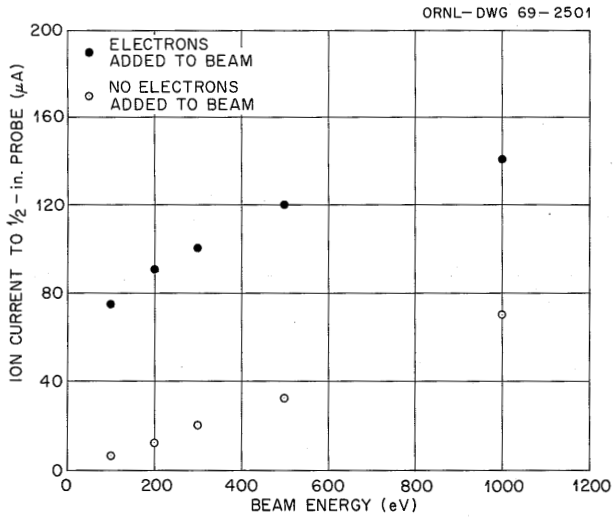

Fig. 10.2. Hydrogen Ion Current With and Without Electron Addition for Improved Space-Charge Neutralization. System pressure 5×10^{-6} torr; probe located 1 m from ion source.

magnitude of the current. Total dc beam currents of 150 mA at energies up to 2 keV were extracted through the tungsten grids with no damage to the grids. The emphasis was only on evaluating the idea of properly adding electrons into the ion beam for space-charge neutralization and comparing this with the identical beam conditions without the electron addition. It is also obvious that the difference will be more dramatic as the pressure in the beam drift region is lowered below 5×10^{-6} torr.

10.3 ION SOURCE FILAMENTS

The dc arc current in the duoplasmatron-type ion source has increased from less than 10 A to more than 50 A in some present applications. No real effort has been made until recently, however, to develop a better filament for these applications. With 50 A arc current (using a four-electrode duoplasmatron ion source) the present filaments (Fig.

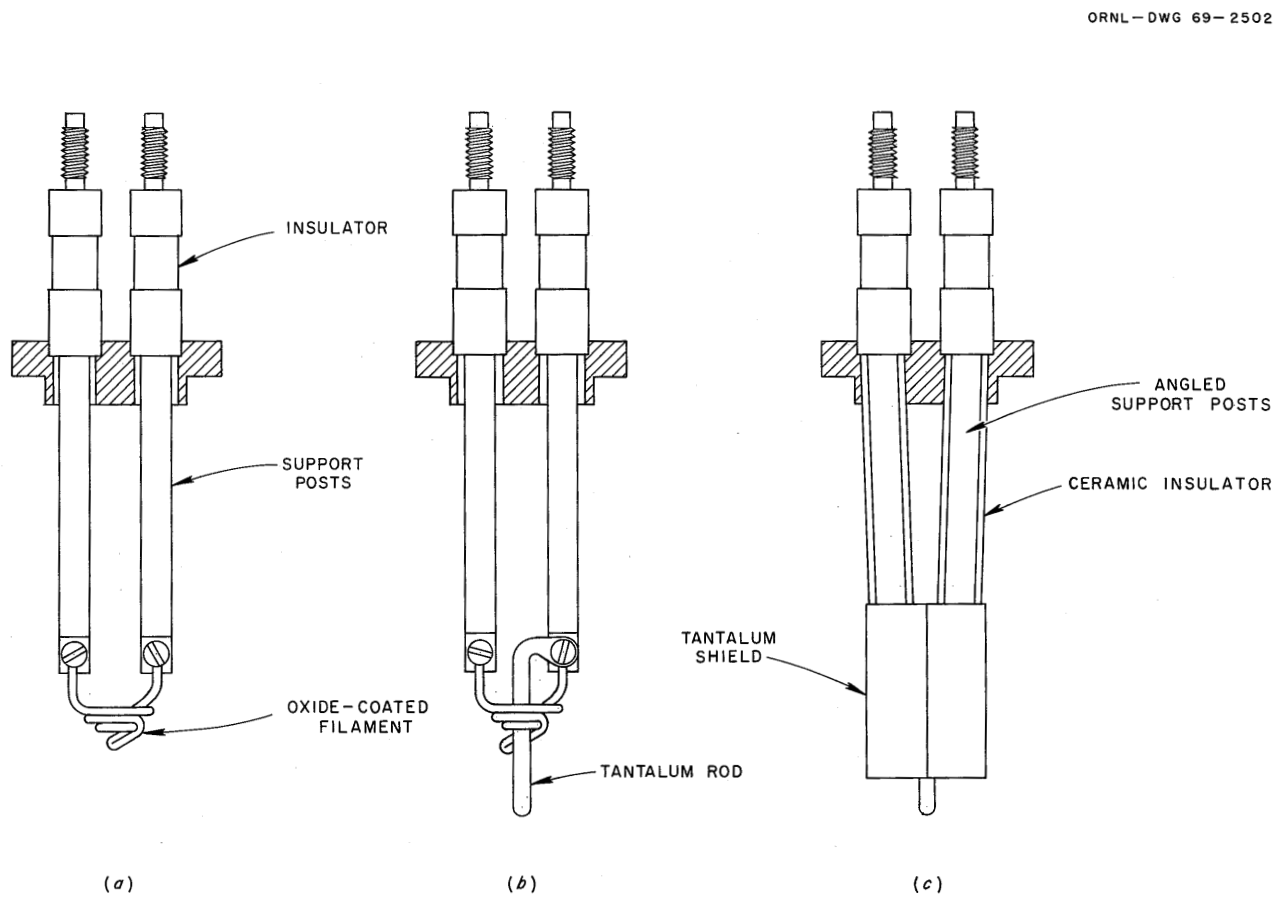

Fig. 10.3. Development of a New Ion Source Filament.

10.3*a*) were found to be limited to a lifetime of a few hours with dc operation. During the lifetime of the filament the current required for adequate emission increased from 18–20 A to 38 A. The arc volts required to start the discharge also increased and resulted in breakdown between the support posts and the intermediate electrode. The incorporation of a tantalum rod (Fig. 10.3*b*) increased the filament lifetime with a 50-A dc arc to 17 hr before breakdown between the support posts and the intermediate electrode terminated the operation. The rod is heated to emission temperatures in ≈15 sec by 10 A or more of arc current. At this time the oxide filament can be turned off. The breakdown problem was eliminated by incorporating a cylindrical tantalum foil shield around the filament (Fig. 10.3*c*). This assembly has been operated for 27 hr with a 50-A dc arc with no noticeable deterioration in performance. A similar filament was also operated for 3 hr at 100 A arc with no appreciable deterioration.

10.4 5-keV H^+–10-keV H_2^+ INJECTOR

The desire to use an intense 5-keV H^0 beam as a diagnostic tool on INTEREM resulted in a re-evaluation of previously obtained beam intensities at this energy.[4] A multiapertured source is used and is shown in Fig. 10.4. Both flat and concave multiapertured electrodes are used, and the ion source location is optimized with respect to the lens. The three-electrode duoplasmatron ion source (Fig. 10.4) was used for H^+ ions and a four-electrode duoplasmatron for H_2^+ ions. An improved method for cooling the electrode is used and is shown in Fig. 10.4. This cooling proved adequate to prevent melting of the aperture webbing.

The injector was evaluated both as a source of ions and of energetic neutral particles by using a magnesium vapor cell. The resulting beams through

[4] *Thermonuclear Div. Semiann. Progr. Rept. Oct. 31, 1965*, ORNL-3908, pp. 105–7.

ORNL-DWG 69-2503

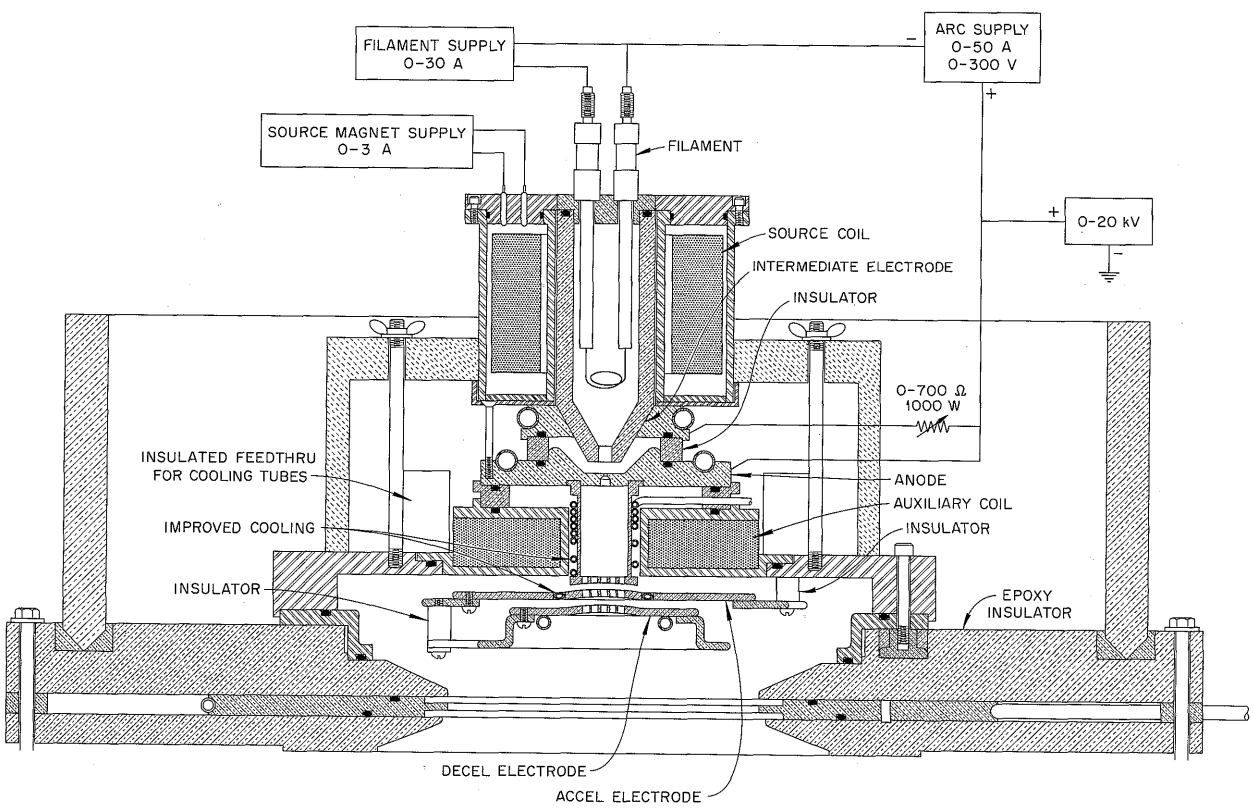

Fig. 10.4. Low-Energy Multiapertured Ion Source System.

Table 10.1. Ion and Neutral-Particle Equivalent Current Through a 5-cm Aperture Located 120 cm from Lens

Neutralizing cell imposes a 4.1-cm constriction 50 cm from lens

Beam Energy (keV)	Ion Current (mA)	H^0 Atom Equivalent Current (mA)
	H^+ Source	
10	34	20
7.5	26	
5	17	8
	H_2^+ Source	
10	28	40
10	20[a]	

[a] 2.5-cm aperture.

a 5-cm aperture located 1.2 m from the lens are summarized in Table 10.1

Unfortunately the results are not significantly better than those obtained earlier.[4] Other techniques have been successful in diagnosing the INTEREM plasma, and this work has been discontinued.

In this energy range a new approach is needed to provide significantly more intense beams. Possible techniques include the use of hydrogen ion clusters (see Sect. 10.6) or the discovery of some means of control of the plasma emission surface.

10.5 SOLAR WIND EXPERIMENT

The 20-kV accelerator system has been altered for use in simulating results of the solar wind upon the moon's surface. This project is being conducted in conjunction with NASA of Houston, Texas.

A 30-g sample of oceanic basalt prepared at Houston and sent to us will be unsealed, bombarded, and resealed while in a vacuum of 0.5 to 1.0×10^{-6} torr. The sample will be spread out on a flat 12-in.-diam water-cooled copper tray. The sample material temperature must not exceed 200°C, so it will be bombarded at the rate of 13 $\mu A/cm^2$ (10 mA H^+ at 10 keV) for a continuous period of ~400 hr. The sample must be stirred and agitated at ~$\frac{1}{2}$-hr intervals to bring fresh material to the surface. This work is being done in cooperation with O. C. Yonts of the Thermonuclear Division.

10.6 HYDROGEN CLUSTERS

Equipment is now being built to evaluate the use of ionized and accelerated condensed hydrogen clusters as an injector for plasma physics experiments. The effort is based on the work of Becker and his co-workers at Karlsruhe,[5,6] who have studied the production and properties of such clusters. The effort at Oak Ridge will attempt to avoid the safety problems associated with the use of liquid hydrogen in these experiments. Liquid-helium vapors warmed to 20–30°K will be used instead of liquid hydrogen. Particular efforts will be devoted to developing an ionizer for an intense stream of clusters. After the ionized clusters are accelerated (up to 100 keV), the entire resulting beam will be analyzed in a transverse magnetic field. The basic question that one hopes to answer rapidly with this technique is whether an intense beam of energetic clusters in a usable mass range can be obtained.

[5] E. W. Becker, R. Klingelhofer, and P. Lohse, *Z. Naturforsch.* **17a**, 432 (1962).

[6] E. W. Becker, K. Bier, and W. Henkes, *Z. Physik* **146**, 333 (1956).

11. Magnetics and Superconductivity

11.1 REVIEW OF OUR BASIC WORK ON SUPERCONDUCTIVITY

K. R. Efferson
W. F. Gauster
J. B. Hendricks[1]
D. M. Kroeger
M. S. Lubell
J. E. Simpkins

As has been mentioned in the previous semiannual report, our basic work on superconductivity is jointly sponsored by the Controlled Thermonuclear Branch of AEC and by the George C. Marshall Space Flight Center of NASA (NASA Government Order No. H-29278A, "Magnetic Flux Flow and Superconductor Stabilization"). The last four of our quarterly NASA progress reports and several of our papers to be published in the open literature contain an almost complete description of our basic research activities on superconductivity during this report period. We therefore restrict ourselves to citing the following abstracts:

1. ORNL-TM-2162 (March 1968), NASA No. H-29278A (covering the period from October 1, 1967, to December 31, 1967).

"Our previously reported work has been continued during this third report period. Extended observations on the flux flow and stability performance of a bare Nb–25% Ti strip showed that for such samples of low heat capacity the value of power dissipation at take-off has minor significance. More important is the sample current (or more specifically, I^2R_n) and its relationship to the minimum propagating current. The flux flow and stability performance of compound conductors has been studied under controlled heat transfer conditions. An analysis of a great number of test cases showed that the flux flow and stability performance for samples with highly varying copper to superconductor ratios can be quantitatively predicted in a broad range of external fields. Conclusions can be drawn about the temperature–heat flux characteristics of the liquid helium cooled short samples employed for these experiments. Our efforts to improve our apparatus for direct measurement of heat transfer from small cylindrical metal surfaces to liquid helium have been continued. Finally, work on "thick" thin films is reported. It includes further developmental work on miniature Hall probes and on vacuum deposition and rf sputtering techniques. These techniques will be used for production of thin films for experimental work on superconductivity and on heat transfer."

2. ORNL-TM-2233 (May 1968), NASA No. H-29278A (covering the period from January 1 to March 31, 1968).

"Our previously reported work has been continued during this fourth report period. The observations on the flux flow and stability performance of bare NbTi strips have been extended to include two additional compositions, viz. Nb–5% Ti and Nb–10% Ti, which have similar critical temperatures but widely different upper critical fields and normal state resistivities. The results obtained with these samples confirm our previous conclusion that heat transfer phenomena rather than electrical effects (or a fortuitous interaction between electrical and heat transfer) were of primary importance in understanding premature take-offs. These results agree well with the observation on temperature fluctuations as described below. It has also been shown that the analysis of the field dependent recovery power can yield the heat flux as a function of temperature for the film boiling regime.

"To improve the analysis of compound conductors, it is necessary to make direct measurements of the magnetoresistance of the stabilizer and of the critical temperature of the superconductor. A new environmental test cell constructed for this purpose is described.

[1]Present address: Montana State University, Bozeman, Montana.

"Additional heat transfer measurements have been performed and reproducible fluctuations in the temperature of the heated sample in nucleate boiling have been observed. They increase in magnitude with the power dissipation and with the height of the liquid helium column above the sample. In the helium bath itself (without operating probes) temperature fluctuations are likewise observed. They are at least two orders of magnitude smaller and they also increase in magnitude with the height of the helium column. Finally, as anticipated, the thin film work has proved to be a useful tool for the manufacturing of new heat transfer probes."

3. ORNL-TM-2350 (August 1968), NASA No. H-29278A (covering the period April 1 to June 30, 1968).

"During this fifth report period, our previously reported work has been continued. For the bare superconducting strips, it is shown how, assuming a linear dependence of minimum propagating current on field, one can predict the anomalous take-off power as a function of field without introducing any arbitrary parameters. Only a measurement of I_c vs H and the known constants R_n, T_c, $H_{c2}(0)$ are needed. A theoretical investigation is made about compound superconductors under the assumption that the filaments are sufficiently thin and well bonded with the nonsuperconducting stabilizer that a uniform compound conductor temperature T can be assumed. If a measured heat transfer characteristic $\tau^* = f(\dot{Q})$ is used, the properties of the flux flow characteristics can be predicted from this function and the expression $(d\tau^*/d\dot{Q})\,[1 - \tau^* + \dot{Q}\,(d\tau^*/d\dot{Q})] = (RI_0^2)^{-1}$. Measurements of the transition temperature and stabilizer magnetoresistance taken with the new test cell are presented for three different types of commercial NbTi stabilized superconductors. Heat transfer experiments with the 0.002 in. wall thickness stainless steel sample have been concluded and a discussion of the large temperature fluctuations which occur in the nucleate boiling region is given. Preliminary results are also presented for the heat transfer from the copper film sample described in the last report. NbTi films deposited on metal substrates with a dielectric film sandwiched between superconductor and substrate are required for certain planned experiments. At the present, it appears that a silicon oxide film deposited on a smooth copper substrate will provide the necessary insulation together with adequate thermal conductivity for these experiments."

An appendix to the preceding report is the following paper:

4. D. M. Kroeger and M. S. Lubell, "Stability of the Flux-Flow State in Superconducting NbTi Strips," *Appl. Phys. Letters* **13**, 63 (1968). Abstract as follows:

"Experiments concerning termination of the flux-flow state have been performed on bare NbTi strips. For those strips of low heat capacity, take-offs occurred at powers less than the maximum heat flux in nucleate boiling. We conclude that take-off resulted from the simultaneous occurrence of a normal zone (caused by a local heat transfer fluctuation) and a current equal to or greater than the minimum propagating current."

5. ORNL-TM-2441 (November 1968), NASA No. H-29278A (covering the period July 1 to September 30, 1968).

"Our previously reported investigations have been continued during this sixth report period. Our work on bare superconducting strips in liquid helium at 4.2°K has been completed and is summarized in a paper which is enclosed as Appendix I. Additional work on the temperature dependence of the critical current of bare superconducting strips is in progress and the experimental arrangement is described. A numerical analysis of a measured steady state *I-V* (current-voltage) characteristic of a commercial compound conductor in constant external field has been made. Our previous investigations assumed that the heat flux is proportional to the 2.5th power of the temperature difference between metal and liquid helium. Furthermore, only the linear dependence of the superconductor current on the temperature has been considered. The present analysis is based on measured heat transfer, and for the zone of low flux flow resistance, the dependence of the superconductor current on temperature and on voltage has been investigated (Appendix II). Improved heat transfer measurements and investigations of the temperature fluctuations have been made (Appendix III)."

Appendixes I to III mentioned in the last NASA report abstract refer to the following papers:

6. M. S. Lubell and D. M. Kroeger, "Flux Flow Studies and Stability Criteria of NbTi Strips" (presented at the 14th Cryogenics Engineering Conference, Cleveland, Ohio, August 1968), to be published in *Advances in Cryogenic Engineering*, Vol. 14, 1969. Abstract as follows:

"Studies of complete flux flow cycles were performed on bare strips of Nb–5%, Nb–10%, and Nb–25% Ti in unrestricted helium flow in an effort to understand the instabilities which lead to termination of the flux flow state. Although the samples studied had large surface to volume ratios and low critical currents, it was nevertheless observed that the power dissipation at take-off (or sudden transition to complete normality) was less than the maximum heat flux in nucleate boiling. It will be shown that the magnitude of the take-off power and its anomalous dependence on magnetic field can be explained by means of temperature fluctuations due to local changes in heat transfer and a field dependent minimum propagating current. It will also be shown that analysis of the field dependent recovery power can give the heat flux as a function of temperature for the film boiling regime which agrees well with conventional heat transfer measurements."

7. W. F. Gauster, "Steady State Performance of Multistrand Superconducting Compound Conductors" (presented at the 1968 Applied Superconductivity Conference, Gatlinburg, Tennessee, October 1968), accepted for publication in *Journal of Applied Physics*, April 1969. Abstract as follows:

"A careful numerical analysis of a measured state *I-V* (current-voltage) characteristic of a superconducting compound conductor with very fine strands is reported. The actual, non-linear heat transfer from copper to the helium bath is considered. It is shown that in the current sharing state the flux flow resistance of the superconductor, R_f, increases from zero to values much greater than the copper resistance, R_{cu}. For $R_f \sim R_{cu}$, the superconductor current I_s is a function of the field H, the voltage V, and the temperature T. For $R_f >> R_{cu}$, I_s is a function of H, independent of V, and a linear function of T. The value of this function extrapolated to the bath temperature T_b is appreciably greater than the critical current. In the absence of flux jumps, the current sharing state could be terminated by the steady state condition $dI/dV = 0$. The actual "take-off" (sudden transition into the normal state) observed, however, took place below the mentioned steady state limit and before the transition from nucleate to film boiling. The new findings of the steady state performance of compound conductors with very thin strands make essential modifications of the usual theoretical approaches necessary. It is shown how the new approach can be applied to compound conductors with thick filaments."

8. K. R. Efferson, "Heat Transfer from Cylindrical Surfaces to Liquid Helium I" (presented at the 1968 Applied Superconductivity Conference, Gatlinburg, Tennessee, October 1968), accepted for publication in *Journal of Applied Physics*, April 1969. Abstract as follows:

"Heat transfer from a cylindrical copper surface to liquid helium at 4°K has been measured. The sample consisted of a horizontally mounted 3 mm O.D., evacuated glass tube, 6.5 cm long, onto which was deposited a 2000 Å thick copper film. It was heated by passing an electrical current through the copper film, and the temperature was monitored by a carbon resistor attached to the inside of the glass tube with varnish. In initial experiments, large temperature fluctuations were observed in the nucleate boiling region. These temperature fluctuations disappeared when the sample was either close to the liquid helium surface or when vertical walls were placed around the sample. The large temperature fluctuations were probably due to interactions of the convective flow of liquid helium with the boundaries of the system (dewar walls, liquid surface, etc.). Similar temperature fluctuations were observed with a stainless steel sample of approximately the same dimensions. The peak heat flux obtained in the nucleate boiling regime was 0.98 watts/cm^2 for Cu and 0.66 watts/cm^2 for stainless steel."

11.2 STEADY-STATE STABILITY OF COMPOSITE SUPERCONDUCTORS

W. F. Gauster

The stability of superconducting magnets can be greatly improved by using composite conductors.[2] They consist of a superconducting part (often in the form of a great number of thin strands) and a nonsuperconducting "stabilizer" (mostly copper; sometimes aluminum or silver), which should be in very good electrical and thermal contact with each other. The stability problem is very complex, since different physical phenomena determine the steady state and the dynamic stability.[3] The

[2]A. R. Kantrowitz and Z. J. J. Stekly, *Appl. Phys. Letters* **6**, 56 (1965); C. Laverick, *Cryogenics* **5**(3), 152 (1965).

[3]P. F. Chester, *Rept. Progr. Phys.* **30**, Part II, 561 (1967).

steady-state stability of composite superconductors is influenced by the flux-flow performance of the superconductor,[4] the interface thermal resistance between superconductor and the stabilizer, and the cooling of the stabilizer.

Z. J. J. Stekly and his co-workers[5] developed a theory of the steady-state stability of composite superconductors. It is based upon the dependence of the superconductor current I_s on two variables, the external field H and the superconductor temperature T, and it is simplified by the assumption of a constant heat transfer coefficient h for the heat flux $\dot{q}$ from the conductor surface to the liquid helium. (This model will be referred to as "model I".) A stability parameter α is introduced which is assumed to characterize the slope of the voltage-current (V-I) characteristic at the onset of the resistance. $\alpha < 1$ indicates stable, $\alpha > 1$ unstable performance. Finally, it has been considered that the steady-state equilibrium is terminated by the maximum nucleate heat flux $\dot{q}_M$.[6]

Tests demonstrated that this simple model is not sufficient for a quantitative prediction of the V-I characteristic[7] and that the $\dot{q}_M$ condition is in general not a criterion for the termination of the steady state.[8]

Recently it was suggested that this simple model could be quantitatively improved by considering instead of a constant h a varying heat-transfer coefficient ("model II").[9] The consequences of this suggestion will be discussed here.

Curve *a* in Fig. 11.1 is a current-voltage (I-V) characteristic of a short sample of a multistrand composite conductor measured by D. L. Coffey.[7] The tests were made under optimum cooling conditions.[8] Curve *b* is calculated with model I (assuming a constant, i.e., average heat transfer coefficient h). The stability parameter α is smaller than 1 (i.e., in accordance with the observed stable performance); however, the difference between the measured and the calculated I-V characteristic is appreciable. The observed termination of the steady state ("takeoff") corresponds to $\dot{q} = 0.25$ W/cm^2, in contrast to the value of $\dot{q}_M$, which was independently measured[10] to be 0.985 W/cm^2. Dynamic stability criteria[3] should be taken into account.

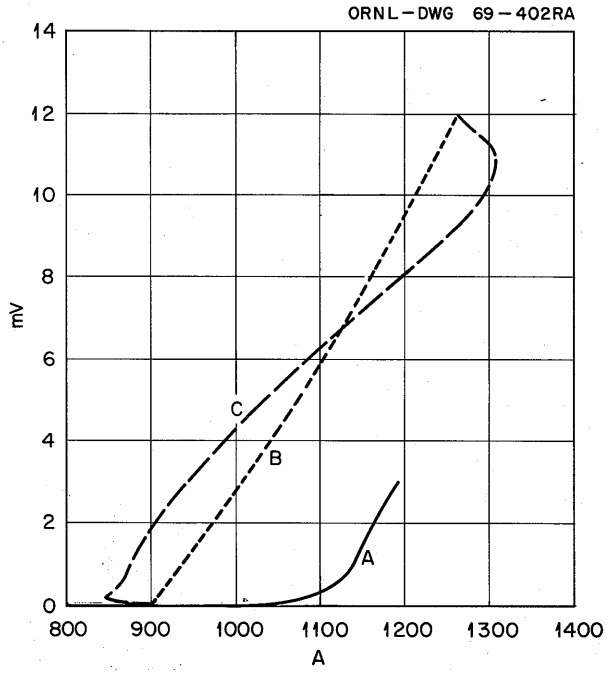

Fig. 11.1. Curve *a* Is the Measured Current-Voltage (I-V) Characteristic [W. F. Gauster, "Steady State Performance of Multistrand Superconducting Composite Conductors," to be published in the *Journal of Applied Physics* (April 1969)] of an NbTi Composite Conductor with 252 Very Fine Filaments at 4.2°K in an External Field of 55 kG. Curve *b* is calculated with "Model I" [Z. J. J. Stekly and J. L. Zar, *IEEE Trans.* NS-12, 367 (1965)]; curve *c* with "Model II" (Z. J. J. Stekly, R. Thome, and B. Strauss, "Principles of Stability in Cooled Superconducting Magnets," Proceedings of the 1968 Summer Study on Superconducting Devices and Accelerators, Brookhaven National Laboratory, June 1968).

Curve *c* in Fig. 11.1 is calculated from model II. Independently measured nonlinear heat transfer has been considered.[10] The calculation with model II

[4] Y. B. Kim, C. F. Hempstead, and A. R. Strnad, *Phys. Rev.* **139**(4A), A1163 (1965).

[5] Z. J. J. Stekly and J. L. Zar, *IEEE Trans.* **NS-12**, 367 (1965).

[6] C. N. Whetstone *et al.*, *IEEE Trans.* **MAG-2**, 307 (1966).

[7] W. F. Gauster, "Steady State Performance of Multistrand Superconducting Composite Conductors," to be published in the *Journal of Applied Physics* (April 1969).

[8] W. F. Gauster and J. B. Hendricks, *J. Appl. Phys.* **39**(6), 2572 (1968).

[9] Z. J. J. Stekly, R. Thome, and B. Strauss, "Principles of Stability in Cooled Superconducting Magnets," Proceedings of the 1968 Summer Study on Superconducting Devices and Accelerators, Brookhaven National Laboratory, June 1968.

[10] K. R. Efferson, "Heat Transfer from Cylindrical Surfaces to Liquid Helium I," to be published in the *Journal of Applied Physics* (April 1969).

indicates initially decreasing I, that is, unstable performance. Therefore model II (which utilizes the actual heat transfer) is in even poorer agreement with the observation than model I (which assumes an average heat transfer coefficient h).

It has been shown[7] that satisfactory agreement with the experiments was obtained when an additional phenomenon was taken into account, namely, that in the flux-flow state the superconductor current depends in general not only on T and H but also on the voltage V along the superconductor. Otherwise, stable performance of a bare superconductor (with a critical current which decreases with temperature) would always be impossible. However, stable flux-flow performance of bare superconductors has been repeatedly observed.[11] In a composite conductor the V dependence can be neglected only if the stabilizer resistance R_{cu} is much smaller than the flux-flow resistance R_f of the superconductor. For currents appreciably larger than the critical current I_c, this is indeed the case. However, at the onset of resistance, the experiments[7] demonstrate $R_f \ll R_{cu}$; that is, the V dependence of I_c cannot be neglected. This explains the discrepancy between the observed values and those calculated with the two models. To consider the V dependence of I_s does not mean the introduction of a new, more complicated "model III" only in order to obtain a better numerical fit of experimental data. It is rather a necessity dictated by the relevant physics and the fact that the other models are not, in general, sufficient to give even qualitatively correct results.

As far as we know, all calculations concerning conductors with thick filaments[12] assume that the current density in the superconductor depends only on H and T. As discussed above, this must lead to unrealistic results.

The valuable assistance of J. L. Horton and G. F. Leichsenring in calculating numerical data is appreciated.

[11] See, for instance, D. M. Kroeger and M. S. Lubell, *Appl. Phys. Letters* 13, 63 (July 1968).

[12] D. F. Fairbanks, paper G-3 presented at the 1968 Cryogenics Engineering Conference, Cleveland, Ohio; D. M. Montgomery *et al.*, "Very High Field Hybrid Magnet Systems," Proceedings of the 1968 Summer Study on Superconducting Devices and Accelerators (Brookhaven National Laboratory, June 1968); Z. J. J. Stekly *et al.*, unpublished.

11.3 WINDING TECHNIQUES FOR SUPERCONDUCTING MAGNETS

R. L. Brown

The electromagnetic forces generated in magnet windings produce stresses in the conductors which must ultimately be transmitted to other coil support structures. Unfortunately, the soft OFHC copper which is used in composite superconductors is a very ductile material capable of withstanding only moderate stresses. Ventilated magnet construction, using conductors with spiral-wrapped insulation,[13,14] increases the local stresses since the partial covering makes the load bearing surfaces smaller.

In layer-wound magnets, specially fabricated filler pieces are required in two places. In making the interlayer transition, it is important that the conductor at the end of one layer not be allowed to simply ride radially outward to the next layer without spacers; such construction causes a scissors action between conductors which damages both insulation and conductors. Rather, the final turn of one layer must rest on a ramp (or wedge) shaped filler piece which guides it to the radial position of the next layer (Fig. 11.2). Second, since the number of turns per layer seldom exactly fills the layer, a filler piece is necessary to eliminate the

[13] *Thermonuclear Div. Semiann. Progr. Rept. Apr. 30, 1967*, ORNL-4150, pp. 142–47.

[14] *Thermonuclear Div. Semiann. Progr. Rept. Oct. 31, 1967*, ORNL-4238, pp. 143–47.

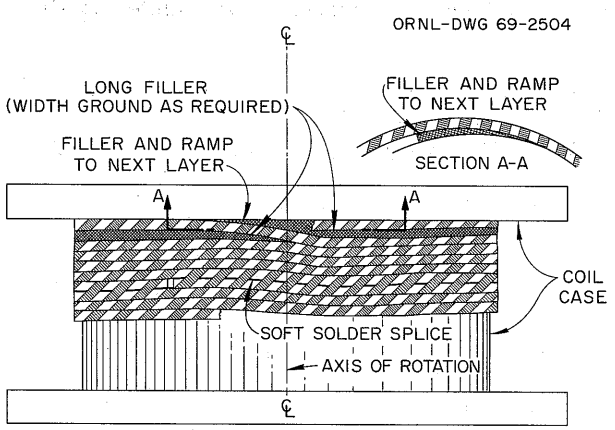

Fig. 11.2. Magnet Coil Fillers and Splices.

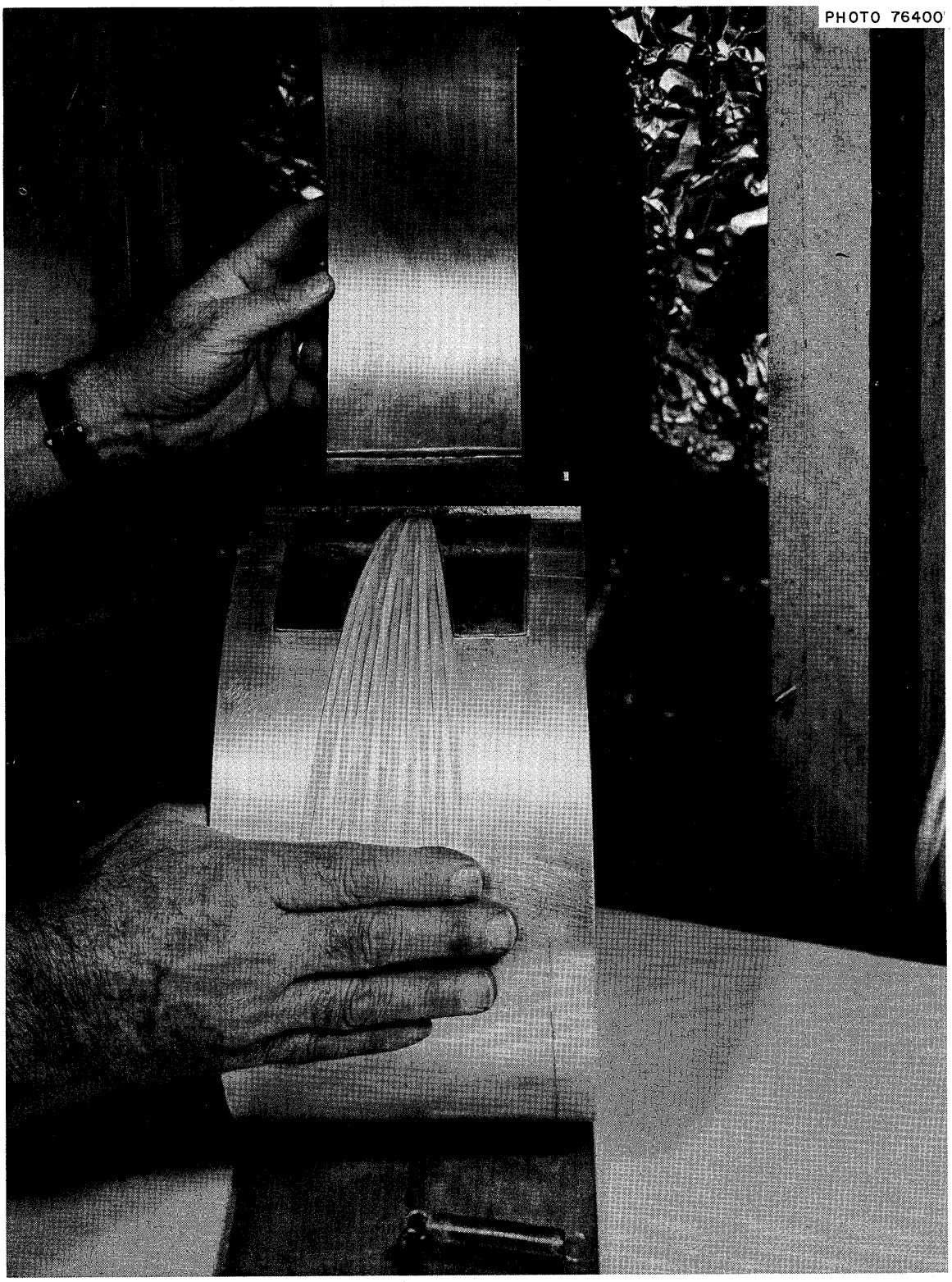

Fig. 11.3. Forming Curved Fillers.

resulting circumferential void. This piece is always less than one conductor width. It generally must be hand fitted to exactly fill the void space. It is convenient to install the circumferential filler piece between the last and the next-to-the-last turn (Fig. 11.2) of the layer. The effect of these filler pieces is to distribute very evenly the forces on the superconducting wire in the critical layer transition area. They greatly reduce the motion of windings subjected to electromagnetic forces and eliminate the "scissors" insulation damage.

The filler pieces must be fabricated of material which is (1) an insulator; (2) mechanically strong, but not brittle at liquid-helium temperatures; and (3) readily machined and formed. A compression test of thermoplastic polycarbonate (Lexan) indicated a yield strength of 3.1×10^4 psi at 77°K (about twice that of soft copper). Though no data are available on the properties of this plastic at lower temperatures, judging from the properties of similar plastics, we expect even greater strength at liquid-helium temperature. The thermoplastic property of polycarbonate makes it possible by heat treating the filler pieces at 150°C for 45 min to form them to the curvature of the magnet winding (Fig. 11.3). From a sheet of polycarbonate, the filler pieces are cut to a width slightly greater than the conductor width. These strips are ground to close tolerance on a rotary grinding wheel (Fig. 11.4). The grinding operation should be fast, since the filler pieces must be custom fitted at the end of each layer. The wedge-shaped filler pieces are fabricated in advance on a manually operated air grinder (Fig. 11.5). It has been found that the wedge-shaped filler piece must provide both a radial ramp and an axial ramp. This requires that

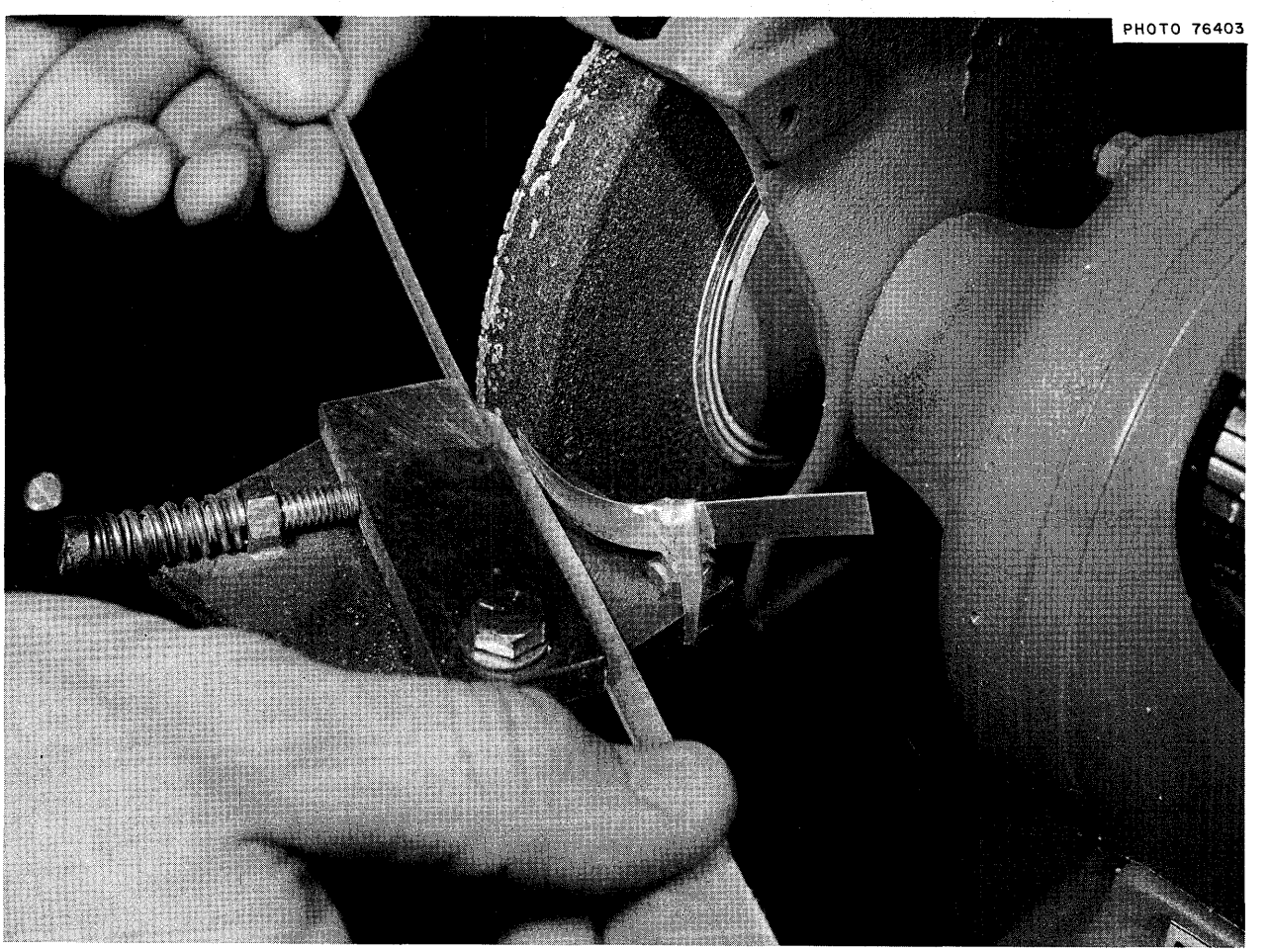

Fig. 11.4. Grinding Straight Rectangular Fillers.

the filler piece have a ramp at each end, with one rotated 90° with respect to the other.

Model winding studies, in connection with the development of IMP magnets, have led to several interesting improvements in the winding technique for layer-wound coils. Uniform conductor winding tension has been maintained by a brake wheel in which the conductor rides on a neoprene disk (Fig. 11.6). The tension is read and maintained by a torque wrench and clutch arrangement. The entire brake assembly is motor driven to move axially so that the conductor is kept in proper alignment with the coil.

Racetrack-shaped coils, for quadrupole magnets, presented another problem. In the straight sections, the windings become very loose since there is no radial force to keep the layers compressed. Attempts to use clamps during winding still did not produce a tightly wound section. It was finally necessary to allow a slight curvature in the "straight section" to maintain radial compression. Several coils with sections of various curvatures were wound to examine the influence of curvature on tightness (Fig. 11.7). A technique was developed to measure relative tightness by compressing the coil surface with 100 lb on a 1-in.-square surface and recording the resulting deflection. As can be seen in Fig. 11.8, with a rise of 0.394 in. at the center of a section with a length of 25 in., the deflection leveled off to approximately 0.0045 in. after about 12 layers of 0.057 × 0.114 in. composite conductor were wound.

Where splices of the composite conductor were required, they were made by soft soldering the

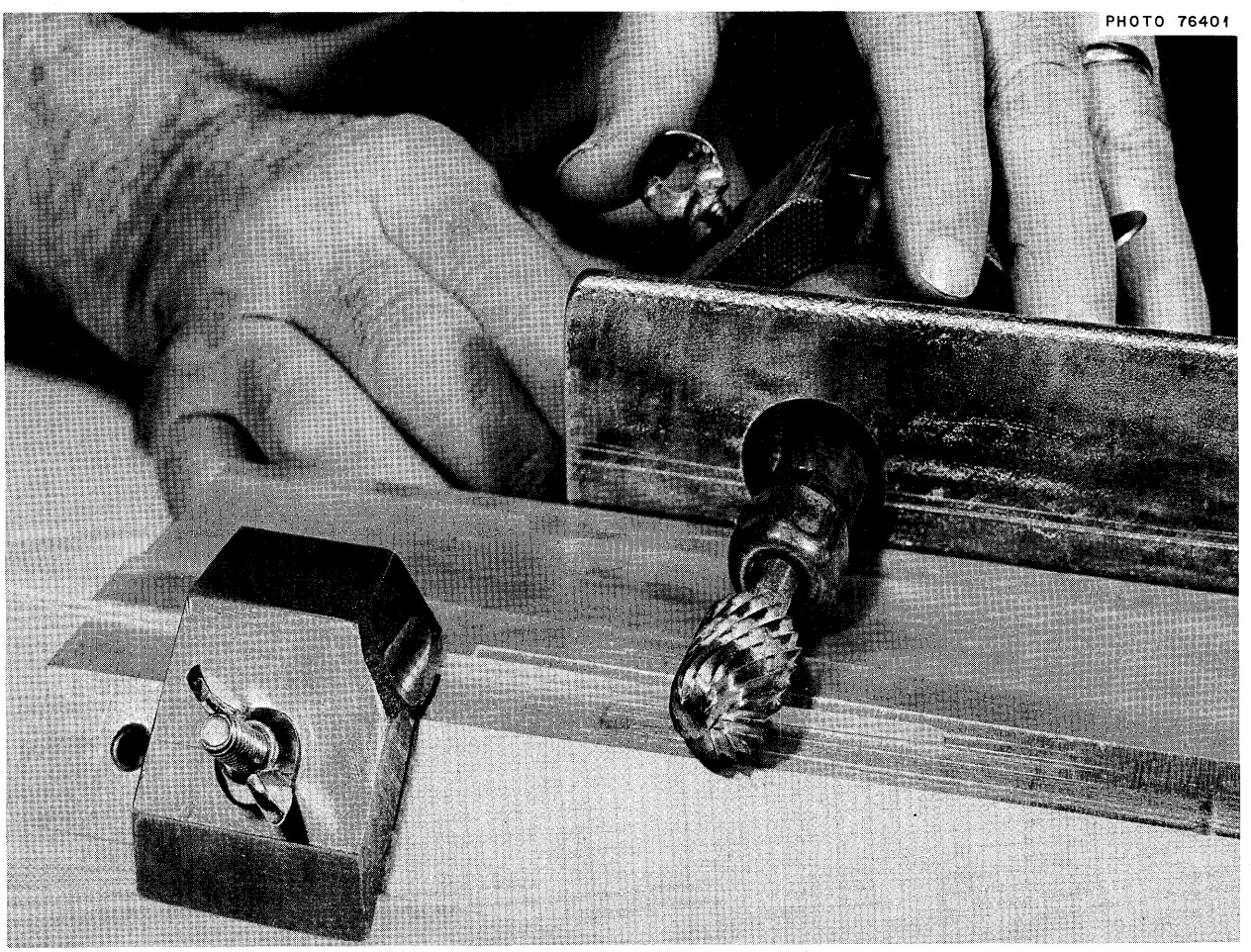

Fig. 11.5. Grinding Wedge-Shape Fillers.

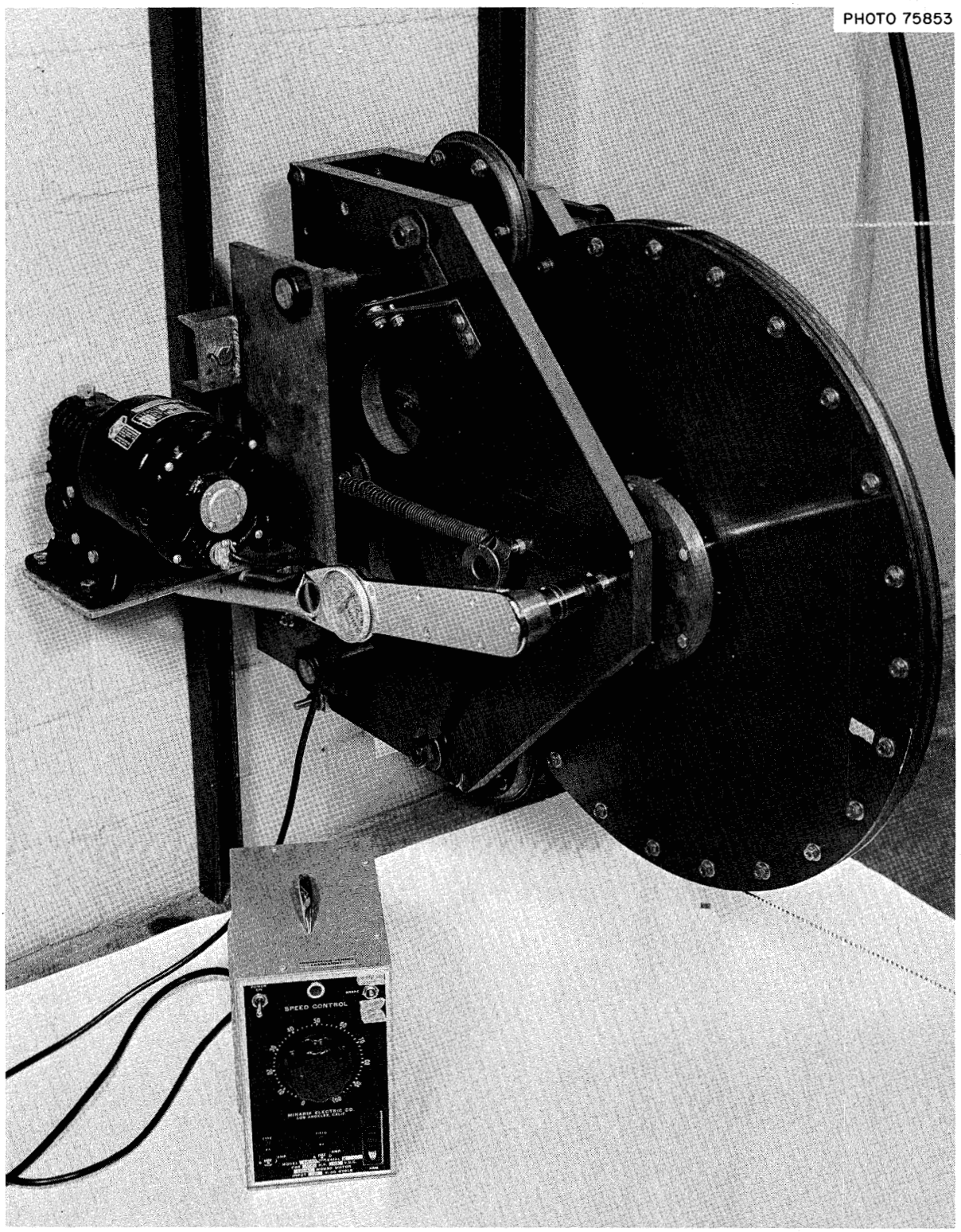

Fig. 11.6. Brake for Conductor Winding Tension.

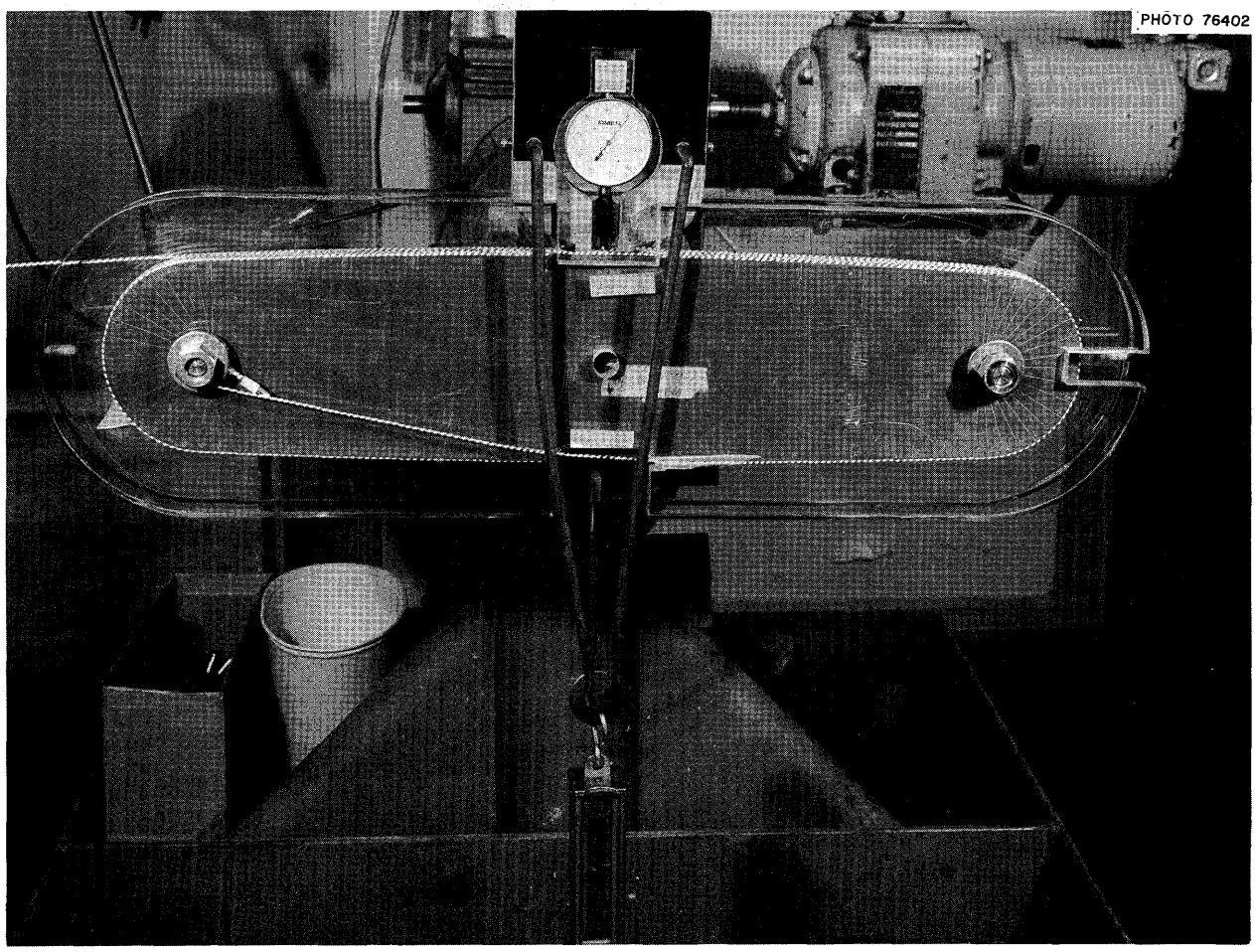

Fig. 11.7. Winding Tightness Test.

narrow edges of the two conductors over a length which is $\frac{1}{8}$ in. less than one turn (Fig. 11.2). This sacrifices one turn but provides a joint which is electrically and mechanically good.

When the decision was made to use Nb_3Sn ribbon[15,16] in the quadrupoles of IMP, it became necessary to find an improved method of making transitions between pancake sections. The transition area is often the location of faults in pancake coils. An added difficulty arose in trying to make reliable transitions between pancakes with different inside radii (Fig. 11.9). A satisfactory solution seems to be the use of a tilted pin, about which the ribbon conductor spirals to move from one pancake plane to the next. It can be seen in Fig. 11.10 that the angle of the pin tilt is proportional to the conductor width. Details of this technique are given elsewhere.[17]

[15] C. D. Graham, Jr., and H. R. Hart, Jr., "Design and Construction of Tape-Wound High Field Superconducting Solenoids," a report by G.E. Research and Development Center, Schenectady, N.Y.

[16] E. R. Schrader, "Design and Construction of Nb_3Sn Superconductive Magnets," a report by RCA, Harrison, N.J.

[17] R. L. Brown, ORNL-TM-2450 (January 1969).

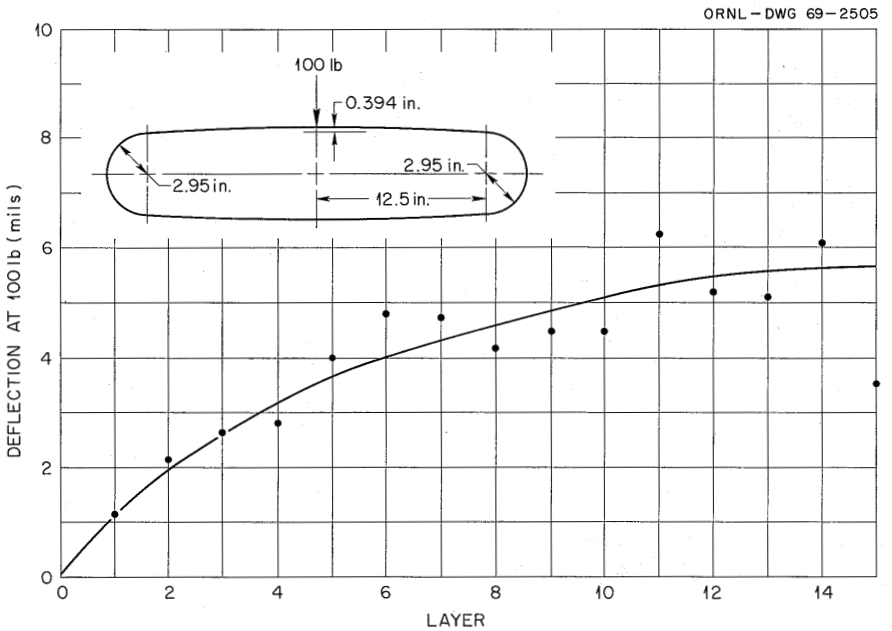

Fig. 11.8. Winding Tightness Test (Deflection vs Layers).

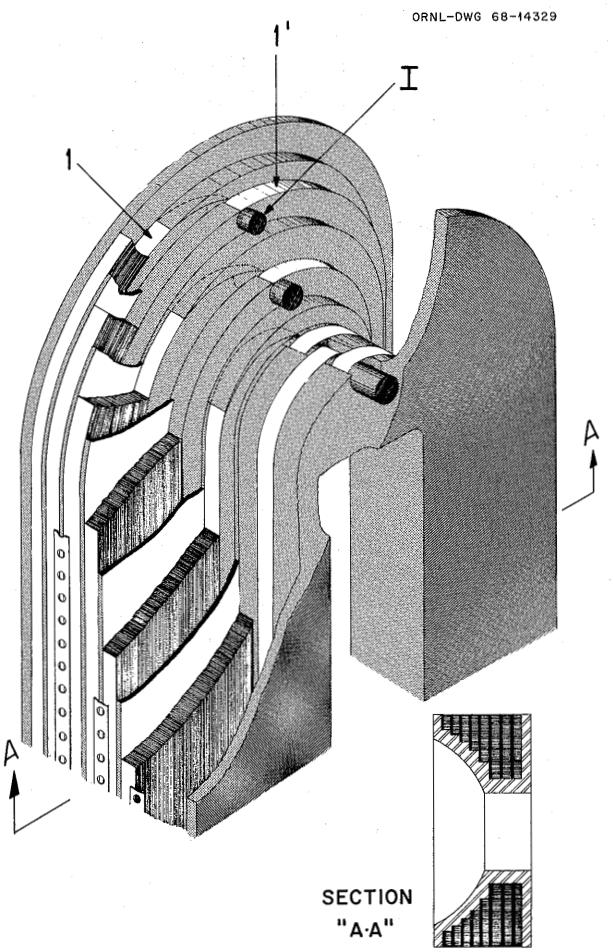

Fig. 11.9. Transition Pins in IMP Quadrupole Coils.

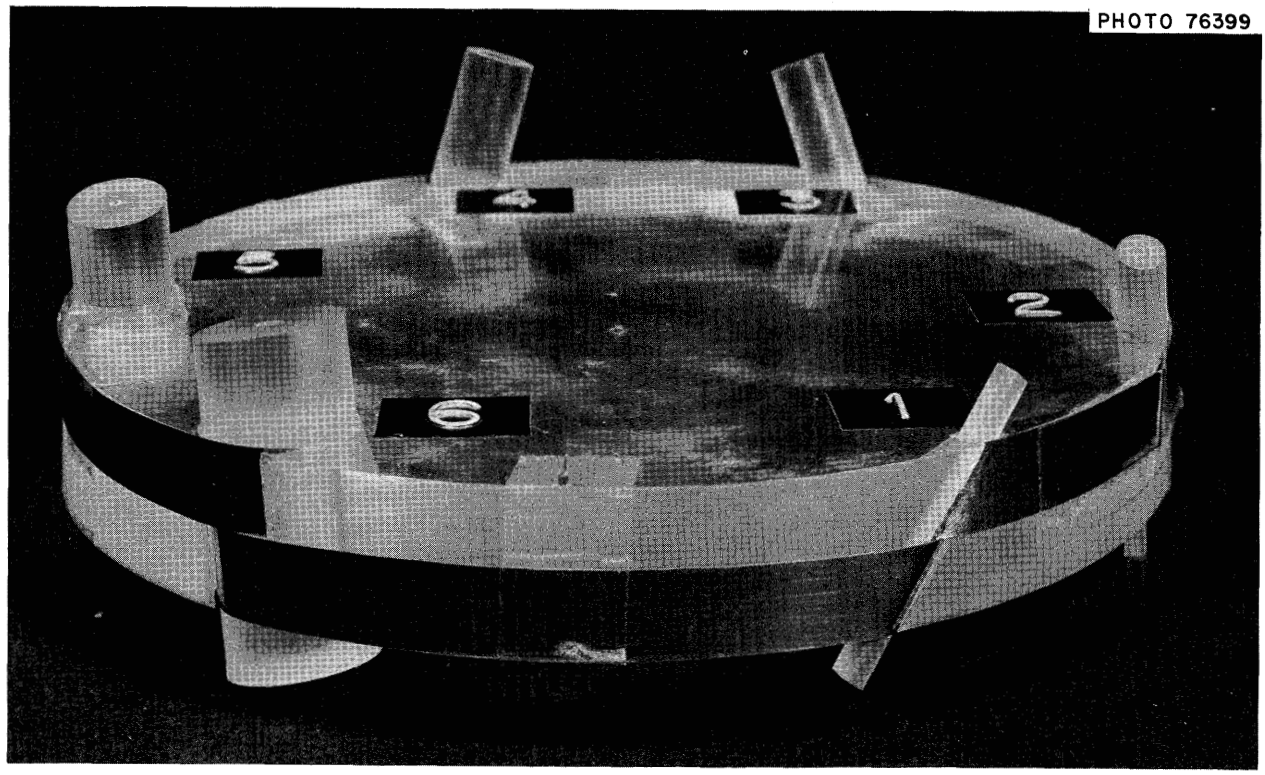

Fig. 11.10. Model Demonstrating Tilt vs Pin Diameter.

11.4 LIQUID-HELIUM LEVEL DETECTOR

K. R. Efferson

11.4.1 Introduction

Superconducting coil systems are usually contained in metal Dewars, so that the liquid-helium level cannot be viewed directly. The liquid level can be monitored at fixed points by means of various level detectors.[18–21] However, a simple detector which can give a continuous indication of liquid level is more desirable than fixed-point detectors. A linear liquid-helium level detector which uses a superconducting element of annealed Ta[22] and another using a Pb-Sn[23] alloy element fulfill the requirement of simplicity; however, neither of them can be expected to work except in very low magnetic fields. Another linear detector, which relies on the measurement of the small capacitance difference between liquid helium and gaseous helium,[24] should work in a magnetic field; however, the associated electronics is complicated, and the system must be constructed with great care.

A new liquid-helium level detector has been designed and tested. The desirable characteristics of this detector are: (1) it gives a continuous linear indication of liquid-helium level, (2) it has a large signal output (0.22 V/cm at 50 mA), (3) it

[18] A. C. Rose-Innes, *Low Temperature Techniques*, p. 9, Van Nostrand, Princeton, N.J., 1964.

[19] R. V. Colvin, S. Arajs, and D. S. Miller, *Rev. Sci. Instr.* **33**, 122 (1962).

[20] A. Wexler and W. S. Corak, *Rev. Sci. Instr.* **22**, 941 (1951).

[21] K. R. Canter and L. O. Roelleg, *Rev. Sci. Instr.* **37**, 1165 (1966).

[22] J. R. Feldmeier and B. Serin, *Rev. Sci. Instr.* **19**, 916 (1948).

[23] R. Ries and C. B. Satterthwaite, *Rev. Sci. Instr.* **35**, 762 (1964).

[24] W. E. Williams and E. Maxwell, *Rev. Sci. Instr.* **25**, 111 (1954); S. Meiboom and J. P. O'Brien, *Rev. Sci. Instr.* **34**, 811 (1963).

works in a high magnetic field (75 kG), and (4) it is relatively easy to construct and requires no complicated electronics. The new level detector utilizes the difference in heat transfer properties of liquid and gas phases of helium to produce and maintain a normal zone only in that portion of a high-field superconducting wire (Nb-Ti) which is above the liquid level.

11.4.2 Construction Details

Figure 11.11 shows a schematic diagram of the new level detector. It consists of a high-field superconducting wire twisted together with a Formvar-insulated heater wire (No. 40 constantan). The combination is then coated with G.E. 7031 insulating varnish to produce good thermal contact between the heater and superconductor. The heater and superconducting wires are soldered together at the lower end so that a series electrical current can be passed through the heater-superconductor combination by a constant-current source. A voltage tap is connected to each end of the superconductor, and the two taps are then connected to an external voltmeter. A light spring holds the heater-superconductor combination in tension to compensate for thermal expansion differences between the insulating tie points and the wires.

Figure 11.12 depicts a finished detector. The small wires are permanently mounted inside a hollow Micarta cylinder (0.95 cm OD, 0.159 cm walls) to protect them from accidental damage. The wires (including the lower potential tap) are stretched against a spring in the lower end and epoxied[25] in place at the upper end. A slot in the side of the Micarta tube ensures that the liquid level inside the tube is the same as it is outside.

[25] "Epoxy Patch," manufactured by Hysol Division of the Dexter Corp.

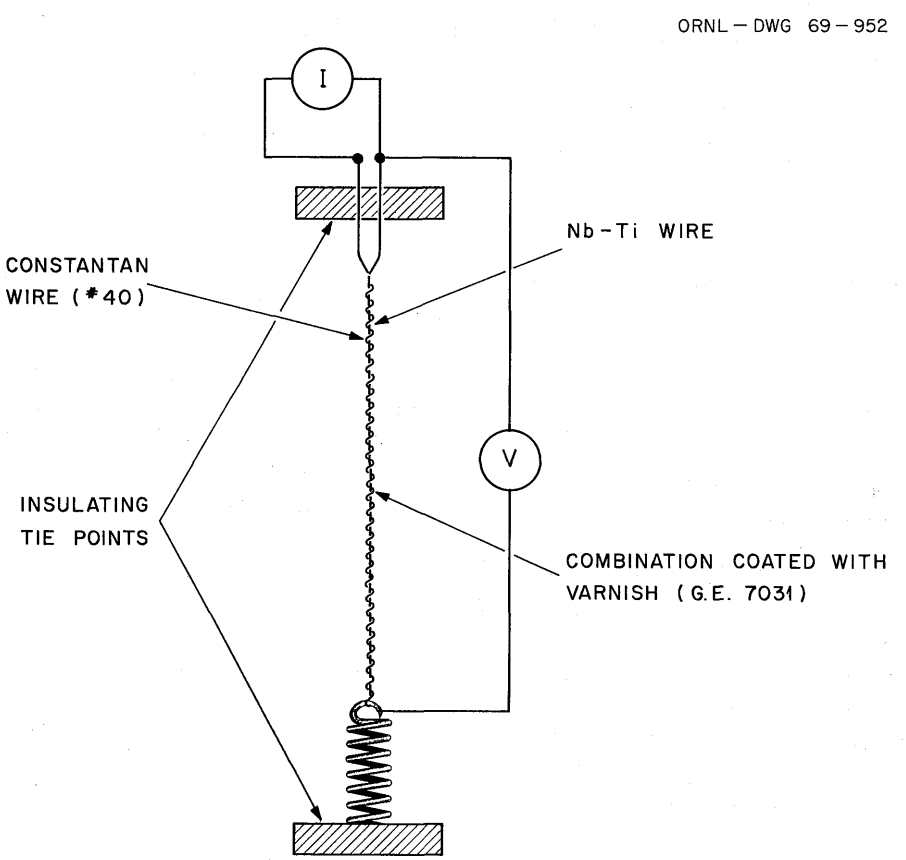

Fig. 11.11. Schematic Diagram of Level Detector. Superconducting wire and heater wire twisted together, covered with varnish, and soldered together at lower end. Current is furnished by constant-current source, and potential drop is measured on superconductor.

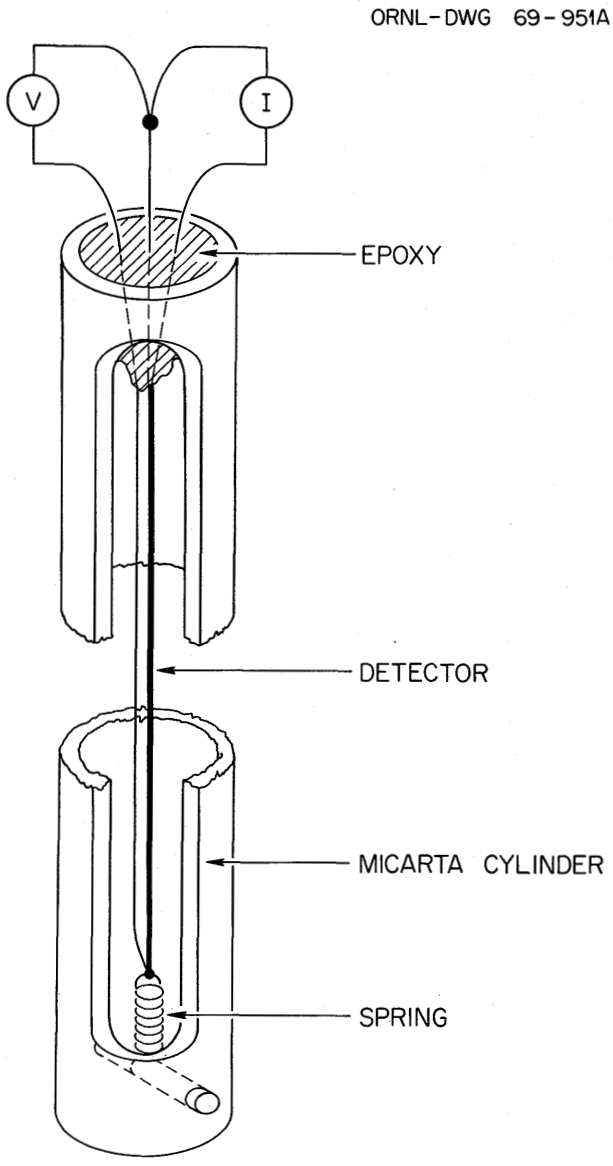

Fig. 11.12. Construction Details for Actual Level Detector.

Niobium-titanium wires of various sizes (0.0038 to 0.0127 cm OD) and Nb-Zr wires (0.0127 cm OD) have been used as superconducting elements in this type of level detector. The 0.0127-cm-OD wire is commercially available as a single strand with copper cladding. This type is convenient since one only has to etch away the copper to form the desired active length of bare superconductor, leaving a small amount of copper on each end for solder joints. Smaller-size wires of Nb-Ti have been obtained by etching the copper away from one of the several multistrand copper-clad superconductors being manufactured commercially. Wires obtained in this way have been used, although they are sometimes nonuniform along the length and are not circular in cross section. Sharp ridges ocurring along the length of this type of wire (sharp points when viewed in cross section) have occasionally shorted to the heater. These wires also had to be copper plated to form the solder contacts on the ends. Finally, small wire (0.00457-cm-OD Nb-Ti, Supercon T48-B with copper cladding) drawn down as a single strand has been obtained as a special item, courtesy of Supercon Corporation. The best detectors have been made of this special wire.

11.4.3 Principle of Operation

When an appropriate constant current is passed through the sample, the heater generates enough heat to drive that portion of the superconductor above the liquid level (where the heat transfer is poor) into the normal state but not enough heat to affect the superconductor below the liquid level. Thus the total voltage drop across the superconducting wire depends on the length of the normal section, and, providing the superconducting wire is uniform and the temperature of the normal region is not so high as to change its resistivity, the voltage is directly proportional to the length of the normal section. Besides ensuring creation of a normal zone in the superconducting wire above the helium level, the heater also makes the sensing element bifilar, so that there are no net forces due to external magnetic fields.

A suitable operating current for a detector constructed of an arbitrary heater-superconductor combination can easily be found experimentally, but is difficult to predict. However, it is informative to consider the physical effects which determine the range of operating currents for the detector. There are three critical values of current associated with this type of detector: (1) I_{max}, the maximum current at which the normal-superconductor boundary can be expected to move with the liquid-gas interface; (2) I_0, the minimum current which when introduced will ensure that the superconductor in the gas phase will be driven into the normal state; and (3) I_{min}, the minimum current below I_0 at which an already-created normal zone in the gas-phase portion of the

superconductor will persist homogeneously to a point near the surface of the liquid and will follow the liquid level variations.

In order to determine I_0, consider the level detector to be partially submerged in liquid helium with about 2 or 3 cm of the detector above the liquid. The detector above the liquid and the gas surrounding it will then be approximately at the bath temperature.[26] If the detector current is gradually increased from zero, a current will be reached where the heat generated in the heater will raise the superconducting wire (in the gas phase) to a critical temperature, ΔT_c, above the bath temperature, at which point the superconductor in the gas phase will be driven into the normal state. The current necessary for the superconductor to reach ΔT_c is I_0. It is obvious that I_0 depends on the size of the wires, how much heat is transferred from the heater to the superconductor, and how much is lost directly from the heater to the surrounding gas (neglecting heat transferred longitudinally to the liquid helium). I_0 decreases as the diameters of the heater and the superconducting wire decrease and as the thermal contact between the heater and the superconductor improves.

Until I_0 is reached, the temperature rise of the superconductor is due only to the heater; however, at I_0 the superconductor becomes resistive and causes an additional temperature rise. Since it is only necessary to maintain the superconductor at ΔT_c, the current can be reduced below I_0 to a value where ΔT_c is just maintained. This current establishes a lower limit below which a normal-to-superconducting transition can occur. Experimentally, a value of current, I_{min}, is found below which the normal-state region of the superconductor will not follow the liquid-helium level as the level falls.

The maximum current, I_{max}, at which the detector will operate is associated with the transition from film boiling to nucleate boiling which occurs in liquid helium.[27] If the detector is completely submerged in liquid helium and the current is increased, the temperature of the detector element will rise. However, superconductivity will persist up to the end of the nucleate boiling region (about 1°K above the bath temperature). A current then will be reached where the heater will cause a transition from the nucleate to the film boiling region with a subsequent large temperature rise (about 20°K) and loss of superconductivity. If the current is now reduced, a current, I_{max}, will be reached where a transition from film boiling to nucleate boiling occurs, with a resultant lowering of temperature of the detector and return to the superconducting state. Film boiling and resultant normal-state regions in that portion of the superconductor below the liquid surface are impossible for currents below I_{max}.

11.4.4 Experimental Results

Detectors 30.5 cm long, constructed from 0.0045-cm-OD Nb-Ti wire, have been tested thoroughly. The critical values of current were determined to be: $I_{min} = 40$ mA, $I_0 = 62$ mA, and $I_{max} = 91$ mA. It was found that the detectors worked well and were linear over the entire range of currents from I_{min} to I_{max}. Figure 11.13 shows linearity checks for a detector operated at I_{min}, I_0, and I_{max}. Note that the zero-voltage intercepts are not the same for the three lines. This is due to the fact that the boundary between the superconducting and normal regions of the Nb-Ti occurs below the liquid-helium surface at high currents and above the surface at low currents. The intercept for the $I = I_0 = 62$ mA line occurs almost exactly at 30.5 cm, that is, at the end of the superconducting detector, signifying that the superconducting-normal boundary must have occurred at the liquid-helium surface. The fact that the voltage per unit length scaled directly with the current for currents between I_{min} and I_{max}, coupled with the linearity of the detector when operated at I_{max}, shows that the gas-phase portion of the detector is not hot enough to affect the normal-state resistivity of the superconductor. Cooling the liquid-helium bath to 2.5°K has also been found to have no effect on the detector characteristics for an arbitrarily chosen operating current of 65 mA. One detector operating at a current of 50 mA was also tested in a longitudinal magnetic field of 75 kG and was found to be unaffected.

Liquid-helium losses due to these detectors were not measured; however, they can be estimated. Because of the poor thermal conductivity of the heater and the superconducting wires, it can be assumed with little error that no heat is transferred

[26] R. T. Swim, *Advan. Cryog. Eng.* 5, 498 (1960).

[27] For example, see R. D. Cummings and J. L. Smith, *Bull. Inst. Intern. Froid, Annexe* 5, 85 (1966).

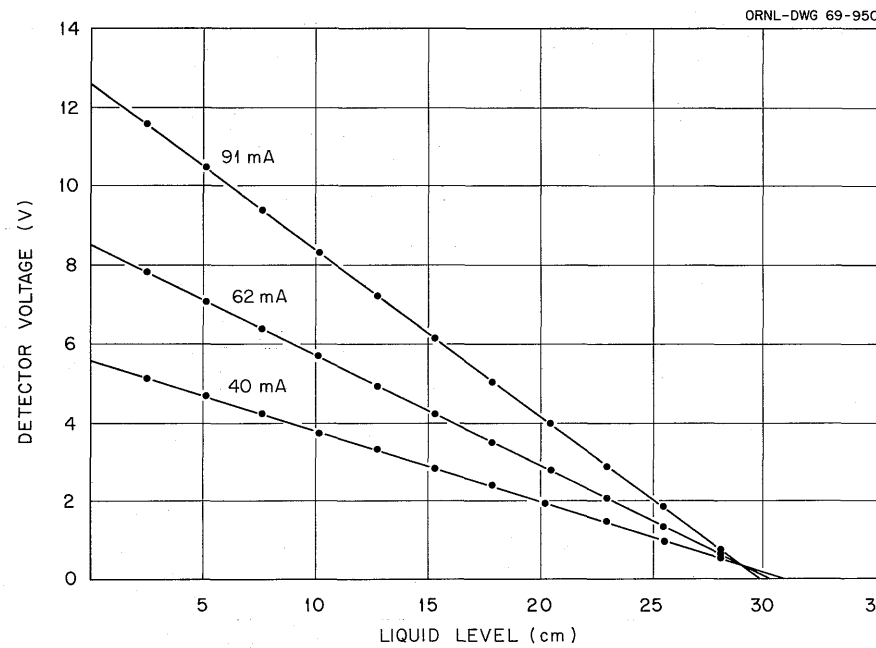

Fig. 11.13. Detector Voltage vs Liquid-Helium Level (Measured from Bottom of Detector) for Three Different Operating Currents. The superconducting element was 0.00457-cm-OD Nb-Ti wire (T48B by Supercon). The length of the detector was 30.5 cm. The heater wire was No. 40 constantan.

along these wires from the gas to the liquid phase of helium. Thus the liquid loss is due primarily to the heat generated below the liquid level. The losses can then be approximated by an expression of the form $L(I^2R)l$, where L is the latent heat of liquid helium, I is the detector current, R the resistance per unit length of the heater wire, and l is the submerged length of the detector. For the heater wire used, $R = 1.0\ \Omega/\text{cm}$; thus the maximum losses from a 30-cm detector operating at $I_0 = 62$ mA would be about 0.15 liter/hr. These losses, though small, can be reduced further by operating at currents close to I_{min} for continuous operation or by operating intermittently when currents above I_0 are used.

11.4.5 Discussion

Level detectors of this type should work very well in closed superconducting coil systems. The IMP mirror coil system now being constructed will be contained in a 71-cm-deep liquid-helium reservoir. This range of liquid levels will be monitored by three overlapping 30.5-cm-long detectors. The advantages of overlapping detectors over a single detector are: (1) The overlapping feature provides an internal check of the consistency of calibration between the three detectors; (2) the top two level detectors both include within their range the lowest point to which the liquid level will be allowed to fall during operation of the magnets, which serves as a safety feature against failure of one of the detectors; and (3) only one level detector will be used at one time, so that the helium losses are determined by a 30.5-cm-long heater element rather than a 71-cm-long element.

11.5 PROGRESS ON THE IMP FACILITY

R. L. Brown
D. L. Coffey
R. J. Colchin
J. L. Dunlap
R. S. Edwards
K. R. Efferson
W. F. Gauster
J. L. Horton[28]
C. E. Parker
H. Postma
E. R. Wells
W. L. Wright

11.5.1 Introduction

During 1968, work on the IMP Facility has reached the construction stage, though several areas of design are also still very active. "Phase

[28]On loan from Instrumentation and Controls Division.

I" operation, in which mirror coils without quadrupole coils will be employed, is nearing final assembly. The central microwave cavity is the only major part not yet completed for this assembly. Preliminary tests of the vacuum tank and the superconducting mirror coils have been successfully completed.

In two areas it has become necessary to make reversals of earlier design decisions, and these midcourse changes have significantly affected the schedule for IMP. Contrary to our expectations, it was not possible to obtain type 310 stainless steel in large forgings in a hard condition. Unfortunately, the strength of type 310 stainless steel in the annealed condition (about 100,000 psi yield strength at 20°K) is not sufficient to withstand the stresses in the quadrupole coil cans; so it was necessary to redesign for Armco 21-6-9 stainless steel with a yield strength of about 190,000 psi. Second, it was felt that (1) the inability to adequately specify NbTi conductor parameters leading to electrical stability, and (2) some concern about the electromagnetic "breathing" motion of the necessarily large winding section in two of the coils, left too much doubt about NbTi quadrupole coil operation. Therefore it was decided that designs for Nb_3Sn quadrupoles were required. These designs have been completed, and quadrupole winding is scheduled to begin in early 1969.

11.5.2 Phase I

The large vacuum tank which will house IMP has been constructed and assembled (Fig. 11.14). The design of the tank provides for complete removal of

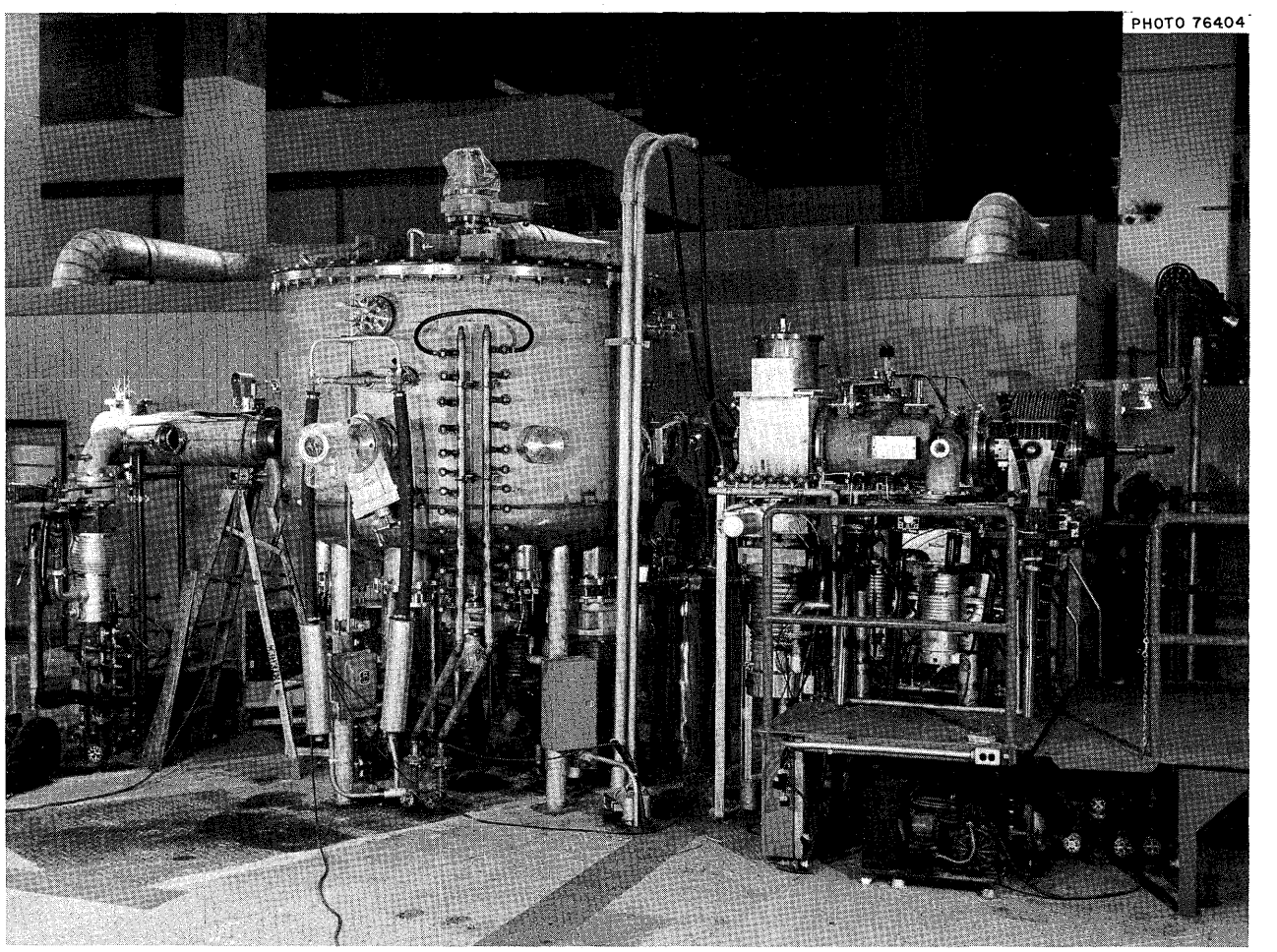

Fig. 11.14. Vacuum Tank for IMP. Also shown are the energetic-neutral injector (right) and the neutral-beam dump (left).

the magnets and the plasma liner assembly by lifting the top off the tank. This provides maximum access for experimental modification. The tank vacuum is established by using a nitrogen gas aspirator (to 23 in. Hg) followed by pumping to 10^{-5} torr with a Linde 150 SN sorption pump. High-vacuum pumping is then provided by a choice of two 10-in. diffusion pumps (with –50°C Freon baffles), titanium evaporation pumping on liquid-nitrogen-cooled surfaces, and an electro-ion pump. Vacuum leak tests have been conducted to 2×10^{-7} torr with the two 10-in. diffusion pumps. Installation of the liquid-nitrogen liners, Freon-cooled baffles, and titanium evaporators is now in progress.

A new control room has been constructed for IMP. It is air-conditioned and soundproof. Instrumentation racks and major wiring construction have been completed, though all instrumentation has not yet been installed.

Major components of the energetic-neutral injector have been fabricated and are being installed. These include the source, neutralizing cell, charged-beam dump, and the final neutral-beam dump. All components of the beam source-dump system have been individually vacuum tested.

Power for resonance heating in the microwave cavity initially will be provided by a single 35-GHz, 1-kW (cw) microwave klystron located near the tank. The microwave power supply and controls presently installed in the Elmo facility will power the microwave tube. Interconnection wiring has been completed to the Elmo control room.

Low-loss current leads[29] have been fabricated for powering the superconducting magnets. The lead design includes a unique motorized electrical and thermal disconnect to reduce standby losses. Special cryogenic-liquid level sensors[30] and selective field sensors have also been installed.

Each of the two superconducting mirror coils has been individually tested; both coils performed satisfactorily. The first test was with a vertical axis (for convenience), and the second test was with a horizontal axis, as will be used in Phase I operation. The two coils were operated to critical currents at 596 and 605 A respectively (600 A ± 1%). This current corresponds to a central field of 60 kG, a maximum field of 66 kG, and an overall current density of 10,300 A/cm^2. These test data showed that the coils performed to the short-sample test data when charged at 0.2 A/sec. Increasing the charging rate to 10 A/sec reduced the critical current to 440 A, in agreement with the rate sensitivity which had been determined earlier in cusp-coil tests. At the 600-A level the normal zone propagated rapidly through the coil so that 90% of the current decayed in less than 4 sec. Under these conditions the coil is self-protecting. The transition at 440 A indicated a much more slowly propagating normal zone, requiring perhaps 15 to 50 sec for current decay. This slow normal-state transition could lead to heat damage in the coil section which first goes normal, and therefore required the use of an external resistance energy dump to effect current decay within 10 sec after a normal zone appears.

11.5.3 Conductor Selection

A wire composed of multifilament NbTi superconductor embedded in OFHC copper was selected for the mirror coils of IMP. Short-sample and cusp-coil tests[31,32] of a number of wire samples from various manufacturers led to a better understanding of the wire design parameters necessary for stable coil operation. These tests indicated that wire stability is enhanced by a high copper:superconductor ratio and by small filament diameters.

In high-current-density magnets the design current (which is, of course, smaller than the critical current) is higher than the minimum propagation current. Therefore even momentary, partial transitions to the normal state must be avoided. During the increase of the magnetic field, shielding currents are induced inside the conductor in loops consisting of parts of the superconducting strands (closed over the high-conductivity copper substrate). Thus the total filament current can locally surpass its critical value. A discontinuous performance of the filament will produce local heating by dissipating the energy stored in the shielding loop concerned. If the heat produced cannot be absorbed by the heat capacity of the conductor or dissipated to the helium effectively, then the local temperature

[29] K. R. Efferson, *Rev. Sci. Instr.* **38**, 1776 (1967).

[30] This report, sect. 11.4.

[31] W. F. Gauster and D. L. Coffey, "Problems in Designing Non-Axisymmetrical Superconducting Magnet Systems," *J. Appl. Phys.* **39**, 6 (1968).

[32] *Thermonuclear Div. Semiann. Progr. Rept. Oct. 31, 1967*, ORNL-4238, pp. 134–40.

disturbance exceeds T_c and leads to a propagating normal region.

In the samples we tested, the minimum propagating current is approximately 400 A almost independent of field. Figures 11.15 and 11.16 show (*a*) cusp-coil and (*b*) short-sample data for some of the materials we evaluated. Since various external fields of up to 60 kG were applied to the cusp coil, several load lines $[B_{max}(I)]$ are shown. In the short-sample test, two conductor types (Fig. 11.15) showed smooth transitions into the current-sharing state. In contrast to the other conductor types (Fig. 11.16), the first mentioned displayed almost short-sample performance in the cusp-coil test when charged at a slow rate. The special conditions of the conductor design which are responsible for achieving a smooth transition from the superconducting to the current-sharing region have not been determined. This is an obvious gap in our understanding of the performance of composite NbTi conductors.

It is possible that by twisting the filaments of the composite conductor, to effect shielding current cancellation,[33] one might avoid the necessity of a smooth superconducting-sharing transition region (since the critical current in the filaments might never be exceeded). However, this technique had not been developed in time for consideration for the IMP magnet system.

In ventilated coil construction, as is the state-of-the-art technique in NbTi composite coils, there is considerable opportunity for the conductor windings to move about under the influence of electromagnetic forces. This "breathing" is worse for coils with large volumes. The possibility of insulation damage caused by conductor motion influenced our decision to build the quadrupole coils of Nb_3Sn rather than NbTi.

Nb_3Sn ribbon conductors with a laminated construction which includes OFHC copper and stainless steel have been chosen for the IMP quadrupole coils. Though almost twice as expensive as NbTi in the quantity required, this conductor seems to

[33] P. F. Smith, Brookhaven Summer Study on Superconductivity, 1968.

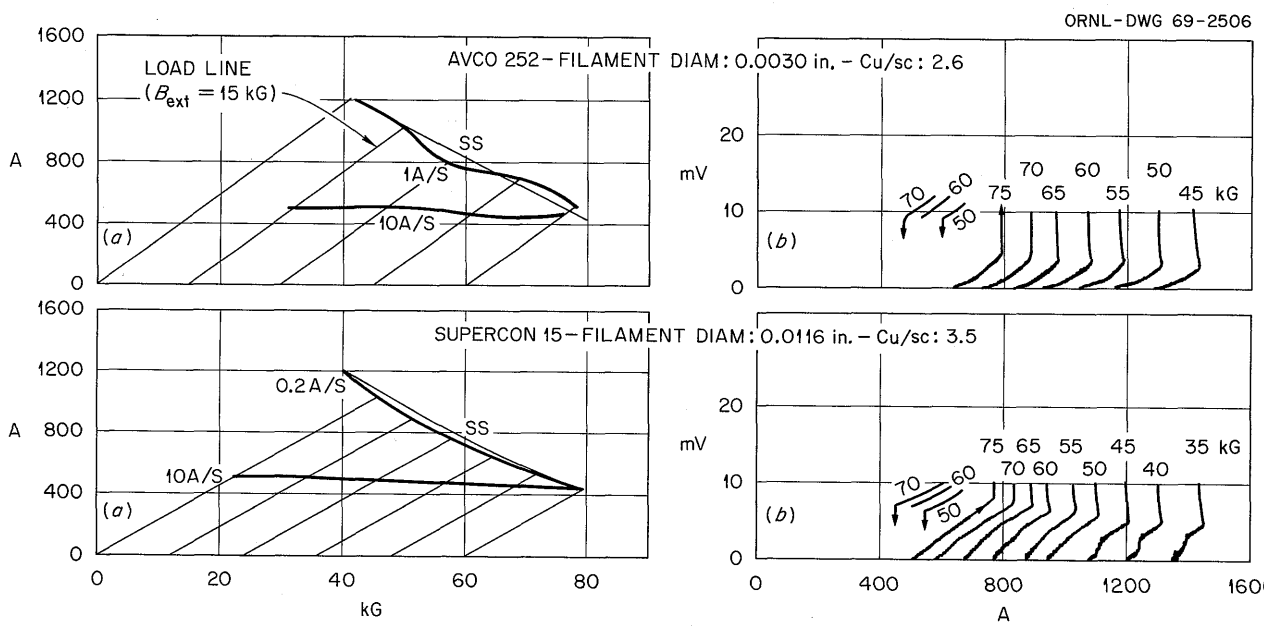

Fig. 11.15. Cusp-Coil and Short-Sample Tests of Various 0.057 × 0.114 in. NbTi compound conductors. Manufacturer, number and diameter of filaments, and copper-to-superconductor ratios are indicated. (*a*) Shows cusp-coil test curves at various rates of current rise (e.g., 10 A/S). "SS" indicates the short-sample critical current characteristic. The short-sample characteristic is reached in the cusp-coil test with slow rates of current rise. (*b*) Represents the current-voltage characteristics in the current-sharing state at various fields (e.g., 70 kG) and as the sample recovers to the superconducting state. The transitions from superconducting to current-sharing state are continuous.

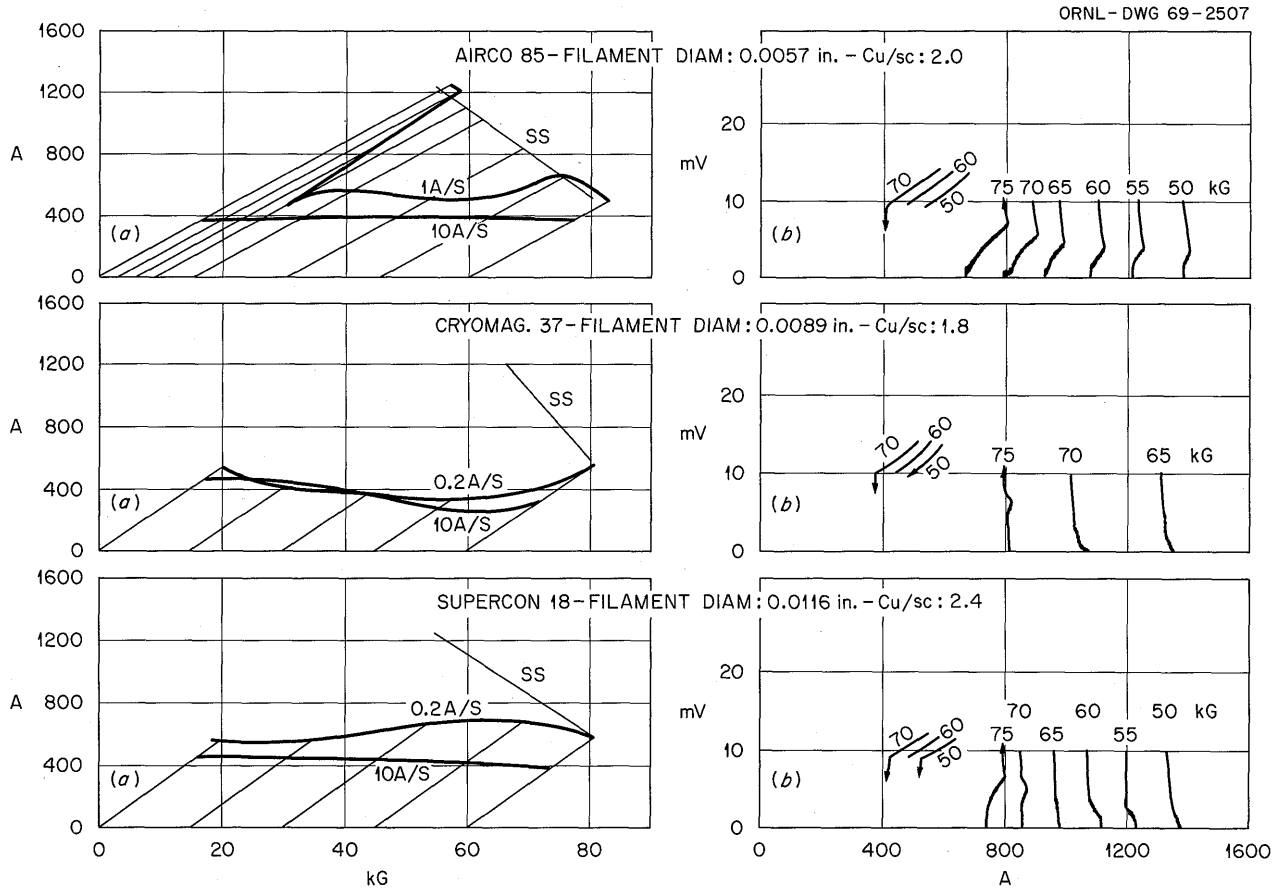

Fig. 11.16. Same as Fig. 11.15. However, (*a*) the cusp-coil test results at slow rates of current rise do not reach the short-sample characteristics at all fields; (*b*) the short-sample transitions from the superconducting to the current-sharing state are partly discontinuous.

have a greater probability of performing satisfactorily in our coils. A number of short-sample and coil tests were conducted with both vapor-deposited and diffusion-formed Nb_3Sn conductors. These tests showed that either material performs very stably (achieves short-sample performance) in the self-field of the cusp coil; however, with an externally superimposed field of even 10 kG the vapor-deposited conductor became unstable. The diffusion-formed conductor remained stable at all external fields available (up to 60 kG applied, 97 kG total field). With an applied field of 30 kG (total field of 78 kG), more than 20,000 A/cm^2 was stably achieved in the cusp-coil test. Since the IMP quadrupoles operate in the field of the mirror coils, the choice of the latter conductor was required. Short-sample critical currents of 600 A + 15%, −10% at the rated field of 80 kG were specified to avoid instabilities caused by excessively high critical current capacities which were observed in some wire samples. The conductor will be 0.0082 in. thick × 0.500 in. wide with 0.002-in.-thick OFHC copper and 0.001-in.-thick stainless steel on each side. For acceptance the conductor must operate in a double pancake coil test to at least 700 A.

A novel technique for making the transition between sections in pancake-wound coils has evolved from the ORNL superconducting magnet test program. It is described elsewhere in this report.[34] The possible influence of high forces on the very ductile soft solder of laminated Nb_3Sn conductors has not been examined. It is unlikely that this

[34]This report, sect. 11.3.

effect would be evident in the early stages of magnet operation, though long periods of high-field operation could cause cold flow of the solder.

The IMP quadrupoles are designed to operate with no turn-to-turn insulation other than the stainless steel of the conductor. This technique has been successful in the cusp-coil tests. Such "shorted" operation makes it extremely difficult to analytically evaluate coil protection requirements. It is anticipated that a propagating normal region in one quadrupole coil will induce normalcy in adjoining coils, so that the stored energy of the quadrupole system will be rather evenly distributed between the four coils. However, scram heaters will be located on the conductor of each coil to assure that each coil can be manually driven normal if self-protection is not apparent.

11.5.4 Structural

Each of the mirror coil cans was machined from an annealed type 310 stainless steel forging. The 0.2% offset yield strength of this steel at 20°K (and presumably at 4.2°K) is approximately 100,000 psi. Stress analysis by Dr. Heinz Parkus, Professor at the University of Technology, Vienna, Austria, and by the Mechanical and Nuclear Engineering Department of the Franklin Institute Research Laboratories under Dr. Zenon Zudans led to the can design. Through the use of heavy interlocking covers and an optimum number of bolts connecting the cover to the coil flanges, the stress is believed to be lower than 70,000 psi at all points in the mirror coil cans.

The quadrupole coil cans are to be fabricated of Armco 21-6-9 stainless steel,[35] which has a 0.2% offset yield strength of more than 190,000 psi at 20°K. The tests of Lawrence Radiation Laboratory indicate that this material is not only stronger than other stainless steels, but it also remains ductile at low temperatures and does not increase in magnetization after thermal cycling. Stress analysis of the quadrupole coil cans is presently in progress in a cooperative effort of ORNL and Franklin Institute personnel. It is anticipated that these studies will be complete in time for winding the quadrupoles in the spring of 1969.

---

[35]The assistance of C. D. Henning and R. L. Nelson of Lawrence Radiation Laboratory in selecting this material is gratefully acknowledged.

12. Fusion Feasibility

12.1 INTRODUCTION

There is no guarantee at present, express or implied, that controlled fusion will be feasible and that, if feasible, it will produce electric power competitive with or cheaper than fission breeders. The resolution of these questions depends greatly on the plasma physics material presented in this report and elsewhere but also on what is called fusion nuclear engineering problems (which are the subject of this section). It is possible, however, to see some encouraging things and to make more definite statements than were previously made, because of a symbiosis of the plasma physics and engineering requirements.

For a variety of reasons the overall fusion problem (partly distinct from only plasma physics) has received an increased emphasis this past year, particularly in the United Kingdom and in the United States. There exist now several studies of the controlled fusion problem in the broader sense, and we give in the remainder of this section several of these studies that were completed this year at Oak Ridge National Laboratory. Since the groups at the various laboratories communicate through technical memoranda, much of what has been defined has appeared in print, and we collect here, mainly in abstract form, only the salient points of these studies.

12.2 THE FEASIBILITY OF CONTROLLED FUSION

D. J. Rose[1]

12.2.1 General Remarks

To obtain useful power from nuclear fusion requires the solution of many problems. In no particular order, these are: (1) plasma confinement and stability; (2) moderation of 14-MeV neutrons and regeneration of tritium with a favorable breeding ratio (for a D-T fusion system); (3) practical development of more complex and less expensive magnetic confinement systems than have presently been used; (4) development of a vacuum wall, resistant to radiation damage over a useful life and permitting high heat transfer; (5) development of plasma injection and pumping techniques; (6) recovery of tritium safely and cheaply; and (7) doing all this cheaply enough to produce electric power competitive with, say, fission breeders of the year 2000.

Of course, in comparing costs, the traditional advantages of fusion power must be assessed. These are: (1) few radioactivity or waste disposal problems; (2) possibility of short fuel doubling times, and, as a corollary, a plentiful neutron economy; and (3) minimal hazards and no continuing nuclear heat source (afterheat) when the device is shut down. This lowers costs, eases siting, reduces electric transmission costs, and permits use of the low-grade steam for space heating.

The economic value of these advantages is not included in these studies. Our concern has been only with the "core" costs, but in doing that, we do incorporate an optimization of the system that involves the first list of desiderata.

Before getting into the detailed discussions, we begin with an engineering idea. The "core" of a fusion reactor would consist of vacuum wall, neutron moderating plus tritium breeding blanket, magnet, mechanical support (mainly for the magnet,

[1]Consultant, Massachusetts Institute of Technology. Most of this work was done while Professor Rose was on sabbatical leave from MIT, and it is greatly condensed from the report *On the Feasibility of Power by Nuclear Fusion*, ORNL-TM-2204 (May 1968).

it turns out), whatever plasma injection is required, and plasma pumping apparatus. All this corresponds roughly to the core of a fission breeder reactor plus some of its auxiliary equipment and fuel processing plants; costs are compared with this in mind.

If we imagine the fusion reactor to be approximated by a long cylinder and neglect end effects, the cost dollars per kilowatt (thermal) will be:

$$\frac{\$}{\text{kW (th)}} = \frac{\dfrac{\text{Cost \$}}{\text{meter length}} \begin{array}{l}\text{of vacuum wall + mod-}\\ \text{erator + magnet}\\ \text{+ support + injector}\\ \text{+ pumps}\end{array}}{\dfrac{\text{net power kW (th)}}{\text{meter length}}} . \quad (1)$$

It turns out that the exact configuration is not important for arriving at these costs, except for specifying the plasma β required (it must be higher in open systems). Thus the calculations to follow are to some extent model-free, and Eq. (1) is in fact meaningful. Plasma physics enters it through the idea of confinement, in the fraction of the injected D-T fuel burned and in the fraction lost in the exhaust. Too short confinement time – that is, too much recycling – raises injection and pumping capital costs and requires power (hence reduces net power).

12.2.2 Some Plasma Considerations

Consider first the general plasma confinement requirements (to be substantiated in part later) of the reactor. For closed systems, confinement for at least 50 Bohm times under fusion conditions will be required for a feasible system (more would be better, of course). Multipoles have given 30 to 40, but not under fusion conditions, and not in fusion-device geometry. Stellarators have sufficiently good *single-particle* confinement, a very important and helpful conclusion. Stellarator plasma confinement ranges from 1 to 100 Bohms but under very nonfusion conditions. The distinction between "closed" and "open" systems is mercifully starting to blur a little, with the practical consideration of effective "loss cones" in stellarators. Perhaps some of the best hopes can be seen in θ-pinch work, where 20 to 30 μsec under near-fusion conditions corresponds to many Bohm times. The stellarator extrapolation is long, but the matter is still unresolved; *if* confinement is satisfactory and *if* β can be made high enough (>0.1?), it is technologically a very desirable configuration. Similar statements could be made for Tokomaks, except for peculiar difficulties to be mentioned later.

Devices that depend on having statistically unlikely velocity distributions to be stable (Max-B, and some mirror concepts) appear statistically less likely to succeed. We must take care with these comments, however, for it is just possible that ZETA could produce a technologically interesting configuration if its remarkable stability persists as fusion conditions are approached.

Open-ended systems ("mirrors") are now getting better understood. A confinement time of (say) ten 90° Coulomb scattering times will be required in a successful device; that implies much better confinement than is possible in simple low-β mirrors. There is thus what seems to be a real requirement for reducing mirror losses, but as yet no one has a convincing and cheap enough (by a large factor) demonstration. Nevertheless, even here there are useful directions to go, and the matter is different than has been sometimes thought. This will be discussed later.

For the most part, extrapolation to fusion reactor conditions involves large extrapolations in size and often in energy. There is some danger in assuming that scaling laws found for our present modest devices will extend that far. Alternately, there is no a priori reason to doubt that extrapolation is valid. If so (a substantial *if*), then present plasma results indicate that scaled confinement times only a few times those presently achieved will suffice for economic fusion. It is therefore important to survey what would come next.

Turning now to more specific things, it is necessary to calculate self-consistent equilibrium plasma quantities (T_e, T_i, energy exchange rate, burning rate, self-heating by fusion alpha particles, plasma radiation, etc.), taking into account all the things that happen. Some input parameters are under our control, and in the examples to be shown, we consider the possibility of heating ions [a parameter V_i (keV) to be seen in subsequent figures], heating electrons (V_e), increasing bremsstrahlung by adding impurities ($C_1 \geqq 1$), altering synchrotron radiation loss by control of vacuum wall properties (C_2 and D). Simple approximate equations have been used so far; more sophisticated analyses are needed, but the general direction seems clear. T_e and T_i depend in a complicated way on plasma confinement

time; for our purpose it is better to replace confinement time by the fraction f_b of the fuel burned in one confinement time. For feasible systems, we should have $f_b \gtrsim 0.05$, to avoid excessive particle injection and other problems.

Figure 12.1 shows typical examples of what might be obtained in self-heated closed systems, with reasonable assumptions about synchrotron radiation. For normal bremsstrahlung ($C_1 = 1$), T_e and T_i rise with increasing burnup f_b, because more fusion alpha particles are present to heat the plasma. For a number of reasons (e.g., burning rate), $T_i \sim 15$ to 20 keV is optimum for closed systems, and we see that T_i is too high at $f_b \sim 0.05$. Enhancing bremsstrahlung ($C_1 = 5$, 10, 15) forces down T_e (very desirable) and T_i via heat transfer. Thus generally reasonable operating conditions can be found: $T_i \sim 15$ to 20 keV, $f_b = 6$ to 7%.

Figure 12.2 shows details of the $C_1 = 5$ case in Fig. 12.1. For rising T_i, T_e and f_b rise as expected, the burning rate (P) drops, and the total plasma radiation per fusion event (U_r) is still modest. More detailed discussion of the variations is beyond our present scope. In summary, closed-system operation appears quite attractive provided β and f_b are high enough.

Open-system analysis is very interesting. Figure 12.3 is complicated but rewards some study. Again, temperatures and other things are plotted vs f_b. The interesting range here is $T_i > 50$ keV (say) for reasonably small mirror loss. At low f_b, alpha heating is small, and T_e (thin dotted lines) is low.

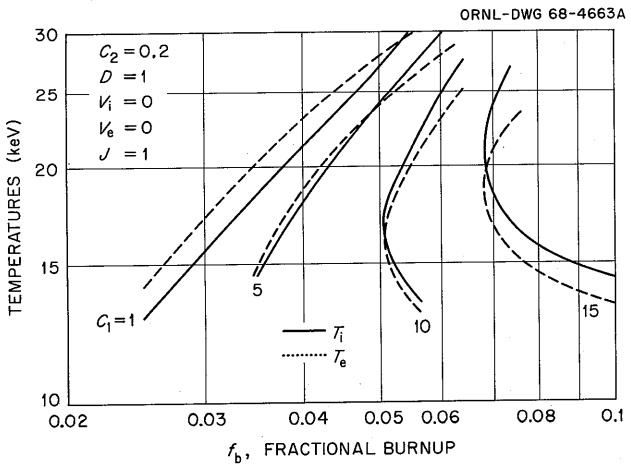

Fig. 12.1. Effect of Normal ($C_1 = 1$) and Enhanced (5×, 10×, 15×) Bremsstrahlung on Equilibrium Conditions in a Self-Heated Fusion Plasma.

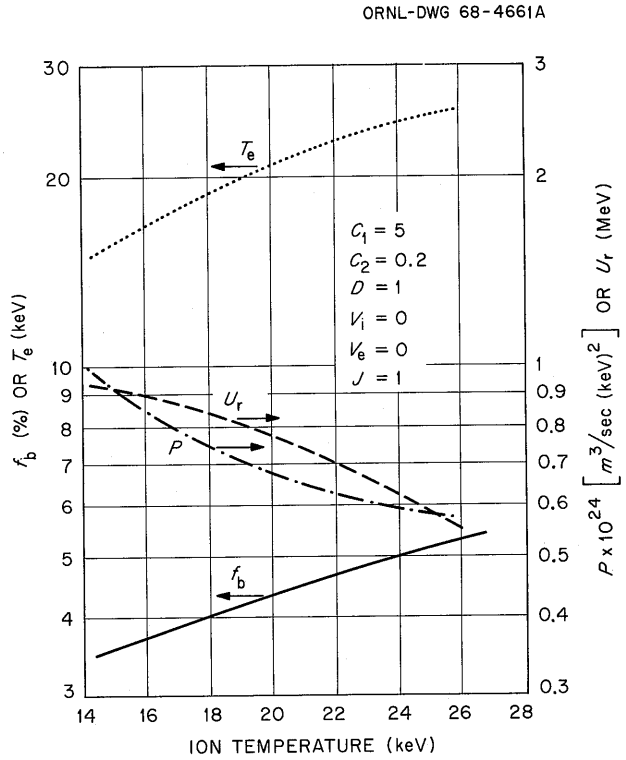

Fig. 12.2. Electron Temperature T_e, Fractional Burnup f_b, Reaction Parameter P, and Radiation/Fusion U_r vs Ion Temperature for a Self-Heated Plasma, with Five Times Normal Bremsstrahlung.

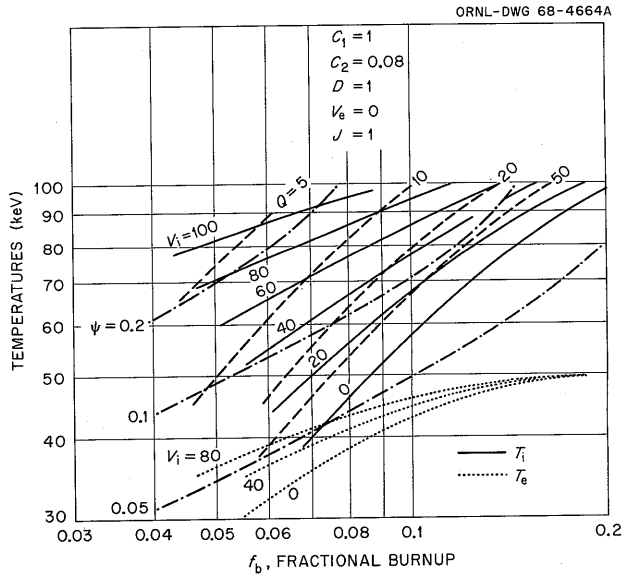

Fig. 12.3. Effect of Ion Heating, and Contours of Constant ψ and Q, for a Plasma Characteristic of Open-Ended Confinement Systems. Low synchrotron radiation; one cold electron injected per ion.

At high f_b, T_e is held down below 45 to 50 keV by synchrotron radiation, which is very energy dependent. The electrons tend to cool the ions, and we see equilibrium ion temperatures (thin solid lines) for various ion injection energies V_i (keV).

Now injection energy implies injection power, and the ratio

$$Q = \frac{\text{fusion power}}{\text{injection power}} \qquad (2)$$

is central to fusion feasibility. $Q < 5$ is surely disastrous, and $Q > 20$ is probably comfortable. Thus we find desirable operating regions in Fig. 12.3, but *not* in the upper left corner.

Unfortunately, ordinary mirror confinement is restricted *entirely* to the upper left of Fig. 12.3. The quantity ψ is the reciprocal of the number of Coulomb scatters to escape, and in ordinary mirrors $\psi \leqq 0.2$ is very improbable. It seems that $\psi = 0.1$ might be satisfactory, implying a stopping of mirrors by a factor of several, and justifying several earlier qualitative remarks.

How this might be done is not clear, but there are hopeful directions. High-β plasmas have large effective mirror ratios, a step in the right direction. All these calculations assume Maxwellian velocity distributions, and there are several reasons (too complicated to discuss here) for suspecting that in the true situation less ion injection energy is required. In that event, the Q contours would move toward the upper left in Fig. 12.3, which is good. Fokker-Planck calculations of open-ended conditions take into account the non-Maxwellian nature of things; but the ones made to date refer to conditions expected off the left side of Fig. 12.3, which is not a region of fusion interest. From all this, we conclude that while open-ended systems *may* not ever have good enough confinement, the old Scottish verdict of "not proven" still applies.

12.2.3 Engineering Considerations

Having discovered something about the plasma, hence of the fusion rate, hence of the denominator

ORNL-DWG 68-4900A

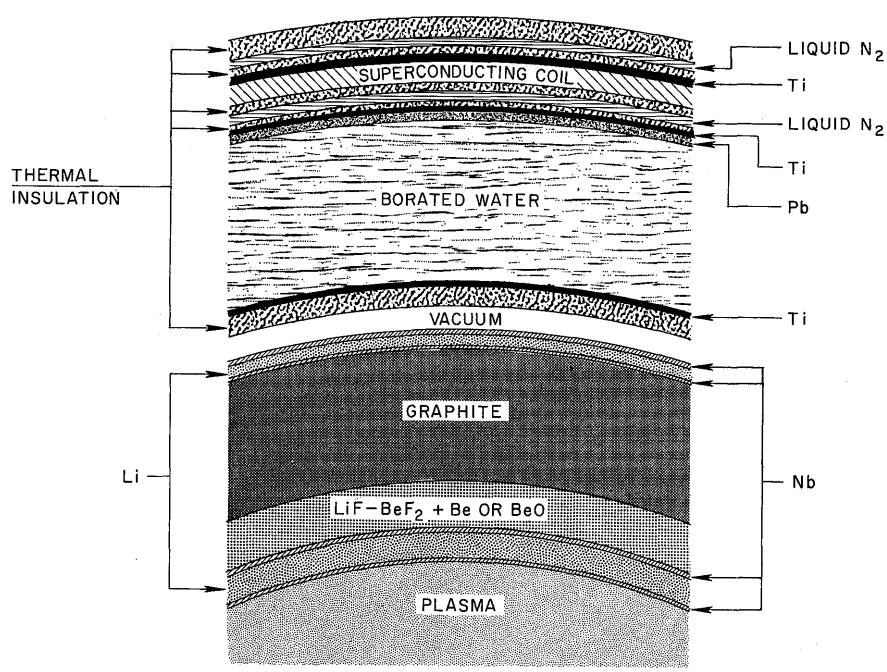

Fig. 12.4. Configuration of a Conceptual Steady-State D-T Fusion System.

of Eq. (1), we turn to the cost appearing in the numerator. Some of the following discussion is based on work by A. P. Fraas and others at ORNL.

Figure 12.4 shows very crudely the stylized configuration. For the vacuum wall and general stiffening structure, niobium seems best. (Molybdenum is neutronically better but has other difficulties.) Ideas about the moderator range from pure lithium, to Li-Be metallic systems, to $(LiF)_2BeF_2$ eutectic salt, all with some added structural material (niobium, carbon, etc.). Crucial to the fusion reactor is the yield T/n of tritons produced in the blanket per fusion neutron. Analyses to date show yields T/n ranging from 1.15 to 1.5 for realistic systems (Sect. 12.3). This presages a quite plentiful neutron economy if fusion comes to pass. The magnet shield is simple and cheap and requires no more discussion. However, the moderator plus shield must be 1.0 to 1.4 m thick, depending on its composition; this very considerable thickness fixes for us much of the scale of the system.

Superconducting magnets appear best for our purpose by far, and present state of the art leads us to be quite optimistic here; already magnets more or less comparable with those required for fusion are being designed and built. To hold the very large magnetic stress, a titanium support structure outside the coils (not shown) must be included in the system and in the cost.

Opinions vary about the precise configuration and of the cost of the components just described, but reasonable figures can be adduced. Examples that now follow are based on a complicated scale of costs, depending on the magnetic field and other things. Roughly, they correspond to the following conservative extrapolations of present costs and technology. For example, some numbers used are as follows: niobium at \$20.00/lb fabricated; magnet coils at \$26,000 per square meter of surface at 50 kG; BeO at \$45.00/lb; $(LiF)_2BeF_2$ at \$7.50/lb; titanium at \$2.00/lb fabricated; thermal fluence at vacuum wall = 10^7 W/m^2 (~15% absorbed there, contributing to local heat transfer problems). The average field at the coils is taken as twice the useful field at the plasma boundary.

Costs of some systems without injectors or pumps (the reactor "core") are shown in Tables 12.1 and 12.2. Table 12.1 compares open and closed systems of vacuum wall radius 5 m, that is, large systems. Costs are independent of configuration in this approximation, but β is not. \$20.00/kW (thermal) is thought reasonable, and \$10.00/kW (thermal) would be very attractive. Note that low magnetic fields are much preferred if β can be made high enough.

Table 12.2 shows several things for closed configurations. As the vacuum wall radius r_w is chosen smaller than 5 m, costs rise, and for "small" systems ($r_w = 1$) reasonable cost implies relatively high β. Two sets of costs are shown. The plain text costs are based upon the conservative magnet estimates just described. The parenthetical costs result if the magnet costs are reduced by a factor of 3. We see that small high-field systems become more attractive.

Descriptions "small" and "large" are relative. In fact, the smallest of these calculated examples is about 3000 MW (thermal), and the larger ones are about 30,000 MW (thermal).

Table 12.1. Cost and Required β of Several Fusion Systems, Assuming 5 m Vacuum Wall Radius

B_{max} at Coils (kG)	Open Systems		Closed Systems	
	Dollars per Kilowatt (Thermal)	β	Dollars per Kilowatt (Thermal)	β
120			22.6	0.067
100	16.9	0.215	16.9	0.096
80	12.0	0.336	12.0	0.15
60	8.25	0.60	8.25	0.27
50	6.9	0.80	6.9	0.38

Table 12.2. Cost and Required β of Several Closed Fusion Systems, with Two Assumptions About Magnet Costs

B_{max} at Coils (kG)	$r_w = 5$ m		$r_w = 3$ m		$r_w = 1$ m	
	Dollars per Kilowatt (Thermal)	β	Dollars per Kilowatt (Thermal)	β	Dollars per Kilowatt (Thermal)	β
120	22.6 (10.7)	0.067	27.0 (12.2)	0.106		
100	16.9 (8.5)	0.096	20.1 (9.5)	0.15	25.5 (11.7)	0.21
80	12.0 (6.7)	0.15	13.6 (7.6)	0.24	17.9 (9.0)	0.34
60	8.25 (5.3)	0.27	9.6 (5.9)	0.43	12 (7.2)	0.50
50	6.9 (4.7)	0.38	7.9 (5.3)	0.61	9.6 (6.1)	0.86

12.2.4 Conclusions

The costs just listed should not be taken as revealed truth, but more as showing optimistic trends. Most importantly, there seems to be every good reason to explore the business more fully. For example, we shall see in Sect. 12.3 that the blanket costs can be reduced substantially from those assumed here by using natural lithium and no beryllium. Further, we see in Sect. 12.4 that the retrieval of tritium generated in the blanket is a fairly simple and cheap process. Thus the "core" cost may eventually be lower.

General directions of the plasma work are fairly clear. We find here some other important plasma problems to explore, but they were already pretty well recognized. In need of work are many more nonplasma things, and space allows hardly more than a partial list by title:

1. Radiation damage. The total fluence of 14-MeV neutrons over a reactor lifetime would be $\sim 10^{23}/\text{cm}^2$. Effects will be severe, but little is known, and a suitable 14-MeV source is not presently available. This problem is being studied at ORNL with increasing attention.
2. Sputtering. We give some first numbers in Sect. 12.5.
3. Injection. For these large systems, getting the D-T fuel into the middle of the plasma may be very difficult. Fast atom beams and high-velocity fuel pellets both seem to be attenuated or ablated near the plasma surface.
4. Startup. No well-analyzed schemes for steady-state devices have been presented.
5. Geometrical and topological problems in the light of real engineering requirements. Here an example is helpful. The Tokomak concept seems in difficulty if $\beta_\theta < 1$, and the Kruskal-Shafranov limit must be well exceeded and not just marginally satisfied. The trouble is that in configurations with large major radius, the main B_z field is too high ($\sim$200 kG); in configurations with small major radius, the finite blanket limits the hole size, and the flux change through it (to produce I_z) becomes excessive.

This list has been extended in other documents. What emerges is that the plasma aspects of fusion are such that we should take an inexpensive look at what would lie beyond. We find there cause for optimism, especially for very large systems. They might be economically very attractive, besides having the desirable properties classically assigned to them, that is, safety, control (technical as well as political), easy neutron economy, and so forth. Perhaps the greatest encouragement to the plasmologist lies in recognizing that economics dictates the large sizes; large sizes in turn may well reduce some of the stringent requirements heretofore placed on plasma confinement.

12.3 NEUTRONICS CALCULATIONS AND COST ESTIMATES FOR FUSION REACTOR BLANKET ASSEMBLIES[2]

Don Steiner[3]

The generation of the tritium fuel through breeding is essential to the D-T fusion reactor. We have investigated a variety of blankets to optimize breeding ratios and minimize cost. The work in ORNL-TM-2360 summarizes the techniques used and presents the blankets which would be useful to more detailed fusion reactor designs. We present this work by abstract:

"We have investigated the tritium breeding potential and the material costs of some thermonuclear blanket assemblies. These assemblies differ from previously proposed assemblies in the following aspects:

(1) Niobium, rather than molybdenum, is employed as the structural material.
(2) Lithium, or a combination of lithium and flibe (lithium-beryllium fluoride), rather than flibe alone, is employed as coolant.
(3) No metallic beryllium is employed; graphite is the only neutron moderator present.

Neutron fluxes and reaction rates were calculated with the ANISN, one dimensional, transport theory code employing an S_8 approximation for the angular flux and a P_3 approximation for the elastic-scatter-source term. In all cases the blanket geometry was idealized as a slab, and one hundred energy groups were employed.

"Blanket assemblies containing only lithium as coolant, yield tritium breeding ratios in the range 1.32–1.57. Blanket assemblies containing both lithium and flibe yield attractive tritium breeding ratios (i.e. $\sim$ 1.2 or greater) only when the volume ratio of lithium to flibe is greater than 1:1.

"It is concluded that the blanket designs considered in this study offer a more attractive combination of tritium breeding ratio and material costs than do the earlier designs."

Preliminary work was done earlier in ORNL-MIT-52.[4] Although the later work of ORNL-TM-2360 gave much more favorable results, we present the MIT Practice School work too by abstract:

"Neutron economy studies of the proposed blanket assembly of a thermonuclear reactor (with deuterium and tritium as fuel) were undertaken. ANISN, a neutron transport code, was used for the calculations. Cross sections were obtained from the cross section tape GAM II. For the calculations the fusion reactor blanket was approximated by a layered slab model, with niobium as a structural material, lithium as a coolant, and graphite and beryllium or beryllium oxide for moderation. Tritium breeding (required to exceed one tritium atom produced per neutron incident on the blanket) was achieved only for very small niobium content in the blanket. Corrections are needed in the GAM II cross section tape before accurate calculations can be made. When future studies are initiated, it is recommended that close attention be directed to minimizing the niobium content of the blanket, and to optimizing the moderation provided by the graphite. Approximation of the layered slab calculational model by homogenizing the blanket into one region was found to be unjustified."

It seems apparent that abundant neutrons will be available and that the regeneration of tritium will not present great difficulties. With suitable and realistic blankets the costs of breeding tritium can be kept much lower than earlier predictions had assumed.

The spectra of neutrons and the power deposition are the current areas of importance. The flux and energy of neutrons, particularly in the niobium vacuum wall, are important in assessing the role of radiation damage. These considerations are now embryonic and will be a subject for the next annual report.

12.4 A DIFFUSION PROCESS FOR REMOVING TRITIUM FROM THE BLANKET OF A THERMONUCLEAR REACTOR[5]

A. P. Fraas[6]

Since the tritium necessary to start the first thermonuclear reactor would cost about $1,000,000/kg and estimates of inventory range up to 220 kg

[2]Don Steiner, *Neutronics Calculations and Cost Estimates for Fusion Reactor Blanket Assemblies*, ORNL-TM-2360 (Nov. 22, 1968).

[3]Reactor Division.

[4]P. J. Wood, W. S. Grow, and D. Steiner (consultant), *Neutron Economy Calculations for Fusion Reactor Blanket Assemblies*, ORNL-MIT-52 (May 3, 1968).

[5]A. P. Fraas, *A Diffusion Process for Removing Tritium from the Blanket of a Thermonuclear Reactor*, ORNL-TM-2358 (December 1968).

[6]Reactor Division.

using "conventional recovery," it is very important to determine a feasible and economical recovery system to remove tritium, minimize inventory, and reduce the doubling time for fuel. ORNL-TM-2358 contains the rationale for using a diffusion process for doing this economically. We reproduce the abstract first and later include some additional remarks.

"The tritium concentration in the blanket of a thermonuclear reactor is important both from the standpoint of its effect on the capital investment required and from the standpoint of possible embrittlement of the structural material. Thus, the size and cost of the system required to keep the tritium concentration to an acceptable level is important from the feasibility standpoint.

"The high diffusion coefficient for hydrogen diffusing through niobium makes it possible to design a tritium removal system for the thermonuclear reactors evolved in the study covered by ORNL-TM-2204. The proposed system entails tritium diffusion from the lithium of the blanket as it circulates through the main heat exchangers built of niobium. These would be operated at about 1800°F and be used to boil potassium for a potassium vapor topping cycle. A stainless steel potassium condenser operating at about 1100°F would serve not only as the boiler for a steam cycle but it would also be designed to concentrate the tritium which would be drawn off as a noncondensable. The incremental cost of the resulting tritium removal system designed to hold the tritium inventory to about 10 kg in a 5000 Mw(t) plant appears to be modest – roughly $4,000,000."

The system proposed in ORNL-TM-2358 shows that only 10 kg of tritium will be necessary as inventory and that the doubling time of the inventory is approximately 90 days, using the breeding ratios determined in Sect. 12.3 of this report.

We can compare the 10-kg inventory of tritium in a proposed fusion reactor with the fission inventory in a comparable size fission reactor. Halfway through the life of a typical fuel inventory the fission reactor has 3000 kg of fission products with at least the same amount of plutonium. The biological hazards of fission products and plutonium are from 10^5 to 10^7 times worse than that of tritium.[7] Thus the hazard potential associated with radioactive material inventory would be at least a factor of 10^{10} lower in a fusion reactor than in a fission reactor.

The afterheat in a fusion reactor is approximately 3×10^{-4}% afterheat/power produced, or for a 30,000 MW (thermal) reactor it is less than 100 kW. For a fission reactor the similar percentage is 1 to 5%.

It thus appears that a simple, economical, and effective tritium recovery system can be designed which keeps inventory low, doubling times short, and hazards very low.

12.5 THE SPUTTERING OF NIOBIUM AT 1000°C BY 20-keV D^+

O. C. Yonts

Niobium has for a variety of reasons gained favor as a vacuum wall material for an eventual fusion reactor. One important parameter needed for an evaluation of the suitability of niobium (or any other material) as a vacuum wall is how fast the wall would erode and the nature of the material ejected into the plasma when the energetic deuterons and tritons from the unburned fuel strike the wall. We have measured the sputtering ratio for niobium and other wall candidates when bombarded by energetic particles appropriate to a D-T fusion reactor.

The simplest and most straightforward method to determine sputtering ratios is to bombard the target material for known time, with known current of ions, and then measure weight loss of the target. For ions that penetrate only a few angstroms into the target lattice, the ions can be ignored, because as the surface erodes the implanted particles leave too. If, however, chemical combination and diffusion are rapid, large quantities of bombarding ions can be trapped.[8]

We found that niobium gains (rather than loses) weight at 1000°C when bombarded by 20-keV D^+ ions; the gain is 0.015 g/A-hr. This corresponds to absorption of 20% of the impinging beam of ions, if we ignore sputtering. Similar gains were found with titanium;[8] there, 95% of impinging D^+ ions were trapped at room temperature. On the other

[7] *Maximum Permissible Body Burdens and Maximum Permissible Concentrations of Radionuclides in Air and Water for Occupational Exposure*, National Bureau of Standards Handbook No. 69, June 5, 1959.

[8] O. C. Yonts and R. A. Strehlow, *J. Appl. Phys.* **33**, 2903 (1962).

ORNL-DWG 69-2508

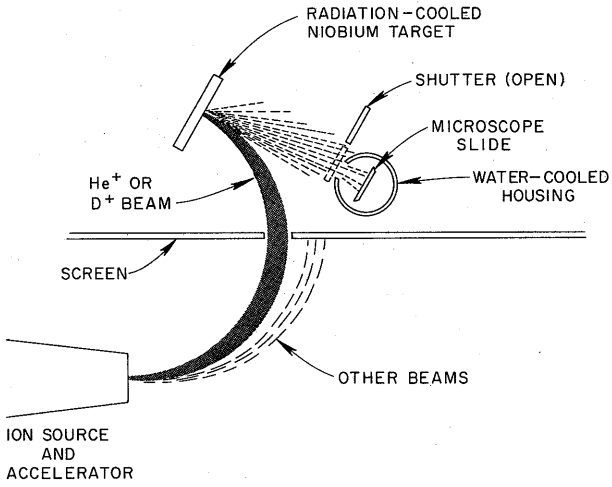

Fig. 12.5. Schematic of Indirect Method of Measuring Sputtering Ratio Within Calutron Unit.

hand, niobium loses weight when bombarded by energetic helium ions, since chemical combination and diffusion are very much reduced; we can therefore measure a sputtering ratio for helium on niobium and use the helium geometry and weight loss as a reference and calibration for the subsequent deuterium sputtering ratio determination by the indirect method. We determined He^+-Nb ratios at 1050 and 1350°C.

We used another method to measure D^+-Nb sputtering ratio, since the direct weight-loss method was not suitable. A schematic is shown in Fig. 12.5. The target ions impinge at normal incidence to the target; sputtered particles are emitted in a $\cos^2 \theta$ distribution about this normal.[9] Sputtered material is collected on a microscope slide. This is done first for He^+-Nb and later again for D^+-Nb. Light transmission is measured, and Beer's law is applied to find the amount of material deposited; this is then related to the number of niobium atoms emitted per incident D^+ ion and per He^+ ion. From these calculations and the knowledge of the direct weight loss for He^+-Nb, we find the D^+-Nb sputtering ratio.

Table 12.3 gives the sputtering ratio for various materials for incident 20-keV D^+; Table 12.4 does the same for incident 20-keV He^+. The data for Nb, Mo, W, and Ti (at 1050°C) are new data.

[9]P. K. Rol, *Sputtering of Copper by Ion Bombardment*, dissertation, University of Amsterdam, Mar. 23, 1960.

Table 12.3. Sputtering by D^+ at 20 keV

Material	Sputtering Ratio	Target Temperature (°C)	Remarks
Al	0.008[a]	50	Water-cooled target
Cu	0.038[a]	50	Water-cooled target
Mo	0.010	50	Water-cooled target
W	0.008	50	Water-cooled target
Nb	0.0006	1050	Radiation cooled
Ti	Estd at 0.02	800	Radiation cooled
Ti	0.35	1050	Includes evaporation from the surface

[a]O. C. Yonts, C. E. Normand, and D. E. Harrison, Jr., *J. Appl. Phys.* 31, 447 (1960).

Table 12.4. Sputtering by He^+ at 20 keV

Material	Sputtering Ratio	Target Temperature (°C)	Remarks
Al	0.022[a]	50	Water-cooled target
Cu	0.197[a]	50	Water-cooled target
Nb	0.044	1350	Radiation cooled
Nb	0.041	1050	Radiation cooled
Ti	0.014	50	Water-cooled target

[a]O. C. Yonts, C. E. Normand, and D. E. Harrison, Jr., *J. Appl. Phys.* 31, 447 (1960).

The ratio for D^+-Nb is 0.0006 and is the smallest ratio we know. We could not measure the sputtering ratio for titanium at room temperature.[8] Why those materials (niobium and titanium), which exhibit great chemical affinity for hydrogen, also have in common very small sputtering ratios will be interesting to investigate! It is distressing to find niobium having such affinity for hydrogen, since the previous section implied high diffusion rates. The 1% zirconium in this sample may be responsible for this discrepancy.

We can now calculate the effect of erosion. For the large [30,000 MW (thermal)] reactors envisioned

in ORNL-TM-2204[10] (p. A-20) we burn 10^{22} D-T/sec; for burnup fractions of 5% (p. 59) we must have 2×10^{23} D-T/sec leaving the system. For uniform radial losses on a wall of 3000 m^2 we have 10^{16} D^+ cm^{-2} sec^{-1}. For sputtering ratios reported here for niobium (6×10^{-4}), we have 6×10^{12} niobium atoms cm^{-2} sec^{-1} leaving the wall, or an erosion rate of 10^{-10} cm/sec. The first wall of the cellular structure recommended in ORNL-TM-2204 has a thickness of ¼ in. (p. A-23). If we allow 20% erosion (1 mm) before we lose wall integrity, the wall would last about 25 years if sputtering were the only criterion. By comparison a molybdenum wall (sputtering ratio of 10^{-2}) would last only 1.5 years before needing replacement. Niobium, then, appears to be an excellent choice as a first wall material. Radiation damage of niobium by 14-MeV neutrons thus is the chief unknown in the further evaluation of structure integrity and economics of the fusion reactor core.

We plan to measure the sputtering ratio of niobium by protons. This ratio, together with that of deuterium, should permit us to assess the effect of energetic tritium on the niobium wall lifetime.

[10] D. J. Rose, *On the Feasibility of Power by Nuclear Fusion*, ORNL-TM-2204 (May 1968).

12.6 WORK IN PROGRESS

The engineering feasibility of a fusion reactor will in large measure depend on the effects of radiation damage by the 14-MeV neutrons striking the vacuum wall. How difficult it will be to design the structure to compensate for damage effects and the lifetime of this system will limit the alternatives we now have. This is a problem not unknown to a fission reactor designer. The Metals and Ceramics and the Solid State Divisions are presently studying the probable radiation damage effects.

The present worth of neutrons is $2300/g. A fusion reactor has very short fuel doubling times and thus has excess neutrons that can be used to lower present costs for various isotope production. Other topics, such as magnetic energy storage in cryogenic or superconducting coils for pulsed systems, are being examined. The engineering problems awaiting solution are many and are vividly displayed in ORNL-TM-2204.[10] One should not lose sight that though the motivation for fusion power is strong and the engineering problems are yielding to careful analyses, the principal problem remains that of adequately confining a plasma.

13. Design and Engineering: Service Report

Design and engineering services are generally reported incidentally with the work of the research groups of the Division. These services include executing or coordinating engineering design, shop fabrication, building operations, and maintenance for the Division.

Design activities for this reporting period are summarized as follows:

Jobs on hand 10-31-67 on which work had not started	3
New jobs received	131
Total jobs	134
Jobs completed	126
Jobs in progress	5
Backlog of jobs 12-31-68	3
Total drawings completed for period (does not include drawings for slides, reports, etc.)	352

Shop fabrication for this reporting period is summarized as follows:

Machine shops	
Completed jobs requiring 16 man-hours or less	196
Completed jobs requiring 17 to 1200 man-hours	182
Completed jobs of miscellaneous character (in plating, carpenter, electrical, glass, lead, and rubber shops)	88
Average manpower (Machine Shop)	11.1
Average manpower (miscellaneous shops)	2
Number of jobs in progress	10
Electromagnet fabrication	
Completed jobs	7
Number of jobs in progress	1
Average manpower	2.3

Publications, ORNL Reports, and Papers

OPEN LITERATURE

Author(s)	Title of Article	Journal (or Book)
I. Alexeff, W. D. Jones, and D. Montgomery[1]	Effects of Electron-Temperature Variation on Ion Acoustic Waves	*Phys. Fluids* **11**, 167 (1968)
H. Doucet,[2] I. Alexeff, and W. D. Jones	Simultaneous Measurements of Ion-Acoustic-Wave Potential and Plasma Density Perturbation to Yield γ_e	*Phys. Fluids* **11**, 2451 (1968)
Igor Alexeff	Letter: Comment on "Measurement of the Anisotropic Energy Distribution of Electrons in an Electron Cyclotron Resonance Plasma," by J. L. Shohet and S. J. Gitomer, *Phys. Fluids* **10**, 1359 (1967)	*Phys. Fluids* **11** (1968)
S. Aksornkitti,[3] H. C. S. Hsuan,[3] K. E. Lonngren,[3] and I. Alexeff	Research Note: Ion Wave Reflections as Observed in a "Perturbed" Plasma	*Phys. Fluids* **8**, 1838 (1968)
I. Alexeff, W. D. Jones, and K. Lonngren[3]	Excitation of Pseudowaves in a Plasma via a Grid	*Phys. Rev. Letters* **21**, 878 (1968)
I. Alexeff, G. E. Guest, R. V. Neidigh, D. J. Rose, and D. Montgomery[1]	Oscillations Present in Plasma-Electron Heating by an Electron Beam	*Phys. Rev. Letters* **21**, 344 (1968)
C. O. Beasley and J. G. Cordey[4]	Convective and Absolute Ion Cyclotron Instabilities in Homogeneous Plasmas	*Plasma Phys.* **10**, 441 (1968)
J. F. Clarke and G. G. Kelley	Instabilities Due to Magnetic Spatial Variations	*Phys. Rev. Letters* **21**, 1041 (1968)
R. J. Colchin, J. L. Dunlap, R. S. Edwards, and H. Postma	A Method for Introducing Energy Spread into Plasmas Formed by High Energy Neutral Injection	*Nucl. Fusion* **7**, 292 (1967)
K. R. Efferson	Helium Vapor Cooled Current Leads	*Rev. Sci. Instr.* **38**, 1776 (1967)
W. M. Farr and R. E. Budwine	High-Frequency Flute-Like Instabilities in Multicomponent Plasmas	*Phys. Fluids* **11**, 883 (1968)
W. F. Gauster and D. L. Coffey	Problems in Designing Non-Axisymmetrical Superconducting Magnet Systems	*J. Appl. Phys.* **39**, 264 (1968)
G. E. Guest and R. A. Dory	Effect of Electron Temperature on Absolute Instabilities in Loss-Cone Plasmas	*Phys. Fluids* **11**, 1775 (1968)

Author(s)	Title of Article	Journal (or Book)
M. O. Krause, T. A. Carlson,[5] and R. D. Dismukes[6]	Double Electron Ejection in the Photoabsorption Process	*Phys. Rev.* **170**, 37 (1968)
R. A. Langley, L. H. Toburen,[7] and M. Y. Nakai[8]	The Measurement of High-Energy Charge Transfer Cross Sections for Incident Protons and Atomic Hydrogen in Various Gases	*Phys. Rev.* **171**, 114 (1968)
J. Rand McNally, Jr.	Further Studies of Excitation-Heating of Ions	*Plasma Phys.* **10**, 903 (1968)
M. Roberts, I. Alexeff, and W. Halchin	Azimuthally Localized Fluctuations in a Levitated Toroidal Quadrupole	*Phys. Letters* **26A**, 590 (1968)
J. E. Simpkins	Microminiature Hall Probes for Use in Liquid Helium	*Rev. Sci. Instr.* **39**, 570 (1968)
N. H. Lazar (ed., Chap. VII)	Plasma Heating Techniques (Other than Shocks)	Pp. 51–57 in *Perspectives on Controlled Thermonuclear Research* (ed. by R. L. Hirsch), USAEC, TID-24804 (October 1968)
F. L. Parker[9] and D. J. Rose	Technical Comment: Wastes from Fusion Reactors	*Science* **159**, 1376 (1968)
C. F. Barnett and H. B. Gilbody[10]	Measurements of Atomic Cross Sections in Static Gases	P. 390 in *Experimental Methods and Physics* (ed. by L. Marton), vol. 7A, chap. 4.2, Academic, 1968
W. F. Gauster and J. B. Hendricks	Performance of Stabilized Superconducting Cables Under Controlled Heat Transfer Conditions	*IEEE Trans. Magnetics* **MAG-4**, 489 (1968)
	Flux Flow and Thermal Stability of Stabilized Superconductors	*J. Appl. Phys.* **39**, 2572 (1968)
D. M. Kroeger and M. S. Lubell	Stability of the Flux Flow State in Superconducting NbTi Strips	*Appl. Phys. Letters* **13**, 63 (1968)
W. F. Gauster	The Large Volume, High Uniformity Magnets at the Oak Ridge National Laboratory	P. 267 in *Proc. Les Champs Magnetiques Intenses: leur Production et leurs Applications*, Grenoble, France, Sept. 12–14, 1966 [Centre National de la Recherche Scientifique, No. 166 (1967)]
G. G. Kelley	An Effect of Finite Plasma Length on Ion Cyclotron Instabilities	Research Note: *Plasma Phys.* **10**, 1105 (1968)
R. A. Dandl,[11] H. O. Eason, P. H. Edmonds,[12] and A. C. England	Electron-Cyclotron Heating by 8-mm Microwave Power in the Magnetic Facility ELMO	Pp. 181–203 in *Relativistic Plasmas* (ed. by O. Buneman and W. B. Pardo), W. A. Benjamin, Inc., New York, 1968
R. C. Davis and G. G. Kelley	The Effect of the Ion Emission Surface on the Optical Properties of Ion Beams	*Nucl. Instr. Methods* **66**(2), 224–28 (1968)
H. Grawe[13]	A Stochastic Model of Electron Cyclotron Heating	*Plasma Phys.* **11**, 151–62 (1969)

[1]Consultant, University of Iowa.
[2]Laboratoire de Physique des Milieux Ionises, Ecole Polytechnique, Paris, France.
[3]University of Iowa.
[4]U.K. Atomic Energy Authority, Culham Laboratory, England.
[5]Chemistry Division, on loan to Physics Division.
[6]U.S. Atomic Energy Commission Health Physics Fellow, Vanderbilt University, Nashville, Tenn.
[7]Battelle Northwest, Richland, Wash.
[8]Osaka Laboratory, Atomic Energy Research Institute, Osaka, Japan.
[9]Department of Sanitary and Water Resources Engineering, Vanderbilt University, Nashville, Tenn.
[10]Consultant, Department of Pure and Applied Physics, Queen's University, Belfast, Northern Ireland.
[11]Instrumentation and Controls Division.
[12]On leave from Culham Laboratory, England.
[13]On leave from Institute for Plasma Physics, Garching, Federal Republic of Germany.

ORNL REPORTS

Author(s)	Title	Number
L. H. Toburen,[1] M. Y. Nakai,[2] and R. A. Langley	The Measurement of High-Energy Charge Transfer Cross Sections for Incident Protons and Atomic Hydrogen in Various Gases	ORNL-TM-1988
Thermonuclear Division Staff	Thermonuclear Division Chrestomathy – 1967	ORNL-TM-2146
D. J. Rose	On the Feasibility of Power by Nuclear Fusion	ORNL-TM-2204
Thermonuclear Division Staff	Thermonuclear Division Semiannual Progress Report for Period Ending October 31, 1967	ORNL-4238
J. F. Clarke, G. G. Kelley, J. F. Lyon, and R. F. Stratton	The Effect of Microinstabilities on a Hot Ion Plasma	ORNL-TM-2333
Glenn Joyce[3] and R. A. Dory	Propagation of Ion Acoustic Waves in a Magnetic Field	ORNL-TM-2341
Ryo Sugihara[4] and Hiroshi Tanaca[5]	Dispersion Relation of Ion Acoustic Waves in a Magnetic field	ORNL-TM-2345
M. S. Lubell and K. R. Efferson	Flux Pumps as Power Supplies in Comparison with Alternatives	ORNL-TM-2351
Thermonuclear Division Staff	Thermonuclear Division Chrestomathy – 1968	ORNL-TM-2337
I. Alexeff, R. V. Neidigh, and W. R. Wing[6]	A Simple Gigacycle Correlator	ORNL-TM-2379
R. A. Dory, W. M. Farr, G. E. Guest, and J. D. Callen[7]	Warm-Plasma Stabilization of Resonant Loss-Cone Instabilities	ORNL-TM-2397
D. A. Ross, M. M. Satterfield, and G. R. Dyer	An Auditory Electrocardiogram Monitor	ORNL-TM-2398
I. Alexeff and D. F. Howell[8]	A Simple Circuit for Obtaining the Electron Velocity Distribution in Plasma	ORNL-TM-2403
J. A. Ray and C. F. Barnett	Detection of Low Energy Heavy Particles with Silicon Barrier Detectors	ORNL-TM-2411
R. L. Brown	Novel Techniques for Winding Superconducting Tapes	ORNL-TM-2450

Author(s)	Title	Number
C. F. Barnett, Director, D. A. Griffin, M. O. Krause, R. A. Langley, J. R. McNally, Jr., J. A. Ray, and I. A. Sellin	Bibliography of Atomic and Molecular Processes, July 1967–December 1967	ORNL-AMPIC-10
	Bibliography of Atomic and Molecular Processes, January 1968–June 1968	ORNL-AMPIC-11
W. F. Gauster, K. R. Efferson, J. B. Hendricks, D. M. Kroeger, and M. S. Lubell	Magnetic Flux Flow and Superconductor Stabilization (December 1, 1967)	ORNL-TM-2075
	Magnetic Flux Flow and Superconductor Stabilization (March 1968)	ORNL-TM-2162
W. F. Gauster, K. R. Efferson, J. B. Hendricks, D. M. Kroeger, M. S. Lubell, and J. E. Simpkins	Magnetic Flux Flow and Superconductor Stabilization (May 17, 1968)	ORNL-TM-2233
	Magnetic Flux Flow and Superconductor Stabilization (August 30, 1968)	ORNL-TM-2350
W. F. Gauster, K. R. Efferson, D. M. Kroeger, M. S. Lubell, and J. E. Simpkins	Magnetic Flux Flow and Superconductor Stabilization (November 1968)	ORNL-TM-2441

[1]Pacific Northwest Laboratory, Battelle Memorial Institute, Richland, Wash.

[2]Osaka Laboratory, Japan Atomic Energy Institute, Neyagawa, Osaka, Japan.

[3]University of Iowa, Iowa City.

[4]On leave from Institute of Plasma Physics, Nagoya University, Nagoya, Japan.

[5]On leave from Institute of Materials Science and Engineering, Yokohama National University, Yokohama, Japan.

[6]Student Guest, University of Iowa, Iowa City.

[7]Institute for Advanced Studies, Princeton, N.J.

[8]Department of Electrical Engineering, University of Tennessee, Knoxville.

PAPERS PRESENTED AT SCIENTIFIC AND TECHNICAL MEETINGS

International Conference on Plasma Confined in Open-Ended Geometry, Gatlinburg, Tennessee, November 1–4, 1967 (Proceedings, CONF-671127)

M. C. Becker,[1] C. W. Blue, R. A. Dandl,[1] H. O. Eason, A. C. England, N. H. Lazar, O. D. Matlock, and M. W. McGuffin, "Target Plasma Experiments in the INTEREM Facility."

R. J. Colchin, J. L. Dunlap, and H. Postma, "Plasma Containment in DCX-1.5."

G. E. Guest, R. A. Dory, C. O. Beasley, Jr., W. M. Farr, and D. J. Sigmar, "Non-Convective Loss-Cone Instabilities."

P. R. Bell, J. F. Clarke, G. G. Kelley, J. F. Lyon, N. H. Lazar, and R. F. Stratton, "DCX-2 Micro-instability Studies."

W. B. Ard and R. A. Dandl,[1] "Studies of Open-Ended Confinement with ECR Plasmas."

American Physical Society, Division of Plasma Physics, Austin, Texas, November 8–11, 1967 [*Bull. Am. Phys. Soc.* 13 (February 1968)]

G. E. Guest, "A Stochastic Model of Electron-Cyclotron Resonant Heating."

G. E. Guest, R. A. Dory, C. O. Beasley, Jr., W. M. Farr, and D. J. Sigmar, "Non-Convective Loss-Cone Instabilities."

E. G. Harris,[2] "Kinetic Theory of Unstable Plasmas."

J. W. Flowers,[3] "Critical Velocities in Rotating Plasmas."

G. G. Kelley, P. R. Bell, N. H. Lazar, J. F. Lyon, and R. F. Stratton, "Energetic Proton Microinstability in the DCX-2 Afterglow."

J. F. Lyon, J. F. Clarke, and R. F. Stratton, "DCX-2 Ion Beam Gyrofrequency Instability. I. Mode Characteristics."

R. V. Neidigh, Ray Hefferlin,[4] Wm. Denver Jones, and S. R. Sowder,[5] "Electron Density in Burnout IV."

C. E. Nielsen[6] and W. L. Stirling, "Electron Density and Potential in a Magnetically Collimated Helium Arc."

M. Roberts, I. Alexeff, and W. Halchin, "Observation of Plasma Injected into a Levitated Toroidal Quadrupole."

W. L. Stirling and C. E. Nielsen,[6] "Power Balance Measurements in a Multi-Kiloampere High Pressure Gas Discharge."

J. F. Clarke, J. F. Lyon, and R. F. Stratton, "DCX-2 Ion Beam Gyrofrequency Instability. II. Landau Damping."

Karl Lonngren,[7] David Montgomery,[8] I. Alexeff, and W. D. Jones, "The Ion-Acoustic Wave Sheath."

1967 Applied Superconductivity Conference and Exhibition, Austin, Texas, November 6–8, 1967 [*Bull. Am. Phys. Soc.* **39** (1968)]

W. F. Gauster and J. B. Hendricks, "Flux Flow and Thermal Stability of Stabilized Superconductors."

W. F. Gauster and D. L. Coffey, "Problems in Designing Nonaxisymmetrical Superconducting Magnet Systems."

Colloquium on the Interaction of Stationary and Progressive Electromagnetic Fields with a Plasma, Saclay, France, January 15–18, 1968

R. A. Dandl,[1] H. O. Eason, P. H. Edmonds, and A. C. England, "Electron Cyclotron Heating by 8-mm Microwave Power in the Magnetic Facility, ELMO."

American Physical Society, Divisions of Chemical Physics, High Polymer Physics, and Solid State Physics, Berkeley, Calif., March 18–21, 1968 [*Bull. Am. Phys. Soc.* **13** (March 1968)]

D. M. Kroeger and M. S. Lubell, "Stability of the Flux-Flow State in Superconducting NbTi Strips."

American Physical Society, Chicago, Illinois, January 29–February 1, 1968 [*Bull. Am. Phys. Soc.* **12** (December 1967)]

C. F. Barnett, "Hydrogen Molecules, Rydberg States, and Autoionization" (invited paper).

M. O. Krause, "Partial Photoabsorption Cross Sections of Krypton in Energy Range from 300 to 1500 eV."

D. J. Rose, "Recent Progress in Fusion Research" (invited paper).

1968 International Conference on Magnetics (INTERMAG), Washington, D.C., April 3–5, 1968 [*IEEE Trans. Magnetics* (September 1968)]

W. F. Gauster and J. B. Hendricks, "Performance of Stabilized Superconducting Cables Under Controlled Heat Transfer Conditions."

Conference on Low Energy Accelerators, Oak Ridge Associated Universities, Inc., Oak Ridge, Tenn., April 8–10, 1968 (CONF-680411, p. 415)

C. F. Barnett, "Atomic and Molecular Collision Physics with Low Energy Accelerators" (invited paper).

American Physical Society, Washington, D.C., April 22–25, 1968 [*Bull. Am. Phys. Soc.* **13** (April 1968)]

K. E. Lonngren,[7] S. Aksornkitti,[7] H. C. S. Hsuan,[7] and I. Alexeff, "Ion Wave Reflections as Observed in Perturbed Plasmas."

M. Roberts, I. Alexeff, and W. Halchin, "Microwave Plasmas Produced in a Levitated Toroidal Quadrupole."

I. Alexeff, W. D. Jones, H. Tanaca, and Karl Lonngren,[7] "Observations of Pseudo-Ion Acoustic Waves in Plasmas."

Annual Sherwood Theory Meeting, Berkeley, California, May 6–7, 1968 (proceedings will not be published)

C. O. Beasley, Jr., R. A. Dory, G. E. Guest, and D. J. Sigmar, "Upper Limits on Electron Temperature in Mirror-Confined Plasmas."

C. C. Cheng[9] and E. G. Harris,[2] "Microinstabilities in Finite Plasmas."

R. A. Dory, C. O. Beasley, Jr., G. E. Guest, and D. J. Sigmar, "Loss-Cone Instabilities at Reactor-Like Densities."

W. M. Farr and G. E. Guest, "Stabilization of Hot, Loss-Cone Plasma with Low-Temperature Ions."

H. Grawe,[10] "A Stochastic Model of Electron Cyclotron Heating."

D. J. Sigmar, G. E. Guest, C. O. Beasley, Jr., and R. A. Dory, "General Properties of Absolute Loss-Cone Instabilities."

Ryo Sugihara,[2] "Ion Acoustic Waves in a Magnetized Plasma."

1968 Summer Study on Superconducting Devices and Accelerators, Brookhaven National Laboratory, Upton, Long Island, New York, June 10–July 19, 1968 (proceedings to be published by Brookhaven National Laboratory)

D. L. Coffey and W. F. Gauster, "Progress on the IMP Facility."

W. F. Gauster, "Standardized Tests for Superconducting Materials."

M. S. Lubell, "Flux Pumps as Power Supplies in Comparison with Alternatives" (invited paper).

American Physical Society, Division of Plasma Physics, Los Alamos, New Mexico, June 17–19, 1968 [*Bull. Am. Phys. Soc.* **13** (June 1968)]

M. Roberts, I. Alexeff, R. A. Dory, W. Halchin, and W. L. Stirling, "Observation of Microwave Plasmas in a Levitated Toroidal Quadrupole."

R. V. Neidigh, D. J. Rose, I. Alexeff, D. Montgomery,[8] and G. E. Guest, "Experimental Strong Turbulent Heating."

R. J. Colchin, J. L. Dunlap, and H. Postma, "Flute Investigations in DCX-1.5."

I. Alexeff, W. D. Jones, and H. Tanaca, "Ion-Acoustic-Wave Speed-Up in a Magnetically Supported Plasma Column."

Annual Meeting, Society of Nuclear Medicine, St. Louis, Missouri, June 27–30, 1968 [*J. Nucl. Med.* **9** (June 1968)]

W. J. McClain,[11] M. M. Satterfield, and G. R. Dyer, "An Evaluation of Scan Data Processing by Digital Computer."

M. M. Satterfield and G. R. Dyer, "A New 'Medical Spectrometer'" (an exhibit and demonstration).

IAEA Third Conference on Plasma Physics and Controlled Nuclear Fusion Research, Novosibirsk, U.S.S.R., August 1–7, 1968 [proceedings to be published]

C. O. Beasley, Jr., R. A. Dory, W. M. Farr, G. E. Guest, and D. J. Sigmar, "Resonant Loss-Cone Instabilities in Mirror-Confined Plasmas."

J. F. Clarke, G. G. Kelley, J. F. Lyon, and R. F. Stratton, "The Effect of Microinstabilities on a Hot Ion Plasma in a Uniform Magnetic Field."

N. H. Lazar, R. A. Dandl,[1] H. O. Eason, P. H. Edmonds, and A. C. England, "Electron Cyclotron Heated 'Target' Plasma Experiments."

M. Roberts, I. Alexeff, R. A. Dory, W. Halchin, and W. L. Stirling, "ORNL Levitated Toroidal Multipole Program."

R. V. Neidigh, I. Alexeff, G. E. Guest, W. D. Jones, D. J. Rose, W. L. Stirling, and D. C. Montgomery,[8] "Experimental Strong Turbulent Heating."

1968 Cryogenic Engineering Conference, Case Western Reserve University, Cleveland, Ohio, August 19–21, 1968 (proceedings to be published in *Advances in Cryogenic Engineering*, vol. 14, ed. by K. D. Timmerhaus, Plenum, New York, 1969)

M. S. Lubell and D. M. Kroeger, "Flux Flow Studies and Stability Criteria of NbTi Strips."

Arnold Sommerfeld Centennial Memorial Meeting and Symposium on Physics of One- and Two-Electron Atoms, University of München, West Germany, September 9–14, 1968 (*Phys. Today*, February 1969, p. 99)

Ivan Sellin, Bailey Donnally,[12] and C. Y. Fan,[13] "Measurement of Triplet-Singlet Transition Probabilities in Two-Electron Heavy Ions."

Southeastern Chapter, Society of Nuclear Medicine, Atlanta, Georgia, October 10–12, 1968 [*Rev. Sci. Instr.* **39** (December 1968)]

G. R. Dyer and W. J. McClain,[11] "A System for Recording and Displaying Scan Data."

J. E. Francis, W. J. McClain,[11] and D. A. Ross, "Scan Analysis by Spectrometry."

M. M. Satterfield, "Compression of Data for Computer-Tape Storage."

Conference on Plasma Instabilities in Astrophysics, Asilomar, Pacific Grove, California, October 14–17, 1968 (proceedings will not be published)

E. G. Harris,[2] "Velocity-Anisotropy Instabilities."

Fifteenth Nuclear Science Symposium, Montreal, Canada, October 23–25, 1968 (proceedings to be published in *IEEE Transactions on Nuclear Science*)

J. A. Ray and C. F. Barnett, "Detection of Low Energy Heavy Particles with Silicon Barrier Detectors."

1968 Applied Superconductivity Conference and Exhibition, Gatlinburg, Tennessee, October 28–30, 1968 [*Bull. Am. Phys. Soc.* **13** (December 1968)]

W. F. Gauster, "Stability Criteria of Compound Conductors Based on Actual Heat Transfer Measurements."

K. R. Efferson, "Heat Transfer from a Cylindrical Copper Surface to Liquid Helium I."

D. L. Coffey, J. L. Dunlap, W. F. Gauster, and J. L. Horton,[1] "A Comparison of NbTi and Nb_3Sn Quadrupole Magnet Systems for IMP."

American Physical Society, Division of Plasma Physics, Miami, Florida, November 13–16, 1968 [*Bull. Am. Phys. Soc.* **13** (November 1968)]

G. E. Guest, W. M. Farr, and R. A. Dory, "Stabilization of Loss-Cone Microinstabilities by Throughput of Warm Plasma."

Owen Eldridge,[2] "Perturbation of a Time Dependent Equilibrium."

D. J. Sigmar, C. O. Beasley, Jr., and G. E. Guest, "Microinstabilities in Hot Electron Plasmas."

J. F. Lyon, J. F. Clarke, G. G. Kelley, and R. F. Stratton, "Effect of the Modified Negative Mass Instability on the DCX-2 Plasma."

J. F. Clarke, "The Negative Mass Instability" (invited paper).

D. J. Rose,[14] "Physics of Fusion Feasibility" (invited paper).

J. E. Robinson[15] and J. F. Clarke, "Low Frequency Fluctuations in the DCX-2."

R. A. Dory, O. C. Eldridge,[2] and S. Fisher,[16] "High-Beta Mirror Equilibrium in Hot Electron Plasma."

E. D. Shipley and O. C. Yonts, "Classical Diffusion in a Negative Potential Well."

G. R. Haste and E. G. Harris,[2] "Stability Analysis of Mirror Plasmas."

W. B. Ard, "Energy Distribution of Electrons in a Decaying Hot Electron Plasma as a Function of Time."

W. L. Stirling, M. Roberts, I. Alexeff, W. Halchin, and R. A. Dory, "Effects of Supports on Microwave Plasma in a Levitated Toroidal Quadrupole.

R. J. Colchin and J. L. Dunlap, "Microinstability with Associated Betatron Oscillations in DCX-1.5."

R. V. Neidigh, I. Alexeff, and W. R. Wing,[17] "A Simple Gigacycle Correlator for Plasma Turbulence Studies."

F. R. Scott,[2] I. Alexeff, W. D. Jones, and R. V. Neidigh, "Observations of Energy and Current Bursts in Burnout V."

N. H. Lazar, J. L. Dunlap, and W. J. Herrmann,[18] "Electron Cyclotron Heated Plasmas in Minimum-*B* Configuration: Instability Studies."

W. J. Herrmann,[18] J. L. Dunlap, G. R. Haste, and N. H. Lazar, "Electron Cyclotron Heated Plasmas in Minimum-*B* Configuration: General Plasma Properties."

W. D. Jones, I. Alexeff, and A. Hirose,[2] "Dispersion Measurements in Electrostatic Ion Cyclotron Waves."

K. Lonngren,[7] S. Aksornkitti,[17] H. C. S. Hsuan,[7] I. Alexeff, and W. D. Jones, "Dispersion of Pseudowaves."

Suthi Aksornkitti,[17] I. Alexeff, and W. D. Jones, "An Experimental Study of the Properties of Pseudowaves."

A. Hirose,[2] N. A. Krall,[19] D. Montgomery,[8] I. Alexeff, and W. D. Jones, "Landau Damping of Ion Acoustic Waves in a Magnetic Field."

Mel Widner,[20] Suthi Aksornkitti,[17] I. Alexeff, and W. D. Jones, "A Sheath Excitation Model for Pseudowave Dispersion."

P. H. Edmonds,[21] R. A. Dandl,[1] and H. O. Eason, "Experiments and Calculations on High-Beta Equilibrium Electron Cyclotron Plasmas."

C. E. Nielsen,[6] "Phase Space Representation of Extended Negative-Mass Modes."

---

[1]Instrumentation and Controls Division.

[2]Consultant, University of Tennessee.

[3]Consultant, University of Florida.

[4]Consultant, Southern Missionary College.

[5]1968 Summer Participant, Southern Missionary College.

[6]Consultant, Ohio State University.
[7]University of Iowa.
[8]Consultant, University of Iowa.
[9]University of Tennessee.
[10]On leave from Institute of Plasma Physics, Garching, Federal Republic of Germany.
[11]On loan from Oak Ridge Gaseous Diffusion Plant.
[12]Lake Forest College.
[13]University of Arizona.
[14]Consultant, Massachusetts Institute of Technology.
[15]1968 Summer Participant, MIT.
[16]New York University.
[17]1968 Student Guest from University of Iowa.
[18]On leave from Institute of Plasma Physics, Garching, West Germany.
[19]University of Maryland.
[20]Summer Participant, 1968, University of Iowa.
[21]On leave from Culham Laboratory, England.